VYSOKÉ UČENÍ TECHNICKÉ V BRNĚ

BRNO UNIVERSITY OF TECHNOLOGY

FAKULTA STROJNÍHO INŽENÝRSTVÍ

FACULTY OF MECHANICAL ENGINEERING

ÚSTAV MATERIÁLOVÝCH VĚD A INŽENÝRSTVÍ

INSTITUTE OF MATERIALS SCIENCE AND ENGINEERING

PŘÍPRAVA A VLASTNOSTI KERAMICKÝCH KOMPOZITŮ

PREPARATION AND PROPERTIES OF CERAMIC COMPOSITES

HABILITAČNÍ PRÁCE

HABILITATION THESIS

AUTOR PRÁCE Ing. Daniel Drdlík, Ph.D.

AUTHOR

BRNO 2024

PODĚKOVÁNÍ

Autor habilitační práce by chtěl poděkovat všem kolegům Ústavu materiálových věd a inženýrství, zejména pracujícím na Odboru keramiky a polymerů, jmenovitě pak prof. RNDr. Jaroslavu Cihlářovi, CSc. a prof. RNDr. Karlu Macovi, Dr. za praktickou pomoc a vedení během jeho vysokoškolské kariéry.

Dále by chtěl poděkovat kolegům a přátelům na pracovišti Středoevropského technologického institutu z výzkumných skupin Pokročilá multifunkční keramika a Pokročilé keramické materiály za pomoc a ochotu při realizaci experimentálních činností, věcné diskuse a rady.

V neposlední řade patří autorův velký dík kolegům a přátelům z Akademie věd ČR, Ústavu fyziky materiálů, Skupina křehkého lomu za nedocenitelný přínos do autorovy nejen vědecké práce.

ABSTRAKT

Tato práce se zabývá popisem vícesložkových keramických materiálů (kompozitů) po stránce jejich přípravy pomocí pokročilých tvarovacích metod a hodnocením jejich základních vlastností. Zaměření práce umožňuje vhled do tří základních typů keramických kompozitů dělených podle typu a tvaru přidané fáze na částicové, vláknové a vrstevnaté. Kromě toho byla také část práce věnována vlivu velikosti a distribuce částic keramického prášku a (fyzikální) modifikaci jejich povrchu na finální vlastnosti keramického výrobku. Všechna čtyři diskutovaná témata obsahují autorovy konkrétní přínosy v dané oblasti ve formě komentovaných publikací.

KLÍČOVÁ SLOVA

Pokročilá keramika; keramické kompozitní materiály; mikrostruktura; vrstvy; částice; vlákna; tvarovací metody; slinování; analýza vlastností

OBSAH

1. ÚVOD

Soudobá poptávka po nových technologiích klade značné nároky na používané materiály, ze kterých jsou moderní výrobky vyráběny. Mnohé z tradičně užívaných materiálů přestávají svými vlastnostmi stačit a je nutné hledat adekvátní náhradu. Jednou z možností je volit pokročilé keramické materiály. Tato skupina materiálů je připravována z velmi čistých chemických prekurzorů a může proto nabídnout mnoho významných užitných vlastností (nízká měrná hmotnost, mechanická a chemická odolnost, optické vlastnosti, piezoelektricita atd.). Nicméně i zde lze narazit na limity. Z této příčiny je značná část vědecké obce zaměřena na optimalizaci nebo modifikaci procesních postupů při výrobě keramických prášků s cílem ovlivnění finální mikrostruktury.

První kategorie si klade za cíl zlepšit zejména chemickou čistotu syntetizovaných keramických částic tak, aby případné nečistoty nebránili difúzním procesům během následného tepelného zpracování – slinování. Opačným přístupem pak může byt cílená modifikace různými příměsemi, které naopak mohou slinování ulehčit (typickým příkladem může být slinování v kapalné fázi). Jinou variantou je pak ovlivnění velikosti, tvaru a distribuce částic. Speciálním případem pak může být úprava povrchu keramických částic, např. studenou plazmou.

Druhá kategorie, na kterou se ve větší míře zaměřuje tato práce, se pak odklání od standardně používaných jednofázových (monolitických) keramických systémů a řešení ve vylepšení finálních vlastností hledá zavedením jedné nebo více dalších fází do struktury. Vzniká tak heterostrukturní (vícefázový) systém; obecně nazývaný kompozit. Keramické kompozity lze rozdělit do několika základních typů. Ve většině případů se jedná o matrici, která tvoří majoritní objem celého kompozitu a o přísadu ve formě částic, whiskerů nebo vláken s různou distribucí nebo orientací. Jiným typem jsou vrstevnaté materiály, kde je mikrostruktura tvořena systémem jednotlivě na sobě ležících vrstev dvou a více keramických materiálů.

Heterostrukturní materiály jsou připravovány ve formě povlaků, vrstev nebo objemových těles pokročilými technikami v jednom nebo dvou krocích. Jedná se vždy o tvarování a slinování. Klasické metody, ať už uvažujme mokrou nebo suchou cestu přípravy, se zakládají na tvarování keramického prášku a jeho následném vysokoteplotním zpracování v druhém kroku. Mezi nejpoužívanější metody, které nevyžadují aplikaci vnějšího tlaku, se řadí dip coating, spin coating, tape casting, slip casting a elektroforetická depozice. Jednoosé lisování a izostatické lisování za studena (CIP) jsou metody, u kterých je prvotního zhutnění dosaženo vyvinutým tlakem, většinou v řádu MPa. Keramické výrobky připravené těmito metodami jsou následně přesunuty do vysokoteplotní pece a v konvenčním nebo nekonvenčním poli zhutněny slinovacím procesem při relativně vysokých teplotách. Existují ale i metody, které fázi tvarování a slinování kombinují. Jedná se předně o metody izostatické lisování za tepla (HIP), horké lisování (HP) a metodu spark plasma sintering (SPS), u kterých je keramický

prášek slisován vysokým tlakem a zároveň je konvenčně nebo nekonvenčně ohříván. Nevýhodou těchto technik je jejich cena (zejména u metody HIP) a příprava keramických těles s omezenou geometrií (u metod HP a SPS).

Tato práce se v menším rozsahu zabývá popisem technik úpravy keramických částic pro zisk jednofázové keramiky s vylepšenými užitnými vlastnostmi a ve větší míře technikami přípravy a hodnocením heterostrukturních keramických systémů, tj. částicových, vláknových a vrstevnatých kompozitů. Kromě literárních zdrojů je použita vlastní vědecká práce autora, která zahrnuje několik typů keramických materiálů a metod přípravy kompozitů.

2. CÍLE PRÁCE

- Modifikace povrchu, velikosti a distribuce částic keramického prášku s cílem ovlivnit finální vlastnosti keramického výrobku připraveného některou z mokrých pokročilých tvarovacích metod.
- Příprava částicových kompozitů pomocí pokročilých tvarovacích metod a analýza jejich vlastností
- Charakterizace přípravy vláknových keramických heterostrukturních systémů se zaměřením na kompozity s polykrystalickými vlákny
- Heterostrukturní vrstevnaté kompozitní keramiky s pevně vázaným rozhraním jednotlivých vrstev – příprava, slinování, vlastnosti

3. MODIFIKACE KERAMICKÝCH PRÁŠKOVÝCH MATERIÁLŮ

Jelikož výroba keramických materiálů neprochází přes kapalnou fázi, tavení, jako je běžné u kovových materiálů a jejich slitin, je zásadním krokem při jejich přípravě tvarování keramických částic. K tomuto účelu se využívá řada pokročilých tvarovacích metod. Ty lze rozdělit na tzv. suché a mokré. Suché tvarování je principiálně jednodušší, zahrnuje většinou různé metody lisování využívající kovové nebo grafitové formy. Keramický prášek je nasypán do formy a za aplikace tlaku dochází k jeho počátečnímu (bez přidaného tepla) nebo finálnímu (metody umožňující souběžné slinování) zhutnění. Nevýhodou tohoto výrobního postupu jsou limitované geometrické možnosti finálního výrobku. Druhou možností jsou mokré tvarovací metody, kde se nachází keramické částice v disperzi polárních nebo nepolárních rozpouštědel. Obecně tyto metody umožňují vyšší stupeň variability na designovou náročnost vyráběné keramiky. Jedním z typických představitelů této kategorie mokrých tvarovacích metod je elektroforetická depozice (EPD), která navíc umožňuje přípravu vícesložkových keramických materiálů.

EPD je metodou tvarování povrchově modifikovaných, nabitých, keramických částic z koloidních roztoků, disperzí nebo suspenzí při průchodu elektrického proudu mezi dvěma elektrodami. Během tohoto procesu dochází k ukládání keramických částic do hutné vrstvy na jednu z elektrod za přispění přitažlivých van der Waalsových sil [1]. Tvar finální keramiky je poté dán tvarem elektrody. Schématické znázornění reálné elektroforetické cely je ukázáno na Obr. 1.

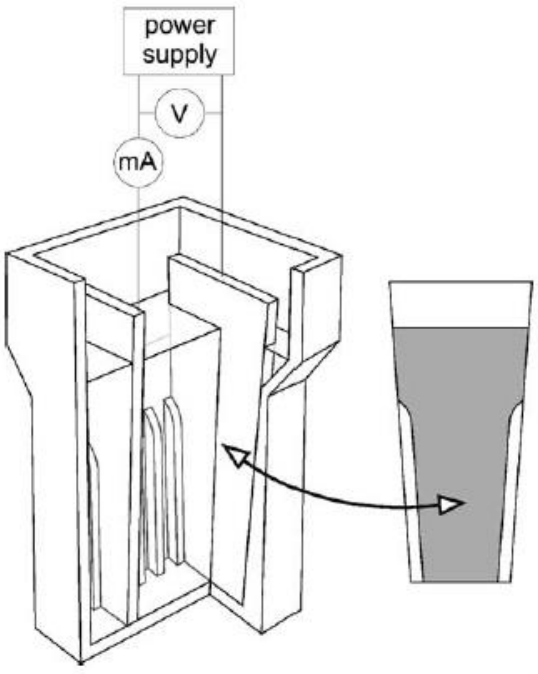

Obr. 1 Řez celou využitelnou pro EPD keramických materiálů (převzato z [2]).

Stability keramických částic v daném polárním nebo nepolárním médiu se dosahuje třemi významnými typy způsoby stabilizace [3]. Prvním stabilizačním mechanismem je reakce dlouhých polymerních řetězců adsorbovaných na povrchu částic. Tento mechanismus se nazývá sterická stabilizace. Příkladem může být adsorpce molekul chitosanu a želatiny na povrch mikrokuliček nebo nanotrubiček [4, 5]. Druhým způsobem je elektrostatická stabilizace, kde je stabilita řízena vznikem náboje o dostatečné velikosti na povrchu keramických částic. Výsledný odpudivý efekt mezi částicemi vykazuje exponenciální charakter, jehož síla závisí na velikosti indukovaného povrchového. Demonstrací tohoto typu stabilizace je například použití indiferentního elektrolytu na povrchu částic oxidu hlinitého [6]. Třetím a zdaleka nejpoužívanějším způsobem je kombinace obou dříve zmíněných mechanismů, tj. stabilizace elektro-sterická. Tento typ stabilizace lze v literatuře často nalézt ve spojení s EPD použitím polyethyleniminu ve vodném [7, 8] nebo nevodném [9] prostředí.

V oblasti elektro-sterické stabilizace byly na našem pracovišti provedeny rozsáhlé experimentální práce zaměřené na systém převážně oxidových keramik (oxid hlinitý, oxid zirkoničitý, hydroxyapatit). Fundamentálním bylo z tohoto pohledu studium vlivu kyselin (monochloroctová, dichloroctová, trichloroctová a sírová) a zásad (dietanolamin, trietanolamin a piperidin) na elektrokinetické chování oxidu hlinitého a zirkoničitého v prostředí bezvodého isopropanolu [I]. V této studii bylo zjištěno, že při interakci těchto oxidů s kyselinami vznikal na jejich povrchu záporný náboj, zatímco v přítomnosti zásad náboj kladný. Tento jev byl vysvětlen nízkými disociačními konstantami kyselin a zásad v isopropanolu. To umožnilo elektro-sterickou stabilizaci částic oxidu hlinitého a zirkoničitého kyselými anionty a zásaditými kationty. Znaménko náboje nebylo určeno pouze pomocí koncentrace protonů, jako by tomu bylo u vodného prostředí, ale strukturou aniontu kyseliny nebo kationtu zásady a jejich koncentrace. Bylo také prokázáno, že síla interakce mezi aniontem kyseliny nebo kationtem zásady a povrchu oxidu má vliv na vlastnosti finálních keramických povlaků připravených EPD. Jelikož depozity s nejvyšší hustotou a minimem defektů byly připraveny pomocí EPD v prostředí monochloroctové, dichloroctové a trichloroctové kyseliny, byly následné experimentální kroky převážně zaměřeny na tyto systémy.

Byl posuzován zejména vliv koncentrace jednotlivých kyselin na velikost elektrické vodivosti v isopropanolové suspenzi obsahující oxid hlinitý jako klíčový parametr k charakterizaci efektivity EPD a kvality výsledné keramiky [II]. V této práci bylo zjištěno, že elektrická vodivost systémů rostla s koncentrací kyselin v isopropanolu a velmi významně ovlivňovala EPD. Vyšší elektrická vodivost suspenze vedla ke snížení rychlosti depozice, což se ukázalo jako určující pro uspořádávání keramických částic do depozitu a povrchovou drsnost výsledného povlaku. Na Obr. 2 je ukázáno, že pro tyto systémy existuje limitní hranice elektrické vodivosti, při které lze připravovat keramiky s hladkým povrchem.

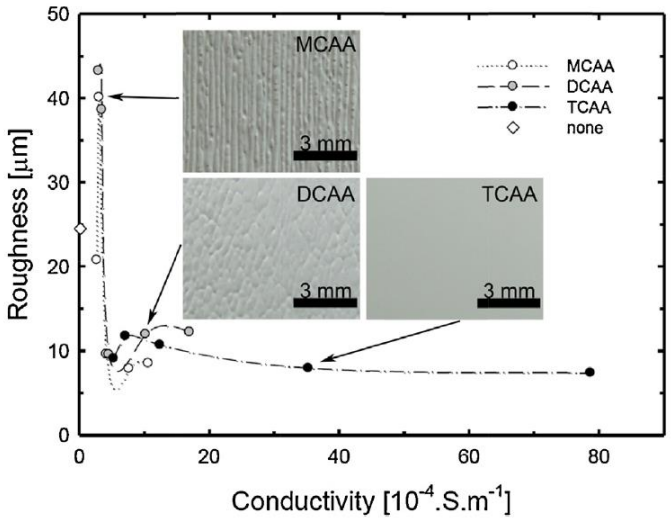

Obr. 2 Závislost povrchové drsnosti keramických povlaků na elektrické vodivosti suspenzí částic oxidu hlinitého stabilizovaných kyselinou monochloroctovou, dichloroctovou a trichloroctovou (převzato z [II]).

Získat kvalitní povrch ovšem znamenalo modifikovat povrch a celou suspenzi vyšším přídavkem kyseliny. Takový postup není ekonomický ani ekologický a vedl tedy k úvaze ovlivnit povrchovou drsnost keramik připravovaných pomocí EPD přídavkem indiferentního elektrolytu. Vybrán byl indiferentní elektrolyt na bázi LiCl [III], který umožnil významně redukovat obsah kyseliny a již při minimálním množství LiCl v suspenzi vyústil v suspenzi s vysokou elektrickou vodivostí. EPD z této suspenze pak vedla přípravě depozitu bez povrchového reliéfu, jak je dokumentováno na Obr. 3.

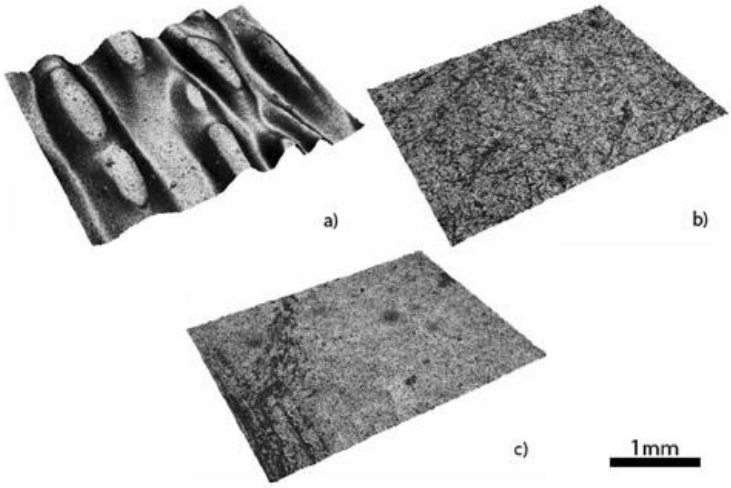

Obr. 3 3D topografie povrchu depozitů připravených ze suspenze a) s nízkou elektrickou vodivostí díky nízkému obsahu stabilizátoru, b) vysokou elektrickou vodivostí díky vysokému obsahu stabilizátoru c) vysokou elektrickou vodivostí díky nízkému obsahu stabilizátoru a přídavku LiCl (převzato z [III]).

Další modifikací keramických částic s cílem ovlivnit výsledné vlastnosti keramiky bylo vysokoenergetické mletí suspenzí obsahující keramický materiál. Toto studium bylo provedeno na biokeramických částicích hydroxyapatitu [IV, V]. Suspenze obsahující hydroxyapatit, kyselinu monochloroctovou a indiferentní elektrolyt byly mlety v planetovém mlýně 0-48 hodin. Mletí mělo za následek rozpad aglomerátů o velikosti 10 μm komerčního hydroxyapatitového prášku. Byla získána unimodální distribuce částic o velikosti ~170 nm. Tyto jemné částice v mleté suspenzi se lépe a rychleji ukládaly na depoziční elektrodu během EPD procesu. Jak modifikace keramického prášku mletím, tak i přídavek indiferentního elektrolytu tedy vedly k optimalizaci přípravy keramiky. Malé částice umožnily slinování při nižších teplotách, což se odrazilo na vysoké finální hustotě a nízké střední velikosti zrn. Výše slinovací teploty a mikrostruktura vzorků ovlivnila rozpad hydroxyapatitu na trikalcium fosfáty, porozitu a s ní spojené mechanické a biologické vlastnosti.

Poslední studovanou povrchovou modifikací keramických částic byla aplikace studené plazmy [VI]. Při experimentech bylo na povrchu částic oxidu hlinitého aktivovaného plazmou detekováno nezanedbatelné množství molekul NO a NO_2. Tyto molekuly sice neovlivnily významně zeta potenciál suspenzí, tj. nepřispěly ke stabilitě systému, ale měly výrazný vliv na depoziční proces ve formě zvýšení elektrické vodivosti suspenze (zpomalení depozice, lepší ukládání částic do depozitu) a kvalitu (drsnost) výsledného depozitu. Překvapivě byla zaznamenána netypická současná katodická i anodická depozice, což vedlo mimo jiné k domněnce, že EPD by mohla zároveň sloužit jako měřící metoda efektivity plazmového opracování. Bylo ukázáno, že plazmové opracování keramických částic umožňuje výrobu homogenních tenkých povlaků pomocí EPD bez použití jakýchkoli stabilizačních činidel, což je velkým benefitem pro životní prostředí.

4. ČÁSTICOVÉ KERAMICKÉ KOMPOZITY

Existence pokročilých heterostrukturních keramických materiálů je odezvou na nízkou křehkolomovou charakteristiku monolitické keramiky. Jedním z přístupů zlepšení této vlastnosti je přídavek druhé (výztužné) fáze ve formě částic. Pro určení mechanického chování kompozitu je pak stěžejní tvar, materiálová podstata a prostorové uspořádání výztužné fáze. Jedním z nejkritičtějších faktorů je rovnoměrná distribuce sekundární fáze, která úzce souvisí s metodikou přípravy. Tu lze obecně rozdělit na dva postupy. Prvním z nich je prosté smíchání původních práškových materiálů a jejich vyvarování některou z pokročilých metod nebo pak vznik sekundární fáze v matrici vnitřní reakcí během výrobního procesu. Objemová tělesa jsou nejběžněji tvarována z keramických směsí částic různých materiálů pomocí lisovacích metod, tj. pomocí uniaxiálního lisování bez nebo s aplikovaným teplotním polem. Mezi nejznámější metody patří metody CIP, SPS nebo HP. Z metod využívající kapalnou fázi pak přicházejí do úvahy metoda slip casting. Pro tvorbu povlaků lze použít různé nástřiky, metody physical nebo chemical vapor depositon, dip coating nebo metodu EPD.

Keramická matrice je běžně vyztužena keramickými nebo kovovými částicemi ve tvaru koulí, desek nebo vloček. Primární mechanismy zodpovědné za zhouževnatění keramického kompozitu jsou interakce mezi čelem trhliny a částicí, stínění trhliny, přemostění trhliny a zbytková napěťová pole vzniklá rozdílným koeficientem teplotní roztažnosti matrice a sekundární fáze [10].

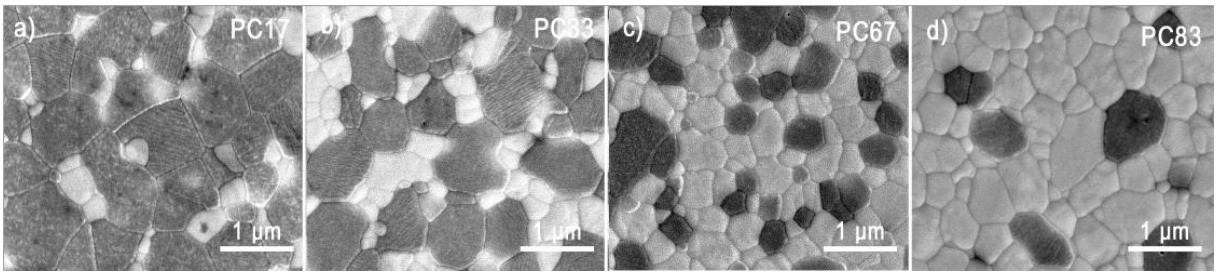

Obr. 4 Typické mikrofotografie mikrostruktur částicových kompozitů na bázi Al_2O_3 a ZrO_2 (převzato a upraveno z [VII]).

Tento typ kompozitů byl připraven pomocí metody EPD, která umožňuje dobrou kontrolu distribuce částic [VII]. V tomto případě se jednalo o materiály Al_2O_3 a ZrO_2, které byly míchány v celém koncentračním rozsahu. Na Obr. 4 jsou ukázány typické mikrostruktury částicových kompozitů, kde tmavou fází je Al_2O_3 a světlou fází ZrO_2. Z Obr. 4a,b) je tedy patrné, že v tomto případě je matricí Al_2O_3 a ZrO_2 slouží jako výztužná fáze, zatímco na Obr. 4c,d) je matricí ZrO_2. Příprava těchto částicových materiálů byla realizována pro důkladný popis slinovacího procesu kompozitů, včetně aplikace modifikované metody Master Sintering

Curve, která slouží pro výpočet aktivační energie slinování. Z výsledků experimentů vyplynulo, že při nižším obsahu ZrO_2 v Al_2O_3 matrici dochází k nárůstu aktivační energie slinování v důsledku zpomalenému zhutnění Al_2O_3 díky pinning efektu malých ZrO_2 zrn. Tento výsledek upravuje současné poznání, které spočívalo v uveřejněné konstantní aktivační energii v celém koncentračním rozsahu [11]. Navíc byly u těchto kompozitů studovány také mechanické vlastnosti měřené indentační technikou. Obecný trend byl zřejmý, se zvyšujícím se množstvím oxidu zirkoničitého klesala jak tvrdost, tak modul pružnosti v důsledku původních vlastností jednotlivých materiálů. Překvapivě bylo zjištěno, že směšovacím pravidlem, které se u těchto kompozitů běžně využívá pro odhad mechanických vlastností, se řídí pouze trend poklesu modulu pružnosti. Trend tvrdosti se od predikce odchyloval. Pozorovaná změna tvrdosti podle Vickerse u připravených částicových kompozitů byla ovlivněna několika společně působícími jevy, jako je propojení fází, přítomná vnitřní tepelná napětí, transformační zpevnění oxidem zirkoničitým a pinning efektem.

U částicových kompozitů samozřejmě záleží také na velikosti a množství sekundární fáze. Pokud jsou částice sekundární fáze oproti matrici řádově menší a jeho množství je v řádu atomových procent, pak hovoříme o dopovaní. Sekundární fáze zde neplní výztužnou funkci, přesto výsledné materiály získávají nové užitné vlastnosti nebo podstatně vylepšují ty stávající [12].

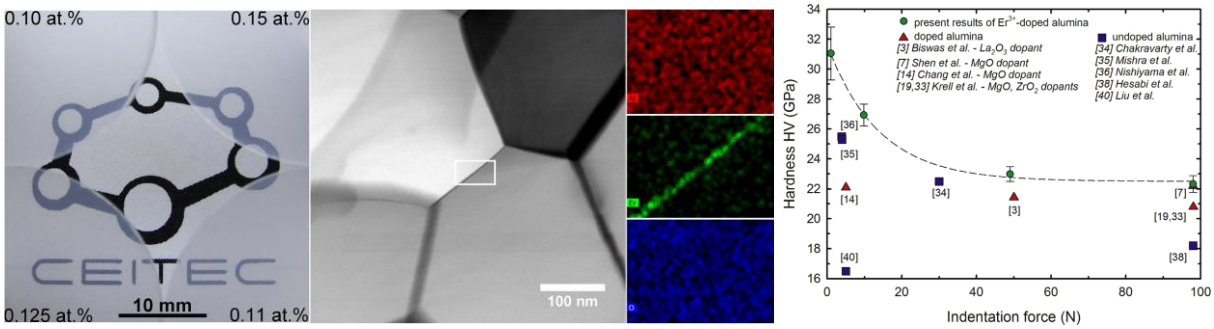

Obr. 5 Erbiem dopovaná Al_2O_3 transparentní keramika (vlevo), její mikrostruktura s EDX plošnou analýzou (uprostřed) a její Vickersova tvrdost v závislosti na použité zátěžné síle (vpravo) (převzato z [VIII, IX]).

Na Obr. 5 je ukázán jeden z příkladů připravené dopované transparentní keramiky, její mikrostruktury a vlivu dopantu na mechanické vlastnosti. Keramický kompozit byl vyroben metodou slip casting, beztlace předslinován do bodu uzavřené porozity zpracovávaného keramického tělesa a následně slinut metodou HIP při aplikovaném tlaku 200 MPa argonu. Dopant oxid erbitý a zvolené tepelné zpracování umožnili výrazně redukovat růst zrn, což se projevilo hodnotou transparentnosti RIT = 56 %, v době publikování nejvyšší dosaženou hodnotou v literatuře pro luminiscenční transparentní Al_2O_3. Erbium segregované na hranici

zrn umožnilo intenzivní zelenou, slabou červenou a infračervenou emisi, jak bylo zjištěno při analýze luminiscenčních vlastností. Navíc bylo zjištěno, že tento materiál vykazuje mimořádnou tvrdost, která byla prověřena v celém rozsahu zátěžných sil a srovnána s literárními daty. Získaná závislost (zelené body proložené čárkovanou čárou na Obr. 5) ukázala, že byl připraven materiál s nejvyšší v literatuře uváděnou tvrdostí dle Vickerse [VIII, IX].

Speciálním případem částicového kompozitu je funkčně gradientní materiál (FGM). Tyto materiály vykazují plynulou (spojitou) změnu strukturního a/nebo chemického složení od jedné fáze ke druhé cílem dosáhnout různých vlastností na opačných stranách materiálu. Na Obr. 6 je demonstrována struktura a vlastnosti FGM a klasického částicového kompozitu. Využití FGM si lze jednoduše představit u materiálu ve tvaru desky, který na jedné straně bude namáhán extrémními teplotami, a na druhé straně teplotami podstatně nižšími. Taková deska pak může sloužit jako tepelný štít, který je z jedné strany velmi odolný proti tepelnému zatížení a z druhé strany má vhodnou houževnatost a pevnost. Příkladů uplatnění FGM lze však nalézt mnohem více, zejména v elektronice [13], optoelektronice [14], řezných nástrojích [15] nebo lékařství [16].

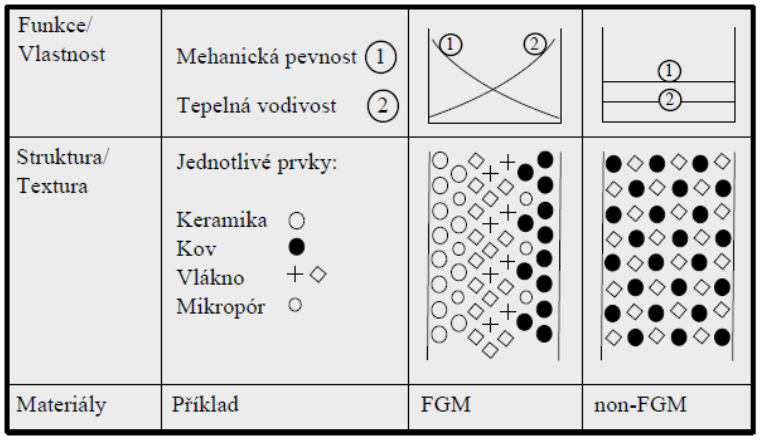

Obr. 6 Porovnání struktury a vlastností funkčně gradientního materiálu a klasického částicového kompozitu (převzato z [17]).

Na pracovišti Ústavu materiálových věd a inženýrství byl připraven pomocí metody EPD biokeramický FGM skládající se z hydroxyapatitu a bioskla [X]. Podobný typ FGM s kontinuální změnou chemického složení se do té doby nepodařilo připravit. Experimentální snahy se soustředily na použití tvarovacích metod využívajících aplikovaného tlaku jako je metoda SPS nebo HP nebo na povlakování metodou plasma spraying. Nicméně, těmito metodami bylo možné připravit kompozit, kde byla změna chemického složení realizována spíše ve formě vrstev [18-20]. O skutečné FGM se tedy nejednalo. Problémem se ovšem ukázalo být tepelné zpracování takového FGM konvenčním slinováním ve vysokoteplotní peci,

protože biosklo krystalizuje již za velmi nízkých teplot. Práce nicméně přinesla nové poznatky o slinování takového kompozitu, které bylo studováno pomocí vysokoteplotní dilatometrie.

5. VLÁKNOVÉ KERAMICKÉ KOMPOZITY

Sekundární fáze celkově modifikující křehkolomové chování keramické matrice může být také ve formě vláken. U vláken hraje důležitou roli jejich materiálová povaha (polymerní, skelná, kovová, keramická), mikrostruktura (monokrystalická nebo polykrystalická), délka (whiskery, krátká vlákna, dlouhá vlákna), orientace (preferenčně nebo nahodile orientované) a distribuce v matrici. Zajištěna musí být také správná adhezní pevnost rozhraní mezi matricí a vláknem, aby mohlo docházet k efektivním mechanismům přenosu napětí, jako jsou odklánění trhliny, vytahování vláken, přemostění trhliny atd. [21] Pro výrobu kompozitů s dlouhými, orientovanými vlákny se využívá zejména infiltračních metod, kdy je keramická matrice infiltrována do předem připravené textury vláken. V případě krátkých vláken je možné využít metod zmíněných v předchozí kapitole. Je ale třeba dbát na důkladnou dispergaci vláken v celém objemu matrice.

Do úvahy je nutné vzít teplotu, za které bude reálná keramická matrice vytužená vlákny využívána. Pokud nepřesáhne maximální provozní teplota 300 °C, je možné použít polymerní vlákna. Pokud bude teplota vyšší, musí to být zohledněno výběrem skelných (do 800 °C), kovových (do 900 °C) nebo keramických vláken (až do 1800 °C) [22]. U keramických vláken je stěžejním parametrem mikrostruktura. Monokrystalická vlákna dosahují výrazně vyšších užitných vlastností než je tomu u polykrystalických vláken, přesto je jejich překážkou vysoká cena a orientace pouze do neoxidových materiálů (SiC, TiN, TiC, Si_3N_4 atd.) [23, 24]. Oxidová vlákna, typicky z Al_2O_3 a ZrO_2, začala být vyráběna v roce 1979 firmou Du Pont v polykrystalické formě [24]. Od té doby vývoj výrobních technik výrazně pokročil a tato vlákna se začala vyrábět v mnoha zemích světa, včetně České republiky ve firmě Pardam s.r.o. Spolupráce s touto firmou přinesla základní poznatky o vlivu ZrO_2 polykrystalických mikrovláken na matrice z oxidu hlinitého a hydroxyapatitu [IV, XI].

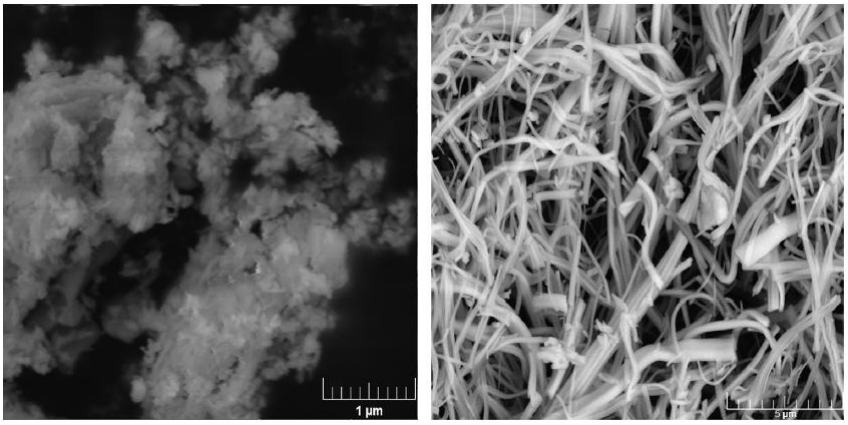

Obr. 7 Mikrofotografie prášku hydroxyapatitu (vlevo) a ZrO_2 vláken (vpravo) (převzato z [IV]).

Metodou EPD byla připravena sada kompozitů, kde bylo v hydroxyapatitové matrici rozptýleno až 16 hm.% ZrO_2 mikrovláken [IV]. Připravené suspenze byly před depozicí mlety kvůli zjemnění částic matrice. Na Obr. 7 jsou ukázány aglomeráty hydroxyapatitových částic před vlastním mletím a amorfní ZrO_2 mikrovlákna, která svou polykrystalickou povahu získají během tepelného zpracování. Redukce velikosti zrn pozitivně ovlivnila mikrostrukturu a mechanické vlastnosti. Kromě toho bylo zjištěno, že mikrovlákna v kompozitu byla orientována rovnoběžně s elektrodou během EPD, a to v důsledku rozložení náboje stabilizátoru na podlouhlých mikrovláknech. Porozita rostla s množstvím ZrO_2 mikrovláken v mikrostruktuře a Vickersova tvrdost a modul pružnosti kompozitů rostly s dobou mletí. Lomová houževnatost kompozitů byla dvojnásobná oproti monolitickému hydroxypatitu při stejné úrovni porozity a to zejména díky orientovaným ZrO_2 mikrovláknům, jemné mikrostruktuře a přítomnosti pórů. Kompozity byly navíc shledány jako bioaktivní testováním v simulované tělní tekutině.

Druhá studie shrnuje přípravu kompozitů s Al_2O_3 matricí vyztužených ZrO_2 mikrovlákny pomocí EPD. Elektroforetická depozice byla provedena z isopropanolových suspenzí stabilizovaných kyselinou monochloroctovou obsahující směs práškového Al_2O_3 a 1 hm.% ZrO_2 mikrovláken. V práci byly použity dva postupy mísení vláken a matrice: pomocí mletí a pomocí ultrazvuku. Mlecí metoda vyústila v kompozity s náhodně orientovanými mikrovlákny uvnitř matrice Al_2O_3, ve kterých bylo pozorováno izotropní šíření trhlin. Depozice ze suspenze podrobené ultrazvukovému poli vedla k získání kompozitů s mikrovlákny uspořádanými rovnoběžně s nanášecí elektrodou. Tento způsob přípravy minimalizoval jejich poškození. Tyto kompozity vykázaly zvýšenou odolnost proti lomu v jednom směru. Na Obr. 8 jsou ukázány mikrofotografie Al_2O_3 matrice se ZrO_2 mikrovlákny a jejich interakce s trhlinou.

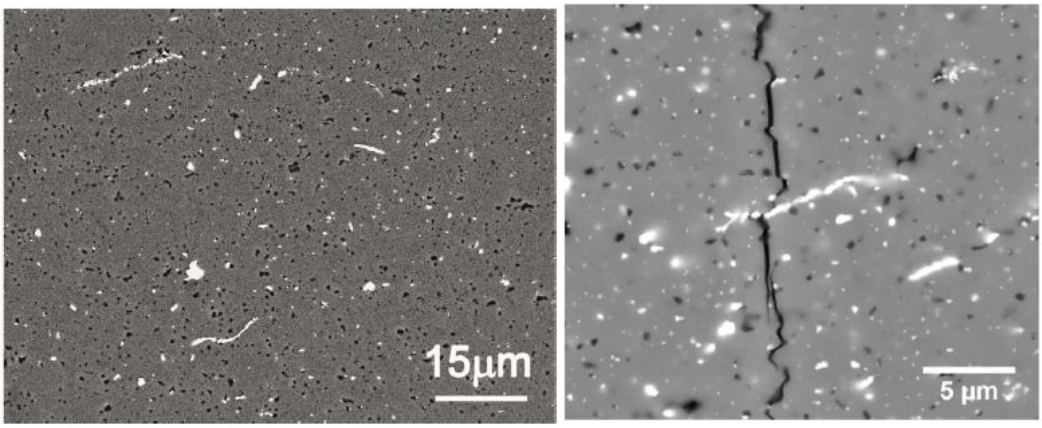

Obr. 8 Mikrofotografie Al_2O_3 matrice se ZrO_2 mikrovlákny (vlevo) a interakce trhliny se ZrO_2 mikrovláknem (vpravo) (převzato z [XI]).

6. VRSTEVNATÉ KERAMICKÉ KOMPOZITY

Posledním typem keramických kompozitů jsou tzv. lamináty, které vznikají vrstvením dvou a více materiálů na sebe. Vlastnosti takového materiálu obvykle nebývají izotropní, což má podle typu jednotlivých zvolených keramik za následek zajímavé mechanické, optické nebo elektrické vlastnosti. V oblasti vlastností bylo nejvíce výzkumných snah věnováno překonání inherentní nízké houževnatosti a spolehlivosti keramiky [25]. Vícefázový materiál složený z vrstev může totiž lépe pracovat s energií trhliny. Neméně aktuálním tématem studia je v oblasti optiky vrstevnatá architektura keramických laserů, které díky této organizaci vykazují lepší nakládání s odpadním teplem [26, 27]. Z hlediska elektrotechniky pak mohou být keramické vrstevnaté konvertory mechanické energie na elektrickou součástmi piezoelektrických harvestorů [28]. Stěžejním pro funkci keramického laminátu je rozhraní mezi vrstvami, kde podle jeho pevnosti rozeznáváme lamináty se slabě nebo silně vázaným rozhraním.

Šířící se trhlina ve vrstevnatém keramickém kompozitu se slabými rozhraními vrstev způsobuje delaminaci vrstev a je vychylována ve směru kolmém ke směru svého šíření. Takové praskliny se stávají nekatastrofickými na rozdíl od obvyklého chování monolitické keramiky. Aby bylo docíleno tohoto typu kompozitu, musí být proveden správný materiálový výběr pro jednotlivé vrstvy. Obecně platí, že tlustší a hutnější vrstvy jsou zodpovědné za mechanickou pevnost a tenčí vrstvy tvořící slabé rozhraní určují houževnatost. Na Obr. 9 je ukázána lomová plocha keramického kompozitu se slabě vázanými vrstvami a schéma šíření trhliny kompozitem způsobující delaminaci vrstev. Tento typ kompozitů lze mimo jiné nalézt v přírodě, zejména u schránek měkkýšů.

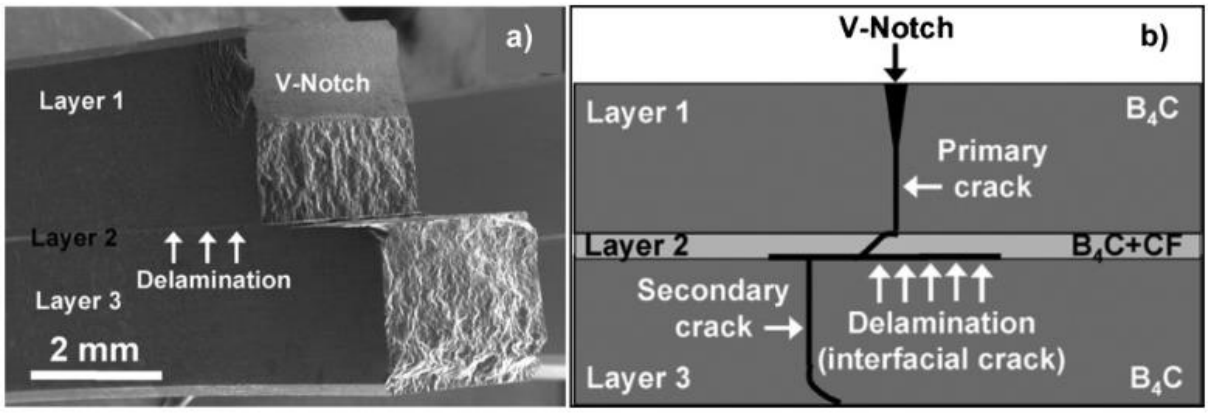

Obr. 9 Lomová plocha keramického kompozitu se slabě vázanými vrstvami (a), schéma šíření trhliny kompozitem (b) (převzato z [29]).

Také vrstevnaté keramické materiály mající silně vázané vrstvy mohou v porovnání s monolitickými keramikami vykazovat pozitivní efekty, zejména ve zvýšené odolnosti proti lomu, lomové houževnatosti a ohybové pevnosti. Tento efekt je docílen použitím dvou chemicky příbuzných materiálů, které jsou vzájemně nerozpustné a mají rozdílný koeficient tepelné roztažnosti, který během chladnutí ze slinovací teploty způsobí vznik vnitřních napětí mezi vrstvami. V případě použití tetragonálního ZrO_2 jako jednoho z materiálů vrstev může navíc docházet k jeho transformaci do monoklinické struktury, což je doprovázeno objemovou změnou [25]. Tyto příspěvky pak významně ovlivňují trajektorii šíření trhliny, jak je demonstrováno na Obr. 10.

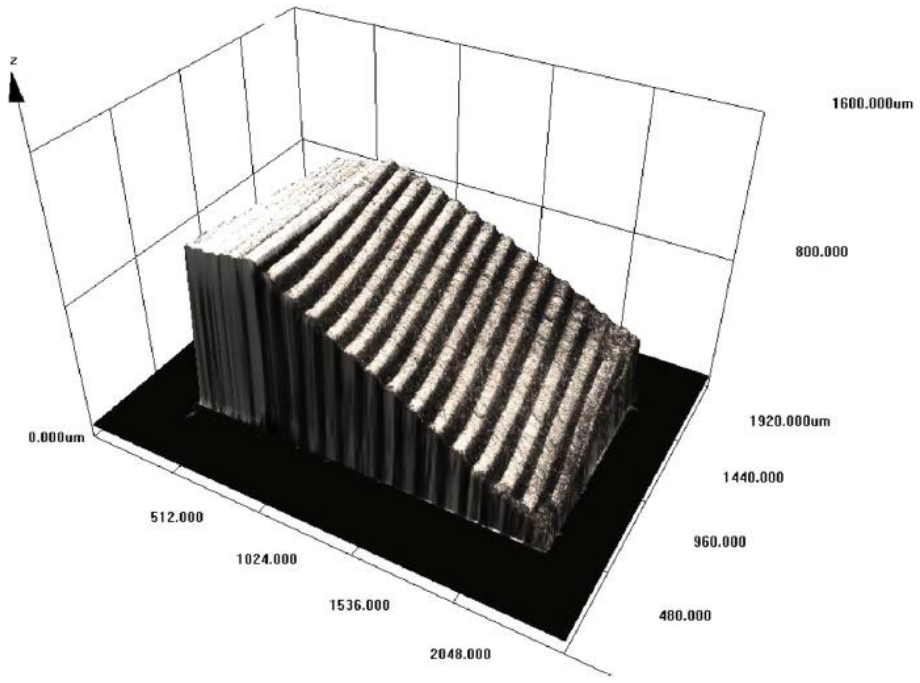

Obr. 10 3D rekonstrukce lomové plochy Al_2O_3/ZrO_2 kompozitu se silně vázanými vrstvami (převzato z [30]).

K výrobě vrstevnatých keramických materiálů může být použito více metod. Mezi nejznámější patří vrstvení keramických plátů připravených metodou tape casting (nutno dále aplikovat externí tlak na vrstvy a slinout v jedno těleso), hutněním keramického prášku ve vrstvách (lisovací metody), odléváním jednotlivých vrstev metodou slip casting, pomocí centrifugace a metoda EPD.

Keramické vrstevnaté materiály s pevně vázaným rozhraním na bázi Al_2O_3/ZrO_2 jsou na Ústavu materiálových věd a inženýrství studovány již od roku 2004. Vznikla celá řada publikací [2, 30-36], které vzhledem ke svým ohlasům ve vědecké komunitě přinesly rozšíření poznání v této tématice. K přípravě těchto kompozitů sloužila zejména metoda EPD a to díky přesně popsané kinetice depozice jednosložkových materiálů, tj. Al_2O_3 a ZrO_2 [34]. Byly

připravovány symetrické i nesymetrické vrstevnaté materiály s proměnnou tloušťkou vrstev díky alternující elektroforetické depozici, kdy je depoziční elektroda přesouvána ze suspenze obsahující jeden keramický materiál v přesném časovém intervalu do suspenze obsahující druhý keramický materiál. Tímto způsobem byly připraveny lamináty obsahující až 150 vrstev, které byly následně hodnoceny po stránce šíření trhlin na rozhraní za použití indentační techniky [31, 32, 36], stanovení vnitřních tahových a tlakových napětí [32] a mechanických vlastností (modul pružnosti, pevnost v ohybu, lomová houževnatost) [30].

V práci Chlup a kol. [XII] byl metodou EPD připraven vrstevnatý Al_2O_3/ZrO_2 kompozit o počtu 100 vrstev, kde tloušťka každé vrstvy byla 50 μm po slinutí. Tento laminát sloužil pro experimentální ověření teoretického modelu, který si klade za cíl stanovit teplotu, při které dochází relaxaci vnitřních napětí. Do té doby byla tato (referenční) teplota určována z teplotního intervalu 1180 – 1300°C, přičemž byla jednou z hodnot, která slouží pro výpočet vnitřních napětí v laminátu. Vnitřní napětí tak mohla být nadhodnocena nebo naopak podhodnocena. Pro stanovení referenční teploty byla provedena série dilatometrických měření a získaná data použita jako vstup pro numerickou simulaci. Výsledky byly porovnány s měřenou deformací na vrstevnatém kompozitu a byla určena referenční teplota pro tento typ kompozitu T_{ref} = 1470 ±40°C, což je hodnota spíše vyšší než byla do té doby používána a je blízko slinovací teplotě (1500°C). Díky znalosti této teploty lze designovat lépe vnitřní napětí ve vrstvách a zabránit tak vzniku nežádoucích trhlin.

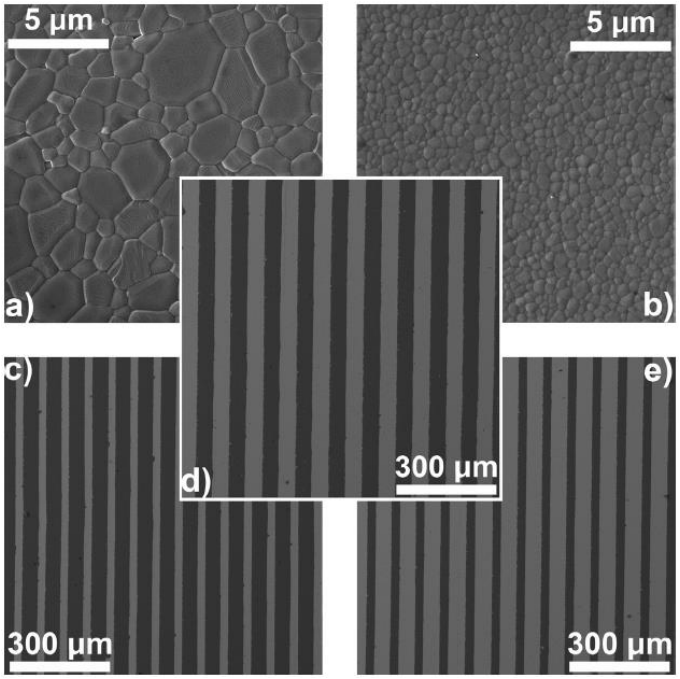

Obr. 11 Mikrostruktury a) Al_2O_3 a b) ZrO_2 monolitů a vrstevnatých Al_2O_3/ZrO_2 kompozitů s poměrem tlouštěk vrstev c) 2:1, d) 1:1 a e) 1:2 (převzato z [XIII]).

Dilatometrická měření vysokoteplotního chování monolitických i vrstevnatých Al_2O_3/ZrO_2 kompozitů s různou tloušťkou vrstev byla předmětem dalšího studia [XIII], přičemž bylo sledováno slinovací smrštění těchto materiálů v příčném (kolmo k vrstvám, tj. ve směru depozice) i v podélném (rovnoběžném s rozhraními vrstev) směru. Na Obr. 11 jsou ukázány typické mikrostruktury monolitů Al_2O_3 a ZrO_2 a vrstevnatých Al_2O_3/ZrO_2 kompozitů s poměrem tlouštěk vrstev 2:1, 1:1 a 1:2 (tmavé oblasti – Al_2O_3, světlé oblasti – ZrO_2). Slinování vrstevnatých kompozitů vykazovalo anizotropní chování. Detailní studie odhalila, že smrštění v podélném směru bylo řízeno oxidem hlinitým (materiál s vyšší slinovací teplotou), zatímco v příčném směru bylo urychlováno směrovým slinováním vrstev oxidu zirkoničitého. Pro interpretaci takové kinetiky anizotropního slinování byl vyvinut a aplikován model Master Shrinkage Curve. Vypočtená aktivační energie slinování byla v podélném směru zvýšená a potvrdila tak omezené možnosti slinování vrstevnatých materiálů.

Samostatnou kapitolou je hodnocení vlivu zbytkových vnitřních napětí na směr dráhy šíření trhliny, která byla ve vrstevnatém kompozitu vytvořena indentační technikou. V tomto případě mohou nastat dvě mezní situace: a) trhlina je kolmá k rovině rozhraní a b) trhlina rovnoběžná s rozhraním. Mimo těchto dvou mezních situací je rozsah úhlů vstupu trhlin (0°,90°), kde by měla hrát významnou roli zbytková vnitřní napětí. Obecně platí, že pokud je vnější zatížení aplikováno v rovině s vrstvami (působící v režimu otevření I), tahová zbytková/vnitřní napětí povedou k naklonění trhliny do normálového směru, zatímco tlaková napětí způsobí deklinaci z normálového směru. Tahová napětí tedy zkrátí cestu trhliny a tlaková napětí ji prodlouží. Přesto se vyskytl zřejmý rozpor v pozorování, když jiné výsledky poskytly povrchové indentační trhliny a lomové plochy vrstevnatých materiálů po ohybových testech. Při konfrontaci těchto výsledků a dodatečných experimentech [XIV] založených na odbrušování povrchu s indentem bylo zjištěno, že odklon indentačních trhlin lze spíše přisoudit elastickým vlastnostem jednotlivých materiálů než úrovni zbytkových vnitřních napětí. Zbytková napětí však velmi ovlivnila dráhu trhlin pod indentem. Informaci o vnitřních napětích a jejich vlivu tak poskytuje pouze pozorování bočního povrchu lomové plochy těles s vrubem (po ohybovém testu).

Materiálové složení jednotlivých vrstev v kompozitu může přinést řadu výzev. Takovou výzvou je příprava symetrického neperiodického keramického harvestoru, kde se střídají vrstvy oxidu hlinitého a zirkoničitého s vrstvami piezoelektrického barium titanátu ($BaTiO_3$). Motivací pro začlenění keramických vrstev Al_2O_3 a ZrO_2 je ochranná funkce z důvodu jejich mechanické odolnosti a také možnosti generovat v těchto vrstvách zbytková vnitřní napětí, která by měla pozitivně ovlivnit křehkolomové chování celého laminátu [28]. Tento typ kompozitu může být úspěšně připraven pomocí EPD, přesto jeho výroba čelí hned několika překážkám. Porozita všech vrstev surového tělesa musí být co nejvíce podobná, aby nedocházelo při jeho sušení k rozvoji vnitřních napětí a vzniku nežádoucích trhlin. Druhý problém nastává během procesu konvenčního slinování, kdy rozdílné koeficienty teplotní roztažnosti jednotlivých materiálů mohou způsobit delaminaci. Dalším pozorovaným

negativním jevem je silná reakce barium titanátu s okolními vrstvami, což vede ke vzniku nových fází [28, 37]. V limitním případě dochází k reakci v celém objemu $BaTiO_3$ vrstvy i vrstvy či vrstev okolních v důsledku výměny atomů v perovskitové struktuře ABO_3 barium titanátu, zejména na A pozici s atomy o valenci 3+. Tyto mechanicky slabší, strukturně komplikované, fáze pak mohou být zdrojem trhlin nebo mohou usnadnit jejich šíření. Z tohoto důvodu byla prověřena možnost výroby podobných typů kompozitů obsahující mechanicky odolné vrstvy ZrO_2 a vrstvy piezokeramiky $BaTiO_3$ nebo $(Ba_{0,85}Ca_{0,15})(Zr_{0,1}Ti_{0,9})O_3$ (BCZT), což je piezoelektrický materiál odvozený od barium titanátu, kombinací EPD a slinutím v nekonvenčním poli pomocí techniky SPS [XV]. Na Obr. 12 jsou ukázány mikrostruktury připravených laminátů slinutých konvenčně ve vysokoteplotní peci a pomocí techniky SPS. Z Obr. 12a,c) je zřejmé, že konvenční slinování $ZrO_2/BaTiO_3$ a ZrO_2/BCZT laminátů při teplotách 1300 °C a 1500 °C (teploty běžně používané pro konvenční slinování těchto materiálů) s dobou výdrže 2 h vedlo ke značným reakčním dějům způsobujícím rozvoj trhlin a destrukci mikrostruktury. Naproti tomu stejné depozity slinuté technikou SPS (viz Obr. 12b,d)), která využívá aplikovaného tlaku (50 MPa) a velmi rychlého ohřevu (100 °C/min), ukázaly potlačený nebo žádný vývoj nežádoucích reakčních fází. Tento výsledek znamená, že kombinace EPD a SPS je slibnou cestou pro přípravu vícevrstvých keramik potenciálně sloužících jako energetické harvestory.

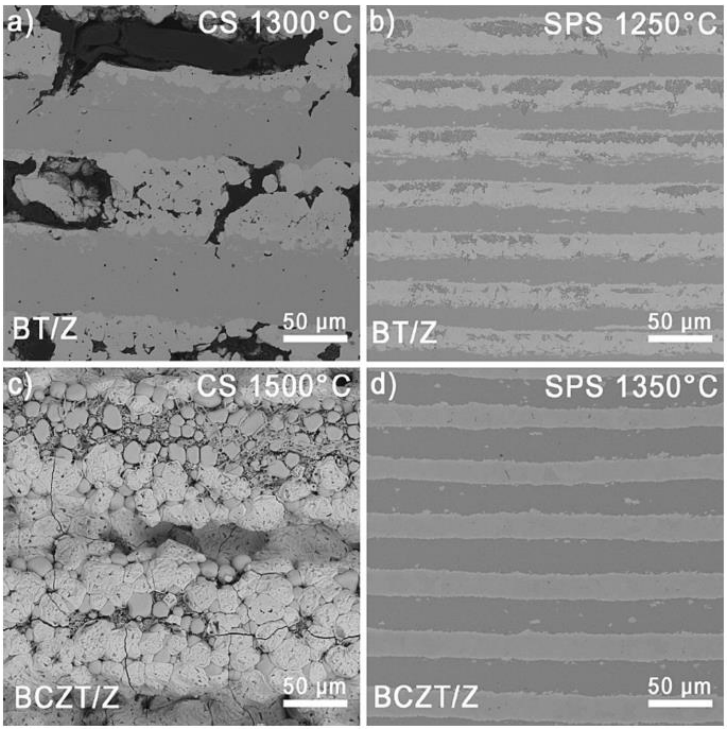

Obr. 12 Mikrostruktury laminátů a, b) $ZrO_2/BaTiO_3$ a c, d) ZrO_2/BCZT slinuté konvenčně (CS) nebo pomocí SPS (převzato z [XV]).

Jak již bylo zmíněno dříve, keramické lamináty mohou být připravovány i jinými technikami než je EPD. Další vhodnou technikou je např. slip casting. Postupným odléváním jednotlivých vrstev byl připraven kompozit o kompozici A/A5SiC/A, kde A byly vrstvy Al_2O_3 a A5SiC byla vrstva obsahující Al_2O_3 a 5 obj. % SiC [XVI]. Kromě tohoto kompozitu byly také připraveny standardy jednotlivých materiálů, jak je ukázáno na Obr. 13. Při odlévání jednotlivých vrstev v laminátu musí být dodržen jistý časový odstup, který zajistí, že spodní vrstva bude na svém povrchu dostatečně prosušená, aby unesla následující vrstvu, přesto však nesmí být úplně suchá, aby došlo k částečnému promísení a spojení materiálů na rozhraní. Nedodržení této výrobní podmínky by vedlo k tvorbě delaminace. Jelikož SiC obecně slinuje velmi špatně, za vysokých teplot a v nepřítomnosti kyslíku, musela být zvolena metoda slinování, která vyhověla všem těmto požadavkům. V této práci byla publikována právě metoda SPS jako vhodná metoda, kdy bylo místo prášku netypicky slinováno celé odlité objemové těleso. Do uveřejnění této práce nebyl tento postup příliš rozšířený. Byl připraven bezdefektní vrstevnatý kompozit, u kterého byla dále studována mikrostruktura, mechanické vlastnosti, a podléhal balistickým testům.

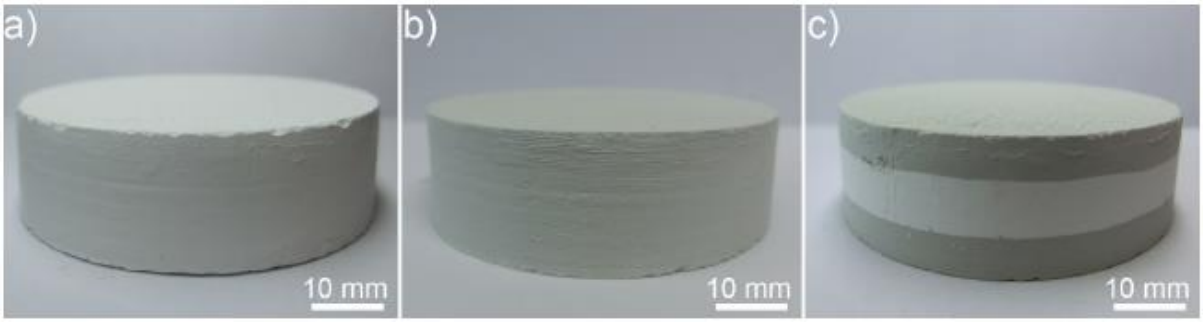

Obr. 13 Standardy a) A, b) A5SiC a c) laminát A/A5SiC/A po odlití metodou slip casting vysušení (převzato z [XVI]).

7. ZÁVĚR

Habilitační práce se svým obsahem zabývá zejména pokročilými keramickými částicovým, vláknovými a vrstevnatými kompozity. Ve třech kapitolách jsou shrnuty základní poznatky o těchto kompozitech doplněné o možné techniky jejich přípravy. Kromě toho byla také zařazena kapitola týkající se modifikace povrchu keramických částic, která byla nezbytná pro uvedení techniky elektroforetické depozice, jež byla majoritně využívána v autorově vědecké práci právě pro výrobu výše uvedených kompozitů. Jednotlivé kapitoly dále obsahují komentované části vybraných publikací upozorňující na technologii přípravy, specifické jevy, nebo hodnocení vlastností.

V první kapitole jsou uvedeny informace o pokročilých tvarovacích metodách a jejich rozdělení se zvláštním zaměřením na techniky přípravy keramických materiálů mokrou cestou. Speciální pozornost je věnována elektroforetické depozici, která je představena a je vysvětlen význam stability suspenzí, ze kterých depozice probíhá. Z tohoto pohledu byla ukázána možnost modifikace povrchu keramických částic v suspenzi různými elektro-sterickými stabilizátory, přídavkem indiferentního elektrolytu, vysokoenergetickým mletím a ošetřením studenou plazmou. Druhá kapitola se týká keramických matricí obsahující příměs ve formě částic. Jsou prezentovány důvody pro existenci těchto kompozitů, zhouževnaťující mechanismy a techniky, které lze využít pro jejich přípravu. Z hlediska distribuce a velikosti přidané keramické fáze byly prezentovány tři práce, ve kterých se ukázala účelnost kompozitů po stránce mechanických, optických a biologických vlastností. Třetí kapitola byla zaměřena na charakterizaci a přípravu keramických materiálů vyztužených vlákny. Opírala se o experimentální spolupráci s firmou Pardam s.r.o., která přinesla informace o chování polykrystalických vláken v různých keramických matricích a posouzení jejich vlivu na lomové chování kompozitů. Ve čtvrté kapitole byly uveřejněny poznatky o vrstevnatých keramických kompozitech, které byly rozděleny a diskutovány dle pevnosti rozhraní mezi jednotlivými vrstvami na slabě a silně vázané. Byly představeny možnosti přípravy kompozitů na bázi Al_2O_3 a ZrO_2 s pevně vázaným rozhraním a demonstrován vliv vnitřních zbytkových napětí na změnu šíření trajektorie lomové trhliny. Byly prezentovány vlivy materiálového složení na slinovací proces, vliv slinovací metody na vznik reakčních vrstev a vhodnost použití metod posuzující vliv zbytkových vnitřních napětí na směr dráhy šíření trhliny.

Za největší autorův přínos v nastíněné tematické oblasti lze považovat nalezení klíčových parametrů EPD pro odstranění povrchové drsnosti připravovaných keramických povlaků. V této technice také jako první využil modifikace keramického prášku studenou plazmou, která pozitivně ovlivnila stabilitu koloidní suspenze a eliminovala použití jakýchkoli stabilizačních činidel, což lze považovat za výrazný benefit ve vztahu k životnímu prostředí. Nedílnou součástí je pak jeho podíl na přípravě transparentní Al_2O_3 keramiky dopované prvky vzácných zemin s vysokou propustností a luminiscenčními vlastnostmi. V této oblasti demonstroval příznivý vliv optimalizované přípravy a dopování na zvýšené hodnoty tvrdosti

transparentní keramiky a provedl ucelené srovnání této mechanické vlastnosti napříč vědeckou literaturou. Při přípravě vrstevnatých keramických materiálů ukázal vhodnost využití slinování pomocí SPS u keramik připravených jinými tvarovacími technikami, což vedlo k úspěšné výrobě jinak obtížně slinutelných vrstevnatých materiálů na bázi Al_2O_3 a SiC nebo potlačení či eliminaci vzniku reakčních fází mezi vrstvami ZrO_2 a silně reaktivních $BaTiO_3$ nebo BCZT.

Lze také konstatovat, že uvedené výsledky byly ve své podstatné většině uveřejněné v předních vědeckých časopisech a ukazují nejen autorův přínos do této tematicky široké oblasti, ale prezentují část experimentálně-vědeckých činností Ústavu materiálových věd a inženýrství na mezinárodní úrovni.

8. SEZNAM KOMENTOVANÝCH PUBLIKACÍ

[I] J. Cihlar, D. Drdlik, Z. Cihlarova, H. Hadraba, Effect of acids and bases on electrophoretic deposition of alumina and zirconia particles in 2-propanol, Journal of the European Ceramic Society, 33 (2013) 1885-1892.

[II] D. Drdlik, E. Bartonickova, H. Hadraba, J. Cihlar, Influence of anionic stabilization of alumina particles in 2-propanol medium on the electrophoretic deposition and mechanical properties of deposits, Journal of the European Ceramic Society, 34 (2014) 3365-3371.

[III] D. Drdlik, Z. Chlup, H. Hadraba, K. Drdlikova, Surface roughness improvement of near net shaped alumina by EPD, Journal of the Australian Ceramic Society, 56 (2020) 721-727.

[IV] D. Drdlik, M. Slama, H. Hadraba, J. Cihlar, Hydroxyapatite/zirconia-microfibre composites with controlled microporosity and fracture properties prepared by electrophoretic deposition, Ceramics International, 41 (2015) 11202-11212.

[V] D. Drdlik, M. Slama, H. Hadraba, K. Drdlikova, J. Cihlar, Physical, mechanical, and biological properties of electrophoretically deposited lithium-doped calcium phosphates, Ceramics International, 44 (2018) 2884-2891.

[VI] D. Drdlik, T. Moravek, J. Rahel, M. Stupavska, J. Cihlar, K. Drdlikova, K. Maca, Electrophoretic deposition of plasma activated sub-micron alumina powder, Ceramics International, 44 (2018) 9787-9793.

[VII] D. Drdlik, I. Sokolov, H. Hadraba, Z. Chlup, K. Drdlikova, K. Maca, Sintering activation energies of anisotropic layered and particle alumina/zirconia-based composites and their mechanical response, Ceramics International, submitted (2024).

[VIII] K. Drdlíková, R. Klement, D. Drdlík, T. Spusta, D. Galusek, K. Maca, Luminescent Er doped transparent alumina ceramics, Journal of the European Ceramic Society, 37 (2017) 2695-2703.

[IX] D. Drdlik, K. Drdlikova, H. Hadraba, K. Maca, Optical, mechanical and fractographic response of transparent alumina ceramics on erbium doping, Journal of the European Ceramic Society, 37 (2017) 4265-4270.

[X] D. Drdlik, K. Drdlikova, K. Maca, Dilatometric and microstructural study of particle and functionally graded composites based on hydroxyapatite and crystalline bioglass, Science of Sintering, 55 (2023) 289-306.

[XI] H. Hadraba, Z. Chlup, D. Drdlik, J. Cihlar, Micro-fibres containing composites prepared by EPD, Journal of the European Ceramic Society, 36 (2016) 365-371.

[XII] Z. Chlup, H. Hadraba, D. Drdlik, K. Maca, I. Dlouhy, R. Bermejo, On the determination of the stress-free temperature for alumina–zirconia multilayer structures, Ceramics International, 40 (2014) 5787-5793.

[XIII] K. Maca, V. Pouchly, D. Drdlik, H. Hadraba, Z. Chlup, Dilatometric study of anisotropic sintering of alumina/zirconia laminates with controlled fracture behaviour, Journal of the European Ceramic Society, 37 (2017) 4287-4295.

[XIV] Z. Chlup, L. Novotná, F. Šiška, D. Drdlík, H. Hadraba, Effect of residual stresses to the crack path in alumina/zirconia laminates, Journal of the European Ceramic Society, 40 (2020) 5810-5818.

[XV] D. Drdlik, V. Marak, H. Hadraba, Z. Chlup, A way for densification of lead-free $BaTiO_3$-based/ZrO_2 laminates for energy harvesting applications prepared by electrophoretic deposition, Materials Letters, 355 (2024) 135424.

[XVI] D. Drdlík, V. Mařák, J. Roleček, K. Drdlíková, J. Kratochvíl, D. Salamon, Study of Alumina and Alumina-Silicon Carbide Layered Composite Sintered by SPS, Key Engineering Materials, 784 (2018) 67-72.

9. SEZNAM POUŽITÉ LITERATURY

[1] P. Sarkar, P.S. Nicholson, Electrophoretic deposition (EPD): Mechanisms, kinetics, and application to ceramics, Journal of the American Ceramic Society, 79 (1996) 1987-2002.

[2] K. Maca, H. Hadraba, J. Cihlar, Electrophoretic deposition of alumina and zirconia: I. Single-component systems, Ceramics International, 30 (2004) 843-851.

[3] J.A. Lewis, Colloidal Processing of Ceramics, Journal of the American Ceramic Society, 83 (2000) 2341-2359.

[4] J. Alipal, S. Saidin, H.Z. Abdullah, M.I. Idris, T.C. Lee, Physicochemical and cytotoxicity studies of a novel hydrogel nanoclay EPD coating on titanium made of chitosan/gelatin/halloysite for biomedical applications, Materials Chemistry and Physics, 290 (2022) 126543.

[5] Z. Zhang, X. Cheng, Y. Yao, J. Luo, Q. Tang, H. Wu, S. Lin, C. Han, Q. Wei, L. Chen, Electrophoretic deposition of chitosan/gelatin coatings with controlled porous surface topography to enhance initial osteoblast adhesive responses, Journal of Materials Chemistry B, 4 (2016) 7584-7595.

[6] B.V. Velamakanni, J.C. Chang, F.F. Lange, D.S. Pearson, New Method for Efficient Colloidal Particle Packing Via Modulation of Repulsive Lubricating Hydration Forces, Langmuir, 6 (1990) 1323-1325.

[7] S. Shehayeb, X. Deschanels, J. Lautru, L. Ghannam, M. Odorico, I. Karamé, G. Toquer, Thin polymeric CuO film from EPD designed for low temperature photothermal absorbers, Electrochimica Acta, 305 (2019) 295-303.

[8] M. Verde, M. Peiteado, A.C. Caballero, M. Villegas, B. Ferrari, Electrophoretic Deposition of Transparent ZnO Thin Films from Highly Stabilized Colloidal Suspensions, Journal of Colloid and Interface Science, 373 (2012) 27-33.

[9] C. Mendoza, Z. González, Y. Castro, E. Gordo, B. Ferrari, Improvement of TiN nanoparticles EPD inducing steric stabilization in non-aqueous suspensions, Journal of the European Ceramic Society, 36 (2016) 307-317.

[10] M. Taya, S. Hayashi, A.S. Kobayashi, H.S. Yoon, Toughening of a Particulate-Reinforced Ceramic-Matrix Composite by Thermal Residual Stress, Journal of the American Ceramic Society, 73 (1990) 1382-1391.

[11] J. Wang, R. Raj, Activation Energy for the Sintering of Two-Phase Alumina/Zirconia Ceramics, Journal of the American Ceramic Society, 74 (1991) 1959-1963.

[12] F. Funabiki, T. Kamiya, H. Hosono, Doping effects in amorphous oxides, Journal of the Ceramic Society Japan, 120 (2012) 447-457.

[13] S. Marković, Č. Jovalekić, L. Veselinović, S. Mentus, D. Uskoković, Electrical properties of barium titanate stannate functionally graded materials, Journal of the European Ceramic Society, 30 (2010) 1427-1435.

[14] I. Bharti, N. Gupta, K. Gupta, Novel applications of functionally graded nano, optoelectronic and thermoelectric materials, International Journal of Materials, Mechanics and Manufacturing, 1 (2013) 221-224.

[15] Y.M. Ko, W.T. Kwon, Y.-W. Kim, Development of Al_2O_3–SiC composite tool for machining application, Ceramics International, 30 (2004) 2081-2086.

[16] Y. Watanabe, Y. Iwasa, H. Sato, A. Teramoto, K. Abe, E. Miura-Fujiwara, Microstructures and mechanical properties of titanium/biodegradable-polymer FGM for bone tissue fabricated by spark plasma sintering method, Journal of Materials Processing Technology, 211 (2011) 1919-1926.

[17] M. Koizumi, FGM activities in Japan, Composites Part B: Engineering, 28 (1997) 1-4.

[18] M. Luginina, D. Angioni, S. Montinaro, R. Orrù, G. Cao, R. Sergi, D. Bellucci, V. Cannillo, Hydroxyapatite/bioactive glass functionally graded materials (FGM) for bone tissue engineering, Journal of the European Ceramic Society, 40 (2020) 4623-4634.

[19] A. Cattini, D. Bellucci, A. Sola, L. Pawłowski, V. Cannillo, Suspension plasma spraying of optimised functionally graded coatings of bioactive glass/hydroxyapatite, Surface and Coatings Technology, 236 (2013) 118-126.

[20] A. Cattini, D. Bellucci, A. Sola, L. Pawłowski, V. Cannillo, Microstructural design of functionally graded coatings composed of suspension plasma sprayed hydroxyapatite and bioactive glass, Journal of biomedical materials research. Part B, Applied biomaterials, 102 (2014) 551-560.

[21] C. Kaya, F. Kaya, E.G. Butler, A.R. Boccaccini, K.K. Chawla, Development and characterisation of high-density oxide fibre-reinforced oxide ceramic matrix composites with improved mechanical properties, Journal of the European Ceramic Society, 29 (2009) 1631-1639.

[22] C.B. Carter, M.G. Norton, Ceramic Materials: Science and Engineering, 2 ed., Springer New York, 2013.

[23] P. Miele, S. Bernard, D. Cornu, B. Toury, Recent Developments in Polymer-Derived Ceramic Fibers (PDCFs): Preparation, Properties and Applications – A Review, Soft Materials, 4 (2007) 249-286.

[24] A.R. Bunsell, M.H. Berger, Inorganic fibres for composite materials, Composites Science and Technology, 51 (1994) 127-133.

[25] F.D. Minatto, P. Milak, A. De Noni, D. Hotza, O.R.K. Montedo, Multilayered ceramic composites – a review, Advances in Applied Ceramics, 114 (2015) 127-138.

[26] A. Ikesue, Y.L. Aung, Origin and Future of Polycrystalline Ceramic Lasers, IEEE Journal of Selected Topics in Quantum Electronics, 24 (2018) 1-7.

[27] A. Ikesue, Y.L. Aung, T. Kamimura, S. Honda, Y. Iwamoto, Composite Laser Ceramics by Advanced Bonding Technology, Materials, 11 (2018) 271-283.

[28] P. Tofel, Z. Machu, Z. Chlup, H. Hadraba, D. Drdlik, O. Sevecek, Z. Majer, V. Holcman, Z. Hadas, Novel layered architecture based on $Al_2O_3/ZrO_2/BaTiO_3$ for SMART piezoceramic electromechanical converters, The European Physical Journal Special Topics, 228 (2019) 1575-1588.

[29] M. Lugovy, V. Slyunyayev, V. Subbotin, F. Liang, J. Gou, N. Orlovskaya, T. Graule, J. Kuebler, Mechanical behavior and failure mechanisms of boron carbide based three-layered laminates with weak interfaces, Ceramics International, 37 (2011) 2255-2261.

[30] Z. Chlup, H. Hadraba, L. Slabáková, D. Drdlík, I. Dlouhý, Fracture behaviour of alumina and zirconia thin layered laminate, Journal of the European Ceramic Society, 32 (2012) 2057-2061.

[31] H. Hadraba, K. Maca, J. Cihlar, Electrophoretic deposition of alumina and zirconia: II. Two-component systems, Ceramics International, 30 (2004) 853-863.

[32] H. Hadraba, J. Klimes, K. Maca, Crack propagation in layered Al_2O_3/ZrO_2 composites prepared by electrophoretic deposition, Journal of Materials Science, 42 (2007) 6404-6411.

[33] H. Hadraba, K. Maca, Z. Chlup, Alumina and Zirconia Based Composites: Part 1 Preparation, Key Engineering Materials, 412 (2009) 221-226.

[34] H. Hadraba, D. Drdlík, Z. Chlup, K. Maca, I. Dlouhý, Control of Electrophoretic Deposition Kinetics for Preparation of Laminated Alumina/Zirconia Ceramic Composites, Key Engineering Materials, 507 (2012) 209-213.

[35] H. Hadraba, D. Drdlik, Z. Chlup, K. Maca, I. Dlouhy, J. Cihlar, Laminated alumina/zirconia ceramic composites prepared by electrophoretic deposition, Journal of the European Ceramic Society, 32 (2012) 2053-2056.

[36] Z. Chlup, H. Hadraba, Alumina and Zirconia Based Layered Composites: Part 2 Fracture Response, Key Engineering Materials, 412 (2009) 227-232.

[37] H. Hadraba, Z. Chlup, D. Drdlík, F. Šiška, Characterisation of mechanical and fracture behaviour of $Al_2O_3/ZrO_2/BaTiO_3$ laminate by indentation, Journal of the European Ceramic Society, 40 (2020) 4799-4807.

PŘÍLOHA – TIŠTĚNÉ VERZE KOMENTOVANÝCH PUBLIKACÍ

PUBLIKACE I

Available online at www.sciencedirect.com

SciVerse ScienceDirect

Journal of the European Ceramic Society 33 (2013) 1885–1892

www.elsevier.com/locate/jeurceramsoc

Effect of acids and bases on electrophoretic deposition of alumina and zirconia particles in 2-propanol

Jaroslav Cihlar[a,*], Daniel Drdlik[a,d], Zora Cihlarova[b,e], Hynek Hadraba[c,f]

[a] CEITEC – Central European Institute of Technology, Brno University of Technology, Brno, Technicka 10, 616 00 Brno, Czech Republic
[b] Faculty of Chemistry, Brno University of Technology, Purkynova 464/118, 612 00 Brno, Czech Republic
[c] CEITEC IPM, Institute of Physics of Materials, Academy of Sciences of the Czech Republic, Zizkova 513/22, 616 62 Brno, Czech Republic

Received 1 November 2012; received in revised form 2 February 2013; accepted 13 February 2013
Available online 17 March 2013

Abstract

The effects of acids (monochloroacetic, dichloracetic, trichloroacetic and sulfuric acids) and bases (diethanolamine, triethanolamine, piperidine) on electrophoretic mobility and electrophoretic deposition (EPD) of particles of amphoteric Al_2O_3 and ZrO_2 in anhydrous 2-propanol were studied. It was found that the ζ-potential of Al_2O_3 and ZrO_2 particles had in acidic and alkaline 2-propanol media opposite charge to that in aqueous medium. This phenomenon was explained by the low dissociation constants of acids and bases in 2-propanol. This enables electrosteric stabilization of Al_2O_3 and ZrO_2 particles by acid anions and base cations. Similar electrophoretic behaviour of Al_2O_3 and ZrO_2 particles in 2-propanolic dispersions stabilized by MCAA allowed the preparation of compact, regular layered laminates with high cohesion at the interface of layers.
© 2013 Elsevier Ltd. All rights reserved.

Keywords: Electrophoretic deposition; Zirconia; Alumina; 2-Propanol; Electrosteric stabilization

1. Introduction

Electrophoretic deposition in non-aqueous medium is a simple colloidal method for the preparation of ceramic coatings, layered composites and laminates,[1,2] functionally gradient materials[3] or components of solid oxide cells[4–6] or porous membranes.[7] The EPD method consists of preparing a stable dispersion of particles with surface charge that can move in the electric field towards the oppositely charged electrode and form a deposit on the electrode surface. A crucial aspect of EPD is the preparation of a stable suspension of ceramic particles in non-aqueous solvent containing usually further additives that prevent agglomeration or flocculation. Ceramic oxide particles dispersed in polar solvents usually acquire a surface charge, which enables electrostatic stabilization. According to the DVLO theory the stabilization of colloidal dispersion depends on the equilibrium of Van der Waals attractive forces and repulsive forces. Besides the repulsive electrostatic forces the steric forces are of significance, in non-aqueous media in particular, which usually appear due to the adsorption of surfactants or polymers on the surface of particles.[8] The most common non-aqueous media used for suspension preparation are alcohols, ethanol in particular[5,6,9] and 2-propanol.[10–12] EPD, especially in an environment of ethanol, is well studied. Comprehensive results have been published in several very good studies.[13–17]

It is generally acknowledged that semi-polar or polar solvents with permittivity >11, which include low-molecular alcohols, behave like water. Oxide particles are usually stabilized electrostatically.[18] The magnitude of the charge on the surface of oxide particles and its charge are given by the donor–acceptor (acidobasic) equilibrium between the particle surface and the dispersive medium.[19,20] In colloidal dispersions of amphoteric oxides (Al_2O_3, ZrO_2, TiO_2,. . .) in ethanol and isopropanol the oxides behave as bases (electron donors) and their surface gets a positive charge.[21] The role of acids in acidobasic equilibria is played by either alcohol molecules or additives and traces of water contained in alcohols.[22] Most of

* Corresponding author. Tel.: +420 541 143 383; fax: +420 541 143 202.
E-mail addresses: jaroslav.cihlar@ceitec.vutbr.cz (J. Cihlar), daniel.drdlik@ceitec.vutbr.cz (D. Drdlik), cihlarova@fch.vutbr.cz (Z. Cihlarova), hadraba@ipm.cz (H. Hadraba).
[d] Tel.: +420 541 143 340; fax: +420 541 143 202.
[e] Tel.: +420 541 149 394.
[f] Tel.: +420 532 290 369; fax: +420 541 218 657.

0955-2219/$ – see front matter © 2013 Elsevier Ltd. All rights reserved.
http://dx.doi.org/10.1016/j.jeurceramsoc.2013.02.017

the works published on the above amphoteric oxides in alcohol media without additives presented a positive ζ-potential of particles and their deposition on the cathode.[5,23] However, the low permittivity of non-aqueous alcohols compared with water results in the reduction of the dissociation degree of electrolytes, reduction of the ionic force of the dispersive medium, and reduction of the electrostatic stabilization of oxide particles.[24,25] On the other hand, low polar dispersive medium supports the adsorption of non-dissociated electrolyte molecules on the surface of particles and the exchange reactions with surface ions. Then the particle surface charge is formed not by protons but by electrolyte cations and anions.[26] This electrosteric mechanism explains why particles stabilized in non-aqueous acid solutions can have the negative charge while particles stabilized by bases can have the positive charge.[14] The electrosteric mechanism enables stabilizing oxide particles (TiO_2) also in non-polar media. TiO_2 particles in hexane in the presence of n-butylamine had the positive charge and were stable due to the steric contribution of n-butylamine adsorbed on the surface of TiO_2.[26] A similar electrosteric mechanism was at work in the stabilization of particles of tetragonal ZrO_2 in acetylaceton medium by ethanolamines[27] or in the stabilization of YBCO particles by the complex cation $CH_3CH_2ICOH^+$ in ethanol medium.[28] Oxide particles in alcohol medium can also be effectively stabilized by surfactants which are effective even in aqueous media. In alcohol medium, however, stabilized particles carry the opposite charge to that in aqueous medium. Al_2O_3 particles stabilized in ethanol by citric acid at pH 4.2 had the negative charge while particles stabilized by tetramethylamoniumhydroxide had at pH 13.6 the positive charge.[14] Westby et al. found that di- and tricarboxylic hydroxyacids combined with di- and trialkylamines led to an effective electrosteric stabilization of Al_2O_3 and SiO_2.[29,30] Basic amine integrated with carboxylic acid and facilitated the dissociation of carboxyl groups of the acid adsorbed on the surface of oxides. This is because the dissociation constants of carboxyl acids are in alcohol media ca. 5 orders lower than in aqueous medium, and carboxyl acids often cannot, without the aid of basic amines, produce the negative charge on the oxide surface (TiO_2).[31] To obtain a sufficient concentration of dissociated carboxyl groups it is necessary to have a considerable amount of stabilizers in non-aqueous dispersive medium. De Riccardis et al. found that maximum stabilization (maximum negative ζ-potential) of Al_2O_3/ZrO_2 particles in ethanol was obtained for a dispersant (citric acid/triethylamine) content of 10 wt%.[32] Monochloroacetic acid is a very effective electrosteric stabilizer of propanol dispersions of amphoteric oxides. We have published a number of papers focused on the study of Al_2O_3/ZrO_2 ceramic composites prepared by electrophoretic deposition of negatively charged ZrO_2 and Al_2O_3 particles in the 2-propanolic dispersions of MCAA.[1–3,33,34] We have not so far published the mechanism of electrophoretic deposition. The present paper is therefore concerned with the mechanism of electrosteric stabilization of Al_2O_3 and ZrO_2 by chloro derivatives of acetic acid and ethanolamines in 2-propanol medium, and with electrophoretic deposition of electrosterically charged Al_2O_3 and ZrO_2 particles.

2. Experimental

For the study of electrokinetic properties and electrophoretic deposition, 2-propanolic dispersions of ceramic powders based on α-Al_2O_3 (HP-DBM, Malakoff Indian, USA) and t-ZrO_2 (TZ-3YS-E, Tosoh, Japan) were used. The dispersions were prepared by ultrasonic mixing of 15 wt% of ceramic powder and 72.25 wt% of dispersion media – anhydrous 2-propanol (180 ppm H_2O), (Lachner, Czech Republic) without additives or with the addition of 0.85–21.25 wt% of stabilizer. Acids and bases were used for electrosteric stabilization. The acids used were monochloroacetic (MCAA) (pa, Aldrich, Germany), dichloracetic (DCAA) (pa, Merck, Germany), trichloroacetic (TCAA) (p, Reachim, Russia), sulfuric acid (SA) (p, ML Chemica, Czech Republic) and the bases used were piperidine (PIP) (p, Lachema, Czech Republic), diethanolamine (DEA) (pa, Penta, Czech Republic), triethanolamine (TEA) (pa, Lachema, Czech Republic).

To measure pH, the pH-metre (model Seven compact, pH/Ion S220, Mettler, Switzerland) was used, which was equipped with a glass electrode for the measurement in anhydrous media (model InLab Science Pro). The pH metre was calibrated by aqueous standards at 25 °C, and the value of operational pH was obtained according to.[35] In the paper, however, not specific pH values but their differences are given. This eliminates errors caused by the asymmetric potential of the glass electrode in nonaqueous medium.

The conductance of dispersions was measured at 25 °C using a conductometer (model Seven compact, Conductivity S230, Mettler, Switzerland) equipped with a probe for the measurement of liquids of low conductance (model Conductivity InLab 710, 0–500 mS).

The content of water in isopropanol was established via the Karl Fischer titration using the Aquameter instrument (Brur, Austria). The content of water and monochloroacetic acid isopropylester in dispersions was established using a gas chromatograph (model Finnigan Trace GC Ultra/DSQ, Thermo Fisher Scientific, USA) with a TG-WAXMS 30 m × 1 μm column.

The measurement of electrokinetic behaviour of dispersions of Al_2O_3 and ZrO_2 was performed at 25 °C by LDV (Laser Doppler Velocimetry) using a Zetasizer 3000 HS (Malvern Instruments, UK). The Henry equation was used to calculate the ζ-potential.[36] To measure the ζ-potential, 2-propanolic dispersions of Al_2O_3 and ZrO_2 were used, prepared for electrophoretic deposition and diluted 100× by anhydrous 2-propanol. In view of the low conductance of 2-propanolic dispersions (about 10 μS) the value of the ζ-potential was slow to steady and at low values of the ζ-potential of particles sediment in the measuring cell. The measurement error was about 30%. Due to the addition of 0.2 mM LiCl and frequent cleaning of the measuring cell the maximum measurement error was reduced to about 15%. The measurement of every ζ-potential value was repeated 15–30 times.

To study the electrophoretic deposition a vertical arrangement of electrodes was used.[34] EPD was conducted with a current intensity of 5 mA between stainless steel electrodes with an effective area of 18.7 cm^2. The distance between the electrodes

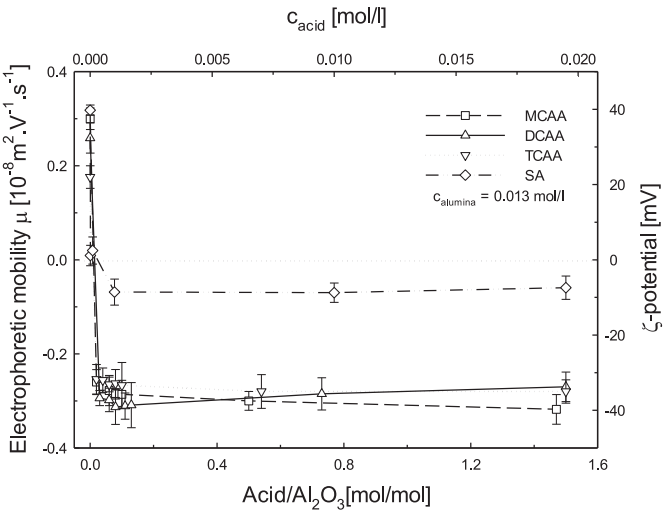

Fig. 1. Dependence of electrophoretic mobility μ (or ζ-potential) of Al_2O_3 particles in 2-propanolic dispersion on the acid/Al_2O_3 molar ratio (MCAA – monochloroacetic acid, DCAA – dichloracetic acid, TCAA – trichloroacetic acid, SA – sulfuric acid).

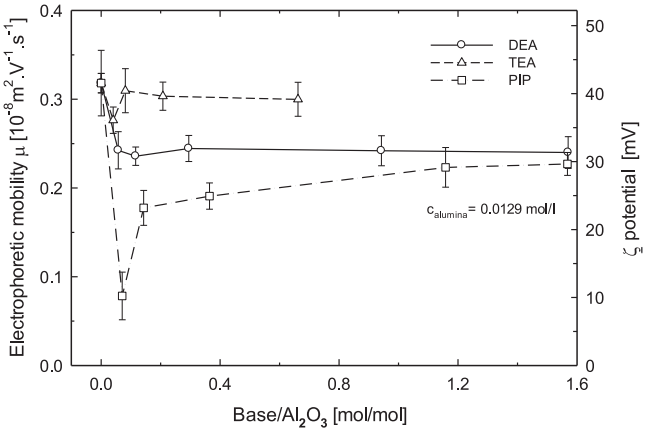

Fig. 2. Dependence of electrophoretic mobility μ (or ζ-potential) of Al_2O_3 particles in 2-propanolic suspension on base/Al_2O_3 molar ratio (DEA – diethanolamine, TEA – triethanolamine, PIP – piperidine).

was set to 26 mm. On the base of the results published in the past[34] the dispersions composed of 15 wt% of oxide, 12.75 wt% of stabilizer and 82.25 wt% of 2-propanol were used for EPD experiments. Ceramic laminates were prepared in the same manner as monolithic ceramics. The deposition of Al_2O_3 and ZrO_2 layers was achieved by moving the electrodes from the cell containing the suspension of alumina to the cell with zirconia. The deposits were dried at 25 °C/24 h and weighed. All deposits were annealed at 800 °C/1 h and sintered at 1500 °C/2 h. The relative densities of deposits after sintering and annealing were measured by Archimedes' method [EN 623-2]. The ceramic laminates were polished and thermally etched at 1450 °C/5 min in air and analyzed on a scanning electron microscope (SEM) (XL 30, Philips, The Netherlands).

3. Results and discussion

3.1. Electrophoretic behaviour of Al_2O_3 and ZrO_2 particles

Fig. 1 illustrates the dependence of electrophoretic mobility or ζ-potential of Al_2O_3 particles in 2-propanol in the presence of monochloroacetic, dichloroacetic, trichloroacetic and sulfuric acid. The electrophoretic mobility of Al_2O_3 in 2-propanol was 0.3×10^{-8} m^2 V^{-1} s^{-1} (ζ-potential amounted to +42 mV). The presence of MCAA, DCAA and TCAA in 2-propanolic dispersions of Al_2O_3 was reflected by the positive ζ-potential changing to a negative one, already at the molar ratio of acid/Al_2O_3 > 0.1. Alumina particles had ζ-potential equal to −39 mV in the presence of MCAA, −38 mV in the presence of DCAA and −37 mV in the presence of TCAA. The values of ζ-potential were practically unchanged in the range of molar ratios of acid/Al_2O_3 > 0.1 – 1.0 (TCAA) and 0.1 – 1.5 (MCAA, DCAA). Al_2O_3 particles in the 2-propanolic dispersions stabilized by sulphuric acid also had negative ζ-potential (−7 mV) at the molar ratio of SA/Al_2O_3 > 0.1. The electrophoretic mobility of Al_2O_3 particles in 2-propanolic dispersions and in the presence of diethanolamine, triethanolamine and piperidine is shown in Fig. 2.

Fig. 2 shows that the initial positive charge of Al_2O_3 particles (+42 mV) remained positive after addition of bases with the base/Al_2O_3 molar ratio > 1.5 (DEA, PIP). After an initial decrease in the ζ-potential, which was most pronounced in the presence of piperidine, the ζ-potential slightly (DEA, TEA) or significantly (PIP) increased and reached values in the range of +25 to +40 mV. Electrophoretic behaviour of 2-propanolic Al_2O_3 suspension without the presence of stabilizer can be described by acidobasic equilibria between the surface of Al–OH groups and traces of water present in the 2-propanolic suspensions in Eq. (1):

$$(\text{=Al–OH})_{\text{surface}} + H_2O \rightleftharpoons (\text{=Al–OH}_2)^+_{\text{surface}} + OH^- \quad (1)$$

This reaction is more probable than the reaction of 2-propanol with the surface of Al_2O_3 according to Eq. (2),

$$(\text{=Al–OH})_{\text{surface}} + 2\text{-}PrOH \rightleftharpoons (\text{=Al–OH}_2)^+_{\text{surface}} + 2\text{-}PrO^- \quad (2)$$

because the dissociation constant of water is more than six orders of magnitude higher than that of 2-propanol.[37] The formation of the negative surface charge of Al_2O_3 particles in 2-propanol in the presence of acids or positive charge in the presence of bases is associated with the low relative permittivity of 2-propanol ($\varepsilon_r = 20.1$). At such a low value of ε_r, a high association of strong electrolytes occurs, together with the formation of ion pairs, triplets and multiplets.[38] These phenomena cause that strong electrolytes become weak (incompletely dissociated) and the dissociation constants of weak electrolytes in 2-propanol are many orders of magnitude lower than in that in water.[37] We therefore assume that the formation of the negative surface charge of Al_2O_3 particles in 2-propanol is the result of adsorption processes (based on donor–acceptor interactions) between the polar surface of Al_2O_3 and weakly dissociated molecules of acids and bases.

Chloro derivatives of acetic acid interact with Al_2O_3 particles by an electrosteric mechanism similar to surface-active

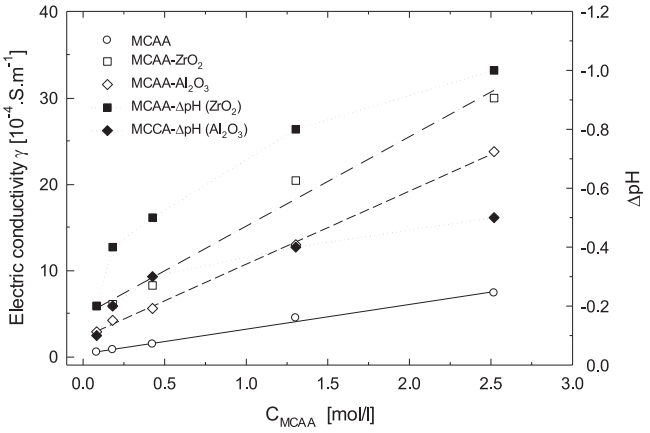

Fig. 3. Dependence of electrical conductivity and pH change of 2-propanolic suspension on concentration of MCAA; without and with addition of Al_2O_3 or ZrO_2.

dispersants based on multifunctional hydroxycarboxylic acids and alkylamines.[29] Chloro derivatives of acetic acid also have in their molecules two polar centres, a carboxyl group which can dissociate, and C–Cl polar bonds, which enable the adsorption of chloroacetic acid onto the surface of oxide particles. This process could in the case of Al_2O_3 and in the presence of MCAA hypothetically be described by equilibrium equations. (3)–(7):

$$(=Al{-}OH)_{surface} + H_2O_{(water\ traces\ in\ 2\text{-}PrOH)} \rightleftharpoons (=Al{-}OH_2)^+ + OH^- \quad (3)$$

$$ClCH_2COOH + OH^- \rightleftharpoons ClCH_2COO^- + H_2O \quad (4)$$

$$(=Al{-})_{surface} + ClCH_2COO^- \rightleftharpoons (=Al{-})_{surface}\cdots ClCH_2COO^- \quad (5)$$

$$(=Al{-})_{surface} + ClCH_2COOH \rightleftharpoons (=Al{-})_{surface}\cdots ClCH_2COOH \quad (6)$$

$$(=Al{-})_{surface}\cdots ClCH_2COOH + H_2O \rightleftharpoons (=Al{-})_{surface}\cdots ClCH_2COO^- + H_3O^+ \quad (7)$$

These equations show that in addition to the changes in the charge of Al_2O_3 particles from positive to negative, there should be a release of hydrogen ions into the 2-propanolic suspension. This process should show the growth of suspension conductivity or reduction of its pH. Fig. 3 describes the dependence of the conductivity and changes in pH in the 2-propanolic solution on the concentration of MCAA without and with the addition of Al_2O_3 or ZrO_2. The Al_2O_3 suspension in 2-propanol with an addition of MCAA had a higher conductivity than the actual 2-propanolic MCAA solution. Addition of Al_2O_3 or ZrO_2 to a 2-propanolic MCAA solution led to a decrease in pH by one unit. The hypothetical mechanism, which was designed for MCAA could also hold for the remaining three acids (dichloroacetic, trichloroacetic and sulfuric), which also caused the sign change of Al_2O_3 surface charge.

In the case of 2-propanolic Al_2O_3 dispersions containing basic substances, it is possible to describe the interaction with the surface of Al_2O_3 by an analogous mechanism such as the interaction of acids. The molecules of aminoalcohols contain one base amino-group capable of dissociation and at least one other polar hydroxy-group capable of interaction with the oxide surface which obtains the positive charge. A similar electrosteric stabilization by the positive charge on ZrO_2 particles in the presence of hydroxyamines in acetylacetone was reported by Xu et al.[27]

The mechanism of diethanolamine interaction with the surface of Al_2O_3 may be described in Eqs. (8)–(11):

$$(=Al{-}OH)_{surface} + H_2O_{(water\ traces\ in\ 2\text{-}PrOH)} \rightleftharpoons (=Al{-}OH_2)^+ + OH^- \quad (8)$$

$$(=A1{-}OH_2)^+ + NH(CH_2CH_2OH)_2 \rightleftharpoons (=A1{-}OH)_{surface} + NH_2^+(CH_2CH_2OH)_2 \quad (9)$$

$$NH_2^+(CH_2CH_2OH)_2 + OH^- \rightleftharpoons NH(CH_2CH_2OH)_2 + H_2O \quad (10)$$

$$(=Al{-}OH)_{surface}\bullet\bullet\bullet\bullet NH(CH_2CH_2OH)_2 + H_2O \rightleftharpoons (=Al{-}OH)_{surface}\bullet\bullet\bullet\bullet NH_2^+(CH_2CH_2OH)_2 + OH^- \quad (11)$$

This description, too, shows that the addition of a base to the suspension of Al_2O_3 should reduce the electrophoretic mobility or the ζ-potential in the limiting case to zero and that higher concentrations of the base cause an increase in conductivity due to the OH^- ions released. This behaviour, i.e. the decrease in the electrophoretic mobility at low base/Al_2O_3 molar ratios, is shown in Fig. 2. The increasing conductivity of the 2-propanolic suspension of Al_2O_3 and ZrO_2 after addition of diethanolamine is shown in Fig. 4.

Electrokinetic behaviour of acidic 2-propanolic ZrO_2 dispersions was similar to the behaviour of dispersions of Al_2O_3 (see Fig. 5 and Table 1). ZrO_2 particles in pure 2-propanol carry a positive charge (ζ-potential of about +33 mV). After the addition of monochloroacetic, dichloroacetic or trichloroacetic acids the charge of ZrO_2 particles changed to negative (ζ-potential reached about −45 mV). The particles in the presence of sulfuric acid had a ζ-potential of about −17 mV. The negative charge of particles remained practically constant at the molar ratio of acid/ZrO_2 > 0.25.

Also the behaviour of basic 2-propanolic ZrO_2 dispersions (see Fig. 6) was similar to that of Al_2O_3 dispersions. The ζ-potential of ZrO_2 particles grew in the range of

Table 1
Yield of electrophoretic deposition and polarity of electrode towards which deposition takes place, depending on type of acid or base.

	Stabilizer	Polarity of electrode	ζ Potential (mV)	Standard deviation	Yield (mg cm^{-2} min^{-1})	Annealed density (%)	Final density (%)
Al_2O_3							
Acids	MCAA	+	−39.42	2.08	8.05	59.67	99.29
	DCAA	+	−37.51	3.41	6.92	59.51	99.10
	TCAA	+	−36.50	4.53	2.07	56.26	99.05
	SA	+	−7.02	2.69	1.56	44.13	96.64
Without stabilizer		–	41.52	1.43	23.93	47.95	97.12
Bases	DEA	–	32.12	2.14	1.99	49.41	98.38
	TEA	–	39.15	2.56	13.50	56.47	98.62
	PIP	–	27.86	2.37	13.02	52.71	98.11
ZrO_2							
Acids	MCAA	+	−45.69	4.31	6.70	47.35	99.92
	DCAA	+	−45.01	3.53	6.42	49.24	99.54
	TCAA	+	−44.51	2.94	2.81	42.58	99.07
	SA	+	−17.10	3.42	2.60	35.45	99.59
Without stabilizer		–	32.71	4.20	23.54	35.70	97.28
Bases	DEA	–	49.87	3.19	1.98	41.17	99.89
	TEA	–	57.28	2.72	5.20	44.56	99.98
	PIP	–	51.69	2.29	10.73	–	–

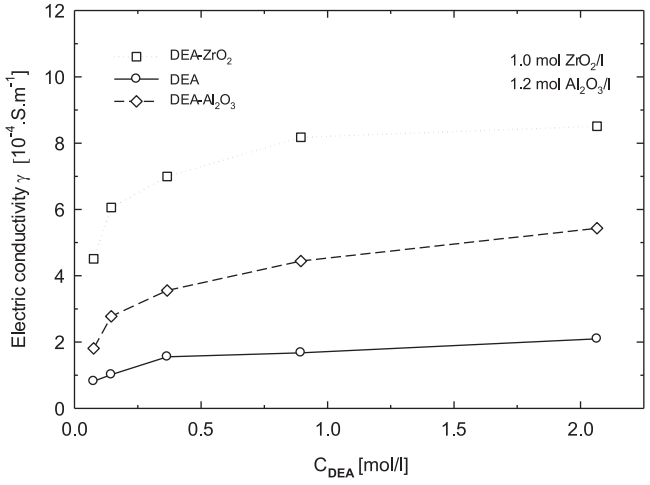

Fig. 4. Dependence of electrical conductivity of 2-propanolic suspension on concentration of DEA with and without addition of Al_2O_3 or ZrO_2.

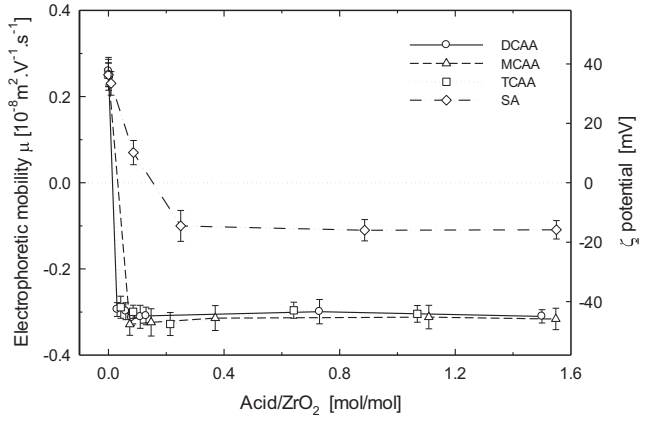

Fig. 5. Dependence of electrophoretic mobility μ (or ζ-potential) of ZrO_2 particles in 2-propanolic suspension on the acid/ZrO_2 molar ratio (MCAA – monochloroacetic acid, DCAA – chloroacetic acid, TCAA – trichloroacetic acid, SA – sulfuric acid).

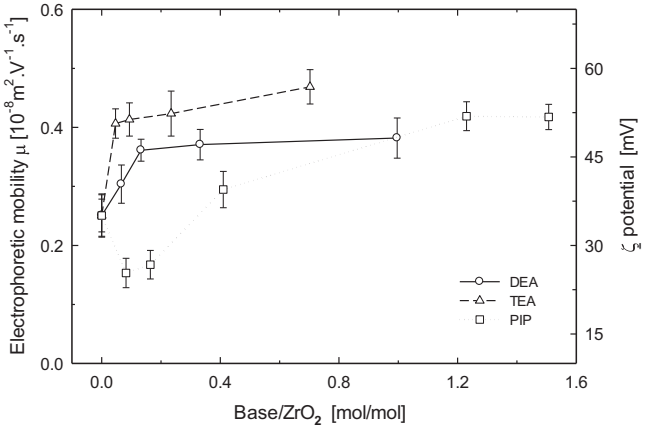

Fig. 6. Dependence of electrophoretic mobility μ (or ζ-potential) of ZrO_2 particles in 2-propanolic suspension on base/ZrO_2 molar ratio (DEA – diethanolamine, TEA – triethanolamine, PIP – piperidine).

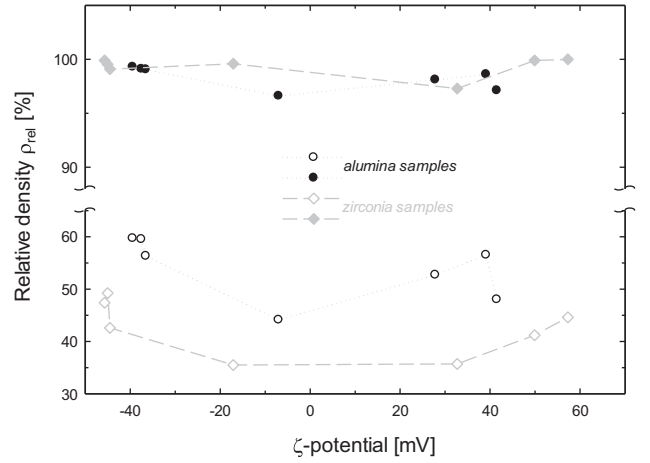

Fig. 7. Influence of ζ-potential on the green and final density of deposits.

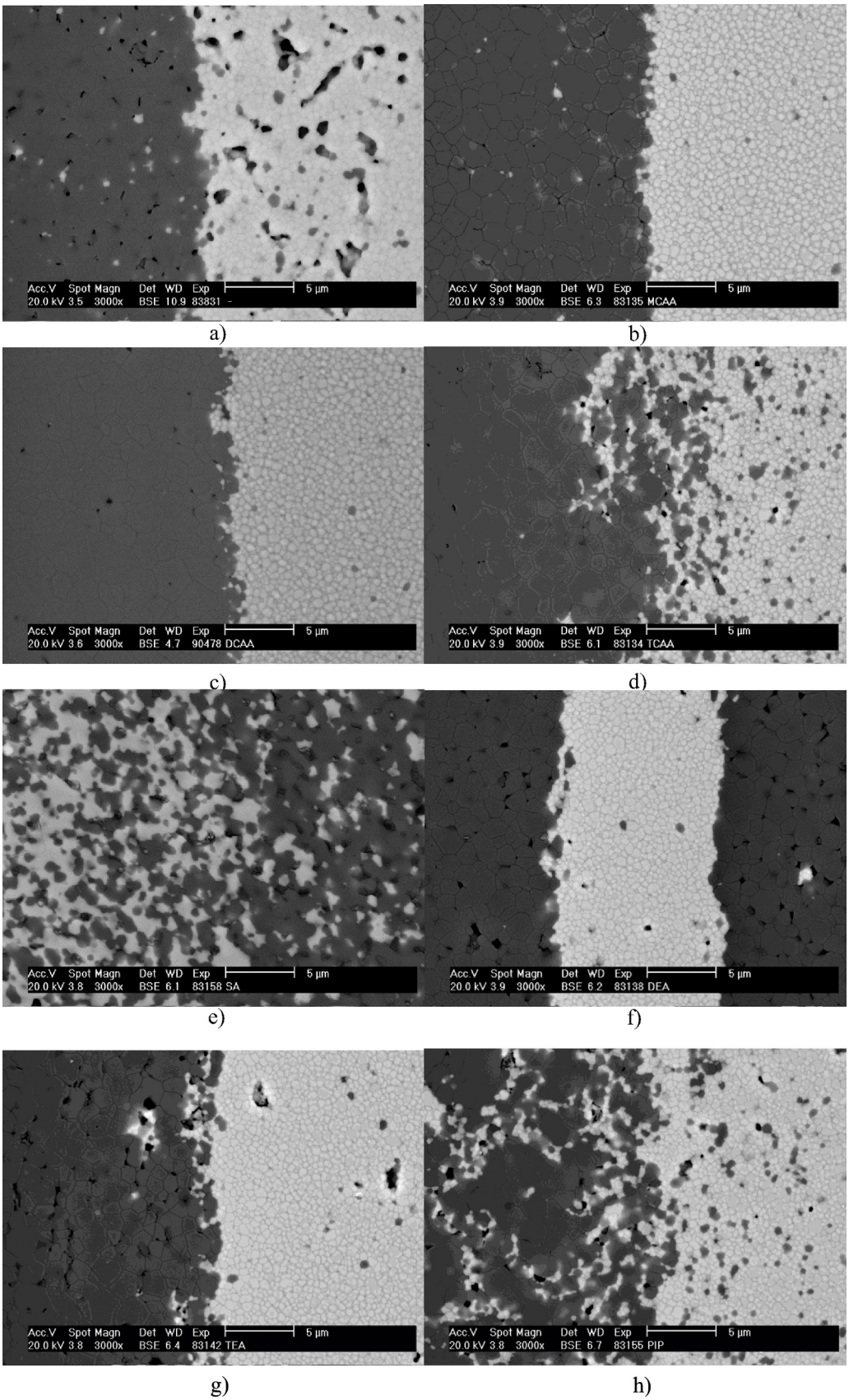

Fig. 8. Morphology of interface in composites of Al_2O_3/ZrO_2 from suspension (a) without stabilization and stabilized dispersions prepared from acids (b) monochloroacetic acid, (c) dichloracetic acid, (d) trichloroacetic acid, (e) sulfuric acid and bases (f) diethanolamine, (g) triethanolamine, (h) piperidine in anhydrous 2-propanol.

base/ZrO_2 molar ratio = 0–0.1, and reached a maximum value of +50 mV (diethanolamine), +58 mV (triethanolamine) and +52 mV (piperidine). The electrokinetic behaviour of 2-propanolic dispersions can therefore be described by the mechanism that was given for 2-propanolic dispersions of Al_2O_3.

3.2. Electrophoretic deposition of 2-propanolic dispersions of Al_2O_3 and ZrO_2

The polarity of the electrodes on which Al_2O_3 was deposited corresponded to the ζ-potential of the Al_2O_3 particles in the dispersion when no stabilizer was present and in the dispersions when monochloroacetic acid, dichloroacetic acid, trichloroacetic acid, piperidine, diethanolamine or triethanolamine were present (see Table 1). The largest yields of Al_2O_3 deposits were established in the 2-propanolic dispersion without stabilizer (23.93 mg cm^{-2} min^{-1}). The yield of Al_2O_3 deposition in the dispersion with MCAA and DCAA was about 3 times lower (8.05 mg cm^{-2} min^{-1} and 6.92 mg cm^{-2} min^{-1}) than that without stabilizer. Deposition yields from dispersions containing trichloroacetic acid and sulfuric acid were also small (1.56–2.07 mg cm^{-2} min^{-1}). Yields from dispersions containing a base ranged from 1.99 to 13.50 mg cm^{-2} min^{-1}.

The ZrO_2 particles were deposited on the electrode in accordance with the observed ζ-potential of particles. As in the case of Al_2O_3, the largest yield of ZrO_2 deposition was observed in the suspension without stabilizer. A sufficiently high yield of deposition was observed in the presence of monochloroacetic acid (6.70 mg cm^{-2} min^{-1}), dichloroacetic acid (6.42 mg cm^{-2} min^{-1}), triethanolamine (5.20 mg cm^{-2} min^{-1}) and piperidine (10.73 mg cm^{-2} min^{-1}).

From the results presented, the following facts can be assumed. Al_2O_3 and ZrO_2 particles have a negative charge in the 2-propanolic medium in the presence of the studied acids, or a positive charge in the presence of bases and have to lose a charge during the electrophoretic deposition on (or near) the electrode if sufficiently dense deposits are to be created. Sarkar and Nicholson[16] first imagined Al_2O_3 deposition from ethanolic suspension on a cathode as a chemical reaction of excessive H^+ ions and counterions in the double layer on the surface of Al_2O_3. Later[17] they came up with the discharge mechanism of discharge-depletion, the essence of which is the reduction of H^+ ions on the cathode to H_2 with the pH of the suspension around the cathode growing up to the isoelectric point of Al_2O_3. For this reason the Al_2O_3 particles lose their charge in the vicinity of the cathode and are deposited on the electrode.

The course of Al_2O_3 or ZrO_2 deposition in 2-propanolic dispersions and in the presence of acids such as MCAA was impossible to describe by any of the above mentioned mechanisms. The Al_2O_3 and ZrO_2 particles were negatively charged and deposited on the anode. The pH change in the vicinity of the electrodes due to the reduction of H^+ ions was therefore out of the question.

Formally, the process of the deposition of Al_2O_3 and ZrO_2 particles in non-aqueous 2-propanolic dispersions and in the presence of acidic and basic stabilizers can be described by Hamaker–Werwey mechanisms[39] in the following steps:

Negatively charged Al_2O_3 or ZrO_2 particles move to the positively charged electrode (anode) in the electric field while positively charged particles of Al_2O_3 or ZrO_2 move to the negatively charged electrode (cathode). The particles accumulate on the electrode and are mutually compressed. Compressed particles coagulate (are deposited) on the electrode.

From Table 1 it is obvious that the highest relative green density and the relative bulk density after sintering were obtained for deposits of Al_2O_3 or ZrO_2 deposited with an average or low yield from dispersions stabilized by MCAA, TCAA, DEA and TEA. All of these deposits had a smooth surface without defects. The effect of acids and bases on the morphology of the interface in the Al_2O_3 and ZrO_2 composites is shown in Fig. 5. The interfaces of most of the composites were blurred and contained pores. The deposit stabilized by DEA had a sharp interface. Dense layers with a sharp interface with minimal defects were only prepared from dispersions of Al_2O_3 and ZrO_2 stabilized by MCAA.

It can be seen from Figs. 7 and 8 that the density of deposits depends on the absolute value of the ζ-potential. The deposits with the highest density were prepared at the highest absolute values of the ζ-potential. During deposition, electrosterically stabilized particles behave similar to the behaviour of electrostatically stabilized particles.

4. Conclusions

The study of the effect of acids and bases on the electrokinetic behaviour and EPD dispersions of amphoteric oxides Al_2O_3 and ZrO_2 in 2-propanol showed that the interaction of these oxides with acids produced a negative surface charge of oxides, while interactions of oxides with bases produced a positive charge. The sign of the charge of electrostatically stabilized Al_2O_3 and ZrO_2 particles in 2-propanol was not determined only by the concentration of protons, as is the case of aqueous medium, but by the structure of the anion of acid or cation of base and their concentrations. Since the strength of the interaction between the anion of acid or cation of base and the oxide surface depended on the nature of the acid or base, their choice could influence the properties of the final ceramic deposits. It turned out that the optimum electrosteric stabilizer providing composite Al_2O_3/ZrO_2 deposits with high relative density, sharp interface and minimal defects was MCAA.

Acknowledgements

The work was supported by the ERDF (CEITEC – CZ.1.05/1.1.00/02.0068), COST LD12004 and Czech Science Foundation under project No. 106/09/H035.

References

1. Hadraba H, Drdlik D, Chlup Z, Maca K, Dlouhy I, Cihlar J. Laminated alumina/zirconia ceramic composites prepared by electrophoretic deposition. *J Eur Ceram Soc* 2012;**32**:2053–6.

2. Hadraba H, Klimes J, Maca K. Crack propagation in layered Al_2O_3/ZrO_2 composites prepared by electrophoretic deposition. *J Mater Sci* 2007;**42**:6404–11.
3. Hadraba H, Maca K, Cihlar J. Electrophoretic deposition of alumina and zirconia – II. Two-component systems. *Ceram Int* 2004;**30**:853–63.
4. Abdoli H, Alizadeh P. Electrophoretic deposition of $(Mn,Co)_3O_4$ spinel nano powder on SOFC metallic interconnects. *Mater Lett* 2012;**80**:53–5.
5. Caproni E, Gouvea D, Muccillo R. Yttria-stabilized zirconia closed end tubes prepared by electrophoretic deposition. *Ceram Int* 2011;**37**: 273–7.
6. Jia L, Lu Z, Huang XQ, Liu ZG, Chen KF, Sha XQ, et al. Preparation of YSZ film by EPD and its application in SOFCs. *J Alloys Compd* 2006;**424**:299–303.
7. Van Hoof V, Dotremont C, Buekenhoudt A. Performance of Mitsui NaA type zeolite membranes for the dehydration of organic solvents in comparison with commercial polymeric pervaporation membranes. *Sep Purif Technol* 2006;**48**:304–9.
8. Morrison ID. Electrical charges in nonaqueous media. *Colloid Surf A* 1993;**71**:1–37.
9. Borojeni IA, Raissi B, Maghsoudipour A, Kazemzad M, Marzbanrad E. Aging behavior of yttria stabilized zirconia (YSZ) in non aqueous suspensions for electrophoretic deposition application. *Key Eng Mater* 2009;**412**:279–85.
10. Ghorbani M, Afshar MR. Electrophoretic deposition of titanium dioxide nano-powders films in isopropanol as a solvent. *Int J Mod Phys B* 2008;**22**:2989–94.
11. Jean J-H. Electrophoretic deposition of Al_2O_3-SiC composite. *Mater Chem Phys* 1995;**40**:285–90.
12. Mohanty G, Besra L, Bliattacharjee S, Singh BP. Optimization of electrophoretic deposition of alumina onto steel substrates from its suspension in iso-propanol using statistical design of experiments. *Mater Res Bull* 2008;**43**:1814–28.
13. Biesheuvel PM, Verweij H. Theory of cast formation in electrophoretic deposition. *J Am Ceram Soc* 1999;**82**:1451–5.
14. Menon M, Decourcelle S, Ramousse S, Larsen PH. Stabilization of ethanol-based alumina suspensions. *J Am Ceram Soc* 2006;**89**:457–64.
15. Menon M, Decourcelle S, Attia N, Ramousse S, Larsen PH. Stabilization of ethanol based ceramic suspensions for electrophoretic deposition. *Ceram Eng Sci Proc* 2005;**26**:239–46.
16. Sarkar P, Nicholson PS. Electrophoretic deposition (EPD): mechanisms, kinetics, and application to ceramics. *J Am Ceram Soc* 1996;**79**:1987–2002.
17. Wang GH, Sarkar P, Nicholson PS. Influence of acidity on the electrostatic stability of alumina suspensions in ethanol. *J Am Ceram Soc* 1997;**80**:965–72.
18. Van Der Hoeven PC, Lyklema J. Electrostatic stabilization in non-aqueous media. *Adv Colloid Interfac* 1992;**42**:205–77.
19. The Jensen WB. Lewis acid-base definitions: a status report. *Chem Rev* 1978;**78**:1–22.
20. Siffert B, Elelilletsango J, Jada A, Papirer E. Experimental-determination of the electron-donor and acceptor numbers of oxides by zetametry in organic media. *Colloid Surf A* 1994;**92**:107–11.
21. Wang GH, Sarkar P, Nicholson PS. Surface chemistry and rheology of electrostatically (ionically) stabilized alumina suspensions in polar organic media. *J Am Ceram Soc* 1999;**82**:849–56.
22. Kosmulski M. Zeta potentials in nonaqueous media: how to measure and control them. *Colloid Surf A* 1999;**159**:277–81.
23. Benehkohal NP, Demopoulos GP. Preparation of DSSC nanotitania thin film photoanodes by electrophoretic deposition in an aqueous suspension. *ECS Trans* 2011;**35**:39–52.
24. Morrison ID. Criterion for electrostatic stability of dispersions at low ionic strength. *Langmuir* 1991;**7**:1920–2.
25. Romo LA. Stability of non-aqueous dispersions. *J Phys Chem A* 1963;**67**:386–9.
26. Siffert B, Jada A, Elelilletsango J. Stability calculations of TiO_2 nonaqueous suspensions – thickness of the electrical double-layer. *J Colloid Interf Sci* 1994;**167**:281–6.
27. Xu H, Shapiro IP, Xiao P. The influence of pH on particle packing in YSZ coatings electrophoretically deposited from a non-aqueous suspension. *J Eur Ceram Soc* 2010;**30**:1105–14.
28. Dusoulier L, Cloots R, Vertruyen B, Moreno R, Burgos-Montes O, Ferrari B. $YBa_2Cu_3O_{7-x}$ dispersion in iodine acetone for electrophoretic deposition: surface charging mechanism in a halogenated organic media. *J Eur Ceram Soc* 2011;**31**:1075–86.
29. Westby WS, Kooner S, Farries PM, Boother P, Shatwell RA. Processing of Nextel 720/mullite composition composite using electrophoretic deposition. *J Mater Sci* 1999;**34**:5021–31.
30. Kooner S, Westby WS, Watson CMA, Farries PM. Processing of Nextel™ 720/mullite composition composite using electrophoretic deposition. *J Eur Ceram Soc* 2000;**20**:631–8.
31. Sun Y, Zhitomirsky I. Electrophoretic deposition of titanium dioxide using organic acids as charging additives. *Mater Lett* 2012;**73**:190–3.
32. De Riccardis MF, Carbone D, Rizzo A. A novel method for preparing and characterizing alcoholic EPD suspensions. *J Colloid Interf Sci* 2007;**307**:109–15.
33. Hadraba H, Maca K, Alumina CZ. Zirconia based composites: part 1 preparation. *Key Eng Mat* 2009;**412**:221–6.
34. Maca K, Hadraba H, Cihlar J. Electrophoretic deposition of alumina and zirconia – I. Single-component systems. *Ceram Int* 2004;**30**:843–52.
35. Bates. Practical measurement of pH in amphiprotic and mixed solvents. Pure Appl Chem, 1969; 18: 419-426.
36. Widegren J, Bergström L. The effect of acids and bases on the dispersion and stabilization of ceramic particles in ethanol. *J Eur Ceram Soc* 2000;**20**:659–65.
37. Izutsu K. Electrochemistry in nonaqueous solutions, Weiheim:Wiley-VCH;2002.p. 182.
38. Safarik L, Stránský Z. *Titrimetric analysis in organic solvents*, vol. 22. Amsterdam: Elsevier; 1986. p. 532.
39. Hamaker HC, Verwey EJW. Part II.-(C) colloid stability. The role of the forces between the particles in electrodeposition and other phenomena. *Trans Faraday Soc* 1940;**35**:180–5.

Jaroslav Cihlar studied physical chemistry at the Faculty of Science of Masaryk University in Brno. He graduated in 1972. In 1973 he defended his dissertation in the field of physical chemistry at the Faculty of Science of Masaryk University. He finished his postgraduate studies in the field of polymer chemistry at the Czechoslovak Academy of Sciences in Prague in 1978.

Presently, he works as professor of materials science and chemistry in the Institute of Materials Science and Engineering of the Faculty of Mechanical Engineering and in the Institute of Materials Chemistry of the Faculty of Chemistry.

In his research work he focuses on the study of advanced inorganic and composite materials (bioceramics, engineering ceramics, nanoceramics, electrochemical and catalytic ceramics), on methods for the preparation of ceramic materials (sol–gel synthesis, injection moulding, CIP, electrophoresis, extrusion) and on the study of high-temperature processes in ceramic materials and in reactive alloys.

He has authored over 60 scientific papers presented in international journals and at conferences, 35 scientific and research papers in Czech scientific journals, conferences and seminars, 2 patents, 40 research reports, and 20 projects of applied research. He is a member of five scientific societies (American Ceramic Society, Materials Research Society, Electrochemical Society, Czech Silicate Society, and Czech Society for Advanced Materials).

PUBLIKACE II

Available online at www.sciencedirect.com

ScienceDirect

Journal of the European Ceramic Society 34 (2014) 3365–3371

www.elsevier.com/locate/jeurceramsoc

Influence of anionic stabilization of alumina particles in 2-propanol medium on the electrophoretic deposition and mechanical properties of deposits

Daniel Drdlik [a,*], Eva Bartonickova [b,1], Hynek Hadraba [c,2], Jaroslav Cihlar [a,3]

[a] CEITEC – Central European Institute of Technology, Brno University of Technology, Technicka 10, Brno 61600, Czech Republic
[b] Materials Research Centre, Faculty of Chemistry, Brno University of Technology, Purkynova 464/118, Brno 61200, Czech Republic
[c] CEITEC IPM, Institute of Physics of Materials, Academy of Sciences of the Czech Republic, Zizkova 513/22, Brno 61662, Czech Republic

Available online 13 May 2014

Abstract

The ceramic dispersions were prepared using 0.85, 1.70, 4.25, 12.75 or 21.25 wt.% of monochloroacetic, dichloroacetic or trichoroacetic acid, 15 wt.% alumina and 2-propanol. The mechanism of anionic stabilization in 2-propanolic media was described. Alumina green bodies were prepared from the stable dispersion via electrophoretic deposition (EPD). It was found that increasing dispersion conductivity significantly influenced the EPD yields. The most effective electrophoretic depositions were performed from dispersions with conductivity in range 4.0–5.3 × 10^{-4} S m^{-1}. Deposits with the highest green density were prepared from the dispersion stabilized by trichloroacetic acid. This behavior was explained by low voltage drop during deposition. The surface roughness was high at low dispersion conductivity and with increasing acid concentration in dispersion the surface of deposits was smoother. The mechanism of particle arrangement in deposit was discussed. Influence of stabilizer amount in the dispersion on the hardness and fracture toughness was described.
© 2014 Elsevier Ltd. All rights reserved.

Keywords: Anionic stabilization; Electric conductivity; Alumina; Electrophoretic deposition

1. Introduction

Electrophoretic deposition (EPD) is an ordinarily used ceramics shaping method utilizing the deposition of ceramic particles from stable dispersions via electric current. This method enables fabrication of fiber composites, laminates, functionally graded materials, thin/thick films, etc., thanks to its simplicity, low cost and versatility.[1–6] EPD can be divided into two processes: electrophoresis and deposition.[7] The electrophoresis is a motion of charged particles through the dispersion and the deposition is an agglomeration of particles near the electrode surface. It is commonly accepted that composition of dispersion has a decisive effect on the physical properties of deposits prepared by electrophoretic deposition.[8]

The organic solvents are used more often than the aqueous solvents for preparation of stable dispersions, because of the electrolysis of water that negatively affects the EPD process.[9] In case of alcoholic solvents the main problem is the description of stabilizing mechanism. Cihlar et al.[10] showed that the control of charge on the surface of amphoteric oxides in 2-propanolic medium is based on addition of acidic or basic stabilizers and measurements of their electrophoretic mobility or ζ-potential, respectively. In this system the interaction of these oxides with acids produced a negative surface charge of oxides, while interactions of oxides with bases produced a positive charge and this phenomenon had a significant impact on the final properties of deposits.

The electric conductivity and its influence on the physical and mechanical properties of deposits is one of the key parameters of electrophoretic deposition, but it is still inadequately studied. Ferrari et al.[11] showed that with high electric conductivity of dispersion the particle motion was slow and the dispersion became unstable. Another result was the observation of electrophoretic deposition at different electric conductivity of dispersion. The obtained results indicated an optimal range of electric conductivity for successful deposition. Stappers et al.[12] studied the

* Corresponding author. Tel.: +420 541 143 340; fax: +420 541 143 202.
E-mail addresses: daniel.drdlik@ceitec.vutbr.cz (D. Drdlik), bartonickova@fch.vutbr.cz (E. Bartonickova), hadraba@ipm.cz (H. Hadraba), jaroslav.cihlar@ceitec.vutbr.cz (J. Cihlar).
[1] Tel.: +420 541 149 366.
[2] Tel.: +420 532 290 369; fax: +420 541 218 657.
[3] Tel.: +420 541 143 383; fax: +420 541 143 202.

http://dx.doi.org/10.1016/j.jeurceramsoc.2014.04.038
0955-2219/© 2014 Elsevier Ltd. All rights reserved.

uniformity of alumina deposits prepared from ethanol dispersion stabilized by HNO_3 at different electric conductivities. It was found that high electric conductivity of dispersion provided uniform deposits while its low electric conductivity resulted in non-uniform ones. This behavior was explained by resistance over the deposit which was caused by the interaction of ions with the deposit and by the depletion of ions at the deposition electrode. Another approach may be the study of influence of pH on the particle agglomeration of yttria stabilized zirconia (YSZ) in acetyl acetone dispersions examined by Xu et al.[13] The low level of an agglomeration of particles was reached at low pH of dispersion, i.e. at high electric conductivity, and the deposit had a high green density. The optimal range of dispersion pH for preparation of deposits with high green density was observed too. In the work of Guo et al.[8], the electrophoretic deposition of YSZ from ethanol–acetyl acetone dispersion stabilized by HCl was made. In this work the mechanism of arrangement of ceramic particles due to pH and electric conductivity was studied. The dispersion composition and conditions of electrophoretic deposition for receiving highest green density were presented within this work.

In the present work, the influence of ceramic dispersion on physical and mechanical properties of deposits prepared by electrophoretic deposition was studied. 2-propanolic dispersion containing submicroscopic particles of alumina anionically stabilized by chloro derivatives of acetic acid were prepared. Addition of monochloroacetic acid, dichloroacetic acid or trichloroacetic acid ensured different electric conductivity in concentrated dispersions. From stable dispersion were prepared alumina deposits by EPD. The yields after EPD, green density and density of sintered bodies were evaluated. The influence of electric conductivity of dispersions on the surface roughness and mechanical properties of sintered deposits were investigated.

2. Experimental

2.1. Materials

Ceramic dispersions used in this paper were composed of alumina (Al_2O_3, Malakoff, Ind., USA), 2-propanol solvent (p.a., Lachner, Czech Republic) and acidic stabilizers: monochloroacetic acid (MCAA, p.a., Aldrich, Germany), dichloroacetic acid (DCAA, p.a., Merck, Germany), trichloroacetic acid (TCAA, p.a., Merck, Germany). The size distribution and surface area of alumina particles were measured by laser diffraction analysis (Horiba LA-500, Japan) and Chembet 3000 machine (Quantachrome, USA), respectively. Alumina particles had the average particle size of 500 nm and the surface area about 7 m^2/g. Ceramic powder was dried before using at 100 °C for at least 2 h in drying chamber. 2-propanol was dried with the calcium metal and re-distilled for keeping water content on the minimum level.

2.2. Preparation of dispersions

Dispersions used for electrophoretic deposition were composed of 15 wt.% of alumina, 0, 0.85, 1.70, 4.25, 12.75, and 21.25 wt.% of acidic stabilizer and 2-propanol. Prepared dispersions were placed into ultrasonic field and mechanically stirred for 30 min. The electric conductivity of dispersions was measured by conductivity probe (InLab 710, Mettler Toledo, Switzerland) and Seven Compact Conductivity machine (S230, Mettler Toledo, Switzerland). The measurement of electrokinetic behavior of alumina dispersions was performed at 25 °C by Laser Doppler Velocimetry (LDV) using a Zetasizer 3000 HS (Malvern Instruments, UK). The Henry equation was used to calculate the ζ-potential.[14]

2.3. Electrophoretic deposition

The 80 ml of dispersion was placed into a vertical electrophoretic cell between two stainless steel electrodes having effective surface area of $S = 18.7\ cm^2$. The distance between electrodes was set to $d = 26$ mm. The electrophoretic deposition was carried out in constant current regime at $I = 5$ mA. To prevent the dispersion from sedimentation of ceramic particles the deposition was interrupted every 5 min and dispersion was mechanically stirred. At the same time the deposit mass was measured in solution of solvent and stabilizer like as was described elsewhere.[15]

2.4. Thermal treatment and testing of mechanical properties

The deposits were then dried at room temperature at least 24 h in desiccator. After drying the deposits were annealed at 800 °C for 1 h and pressurelessly sintered at 1500 °C for 2 h in air.

The relative density of the annealed deposits was established from soaking capacity and the relative density of the sintered deposits was established by the Archimedes method (EN 623-2). Samples were grinded, polished and thermally etched. The Vickers hardness *HV* of the prepared deposits was measured by the instrumented hardness tester (Z2.5, Zwick/Roel, Germany) by using load *F* of 5 kg (49 N). Values of indentation fracture toughness were calculated from crack length after hardness indentation. For calculation the Anstis equation was used[16]:

$$K_{Ic} = 0.018 \cdot \sqrt{\frac{E}{HV}} \cdot \frac{F}{c^{3/2}}, \quad (1)$$

where *F* is the applied load, *E* is Young's modulus, *HV* is the Vickers hardness, and *c* is the length of the surface trace of the crack measured from the center of the indent.

The microstructure of the sintered deposits was observed by using the FEG/FIB scanning electron microscope (Lyra 3, Tescan, Czech Republic).

3. Results and discussion

3.1. Mechanism of stabilization

The 2-propanolic dispersion used in this work for electrophoretic deposition of alumina particles contained stabilizing

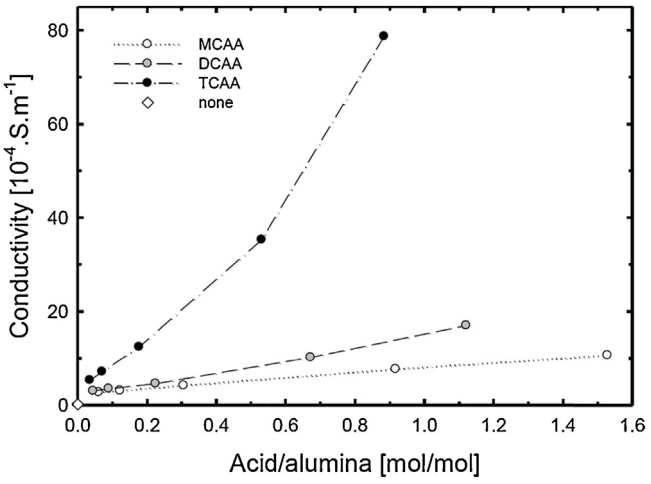

Fig. 1. Dependence of electric conductivity of dispersions on acid/alumina molar ratio (MCAA – monochloroacetic acid, DCAA – dichloroacetic acid, TCAA – trichloroacetic acid, none – without stabilization).

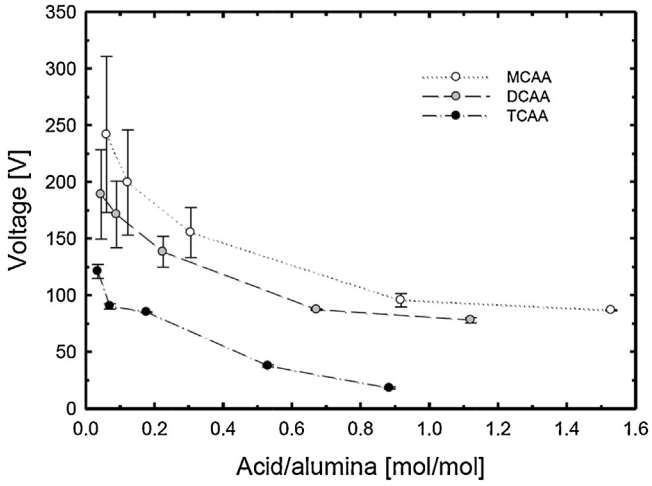

Fig. 2. Dependence of average voltage during electrophoretic deposition on acid/alumina molar ratio (MCAA – monochloroacetic acid, DCAA – dichloroacetic acid, TCAA – trichloroacetic acid).

additives of monochloroacetic acid, dichloroacetic acid or trichloroacetic acid. Chloro derivates of acetic acid interacted with alumina particles by an electrosteric mechanism similar to surface-active dispersants based on multifunctional hydroxycarboxylic acids and alkylamines.[10,17] In case of chloro derivatives of acetic acid the important role play two polar centers. The first one is the carboxyl group which can dissociate and the second one is C–Cl polar bond which enable the adsorption of the chloroacetic acid onto the surface of oxide particles. For this reason, we can assume that the formation of negative surface charge on the alumina particle surface in 2-propanolic medium is a result of adsorption process (i.e. donor–acceptor interactions) between the polar surface of alumina particles and molecules of difunctional weak acids. This mechanism was schematically described for monochloroacetic acid by Cihlar et al.[10]:

$$(=\mathrm{Al}-)_{surface} + \mathrm{ClCH_2COOH} \leftrightarrow (=\mathrm{Al}-)_{surface}\ldots\mathrm{ClCH_2COOH}, \quad (2)$$

$$(=\mathrm{Al}-)_{surface}\ldots\mathrm{ClCH_2COOH} + \mathrm{H_2O} \leftrightarrow (=\mathrm{Al}-)_{surface}\ldots\mathrm{ClCH_2COO^-} + \mathrm{H_3O^+}. \quad (3)$$

This proposed mechanism is in the modified form valid for stabilization of alumina particles by dichloroacetic acid and trichloroacetic acid.[10]

3.2. Electrophoretic deposition

In Fig. 1, the dependence between electric conductivity of dispersions and content of stabilizer (monochloroacetic acid – MCAA, dichloroacetic acid – DCAA and trichloroacetic acid – TCAA) added to the dispersions is given. The electric conductivity of dispersion increased nearly linearly with amount of acid added as was reported in previous works.[8,18] Differences in electric conductivity of the dispersions containing MCAA, DCAA and TCAA can be related to dissociation constants of the acids. The highest electric conductivities were found in the case of TCAA having the relatively high of dissociation constant ($pK_a = 0.66$, valid for water). On the other hand, by adding acids having lower dissociation constants (pK_a for MCAA is 2.86, for DCAA is 1.35, both valid for water) the electric conductivities were lowered.

In the previous work[10] it was shown that simply adding relatively small amount of MCAA, DCAA or TCAA acid led to achieving the similar ζ-potential values of alumina powder: ∼−39.5 mV for MCAA, ∼−37.5 mV for DCAA and ∼−36.5 mV for TCAA. These ζ-potentials were almost constant for the entire range of acid/alumina molar ratios. From this perspective the surface of alumina particles is saturated by a small amount of ions coming from acids. The rest of the acid concentration leads to increase of the dispersion electric conductivity by increase of ion concentration, i.e. ionic strength of dispersion.

This assumption was experimentally proven by measuring the voltage course during electrophoretic deposition results of which are given in Fig. 2 where the dependence of voltage during EPD on the acid concentration in the dispersion is plotted. The voltage decreases with increasing acid/alumina concentration which corresponds to the increasing electric conductivity of dispersion (as it is given in Fig. 1).

Final density of the deposits depends on the particle arrangement on the electrode while coagulating onto dense mass. Generally, high voltage applied between the electrodes causes high speed particle movement and results in low density deposits.[3] High velocity of particles reaching electrode make the dense arrangement of particles impossible. Also retrograde electro-osmotic flow of liquid phase damages growing deposit. The deposit growing onto electrode causes resistivity increasing during deposition and subsequent voltage drop. Ji et al.[19] showed that the final deposited mass increased with increasing the voltage drop during deposition and the final density of deposit was then decreased. From Fig. 2 it is obvious that the

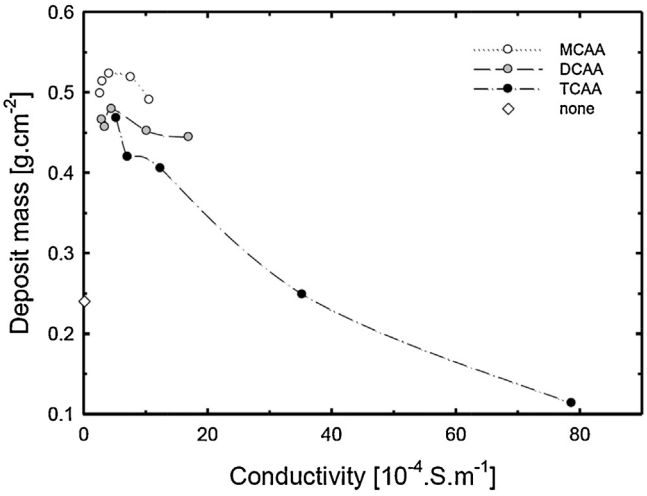

Fig. 3. Dependence of deposited mass on the electric conductivity of dispersion.

voltage drop decreases with increasing acid/alumina molar ratio and with decreasing value of dissociation constant. Acids having high dissociation constant can be easily dissociated which leads to increasing concentration of ions in dispersion.

In Fig. 3, the dependence of deposit mass on the electric conductivity of dispersion is given. The observed increase of the deposited mass with increasing dispersion conductivity was found in the case of MCAA and DCAA acids. From Fig. 3 is obvious that the most effective electrophoretic depositions were achieved using dispersions with electric conductivity in range 4.0–5.3 × 10^{-4} S m^{-1}. Deposited mass increase is connected to the electric conductivity of dispersion (see Fig. 1) and the high voltage drop (see Fig. 2). With increasing electric conductivity of dispersion (see Fig. 1) the green density of deposit was also slightly increased, as it is shown in Fig. 4.

From the point of view of the deposited mass there is an optimal concentration of stabilizing acid for which the electrophoretic deposition is most efficient. This was shown also in the work of Ferrari.[11] Important finding is that just high electric conductivity of dispersions containing the TCAA is not

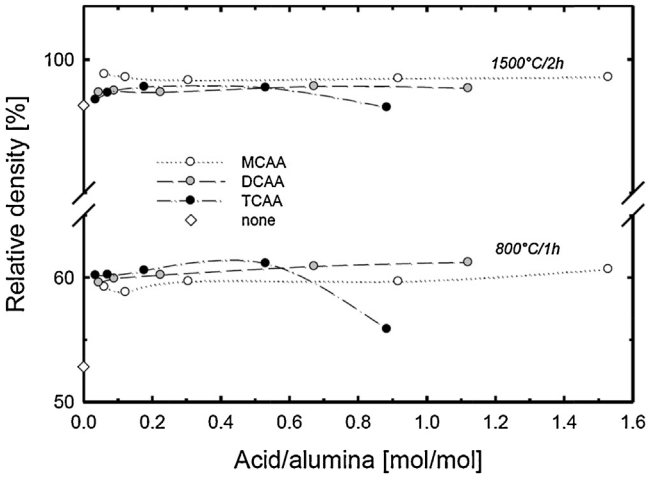

Fig. 4. Dependence of green and final density of deposits on acid/alumina molar ratio.

sufficient to achieve the high dense deposit. With increasing TCAA content the green density is decreasing, probably due to the high retrograde electro-osmotic flow of ions from the depositing electrode. On the other hand the dispersions stabilized with MCAA achieved the lowest green densities but the highest final densities. In the case of MCAA the concentration of charge carried ions in liquid was optimal for ensuring both stabilization of alumina particles and electric conductivity of dispersion.

The relative density of deposit prepared from the non-stabilized dispersion was lower than in the case of deposits prepared from the stabilized dispersions. This difference was probably caused by different type of stabilization. The charge on the alumina surface in non-stabilized dispersion can be described by acidobasic equilibrium between Al–OH groups on the particle surface and water traces in 2-propanol. From this point of view the ζ-potential was positive (41.52 mV).[10] The low electric conductivity and high voltage drop (1200 V) caused high velocity of alumina particles and low final density after annealing and sintering.

From the published data it can be concluded that the dispersion conductivity had a little significance in relation to final relative density of deposits. The greater importance of dispersion conductivity seems to be in particle rearrangement mechanism during electrophoretic deposition.

3.3. Structure of deposits

Particles reaching depositing electrode coagulate under Van der Waals forced to dense mass. For achieving this it is necessary to bring particles close to the each other. The earlier explanation of mechanism of electrophoretic deposition proposed by Hamaker and Verwey[20] presumed pressing particles just by external pressure of moving particles. Sarkar and Nicholson[7] added to the model a concept of coagulation of particles near depositing electrode caused by thinning of ionic atmosphere around particles. There is cooperation of two mechanisms near the depositing electrode: (i) coagulation of particles and (ii) external pressure of moving particles.

In Fig. 5, the dependence of deposit's surface roughness on electric conductivity of dispersions used for electrophoretic deposition is given. From Fig. 5 it is evident that the surface roughness of deposits strongly depends on the electric conductivity. The similar observation at high voltage of EPD was mentioned, but not clearly discussed, in the work of Ji et al.[19] The deposits obtained by EPD from dispersions containing TCAA had smooth surface. Opposite to this the deposits obtained by EPD from dispersions stabilized by small amount of MCAA and DCAA had high surface roughness (see photographs of surfaces given in Fig. 5) containing bulbs aligned to vertical strips (in the case of MCAA).

This behavior can be probably connected to the dependence of dispersion conductivity given in Fig. 1. The dispersions stabilized by TCAA contained several times more free ions than those stabilized by DCAA and MCAA. After increasing the MCAA and DCAA content (and thus content of free ions), the roughness of deposit surface decreased and we have obtained perfectly

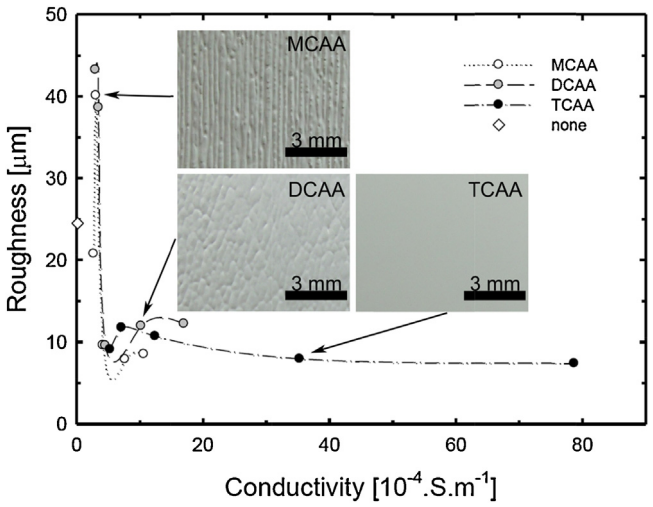

Fig. 5. Dependence of deposit surface roughness on the electric conductivity of dispersion.

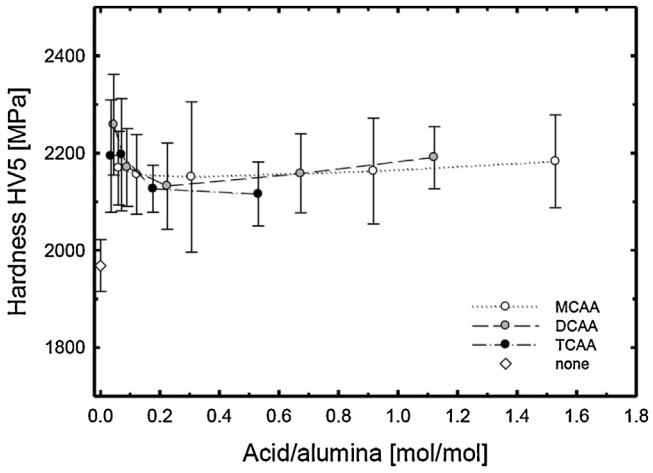

Fig. 7. Dependence of the deposit hardness on the acid/alumina molar ratio (MCAA – monochloroacetic acid, DCAA – dichloroacetic acid, TCAA – trichloroacetic acid, none – without stabilization).

smooth deposits. As it was discussed above, at low concentrations of stabilizers the surface of particles is fully covered by ions and the liquid contains relatively small amount of free ions acting as charge carriers. These dispersions contain probably also a large amount of coagulated particles caused development of bulbs in the deposits.

In Fig. 6 are given microstructures of bulbs found in fired deposits. The formation of bulbs is probably associated with the electric conductivity of dispersion, where at low electric conductivity there is relatively intense particle motion.[8,11] From Fig. 6 it is evident that development of the bulbs was caused by deposition of large precipitates. These precipitates were deposited on the electrode at low electric conductivity via power of electric current and pressure of outer layers of particles according to Hamaker[20] mechanism. These precipitates were then covered by alumina particles and copied to the outer layers of the deposits. These precipitates are still visible (in the fired microstructure) as badly-sintered areas with low density (see Fig. 6a). If electric conductivity of dispersion is relatively high than the particle motion is slow. In this case the large precipitates settle on the bottom of the electrophoretic cell due to gravity force. In Fig. 6b the deposit prepared from the high conductive dispersion (TCAA) is shown. The surface of this deposit was smooth and the precipitates were not observed in the structure.

3.4. Mechanical properties

Fig. 7 shows results of hardness measurement of deposits prepared from dispersions with increasing amount of MCAA, DCAA or TCAA. The curves indicate that the hardness values vary only slightly over the entire range of acid/alumina molar ratios. It was hard to decide about trends because the all measured values had large errors. However, hardness values seem to be higher by up to 100 HV at low acid/alumina molar ratios (low electric conductivity) when compared to the hardness values at high acid/alumina molar ratios. Another comparison of hardness can be done between the deposits prepared from dispersions with and without stabilizers (white rhombus in Fig. 7). Generally, the difference between the values of hardness is about 200 HV. This disproportion was caused by lower final density of

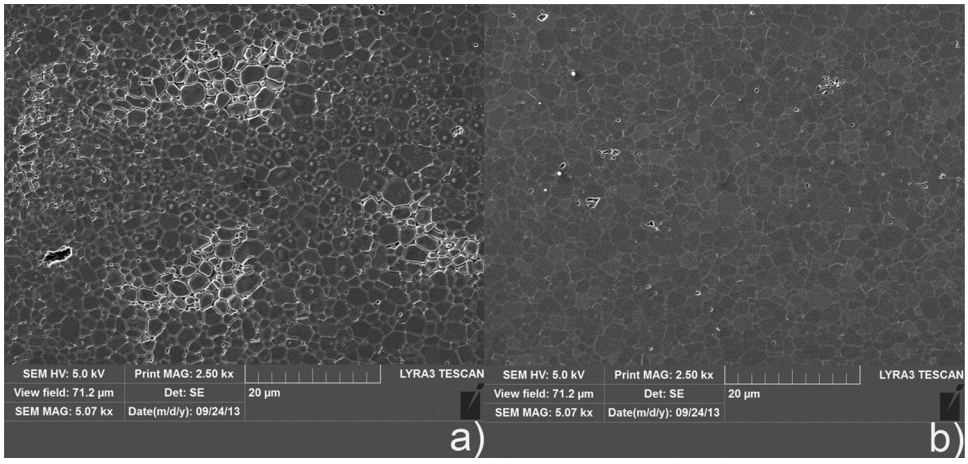

Fig. 6. Microstructures of sintered alumina deposited from dispersions with (a) low (DCAA) and (b) high (TCAA) electric conductivities.

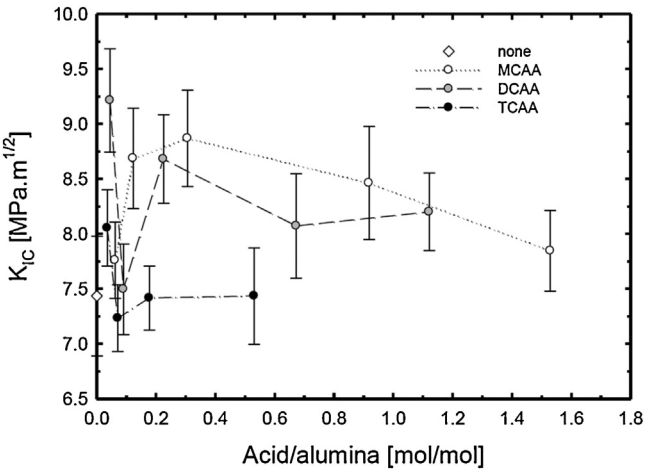

Fig. 8. Dependence of the indentation fracture toughness on the acid/alumina molar ratio (MCAA – monochloroacetic acid, DCAA – dichloroacetic acid, TCAA – trichloroacetic acid, none – without stabilization).

deposit, which was prepared from the non-stabilized dispersion (see Fig. 4).

The dependence of the indentation fracture toughness of deposits on the acid/alumina molar ratio is shown in Fig. 8. In the case of deposits prepared from dispersion stabilized by MCAA it was observed that indentation fracture toughness grows from 7.76 MPa m$^{1/2}$ to 8.87 MPa m$^{1/2}$ for acid/alumina molar ratios 0.06 and 0.31, respectively. With increasing acid amount or electric conductivity of the dispersion the indentation fracture toughness decreased. In the case of deposits prepared from dispersion stabilized by DCAA or TCAA the situation were similar. The highest values of indentation fracture toughness 9.21 MPa m$^{1/2}$ (DCAA) and 8.05 MPa m$^{1/2}$ (TCAA) were reached at relatively low acid/alumina molar ratios 0.05 and 0.04, respectively. At other higher molar ratios the indentation fracture toughness decreased for all three stabilizers.

This behavior can be connected with presence of structural defects described in Section 3.3. The badly sintered areas (see Fig. 6a) could cause crack tip branching and dissipation of crack energy. This effect could lead to underestimating the length of indentation cracks developed. Indentation fracture toughness values determined from the indentation crack length are then overestimated according to Eq. (1). Based on these data we can conclude that the best fracture toughness can be achieved for the deposits prepared from stable dispersions at low acid/alumina molar ratios. Very similar behavior was observed in the case of measurements of yields after EPD, roughness and hardness.

4. Conclusions

The aim of this paper was to describe the influence of properties of ceramic dispersions used for electrophoretic deposition on the physical and mechanical properties of prepared deposits. The 2-propanol dispersions containing submicrometric alumina particles and chloro derivatives of acetic acid as the anionic stabilizer were prepared. The electric conductivity of dispersions increased with increasing concentration of acids in 2-propanolic dispersions and significantly affected yields of electrophoretic deposition. The optimal conductivities of dispersions for most effective electrophoretic deposition were identified at lower acid/alumina molar ratios. It was found that the electric conductivity of dispersion had a little influence on the relative density of deposit. On the other hand the electric conductivity of dispersions had a great influence on the surface roughness of deposits. Observation of the microstructure of deposits showed that the relatively high rate of deposition occurred at low electric conductivity of dispersion. At these conditions the large precipitates were deposited. During deposition the precipitates were covered another alumina particles which resulted in rough deposit surface. The measurement of hardness and fracture toughness showed decreasing mechanical properties with increasing dispersion conductivity. The obtained experimental data suggest the existence of the optimal composition of dispersion for the preparation of alumina parts with very good physical and mechanical properties by electrophoretic deposition.

Acknowledgments

The work was supported by action COST LD12004 and realized in CEITEC – Central European Institute of Technology with research infrastructure supported by the project CZ.1.05/1.1.00/02.0068 financed from European Regional Development Fund and under project “Excellent Teams” No. CZ.1.07/2.3.00/30.0005.

References

1. Kaya C, Kaya F, Boccaccini AR, Chawla KK. Fabrication and characterisation of Ni-coated carbon fibre-reinforced alumina ceramic matrix composites using electrophoretic deposition. *Acta Mater* 2001;**49**:1189–97.
2. Chlup Z, Hadraba H, Slabakova L, Drdlik D, Dlouhy I. Fracture behaviour of alumina and zirconia thin layered laminate. *J Eur Ceram Soc* 2012;**32**:2057–61.
3. Hadraba H, Drdlik D, Chlup Z, Maca K, Dlouhy I, Cihlar J. Laminated alumina/zirconia ceramic composites prepared by electrophoretic deposition. *J Eur Ceram Soc* 2012;**32**:2053–6.
4. Hadraba H, Maca K, Cihlar J. Electrophoretic deposition of alumina and zirconia—II. Two-component systems. *Ceram Int* 2004;**30**:853–63.
5. Hvizdos P, Puchy V, Drdlik D, Cihlar J. Mechanical and tribological properties of Al_2O_3–ZrO_2 based composites prepared by EPD. *Key Eng Mater* 2012;**507**:191–5.
6. Hosomi T, Matsuda M, Miyake M. Electrophoretic deposition for fabrication of YSZ electrolyte film on non-conducting porous NiO–YSZ composite substrate for intermediate temperature SOFC. *J Eur Ceram Soc* 2007;**27**:173–8.
7. Sarkar P, Nicholson PS. Electrophoretic deposition (EPD): mechanisms, kinetics, and application to ceramics. *J Am Ceram Soc* 1996;**79**:1987–2002.
8. Guo FW, Shapiro IP, Xiao P. Effect of HCl on electrophoretic deposition of ytrria stabilized zirconia particles in organic solvents. *J Eur Ceram Soc* 2011;**31**:2005–11.
9. Besra L, Uchikoshi T, Suzuki TS, Sakka Y. Application of constant current pulse to suppress bubble incorporation and control deposit morphology during aqueous electrophoretic deposition (EPD). *J Eur Ceram Soc* 2009;**29**:1837–45.
10. Cihlar J, Drdlik D, Cihlarova Z, Hadraba H. Effect of acids and bases on electrophoretic deposition of alumina and zirconia particles in 2-propanol. *J Eur Ceram Soc* 2013;**33**:1885–92.

11. Ferrari B, Moreno R. The conductivity of aqueous Al_2O_3 slips for electrophoretic deposition. *Mater Lett* 1996;**28**:353–5.
12. Stappers L, Zhang L, Van Der Biest O, Fransaer J. The effect of electrolyte conductivity on electrophoretic deposition. *J Colloid Interface Sci* 2008;**328**:436–46.
13. Xu H, Shapiro IP, Xiao P. The influence of pH on particle packing in YSZ coatings electrophoretically deposited from a non-aqueous suspension. *J Eur Ceram Soc* 2010;**30**:1105–14.
14. Widegren J, Bergstrom L. The effect of acids and bases on the dispersion and stabilization of ceramic particles in ethanol. *J Eur Ceram Soc* 2000;**20**:659–65.
15. Hadraba H, Drdlik D, Chlup Z, Maca K, Dlouhy I, Cihlar J. Layered ceramic composites via control of electrophoretic deposition kinetics. *J Eur Ceram Soc* 2013;**33**:2305–12.
16. JIS R 1607. *Testing Methods for Fracture Toughness of High Performance Ceramics*; 1990.
17. Westby WS, Kooner S, Farries PM, Boother P, Shatwell RA. Processing of Nextel 720/mullite composition composite using electrophoretic deposition. *J Mater Sci* 1999;**34**:5021–31.
18. Hadraba H, Klimes J, Maca K. Crack propagation in layered Al_2O_3/ZrO_2 composites prepared by electrophoretic deposition. *J Mater Sci* 2007;**42**:6404–11.
19. Ji CZ, Lan WH, Xiao P. Fabrication of yttria-stabilized zirconia coatings using electrophoretic deposition: packing mechanism during deposition. *J Am Ceram Soc* 2008;**91**:1102–9.
20. Hamaker HC, Verwey EJW. The role of the forces between the particles in electrodeposition and other phenomena. *Trans Faraday Soc* 1940;**36**:180–5.

PUBLIKACE III

Journal of the Australian Ceramic Society (2020) 56:721–727
https://doi.org/10.1007/s41779-019-00390-y

RESEARCH

Surface roughness improvement of near net shaped alumina by EPD

Daniel Drdlik[1,2] · Zdenek Chlup[3] · Hynek Hadraba[3] · Katarina Drdlikova[1]

Received: 1 August 2018 / Revised: 12 March 2019 / Accepted: 26 June 2019 / Published online: 4 July 2019
© Australian Ceramic Society 2019

Abstract

The high surface roughness of thick and dense alumina deposits prepared by long-term electrophoretic deposition (EPD) caused by surface inhomogeneities could be eliminated by changing the suspension composition or EPD parameters. This work is aimed at the influence of the suspension composition, more precisely on the increase of electrical conductivity through indifferent electrolyte (lithium chloride) addition and its effect on the surface roughness. At first, the electrical conductivity was adjusted by the various amounts of the stabilisers of mono-, di- and trichloroacetic acid in the range of 0.85–21.25 wt%. It was demonstrated that deposits prepared from these suspensions were several millimetres thick, dense with a relatively low surface roughness ($R_a \approx$ 10 μm) only when the electrical conductivity was higher than 4 μS/cm. If a portion of the stabiliser was replaced with indifferent electrolyte, it resulted in the significantly smoother surface with a roughness $R_a \approx 2$ μm preserving all other benefits. Suggested optimization represents a useful novel approach for the preparation of dense, thick and near net-shaped alumina deposits with low surface roughness via EPD.

Keywords Alumina · Electrophoretic deposition · Electrical conductivity · Surface roughness · Thick layer

Introduction

The structural ceramics are still interesting attractive materials for the industry but their cost strongly determines their utilization in advanced applications instead of commonly used materials (e.g. metals and polymers) with lower durability. Therefore, the selection of the cost-effective ceramic material prepared by a simple processing method allowing minimal post-processing steps guaranties economic benefits in favour of ceramic products. From this point of view, it is more than adequate to manufacture products in a near net shape to eliminate a machining process before or after sintering of ceramic parts.

To fulfil such condition, the appropriate ceramic material and shaping method have to be selected. The most frequently used ceramic material is alumina due to its price to performance ratio. The determining advantage of alumina is its appropriate mechanical, chemical, electrical and optical properties and cost efficiency. The simple processing method which requires uncomplicated apparatus and enables preparation of the near net shape products is electrophoretic deposition (EPD) [1]. The EPD is based on the movement of ceramic particles dispersed in the stable colloidal suspension to the deposition electrode under the applied electric field. The particles agglomerate to the bulk layer on the electrode and replicate its shape. Therefore, EPD allows preparation of complex shapes.

The surface quality is the main parameter for near net shape ceramic productions. Unfortunately, some surface inhomogeneities such as bubbles, cracks or surface relief may occur during EPD, especially when the long-term deposition is applied. The bubble formation is mostly caused by the evolution of gasses by the electrolysis of water. In the aqueous suspension, the suppression of gas bubble evolution requires reduction of voltage during deposition or using of pulsed DC instead of the conventionally used continuous DC [2]. Another approach is a fabrication of bubble-free deposits from a non-aqueous suspension. The cracks may be formed in the deposits directly during the deposition as a consequence of high moving energy of ceramic particles or during drying after deposition. There are several solutions that can be taken to avoid the cracking: reduction of the electrical power transferred during deposition [3], changing the

✉ Daniel Drdlik
daniel.drdlik@ceitec.vutbr.cz

[1] CEITEC BUT, Brno University of Technology, Purkynova 123, 612 00 Brno, Czech Republic

[2] Institute of Materials Science and Engineering, Brno University of Technology, Technicka 2, 616 00 Brno, Czech Republic

[3] CEITEC IPM, Institute of Physics of Materials, Academy of Sciences of the Czech Republic, Zizkova 22, 616 62 Brno, Czech Republic

electrical conductivity of the suspension, using a chamber with the controlled atmosphere or using a substrate that shrinks with the deposit during drying [4].

The formation of the surface relief is still weakly discussed phenomena occurring during the EPD. In general, the surface quality can be adjusted by two approaches: (i) suspension optimization or and (ii) adjusting of deposition parameters. In the first approach, the uniformity, density and roughness of the deposit can be affected by the stability of the suspension, its concentration and the size of suspended particles [5–7]. In the second approach, the surface quality is influenced by the change in the deposition time, current density, substrate conductivity etc. [8–10, 7]. Mentioned approaches according to the literature were demonstrated especially during the preparation of thin films or coatings. On the other hand, surface quality control of thick deposits which becoming to be increasingly used for fabrication of bulk ceramics mainly layered structures is marginalized [11–13]. Although the EPD parameters and their optimisation are still widely studied [14–19], it is still necessary to examine the factors influencing the surface quality of the thick deposits or layers in laminates.

One of the key parameters for EPD, which is responsible for obtaining the deposit, is the abovementioned electrical conductivity of the suspension. For successful deposition of the ceramic particles, the electrical conductivity value must be in a given region and it is driven by the stabiliser content and solvent used [20]. A concentration of the stabiliser determines also the suspension stability expressed by the zeta potential. The zeta potential increases in absolute value with increasing the concentration of the stabiliser up to a certain value when the stability of the suspension is achieved. If the stabiliser dissociates in a solvent, the further addition results in electrical conductivity increase. However, the higher conductivity can be attained also by an appropriate amount of the indifferent electrolyte [21]. This approach can reduce the consumption of acidic or alkaline reagents and only increases the ionic strength of the solution without affecting overall stability [22, 23].

This work aims mainly on the preparation of several millimetres thick and dense alumina deposits with low surface roughness (R_a lower than 9 μm). The target of the paper is fulfilled through the variation of the suspension electrical conductivities by using various types of stabilisers and/or adding an amount of the indifferent electrolyte. The relationship between suspension properties, surface quality and physical properties of deposits is discussed.

Methods and procedures

Suspensions contained 15 wt% of alumina, a certain amount of stabiliser (0, 0.85, 1.70, 4.25, 12.75 or 21.25 wt%) and 2-propanol. Ceramic powder used in this study was alumina (Al_2O_3, Malakoff, Ind., USA) with a surface area of 7 m^2/g and an average particle size of 500 nm determined by a Chembet 3000 (Quantachrome, USA) and a laser diffraction analysis (Horiba LA-500, Japan), respectively. Monochloroacetic acid (MCAA, p.a., Aldrich, Germany), dichloroacetic acid (DCAA, p.a., Merck, Germany) and trichloroacetic acid (TCAA, p.a., Merck, Germany) were used as stabilisation aids. Moreover, lithium chloride (LiCl, p.a., Spolana, Czech Republic) was added to the selected suspensions in concentrations of 0.01, 0.15 and 0.30 g/L. The electric conductivity of suspensions was measured using a Seven Compact Conductivity (S230, Mettler Toledo, Switzerland) equipped with a conductivity probe InLab 710 (Mettler Toledo, Switzerland). After mixing all components, the suspensions were stirred for 30 min using a shaft stirrer at 200 rpm in the ultrasonic field with a power of 300 W.

The glass electrophoretic cell with two stainless steel electrodes (active surface = 18.7 cm^2) placed in the distance of 26 mm between them was used for the preparation of alumina deposits. The constant current mode of 5 mA was selected. The deposition was interrupted after every 5 min and the suspension was vigorously stirred by hand and the electrode with the deposit was weighted. The deposits were removed from electrodes after 24 h of drying and they were subsequently annealed at 800 °C for 1 h and sintered at 1500 °C for 2 h in ambient atmosphere.

The deposit densities were determined by the Archimedes method using the theoretical density to be 3.99 g/cm^3. The micrographs and roughness of deposit surfaces were obtained using a laser confocal microscope (Lext OLS3100, Olympus, Japan).

Results and discussion

The influence of stabiliser type on EPD and deposit properties

The stable suspension is necessary to obtain a thick deposit with high packing density on the deposition electrode during long-term EPD [24, 4]. To ensure this, a certain amount of MCAA, DCAA or TCAA was added into the suspension. Cihlar et al. showed that the stability of suspension using such type of stabiliser is already attained after adding a small amount of the acid (a zeta potential of − 39 mV for MCAA, − 38 mV for DCAA and − 37 mV for TCAA). Further addition of the stabiliser does not decrease the zeta potential anymore [25]. Therefore, it can be assumed that only part of acid stabilises the alumina particles and the excess of it increases the electrical conductivity of the suspension. The effect of higher electrical conductivity should manifest in the decrease of deposition mass and deposition rate [20].

Figure 1 shows the dependence of deposited mass on time of EPD from suspensions stabilised by different amounts of

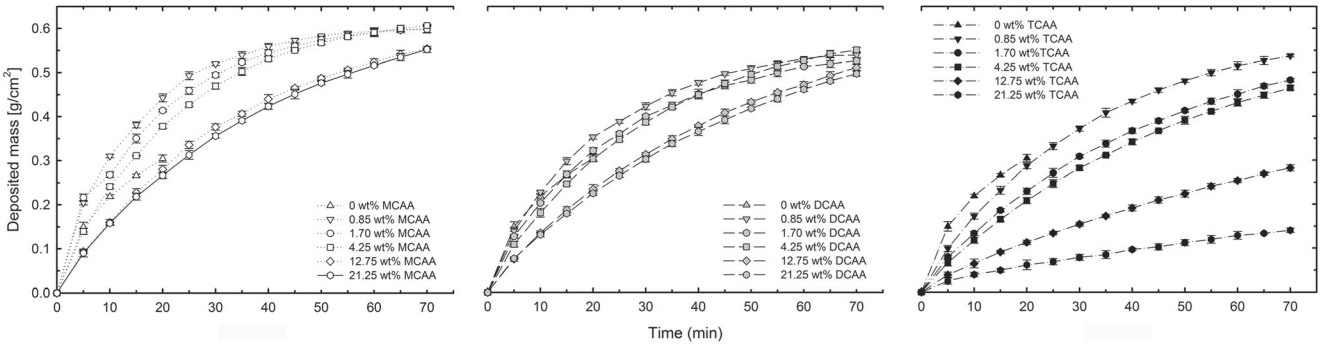

Fig. 1 Dependence of deposited mass on time of EPD from suspensions stabilised by different amounts of MCAA (left), DCAA (middle) and TCAA (right)

MCAA (white symbols), DCAA (grey symbols), and TCAA (black symbols). The deposition curves confirmed the decrease of the deposited mass with increased concentration of the stabiliser. This result is consistent with the measurements of the electrical conductivities in suspensions used as shown in Table 1. The electrical conductivity increased with the amount of acid in the suspension. The deposition rate given by the slope of the deposition curve was different for used stabilisers accordingly to their dissociation constants. It can be demonstrated for dissociation constants decreasing in a polar solvent (water, $pK_a = 2.86$ (MCAA); $pK_a = 1.35$ (DCAA); $pK_a = 0.66$ (TCAA)) as well as in the nonpolar solvents (methanol or ethanol are $pK_a = 7.80$ or 8.50 (MCAA) and $pK_a = 4.90$ or 5.70 (TCAA)) [26, 27]. The electrical conductivity increase led to the decrease in the deposition rate which negatively affected deposited mass [28, 29, 6], as shown in Fig. 1, and resulted in a less-effective deposition.

The change of the electrical conductivity also affected the deposit thicknesses (after drying) as given in Fig. 2. The highest thickness of 3.5 mm was obtained from the suspension stabilised by 0.85 wt% of MCAA. It can be considered as a very good result in comparison with literature data where the deposits with thickness up to 1 mm are mostly discussed [30–32, 7]. Nevertheless, a lower deposition rate resulted in a decrease of deposit thickness with the increased amount of the stabiliser. The deposit thickness decrease was also depended on the type of acid used. The thickness of the deposits decreased in the range of 2.6–3.5 mm (MCAA), 2.2–2.9 mm (DCAA) and 0.6–2.6 mm (TCAA), respectively, as the electrical conductivity of the suspensions increased.

Similarly, the lower velocity of alumina particles should lead to an improvement of the deposit density because particles should have enough time to occupy a favourable position in a deposited layer [33]. This effect is not clearly evident from the measured final densities listed in Table 1. On the contrary, the deposits prepared from suspensions stabilised by MCAA which had the lowest electrical conductivities, i.e. the high deposition rates, exhibited the highest densities. The more effective mechanism of particle arrangement proposed by Hamaker can be an explanation of this effect [34]. The high particle velocity at the lower electrical conductivities of the suspensions caused a high pressure in the external part of the created deposit; therefore, more efficient particle densification occurred.

From Table 1, it is obvious that the majority of prepared deposits had a very rough surface (the rough surface corresponds to the R_a value higher than 9 μm based on the laser profilometry measurements). The typical micrographs of the deposit surfaces are shown in Fig. 3. The morphology of the surface reliefs in shapes of (i) vertical lines (see Fig. 3a), (ii)

Table 1 Summary of electrical conductivity of suspensions stabilised by different amounts of MCAA, DCAA, TCAA and selected physical properties of deposits

Stabiliser (wt%)	MCAA			DCAA			TCAA		
	Electrical conductivity (μS/cm)	Final density (%)	R_a (μm)	Electrical conductivity (μS/cm)	Final density (%)	R_a (μm)	Electrical conductivity (μS/cm)	Final density (%)	R_a (μm)
0	0.16	98.28	24.50	0.16	98.28	24.50	0.16	98.28	24.50
0.85	2.70	99.45	40.66	2.98	98.76	43.26	5.29	98.49	10.10
1.70	3.06	99.33	40.11	3.46	98.83	38.64	7.10	98.75	11.75
4.25	4.16	99.22	9.59	4.55	98.77	9.56	12.41	98.97	10.70
12.75	7.64	99.29	7.88	10.19	98.99	11.95	35.30	98.94	7.92
21.25	10.61	99.33	8.50	17.00	98.92	12.21	78.70	98.20	7.37

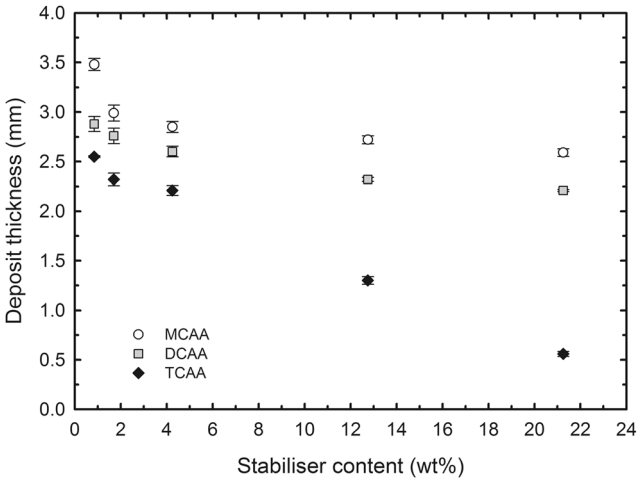

Fig. 2 Dependence of deposit thickness (after drying) on the content of MCAA, DCAA and TCAA in the suspensions

together connected spurs or (iii) humps (see Fig. 3b) was determined. This behaviour is probably caused by randomly ordered deposition of large agglomerates or aggregates at the low electrical conductivity of the suspension and their overlapping with other fine deposited particles [9, 35]. Moreover, a dynamic flow invoked due to turbulence located close to the deposited layer can also increase the surface roughness of the deposit [28, 36]. From Table 1, it is obvious that the surface roughness can be eliminated at the depositions using suspensions with higher electrical conductivities.

From this point of view, only suspensions containing MCAA or TCAA stabiliser in amounts equal or higher than 12.75 wt% allowed the preparation of deposits with the smooth surface (see Fig. 3c).

The best results in terms of the most effective EPD with the satisfactory deposition yields, thickness and the highest final density of the deposits were achieved using suspensions stabilised by MCAA. In the case of the higher content of the MCAA, the low surface roughness was obtained as well. On the other hand, the high content of the stabiliser in the suspension is undesirable because of its toxic nature.

The influence of electrolyte addition on EPD and properties of deposits

The excess of stabiliser which induced desired higher electrical conductivity was replaced by a small addition of the indifferent electrolyte (LiCl), which was added into the suspension containing the lowest amount of the stabiliser (0.85 wt% of MCAA). The effect of the indifferent electrolyte on the electrical conductivity was already described by Cruz et al. [22]. It can be supposed that the electrolyte affects the suspension stability not appreciably; i.e. the zeta potential could be slightly decreased due to thinning of the double layer [37]. As was expected, the electrolyte addition increased the electrical conductivity of the suspension and consequently decreased the deposition rate and deposited mass. This was due to a reduction in the voltage between the electrodes because of the increased ionic strength of the suspension. The dependence of deposited mass on time of EPD from the suspensions stabilised by different amounts of MCAA and with LiCl addition is shown in Fig. 4. It is obvious that the addition of 0.01 g/L of indifferent electrolyte led to a significant reduction of the deposited mass and the electrical conductivity of the suspension was increased from 2.70 to 7.04 μS/cm. For comparison, the black continuous line in Fig. 4 representing a typical deposition from the suspension stabilised by 12.75 wt% of MCAA is displayed. The deposited masses are similar for depositions from the suspension stabilised by 12.75 wt% of MCAA and suspension containing 0.85 wt% of MCAA with 0.01 g/L of the indifferent electrolyte. Therefore, the amount of the stabiliser

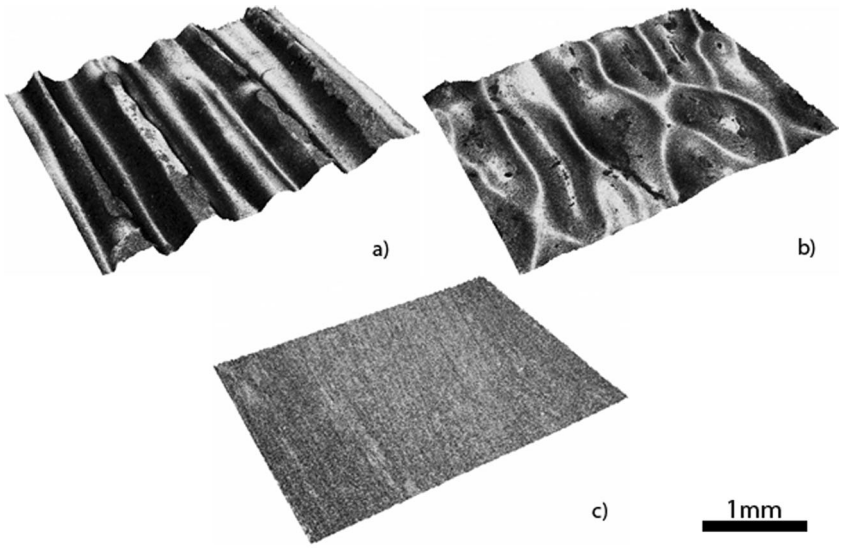

Fig. 3 3D topography of deposit surfaces prepared from suspensions containing 1.70 wt% of MCAA (**a**), 4.25 wt% of DCAA (**b**) and 21.25 wt% of TCAA (**c**)

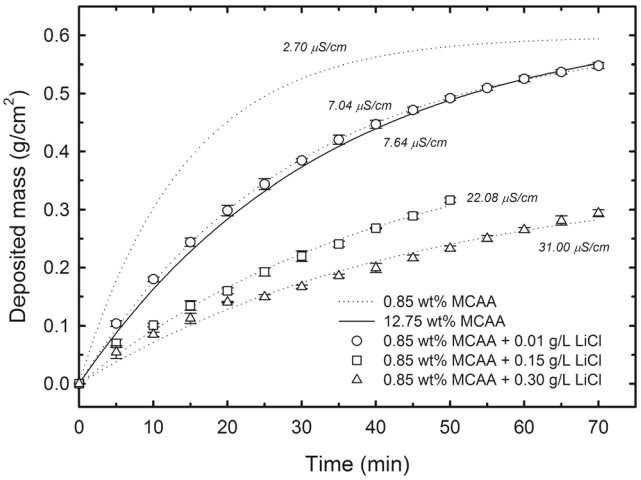

Fig. 4 Dependence of deposited mass on time of EPD from suspensions stabilised by different amounts of MCAA and with LiCl addition

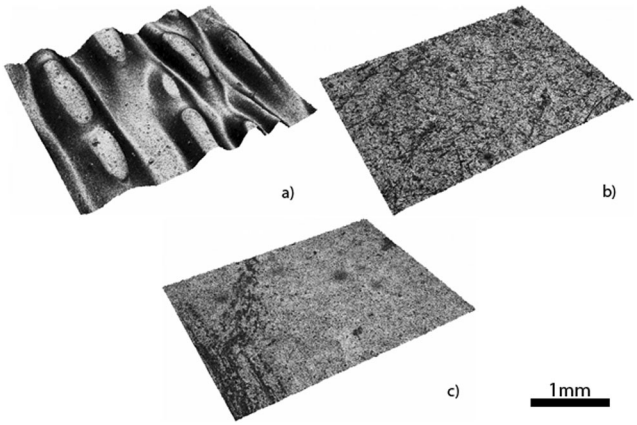

Fig. 5 3D topography of deposit surfaces prepared from suspensions containing 0.85 wt% of MCAA (**a**), 12.75 wt% of MCAA (**b**) and 0.85 wt% of MCAA (**c**) with 0.01 g/L of LiCl addition

can be effectively reduced while an appropriate value of the electrical conductivity of the suspension is preserved. Further increasing of indifferent electrolyte amount led to the subsequent reduction of the deposited mass and increase of the electrical conductivity up to 31.00 μS/cm.

To maintain efficient yields during deposition, it seems to be appropriate to use the lowest concentration of LiCl despite the slightly higher final density of the deposits prepared from the suspensions with higher LiCl addition. The final density of the deposit prepared from a suspension containing 0.01 g/L of LiCl was 99.22% whereas from suspensions enriched with 0.15 and 0.30 g/L of LiCl allowed preparation of deposits with the final densities of 99.33 and 99.45%, respectively. Here, the aforementioned first mechanism of the particles rearrangement during the deposition presumably took place. Likewise, the thickness of the deposits was almost the same as in the case of the deposit prepared from the suspension stabilised by 12.75 wt% of MCAA. As a consequence of increasing LiCl concentration in the suspension, the thickness decreased from 2.5 to 1.4 mm due to lower deposition yields (see Fig. 4).

Another benefit of indifferent electrolyte addition is clearly visible in Fig. 5 where the 3D topography of deposit surfaces prepared from suspensions containing (a) 0.85 wt% of MCAA, (b) 12.75 wt% of MCAA and (c) 0.85 wt% of MCAA with 0.01 g/L of LiCl are displayed. The surface roughness of the deposit prepared from suspensions containing only 0.85 wt% of MCAA was 34.96 μm (see Fig. 5a). When the deposition rate slows down due to stabiliser addition as a result of the electrical conductivity increase, then the surface roughness of such deposit was 7.88 μm (see Fig. 5b). Furthermore, the replacement of the portion of the stabiliser with indifferent electrolyte resulted in the smoother surface roughness of 2.21 μm (see Fig. 5c). The proposed approach could be considered as an effective tool for preparation of dense and thick alumina deposits with low surface roughness via EPD.

Conclusions

The preparation of thick and dense alumina deposits with low surface roughness via EPD was studied. The alumina particles dispersed in 2-propanol suspensions stabilised by monochloroacetic acid (MCAA), dichloroacetic acid (DCAA) or trichloroacetic acid (TCAA) were stable in the chosen concentration range (0.85–21.25 wt%) and they allowed fabrication of deposits with a thickness exceeding several millimetres. The higher amount of stabiliser in the suspension resulted in an increase of the electrical conductivity; i.e. deposition rate decreased. Consequently, the surface roughness was reduced. The indifferent electrolyte (LiCl) was added to substitute relative high content of the stabiliser in the suspension. Only a small amount of LiCl (0.01 g/L) dispersed in a suspension containing 0.85 wt% of MCAA resulted to the preparation of dense (final density of 99.22%) and thick (2.5 mm) alumina deposits with a smooth surface (surface roughness of 2.21 μm). The proposed modification of the suspension allows electrophoretic deposition of alumina deposits with low surface roughness, high final density and sufficient thickness suitable for a cost-effective near net shape ceramic production.

Funding information The authors acknowledge the support of the Grant Agency of the Czech Republic under grant no. 17-08153S. This research was also carried out under the project CEITEC 2020 (LQ1601) with financial support from the Ministry of Education, Youth and Sports of the Czech Republic under the National Sustainability Programme II.

Compliance with ethical standards

Conflict of interest The authors declare that they have no conflict of interest.

References

1. Sarkar, P., Nicholson, P.S.: Electrophoretic deposition (EPD): mechanisms, kinetics, and application to ceramics. J. Am. Ceram. Soc. **79**(8), 1987–2002 (1996). https://doi.org/10.1111/j.1151-2916.1996.tb08929.x
2. Besra, L., Uchikoshi, T., Suzuki, T.S., Sakka, Y.: Application of constant current pulse to suppress bubble incorporation and control deposit morphology during aqueous electrophoretic deposition (EPD). J. Eur. Ceram. Soc. **29**(10), 1837–1845 (2009). https://doi.org/10.1016/j.jeurceramsoc.2008.07.031
3. Tahmasbi Rad, A., Solati-Hashjin, M., Osman, N.A.A., Faghihi, S.: Improved bio-physical performance of hydroxyapatite coatings obtained by electrophoretic deposition at dynamic voltage. Ceram. Int. **40**(8, Part B), 12681–12691 (2014). https://doi.org/10.1016/j.ceramint.2014.04.116
4. Besra, L., Liu, M.: A review on fundamentals and applications of electrophoretic deposition (EPD). Prog. Mater. Sci. **52**(1), 1–61 (2007). https://doi.org/10.1016/j.pmatsci.2006.07.001
5. Diba, M., Fam, D.W.H., Boccaccini, A.R., Shaffer, M.S.P.: Electrophoretic deposition of graphene-related materials: a review of the fundamentals. Prog. Mater. Sci. **82**, 83–117 (2016). https://doi.org/10.1016/j.pmatsci.2016.03.002
6. Ferrari, B., Moreno, R.: Electrophoretic deposition of aqueous alumina slips. J. Eur. Ceram. Soc. **17**(4), 549–556 (1997). https://doi.org/10.1016/S0955-2219(96)00113-6
7. Milani, M., Zahraee, S.M., Mirkazemi, S.M.: Influence of electrophoretic deposition parameters on pore size distribution of doped nano alumina plates. Ceramics-Silikáty. **60**(4), 299–307 (2016). https://doi.org/10.13168/cs.2016.0045
8. Hasanpoor, M., Aliofkhazraei, M., Delavari, H.,.H.: In-situ study of mass and current density for electrophoretic deposition of zinc oxide nanoparticles. Ceram. Int. **42**(6), 6906–6913 (2016). https://doi.org/10.1016/j.ceramint.2016.01.076
9. Javidi, M., Javadpour, S., Bahrololoom, M.E., Ma, J.: Electrophoretic deposition of natural hydroxyapatite on medical grade 316L stainless steel. Mater. Sci. Eng. C. **28**(8), 1509–1515 (2008). https://doi.org/10.1016/j.msec.2008.04.003
10. Meng, X., Kwon, T.Y., Yang, Y., Ong Joo, L., Kim, K.H.: Effects of applied voltages on hydroxyapatite coating of titanium by electrophoretic deposition. J Biomed Mater Res B Appl Biomater. **78B**(2), 373–377 (2006). https://doi.org/10.1002/jbm.b.30497
11. Hadraba, H., Chlup, Z., Drdlik, D., Cihlar, J.: Micro-fibres containing composites prepared by EPD. J. Eur. Ceram. Soc. **36**(2), 365–371 (2016). https://doi.org/10.1016/j.jeurceramsoc.2015.07.031
12. Maca, K., Pouchly, V., Drdlik, D., Hadraba, H., Chlup, Z.: Dilatometric study of anisotropic sintering of alumina/zirconia laminates with controlled fracture behaviour. J. Eur. Ceram. Soc. **37**(14), 4287–4295 (2017). https://doi.org/10.1016/j.jeurceramsoc.2017.04.030
13. Hung, C.-W., Chang, C.-H., Chen, W.-C., Chen, C.-C., Chen, H.-I., Tsai, Y.-T., Tsai, J.-H., Liu, W.-C.: A Pt/AlGaN/GaN heterostructure field-effect transistor (HFET) prepared by an electrophoretic deposition (EPD)-gate approach. Solid State Electron. **124**, 5–9 (2016). https://doi.org/10.1016/j.sse.2016.06.011
14. Keller, F., Nirschl, H., Dörfler, W., Woldt, E.: Efficient numerical simulation and optimization in electrophoretic deposition processes. J. Eur. Ceram. Soc. **35**(9), 2619–2630 (2015). https://doi.org/10.1016/j.jeurceramsoc.2015.02.031
15. Michaud, X., Shi, K., Zhitomirsky, I.: Electrophoretic deposition of LiFePO4 for Li-ion batteries. Mater. Lett. **241**, 10–13 (2019). https://doi.org/10.1016/j.matlet.2019.01.032
16. Esfahani, S.L., Rouhani, S., Ranjbar, Z.: Optimization the electrophoretic deposition fabrication of graphene-based electrode to consider electro-optical applications. Surf. Interfaces. **9**, 218–227 (2017). https://doi.org/10.1016/j.surfin.2017.10.001
17. Song, G., Xu, G., Quan, Y., Yuan, Q., Davies, P.A.: Uniform design for the optimization of Al2O3 nanofilms produced by electrophoretic deposition. Surf. Coat. Technol. **286**, 268–278 (2016). https://doi.org/10.1016/j.surfcoat.2015.12.039
18. Drdlik, D., Moravek, T., Rahel, J., Stupavska, M., Cihlar, J., Drdlikova, K., Maca, K.: Electrophoretic deposition of plasma activated sub-micron alumina powder. Ceram. Int. **44**(8), 9787–9793 (2018). https://doi.org/10.1016/j.ceramint.2018.02.215
19. Ervina, J., Ghaleb, Z.A., Hamdan, S., Mariatti, M.: Colloidal stability of water-based carbon nanotube suspensions in electrophoretic deposition process: effect of applied voltage and deposition time. Compos. A: Appl. Sci. Manuf. **117**, 1–10 (2019). https://doi.org/10.1016/j.compositesa.2018.11.002
20. Ferrari, B., Moreno, R.: The conductivity of aqueous Al2O3 slips for electrophoretic deposition. Mater. Lett. **28**(4), 353–355 (1996). https://doi.org/10.1016/0167-577X(96)00075-4
21. Lefrou, C., Fabry, P., Poignet, J.C.: Electrochemistry: the Basics, with Examples. Springer, Berlin Heidelberg (2012)
22. Cruz, R.C.D., Reinshagen, J., Oberacker, R., Segadães, A.M., Hoffmann, M.J.: Electrical conductivity and stability of concentrated aqueous alumina suspensions. J. Colloid Interface Sci. **286**(2), 579–588 (2005). https://doi.org/10.1016/j.jcis.2005.02.025
23. Liu, X., Maki-Arvela, P., Aho, A., Vajglova, Z., Gun'ko, V.M., Heinmaa, I., Kumar, N., Eranen, K., Salmi, T., Murzin, D.Y.: Zeta potential of beta zeolites: influence of structure, acidity, pH, temperature and concentration. Molecules (Basel, Switzerland). **23**(4), (2018). https://doi.org/10.3390/molecules23040946
24. Krüger, H.G., Knote, A., Schindler, U., Kern, H., Boccaccini, A.R.: Composite ceramic-metal coatings by means of combined electrophoretic deposition and galvanic methods. J. Mater. Sci. **39**(3), 839–844 (2004). https://doi.org/10.1023/B:JMSC.0000012912.96350.d2
25. Cihlar, J., Drdlik, D., Cihlarova, Z., Hadraba, H.: Effect of acids and bases on electrophoretic deposition of alumina and zirconia particles in 2-propanol. J. Eur. Ceram. Soc. **33**(10), 1885–1892 (2013). https://doi.org/10.1016/j.jeurceramsoc.2013.02.017
26. Safarík, L., Stránský, Z.: Titrimetric Analysis in Organic Solvents. Elsevier, Amsterdam (1986)
27. Izutsu, K.: Electrochemistry in Nonaqueous Solutions. Wiley, (2009)
28. Ji, C., Lan, W., Xiao, P.: Fabrication of yttria-stabilized zirconia coatings using electrophoretic deposition: packing mechanism during deposition. J. Am. Ceram. Soc. **91**(4), 1102–1109 (2008). https://doi.org/10.1111/j.1551-2916.2008.02261.x
29. Guo, F., Shapiro, I.P., Xiao, P.: Effect of HCl on electrophoretic deposition of yttria stabilized zirconia particles in organic solvents. J. Eur. Ceram. Soc. **31**(14), 2505–2511 (2011). https://doi.org/10.1016/j.jeurceramsoc.2011.02.027
30. Anné, G., Vanmeensel, K., Neirinck, B., Van der Biest, O., Vleugels, J.: Ketone-amine based suspensions for electrophoretic deposition of Al2O3 and ZrO2. J. Eur. Ceram. Soc. **26**(16), 3531–3537 (2006). https://doi.org/10.1016/j.jeurceramsoc.2006.01.019
31. Hirata, Y., Nishimoto, A., Ishihara, Y.: Forming of alumina powder by electrophoretic deposition. J. Ceram. Soc. Jpn. International ed. **99**(2), 105–109 (1991)
32. Kreethawate, L., Larpkiattaworn, S., Jiemsirilers, S., Besra, L., Uchikoshi, T.: Application of electrophoretic deposition for inner surface coating of porous ceramic tubes. Surf. Coat. Technol. **205**(7), 1922–1928 (2010). https://doi.org/10.1016/j.surfcoat.2010.08.069
33. Basu, R.N., Randall, C.A., Mayo, M.J.: Fabrication of dense zirconia electrolyte films for tubular solid oxide fuel cells by

electrophoretic deposition. J. Am. Ceram. Soc. **84**(1), 33–40 (2001). https://doi.org/10.1111/j.1151-2916.2001.tb00604.x
34. Hamaker, H.C., Verwey, E.J.W.: The role of the forces between the particles in electrodeposition and other phenomena. Trans. Faraday Soc. **36**, 180–185 (1940)
35. Zhitomirsky, I., Gal-Or, L.: Electrophoretic deposition of hydroxyapatite. J. Mater. Sci. Mater. Med. **8**(4), 213–219 (1997)
36. Trau, M., Seville, D.A., Aksay, I.A.: Field-induced layering of colloidal crystals. Science. **272**(5262), 706–709 (1996)
37. Meyers, D.: Surfaces, Interfaces, and Colloids, vol. 2. Wiley-VCH, New York (1999)

Publisher's note Springer Nature remains neutral with regard to jurisdictional claims in published maps and institutional affiliations.

PUBLIKACE IV

Available online at www.sciencedirect.com

ScienceDirect

Ceramics International 41 (2015) 11202–11212

CERAMICS INTERNATIONAL

www.elsevier.com/locate/ceramint

Hydroxyapatite/zirconia-microfibre composites with controlled microporosity and fracture properties prepared by electrophoretic deposition

Daniel Drdlik[a,*], Martin Slama[b,1], Hynek Hadraba[c,2], Jaroslav Cihlar[a,3]

[a]CEITEC – Central European Institute of Technology, Brno University of Technology, Technicka 10, Brno 616 00, Czech Republic
[b]Institute of Materials Science and Engineering, Brno University of Technology, Technicka 2, Brno 616 00, Czech Republic
[c]CEITEC IPM, Institute of Physics of Materials, Academy of Sciences of the Czech Republic, Zizkova 513/22, Brno 616 62, Czech Republic

Received 27 January 2015; received in revised form 12 May 2015; accepted 14 May 2015
Available online 20 May 2015

Abstract

The stabilisation of hydroxyapatite (HA) particles in dispersions containing 2-propanol and monochloroacetic acid (MCAA) was studied. The surface of HA (Ca^{2+} cations) was stabilized by chemical adsorption of non-dissociated MCAA molecules via polar Cl atoms followed by dissociation (cleavage of the protons), which led to negative charging of the HA particles. Colloidal dispersions were milled for 0, 2 and 24 h in a planetary ball mill before electrophoretic deposition (EPD). The electrical conductivity of dispersions was modified by adding an indifferent electrolyte (LiCl) to obtain crack-free deposits with a smooth surface. HA and HA/t-ZrO_2 composites containing 2, 4, 8 and 16 wt% zirconia microfibres were prepared by EPD. HA decomposed into α-TCP, β-TCP and partially substituted calcium phosphate by the action of Li^+ cations during sintering. Elastic modulus and Vickers hardness of composites increased with milling time of the dispersions prior to EPD and decreased with the quantity of zirconia microfibres in the deposits, depending on the composite density. Fracture toughness of the composites was twice as high as that of pure HA due to the presence of orientated zirconia microfibres, finer microstructure, tougher β-TCP phase and pores. The two-week soaking in simulated body fluid revealed the bioactivity of all prepared materials.
© 2015 Elsevier Ltd and Techna Group S.r.l. All rights reserved.

Keywords: Hydroxyapatite; Zirconia; Composite; Electrophoretic deposition; Porosity

1. Introduction

Hydroxyapatite (HA) has widely been studied as a structural material for medical applications in the last decade. This material has a similar structural and chemical composition as human hard tissue and is biocompatible and is resorbable [1]. The main disadvantage of HA is its low strength and fracture toughness, which is a barrier for load-bearing applications [2]. To fulfil the function of HA as a biological and structural material, an appropriate compromise between its mechanical properties (strength, fracture toughness) and a microstructure suitable for biological applications (porosity) must be found.

The porosity inside a ceramic body can be closed, in the form of isolated pores or open, forming a net of interconnected pores. Interconnection between pores in a bone-substituting material is required to allow the transportation of nutrients to form new bone tissue; it allows for the migration of cells and removal of waste products [3–5]. In bone-substituting materials we can distinguish between macroporosity (pores >50 μm) and microporosity (pores <20 μm). Macroporosity allows osteogenesis through the transportation of cells and ions [3]. Due to its high surface area, microporosity allows protein adsorption [4], provides more preferential places for the interception and growth of cells [3] and accelerates osteointegration [4]. It is well known that porous ceramics exhibit poorer elastic, plastic properties and fracture resistance. An enhancement of the mechanical properties can be achieved by

*Corresponding author. Tel.: +420 541 143 340; fax: +420 541 143 202.
E-mail addresses: daniel.drdlik@ceitec.vutbr.cz (D. Drdlik), y116044@stud.fme.vutbr.cz (M. Slama), hadraba@ipm.cz (H. Hadraba), jaroslav.cihlar@ceitec.vutbr.cz (J. Cihlar).
[1]Tel.: +420 541 143 340; fax: +420 541 143 202.
[2]Tel.: +420 532 290 369; fax: +420 541 218 657.
[3]Tel.: +420 541 143 383; fax: +420 541 143 202.

http://dx.doi.org/10.1016/j.ceramint.2015.05.070
0272-8842/© 2015 Elsevier Ltd and Techna Group S.r.l. All rights reserved.

milling HA powder to reduce the particle size or by adding other materials (Al_2O_3, TiO_2, etc.) to serve as toughening phases [6–8]. In the case of adding a second phase, its biocompatibility must be ensured to allow the composite to be used in medical applications. The next important factor affecting the final porosity is the sintering temperature and the associated decomposition of HA. Increasing the sintering temperature leads to decreasing material porosity and thus influences the balance between the volumes of macroporosity and microporosity in a biomaterial. Moreover, HA decomposes into single phases: oxyapatite, α-tricalcium phosphate, β-tricalcium phosphate or into tetra-calcium phosphate (OA, α-TCP, β-TCP or TTCP) [9–11]. On the one hand, the decomposition is beneficial because α-TCP or β-TCP have a higher rate of biodegradation than HA [12,13]; however, the decomposition brings about increased material porosity, which can deteriorate the final mechanical properties [14]. The preparation method has the greatest influence on the porosity of biomaterials. The commonly used methods for the preparation of porous ceramic structures are microsphere burn-out, direct foaming, colloidal crystals method or rapid prototyping.

Another useful method for the preparation of porous HA can be electrophoretic deposition (EPD) [15]. It is a relatively simple and cheap method for the preparation of ceramic monoliths [16], functionally gradient materials [17], laminates [18,19] or thin films and layers [3] from a stable colloidal dispersions [20,21]. In recent years, attention has mostly been paid to the preparation of thin coatings and films of HA, α-TCP or β-TCP on ceramic or metal substrates via EPD. On the other hand, the preparation of thick deposits with interesting structural and mechanical properties has been neglected. Moreover, EPD is a suitable method for the preparation of porous biomaterials. Ma et al. [22] prepared a uniform crack-free HA scaffold with interconnected porosity by EPD. They experienced some inconvenience as the deposit was cracking during deposition. This problem was solved by repeated deposition. Generally, the presence of micro-cracks in HA materials is a frequent phenomenon, which has been solved by several authors [2,22,23].

The aim of this work was the preparation of thick HA reinforced with zirconia microfibres (ZF) with controlled microporosity. Stable dispersions consisting of a mixture of HA powder and ZF were prepared by colloidal milling. Electrical conductivity of the dispersions was modified to obtain deposits of controlled quality. Thick, porous, crack-free deposits without surface roughness were deposited by utilising EPD. The physical (density, porosity, microstructure, etc.) and mechanical (Vickers hardness, Young's modulus) properties of HA monoliths and HA/ZrO_2 composites were studied. The effect of ZF in the HA matrix on composite fracture toughness was examined. The prepared composites were also studied as a potential biomaterial for the replacement of living hard tissues.

2. Experimental

2.1. Materials

HA and polycrystalline yttria stabilized tetragonal ZF used for the preparation of the composites are listed in Table 1 and shown in Fig. 1. The surface area and particle size distribution of ceramic powders were measured using Chembet – 3000 (Fa Quantachrome, USA) and LA 950 (Horiba, Japan), respectively.

Table 1
Characteristics of materials used.

Chemical composition	Designation	Surface area (m^2/g)	Average particle size (μm)	Producer
$Ca_5(OH)(PO_4)_3$	HA	33.8	Diameter 10	Fluka, Switzerland
t-(Y)ZrO_2 fibres	ZF	8.0	Diameter 0.15–0.40/length 2–400	Pardam, Czech Republic

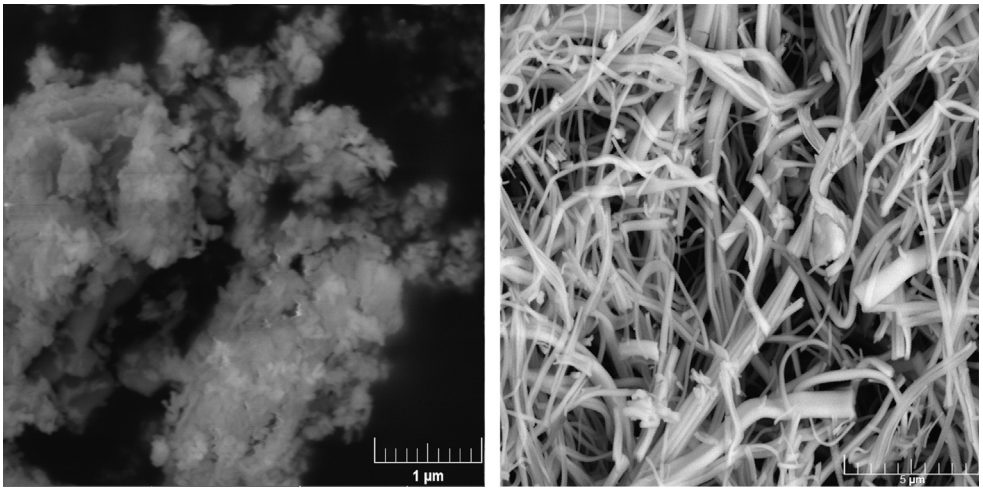

Fig. 1. Micrographs of hydroxyapatite powder (left) and tetragonal zirconia fibres (right).

2.2. Dispersion preparation

Dispersions contained 15 wt% of ceramic load (HA and ZF), 0.85–21.25 wt% of monochloroacetic acid (MCAA, p.a., Sigma-Aldrich, Germany) as a stabilizing aid and 84.15–63.75 wt% of 2-propanol (p.a., Lachner, Czech Republic) as a dispersion medium. The dispersion used for the preparation of HA/ZF composites contained 2, 4, 8 or 16 wt% ZF. After mixing all of the components, one set of dispersions was directly used for EPD (denoted as AM0) and the other two sets were milled in a planetary ball mill prior to EPD for 2 h (denoted as AM2) and 24 h (denoted as AM24). Zirconia milling elements of 5 mm in diameter and balls to powder milling ratio (BPR) of 11:1 were used. The milling ratio can be referenced elsewhere [14]. To prevent the HA and ZF particles from settling, the dispersions were ultrasonically agitated and mechanically stirred for 30 min prior to EPD. Lithium chloride (LiCl, p.a., Spolana, Czech Republic) as indifferent electrolyte in amounts of 0.05 g/L, 0.10 g/L, 0.15 g/L and 0.25 g/L was added into the dispersion to increase electrical conductivity. The electrical conductivity of the dispersions was measured at room temperature using a SevenCompact Conductivity S230 device (Mettler Toledo AG, Switzerland). The electrokinetic behaviour of the colloidal dispersions was measured at room temperature via LDV (Laser Doppler Velocimetry) using a Zetasizer 3000 HS device (Malvern Instruments, UK) on dispersions diluted by anhydrous 2-propanol. Henry's equation was used to calculate the zeta potential [24].

2.3. Electrophoretic deposition

EPD with vertical electrode arrangement under a constant current of 5 mA (current density of 0.27 mA cm^{-2}) was carried out. Stainless steel electrodes with polished surfaces and a surface area of 18.2 cm^2 were placed into a glass container and spaced 26 mm apart. During deposition lasting 40 min, a direct weight measurement of the deposit was performed according to [18].

2.4. Study of deposits

The deposits were dried at room temperature in a desiccator and then annealed and sintered in air at 600 °C for 2 h and 1250 °C for 3 h. The thermal stability and phase composition of the composites were determined using a Seiko TG/DTA 6300 thermogravimeter (+20 °C/min, Seiko Company, Japan) and X-ray diffraction (XRD) equipment with Cu Kα radiation (Smartlab, Rigaku, Japan), respectively. The average density of the deposits was determined by the Archimedes method (EN 623-2) from three measurements. The microstructure of materials prepared was observed using a Lyra3 scanning electron microscope (FEG/FIB, Tescan, Czech Republic). The linear intercept method was used to calculate the average grain size of the composites. After calculation, the values of grain size were multiplied by a shape correction factor of 1.56 [25]. Vickers hardness and indentation Young's modulus was determined by means of an instrumented hardness tester (Z2.5, Zwick/Roel, Germany). Indentation fracture toughness was determined using cracks propagating from corners of indents as [26]:

$$K_{Ic} = 0.018\left(E/HV\right)^{0.5}\left(P/c^{1.5}\right), \quad (1)$$

where E is Young's modulus, HV is Vickers hardness, P is the load and c is the length of the crack. Average values of E, HV and K_{IC} were evaluated from at least 10 independent indentation measurements.

Samples prepared from 2 and 24 h milled dispersions containing 0, 2, 8 and 16 wt% ZF were selected for biological activity testing. Biological activity was qualified after soaking the samples in simulated body fluid (SBF) for two weeks at 36.5 °C. The recipe for SBF was prepared according to the work of Kokubo et al. [27].

3. Results and discussion

3.1. Stabilisation of HA particles

Colloidal dispersions containing 2-propanol as the dispersing medium and monochloroacetic acid as a stabiliser were used for EPD of HA and HA/ZF composites. EPD and electrokinetic behaviour of 2-propanol dispersions of Al_2O_3 and ZrO_2 stabilized chloro derivatives of acetic acid have been previously studied and the results were published [28,29]. The electrokinetic behaviour of HA dispersions, whose properties are shown in Table 2, was studied in the same manner as in the work of Cihlar et al. [28].

The zeta potential of HA (HA AM0) in 2-propanol in the absence of MCAA was positive (+4.8 mV). After the addition of MCAA the positive charge of HA particles changed to negative (−31.4 mV) (see Table 2). We expect that this change occurred by the same mechanism that was proposed

Table 2
Electrokinetic properties of HA and HA/ZF colloidal dispersions.

Samples	Zeta potential (mV)	Electrophoretic mobility μ (μm cm V^{-1} s^{-1})
HA AM0[a]	+4.80	+0.04
HA AM0	−31.40	+0.24
HA AM2	−31.90	−0.22
HA AM24	−33.00	−0.25
HA/16ZF AM2	−32.20	−0.25
HA/16ZF AM24	−35.10	−0.27

[a]Without stabilising aid.

for alumina [28]. The molecules of chloroacetic acid have two polar centres, a carboxyl group (which can dissociate) and a C–Cl polar bond, which enable the adsorption of chloroacetic acid onto the surface of oxide particles. The MCAA molecule in the non-dissociated state is first adsorbed on the surface of HA (probably in the vicinity of Ca^{2+} cations) via a Cl atom with a partial negative charge, then MCAA dissociates (cleaves the proton) and the anion of MCAA bound to the HA particle gives it a negative charge. The mechanism can be described by Eqs. (2) and (3):

$$\left(Ca_5(PO_4)_3(OH)\right)_{surface} + ClCH_2COOH \rightarrow \left(Ca_5(PO_4)_3(OH)\right)_{surface} \ldots ClCH_2COOH, \quad (2)$$

$$\left(Ca_5(PO_4)_3(OH)\right)_{surface} \ldots ClCH_2COOH \rightarrow \left(Ca_5(PO_4)_3(OH)\right)_{surface} \ldots ClCH_2COO^- + H^+. \quad (3)$$

3.2. Colloidal milling

The dispersions containing HA powder were colloidally milled in a planetary ball mill (denoted as AM-automatic milling). The particle size distribution was observed to change with milling time (1, 2, 4, 6, 12 and 24 h) (see Fig. 2). The HA starting powder consisted of agglomerates (see Fig. 1) having an unimodal size distribution function with an average size of approximately 10 μm (solid grey line in Fig. 2). After colloidal milling the bimodal distribution of particle sizes in the dispersion was observed. The average size of agglomerates in the dispersion decreased with milling time (see the high peaks on the right) from approximately 3.50 μm to 750 nm for milling times of 1 and 24 h, respectively. The low peaks at 250 nm probably represent primary HA particles released from agglomerates during milling (compare with Fig. 1).

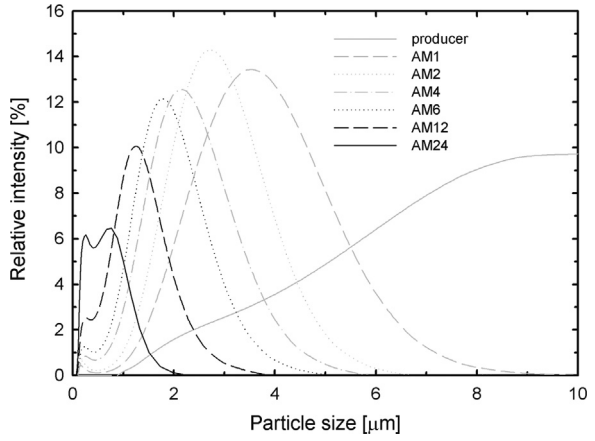

Fig. 2. Graph of the particle size distribution function of HA dispersions for different milling times.

3.3. Electrophoretic deposition

The set of dispersions consisting of 2-propanol, HA and only a minimal amount of stabiliser (0.85 wt% MCAA) were milled for 0, 2 or 24 h. The EPD of these dispersions led to deposits having a rough surface due to the low electrical conductivity of dispersions and thus high velocity of particles during the deposition (see Fig. 3a). This behaviour was observed for different material in a previous work [29]. Moreover, cracks developed during EPD in some cases, which led to the separation of the deposit from the electrode during deposition. We believe that the development of cracks is related to the high moving energy of particles. These particles create a pressure on the weakened spots of the deposit (micro-cracks, clusters of agglomerates, edges of deposit, etc.), causing an enlargement of the defects with increasing deposition time. The penetration of particles into the defect results in an optically observable crack. The problem can be overcome by adjusting the electrical conditions during deposition. Rad et al. [23] reduced the electrical power transferred during deposition at the cost of increased deposition time. Another approach consists of changing the electrical conductivity of the dispersion. The electrical conductivity of the dispersion stabilized with 0.85 wt% of MCAA was only 0.38 μS cm^{-2}. For this reason the concentration of monochloroacetic acid in the dispersion was raised up to

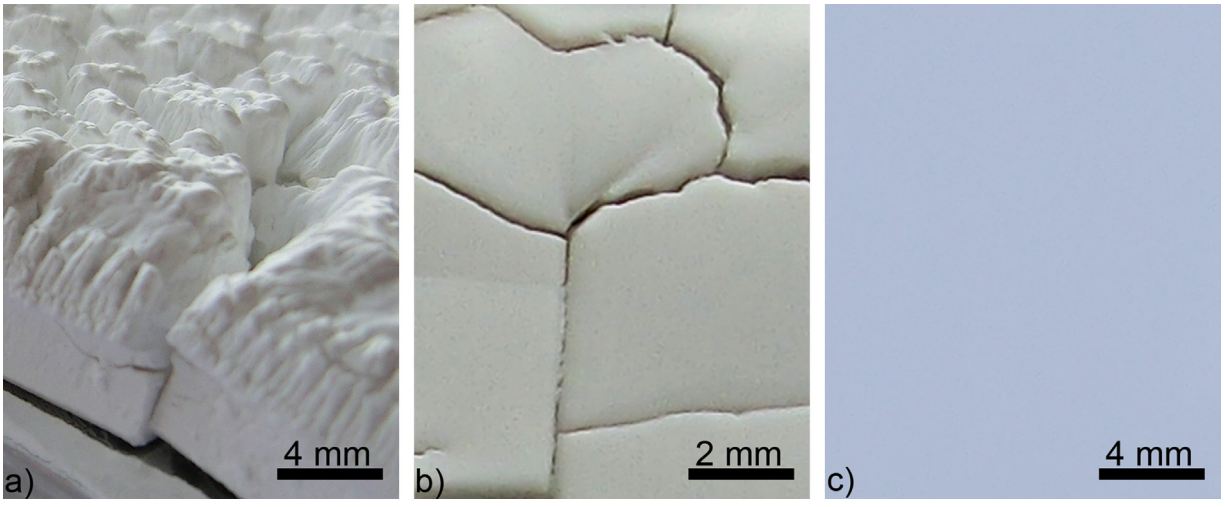

Fig. 3. Digital photos of deposit surfaces: a) side view of a deposit prepared from the dispersion containing 0.85 wt% MCAA; front view of deposits prepared from dispersions containing, b) 21.25 wt% MCAA, and c) 21.25 wt% MCAA and 0.10 g/L of LiCl.

21.25 wt%. The electrical conductivity of the dispersion grew with MCAA concentration: for 1.70 wt%, it was 0.93 μS cm^{-2}; for 4.25 wt%, 1.29 μS cm^{-2}; for 12.25 wt%, 3.76 μS cm^{-2}; for 21.25 wt%, 5.48 μS cm^{-2}. The increase in electrical conductivity led to a decrease in deposition rate and reduced deposition yield and surface roughness of the deposit. For further study the dispersion with 21.25 wt% of MCAA was selected.

The electrokinetic behaviour of this dispersion was measured for various milling times and quantities of ZF. The values of zeta potentials and electrophoretic mobility are listed in Table 2. The absolute values of the zeta potential of these dispersions were over 30 mV. The absolute zeta potentials of dispersions milled for 24 h were higher than the absolute zeta potential of dispersions milled for 2 h or that of non-milled dispersions. The addition of ZF slightly increased the absolute zeta potential. A possible reason for increased zeta potential as a results of long time milling and ZF addition could be explained by the increase of HA surface area after milling and high ZF surface area. It should be noted that statistical variance of the zeta potential values was caused by the low electrophoretic mobility in 2-propanol dispersions.

Smooth deposits obtained by deposition from a highly conductive dispersion containing 21.25 wt% MCAA still contained cracks (see Fig. 3b). The electrical conductivity of the dispersion was further increased by adding an indifferent electrolyte (LiCl). The indifferent electrolyte did not participate in the stabilisation but only increased the electrical conductivity of the dispersion. The measurement of the zeta potential supported this fact because a non-milled dispersion containing 2-propanol, HA and MCAA with an addition of LiCl had a negative zeta potential of −29.80 mV. This value is approximately 10% lower than for other dispersions in Table 2. The decrease in zeta potential was caused by electric double layer thinning due to dissociated ions of LiCl [30].

The time dependence of the HA mass deposited from dispersions stabilized by 21.25 wt% MCAA with added LiCl is shown in Fig. 4. The addition of LiCl had a significant impact on the decrease of the deposition rate up to a concentration of 0.10 g/L. The electrical conductivity of the dispersion increased from 5.48 μS cm^{-2} to 11.72 μS cm^{-2}. A minimal addition of 0.10 g/L of indifferent electrolyte into the dispersion resulted in

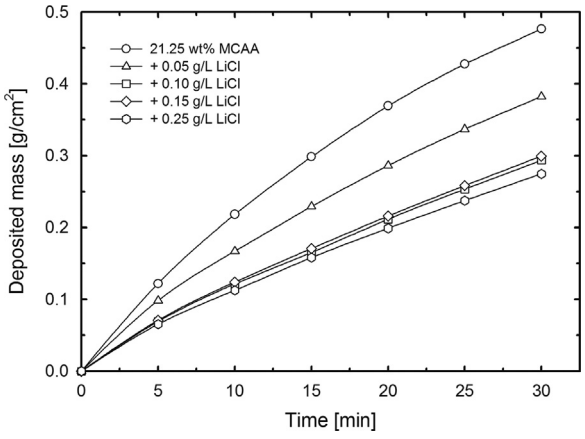

Fig. 4. Dependence of the deposited mass during EPD on time and indifferent electrolyte addition.

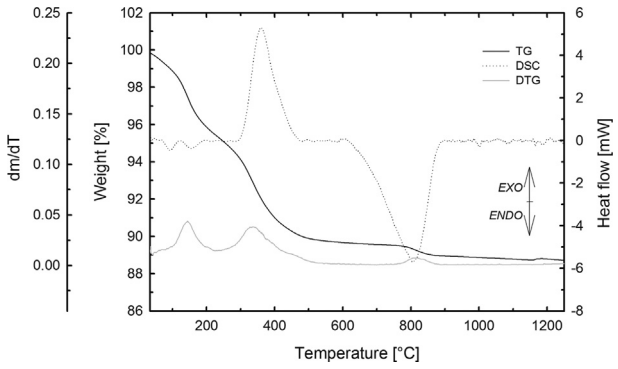

Fig. 5. Thermogravimetric analysis of the deposit prepared from HA milled for 24 h with 16 wt% ZF.

deposits having a smooth surface without cracks (see Fig. 3c). For further preparation of HA and HA/ZF deposits by EPD a dispersion was used that contained a maximum amount of MCAA and 0.10 g/L of LiCl. The electrical conductivity of these dispersions was approximately 10.59 μS cm^{-2}.

The addition of indifferent electrolyte to the dispersion used for EPD significantly improved the quality of the deposit obtained. On the other hand, LiCl may not be the best choice for potential application in medicine. However, for future experiments it could simply be replaced by any other environmentally friendly indifferent electrolyte (e.g., tetramethylammonium chloride).

3.4. Thermal stability of composites

The thermogravimetric analysis of a composite prepared from HA dispersion milled for 24 h and containing 16 wt% ZF is shown in Fig. 5. Three exo- and/or endo-thermic events were identified. The first one (80–200 °C) can be linked to the evaporation of water adsorbed on HA/ZF particles. The second exothermic peak (250–500 °C) was probably caused by the oxidation of monochloroacetic acid. The third endothermic peak observed in the temperature range of 610–900 °C was caused by the decomposition of HA into OA and TCP phases [11]. No additional thermal events were observed with the temperature increasing up to 1250 °C.

Results of an XRD analysis showed that the temperature of thermal treatment had a significant impact on the phase composition of the HA and HA/ZF composites (see Table 3). After annealing at 600 °C, no new phases were detected that would have been incurred by thermal decomposition of HA or solid state reaction (SSR) of HA with t-(Y)ZrO_2. After sintering at 1250 °C the thermal decomposition of HA took place in both samples. The HA sample decomposed into α-$Ca_3(PO_4)_2$ and β-$Ca_3(PO_4)_3$. The mechanism and kinetics of HA decomposition were proposed earlier by Cihlář [11]. The HA/ZF composite decomposed into α-$Ca_3(PO_4)_2$ and another trigonal phase structurally similar to the $Ca_{2.89}Mg_{0.11}(PO_4)_2$ compound that can be characterised as β-TCP partially substituted by Mg [31].

Instead of Mg the Li from LiCl (used as an indifferent electrolyte) was detected by EDS in the products of the solid state reaction. It can be assumed that the second identified

Table 3
Influence of temperature on the phase composition of HA and HA/ZF composites.

Sample composition before SSR (wt%)		Temperature of SSR	Sample composition after SSR (wt%)				
HA	t-ZrO_2	(°C)	HA	t-ZrO_2	α-TCP	β-TCP	Li, Ca–P
100		600	100				
100		1250			67	33	
84	16	600	83	17			
84	16	1250		17	52		31

phase was β-TPC partially substituted by Li^+ cations. The process of thermal decomposition of HA and solid state reaction of HA and t-(Y)ZrO_2 in the presence of Li^+ cations can be described by Eqs. (4)–(7):

$$2Ca_5(PO_4)_3OH \xrightarrow{\Delta T} Ca_{10}(PO_4)_6O + H_2O, \quad (4)$$

$$Ca_{10}(PO_4)_6O \xrightarrow{\Delta T} 3\alpha - Ca_3(PO_4)_2 + CaO, \quad (5)$$

$$Ca_{10}(PO_4)_6O \xrightarrow{xLi^+} 2\alpha - Ca_3(PO_4)_2 + Ca_{3-\frac{x}{2}}Li_x(PO_4)_2 + 1 + \frac{x}{2}CaO, \quad (6)$$

$$t - (Y)ZrO_2 + CaO \xrightarrow{\Delta T} t - (Y,Ca)ZrO_2. \quad (7)$$

CaO resulting from the HA decomposition was probably dissolved in the tetragonal lattice of ZF stabilized with yttria. The concentration of Ca in t-(Y,Ca)ZrO_2 was low and therefore t-(Y,Ca)ZrO_2 did not transform into the cubic phase.

3.5. Study of microstructure

The microstructure of HA and HA/ZF deposits prepared from dispersions milled for 0, 2 and 24 h is shown in Fig. 6. The influence of colloidal milling on the grain size and porosity of the deposits prepared is obvious as shown in Fig. 6 (compare with Table 4). The grain size of sets milled for 0, 2 and 24 h was measured. With increasing quantity of ZF in HA the grain size decreased (see Table 4), as shown in Fig. 6. The grain size of HA was probably influenced by the presence of the secondary phase (fibres or particles of zirconia), which inhibited the grain growth of HA during sintering [32]. This process is known as "pinning effect" or "Zener pinning" [33,34].

In the case of deposits milled for 0 or 2 h before EPD, a relatively low density and high porosity were observed (see Fig. 7 and Table 4). The decrease in final density of deposits with increasing quantity of ZF probably relates to i) deposition of large ZF clusters in the deposit structure, ii) shortening of ZF with increased milling time, iii) decomposition of HA during thermal treatment. Clusters of ZF and agglomerates of primary particles were identified in deposits prepared from non-milled dispersions (see Fig. 6 (ZF8 AM0)). Moreover, after the addition of a maximum quantity of ZF, the HA/ZF composite was at the cohesion limit (see Fig. 6 (ZF16 AM0)). The composites prepared from the dispersions milled for 2 h contained smaller clusters of ZF than the composites prepared from the non-milled dispersions. To a certain degree, this milling time was sufficient for an effective separation of the fibres because single ZF or particles released from the fibres during milling were observed at the grain-pore interfaces (see Fig. 6). For the deposits prepared from dispersions milled for 24 h before EPD, the microstructural analysis showed single ZF, shortened fibres and single zirconia particles in the structure. There were no agglomerates or clusters of ZF in the HA/ZF composite. For this reason, the volume and the size of pores in this composite were lower than in the other two sets of composites, and the final density of deposits was higher (see Fig. 6 (ZF8 and ZF16 for the sets AM2 and AM24)). By comparing all three sets of samples investigated in Fig. 7 it was found that the final density of sets milled for 2 and 24 h was approximately 16% and 30% higher, respectively, than that of non-milled sets.

In summary, the grain size and the amount and size of pores in the microstructure can effectively be influenced by the time of colloidal milling of the dispersions and by choosing the quantity of ZF in the dispersions.

3.6. Mechanical properties of HA and HA/ZF composites

The mechanical properties of sintered HA and HA/ZF composites were evaluated using the indentation method with a Vickers indenter. Instrumented indentation allowed us to measure Vickers hardness and also evaluate Young's elastic modulus from the unloading part of the force–time dependence. The dependence of elastic modulus and hardness of composites on the quantity of ZF and milling time is shown in Fig. 8.

Both the elastic modulus and the hardness increased with the milling time and decreased with the quantity of ZF. The increase in elastic modulus and hardness of deposits with the milling time can be linked to the microstructure refinement caused by the decreasing size of HA agglomerates and by the separation of ZF from clusters during milling of the dispersion. The dependence of elastic modulus and hardness on the quantity of ZF and the milling time had the same tendency as density (compare Figs. 6 and 8). Generally the elastic and plastic properties of ceramics are functions of grain size, porosity and presence of secondary phases. The hardness and/or elastic modulus of single-phase ceramics decreased with increasing internal porosity [35,36]. The dependence of elastic modulus and hardness of the composites on density is shown in Fig. 9. Crosses represent the elastic modulus and Vickers hardness of HA as published in the literature [36,37]. The dependence of elastic modulus E on porosity level φ can be described by a symmetric-cell average

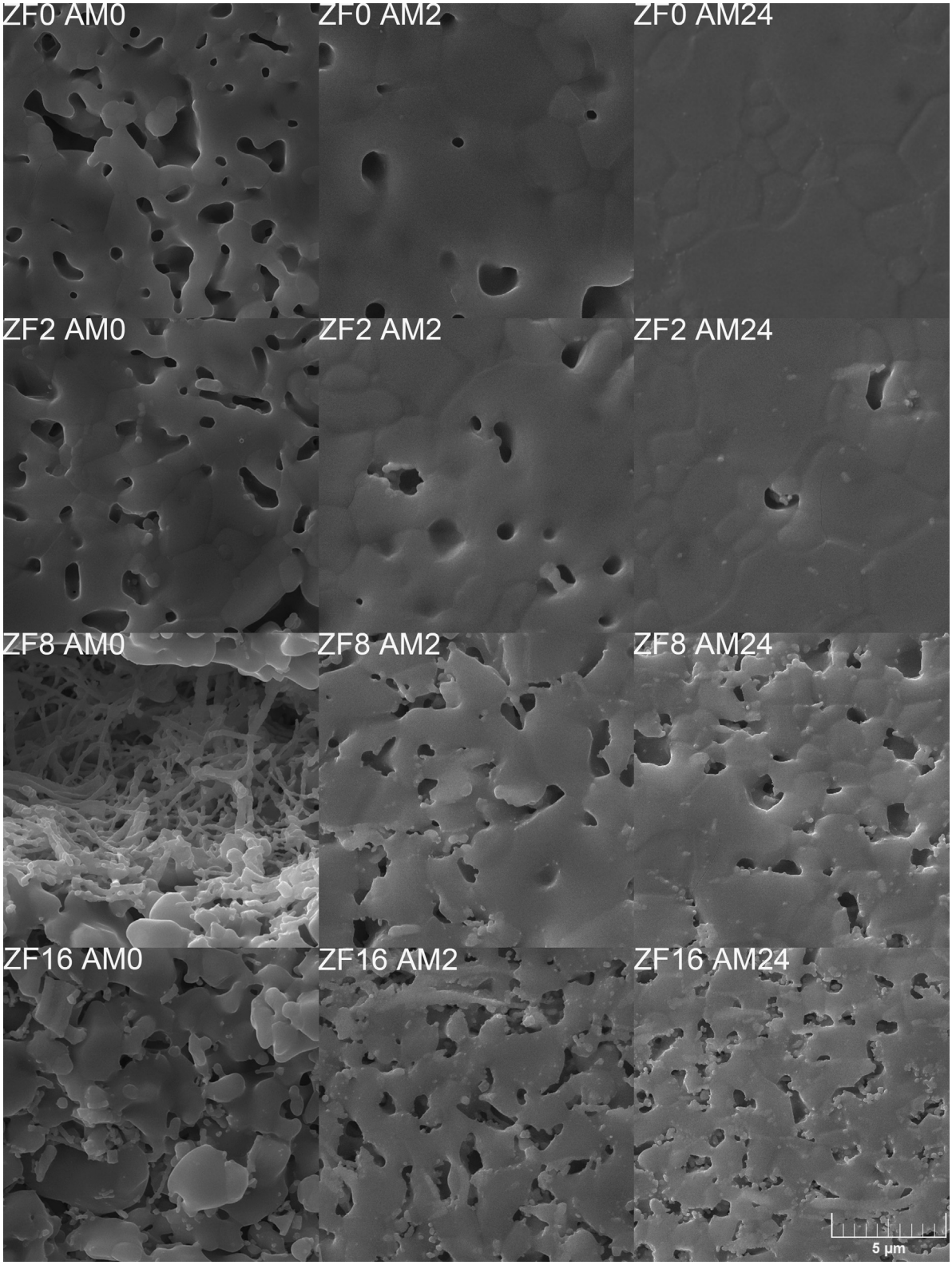

Fig. 6. Micrographs of HA and HA/ZF deposits prepared from dispersions milling (AM) for 0, 2 and 24 h.

model based on the Hashin-Shtrikman bound [35]:

$$E = E_0\left(\frac{(1-\varphi)^2}{1+\varphi}\right), \tag{8}$$

where E_0 is the elastic modulus of a specimen with zero porosity. The value of E_0, 120 GPa, was established from an aggregate average of elastic modulus data for high-dense pure HA [37]. The Vickers hardness HV dependence on porosity

Table 4
Porosity and grain size of the composites prepared.

ZF (wt%)	Porosity (vol%)			Grain size (μm)		
	AM0	AM2	AM24	AM0	AM2	AM24
0	28.92	17.54	7.42	6.19	4.53	4.19
2	30.61	15.10	9.24	4.87	4.61	3.69
4	32.68	22.27	12.17	4.39	4.05	2.99
8	38.59	32.56	20.26	3.45	3.01	2.81
16	53.28	38.90	34.67	–	–	–

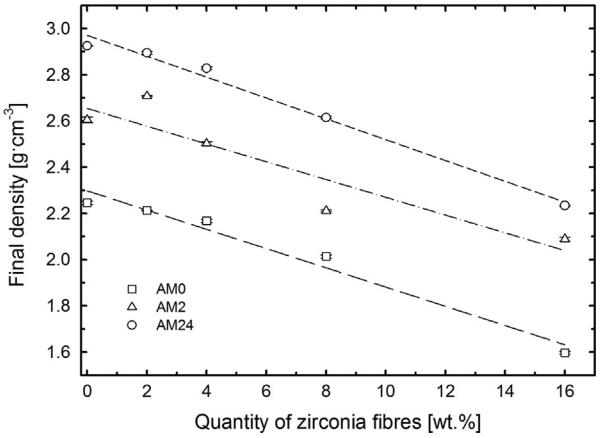

Fig. 7. Dependence of final density of deposits on the quantity of ZF and milling time.

level φ can be described by an exponential model based on the minimum solid area proposed by Rice [36]:

$$HV = HV_0 \cdot exp^{-b \cdot \varphi}, \quad (9)$$

where HV_0 is the Vickers hardness of a specimen with zero porosity and b is the material constant. The least square fit to Eq. (9) yielded values of 6.04 GPa for HV_0 and 6.03 for material constant b. The value of HV_0 is very close to the Vickers hardness of high-dense pure HA with porosity ˂0.01 (6 GPa) as found in work [38].

The predictions of elastic modulus and hardness of HA ceramics based on Eqs. (8) and (9) described well the elastic modulus and Vickers hardness dependence found for HA and HA/ZF composites in this study. It means that the major influence on the mechanical properties was porosity level rather than the presence of ZF in the microstructure. The slight deviation of the measured data from the predictions can be explained by inaccuracies in the determination of either porosity or elastic modulus and hardness. In particular, the elastic modulus was calculated assuming pure elastic deformation during unloading of the specimen. Additionally, Eqs. (8) and (9) were derived assuming spherical pores, which may not be valid in the case of fibre-reinforced composites.

The dependence of the fracture toughness of HA and HA/ZF on the quantity of ZF is shown in Fig. 10. The indentation fracture toughness of HA was approximately 0.6 MPa m$^{-1/2}$, which is comparable with indentation fracture toughness data found in the literature [39]. Incorporation of 2 wt% ZF did not affect either the crack length or final fracture toughness. Increasing the quantity of ZF (from 4 wt% to 16 wt%) led to a monotonic crack length decrease and thus to a fracture toughness increase of up to 1 MPa m$^{-1/2}$. In Fig. 10 the dependence of fracture toughness data on the porosity of deposits (white circles) is given. Crosses represent fracture toughness data found in the literature [40]. The fracture toughness of a pure HA deposit is approximately 30% lower than that from the literature. This could be due to several reasons. The fracture toughness data compared were obtained by different methods: data from the literature had been obtained on notched bars, while an indentation technique was used in this study. Another reason could be the slight difference in the chemical composition of HA (Ca:P ratio). However, it is evident that a composite containing 16 wt% ZF prepared in this study had twice the fracture toughness of pure HA with comparable porosity.

The observed crack length decrease with the quantity of ZF (see Fig. 10) was probably caused by: i) the shortening of the linear crack length and ii) arrest of the crack. The first mechanism would be caused by the meandering of the crack path on grains and fibres, especially in the case of composites with a fine microstructure deposited from a dispersion highly agitated by milling (see Section 3.5) [41,42]. The crack arrest was caused either by the presence of a tougher phase (zirconia or β-TCP) or by the crack energy consumption due to crack re-initiation in the pores. In Fig. 11 the crack path is documented showing a crack crossing the pores (white arrows) and a crack deflected by ZF (black arrows), which were oriented parallel to the electrode.

3.7. Bioactivity of composites

An apatite layer similar to bone is important for ensuring a bone-bonding interface between the bioactive material and the living tissue [27,43]. For this reason, most papers focus on the testing of biomaterials in SBF. The time of sample soaking was selected based on work by Yugeswaran et al. [44], which dealt with a similar material system where the apatite layer was created in 10–15 days of soaking in the SBF. The surface morphologies of HA (Fig. 12a) and HA/ZF composites (Fig. 12b–d) after two weeks of soaking in the SBF are shown in Fig. 12. The apatite layers were formed from spherulites. These spherulites were composed of many small crystallites, which indicated a high rate of nucleation of the calcium and phosphorus species. Fig. 12a and d shows the first apatite layer overlapped by a new layer of finer spherulites. A similar progression of apatite layer growth was

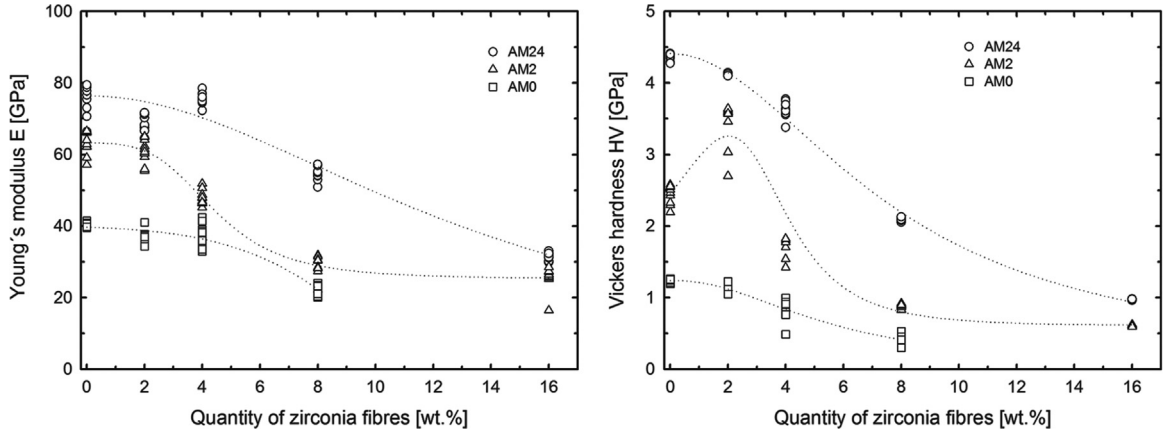

Fig. 8. Dependence of elastic modulus (left) and hardness (right) of HA and HA/ZF composites on quantity of ZF and milling time.

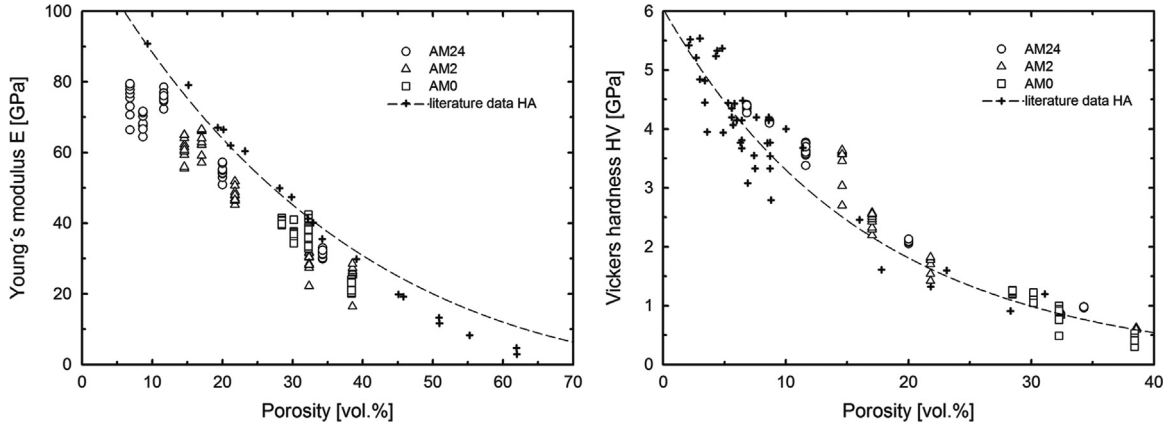

Fig. 9. Dependence of elastic modulus (left) and Vickers hardness (right) of HA and HA/ZF composites on porosity content (symbols indicate measured values; lines represent exponential fits).

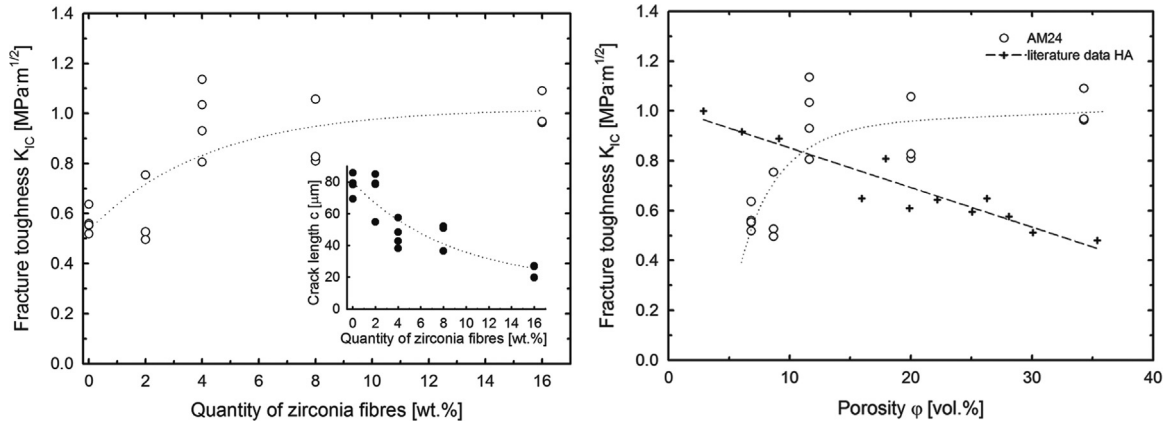

Fig. 10. Dependence of indentation fracture toughness of HA and HA/ZF composites on quantity of ZF (left) and on porosity content (right).

reported by other authors [45]. The apatite layers covering surfaces of our samples did not contain micropores, which are usually observed in the case of composite materials and which are caused by ion diffusion from the sample surface to the SBF [46]. Exclusively local formation of spherulites was observed on a few of the samples (see Fig. 12c).

All of the composites prepared supported the creation of apatite layers from SBF and thus are capable of providing a connexion with living hard tissue through the apatite interlayer [27]. From this point of view, HA/ZF composites have potential in regenerative medicine as a replacement for living hard tissues.

4. Conclusions

HA/ZF composites prepared by EPD from optimised dispersions were studied through characterisation of their microstructure

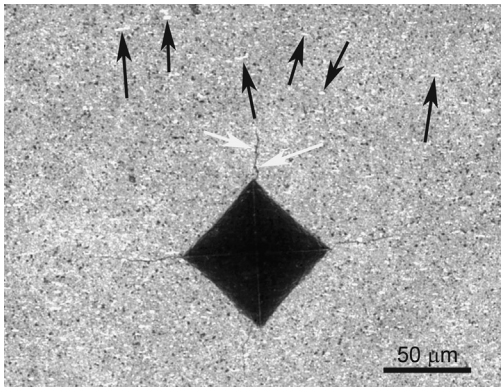

Fig. 11. Micrographs of ZF8 AM24 composite after Vickers indentation.

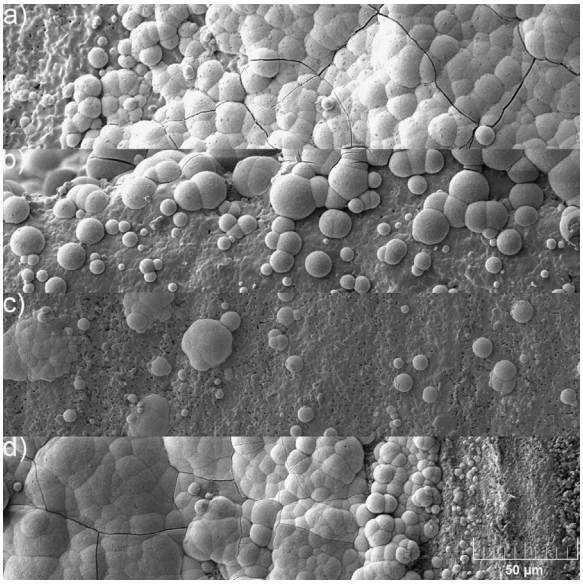

Fig. 12. Micrographs of HA/ZF composite microstructures after soaking in SBF: a) ZF0 AM2, b) ZF2 AM24, c) ZF8 AM2, and d) ZF16 AM24.

and physical, mechanical and biological properties. Dispersions were optimised by long-term colloidal milling and increasing electrical conductivity. The electrical conductivity of dispersions was increased up to 10.59 μS cm^{-2} by adding LiCl as an indifferent electrolyte to obtain thick crack-free deposits with smooth surfaces prepared by EPD. The colloidal milling reduced particle sizes in the dispersions and led to reduction of grain size in sintered composites. The grain size reduction positively affected the microstructure and mechanical properties of the composites. Moreover, it was found that the ZF in composites were oriented parallel to the electrode during EPD. With respect to the physical and mechanical properties of the composites, it was found that the porosity increased with the quantity of ZF and the elastic modulus and Vickers hardness increased with the milling time. The fracture toughness was twice that of pure HA at the same porosity level due to the orientation of ZF, the finer microstructure and the presence of pores in the composites. The study of composites in SBF revealed the bioactive behaviour of HA/ZF composites.

Acknowledgements

The authors are grateful for the financial support from the COST LD14072 project and the GAP108-11-1644 project of the Czech Science Foundation. This work was carried out at CEITEC – Central European Institute of Technology with the research infrastructure supported by the project CZ.1.05/1.1.00/02.0068 financed by the European Regional Development Fund.

References

[1] M. Maas, P.M. Bodnar, U. Hess, L. Treccani, K. Rezwan, Towards the synthesis of hydroxyapatite/protein scaffolds with controlled porosities: bulk and interfacial shear rheology of a hydroxyapatite suspension with protein additives, J. Colloid Interface Sci. 407 (2013) 529–535.
[2] H.B. Guo, K.A. Khor, Y.C. Boey, X.G. Miao, Laminated and functionally graded hydroxyapatite/yttria stabilized tetragonal zirconia composites fabricated by spark plasma sintering, Biomaterials 24 (4) (2003) 667–675.
[3] A. Bignon, J. Chouteau, J. Chevalier, G. Fantozzi, J.P. Carret, P. Chavassieux, G. Boivin, M. Melin, D. Hartmann, Effect of micro- and macroporosity of bone substitutes on their mechanical properties and cellular response, J. Mater. Sci. Mater. Med. 14 (12) (2003) 1089–1097.
[4] K.A. Hing, B. Annaz, S. Saeed, P.A. Revell, T. Buckland, Microporosity enhances bioactivity of synthetic bone graft substitutes, J. Mater. Sci. Mater. Med. 16 (5) (2005) 467–475.
[5] T. Kaito, A. Myoui, K. Takaoka, N. Saito, M. Nishikawa, N. Tamai, H. Ohgushi, H. Yoshikawa, Potentiation of the activity of bone morphogenetic protein-2 in bone regeneration by a PLA-PEG/hydroxyapatite composite, Biomaterials 26 (1) (2005) 73–79.
[6] L. Boilet, M. Descamps, E. Rguiti, A. Tricoteaux, J.X. Lu, F. Petit, V. Lardot, F. Cambier, A. Leriche, Processing and properties of transparent hydroxyapatite and beta tricalcium phosphate obtained by HIP process, Ceram. Int. 39 (1) (2013) 283–288.
[7] S.J. Kim, H.G. Bang, J.H. Song, S.Y. Park, Effect of fluoride additive on the mechanical properties of hydroxyapatite/alumina composites, Ceram. Int. 35 (4) (2009) 1647–1650.
[8] A. Kumar, K. Biswas, B. Basu, On the toughness enhancement in hydroxyapatite-based composites, Acta Mater. 61 (14) (2013) 5198–5215.
[9] J. Cihlar, M. Trunec, Injection moulded hydroxyapatite ceramics, Biomaterials 17 (19) (1996) 1905–1911.
[10] I. Mobasherpour, M.S. Hashjin, S.S.R. Toosi, R.D. Kamachali, Effect of the addition ZrO_2–Al_2O_3 on nanocrystalline hydroxyapatite bending strength and fracture toughness, Ceram. Int. 35 (4) (2009) 1569–1574.
[11] J. Cihlar, A. Buchal, M. Trunec, Kinetics of thermal decomposition of hydroxyapatite bioceramics, J. Mater. Sci. 34 (24) (1999) 6121–6131.
[12] J.X. Lu, M. Descamps, J. Dejou, G. Koubi, P. Hardouin, J. Lemaitre, J.P. Proust, The biodegradation mechanism of calcium phosphate biomaterials in bone, J. Biomed. Mater. Res. 63 (4) (2002) 408–412.
[13] J. Wiltfang, H.A. Merten, K.A. Schlegel, S. Schultze-Mosgau, F.R. Kloss, S. Rupprecht, P. Kessler, Degradation characteristics of alpha and beta tri-calcium- phosphate (TCP) in minipigs, J. Biomed. Mater. Res. 63 (2) (2002) 115–121.
[14] M. Aminzare, A. Eskandari, M.H. Baroonian, A. Berenov, Z.R. Hesabi, M. Taheri, S.K. Sadrnezhaad, Hydroxyapatite nanocomposites: synthesis, sintering and mechanical properties, Ceram. Int. 39 (3) (2013) 2197–2206.
[15] I. Zhitomirsky, L. Gal-Or, Electrophoretic deposition of hydroxyapatite, J. Mater. Sci. Mater. Med. 8 (4) (1997) 213–219.
[16] H. Hadraba, D. Drdlik, Z. Chlup, K. Maca, I. Dlouhy, J. Cihlar, Laminated alumina/zirconia ceramic composites prepared by electrophoretic deposition, J. Eur. Ceram. Soc. 32 (9) (2012) 2053–2056.
[17] H. Hadraba, K. Maca, J. Cihlar, Electrophoretic deposition of alumina and zirconia – II. Two-component systems, Ceram. Int. 30 (6) (2004) 853–863.

[18] H. Hadraba, D. Drdlik, Z. Chlup, K. Maca, I. Dlouhy, J. Cihlar, Layered ceramic composites via control of electrophoretic deposition kinetics, J. Eur. Ceram. Soc. 33 (12) (2013) 2305–2312.
[19] Z. Chlup, H. Hadraba, L. Slabakova, D. Drdlik, I. Dlouhy, Fracture behaviour of alumina and zirconia thin layered laminate, J. Eur. Ceram. Soc. 32 (9) (2012) 2057–2061.
[20] A.R. Boccaccini, I. Zhitomirsky, Application of electrophoretic and electrolytic deposition techniques in ceramics processing, Curr. Opin. Solid State Mater. Sci. 6 (3) (2002) 251–260.
[21] L. Besra, M. Liu, A review on fundamentals and applications of electrophoretic deposition (EPD), Prog. Mater. Sci. 52 (1) (2007) 1–61.
[22] J. Ma, C. Wang, K.W. Peng, Electrophoretic deposition of porous hydroxyapatite scaffold, Biomaterials 24 (20) (2003) 3505–3510.
[23] A.T. Rad, M. Solati-Hashjin, N.A. Abu Osman, S. Faghihi, Improved bio-physical performance of hydroxyapatite coatings obtained by electrophoretic deposition at dynamic voltage, Ceram. Int. 40 (8) (2014) 12681–12691.
[24] J. Widegren, L. Bergstrom, The effect of acids and bases on the dispersion and stabilization of ceramic particles in ethanol, J. Eur. Ceram. Soc. 20 (6) (2000) 659–665.
[25] J.C. Wurst, J.A. Nelson, Linear intercept technique for measuring grain-size in 2-phase polycrystalline ceramics, J. Am. Ceram. Soc. 55 (2) (1972) 109.
[26] G.R. Anstis, P. Chantikul, B.R. Lawn, D.B. Marshall, A critical-evaluation of indentation techniques for measuring fracture-toughness.1. Direct crack measurements, J. Am. Ceram. Soc. 64 (9) (1981) 533–538.
[27] T. Kokubo, H. Takadama, How useful is SBF in predicting in vivo bone bioactivity?, Biomaterials 27 (15) (2006) 2907–2915
[28] J. Cihlar, D. Drdlik, Z. Cihlarova, H. Hadraba, Effect of acids and bases on electrophoretic deposition of alumina and zirconia particles in 2-propanol, J. Eur. Ceram. Soc. 33 (10) (2013) 1885–1892.
[29] D. Drdlik, E. Bartonickova, H. Hadraba, J. Cihlar, Influence of anionic stabilization of alumina particles in 2-propanol medium on the electrophoretic deposition and mechanical properties of deposits, J. Eur. Ceram. Soc. 34 (14) (2014) 3365–3371.
[30] D. Meyers, Surfaces, Interfaces, and Colloids, second ed., Wiley-VCH, New York, 1999.
[31] X.L. Yin, L. Calderin, M.J. Stott, M. Sayer, Density functional study of structural, electronic and vibrational properties of Mg- and Zn-doped tricalcium phosphate biomaterials, Biomaterials 23 (20) (2002) 4155–4163.
[32] X.G. Miao, Y.M. Chen, H.B. Guo, K.A. Khor, Spark plasma sintered hydroxyapatite–yttria stabilized zirconia composites, Ceram. Int. 30 (7) (2004) 1793–1796.
[33] L. Vanherpe, N. Moelans, B. Blanpain, S. Vandewalle, Pinning effect of spheroid second-phase particles on grain growth studied by three-dimensional phase-field simulations, Comp. Mater. Sci. 49 (2) (2010) 340–350.
[34] D.J. Curran, T.J. Fleming, M.R. Towler, S. Hampshire, Mechanical properties of hydroxyapatite–zirconia compacts sintered by two different sintering methods, J. Mater. Sci. Mater. Med. 21 (4) (2010) 1109–1120.
[35] Z. Zivcova, M. Cerny, W. Pabst, E. Gregorova, Elastic properties of porous oxide ceramics prepared using starch as a pore-forming agent, J. Eur. Ceram. Soc. 29 (13) (2009) 2765–2771.
[36] T.P. Hoepfner, E.D. Case, The influence of the microstructure on the hardness of sintered hydroxyapatite, Ceram. Int. 29 (6) (2003) 699–706.
[37] X. Fan, E.D. Case, F. Ren, Y. Shu, M.J. Baumann, Part II: fracture strength and elastic modulus as a function of porosity for hydroxyapatite and other brittle materials, J. Mech. Behav. Biomed. Mater. 8 (2012) 99–110.
[38] G. Muralithran, S. Ramesh, The effects of sintering temperature on the properties of hydroxyapatite, Ceram. Int. 26 (2) (2000) 221–230.
[39] S. Kobayashi, W. Kawai, Development of carbon nanofiber reinforced hydroxyapatite with enhanced mechanical properties, Compos. Part A-Appl. Sci. Manuf. 38 (1) (2007) 114–123.
[40] W. Suchanek, M. Yoshimura, Processing and properties of hydroxyapatite-based biomaterials for use as hard tissue replacement implants, J. Mater. Res. 13 (1998) 94–117.
[41] R. Kumar, K.H. Prakash, P. Cheang, K.A. Khor, Microstructure and mechanical properties of spark plasma sintered zirconia–hydroxyapatite nano-composite powders, Acta Mater. 53 (8) (2005) 2327–2335.
[42] J.W. Wang, L.L. Shaw, Nanocrystalline hydroxyrapatite with simultaneous enhancements in hardness and toughness, Biomaterials 30 (34) (2009) 6565–6572.
[43] P. Li, I. Kangasniemi, K. de Groot, Bonelike hydroxyapatite induction by a gel-derived titania on a titanium substrate, J. Am. Ceram. Soc. 77 (1994) 1307–1312.
[44] S. Yugeswaran, C.P. Yoganand, A. Kobayashi, K.M. Paraskevopoulos, B. Subramanian, Mechanical properties, electrochemical corrosion and in-vitro bioactivity of yttria stabilized zirconia reinforced hydroxyapatite coatings prepared by gas tunnel type plasma spraying, J. Mech. Behav. Biomed. 9 (2012) 22–33.
[45] J.D. Santos, L.J. Jha, F.J. Monteiro, In vitro calcium phosphate formation on SiO_2–Na_2O–CaO–P_2O_5 glass reinforced hydroxyapatite composite: a study by XPS analysis, J. Mater. Sci. Mater. Med. 7 (3) (1996) 181–185.
[46] Y.W. Gu, K.A. Khor, P. Cheang, In vitro studies of plasma-sprayed hydroxyapatite/Ti–6Al–4V composite coatings in simulated body fluid (SBF), Biomaterials 24 (9) (2003) 1603–1611.

PUBLIKACE V

Ceramics International 44 (2018) 2884–2891

Contents lists available at ScienceDirect

Ceramics International

journal homepage: www.elsevier.com/locate/ceramint

Physical, mechanical, and biological properties of electrophoretically deposited lithium-doped calcium phosphates

Daniel Drdlik[a,b,*], Martin Slama[b], Hynek Hadraba[c], Katarina Drdlikova[a], Jaroslav Cihlar[a]

[a] CEITEC BUT, Brno University of Technology, Purkynova 123, 612 00 Brno, Czech Republic
[b] Institute of Materials Science and Engineering, Brno University of Technology, Technicka 2, 616 00 Brno, Czech Republic
[c] CEITEC IPM, Institute of Physics of Materials, Academy of Sciences of the Czech Republic, Zizkova 513/22, 616 62 Brno, Czech Republic

ARTICLE INFO

Keywords:
Lithium
Calcium phosphate
Colloidal milling
Electrophoretic deposition
Material properties

ABSTRACT

In the present work, the preparation of sintered lithium-doped tricalcium phosphates was studied, along with their physical, mechanical, and biological properties. Calcium phosphates were shaped via the use of electrophoretic deposition (EPD), using colloidally milled dispersions of hydroxyapatite (HAp) particles. The dispersions were stabilised with monochloroacetic acid. Lithium was incorporated into the structure via an addition of lithium chloride, which also served to optimise the deposition process. The dispersions were milled colloidally for periods of 0–48 h. The colloidal milling resulted in two effects: i) disintegration of the commercial HAp powder (10 μm) agglomerates, ii) unimodal distribution of the HAp particles (~ 170 nm). The fine particles of the milled HAp dispersions accelerated the deposition rate, and increased the mass of the deposit. The reduced size of the initial particles, owed to the milling, led to the superior arrangement of the particles during deposition and to reduced porosity after sintering (1050–1250 °C). The HAp decomposed into tricalcium phosphate phases during sintering. At a sintering temperature of 1250 °C, grain growth occurred, which consequently resulted in a slight degradation of the mechanical properties (reduction in hardness and Young's modulus). In contrast, the hardness and Young's modulus increased as the dispersion milling time increased (smaller grain size after sintering); however, the fracture toughness did not change. The results of the biological testing confirmed the bioactivity of the material through the growth of the apatite layer in the simulated body fluid (SBF), and the biodegradation of the prepared materials in the Tris-HCl solution. With regard to the preparation of compact lithium-doped tricalcium phosphates, the best results were obtained in the case of the sample that utilised the dispersion that was milled for 48 h, and was sintered at 1050 °C.

1. Introduction

In the past decade, there has been considerable emphasis on the study of ceramic materials and their interaction with living hard tissue. These materials should offer, in particular, bioactivity, biocompatibility, chemical stability, non-toxicity, and appropriate physical and mechanical properties for biomedical applications. From this perspective, the most widely studied ceramic material is hydroxyapatite (HAp), which has a chemical composition similar to that of bones or teeth. At increased temperatures, HAp decomposes into several phases, namely oxyapatite (OA), α-tricalcium phosphate (α-TCP), β-tricalcium phosphate (β-TCP), or tetra-calcium phosphate (TTCP) [1–3]. Moreover, HAp can be doped with biogenic elements such as lithium, zinc, magnesium, manganese, etc. These trace elements promote osteogenesis and neovascularisation; their positive effect on the natural health of bones is well documented [4].

Lithium, which is an alkaline metal and bioelectric material [5], is a relatively novel and interesting additive in the field of bone replacements [4]. In general, lithium is used for the treatment of bipolar disorder and other psychiatric disorders. However, lithium can affect the formation of bone tissue, as shown in a previous study [6]. In the aforementioned study, 150 subjects were compared, out of which 75 were administered lithium. With regard to the spinal column, femur cervix, and trochanter, the bone mass of the patients that were administered lithium increased by several percentage points (4.5–7.5%). On the other hand, the use of lithium is occasionally associated with hyperparathyroidism [7], which can cause loss of bone mass. Lithium is also associated with the activation of β-catenin, which contributes to the healing of fractures [8]. β-catenin is known as a signalling mediator in the canonical Wnt signalling pathway, which is one of the most important signalling cascades in bone formation and re-formation processes [4,9,10].

* Corresponding author at: CEITEC BUT, Brno University of Technology, Purkynova 123, 612 00 Brno, Czech Republic.
E-mail address: drdlik@volny.cz (D. Drdlik).

https://doi.org/10.1016/j.ceramint.2017.11.035
Received 1 September 2017; Received in revised form 19 October 2017; Accepted 7 November 2017
Available online 08 November 2017
0272-8842/ © 2017 Elsevier Ltd and Techna Group S.r.l. All rights reserved.

There are very few studies on the targeted doping of biomaterials with lithium. In a study by Kaygili et al. [11], lithium-doped calcium phosphates (10 and 20 at%) were synthesised using the sol-gel method, where the apatite structure of HAp was modified to a phase containing lithium. Lithium doping can affect the thermal stability of HAp [12] and enhance cell adhesion and proliferation [13]. An alternative approach involves the employment of lithium compounds (e.g., lithium chloride, lithium carbonate) that have already been used in ceramic manufacture; here, lithium is incorporated into the structure of the ceramic material. Electrophoretic deposition (EPD) is considered a suitable method for this purpose.

EPD is a relatively simple and cheap method that is used for preparing coatings and layers with both planar and complex shapes [14]. To prepare ceramic materials with a defined structure, stable colloidal dispersions with appropriate dispersion parameters should be used for EPD [15]. In particular, electrical conductivity was found to be one of the key parameter that influences the quality of the prepared deposit. Electrical conductivity can be affected by high stabiliser concentration [16], which do not participates in the stabilisation of the dispersion. It can also be influenced by the addition of an indifferent electrolyte (e.g., lithium chloride). The optimisation of the dispersion system parametres can affect the structure and properties of the final product, which can be influenced by further optimisation of the dispersions, for example by colloidal milling [17].

The present study combines and utilises the knowledge obtained from our earlier studies on the optimisation of the preparation of diverse ceramic materials via EPD [16–18]. Specifically, we previously studied [16] and [17] the preparation of thick Al_2O_3 layers, where the deposition process was simultaneously optimised with respect to the electrical conductivity of the used dispersions. We also studied thick layers of HAp-ZrO_2 composites, where ZrO_2 fibres were employed for toughening. The proven effectivity of the HAp dispersions milling [17], and the positive effect of the lithium chloride addition on the properties of deposits [18] were utilised in the present work with regard to the preparation of compact lithium-doped calcium phosphates. It is important to optimise the preparation of these materials, and to characterise their structural, physical, mechanical, and biological properties to improve knowledge on HAp-based compact biomaterials, as well as their preparation and properties.

2. Experimental methods

2.1. Materials

Commercial HAp (Fluka, Switzerland), with a specific surface area of 33.8 $m^2 g^{-1}$ and a mean particle size of 10 μm, was used. The specific surface area was measured using the Chembet 3000 analyser (Quantachrome, USA), while the mean particle size was measured via laser diffraction using the LA950 analyser (Horiba, Japan). HAp was supplied by the producer in the form of agglomerated nanorods. The typical agglomerate and detail of the HAp particles are shown in Fig. 1.

2.2. Preparation of dispersions

The dispersions contained 15 wt% HAp, 21.25 wt% monochloroacetic acid stabiliser (MCAA, p.a., Sigma-Aldrich, Germany), 0.10 g L^{-1} of an indifferent electrolyte (Lithium chloride, p.a., Spolana, Czech Republic), and isopropanol solvent (p.a., Lachner, Czech Republic). After mixing, the dispersions were milled within a planetary ball mill for 0, 6, 12, 24, 36, and 48 h. The milling was performed using zirconia milling balls with a diameter of 5 mm, at a milling ratio of 11:1. The dispersions were subjected to a measurement of the zeta potential using a Zetasizer Nano ZS (Malvern Instruments Ltd., UK). For this purpose a whole set of the dispersions without indifferent electrolyte was also prepared.

2.3. Electrophoretic deposition

After milling, the dispersions were mechanically mixed under an ultrasonic field for 30 min. The electrical conductivity of the dispersions was measured at a temperature of 25 °C using a SevenCompact Conductivity S230 conductometer (MettlerToledo AG, Switzerland) equipped with a platinum 4-plate conductivity probe (0–500 mS cm^{-1}, 0–100 °C, 0.80 cm^{-1}). The dispersion was then poured into an EPD cell with a volume of 80 mL. The cell was equipped with two polished, trapezoidal-shaped stainless steel electrodes, which had a total effective surface area of 18.2 cm^2. The effective surface area of the electrode was calculated using the dimensions of the bases (2.3 and 2.9 cm) and height (7 cm). The electrodes, which were 26 mm apart, were connected to a stabilised source, with the deposition process operating at a constant current of 5 mA (current density of 0.27 mA cm^{-2}). The variation in the voltage (from 54 to 92 V) was monitored during the deposition using a voltmeter. Each deposition process occurred over a period of 25 min, and was interrupted at 5-min intervals to conduct mixing; this was to prevent the HAp particles from settling on the cell base. During each interruption, the electrode with the deposit was weighed [19].

2.4. Study of deposits

Following drying, the deposits were removed from the deposition electrodes. The density of the deposits was measured after annealing (600 °C/1 h in air) and sintering (1050 °C, 1150 °C, and 1250 °C for 3 h in air) using the Archimedes method (EN 623-2). The microstructure of each deposit was observed using a Lyra3 scanning electron microscope (SEM, FEG/FIB, Tescan, Czech Republic). The mean grain size (MGS) was determined using the linear intercept method, and the result was multiplied by a shape correction coefficient of 1.56 [20]. The phase analysis was conducted using X-ray diffraction (XRD, SmartLab, Rigaku, Japan). The lithium content was determined using an inductively coupled plasma mass spectrometer Agilent 7500ce (ICP, Agilent Technologies, USA). The measurements were performed using isotope ^7Li. Isotope ^{23}Na was used as an internal standard to compensate for the matrix effects. All samples were diluted by a factor of 10 prior to the measurements. The thermal stability of the prepared materials was evaluated using the Seiko TG/DTA 6300 analyser (+20 °C/min, Seiko Company, Japan). The hardness and Young's modulus of the deposits were established using an instrumented hardness tester (Z2.5, Zwick/Roell, Germany) at a load force of 10 N. The indentation fracture toughness was calculated using the following equation [21]:

$$K_{Ic} = 0.018(E/HV)^{0.5}(P/c^{1.5}), \quad (1)$$

where E is the Young's modulus, HV is the Vickers hardness, P is the load, and c is the crack length. The lengths of the indent diagonals and cracks were measured using a confocal microscope, LEXT OLS3100 (Olympus, Japan). The growth of an apatite layer on sintered deposits immersed in simulated body fluid (SBF) was studied for 14 days at a temperature of 36.5 °C [22]. The composition of the SBF was taken from a report by Kokubo et al. [23]. In addition, the degradation of the prepared materials was studied by measuring their weight loss in the Tris-HCl solution. The composition of the Tris-HCl solution was taken from an article by Lin et al. [24]. To determine the degradation rate, three samples were always tested for each milling time and sintering temperature. The samples were placed in plastic containers filled with Tris-HCl solution, with a solid phase/liquid ratio of 0.1 g/15 mL. The plastic containers were placed into a shaker incubator, with an ambient temperature of 36.5 °C, for 21 days. The weight loss of the samples was measured after 1, 3, 7, 14, and 21 days. Prior to weighting, the samples were removed from the Tris-HCl solution, rinsed in distilled water, and dried for 3 h at 200 °C. The Tris-HCl solution was renewed after three days, in accordance with a previous experiment [25].

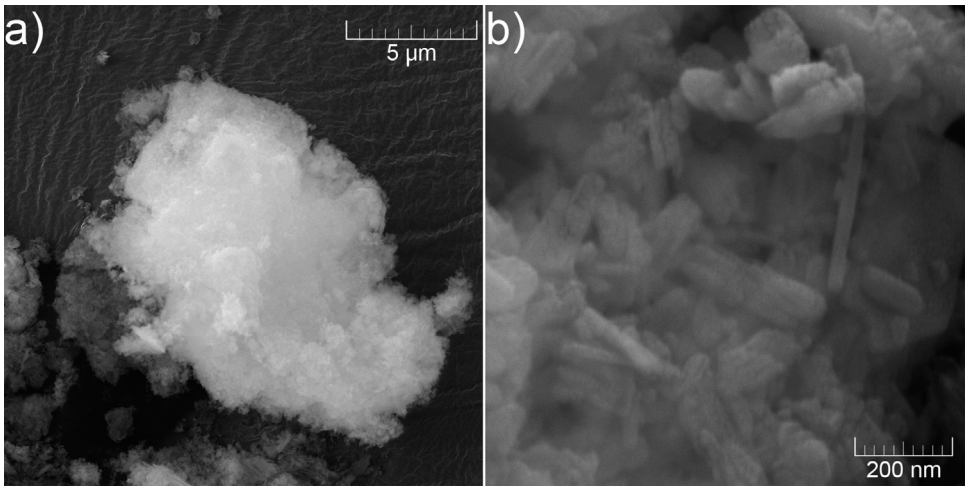

Fig. 1. Micrographs of commercial HAp powder: a) typical agglomerate and b) primary particles.

3. Results and discussion

3.1. Milling of dispersions

The dispersions consisted of HAp particles; with dissociated monochloroacetic acid was adsorbed to their surface via a mechanism described in [17]. Lithium chloride was added to the electrosterically stabilised HAp particles to increase the ionic strength (and electrical conductivity) of the dispersion; consequently, the final structure was doped with lithium.

The dispersions were milled in a planetary ball mill for 6, 12, 24, 36, and 48 h. The dependence of the size of the particles in the dispersion on the milling time is shown in Fig. 2. The non-milled HAp dispersion had a unimodal particle size of 10 μm. As shown in Fig. 1, the HAp powder, as supplied by the manufacturer, was predominantly formed by agglomerates of primary particles. Initially, the colloidal milling yielded dispersions with a bimodal distribution of particles, in which the size of the agglomerates was effectively reduced according to the curve shown in the detailed graph of Fig. 2. Simultaneously, primary particles with sizes of 170–250 nm were released from the agglomerates via the milling; their quantity increased as the milling time increased until a unimodal distribution was again obtained (dot-and-dash line).

The higher amount of the primary particles in the milled dispersions is also associated with increase of the zeta potential. The influence of milling time on the zeta potential of the dispersions is summarized in Table 1. The zeta potential of the dispersion increased with milling time as the result of an increase in amount of active centres where the stabiliser (MCAA) could be adsorbed.

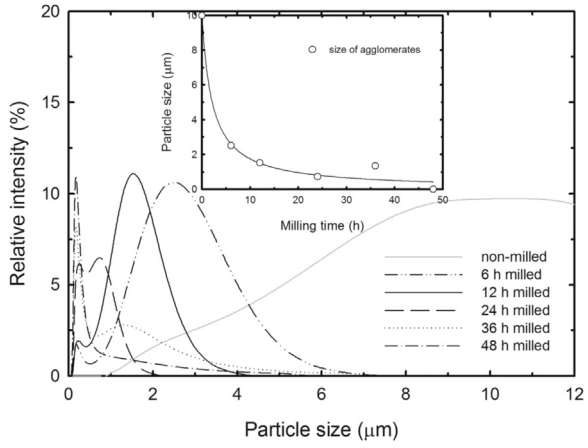

Fig. 2. Dependence of particle size of HAp on the dispersion milling time.

Table 1
Zeta potential measurement of milled dispersions.

Milling time (h)	Zeta potential (mV)	
	Without LiCl	With LiCl
0	−31.4	−29.8
24	−37.6	−32.5
48	−40.8	−38.5

The milling time had another effect, which was visible to the naked eye; there was a change in the viscosity of the dispersions that were prepared. The viscosity of the dispersions increased considerably as the milling time was extended, which, considering the reduction of the particle size, was to be expected [26].

3.2. Electrophoretic deposition

The quality of the products formed through EPD (i.e., bodies without cracks, surface roughness, etc.) is greatly affected by the zeta potential and electrophoretic mobility, as well as the electrical conductivity of the dispersions [17]. Consequently, an indifferent electrolyte was added to the dispersions. Indifferent electrolytes increase the electrical conductivity of colloidal systems [27]; this is owing to an increase in the ion concentration, i.e., the ionic strength of the dispersion. Therefore, there is a reduction in the voltage between the electrodes [16], and the deposition rate decreases. Consequently, there is more time available for ceramic particles to occupy an advantageous position within the deposit, which affects the quality of the deposit, in particular, the density. However, the deposition yields decreased, as demonstrated in Fig. 3a); here, the addition of the indifferent electrolyte increased the electrical conductivity of the non-milled dispersion from 5.10 μS cm^{-1} to 15.89 μS cm^{-1}.

Another phenomenon was studied; in the case of the dispersions that were enriched by an addition of lithium chloride, the concentration of the primary HAp particles increased as the milling time was extended. The dependence of the deposited mass on the deposition time of the milled dispersions that contained lithium chloride is shown in Fig. 3b). As shown in Fig. 3b), as the milling time was extended, the average deposition rate, v_x, increased; this is demonstrated by the secant slope for the time interval, t (5, 25). In this interval, the average EPD rates achieved using the dispersions that were milled for 24 and 48 h (v_{24} and v_{48}) were twice that achieved using the non-milled dispersion (v_0). The mutual shift of the curves is given by the initial time interval, t (0, 5); when the particle concentration was at its highest, the deposition rate was greater than that achieved with longer deposition

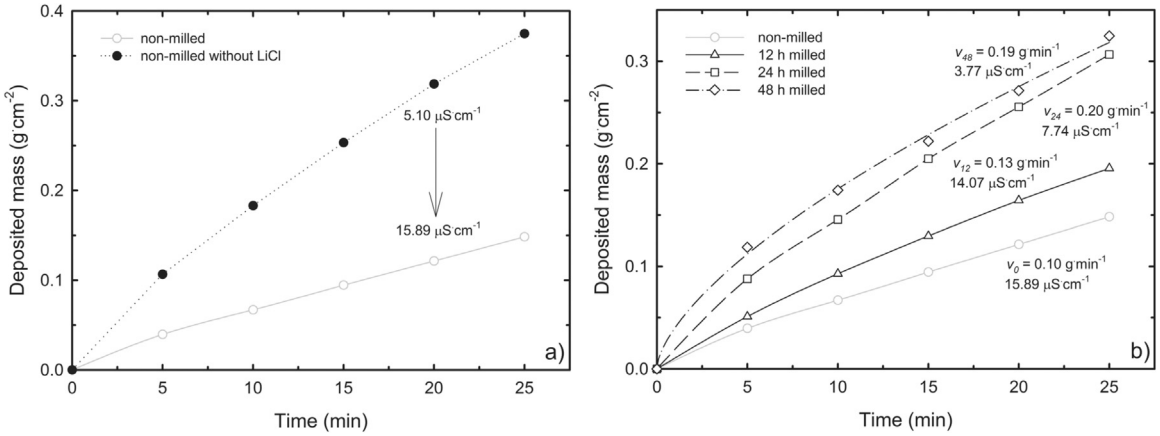

Fig. 3. Dependence of deposited mass on deposition time for: a) non-milled dispersion with and without LiCl addition, and b) various milled dispersions.

times [14]. It can be assumed that when the milling time is over 48 h, the average deposition rate would decrease because long-term milling can lead to repeated agglomeration of the fine ceramic particles owing to their mechanical activation [28]. As shown in Fig. 3b), the deposition yields (or thickness of deposits) increased as the dispersion milling time was extended. The deposit thickness increased, from 0.93 to 1.54 mm, as the dispersion milling time was extended. Therefore, EPD can be considered a useful method for the fabrication of thick planar hard-tissue replacements. Moreover, thick deposits, as well as very thin coatings, are beneficial with regard to preventing cracks from forming within the deposits during drying. In our case, several macroscopic cracks were observed within the deposits. However, these cracks could be avoided by controlling the evaporation of the solvent during drying.

When the lithium chloride was added to the non-milled dispersions, the electrical conductivity increased. However, when the milling time was extended, the overall electrical conductivity of the dispersions decreased. As a result of milling, the specific surface area of ceramic powder increases [28]; therefore, on the surfaces of the HAp particles, there was an increase in the concentration of oxygen atoms with a negative fractional electric charge. In the case of the used dispersions, the charge carriers consisted of H^+ and Li^+ protons; therefore, it is assumed that the lower electrical conductivity may have been caused by H^+ and Li^+ adsorption on the HAp, which had a greater specific surface area. This resulted in the reduced electrical conductivity of the dispersions, and the increased voltage across the electrodes. Concurrently, such dissociated ions caused thinning of the electric double layer [29] which resulted to slight decrease of absolute value of zeta potential as is documented in Table 1.

With regard to EPD, it is necessary to select optimal processing conditions. By utilising the favourable effects of an indifferent electrolyte and appropriate milling time, crack-free deposits, with satisfactory densities and low surface roughness, can be prepared while maintaining relatively high deposition yields, i.e., deposition rates. From this perspective, the apparently optimal deposits were those that were formed using the dispersions that were milled for 24 and 48 h. This is because their electrical conductivity was close to that required for effective EPD; in addition, the potential formation of a relief surface was suppressed by the absence of agglomerates [16]. This statement can be compared with a study [17] where the lower concentrated dispersions and dispersions without an indifferent electrolyte were used.

3.3. Characterisation of deposits

Following the EPD, the deposits were evaluated using thermogravimetric analysis at temperatures up to 1250 °C, as shown in Fig. 4. The analysis revealed that water evaporated from the surfaces of HAp particles, which continued up to 200 °C. Subsequently, an exothermic

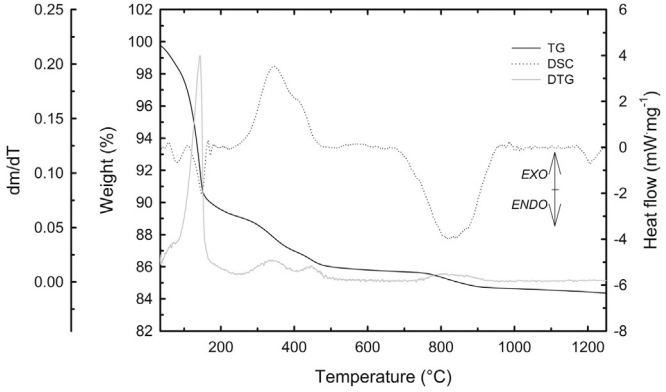

Fig. 4. Thermogravimetric analysis results obtained for prepared deposit.

reaction occurred owing to the oxidation of the residual organic products of the monochloroacetic acid, and the impurities of the HAp. Further heating resulted in the decomposition of HAp into OA and TCP phases over the 650–970 °C interval [3].

The X-ray diffractograms shown in Fig. 5 demonstrate that the initial material consisted of HAp with a small addition of $Ca(HPO_4)$. After annealing, only the HAp phase was found within the deposits. The sintering process at 1050 °C resulted in the decomposition of HAp, primarily into β-TCP with an admixture of α-TCP and β-DCP (dicalcium phosphate). In the case of the deposits sintered at higher temperatures (1150 °C and 1250 °C), the HAp could no longer be detected; β-TCP was

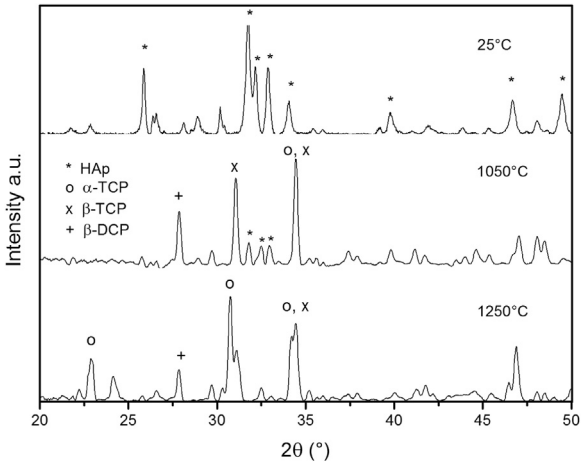

Fig. 5. X-ray diffractograms of HAp powder, and deposits sintered at 1050 °C and 1250 °C.

transformed into α-TCP and the quantity of the β-DCP phase decreased, as shown in Fig. 5.

Only a small amount of lithium chloride was used for the preparation of the deposits, and therefore, it was not detected during the XRD analysis. The Li^+ ions are assumed to have substituted the TCP, according to the following formula:

$$Ca_{10}(PO_4)_6O + xLi^+ \rightarrow 2Ca_3(PO_4)_2 + Ca_{(3-\frac{x}{2})}Li_x(PO_4)_2 + (1+\frac{x}{2})CaO. \quad (2)$$

The lithium content of two samples was determined using ICP; these samples were milled for 0 and 48 h prior to the analysis. It was established that the sample prepared from non-milled dispersion contained 14.7 ppm of lithium, while the sample that was prepared from the dispersion that was milled for 48 h contained 67.3 ppm of lithium. These values are higher than the average value detected for healthy human bone, namely 1.3 ppm [30]. Based on the results, the amount of lithium chloride electrolyte within the dispersion could be reduced to approximately 0.005 g L^{-1} to maintain the natural trace amount of this element in human bone. However, slightly higher amounts of lithium can potentially have therapeutic effects with regard to the activation of β-catenin [8].

The dependence of the relative density and MGS on the annealing and sintering temperatures, and milling time is given in Table 2. The relative density of the deposits after annealing increased with the dispersion milling time. This result indicates that during the EPD, the small particles of the dispersions that were milled for long time were more appropriately arranged within the deposit structures. There was a 20.4% t.d. difference between the relative densities of the deposits prepared from the non-milled dispersion and the dispersion milled for 48 h; this represents a 55% increase in the green body density.

The deposit prepared from the non-milled dispersion that was sintered at 1050 °C had a density of 54% t.d. By increasing the sintering temperature to 1250 °C, the density of the deposit prepared from the non-milled HAp could be increased to a value of approximately 75% t.d. The heating during sintering resulted in the thermal decomposition of the HAp into TCP (see Fig. 5), as well as considerable grain growth (see Table 2). Owing to the dispersion milling, the disintegration of the agglomerates and the refinement of the HAp particles led to a pronounced increase in the density of the sintered deposits. These deposits had densities of about 95% t.d., even at a low sintering temperature (1050 °C).

Table 2 shows the effects of the dispersion milling time and sintering temperature on the MGS of the structure of the deposits. While the MGS decreased as the milling time was extended, the temperature had an opposite effect. In the case of the deposits sintered at 1050 °C and 1150 °C, the MGS decreased by approximately 0.5 μm, which was owed to the milling of the HAp particles. However, when the sintering temperature was increased, the grains grew by approximately 0.8 μm. Considerable grain growth was observed under the highest sintering temperature (1250 °C). Fig. 6 shows the microstructures of the deposits prepared with a 25-min EPD process using the dispersions that were milled for 48 h, which were sintered at 1050 °C to 1250 °C.

Table 2
Relative density and mean grain size of deposits after annealing and sintering.

Milling time (h)	ρ_{rel} (%)/MGS(μm)			
	600 °C	1050 °C	1150 °C	1250 °C
0	36.9/-	54.3/1.12	73.0/1.99	74.9/-
12	42.8/-	64.2/0.84	92.5/1.90	86.5/7.62
24	46.1/-	73.1/0.72	95.6/1.69	91.5/6.69
36	49.7/-	80.9/0.74	96.4/1.55	93.3/6.43
48	57.3/-	94.9/0.65	96.5/1.44	94.3/5.37

3.4. Mechanical behaviour of deposits

Fig. 7a) shows the dependence of the Vickers hardness of the sintered deposits on the dispersion milling time and sintering temperature. As the dispersion milling time was extended and the sintering temperature increased, the Vickers hardness increased to 4–5 GPa. The dependence of the Vickers hardness of the deposits on the level of porosity is given in Fig. 7b). It is obvious that the Vickers hardness of the deposits is primarily affected by the level of porosity because the mechanical properties of the solid body are greatly influenced by the presence of pores [31,32]. Pores reduce the effective loaded cross-section of the material, and they collapse under mechanical loading. Consequently, the values of established mechanical characteristics (hardness, elastic modulus, fracture toughness) decrease as the level of porosity of the material increases. The dependence of the Vickers hardness, *HV*, of the deposit on the porosity of the material, φ, can be described by an exponential model [33]:

$$HV = HV_0 \cdot exp^{-b\cdot\varphi}, \quad (3)$$

where HV_0 is the Vickers hardness of the compact HAp, and b is a material constant. Fig. 7b) gives the theoretical dependence for HV_0 and b, which are 6.04 GPa and 6.03, respectively. These values were established based on a huge amount of literary data, and were reported in a previous study [17]. In this study, the measured hardness values of the deposit correlate with those of the valid theoretical model for pure HAp. The hardness values of both TCP phases are very close to the value of HAp, and with regard to their mechanical properties, it is not possible to distinguish their behaviour [34].

Fig. 8a) shows the dependence of the Young's modulus of the sintered deposits on the dispersion milling time and sintering temperature. As shown in the case of the Vickers hardness, the elastic modulus increased with the milling time of the dispersions used to prepare the deposits. The dependence of the elastic modulus on the level of porosity is given in Fig. 8b). It is obvious that in addition to the Vickers hardness of the deposits, the elastic modulus is greatly dependent on the level of porosity. The dependence of the Young's modulus, *E*, on the pore content, φ, is governed by the following equation [31]:

$$E = E_0\left(\frac{(1-\varphi)^2}{1+\varphi}\right), \quad (4)$$

where E_0 is the elastic modulus of the non-porous HAp. The value of E_0 = 120 GPa, which is valid for a monocrystal of HAp, was taken from a previous report [35]. An identical E_0 value was determined for a single crystal of TCP by Viswanath et al. [34]. The differences between the determined elastic modulus and the theoretical prediction can be attributed to the method of determination; this is based on an estimation from the unloading part of a loading curve obtained at instrumented hardness measurement.

The dependence of the indentation fracture toughness of the deposits on the sintering temperature, milling time, and porosity is shown in Fig. 9. The dependence of the fracture toughness of HAp on its porosity is described, in the literature, as a monotonically falling function; a fracture toughness of approximately 1 MPa $m^{0.5}$ was determined for HAp with a density close to the theoretical density, while a value of approximately 0.5 MPa $m^{0.5}$ was determined for HAp with a density of 65% t.d. (porosity of 35%) [36].

Fig. 9b) shows the dependence of the indentation fracture toughness of the deposits on the porosity level and sintering temperature. In contrast to the literary data, it can be observed that as the level of porosity increases, the fracture toughness increases from a value of around 0.55 MPa $m^{0.5}$, obtained for deposits that have a density close to the theoretical density, up to a value of 0.85 MPa $m^{0.5}$, obtained for deposits with densities of around 70% t.d. In all cases, when the Vickers indenter impressions on the deposit surface were gradually polished, it was observed that Palmqvist-type cracks were formed in the material;

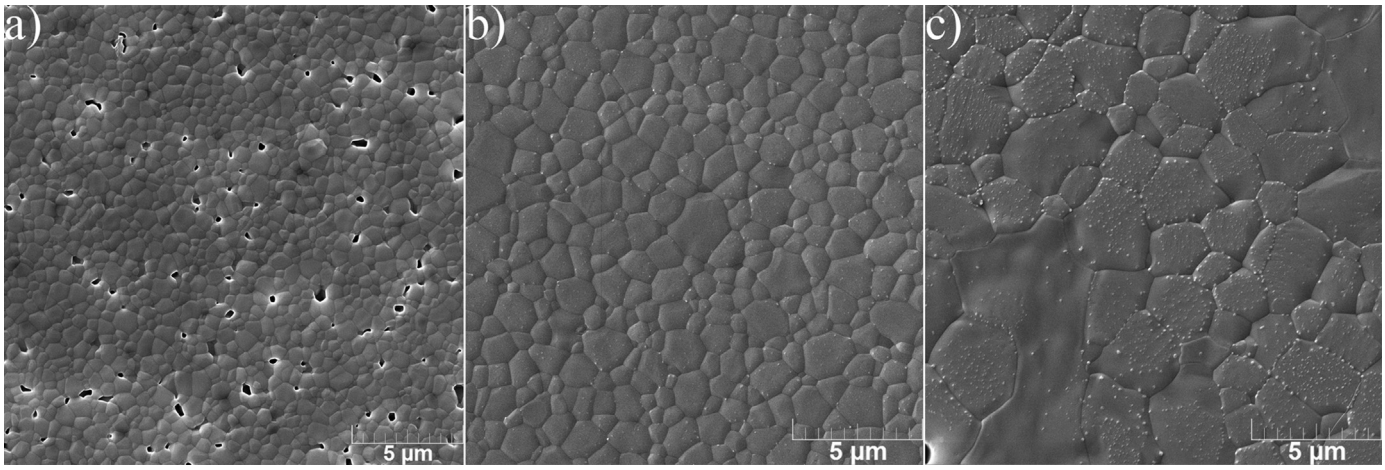

Fig. 6. SEM micrographs of deposit microstructures prepared from dispersions milled for 48 h, and sintered at: a) 1050 °C, b) 1150 °C, and c) 1250 °C.

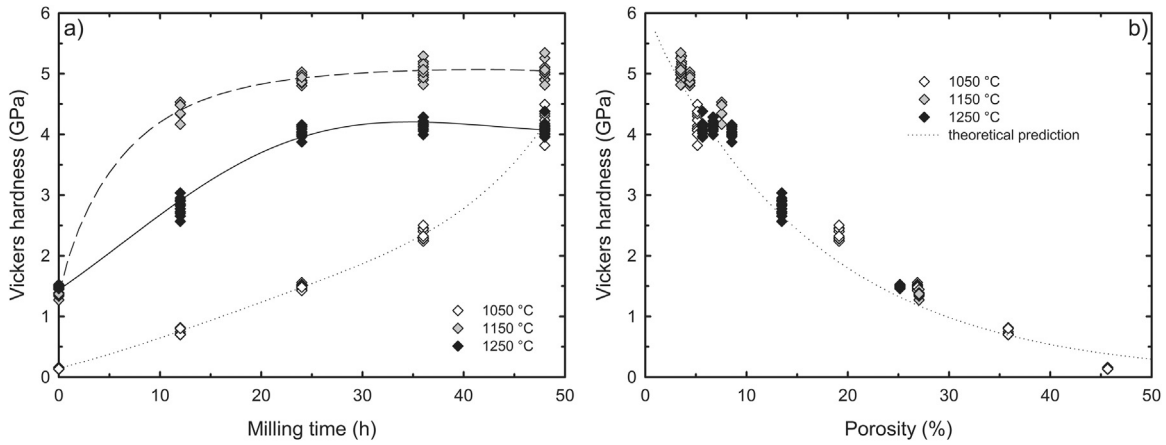

Fig. 7. Dependence of Vickers hardness of deposits on the sintering temperature, and: a) dispersion milling time, and b) porosity level of deposits.

thus, the equation used for determining the indentation fracture toughness was determined to be valid. The observed increase in the indentation fracture toughness was due to the increased porosity of the deposits. In all cases, the length of the indentation cracks decreased; this is owed to the stoping of the indentation cracks at the pores and the necessity of their subsequent re-initiation. This phenomenon is responsible for the apparent increase in the indentation fracture toughness with the increased porosity level of the deposit.

3.5. Biological properties of deposits

A layer of newly formed apatite was identified on the deposits that had been immersed in the SBF for 14 days. In some cases, the individual apatite layers overlapped, as shown in Fig. 10a). A similar phenomenon was also observed by other authors [37]. It was observed that the apatite layers were formed by speherical shapes, with sizes in the range of tens of micrometres. A detail of the interface between the two spherical shapes and their composition of fine apatite crystals is shown in Fig. 10b). The above result indicates that the addition of lithium into

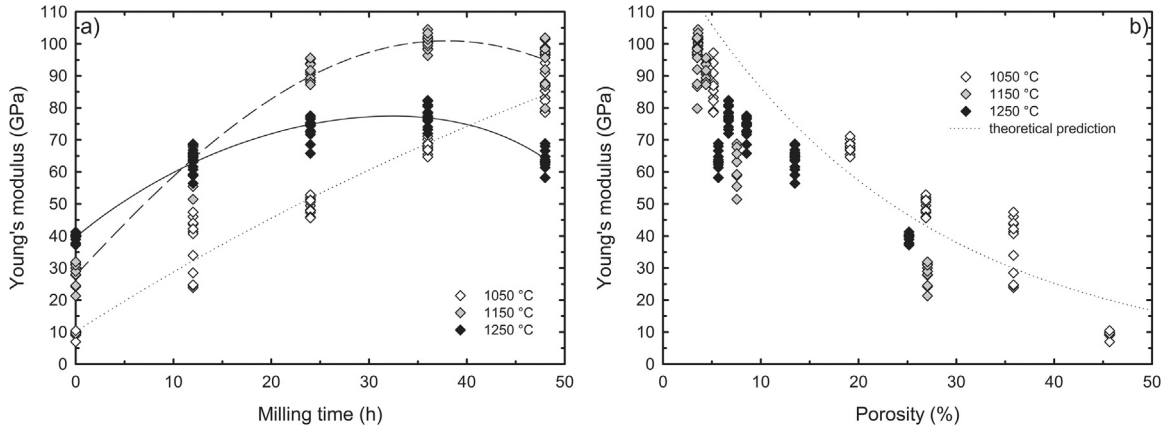

Fig. 8. Dependence of Young's modulus of deposits on the sintering temperature, and: a) dispersion milling time, and b) porosity level of deposits.

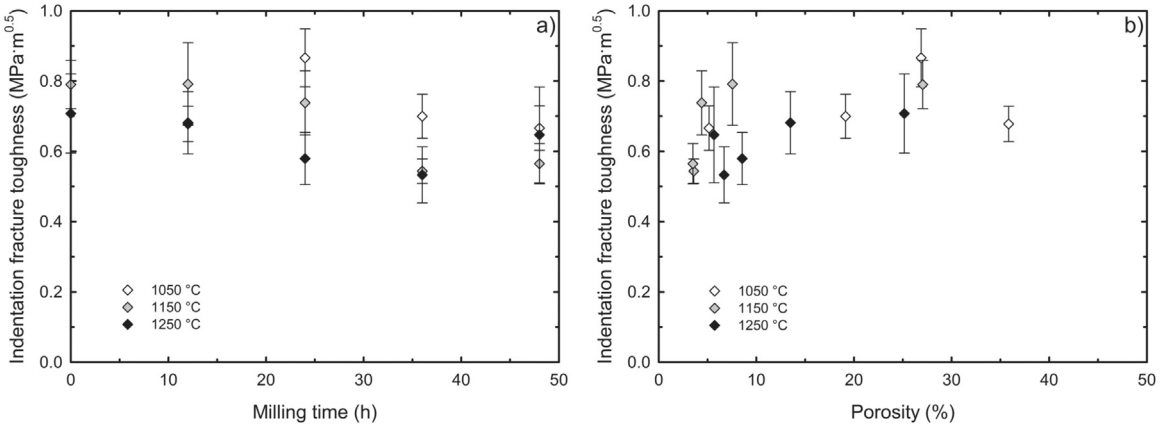

Fig. 9. Dependence of indentation fracture toughness of deposits on the sintering temperature, and: a) dispersion milling time, and their b) porosity level of deposits.

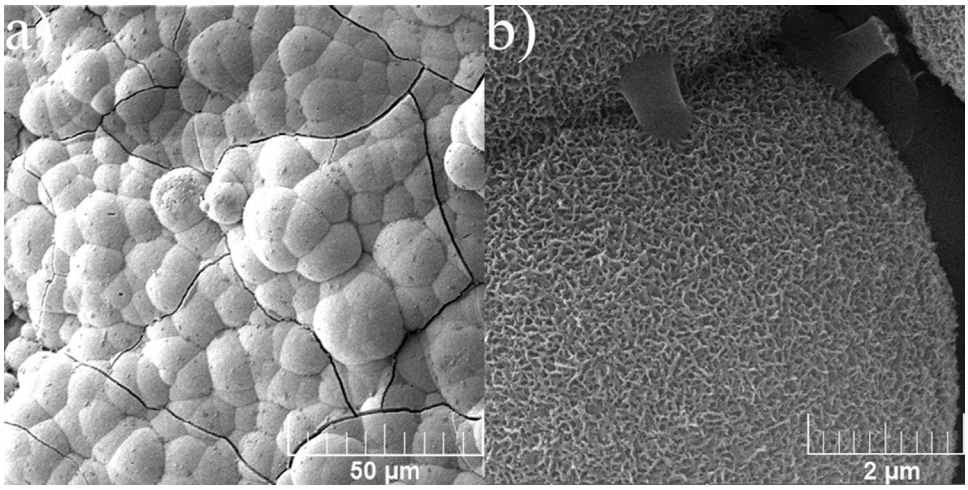

Fig. 10. SEM micrographs of: a) surface of deposit covered with apatite layer, b) fine apatite crystals.

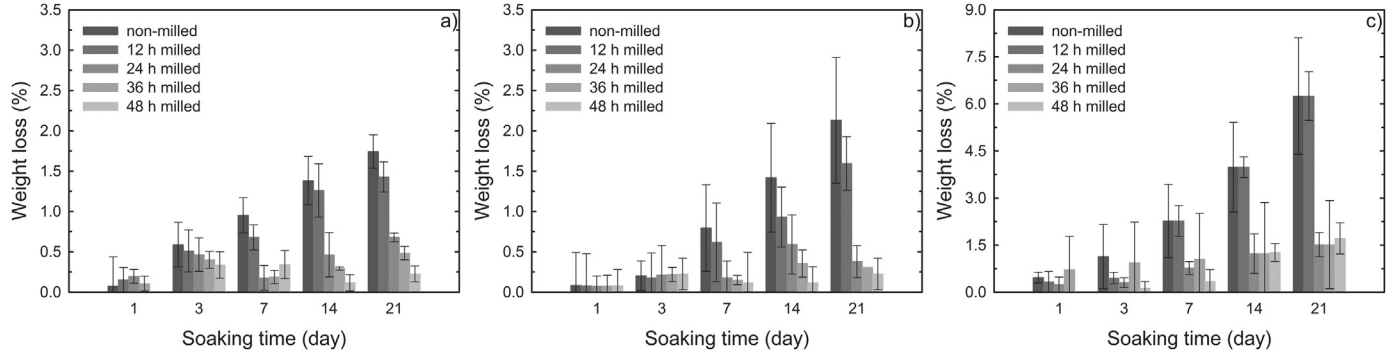

Fig. 11. Weight loss of deposits prepared from various milled dispersions sintered at: a) 1050 °C, b) 1150 °C, and c) 1250 °C, which were immersed in Tris-HCl solution for 1, 3, 7, 14, and 21 days.

the TCP structure did not impair the formation of the apatite layer. The prepared materials are bioactive and can potentially be used in the field of transplant medicine.

Fig. 11 shows the weight losses of the sintered deposits prepared from the non-milled and milled dispersions, which were immersed in the Tris-HCl solution for 21 days. During soaking, the weight of each sample decreased. As shown in Fig. 11, the weight losses of the samples decreased with the milling time and increased as the sintering temperature increased. The milling of the dispersions markedly affected the porosity of deposits; thus, in the cases of the structures with a lower porosity level, the Tris-HCl solution only dissolved the individual phases to a certain extent. The results correspond well with the results of the density measurements, shown in Table 2. However, the sintering temperature also affects the disintegration of HAp into the TCP phases (see Fig. 5), which dissolve more rapidly than the HAp itself. The solubility product of HAp is $^{HA}K_{sp} = 10^{-59}$ at pH 7.4, while the solubility products for α-TCP and β-TCP are $^{\alpha}K_{sp} = 10^{-26}$ and $^{\beta}K_{sp} = 10^{-30}$, respectively [38–40]. However, based on the above results, the effect of the porosity on the weight loss of the deposits is more significant than the dissolution rate of the TCP phases. In this study, the greatest weight loss, 6.25%, was determined for a deposit prepared from the non-milled dispersion, which was sintered at 1250 °C. This result is comparable with the literary data regarding structures of similar porosity [41].

4. Conclusions

In this study, we proposed that the physical, mechanical, and biological properties of deposits can be tuned by controlling the milling (0–48 h) of lithium-enriched dispersions, which are applied prior to EPD, and the sintering conditions. Both the addition of lithium, and the milling process optimised the preparation of the bioceramics by modifying the electrical conductivity of the fine primary particles in the dispersions, and increasing their quantity. The optimised dispersions allowed the preparation of good quality lithium-doped HAp deposits (14.7–67.3 ppm), which could potentially have therapeutic effects with regard to bone-tissue engineering. From the perspective of material density and homogeneity, long-term milling (up to 48 h) is advantageous because materials can be sintered at a lower temperature (1050 °C), attaining a high final density of around 95% t.d., along with a small MGS. During the thermal treatment of the deposits, the HAp decomposed into α-, β-TCP, and β-DCP. The Vickers hardness and Young's modulus of the deposits increased as their level of porosity decreased; these were governed by two-parameter exponential functions. On the other hand, the indentation fracture toughness of the deposits increased with increasing pore content as a consequence of the indentation crack stoping on the pores and of the necessity of their subsequent re-initiation. The prepared materials exhibited good bioactivity and biodegradability, and therefore they could potentially be used in the field of transplant medicine.

Acknowledgements

The authors gratefully acknowledge support from the COST LD14072 project.

References

[1] J. Cihlar, M. Trunec, Injection moulded hydroxyapatite ceramics, Biomaterials 17 (1996) 1905–1911.
[2] I. Mobasherpour, M.S. Hashjin, S.S.R. Toosi, R.D. Kamachali, Effect of the addition ZrO2-Al2O3 on nanocrystalline hydroxyapatite bending strength and fracture toughness, Ceram. Int 35 (2009) 1569–1574.
[3] J. Cihlar, A. Buchal, M. Trunec, Kinetics of thermal decomposition of hydroxyapatite bioceramics, J. Mater. Sci. 34 (1999) 6121–6131.
[4] S. Bose, G. Fielding, S. Tarafder, A. Bandyopadhyay, Understanding of dopant-induced osteogenesis and angiogenesis in calcium phosphate ceramics, Trends Biotechnol. 31 (2013) 594–605.
[5] O. Kaygili, C. Tatar, The investigation of some physical properties and microstructure of Zn-doped hydroxyapatite bioceramics prepared by sol-gel method, J. Sol Gel Sci. Technol. 61 (2012) 296–309.
[6] A. Zamani, G.R. Omrani, M.M. Nasab, Lithium's effect on bone mineral density, Bone 44 (2009) 331–334.
[7] J.L. Marti, C.S. Yang, T. Carling, S.A. Roman, J.A. Sosa, P. Donovan, M.S. Guoth, K.S. Heller, R. Udelsman, Surgical approach and outcomes in patients with lithium-associated hyperparathyroidism, Ann. Surg. Oncol. 19 (2012) 3465–3471.
[8] Y. Chen, H.C. Whetstone, A.C. Lin, P. Nadesan, Q.X. Wei, R. Poon, B.A. Alman, Beta-catenin signaling plays a disparate role in different phases of fracture repair: implications for therapy to improve bone healing, PLoS Med. 4 (2007) 1216–1229.
[9] D.G. Monroe, M.E. McGee-Lawrence, M.J. Oursler, J.J. Westendorf, Update on Wnt signaling in bone cell biology and bone disease, Gene 492 (2012) 1–18.
[10] F. Milat, K.W. Ng, Is Wnt signalling the final common pathway leading to bone formation? Mol. Cell. Endocrinol. 310 (2009) 52–62.
[11] O. Kaygili, S. Keser, T. Ates, F. Yakuphanoglu, Synthesis and characterization of lithium calcium phosphate ceramics, Ceram. Int. 39 (2013) 7779–7785.
[12] N. Matsumoto, K. Yoshida, K. Hashimoto, Y. Toda, Thermal stability of beta-tricalcium phosphate doped with monovalent metal ions, Mater. Res. Bull. 44 (2009) 1889–1894.
[13] J.W. Wang, K. de Grootb, C. van Blitterswijk, J. de Boet, Electrolytic deposition of lithium into calcium phosphate coatings, Dent. Mater. 25 (2009) 353–359.
[14] P. Sarkar, P.S. Nicholson, Electrophoretic deposition (EPD): mechanisms, kinetics, and application to ceramics, J. Am. Ceram. Soc. 79 (1996) 1987–2002.
[15] J. Cihlar, D. Drdlik, Z. Cihlarova, H. Hadraba, Effect of acids and bases on electrophoretic deposition of alumina and zirconia particles in 2-propanol, J. Eur. Ceram. Soc. 33 (2013) 1885–1892.
[16] D. Drdlik, E. Bartonickova, H. Hadraba, J. Cihlar, Influence of anionic stabilization of alumina particles in 2-propanol medium on the electrophoretic deposition and mechanical properties of deposits, J. Eur. Ceram. Soc. 34 (2014) 3365–3371.
[17] D. Drdlik, M. Slama, H. Hadraba, J. Cihlar, Hydroxyapatite/zirconia-microfibre composites with controlled microporosity and fracture properties prepared by electrophoretic deposition, Ceram. Int. 41 (2015) 11202–11212.
[18] D. Drdlik, M. Slama, H. Hadraba, K. Drdlikova, J. Cihlar, On the role of the indifferent electrolyte LiCl in electrophoretic deposition of hydroxyapatite from 2-propanol dispersions, Ceram. Int. 42 (2016) 16529–16534.
[19] H. Hadraba, D. Drdlik, Z. Chlup, K. Maca, I. Dlouhy, J. Cihlar, Layered ceramic composites via control of electrophoretic deposition kinetics, J. Eur. Ceram. Soc. 33 (2013) 2305–2312.
[20] J.C. Wurst, J.A. Nelson, Linear intercept technique for measuring grain-size in 2-phase polycrystalline ceramics, J. Am. Ceram. Soc. 55 (1972) 109.
[21] G.R. Anstis, P. Chantikul, B.R. Lawn, D.B. Marshall, A critical-evaluation of indentation techniques for measuring fracture-toughness. 1. Direct crack measurements, J. Am. Ceram. Soc. 64 (1981) 533–538.
[22] S. Yugeswaran, C.P. Yoganand, A. Kobayashi, K.M. Paraskevopoulos, B. Subramanian, Mechanical properties, electrochemical corrosion and in-vitro bioactivity of yttria stabilized zirconia reinforced hydroxyapatite coatings prepared by gas tunnel type plasma spraying, J. Mech. Behav. Biomed. 9 (2012) 22–33.
[23] T. Kokubo, H. Takadama, How useful is SBF in predicting in vivo bone bioactivity? Biomaterials 27 (2006) 2907–2915.
[24] K.L. Lin, L. Chen, H.Y. Qu, J.X. Lu, J. Chang, Improvement of mechanical properties of macroporous beta-tricalcium phosphate bioceramic scaffolds with uniform and interconnected pore structures, Ceram. Int. 37 (2011) 2397–2403.
[25] J.X. Lu, J. Wei, Q. Gan, X. Lu, J. Hou, W.H. Song, Y.G. Yan, J. Ma, H. Guo, T.Q. Xiao, C.S. Liu, Preparation, bioactivity, degradability and primary cell responses to an ordered mesoporous magnesium-calcium silicate, Microporous Mesoporous Mater. 163 (2012) 221–228.
[26] S.M. Seo, D.M. Kim, T.J. Chung, J.J. Yoo, H.J. Kim, H.J. Chun, J.W. Jang, K.S. Oh, Effect of milling time on the viscosity of hydroxyapatite suspension, Curr. Appl. Phys. 12 (2012) S71–S75.
[27] R.C.D. Cruz, J. Reinshagen, R. Oberacker, A.M. Segadaes, M.J. Hoffmann, Electrical conductivity and stability of concentrated aqueous alumina suspensions, J. Colloid Interface Sci. 286 (2005) 579–588.
[28] Morphology Control of Materials and Nanoparticles: Advanced Materials Processing and Characterization, 1st ed., Springer-Verlag, Berlin Heidelberg, 2004.
[29] D. Meyers, Surfaces, Interfaces, and Colloids, 2nd ed., Wiley-VCH, New York, 1999.
[30] J. Emsley, Nature's Building Blocks: An A-Z Guide to the Elements, OUP, Oxford, 2011.
[31] Z. Zivcova, M. Cerny, W. Pabst, E. Gregorova, Elastic properties of porous oxide ceramics prepared using starch as a pore-forming agent, J. Eur. Ceram. Soc. 29 (2009) 2765–2771.
[32] T.P. Hoepfner, E.D. Case, The influence of the microstructure on the hardness of sintered hydroxyapatite, Ceram. Int. 29 (2003) 699–706.
[33] R.W. Rice, Evaluation and extension of physical property-porosity models based on minimum solid area, J. Mater. Sci. 31 (1996) 102–118.
[34] B. Viswanath, R. Raghavan, N.P. Gurao, U. Ramamurty, N. Ravishankar, Mechanical properties of tricalcium phosphate single crystals grown by molten salt synthesis, Acta Biomater. 4 (2008) 1448–1454.
[35] X. Fan, E.D. Case, F. Ren, Y. Shu, M.J. Baumann, Part II: fracture strength and elastic modulus as a function of porosity for hydroxyapatite and other brittle materials, J. Mech. Behav. Biomed. 8 (2012) 99–110.
[36] W. Suchanek, M. Yoshimura, Processing and properties of hydroxyapatite-based biomaterials for use as hard tissue replacement implants, J. Mater. Res. 13 (1998) 94–117.
[37] J.D. Santos, L.J. Jha, F.J. Monteiro, In vitro calcium phosphate formation on SiO2-Na2O-CaO-P2O5 glass reinforced hydroxyapatite composite: a study by XPS analysis, J. Mater. Sci. Mater. Med. 7 (1996) 181–185.
[38] M. Bohner, J. Lemaitre, T.A. Ring, Kinetics of dissolution of beta-tricalcium phosphate, J. Colloid Interface Sci. 190 (1997) 37–48.
[39] E. Fernandez, F.J. Gil, M.P. Ginebra, F.C.M. Driessens, J.A. Planell, S.M. Best, Calcium phosphate bone cements for clinical applications – Part I: solution chemistry, J. Mater. Sci. Mater. Med. 10 (1999) 169–176.
[40] A. Ravaglioli, A. Krajewski, Bioceramics, Springer, Netherlands, 1992.
[41] M.C. Xu, D. Zhai, J. Chang, C.T. Wu, In vitro assessment of three-dimensionally plotted nagelschmidtite bioceramic scaffolds with varied macropore morphologies, Acta Biomater. 10 (2014) 463–476.

PUBLIKACE VI

Ceramics International 44 (2018) 9787–9793

Contents lists available at ScienceDirect

Ceramics International

journal homepage: www.elsevier.com/locate/ceramint

Electrophoretic deposition of plasma activated sub-micron alumina powder

Daniel Drdlik[a,b,*], Tomas Moravek[c], Jozef Rahel[c], Monika Stupavska[c], Jaroslav Cihlar[a], Katarina Drdlikova[a], Karel Maca[a,b]

[a] CEITEC BUT, Brno University of Technology, Purkynova 123, 61200 Brno, Czech Republic
[b] Institute of Materials Science and Engineering, Brno University of Technology, Technicka 2, 61600 Brno, Czech Republic
[c] Department of Physical Electronics, CEPLANT, Masaryk University, Kotlarska 2, 61137 Brno, Czech Republic

ARTICLE INFO

Keywords:
Alumina
Non-thermal plasma
DCSBD
Electrophoretic deposition

ABSTRACT

The positive effect of plasma mediated treatment of powder fraction in water-based dispersion is a rather well documented fact. Despite its importance for ceramic processing, the applicability of plasma treatment of ceramic particles in a non-aqueous dispersions remains unexplored. In the presented article, a specific planar type of dielectric barrier discharge - Diffuse Coplanar Surface Barrier Discharge (DCSBD), operated in atmospheric pressure air was used for the surface activation of sub-micron alumina particles. These were consequently dispersed in organic solvent of 2-propanol and evaluated for the performance during the process of electrophoretic deposition (EPD). The surface of ceramic particles and the dispersion behaviour were investigated using thermogravimetric analysis, XPS, measurement of zeta potential and particle size distribution. Plasma treatment of ceramic particles had a substantial effect on the deposition rate, which caused a significant reduction of surface roughness and slight improvement of the density and mean grain size of the fabricated coatings. Moreover, the plasma treatment resulted in a simultaneous anodic and cathodic EPD.

1. Introduction

Structural ceramic materials play an important role in nowadays technologies, especially automotive, medicine, space and military industries [1]. In all these various applications the different final properties are required. The basic properties, both strengths and weaknesses, of commonly used oxide or non-oxide ceramics (Al_2O_3, ZrO_2, SiC, Si_3N_4 etc.) are known for a very long time. Many scientists therefore focus their attention to improve one or more material characteristic by changing of the chemical nature by addition of another type of the material in form of atoms, particles, whiskers, tubes, fibres etc. [2–4]. Different approach is based on optimising of appropriately chosen manufacturing method with the aim to influence and properly "tailor" a microstructure, because all properties of sintered ceramics depend directly on the microstructure (defects, porosity, grain size, impurities). This optimisation should be optimally done right at the beginning of the manufacturing process.

It is known that the macroscopic properties of the ceramic powder are influenced by its surface properties [5]. Non-thermal plasma treatment is a known method to alter the surface characteristics of a number of materials in quite diverse forms, including the powdered ones. Most of the reported literature deals with the polymer powders. Using a vacuum plasma system, the wetting or rheological properties of powder was improved either by direct plasma exposure [6,7], which introduce new polar functional groups to the surface (carbonyls, carboxyl or amino groups), or by a thin film deposition from a suitable organosilicon precursor [8]. The benefit of using the direct plasma exposure lays in the simplified control of processing parameters. Co-deposition on the other hand delivers a surface modification which is more stable in time. The list of literature addressing the plasma modification of inorganic powders is substantially shorter. In [9] the RF (13.56 MHz) plasma, low-pressure air treatment of kaolinite powders led to a significant improvement of its water wettability. Similar type of capacitively coupled RF reactor was use to improve the stability of TiO_2 particles in water, through the plasma polymerization of acrylic acid onto the particles surface [10]. Inductively coupled RF (13.56 MHz) plasma reactor was used in [11] to make uniform deposition of ultra-thin polymer films of 2 nm on the surfaces of alumina nanoparticles.

In general, the low-pressure plasma treatment requires relatively long treatment times of 10–300 min, which in some cases may be of concern. With this respect, the use of non-thermal plasma generated and atmospheric pressure is a feasible option. In [12] the volume geometry of dielectric barrier discharge (DBD) [13] was used to create active amino groups by forming an aminosilane coatings on porous alumina microspheres, with the deposition times below 5 min. Paper of Szalay et al. [14] reported, that a 30 s direct air plasma treatment of

* Corresponding author at: CEITEC BUT, Brno University of Technology, Purkynova 123, 61200 Brno, Czech Republic.
E-mail address: drdlik@volny.cz (D. Drdlik).

https://doi.org/10.1016/j.ceramint.2018.02.215
Received 10 January 2018; Received in revised form 15 February 2018; Accepted 26 February 2018
Available online 02 March 2018
0272-8842/ © 2018 Elsevier Ltd and Techna Group S.r.l. All rights reserved.

submicron alumina, using a specific co-planar type of DBD – DCSBD, improved substantially the stability of water-Al_2O_3 colloidal dispersion. This was in agreement e.g. which the earlier results of Gibson et al. [15] who studied water dispersion of DBD plasma modified nanodiamond particles.

Clearly, a positive effect of plasma treatment (low-pressure or DBD) on water-based dispersions, by improving the powder hydrophilicity, is now a well-proven experimental fact. However, a possibility of employing plasma pre-treatment for non-aqueous (i.e. non-polar organic solvents) dispersions remains an open question, despite its indisputable importance for many of the ceramics wet shaping methods. For example, to our best knowledge the effect of plasma pre-treatment on electrophoretic deposition (EPD) has not been studied yet.

EPD is a versatile shaping method using the stable colloidal dispersions for fabrication of ceramics films [16] or layers [17]. In EPD, charged ceramic particles, dispersed in a liquid medium, are attracted and deposited onto a conductive substrate of opposite charge on application of an electric field. The key factors affecting of EPD are particle size, zeta potential (stability) and electrical conductivity of dispersion [18]. From this point of view the combination of DBD and EPD seems to be a new unstudied approach how to optimise fabrication method and/or properties of the ceramic body.

In the presented article, the EPD from the as-received and DCSBD activated sub-micron alumina powders are thoroughly compared, to evaluate the effect of plasma pre-treatment on raw and sintered ceramic material. The EPD was carried out in a non-aqueous dispersion, namely in 2-propanol, with and without the presence of stabiliser. As we will show, plasma-induced surface changes will bring a beneficial effect also in this type of non-aqueous environment.

2. Experimental

2.1. Powder pre-treatment

Sub-micron alumina powder (D_{BET} = 150 nm, TM-DAR, Taimei Chemicals, Japan) was plasma treated by the Diffuse Coplanar Surface Barrier Discharge (DCSBD). Thin (< 0.3 mm) layer of non-thermal plasma was generated above the 0.6 mm thick flat dielectric panel made of 96% Al_2O_3 by the pair of screen printed comb-like high voltage electrodes, situated on the opposite panel face (Fig. 1). The width of electrode strips was 1.5 mm, their mutual distance was 1 mm. The system was powered by sinusoidal HV of 14 kHz at 20 kV peak-to-peak and 400 W input power, supplied by in-house build power generator. The energizing electrodes were cooled by circulating transformer oil, which served also as their electrical insulation. Discharge was operated in still (no flow) atmospheric pressure air of absolute humidity within the range of 3–8 g/m^3. Active area of generated plasma of used DCSBD unit was 8 × 20 cm. Maximum temperature of DCSBD dielectric panel was less than 70 °C.

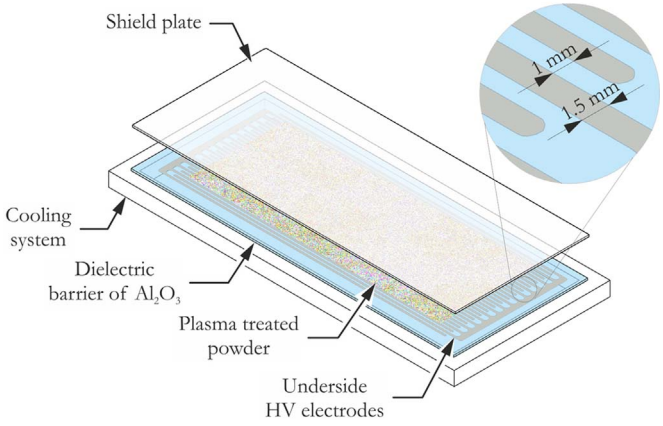

Fig. 1. Scheme of DCSBD generator.

The treatment was done in the discontinuous regime. A small amount (approximately 0.4 g) of alumina powder was sifted on the surface of DCSBD panel, to form a very thin powder layer which was found to be a necessary condition for uniform plasma exposure of the whole powder bed. The thin powder layer was covered with the shield alumina plate to prevent its loss due the ionic wind during the plasma treatment. Ionic wind, on the other hand, provided a useful mixing of the layered powder, which help to the uniform plasma exposure of powder particles. After the set treatment time (typically 1 min), the treated powder was scraped away, collected for further processing, and the whole process was repeated again. The treated powder exhibited no static charge on its surface.

Chemicals adsorbed or bound on the surface of both as-received and plasma treated alumina powders were determined by simultaneous thermogravimetric and mass spectrometric analysis using the STA 409C / CD analyser (Netzsch, Germany). X-ray photoelectron spectroscopy (XPS) measurements were done on the ESCALAB 250Xi (Thermo Fisher Scientific, USA) equipped with microfocused Al Kα monochromated X-ray source (1486.6 eV). The X-ray beam of 200 W with the diameter of 650 μm was used. The survey spectra were acquired with a pass energy of 50 eV and a resolution of 1 eV. High-resolution scans were acquired with a pass energy of 20 eV and a resolution of 0.05 eV. To prevent any charging of the surface, an electron flood gun was used. Spectra were referenced to the hydrocarbon type C 1s component set at a binding energy of 284.8 eV. The spectra calibration, processing and fitting routines were done using Avantage software.

2.2. Preparation of dispersions

The both as received and plasma treated alumina powders were dispersed in the non-stabilised or stabilised 2-propanolic dispersions. The dispersions contained 15 wt% of alumina and dried 2-propanol (p.a., Lachner, Czech Republic). The stabilisation was attained by adding of 4.25 wt% of monochloroacetic acid (MCAA, p.a., Sigma-Aldrich, Germany); the amount of 2-propanol was appropriately reduced to retain the same solid phase content.

The dispersions were mechanically stirred in an ultrasonic bath for 30 min. The electrical conductivity of the dispersions was determined by using a SevenCompact Conductivity S230 device (Mettler Toledo AG, Switzerland) equipped with a platinum 4-plate conductivity probe (0–500 mS cm^{-1}, 0–100 °C, 0.80 cm^{-1}). The particle size distribution of alumina particles dispersed in 2-propanol was measured via laser diffraction using the LA950 analyser (Horiba, Japan). The zeta potential of the dispersions was determined using a Zetasizer Nano ZS (Malvern Instruments, UK).

2.3. Electrophoretic deposition

Vertically oriented EPD under a constant current of 5 mA (current density of 0.57 mA/cm^2) was used. Two stainless steel electrodes with polished surface areas of 8.8 cm^2 were placed into glass container with volume of 40 mL. The distance between electrodes was set to 26 mm. The total time of deposition was 30 min. The deposition was interrupted each 5 min and mechanically stirred to avoid particle sedimentation. At the same time, the deposition yield was recorded by weighting of deposited mass on the deposition electrode in 2-propanol or solution of 2-propanol with MCAA, respectively.

2.4. Study of deposits

The deposits were dried at 120 °C for 20 min immediately after deposition. Then the deposits were removed from the electrodes and annealed and sintered at 800 °C and 1300 °C for 1 h in air, respectively. The relative densities of thermally treated deposits were measured

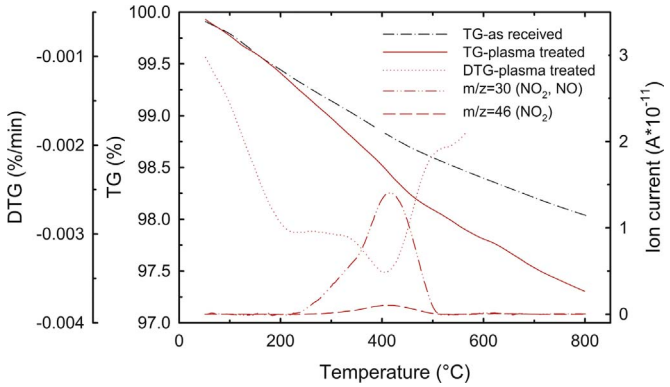

Fig. 2. TG/DTG/MS curves of as received and plasma treated alumina powders.

using the Archimedes method (EN 623-2). The theoretical density of alumina used for calculations was 3.987 g/cm^3. The microstructure of deposits was observed using a Lyra 3 scanning electron microscopy (SEM, FEG/FIB, Tescan, Czech Republic). The mean grain size (MGS) was determined using the linear intercept method with a correction factor of 1.56 [19]. The deposit surface roughness was observed using a Lext OLS3100 confocal microscope (Olympus, Japan).

3. Results

3.1. Characterisation of the powders and dispersions

Both as received and plasma treated powders were evaluated using simultaneous thermogravimetric/mass spectrometric analysis at temperature of 20–800 °C, as shown in Fig. 2. The analysis revealed the differences in weight decrease with increasing temperature. The DTG curve of as received powder did not exhibit any significant effects. The DTG curve of plasma treated powder exhibited one broad maximum in the temperature range of 200–500 °C. In this temperature range the loss in mass of plasma treated powder was higher by ca 0.5% than the mass loss of as received powder, and was presumably attributed to NO (m/z = 30) and NO_2 (30 and 46) molecules detected by quadrupole mass spectrometer. DCSBD (as well as other DBD systems) operated in the ambient air is known to be an effective generator of all varieties of nitrogen oxide molecules [20,21]. Their presence in the TGA mass spectra is therefore to be expected. From this point of view, our measurement is consistent with the adsorption of NO_2 and NO_3 after plasma treatment of flat aluminium surface that was reported in a recent study of Bonova et al. [22].

The survey XPS spectra revealed three major components – Al, O and C. Plasma treatment had only a minimal effect to their mutual ratio, which is contrary to the typical XPS outcome of plasma treated polymer materials/powders [23]. Some insight to character of plasma induced changes was gained by deconvoluting the Al 2p and C 1s peaks. Aluminium oxides and hydroxides are extremely difficult to differentiate by XPS, because the values for the varying oxides and hydroxides overlap each other. The left column in Fig. 3 shows high resolution scans of Al 2p for untreated and plasma-activated alumina powder deconvoluted into three components: Al_2O_3 (74.1 eV), $Al(OH)_3$ (74.8 eV) and AlOOH (75.2 eV). Corresponding concentrations are listed in Table 1. The most significant changes resulting from plasma treatment are the decrease of alumina component and increase of AlOOH chemical bond. For these components, relative areas are changed by a factor of 5.7 and 10.8, respectively. The relative area corresponding to $Al(OH)_3$ component was not affected by the plasma treatment. This agrees with former findings of Szalay et al. [14] whose pair comparison of NIR spectra for as received and plasma activated alumina powders same showed the presence of differently bound OH groups. High-resolution scans of C 1s peaks (see right column in Fig. 3) were decomposed into four components: C–C/C–H at 284.8 eV, C–O at 286.3 eV, C = O at 287.8 eV, O–C = O at 289.2 eV and carbonate CO_3^{2-} at 290.9 eV. Differences in peak areas are summarized in Table 1. The most significant change due to the plasma treatment is the increase of C-O and C = O chemical state at the expense of C-C/C-H component. Exposure to plasma resulted in more than fivefold increase of C-O peak areas. For C = O component, a plasma-treated process enhanced relative area by a factor of 3. The presence of carbonates on the surface can be explained by the reaction of hydroxylated surface sites with the atmospheric CO_2 [24].

After dispersing of the both powders in 2-propanol or solution of 2-propanol and MCCA the zeta potential was measured. The dispersions containing as received or plasma treated alumina with 2-propanol only had positive zeta potentials of + 4.7 mV or + 4.8 mV, respectively. This result suggests that the dispersions were unstable because a lower limit of the dispersion stability is approximately of |30| mV [25]. The zeta potential of the stabilised dispersion by MCAA containing as received powder was − 25.6 mV whereas the dispersion containing plasma treated alumina had the zeta potential of − 22.0 mV.

Particle size distribution of as received and plasma treated alumina powders dispersed in non-stabilised and stabilised 2-propanolic dispersion is shown in Fig. 4. The dispersed as received alumina particles had a unimodal particle size distribution with peak maxims at 170 and 270 nm for stabilised and non-stabilised dispersions, respectively. In contrast, both dispersions containing plasma treated alumina had a bimodal particle size distribution with primary particle size of 200 nm and aggregates size of 1.65 μm (or 1.94 μm). It is evident that the bimodal distribution was caused by the plasma treatment.

3.2. Electrophoretic deposition

The dependence of deposited mass on deposition time of non-stabilised and stabilised dispersions containing the as received (black diamonds) or plasma treated (red circles) alumina is shown in Fig. 5a. The as received alumina particles in non-stabilised dispersion moved to the cathode and cathodic electrophoretic deposition took place. In agreement with our expectations, the small amount of charge carriers resulted in a low electrical conductivity of the dispersion (0.01 μS/cm). To sustain the fixed current value, high voltage was needed, which in turn promoted the high deposition rate [26,27]. The EPD had to be terminated after 10 min due to the voltage exceeding the limits of EPD power supply. Contrary, if the MCCA was added to the dispersion then the alumina particles coated the anode (anodic deposition). The alumina particles covered deposition electrode relatively fast, because the low dispersion electrical conductivity of 1.37 μS/cm still gave rise to a relatively high voltage. Due to high velocity of particles the both coatings had high surface roughness, as is documented in Fig. 5b and Fig. 5c.

The plasma treatment of alumina powder dispersed in 2-propanol affected EPD substantially. The electrical conductivities of non-stabilised and stabilised dispersions increased significantly up to 7.59 μS/cm and 23.70 μS/cm, respectively. As a result, the deposition rate as well as the deposition mass decreased. The most surprising phenomenon occurred during the deposition from the non-stabilised dispersion. An atypical anodic together with cathodic electrophoretic deposition were observed (see Fig. 5e). Contrary to cathodic deposition made with as received alumina powder, which resulted in rough surface deposit, the thin, smooth and homogenous coating of plasma treated alumina particles was formed on the anode. Less intensive cathode deposition of Fig. 5e formed an inhomogeneous coating of alumina agglomerates or aggregates. The EPD of plasma treated alumina from the stabilized dispersion resulted in the smooth coating on the anode as well (see Fig. 5d). For further evaluation of plasma treated samples, only the coatings fabricated on the anode were used.

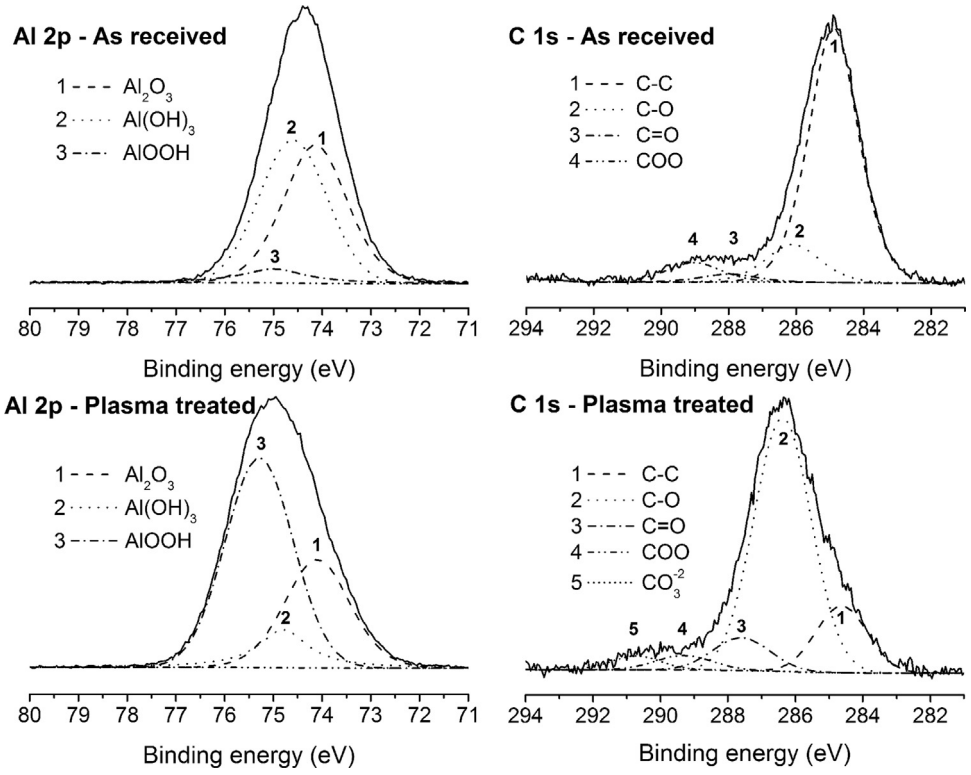

Fig. 3. Deconvoluted XPS spectra of Al 2p and C 1s peaks, for as received and plasma treated alumina powders.

Table 1
XPS results: atomic composition and relative area of chemical bonds.

	Name	Ref[a]	Treated[b]
survey	Al	35%	33%
	O	51%	51%
	C	14%	16%
C 1s	C–C	78%	16%
	C–O	13%	68%
	C=O	3%	9%
	COO	6%	4%
	CO_3^{2-}	0%	3%
Al 2p	Al_2O_3	44%	20%
	$Al(OH)_3$	50%	11%
	AlOOH	6%	59%

[a] i.e. as received alumina powder.
[b] i.e. plasma treated alumina powder.

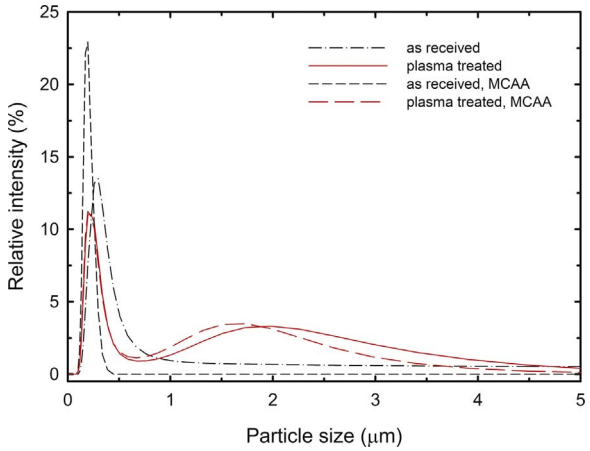

Fig. 4. Particle size distribution of as received and plasma treated alumina powders.

3.3. Physical properties of deposits

The demonstration of the plasma treatment on the final properties of deposits fabricated by EPD is given in Table 2. In general, the plasma treatment significantly affects the surface roughness of the deposits and slightly improves other properties (density, MGS).

The density of the green body (ρ_{an}) fabricated from quasi stable suspension (as received powder, no MCAA) was 48.0% of theoretical density (t.d.). When the stabilised dispersion was used then density of green body increased to 54.6% t.d. The same deposition conditions allowed fabrication of deposits with densities of 49.1% and 51.3% t.d from plasma treated alumina. After sintering at 1300 °C/1 h the differences in the densities (ρ_{sin}) of all deposits were in the range only of 0.5–0.7% with the highest values belonging to the plasma treated alumina.

The more significant difference was observed by MGS measurement. The deposits electrophoretically deposited from the non-stabilised dispersions reached MGS of 0.61 μm and 0.52 μm for as received and plasma treated alumina, respectively. In the case of stabilised dispersion, the coating formed from as received alumina had MGS of 0.73 μm contrary to plasma treated alumina one with MGS of 0.57 μm. Thus, the plasma treatment resulted in more dense ceramics with finer microstructure.

However, the most positive effect of plasma treatment of alumina powder can be seen in the optimisation of the surface quality of the deposits. The surface roughness of plasma treated deposits is significantly lower related to samples prepared from as received alumina (see Table 2). Moreover, the surface roughness dramatically increased thickness of the coatings. The deposits with rough surface had coating thicknesses of 4.5 and 6.2 mm while the deposits fabricated from plasma treated powder was approximately 1.0 mm thick.

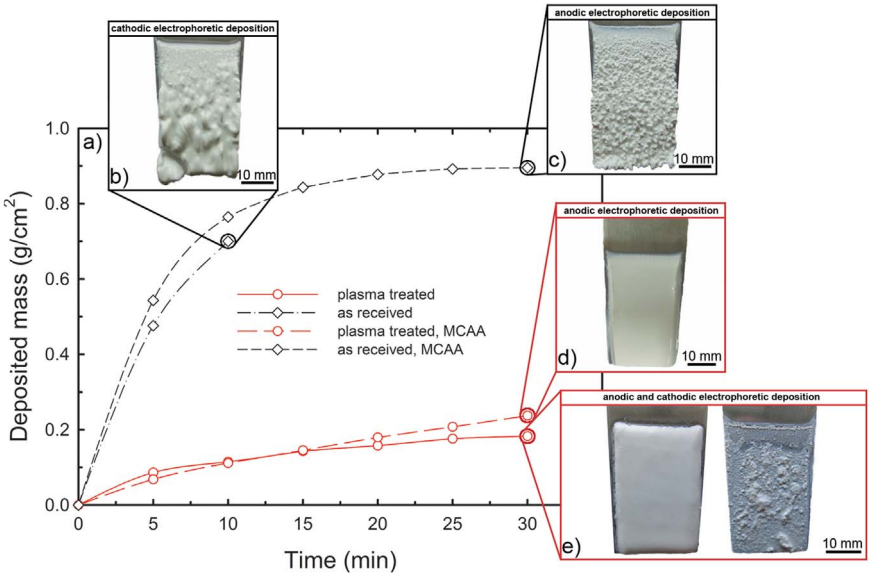

Fig. 5. Dependence of a) deposited mass on the deposition time and photographs insets of coatings prepared from dispersions containing b) 2-propanol and as received alumina, c) 2-propanol, MCAA and as received alumina, d) 2-propanol, MCAA and plasma treated alumina, e) 2-propanol and plasma treated alumina.

Table 2
Relative densities (annealed ρ_{an} and sintered ρ_{sin}), mean grain size (MGS) and surface roughness (R_a) of the deposits manufactured from non-stabilised and stabilised dispersions.

	ρ_{an} (%)		ρ_{sin} (%)		MGS (μm)		R_a (μm)	
	Ref[a]	Treated[b]	Ref	Treated	Ref	Treated	Ref	Treated
no MCAA	48.0	49.1	98.2	98.7	0.61 ± 0.09	0.52 ± 0.06	70.3 ± 14.8	2.2 ± 0.2
MCAA	55.7	51.3	98.2	98.9	0.73 ± 0.12	0.57 ± 0.09	155.0 ± 22.1	2.1 ± 0.2

[a] i.e. manufactured from as received alumina.
[b] i.e. manufactured from plasma treated alumina.

4. Discussion

4.1. Characterisation of the powders and dispersions in relation to EPD process

The plasma treatment of alumina powder followed by dispersing in 2-propanol and electrophoretic deposition has brought some surprising results, the explanation of which will require further detailed study. One of them is the insignificant change of the zeta potential observed on the plasma treated powder, which is in some conflict with the treated powder behaviour during the EPD process.

From the aforementioned measurement of the zeta potential it is obvious that the as received alumina particles dispersed in 2-propanol without stabilisation aid had a positive surface charge (zeta potential of + 4.7 mV). This surface charge originates from traces of water adsorbed on the particle surface because the coordinatively unsaturated surface Al ions provide strong Lewis acid (electron-acceptor) sites [28]. When the dispersion contains MCAA, the surface charge of alumina particles become negative due to the electrosteric stabilisation mechanism proposed by Cihlar et al. [29]. Nevertheless, the zeta potentials of both type dispersions was similar and thus the plasma treatment of alumina powder had no significant effect on it. The similar conclusion was published by Szalay et al. [14] who observed higher colloidal stability of plasma treated alumina powder dispersed in water, but the zeta potential measurement was practically unchanged related to the reference powder.

Despite of positive value of zeta potential in the case of non-stabilised dispersion containing plasma treated alumina, the most of particles had negative charge were deposited on the anode (see Fig. 5e). Unfortunately, we cannot entirely explain such mismatch between the zeta potential measurement and deposition process at this time.

A possible explanation of the anodic deposition can be attributed to the ample amount of NO_x species detected by TGA mass spectra on surface of plasma treated powders. According to DFT models of NO_x species on alumina surfaces [30–32], the major part of NO_x species is bonded to the alumina surface through Al-O-N bound. The most preferred orientation of NO_x species is that of oxygen atom pointing out from the surface. In such manner, the most outbound oxygen atom of NO_x would create a negative surface charge on the particle surface, opposite to the natural positive charge of alumina. In the same manner, the increase of dispersion conductivity can be explained by desorption of plasma introduced species to the particles surface, because the NO_x species are known to be solvable in organic solvents [33,34], or other, currently unresolved species. An alternate explanation is based on the XPS observed increase of C-O, C = O and CO_3^{2-} bonds on plasma treated powders. Each of these functional groups provides negative surface charge, and can be therefore responsible for the anodic deposition. At the moment it can be only speculated, which of these two mechanisms is more dominant.

The coating simultaneously formed on cathode is then most likely caused by insufficiently plasma treated powder. The presence of the bimodal particle size distribution (see Fig. 4) similarly supports the idea of partial or imperfect plasma treatment resulting in simultaneous presence of positively and negatively charged particles within the dispersion. Their mutual attraction subsequently creates aggregates or agglomerates. Future experiments are planned for confirmation of this assumption and positive results can then establish the EPD as a useful and simple method for determination of efficiency of powders plasma treatment.

In the case of stabilised dispersion containing the plasma treated

alumina, the particles surface was covered completely by negative charge of plasma introduced functionalities and MCAA. Moreover, the stabilisation aid further increased ionic strength of the dispersion and thus could promote the further increase of electrical conductivity of 23.70 μS/cm via more intensive desorption of adsorbed species. However, following similarity of the both red curves in Fig. 5a one can conclude that the use of plasma treatment of ceramic particles should be considered as an alternative way how to use EPD without any stabilising aids which are in many cases dangerous or even toxic to the environment.

4.2. Physical properties of deposits

The exceptionally high green density was measured at coating fabricated from stabilised dispersion containing as received alumina powder. It could probably be caused by the high external pressure of rapidly moved particles according to mechanism proposed by Hamaker et al. [35] and the long-time deposition because the lower deposition rate at a later stage of EPD (see Fig. 5a) is more favourable for particles to find optimal positions [27]. Nevertheless, after sintering process the densities of the deposits fabricated from the plasma treated alumina were of about 0.5–0.7% t.d. higher to that of as received powder. For comparison, Szalay et al. [14] measured the same densities at same temperature for both reference and plasma processed alumina samples, although dry process of axial pressing with following cold isostatic press has been used in their case.

The same authors have shown that the plasma treatment of alumina powder affects positively the MGS. They reported 30% decrease of MGS for sample prepared from plasma treated powder. We have observed a similar MGS decrease for the plasma treated samples processed at the same sintering temperature that had lower MGS contrary to deposits fabricated from as received alumina. In our case, the decrease of the MGS was 15% (from non-stabilised dispersion) and 22% (from stabilised dispersion). These results suggests that plasma treatment of the fine alumina powder allows microstructure refinement during EPD, which results in the higher homogeneity of green body.

The surface smoothing as well as density improving can be attributed to the decrease of deposition rate, caused by the higher electrical conductivity of the dispersions [26,27,36]. During the EPD, the particle deposition and particle rearrangement occur concurrently. Final deposit porosity is a combined result of the deposition rate and the rearrangement ability of particles [27]. Therefore, the as received particles had too high deposition rate at the beginning of EPD and too short time to move into optimum positions at the deposit surface, resulting in a loose packing structure. Moreover, all particles (primary particles and large agglomerates or aggregates) are deposited at the high deposition rates, i.e. low electrical conductivities. In such situation the rough surface of the deposit could be expected. It should be noted however, that the decrease of deposition rate resulted in the decrease of the deposit coating thickness.

5. Conclusions

The effect of atmospheric air plasma treatment on electrophoretically deposited alumina powder was investigated. A considerable quantity of NO and NO_2 were detected on the surface of the plasma treated powder. Although these species did not significantly affect the stability of the dispersion, they have significant impact on the electrophoretic deposition and quality of the coatings. The atypical simultaneous anodic with cathodic electrophoretic deposition were observed. The products of plasma treatment reduced deposition rate which significantly improved surface roughness of coatings and slightly improved their density and mean grain size. It was shown, that the plasma treatment of ceramic particles allows fabrication of homogeneous thin coatings via EPD without use of any stabilising aid. The results also indicate the EPD potential usage for determination of plasma treatment efficiency of ceramics powders. This assumption will be investigated and discussed in detail in our follow-up article.

Acknowledgements

The authors acknowledge the support of the Grant agency of the Czech Republic under grant no. 17-05620S. This research was also carried out under the project CEITEC 2020 (LQ1601) with financial support from the Ministry of Education, Youth and Sports of the Czech Republic under the National Sustainability Programme II. We also thank to CEITEC Nano RI, MEYS CR, 2016–2019 for allowing the SEM analyses. TM and JR would like to acknowledge the support of project CZ.1.05/2.1.00/03.0086 funded by European Regional Development Fund and project LO1411 (NPU I) funded by Ministry of Education Youth and Sports of Czech Republic.

References

[1] J.J. Wachtman, Structural Ceramics, Academic Press, London, 1989.
[2] D. Drdlik, K. Drdlikova, H. Hadraba, K. Maca, Optical, mechanical and fractographic response of transparent alumina ceramics on erbium doping, J. Eur. Ceram. Soc. 37 (2017) 4265–4270.
[3] J. Homeny, W.L. Vaughn, M.K. Ferber, Silicon carbide whisker/alumina matrix composites: effect of whisker surface treatment on fracture toughness, J. Am. Ceram. Soc. 73 (1990) 394–402.
[4] D.-Y. Lee, D.-H. Yoon, Properties of alumina matrix composites reinforced with SiC whisker and carbon nanotubes, Ceram. Int. 40 (2014) 14375–14383.
[5] S.H. Jung, S.M. Park, S.H. Park, S.D. Kim, Surface modification of fine powders by atmospheric pressure plasma in a circulating fluidized bed reactor, Ind. Eng. Chem. Res. 43 (2004) 5483–5488.
[6] C. Arpagaus, A. Sonnenfeld, P.R. von Rohr, A downer reactor for short-time plasma surface modification of polymer powders, Chem. Eng. Technol. 28 (2005) 87–94.
[7] M. Horakova, P. Spatenka, J. Hladik, J. Hornik, J. Steidl, A. Polachova, Investigation of adhesion between metal and plasma-modified polyethylene, Plasma Process. Polym. 8 (2011) 983–988.
[8] C. Roth, Z. Künsch, A. Sonnenfeld, P. Rudolf von Rohr, Plasma surface modification of powders for pharmaceutical applications, Surf. Coat. Technol. 205 (2011) S597–S600.
[9] L. Lapcik, B. Lapcikova, I. Krasny, I. Kupska, R.W. Greenwood, K.E. Waters, Effect of low temperature air plasma treatment on wetting and flow properties of kaolinite powders, Plasma Chem. Plasma Process. 32 (2012) 845–858.
[10] A. Solís-Gómez, M.G. Neira-Velázquez, J. Morales, M.A. Sánchez-Castillo, E. Pérez, Improving stability of TiO_2 particles in water by RF-plasma polymerization of poly (acrylic acid) on the particle surface, Colloids Surf. A: Physicochem. Eng. Asp. 451 (2014) 66–74.
[11] D. Shi, S.X. Wang, W.Jv Ooij, L.M. Wang, J. Zhao, Z. Yu, Uniform deposition of ultrathin polymer films on the surfaces of Al_2O_3 nanoparticles by a plasma treatment, Appl. Phys. Lett. 78 (2001) 1243–1245.
[12] M.G. Trulli, N. Claes, J. Pype, S. Bals, K. Baert, H. Terryn, E. Sardella, P. Favia, A. Vanhulsel, Deposition of aminosilane coatings on porous Al_2O_3 microspheres by means of dielectric barrier discharges, Plasma Process. Polym. 14 (2017).
[13] R. Brandenburg, Dielectric barrier discharges: progress on plasma sources and on the understanding of regimes and single filaments, Plasma Sources Sci. Technol. 26 (2017).
[14] Z. Szalay, K. Bodisova, H. Palkova, P. Svancarek, P. Durina, J. Rahel, A. Zahoranova, D. Galusek, Atmospheric pressure air plasma treated alumina powder for ceramic sintering, Ceram. Int. 40 (2014) 12737–12743.
[15] N. Gibson, O. Shenderova, T.J.M. Luo, S. Moseenkov, V. Bondar, A. Puzyr, K. Purtov, Z. Fitzgerald, D.W. Brenner, Colloidal stability of modified nanodiamond particles, Diam. Relat. Mater. 18 (2009) 620–626.
[16] P. Sarkar, P.S. Nicholson, Electrophoretic deposition (EPD): mechanisms, kinetics, and application to ceramics, J. Am. Ceram. Soc. 79 (1996) 1987–2002.
[17] D. Drdlik, M. Slama, H. Hadraba, K. Drdlikova, J. Cihlar, Physical, mechanical, and biological properties of electrophoretically deposited lithium-doped calcium phosphates, Ceram. Int (2017).
[18] L. Besra, M. Liu, A review on fundamentals and applications of electrophoretic deposition (EPD), Prog. Mater. Sci. 52 (2007) 1–61.
[19] M.I. Mendelson, Average grain size in polycrystalline ceramics, J. Am. Ceram. Soc. 52 (1969) 443–446.
[20] J. Cech, A. Brablec, M. Cernak, N. Puac, N. Selakovic, Z.L. Petrovic, Mass spectrometry of diffuse coplanar surface barrier discharge: influence of discharge frequency and oxygen content in N-2/O-2 mixture, Eur. Phys. J. D 71 (2017).
[21] I. Jõgi, E. Levoll, J. Raud, Plasma oxidation of NO in O_2:N_2 mixtures: the importance of back-reaction, Chem. Eng. J. 301 (2016) 149–157.
[22] L. Bonova, A. Zahoranova, D. Kovacik, M. Zahoran, M. Micusik, M. Cernak, Atmospheric pressure plasma treatment of flat aluminum surface, Appl. Surf. Sci. 331 (2015) 79–86.
[23] P. Klímek, T. Morávek, J. Ráhel, M. Stupavská, D. Děcký, P. Král, J. Kúdela, R. Wimmer, Utilization of air-plasma treated waste polyethylene terephthalate particles as a raw material for particleboard production, Compos. Part B: Eng. 90

(2016) 188–194.
[24] C. Weilach, C. Spiel, K. Fottinger, G. Rupprechter, Carbonate formation on Al_2O_3 thin film model catalyst supports, Surf. Sci. 605 (2011) 1503–1509.
[25] S. Myhra, J.C. Rivière, Characterization of Nanostructures, CRC Press, Boca Raton, 2012.
[26] B. Ferrari, R. Moreno, The conductivity of aqueous Al_2O_3 slips for electrophoretic deposition, Mater. Lett. 28 (1996) 353–355.
[27] F.W. Guo, I.P. Shapiro, P. Xiao, Effect of HCl on electrophoretic deposition of yttria stabilized zirconia particles in organic solvents, J. Eur. Ceram. Soc. 31 (2011) 2505–2511.
[28] K.C. Hass, W.F. Schneider, A. Curioni, W. Andreoni, The chemistry of water on alumina surfaces: reaction dynamics from first principles, Science 282 (1998) 265–268.
[29] J. Cihlar, D. Drdlik, Z. Cihlarova, H. Hadraba, Effect of acids and bases on electrophoretic deposition of alumina and zirconia particles in 2-propanol, J. Eur. Ceram. Soc. 33 (2013) 1885–1892.
[30] H.H. Ingelsten, A. Hellman, H. Kannisto, H. Gronbeck, Experimental and theoretical characterization of NO_x species on Ag/alpha-Al_2O_3, J. Mol. Catal. a-Chem. 314 (2009) 102–109.
[31] A. Hellman, H. Gronbeck, First-principles studies of NOx chemistry on Ag-n/alpha-Al_2O_3, J. Phys. Chem. C 113 (2009) 3674–3682.
[32] Z.M. Liu, L.L. Ma, A.S.M. Junaid, NO and NO_2 Adsorption on Al_2O_3 and Ga modified Al_2O_3 surfaces: a density functional theory study, J. Phys. Chem. C 114 (2010) 4445–4450.
[33] A.W. Shaw, A.J. Vosper, Solubility of nitric-oxide in aqueous and non-aqueous solvents, J. Chem. Soc. Farady Trans. 1 73 (1977) 1239–1244.
[34] S. Signorelli, M.N. Moller, E.L. Coitino, A. Denicola, Nitrogen dioxide solubility and permeation in lipid membranes, Arch. Biochem. Biophys. 512 (2011) 190–196.
[35] H.C. Hamaker, E.J.W. Verwey, Part II.-(C) Colloid stability. The role of the forces between the particles in electrodeposition and other phenomena, Trans. Faraday Soc. 35 (1940) 180–185.
[36] D. Drdlik, E. Bartonickova, H. Hadraba, J. Cihlar, Influence of anionic stabilization of alumina particles in 2-propanol medium on the electrophoretic deposition and mechanical properties of deposits, J. Eur. Ceram. Soc. 34 (2014) 3365–3371.

PUBLIKACE VII

Ceramics International

Sintering activation energies of anisotropic layered and particle alumina/zirconia-based composites and their mechanical response

--Manuscript Draft--

Manuscript Number:	
Article Type:	SI: Sintering2023
Keywords:	Sintering; activation energy; high-temperature dilatometry; laminate; particle composite
Corresponding Author:	Karel Maca Vysoké učení technické v Brně Brno, CZECH REPUBLIC
First Author:	Daniel Drdlik
Order of Authors:	Daniel Drdlik
	Ilya Sokolov
	Hynek Hadraba
	Zdenek Chlup
	Katarina Drdlikova
	Karel Maca
Abstract:	Information on the sintering activation energy is currently focused on evaluation of single-phase ceramic systems. This work shows the results of high-temperature dilatometry measurements of layered and particle composites based on alumina and zirconia. Layered composites with different layer thickness ratios and particle composites with variable composition in the entire concentration range were prepared by electrophoretic deposition allowing manufacturing composites with precious design and strongly bonded interfaces. The phenomena observed during the high-temperature dilatometry measurements are discussed, and the data were used to calculate the sintering activation energies of composites using the modified Master Sintering Curve concept. By covering a wide range of composite designs, it was possible to determine differences in activation energies and to show their dependence on the direction in the case of laminate composites given by the directionally dependent sintering behaviour. Sintering activation energies of layered composites were always higher than for nominally pure monoliths due to constrained sintering showing maximum sintering activation energies at lower volumes of zirconia in the layers for longitudinal and transversal orientation of the samples. A similar trend was identified in particle composites due to slowed down alumina densification by the pinning effect. Additionally, mechanical properties represented by Vickers hardness and indentation elastic modulus were related to the microstructure developed during sintering. The effects of interconnectivity of phases present in the composites together with other parameters of the microstructure were described.
Suggested Reviewers:	Mathias Herrmann mathias.herrmann@ikts.fraunhofer.de He is well known scientist in the field of sintering and characterization of advanced ceramics.
	Raul Bermejo raul.bermejo@unileoben.ac.at He is well known scientist in the field of design and processing of ceramic composite architectures for optimal strength and toughness.
	Csaba Balazsi balazsi.csaba@energia.mta.hu He is well known scientist in the field of ceramic materials (shaping, sintering, analysis).
Opposed Reviewers:	

Powered by Editorial Manager® and ProduXion Manager® from Aries Systems Corporation

Manuscript Click here to view linked References

Sintering activation energies of anisotropic layered and particle alumina/zirconia-based composites and their mechanical response

Daniel Drdlik[a,b], Ilya Sokolov[a], Hynek Hadraba[c], Zdenek Chlup[c], Katarina Drdlikova[a], Karel Maca[a,b*]

[a] *CEITEC BUT, Brno University of Technology, Purkynova 123, 612 00 Brno, Czech Republic*

[b] *Institute of Materials Science and Engineering, Brno University of Technology, Technicka 2, 616 00 Brno, Czech Republic*

[c] *Institute of Physics of Materials of the Czech Academy of Sciences, Zizkova 22, 616 00 Brno, Czech Republic*

* Corresponding author: maca@fme.vutbr.cz

Abstract

Information on the sintering activation energy is currently focused on evaluation of single-phase ceramic systems. This work shows the results of high-temperature dilatometry measurements of layered and particle composites based on alumina and zirconia. Layered composites with different layer thickness ratios and particle composites with variable composition in the entire concentration range were prepared by electrophoretic deposition allowing manufacturing composites with precious design and strongly bonded interfaces. The phenomena observed during the high-temperature dilatometry measurements are discussed, and the data were used to calculate the sintering activation energies of composites using the modified Master Sintering Curve concept. By covering a wide range of composite designs, it was possible to determine

differences in activation energies and to show their dependence on the direction in the case of laminate composites given by the directionally dependent sintering behaviour. Sintering activation energies of layered composites were always higher than for nominally pure monoliths due to constrained sintering showing maximum sintering activation energies at lower volumes of zirconia in the layers for longitudinal and transversal orientation of the samples. A similar trend was identified in particle composites due to slowed down alumina densification by the pinning effect. Additionally, mechanical properties represented by Vickers hardness and indentation elastic modulus were related to the microstructure developed during sintering. The effects of interconnectivity of phases present in the composites together with other parameters of the microstructure were described.

Keywords

Sintering; activation energy; high-temperature dilatometry; laminate; particle composite

1. Introduction

Generally, sintering is the densification of free powder or powder compact at a temperature below the material's melting point. Such a thermally driven process has been known for thousands of years; however, in the last century, considerable efforts have been made in the development of sintering methods and the sintering of various advanced ceramic materials. Along with this, various sintering models were derived, which are subject to constant refinement. One of the significant parameters allowing a better insight into the physical background of the sintering is the activation energy of sintering also referred to as apparent activation energy.

The beginnings of the study of the sintering activation energy are related to the work of Young and Cutler [1] who studied the densification of alumina, zirconia and titania at constant rates of heating to describe solid-solid reactions. Their work was followed up by Wang and Raj [2, 3] who used constant-heating-rate experiments to estimate activation energy in alumina, alumina/titania and alumina/zirconia particle composites. Since then, many scientific works have been published reporting the sintering activation energies of various ceramics. Afterwards, an engineering tool based on non-isothermal sintering for predicting the sintering process and also determining sintering activation energies was developed [4].

Su and Johnson [4] developed the concept of master sintering curve (MSC) assuming that the geometric parameters related to the sintering are functions only of green body microstructure (and therefore independent on the heating profile) and that only one prevalent diffusion mechanism is dominant in the sintering process. The MSC gives the relation between the thermal history of the sintering (using the parameter Q describing the activation energy of sintering) and density. The experimental approach of the concept is based on the time-consuming mathematical iterations drawing data from the number of sintering experiments conducted at different heating regimes. However, the following works brought simplification

in the construction of the MCS using computer programs [5] together with dilatometric data [6, 7] reducing computing time dramatically.

A lot of works have been published up to now to establish activation energies of nominally monolithic ceramics. The most attention was paid to alumina [1-3, 7-13], zirconia [3, 7, 9, 14-16], silicon nitride [17], zinc oxide [8], uranium dioxide [18, 19], yttrium oxide [20], etc. Moreover, it was found that the sintering technique can also play a role in diffusion mechanisms in studied materials affecting the activation energy of sintering [8]. Therefore, not only conventional sintering [1-3, 7-9] but also microwave sintering [8], sintering in microwave-induced oxygen plasma [21], spark plasma sintering [22], and liquid phase sintering [17] were considered to report complex data concerning activation energy of sintering at different conditions.

However, a more complex situation arises when multiple phases appear in the material. The volume of these phases can be distributed in an ordered manner in the form of individual particles (grains) or layers. The sintering activation energy of the particle composites based on alumina and zirconia ceramics was studied for the very first time by Wang and Raj [2, 3]. They showed that the activation energy remains in the range of 700 ± 100 kJ/mol when the composition changes from 5 to 95 vol.% zirconia [3]. Although the authors reported full range composition, only concentrations of 0, 5, 50, 95 and 100 vol.% zirconia were investigated. Therefore, a substantial part of the concentration profile of this ceramic particle composite is missing. Even less data is known about layered materials. Maca et al. [9] recently showed layered composites where alternating layers with different thicknesses and/or volumes of alumina and zirconia were evaluated in terms of sintering activation energies. For this geometrical purpose, the MCS concept using dilatometric measurements had to be modified to the so-called Master Shrinkage Curve [9]. It was found that strongly bonded layers exhibit sintering anisotropy demonstrated by different sintering activation energies in the two

measurement directions of the sintered samples. However, as with particle composites [3], only a small concentration range was studied in this work, i.e., the composite that had 50 vol.% represented by layers of alumina and the rest by zirconia. Thus, a much more precise insight into this issue is necessary for a better understanding of the sintering process in particle and layered ceramics.

These materials are very interesting from the point of view of their microstructural and mechanical properties. The alumina and zirconia particle composites can be divided into two categories depending on the major phase on Zirconia Toughened Alumina (ZTA, alumina is a major phase) and Alumina Toughened Zirconia (ATZ, zirconia is a major phase) providing improved strength, fracture resistance, elasticity, hardness, toughness, and/or wear resistance etc. These composites are widely employed in various structural applications across different industries such as cutting tools [23-25], aerospace applications [26], electrical insulators [27], wear-resistant products (nozzles, pump parts, valves etc.) [28], dental implants [29, 30], orthopaedic replacements [31, 32], coatings [29, 33] etc. Layered architectures which are composed of alternating layers of two or more different ceramic materials, offer unique fracture behaviour if the internal stresses are generated in the layers during sintering and cooling. In the case of alumina/zirconia layered material, the internals stresses arise during densification of the composite at the heating stage and dwell time on the sintering temperature [34]. However, such internal stresses are relatively small and can relax during the dwell time at the sintering temperature via the diffusion processes. More significant are internal stresses developed when reference (stress-free) temperature is exceeded [35] at the cooling stage of sintering. The stresses inside the strongly bonded layered structure originate from the thermal expansion mismatch of the ceramic materials resulting, among others, in a crack deflection behaviour [36]. Moreover, the presence of zirconia might originate transformation toughening mechanisms, which operate at the microstructural level [37].

The paper substantially expands the existing knowledge about the sintering activation energy of the particle and layered structures that are composed of alumina and zirconia in the full volume (concentration) range. This is achieved by using a modified MSC concept and high-temperature dilatometry. The sintering behaviour is correlated with the mechanical response of composite materials and discussed.

2. Experimental

Alumina (HP-DBM, Malakoff Ind., USA) and zirconia (TZ-3YS-E, Tosoh, Japan) ceramic powders with mean particle sizes of 0.47 and 0.14 μm, respectively, were dispersed in colloidal suspensions for their wet shaping via electrophoretic deposition (EPD). To this purpose, the suspensions were composed of 15 wt.% alumina and/or zirconia, 12.75 wt.% monochloroacetic acid (99 %, Merck, Germany) acting as a stabiliser, and 2-propanol dispersant (p.a., Lachner, Czech Republic) in the amount of 72.25 wt.%. Suspensions were stirred mechanically in an ultrasonic bath (output power 320 W) for 30 min prior to EPD.

The vertical position of two stainless steel electrodes with an effective surface area of 18.2 cm^2 placed at a distance of 26 mm between them was used for EPD in a glass cell. The electrodes connected with a stabilised source allowed to set a circuit with a constant current of 5 mA. Three types of ceramic materials were prepared i) monoliths (standards – nominally pure alumina or zirconia denoted as A and Z) ii) particle composites (i.e., homogeneous mixture of alumina and zirconia with given volume fraction), and iii) layered composites (i.e., alternating alumina and zirconia layers with various thickness). The particle composites (denoted as PC) were prepared by mixing of certain volume fraction of zirconia (i.e., 17, 25, 33, 45, 50, 55, 66, 75, and 83 vol.%) into alumina. The depositions lasting 30 min were interrupted each 5 min and the suspensions were thoroughly stirred to prevent sedimentation of the particles. Based on our previous results [38, 39] concerning deposition kinetic studies of alumina and zirconia we were able to fabricate layered structures (laminates; denoted as LC) with a precise thickness of layers. The laminates were designed with the same volume fractions of alumina and zirconia as in particle composites and the desired concentrations were set by different layers thickness ratios. The thickness ratios (A:Z) of 5:1, 3:1, 1.2:1 and vice versa were prepared by the repeated moving of deposition electrode from suspension containing alumina to zirconia suspension at strictly defined time segments. The total number of layers was set to 100. The information about

prepared samples including volume fractions of ceramic materials is summarised in Table 1. The deposits were dried at room temperature for 24 hours after deposition. Subsequently, they were removed from deposition electrodes and annealed at 800°C for 1 h in an ambient atmosphere.

The prepared samples were cut out from the green bodies in longitudinal (perpendicular to the deposition direction) and transversal orientation (parallel to the deposition direction) in the form of bars (4 × 4 × 10 mm) or cylinders (ø5 × ca 5 mm), respectively. The samples underwent high-temperature dilatometry sintering using L70/1700 (Linseis, Germany) at 1500°C with heating rates 2, 5, 10, and 20°C/min for 2 h at sintering temperature. The samples intended for mechanical testing were sintered in a conventional furnace at 1500°C with a heating rate of 10°C/min and a dwell time of 2 h.

The coefficient of thermal expansion was calculated using Equation (1):

$$\alpha = \frac{\varepsilon_{T\,room} - \varepsilon_{T\,max}}{(T_{room} - T_{max}) \cdot 100}, \quad (1)$$

where $\varepsilon_{T\,room}$ is the shrinkage after cooling, ε_{max} is the shrinkage at the end of the dwell, T_{room} is the temperature after cooling, and T_{max} is the dwell temperature.

The sintering shrinkage was calculated using Equation (2):

$$\varepsilon(t,T) = \varepsilon_{instant}(t,T) - \alpha \cdot 100 \cdot (T - T_{room}), \quad (2)$$

where $\varepsilon_{instant}$ (t,T) is the instantaneous measured shrinkage, t is the time, and T is the actual temperature.

To examine activation energies, allowing deeper insight into the physical background of the sintering process of anisotropic layered and particle composites, the modified Master Sintering Curve model [9] was applied for the construction of Master Shrinkage Curves. Assuming the work of Hansen et al. [40], it includes the relationship between the thermal history of the sintering and linear shrinkage under the following Equation (2):

$$\frac{-k}{\gamma\Omega D_0}\int_0^{\varepsilon_f}\frac{(G(\varepsilon))^n}{\Gamma(\varepsilon)}d\varepsilon=\Theta=\int_0^t\frac{1}{T}\exp\left(-\frac{Q}{RT}\right)dt, \quad (3)$$

where function Θ describes the thermal history of the sintering with the activation energy of sintering Q, k is the Boltzmann constant, γ is the surface energy, Ω is the atomic volume, D_0 is the coefficient of a diffusion process, G is the mean grain size, Γ represents scaling parameters, ε is the linear shrinkage, T is the thermodynamic temperature, R is the gas constant and t is the time. The four heating regimes were conducted for all samples to obtain sufficient data sets to find the best overlap of individual curves calculated using Eq. 1. The criterion of Mean Perpendicular Curve Distance was used to find the best overlap [41].

The densities of the green bodies and sintered samples were measured using the soaking method and Archimedes principle. The microstructure of the samples was observed using scanning electron microscopy Verios 460L (SEM, FEI, Czech Republic). The mean grain size (MGS) was determined using the linear intercept method from at least 5 images and the results were multiplied by a correction factor of 1.56 [42].

Cooling from the sintering temperature can cause the development of internal stresses as was mentioned in the introduction chapter. The theoretically estimated internal stresses for laminate based on the volume fraction of individual phases independent of the layer design are shown in Fig. 1a) [43]. The input values for internal stress calculation were taken from our previous works [35, 44]. Similarly to laminates, the internal stresses are also developed in the particle composite materials due to CTE mismatch and can influence hardness, modulus and/or strength in the dependence of design and phase volume fraction. In the particle composite, the level of internal stresses within individual phases is estimated by Eshelby's inclusion model in the dependence on the volume fraction, see Fig. 1b) [45, 46]. The model estimates stresses based on the fact of which phase forms the matrix (σ_m) and which reinforcement (σ_f).

$$\sigma_f=\frac{-2E_m(1-v_f)\beta\alpha^*}{A}, \quad (4)$$

$$\sigma_m = \frac{2E_m v_f \beta \alpha^*}{A}, \quad (5)$$

$$A = \left(1 - v_f\right)(\beta + 2)(1 + \mu_m) + 3\beta v_f (1 - \mu_m), \quad (6)$$

$$\beta = \frac{E_f(1 + \mu_m)}{E_m\left(1 - 2\mu_f\right)}, \quad (7)$$

$$\alpha = \left(\alpha_f - \alpha_m\right)\Delta T, \quad (8)$$

where $\Delta T = T - T_{room}$ similarly as in Equation 1, $v, E, \mu \; and \; \alpha$ are the volume fraction, elastic modulus, Poisson's ratio and CTE for given phase, indexes *m* and *f* mean matrix or reinforcement, respectively.

The microhardness of the particle composites was measured on the polished cross-section surfaces using an instrumented Vickers indentation technique using an electromechanical machine Z2.5 equipped with a ZHU0.2 indentation head (Zwick/Roell, Germany). The indentation load of 5 kg (~49 N) was selected to incorporate into the indentation imprint a significant number of grains to sufficiently describe the mechanical behaviour of particle composite (i.e., compare imprint diagonals of 70-80 μm vs 0.5-1.0 μm grain size). The instrumented indentation was used to estimate the indentation elastic modulus calculated from the unloading part of the recorded loading curve.

Experimental data used for this paper are available in a general-purpose open repository [47], Zenodo, developed under the European OpenAIRE program and operated by CERN.

3. Results and discussion

The alumina and zirconia green bodies prepared by EPD reached the relative density of 61.0% and 47.4% t.d., respectively (see Table 1). One could expect that the layered or particle materials composed from these ceramics using the same fabrication technique should follow the superposition of alumina and zirconia densities. This assumption is confirmed in Fig. 2 showing relative densities of annealed layered composites and particle composites prepared by EPD. Newly acquired data was supplemented with information from recently published results (red symbols) [9]. The linear dependence of measured values is visible for both types of composites. Moreover, the recently published values fit very well the trend of the newly acquired data (see Fig. 2a) demonstrating good reproducibility of the experiment. The EPD shaping technique makes it possible to obtain composites, whether they are made up of bulk layers or dispersed particles, which have the same density for individual material compositions.

The lower green density of the zirconia monolith resulted in higher shrinkage in the longitudinal and transversal orientation of the measured sample during sintering than that of the alumina. This is documented in Fig. 3 where the sintering shrinkage and sintering shrinkage rate of monoliths and layered composites in longitudinal and transversal orientations are given. Alumina and zirconia shrinkage in longitudinal and transversal orientation shows sintering shrinkage anisotropy. Figs. 3a,b show that the total difference in sintering shrinkage in longitudinal and transversal orientations for alumina was 4.8% (ε_L = 13.1% vs. ε_T = 17.9%) whereas for zirconia it was 1.9% (ε_L = 22.3% vs. ε_T = 24.2%). The origin of the anisotropy can be found in the anisotropic (oval) shape of alumina particles contrary to more less spherical shape of zirconia particles [38] resulting in shape-oriented packing of charged particles in an electrical field during EPD [48].

The sintering shrinkage curves of layered samples in longitudinal orientation (see Fig. 3a) are more inclined to the shrinkage curve of alumina monolith even when a high volume of

zirconia is present in the layers, e.g. see sample LC83. It means, that the sintering in longitudinal orientation is more controlled by the alumina than zirconia content in layered structures. To explain this behaviour, the initial particle size must be considered. Zirconia layers composed of smaller particles tend to shrink earlier than alumina layers because the sintering temperature decreases with decreasing particle size [49]. Therefore, zirconia layers shrink at lower temperatures (of around 1300°C for zirconia monolith) with a higher sintering shrinkage rate at a lower sintering shrinkage maximum, as can be seen in Fig. 3c. Together with the fact that alumina does not yet sinter/shrink at this temperature and many interfaces between alumina and zirconia layers exist, zirconia layers can densify in transversal orientation predominantly [50]. As a result of this, a constrained sintering takes place demonstrated by lower sintering shrinkage of zirconia layers in longitudinal orientation than in transversal one.

The sintering shrinkage in transversal orientation was even higher for most of the layered composites than for zirconia monolith (see Fig. 3b). To explain this abnormality, relative volume change was calculated for pure materials and layered composites (see Fig. 4). As expected, the volume shrinkage gradually increases with increasing zirconium content. It means, that high shrinkage in transversal orientation only compensates for the shrinkage deceleration in the longitudinal orientation and the effect is more pronounced with increasing zirconia content. In pure zirconia, of course, this „compensation“ does not occur.

When comparing Fig. 3c and Fig. 3d, the sintering shrinkage curves in longitudinal orientation show a shift of the maximal shrinkage rate values of layered composites with increasing alumina content to higher temperature into the area appropriate for alumina sintering (around 1400°C). However, the sintering shrinkage rates of layered composites measured in transversal orientation are similar or close to the sintering shrinkage rate of zirconia monolith.

The sintering shrinkage and sintering shrinkage rates of monoliths and particle composites are given in Fig. 5. The samples were measured in longitudinal orientation only.

The sintering shrinkage of particle composites was the superposition of the alumina and zirconia shrinkages. Surprisingly, the maximal shrinkage rate occurred at a temperature close to 1500°C in the particle composite with the lowest zirconia volume fraction, see Fig. 5b. It means, that the sintering was retarded due to the microstructural events discussed below. However, as the volume of zirconia grains in the samples increased, the curves of the shrinkage rate shifted to lower temperatures towards the curve of the zirconia monolith.

Fig. 6 shows the sintering activation energies of monoliths, layered composites in longitudinal and transversal orientations and particle composites. It was found that activation energies of nominally pure alumina and zirconia were 670 and 580 kJ/mol in longitudinal orientation and 700 and 550 kJ/mol in transversal orientation, respectively. These values fit the previously reported data in the literature covering a big scatter in the range of 342 – 1163 kJ/mol for alumina [1-4, 7-13, 21, 22, 51] and 310 – 990 kJ/mol for zirconia [3, 9, 14-16, 22]. The broad values spread is given by evaluation method, morphology [7] and purity of the powder used, considered density interval [14, 52, 53], different microstructure before sintering and temperature range [9]. In the case of layered composites, the activation energies were always higher than for nominally pure monoliths due to constrained sintering [54]. The highest activation energies were found for samples with higher alumina content. For longitudinally oriented samples the highest sintering activation energy of 1250 kJ/mol was obtained for the sample with 17 vol.% of zirconia, for transversely oriented one it was for the sample with 25 vol.% of zirconia (880 kJ/mol). It is also evident that the absolute values of the activation energies were lower in transversal orientation because of the preferential sintering of zirconia.

The activation energies of the particle composites showed a similar trend to that observed for layered ceramics. At low zirconia content, the densification of alumina is slowed down by the so-called pinning effect. It is manifested by an increase in activation energy related to reduced shrinkage rate and the shift of the sintering temperature to higher values (see

Fig. 5b). Even at higher zirconia concentrations, the activation energy remains relatively high probably because of the slightly retarded diffusion of atoms in the two-phase material during sintering. The newly obtained results significantly modify the data reported by Wang and Raj [3], who established an activation energy of about 700 kJ/mol for the entire concentration range for this type of particle composite.

Fig. 7 shows typical microstructures of layered and particle composites. Generally, the layered structures can be divided into two groups regarding the strength of the interfaces between layers. The first one is layered structures with weak interfaces findable also in nature (e.g., tooth enamel and sea shells [55]) overcoming their inherent brittleness at static or dynamic loads by deflection or delamination of the propagating crack to generate toughening mechanisms [56, 57]. The second group resists against crack propagation by energy-dissipating mechanisms such as crack deflection or bifurcation phenomena due to the presence of compressive residual stresses whose intensity is given by the thickness of layers [58, 59]. These layered structures, typically composed of alumina and zirconia [58-61], have strongly bonded interfaces.

Figs. 7a-d show layered composites with different layer thickness ratios. The EPD allowed to fabrication of multilayer ceramics with sharp, narrow, defect-free and strongly bonded interfaces. However, a certain level of porosity was observed in layered composites, see Table 1, that decreased with zirconia volume. The typical microstructures of the alumina and zirconia individual layers in a layered composite are shown in Fig. 8. Some porosity is evident in alumina while the zirconia layer is fully dense which corresponds with the density measurements of monoliths. Therefore, the density in layered composites depends on the thickness of the alumina layers (alumina volume) in particular.

The second benefit of the fabrication method is nicely dispersed alumina and zirconia grains in the sintered microstructures of the particle composites, as demonstrated in Figs. 7e-h.

The mean grain size of the particle as well as layered composites is shown in Fig. 9. The graph shows the usefulness of adding a dispersed second phase to control grain growth during sintering. The MGS of alumina in particle composites decreased at low zirconia contents as a consequence of the pinning effect [54]. Subsequently, the MGS size was mainly affected by retarded diffusion caused by an increasing zirconia concentration. On the other hand, the MGS of zirconia remained unaffected in particle composite microstructures because it is widely believed that alumina grains effectively impede the mobility of zirconia grain boundaries in Alumina Toughened Zirconia composites [62]. Approximately 50 vol.% of alumina in the microstructure seems to be beneficial for stabilising MGS on the minimal level possible. However, a higher volume of alumina in the composite resulted in lower density, see Table 1. As a confirmation of this, certain porosity is present in the microstructures in Figs. 7e,f. Contrary, two distinct populations of MGSs were measured in layered composites. There is no reason for pining effect application, so the grain growth is driven by original particle size, chemical nature, packing density and sintering temperature.

The mechanical properties of laminates according to their layer design and total volume fraction of phases are in the literature well described [43, 61, 63]. The apparent fracture toughness and flexural strength depend on the developed internal stresses (see Fig. 1a) due to CTE mismatch given by alumina-zirconia laminate prepared by EPD similar to the laminate used in this work [39, 44]. The laminate prepared for this study contains a higher number of layers which is not optimal for the strength and fracture toughness [43]. The crack behaviour during indentation for laminates was clearly described here [64] showing that the indentation method is not suitable to characterize fracture behaviour when internal stresses are present.

However, Vickers hardness and indentation elastic modulus development with increasing addition of zirconia to the alumina matrix determined for particle composite can provide valuable information. The dependencies are shown in Fig. 10 where average values

together with indicated standard deviation by error bars are plotted. The general trend is obvious that with increasing amounts of zirconia, both hardness and elastic modulus decreases.

When a single-phase material is loaded, the corresponding deformation is uniformly distributed over the whole body. In a material composed of two phases, the deformation is distributed between the phases according to their stiffness. A standard method used for estimating the overall mechanical properties of a composite material is based on the rule of mixtures (RoM). The simplest linear combination of the Vickers hardness HV (or elastic modulus E) versus the volume fraction of the phases is given by the iso-stress model (Voigt) [65]:

$$HV_c = HV_f \cdot v_f + HV_m \cdot (1 - v_f), or\ E_c = E_f \cdot v_f + E_m \cdot (1 - v_f) \quad (9)$$

where v_f is the reinforcement volume fraction, HV_m and HV_f are the Vickers hardness and E_m, E_f is the elastic modulus of the matrix and reinforcement, respectively. When materials with large differences in hardness are combined, it is clear that the deformation of the soft matrix is greater than that of the hard particles. On the other hand, the deformation of the hard matrix containing soft particles increases and the hardness can be lower than predicted by Eq. 9. In these cases, to estimate the Vickers hardness HV (or elastic modulus E), Reuss proposed the iso-strain model as a lower bound of the RoM method [65]:

$$HV_c = \left(\frac{v_f}{HV_f} + \frac{(1 - v_f)}{HV_m}\right)^{-1}, or\ E_c = \left(\frac{v_f}{E_f} + \frac{(1 - v_f)}{E_m}\right)^{-1}. \quad (10)$$

The predictions of the Vickers hardness HV and indentation elastic modulus E_{IT} of the fabricated particle composites based on Eq. 9 and Eq. 10 are given in Fig. 10 by the dashed lines. The indentation elastic modulus keeps the trend given by the mixture law (Eq. 9) given by input values of pure alumina and zirconia as can be seen in Fig. 10. In contrast, the Vickers hardness of the prepared particle composites significantly differs from the predictions given by the RoM methods. The observed change in Vickers hardness of the prepared particle composites

is influenced by several jointly acting effects such as interconnection of phases, internal thermal stresses present, transformation toughening by zirconia and grain size pinning effect.

The main effect can be attributed to the developed internal stresses. According to the literature, experimental data lay mostly close to the zirconia matrix inclusion bounds (see Fig. 1b) - full line) even for higher concentrations of reinforcement (i.e. forming continuous phase) [46, 66, 67]. This influence can be affected by the development of additional stresses caused by volume change during the stress-induced transformation of partially stabilised tetragonal zirconia grains during loading [25, 68-71]. This effect can be weakened by spontaneous transformation due to the development of internal stresses during cooling from sintering temperature [71].

Interconnectivity and gain pinning effect are other factors influencing mechanical behaviour. The isolated grains of the secondary (reinforcing) phase are restricted in their growth due to a lack of material in the surrounding eliminating diffusion processes during sintering. On the other hand, the grains in the matrix are also restricted in the grain growth by the pinning effect [72]. Therefore, the development of grain size distributions for both phases is very dependent except the volume fraction also on the processing conditions (temperature, dwell time etc.) and the initial particle size and level of dispersion of the reinforcing phase. The development of the grain size for all composites under investigation is shown in Fig. 9. Some relations can be found between the restricted gain growth and activation energies determined during sintering, see Fig. 6.

Generally, the interconnectivity of two phases should change symmetrically at a reinforcement volume fraction equal to 50%. In our particle composite is the situation more complex because the particle/grain sizes are different for each phase and each composition because of geometrical and physical reasons. The breakpoint will be shifted from the equilibrium of 50 volume % to between 55-67%. This fact corresponds well to the hardness

development shown in Fig. 10 where two different trends (slopes) depending on the composition can be observed. The first slope can be seen for 0-55% of zirconia and the second one is steeper from 67% to 100% of zirconia. We believe that the dominance of the interconnected phase is responsible for this behaviour. The enhanced hardness values (above the RoM upper bound) can be explained by the synergism of developed internal stresses, transformation toughening, and formation of interconnected phases and therefore the number of biphase interfaces [73].

Contrary to hardness, the indentation elastic modulus keeps the trend given by the RoM given by values of alumina and zirconia as can be seen in Fig. 10. Also, here is an effect of relative densities (shown in Table 1) mirrored to the scattering of values and slight differences from the linear dependence. The effect of the interconnected phase is not observable as in the case of Vickers hardness because the level of internal stresses and grain size does not change elastic modulus.

Summing all together the above-mentioned effects acting and affecting the mechanical properties can be concluded that there is no direct relationship between the activation energy of sintering. The only relationship through the resulting microstructure and amount of bi-phase interfaces can be found. The number of interfaces is higher for the particle composite than in the case of laminates having the same volume fraction. Also, the grain size pinning effect is more pronounced in particle composites because in laminates the majority of grains within one phase are interconnected.

4. Conclusions

The complex evaluation of particulate and laminate composites by the modified Master Sintering Curve concept was done for the whole range of compositions for the first time. The alumina/zirconia composites designed as layers in various thickness ratios or dispersed particles covering the entire concentration profile were successfully prepared using electrophoretic deposition (EPD). The composites with strongly bounded interfaces were obtained.

Sintering of the composites was monitored by high-temperature dilatometry in the longitudinal and transversal orientation of the samples. The pure alumina and zirconia monoliths showed shrinkage anisotropy due to the morphology of starting ceramic particles. In the case of layered composites, the sintering in longitudinal orientation was more controlled by the alumina than zirconia content resulting in constrained sintering. On the other hand, in the transversal orientation, the shrinkage only compensates for the shrinkage deceleration in the longitudinal orientation. The effect was more pronounced with increasing zirconia content. Therefore, the sintering shrinkage in transversal orientation was even higher for most layered composites than for zirconia monolith. The sintering shrinkage of particle composites was the superposition of the alumina and zirconia shrinkages.

Sintering activation energies of layered composites were always higher than for nominally pure monoliths due to constrained sintering. However, the absolute values of the activation energies were lower in transversal orientation because of the preferential sintering of zirconia. In both orientations, the highest sintering activation energies were calculated for samples with lower content of zirconia, i.e. 17 vol.% (1250 kJ/mol - transversal orientation) and 25 vol.% (880 kJ/mol - transversal orientation). In the case of particle composites, the increase of sintering activation energy (~1100 kJ/mol) at low zirconia content was attributed to the slowed-down densification of alumina by the pinning effect caused by smaller zirconia particles. These results significantly modify reported knowledge to date.

The microstructural analysis showed that EPD allowed to fabrication of multilayer ceramics with sharp, narrow, defect-free and strongly bonded interfaces and particle composites with nicely dispersed alumina and zirconia grains in the sintered microstructures. Moreover, in the particle composites, the mean grain size of alumina decreased at low zirconia contents confirming the pinning effect.

The mechanical properties represented by Vickers hardness measured for particle composite varied from the theoretical predictions, especially for the compositions exhibiting the highest activation energies, however, no direct relationship between the hardness and activation energy was found. The observed behaviour was interpreted with the help of microstructural interconnectivity between phases given by initial particle size, development of internal stresses during cooling down from the sintering temperature and grain size pinning effect. Contrary to the hardness the indentation elastic modulus respects well the upper bound of the rule of mixture given by Voigt's iso-stress model.

Acknowledgements

This publication was supported by the project "Mechanical Engineering of Biological and Bio-inspired Systems", funded as project No. CZ.02.01.01/00/22_008/0004634 by Programme Johannes Amos Commenius, call Excellent Research. We acknowledge CzechNanoLab Research Infrastructure supported by MEYS CR (LM2023051) and Brno University of Technology for grant No. FSI-S-23-8226.

Figure captions

Fig. 1 Theoretically estimated internal stresses developed due to thermal expansion mismatch for each phase in a) laminates and b) particle composites with two limit situations, i.e. upper and lower bounds for each phase. LC – Layered Composite, PC – Particle Composite.

Fig. 2 Dependence of relative density on zirconia content in monoliths and a) layered and b) particle composites in their green state (red symbols – reported data from Maca et al. [9]).

Fig. 3 Sintering shrinkage a, b) and sintering shrinkage rate c, d) of monoliths and layered composites in the longitudinal and transversal orientation of the samples. LC – Layered Composite.

Fig. 4 Dependence of relative volume shrinkage on zirconia content in layered composites.

Fig. 5 Sintering shrinkage a) and sintering shrinkage rate b) of monoliths and particle composites. PC – Particle Composite.

Fig. 6 Sintering activation energies of monoliths, a) layered composites in longitudinal and transversal orientations and b) particle composites (red columns – reported data from Maca et al. [9]). LC – Layered Composite, PC – Particle Composite.

Fig. 7 Micrographs a-d) layered and e-h) particle composite microstructures (alumina – dark fields, zirconia – bright fields). LC – Layered Composite, PC – Particle Composite.

Fig. 8 Microstructures of a) alumina layer and b) zirconia layer in the layered composite LC75.

Fig. 9 Dependence of mean grain size on zirconia content in monoliths, layered and particle composites (in longitudinal orientation) sintered at 1500°C for 2 h with a heating rate of 10°C/min (pink symbols – reported data from Maca et al. [9]). LC – Layered Composite, PC – Particle Composite.

Fig. 10 Dependence of a) Vickers hardness HV and b) indentation elastic modulus E_{IT} on zirconia content in the particle composites.

Table captions

Table 1 Summarization of sample's compositions and their microstructural properties

References

[1] W.S. Young, I.B. Cutler, Initial sintering with constant rates of heating, J. Am. Ceram. Soc., 53 (1970) 659-663. https://doi.org/10.1111/j.1151-2916.1970.tb12036.x

[2] J. Wang, R. Raj, Estimate of the activation energies for boundary diffusion from rate-controlled sintering of pure alumina, and alumina doped with zirconia or titania, J. Am. Ceram. Soc., 73 (1990) 1172-1175. https://doi.org/10.1111/j.1151-2916.1990.tb05175.x

[3] J. Wang, R. Raj, Activation energy for the sintering of two-phase alumina/zirconia ceramics, J. Am. Ceram. Soc., 74 (1991) 1959-1963. https://doi.org/10.1111/j.1151-2916.1991.tb07815.x

[4] H.H. Su, D.L. Johnson, Master sintering curve: A practical approach to sintering, J. Am. Ceram. Soc., 79 (1996) 3211-3217. https://doi.org/10.1111/j.1151-2916.1996.tb08097.x

[5] M.H. Teng, Y.C. Lai, Y.T. Chen, A computer program of master sintering curve model to accurately predict sintering results, Western Pacific Earth Sciences, 2 (2002) 171-180

[6] D.C. Blaine, S.-J. Park, R.M. German, Linearization of master sintering curve, J. Am. Ceram. Soc., 92 (2009) 1403-1409. https://doi.org/10.1111/j.1551-2916.2009.03011.x

[7] V. Pouchly, K. Maca, Master sintering curve: A practical approach to its construction, Sci. Sinter., 42 (2010) 25-32. https://doi.org/10.2298/SOS1001025P

[8] F. Zuo, A. Badev, S. Saunier, D. Goeuriot, R. Heuguet, S. Marinel, Microwave versus conventional sintering: Estimate of the apparent activation energy for densification of α-alumina and zinc oxide, J. Eur. Ceram. Soc., 34 (2014) 3103-3110. https://doi.org/10.1016/j.jeurceramsoc.2014.04.006

[9] K. Maca, V. Pouchly, D. Drdlik, H. Hadraba, Z. Chlup, Dilatometric study of anisotropic sintering of alumina/zirconia laminates with controlled fracture behaviour, J. Eur. Ceram. Soc., 37 (2017) 4287-4295. https://doi.org/10.1016/j.jeurceramsoc.2017.04.030

[10] Z. He, J. Ma, Densification and grain growth during interface reaction controlled sintering of alumina ceramics, Ceram. Int., 27 (2001) 261-264. https://doi.org/10.1016/S0272-8842(00)00073-0

[11] W.Q. Shao, S.O. Chen, D. Li, H.S. Cao, Y.C. Zhang, S.S. Zhang, Prediction of densification and microstructure evolution for α-Al_2O_3 during pressureless sintering at low heating rates based on the master sintering curve theory, Sci. Sinter., 40 (2008) 251-261. https://doi.org/10.2298/SOS0803251S

[12] M. Aminzare, M. Mazaheri, F. Golestani-fard, H.R. Rezaie, R. Ajeian, Sintering behavior of nano alumina powder shaped by pressure filtration, Ceram. Int., 37 (2011) 9-14. https://doi.org/10.1016/j.ceramint.2010.07.027

[13] T.-T. Fang, J.-T. Shiue, F.-S. Shiau, On the evaluation of the activation energy of sintering, Mater. Chem. Phys., 80 (2003) 108-113. https://doi.org/10.1016/S0254-0584(02)00373-5

[14] G. Bernard-Granger, C. Guizard, Apparent activation energy for the densification of a commercially available granulated zirconia powder, J. Am. Ceram. Soc., 90 (2007) 1246-1250. https://doi.org/10.1111/j.1551-2916.2006.01415.x

[15] R.F. Marcomini, V.L. Arantes, Sintering mechanisms of partially stabilized zirconia (TZ3Y) with ZnO and Co_3O_4 as sintering additives, Cerâmica, 67 (2021) 244-249. https://doi.org/10.1590/0366-69132021673823099

[16] K. Matsui, N. Ohmichi, M. Ohgai, N. Enomoto, J. Hojo, Sintering kinetics at constant rates of heating: Effect of Al_2O_3 on the initial sintering stage of fine zirconia powder, J. Am. Ceram. Soc., 88 (2005) 3346-3352. https://doi.org/10.1111/j.1551-2916.2005.00620.x

[17] C.C. Ye, W.Q. Wei, X. Fu, C.H. Wang, H.Q. Ru, Effect of sintering activation energy on Si_3N_4 composite ceramics, Ceram. Int., 48 (2022) 4851-4857. https://doi.org/10.1016/j.ceramint.2021.11.021

[18] P. Dehaudt, L. Bourgeois, H. Chevrel, Activation energy of UO_2 and UO_{2+x} sintering, J. Nucl. Mater., 299 (2001) 250-259. https://doi.org/10.1016/S0022-3115(01)00661-4

[19] D. Lahiri, S.V.R. Rao, G.V.S.H. Rao, R.K. Srivastava, Study on sintering kinetics and activation energy of UO_2 pellets using three different methods, J. Nucl. Mater., 357 (2006) 88-96. https://doi.org/10.1016/j.jnucmat.2006.05.046

[20] K. Nakajima, R.H.R. Castro, Thermodynamics and kinetics of sintering of Y_2O_3, J. Am. Ceram. Soc., 103 (2020) 4903-4912. https://doi.org/10.1111/jace.17273

[21] H. Su, D.L. Johnson, Sintering of alumina in microwave-induced oxygen plasma, J. Am. Ceram. Soc., 79 (1996) 3199-3210. https://doi.org/10.1111/j.1151-2916.1996.tb08096.x

[22] V. Pouchly, K. Maca, Y. Xiong, J.Z. Shen, Master Sintering Surface – A practical approach to its construction and utilization for spark plasma sintering prediction, Sci. Sinter., 44 (2012) 169-175. https://doi.org/10.2298/SOS1202169P

[23] A. Okada, Automotive and industrial applications of structural ceramics in Japan, J. Eur. Ceram. Soc., 28 (2008) 1097-1104. https://doi.org/10.1016/j.jeurceramsoc.2007.09.016

[24] S.R. Banik, I.M. Iqbal, R. Nath, L.J. Bora, B.K. Singh, N. Mandal, M.R. Sankar, State of the art on zirconia toughened alumina cutting tools, Mater. Today: Proc., 18 (2019) 2632-2641. https://doi.org/10.1016/j.matpr.2019.07.123

[25] M.M. Basha, S.M. Basha, B.K. Singh, N. Mandal, M.R. Sankar, A review on synthesis of zirconia toughened alumina (ZTA) for cutting tool applications, Mater. Today: Proc., 26 (2020) 534-541. https://doi.org/10.1016/j.matpr.2019.12.134

[26] T.E. Steyer, Shaping the future of ceramics for aerospace applications, Int. J. Appl. Ceram. Technol., 10 (2013) 389-394. https://doi.org/10.1111/ijac.12069

[27] E. Yousefi, M. Adineh, M.B. Askari, An investigation on microstructural and mechanical properties of porous zirconia-alumina nanocomposite prepared by solid state sintering method,

Anti-Corros. Methods Mater., 65 (2018) 138-145. https://doi.org/10.1108/ACMM-03-2017-1773

[28] J. Lalande, S. Scheppokat, R. Janssen, N. Claussen, Toughening of alumina/zirconia ceramic composites with silver particles, J. Eur. Ceram. Soc., 22 (2002) 2165-2171. https://doi.org/10.1016/S0955-2219(02)00031-6

[29] G. Schierano, F. Mussano, M.G. Faga, G. Menicucci, C. Manzella, C. Sabione, T. Genova, M.M.v. Degerfeld, B. Peirone, A. Cassenti, P. Cassoni, S. Carossa, An alumina toughened zirconia composite for dental implant application: In vivo animal results, Biomed Res. Int., 2015 (2015) 157360. https://doi.org/10.1155/2015/157360

[30] F. Mussano, T. Genova, L. Munaron, M.G. Faga, S. Carossa, Ceramic biomaterials for dental implants: Current use and future perspectives, in: A. Mazen Ahmad Jawad Amin (Ed.) Dental Implantology and Biomaterial, IntechOpen, Rijeka, 2016, pp. Ch. 4.

[31] S. Sequeira, M.H. Fernandes, N. Neves, M.M. Almeida, Development and characterization of zirconia–alumina composites for orthopedic implants, Ceram. Int., 43 (2017) 693-703. https://doi.org/10.1016/j.ceramint.2016.09.216

[32] S.M. Kurtz, S. Kocagöz, C. Arnholt, R. Huet, M. Ueno, W.L. Walter, Advances in zirconia toughened alumina biomaterials for total joint replacement, J. Mech. Behav. Biomed. Mater., 31 (2014) 107-116. https://doi.org/10.1016/j.jmbbm.2013.03.022

[33] B.J. McEntire, B.S. Bal, M.N. Rahaman, J. Chevalier, G. Pezzotti, Ceramics and ceramic coatings in orthopaedics, J. Eur. Ceram. Soc., 35 (2015) 4327-4369. https://doi.org/10.1016/j.jeurceramsoc.2015.07.034

[34] D.J. Green, P.Z. Cai, G.L. Messing, Residual stresses in alumina–zirconia laminates, J. Eur. Ceram. Soc., 19 (1999) 2511-2517. https://doi.org/10.1016/S0955-2219(99)00103-X

[35] Z. Chlup, H. Hadraba, D. Drdlik, K. Maca, I. Dlouhy, R. Bermejo, On the determination of the stress-free temperature for alumina–zirconia multilayer structures, Ceram. Int., 40 (2014) 5787-5793. https://doi.org/10.1016/j.ceramint.2013.11.018

[36] H. Moon, M.G. Pontin, F.F. Lange, Crack interactions in laminar ceramics that exhibit a threshold strength, J. Am. Ceram. Soc., 87 (2004) 1694-1700. https://doi.org/10.1111/j.1551-2916.2004.01694.x

[37] J. Gurauskis, A.J. Sánchez-Herencia, C. Baudín, Alumina–zirconia layered ceramics fabricated by stacking water processed green ceramic tapes, J. Eur. Ceram. Soc., 27 (2007) 1389-1394. https://doi.org/10.1016/j.jeurceramsoc.2006.04.081

[38] H. Hadraba, D. Drdlik, Z. Chlup, K. Maca, I. Dlouhy, Control of electrophoretic deposition kinetics for preparation of laminated alumina/zirconia ceramic composites, Key Eng. Mater., 507 (2012) 209-213. https://doi.org/10.4028/www.scientific.net/KEM.507.209

[39] H. Hadraba, D. Drdlik, Z. Chlup, K. Maca, I. Dlouhy, J. Cihlar, Layered ceramic composites via control of electrophoretic deposition kinetics, J. Eur. Ceram. Soc., 33 (2013) 2305-2312. https://doi.org/10.1016/j.jeurceramsoc.2013.01.026

[40] J.D. Hansen, R.P. Rusin, M.-H. Teng, D.L. Johnson, Combined-stage sintering model, J. Am. Ceram. Soc., 75 (1992) 1129-1135. https://doi.org/10.1111/j.1151-2916.1992.tb05549.x

[41] K.J. An, M.K. Han, H.J. Kim, The pressure-assisted master sintering surface of metallic powder mixture, Mater. Trans., 51 (2010) 822-825. https://doi.org/10.2320/matertrans.M2009303

[42] M.I. Mendelson, Average grain size in polycrystalline ceramics, J. Am. Ceram. Soc., 52 (1969) 443-446. https://doi.org/10.1111/j.1151-2916.1969.tb11975.x

[43] L. Sestakova, R. Bermejo, Z. Chlup, R. Danzer, Strategies for fracture toughness, strength and reliability optimisation of ceramic-ceramic laminates, Int. J. Mater. Res., 102 (2011) 613-626. https://doi:10.3139/146.110523

[44] Z. Chlup, H. Hadraba, L. Slabáková, D. Drdlik, I. Dlouhy, Fracture behaviour of alumina and zirconia thin layered laminate, J. Eur. Ceram. Soc., 32 (2012) 2057-2061. https://doi.org/10.1016/j.jeurceramsoc.2011.09.006

[45] J.D. Eshelby, The determination of the elastic field of an ellipsoidal inclusion, and related problems, Proc. R. Soc. A: Math. Phys. Eng. Sci., 241 (1957) 376-396. https://doi.org/10.1098/rspa.1957.0133

[46] Y. Akiniwa, K. Tanaka, N. Minakawa, Y. Morii, Neutron diffraction study of thermal residual stress in ceramic composite, J. Soc. Mater. Sci. Jap., 49 (2000) 281-286. https://doi.org/10.2472/jsms.49.12Appendix_281

[47] [Dataset] D. Drdlik, I. Sokolov, H. Hadraba, Z. Chlup, K. Drdlikova, K. Maca, Data for "Sintering activation energies of anisotropic layered and particle alumina/zirconia-based composites and their mechanical response", Zenodo, v1, 2024, https://doi.org/10.5281/zenodo.10592589.

[48] S. Yang, W. Cai, G. Liu, H. Zeng, From nanoparticles to nanoplates: Preferential oriented connection of Ag colloids during electrophoretic deposition, J. Phys. Chem. C, 113 (2009) 7692-7696. https://doi.org/10.1021/jp901961h

[49] M.J. Mayo, Processing of nanocrystalline ceramics from ultrafine particles, Int. Mater. Rev., 41 (1996) 85-115. https://doi.org/10.1179/imr.1996.41.3.85

[50] A.J. Sánchez-Herencia, J. Gurauskis, C. Baudín, Processing of Al_2O_3/Y-TZP laminates from water-based cast tapes, Compos. B. Eng., 37 (2006) 499-508. https://doi.org/10.1016/j.compositesb.2006.02.002

[51] B. Baruah, R. Anand, S.K. Behera, Master sintering curve and activation energy of sintering of ZrO_2-doped Al_2O_3, Ceram. Int., 47 (2021) 7253-7257. https://doi.org/10.1016/j.ceramint.2020.11.001

[52] V. Pouchly, K. Maca, Z. Shen, Two-stage master sintering curve applied to two-step sintering of oxide ceramics, J. Eur. Ceram. Soc., 33 (2013) 2275-2283. https://doi.org/10.1016/j.jeurceramsoc.2013.01.020

[53] K. Maca, V. Pouchlý, K. Bodišová, P. Švančárek, D. Galusek, Densification of fine-grained alumina ceramics doped by magnesia, yttria and zirconia evaluated by two different sintering models, J. Eur. Ceram. Soc., 34 (2014) 4363-4372. https://doi.org/10.1016/j.jeurceramsoc.2014.06.030

[54] F.F. Lange, M.M. Hirlinger, Hindrance of grain growth in Al_2O_3 by ZrO_2 inclusions, J. Am. Ceram. Soc., 67 (1984) 164-168. https://doi.org/10.1111/j.1151-2916.1984.tb19734.x

[55] M.A. Meyers, P.-Y. Chen, A.Y.-M. Lin, Y. Seki, Biological materials: Structure and mechanical properties, Prog. Mater. Sci., 53 (2008) 1-206. https://doi.org/10.1016/j.pmatsci.2007.05.002

[56] H. Tomaszewski, H. Węglarz, A. Wajler, M. Boniecki, D. Kalinski, Multilayer ceramic composites with high failure resistance, J. Eur. Ceram. Soc., 27 (2007) 1373-1377. https://doi.org/10.1016/j.jeurceramsoc.2006.04.030

[57] A. Ceylan, P.A. Fuierer, Fracture toughness of alumina/lanthanum titanate laminate composites with a weak interface, Mater. Lett., 61 (2007) 551-555. https://doi.org/10.1016/j.matlet.2006.05.021

[58] A.J. Blattner, R. Lakshminarayanan, D.K. Shetty, Toughening of layered ceramic composites with residual surface compression: effects of layer thickness, Eng. Fract. Mech., 68 (2001) 1-7. https://doi.org/10.1016/S0013-7944(00)00096-5

[59] R. Bermejo, Y. Torres, A.J. Sánchez-Herencia, C. Baudín, M. Anglada, L. Llanes, Residual stresses, strength and toughness of laminates with different layer thickness ratios, Acta Mater., 54 (2006) 4745-4757. https://doi.org/10.1016/j.actamat.2006.06.008

[60] R. Lakshminarayanan, D.K. Shetty, R.A. Cutler, Toughening of layered ceramic composites with residual surface compression, J. Am. Ceram. Soc., 79 (1996) 79-87. https://doi.org/10.1111/j.1151-2916.1996.tb07883.x

[61] R. Bermejo, Y. Torres, C. Baudín, A.J. Sánchez-Herencia, J. Pascual, M. Anglada, L. Llanes, Threshold strength evaluation on an Al_2O_3–ZrO_2 multilayered system, J. Eur. Ceram. Soc., 27 (2007) 1443-1448. https://doi.org/10.1016/j.jeurceramsoc.2006.05.037

[62] M.K.G. Abbas, S. Ramesh, S.F.H. Tasfy, K.Y.S. Lee, A state-of-the-art review on alumina toughened zirconia ceramic composites, Mater. Today Commun., 37 (2023) 106964. https://doi.org/10.1016/j.mtcomm.2023.106964

[63] R. Bermejo, Y. Torres, A.J. Sánchez-Herencia, C. Baudín, M. Anglada, L. Llanes, Fracture behaviour of an Al_2O_3–ZrO_2 multi-layered ceramic with residual stresses due to phase transformations, Fatigue Fract. Eng. Mater. Struct., 29 (2006) 71-78. https://doi.org/10.1111/j.1460-2695.2006.00962.x

[64] Z. Chlup, L. Novotná, F. Šiška, D. Drdlík, H. Hadraba, Effect of residual stresses to the crack path in alumina/zirconia laminates, J. Eur. Ceram. Soc., 40 (2020) 5810-5818. https://doi.org/10.1016/j.jeurceramsoc.2020.06.044

[65] H.S. Kim, On the rule of mixtures for the hardness of particle reinforced composites, Mater. Sci. Eng. A, 289 (2000) 30-33. https://doi.org/10.1016/S0921-5093(00)00909-6

[66] G. Pezzotti, V. Sergo, O. Sbaizero, N. Muraki, S. Meriani, T. Nishida, Strengthening contribution arising from residual stresses in Al_2O_3/ZrO_2 composites: a piezo-Spectroscopy investigation, J. Eur. Ceram. Soc., 19 (1999) 247-253. https://doi.org/10.1016/S0955-2219(98)00195-2

[67] Q. Ma, W. Pompe, J.D. French, D.R. Clarke, Residual stresses in Al_2O_3-ZrO_2 composites: A test of stochastic stress models, Acta Metall. et Mater., 42 (1994) 1673-1681. https://doi.org/10.1016/0956-7151(94)90377-8

[68] B. Basu, J. Vleugels, O. Van Der Biest, ZrO_2–Al_2O_3 composites with tailored toughness, J. Alloys Compd., 372 (2004) 278-284. https://doi.org/10.1016/j.jallcom.2003.09.157

[69] V. Naglieri, P. Palmero, L. Montanaro, J. Chevalier, Elaboration of alumina-zirconia composites: Role of the zirconia content on the microstructure and mechanical properties, Materials, 2013, 2090-2102.

[70] D. Casellas, M.M. Nagl, L. Llanes, M. Anglada, Fracture toughness of alumina and ZTA ceramics: microstructural coarsening effects, J. Mater. Process. Technol., 143-144 (2003) 148-152. https://doi.org/10.1016/S0924-0136(03)00396-0

[71] J. Wang, R. Stevens, Zirconia-toughened alumina (ZTA) ceramics, J. Mater. Sci., 24 (1989) 3421-3440. https://doi.org/10.1007/BF02385721

[72] K. Okada, T. Sakuma, The role of Zener's pinning effect on the grain growth in Al_2O_3-ZrO_2, J. Ceram. Soc. Jap., 100 (1992) 382-386. https://doi.org/10.2109/JCERSJ.100.382

[73] R.M. German, Particulate Composites, first ed., Springer Cham, 2016.

Brno, January 30, 2024

Dear Editor,

Please find enclosed the manuscript of our paper:
D. Drdlik, I. Sokolov, H. Hadraba, Z. Chlup, K. Drdlikova, K. Maca **"Sintering activation energies of anisotropic layered and particle alumina/zirconia-based composites and their mechanical response"**.

This paper follows my invited lecture on the conference "*Sintering 2023*" held in 27th – 31st August 2023 in Gifu, Japan. The article manuscript aims on activation energy of sintering as one of the significant parameters allowing a better insight into the physical background of the sintering of ceramic materials. However, information on the sintering activation energy is mostly focused on evaluation of single-phase ceramic systems. The novelty of the work lies in the high-temperature dilatometry measurements of layered and particle composites based on alumina and zirconia which were used to calculate the sintering activation energies using the modified Master Sintering Curve concept. The results, which also include the evaluation of the mechanical properties of the composites, significantly expand the previously published knowledge, especially the understanding of the sintering process of multilayer and particle ceramic structures.

Therefore, we believe the submitted manuscript will be of interest for publication in the Ceramics International.

Under our ethical responsibility, we declare that the article is original and has not been or has been previously submitted for publication elsewhere. We also certify that all authors have seen and approved the final version of this manuscript and that there is no conflict of interest. The important dataset is publicly available online on zenodo.org (https://doi.org/10.5281/zenodo.10592589). To disseminate the results of our research worldwide and support the idea of the open science, the article is submitted as a golden open access.

On behalf of all authors,

Prof. Karel Maca
CEITEC - Central European Institute of Technology
Brno University of Technology
Purkyňova 123
612 00 Brno
Czech Republic
Email: maca@fme.vutbr.cz

Declaration of interests

☒ The authors declare that they have no known competing financial interests or personal relationships that could have appeared to influence the work reported in this paper.

☐The authors declare the following financial interests/personal relationships which may be considered as potential competing interests:

Table 1 Summarization of sample's compositions and their microstructural properties

Sample	Z content (vol.%)	A/Z thickness ratio	green density (%t.h.)	final density (%t.h.)	A/Z grain size (μm/μm)
monoliths					
A	0	-	61.0	98.3	1.3/-
Z	100	-	47.4	99.7	-/0.3
particle composites					
PC17	17	-	57.6	97.7	1.0/0.5
PC25	25	-	56.4	97.9	0.9/0.5
PC33	33	-	55.6	98.1	0.8/0.5
PC45	45	-	53.4	98.4	0.7/0.4
PC50	50	-	53.1	98.6	0.7/0.5
PC55	55	-	53.1	99.0	0.7/0.5
PC66	66	-	51.1	99.2	0.7/0.5
PC75	75	-	51.0	99.5	0.6/0.5
PC83	83	-	50.6	99.8	0.6/0.5
layered composites – longitudinal orientation					
LC17	17	5:1	58.1	97.6	1.6/0.6
LC25	25	3:1	57.1	98.7	1.7/0.6
LC45	45	1.2:1	54.8	98.6	1.8/0.6
LC55	55	1:1.2	54.7	99.9	1.6/0.6
LC75	75	1:3	51.1	99.6	1.5/0.6
LC83	83	1:5	50.4	99.9	1.5/0.6

A, Z – Alumina, Zirconia; PC – Particle Composite; LC – Layered Composite

Sintering regime 1500°C/2h; heating rate of 10°C/min

Figure 1

Click here to access/download;Figure;Fig. 1.tif

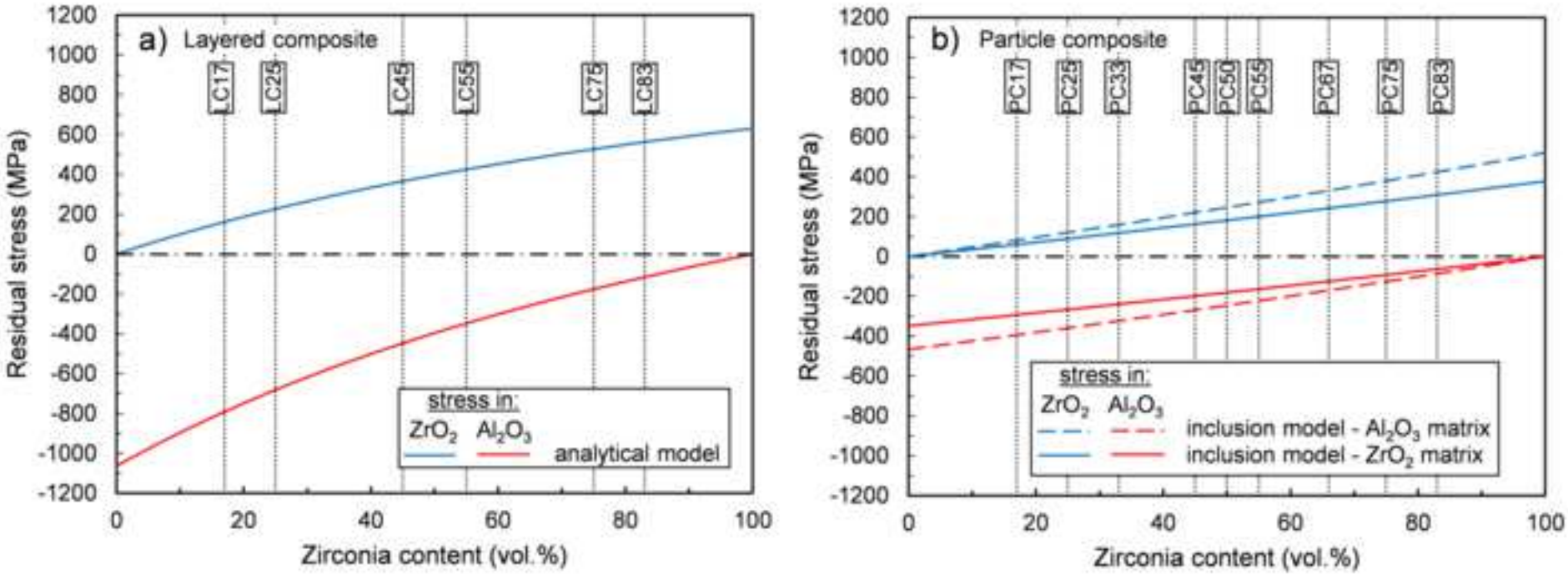

Figure 2

Click here to access/download;Figure;Fig. 2.tif

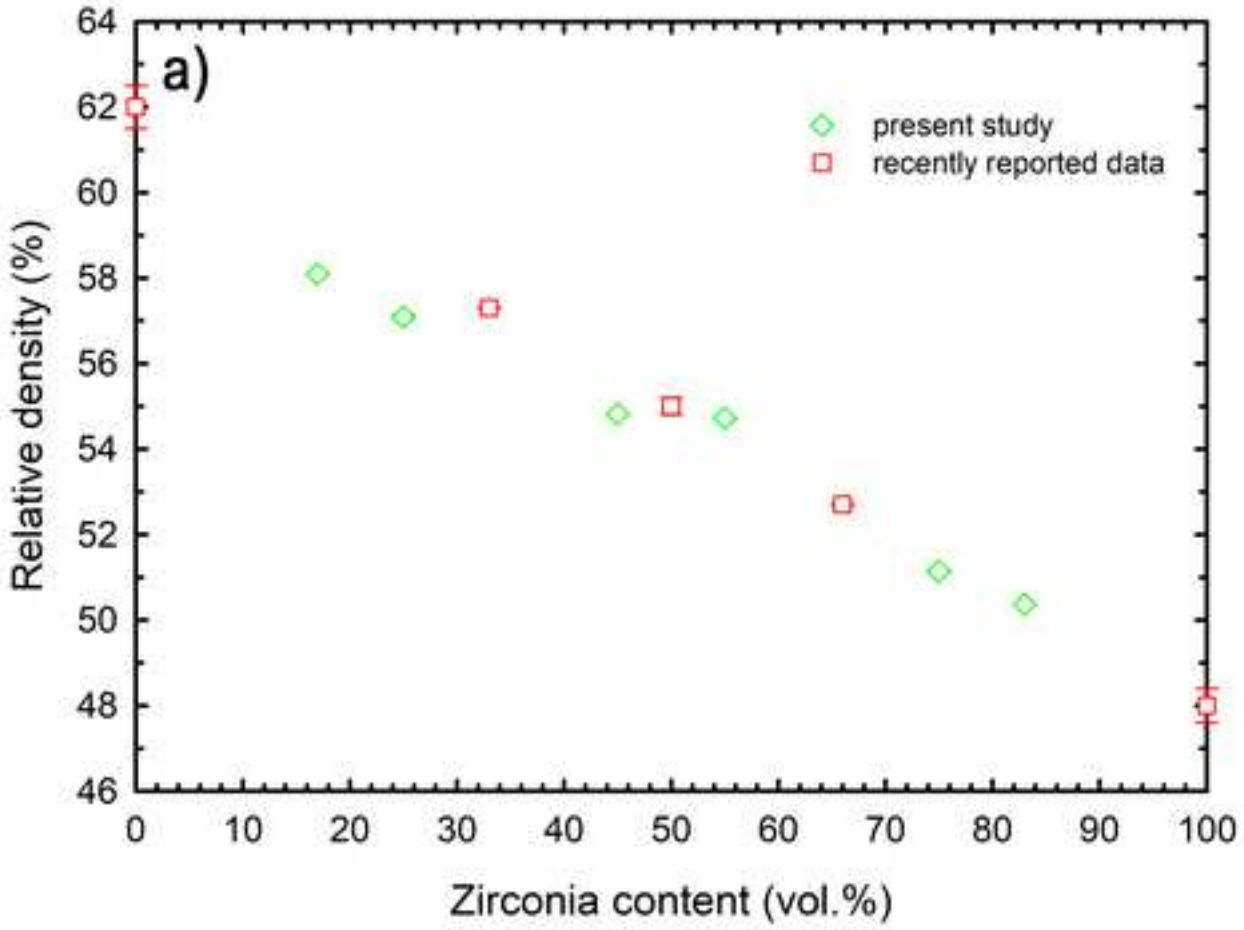

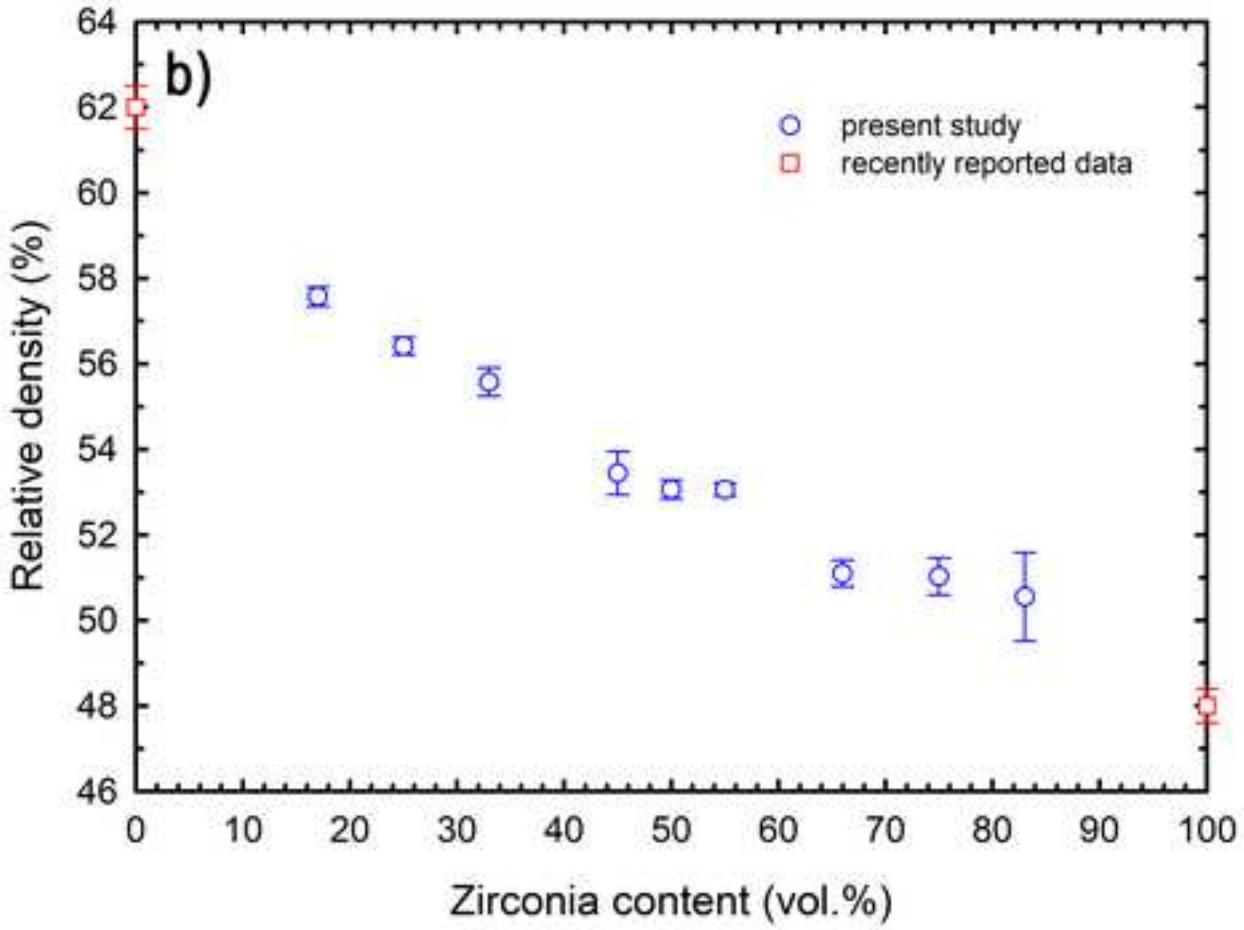

Figure 3

Click here to access/download;Figure;Fig. 3.tif

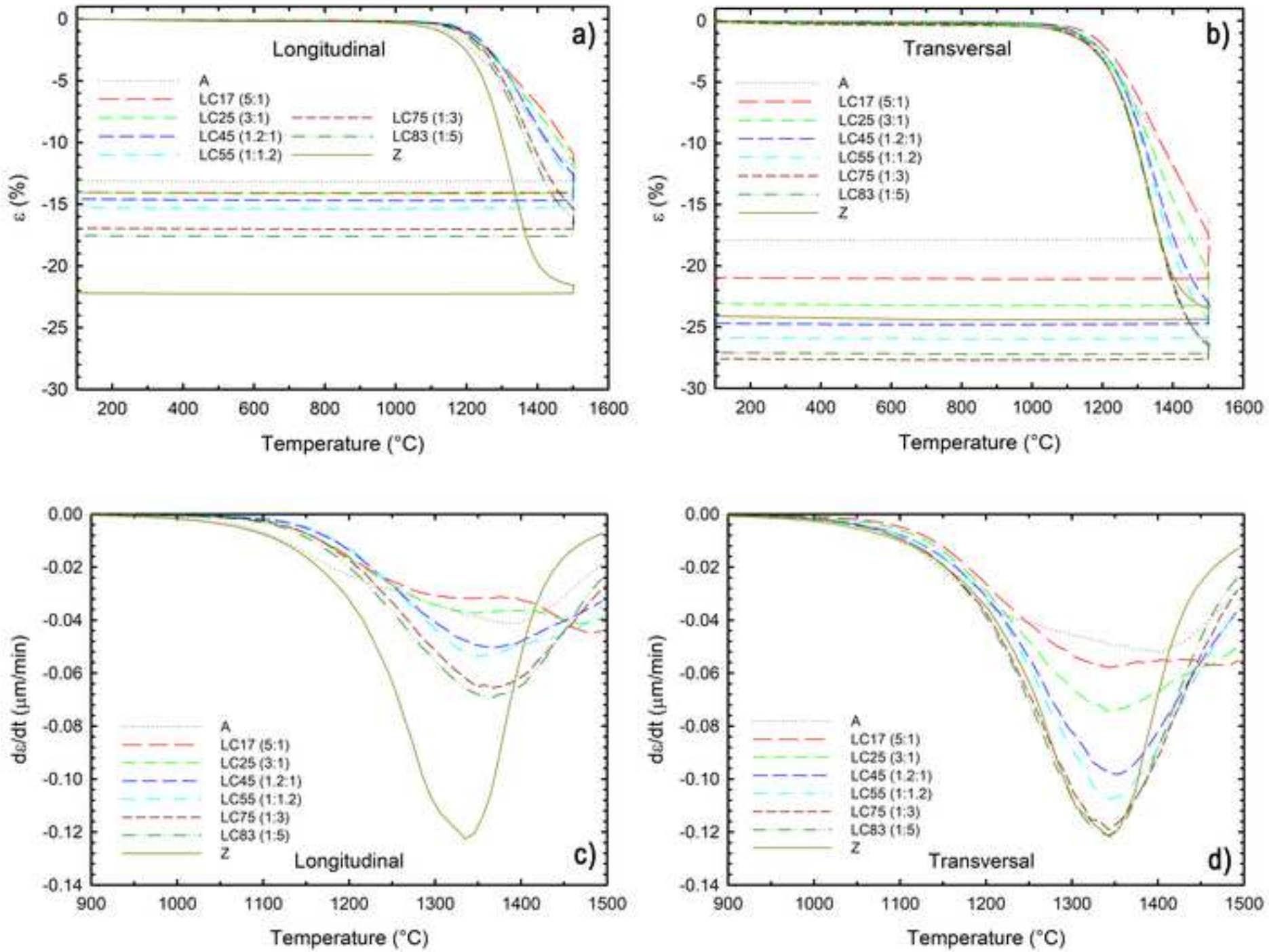

Figure 4

Click here to access/download;Figure;Fig. 4.tif

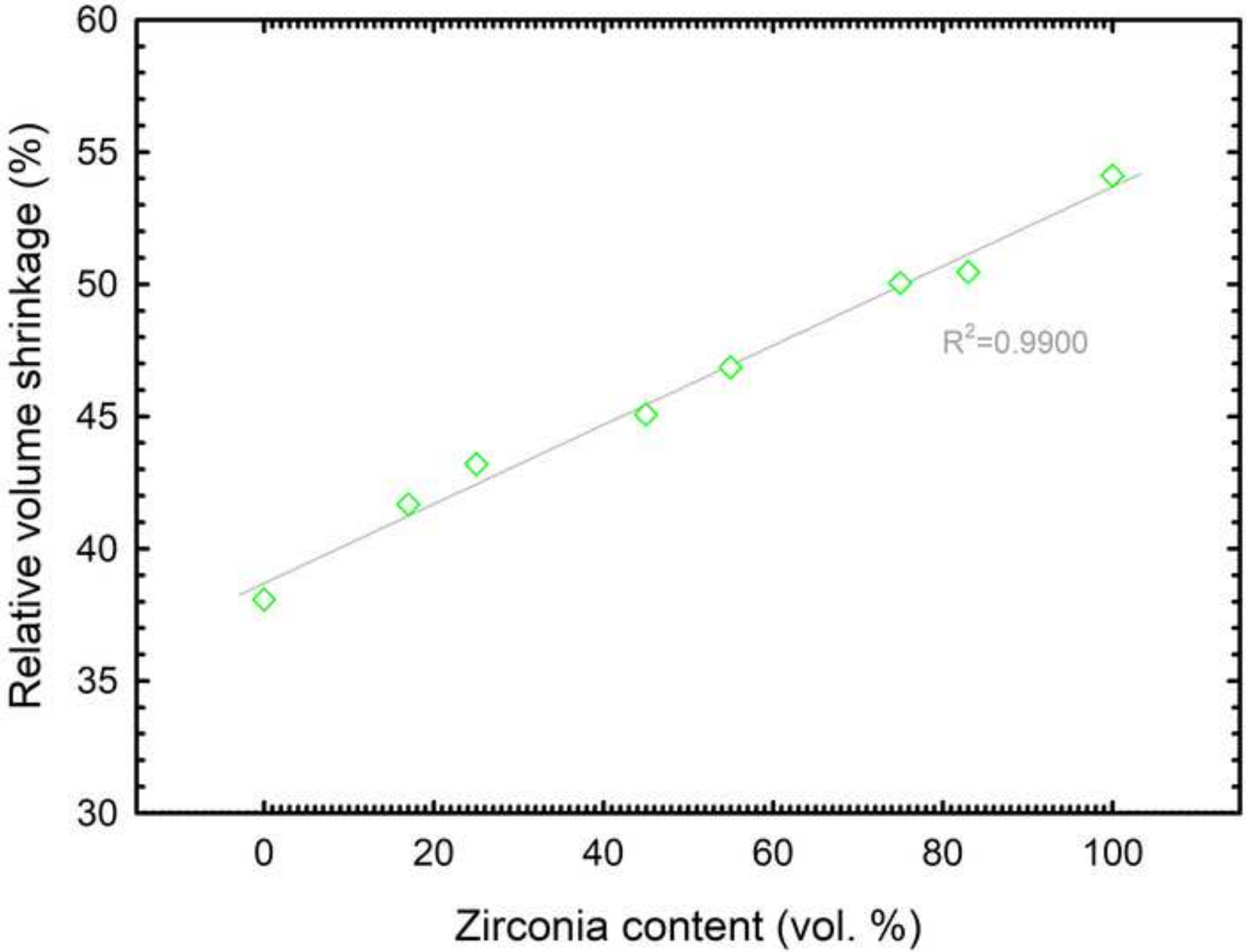

Figure 5

Click here to access/download;Figure;Fig. 5.tif

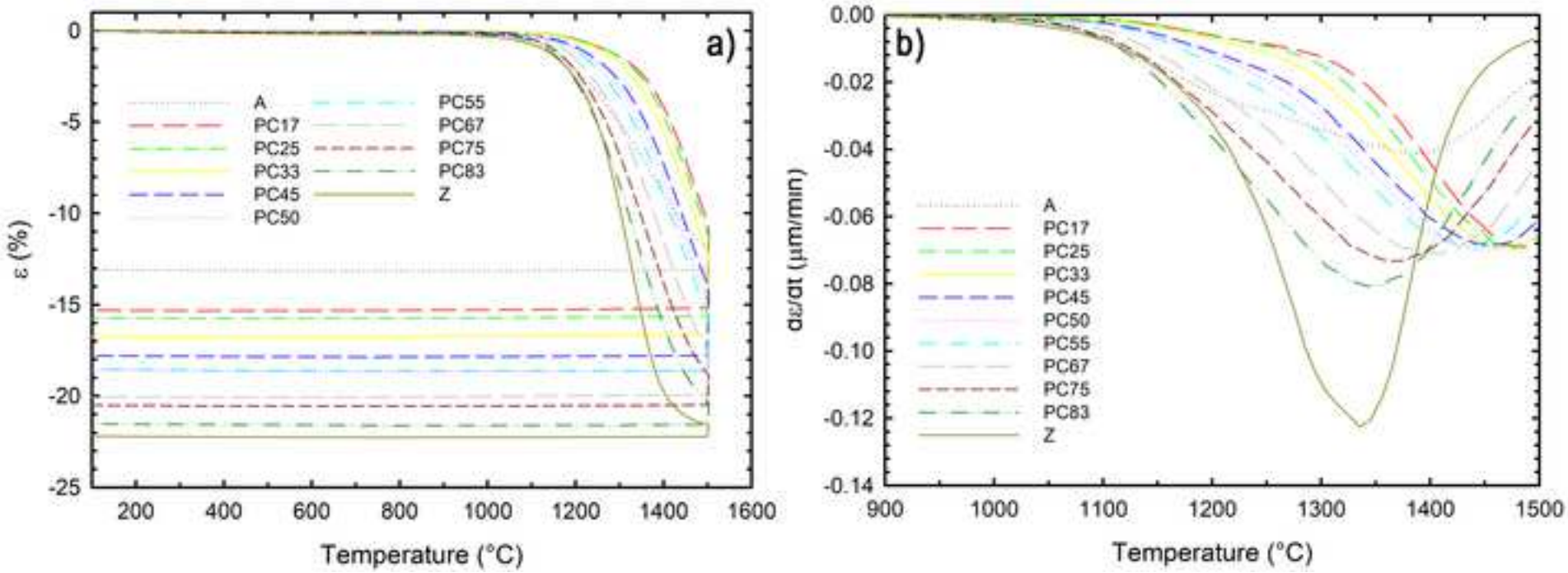

Figure 6

Click here to access/download;Figure;Fig. 6.tif

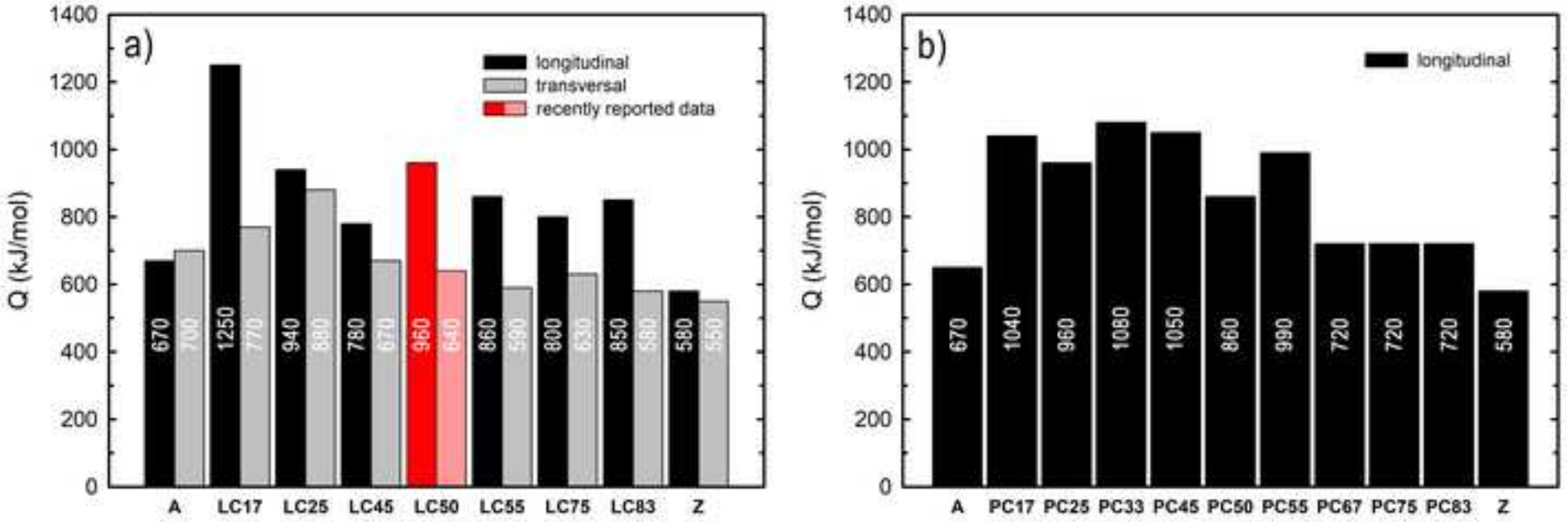

Figure 7

Click here to access/download;Figure;Fig. 7.tif

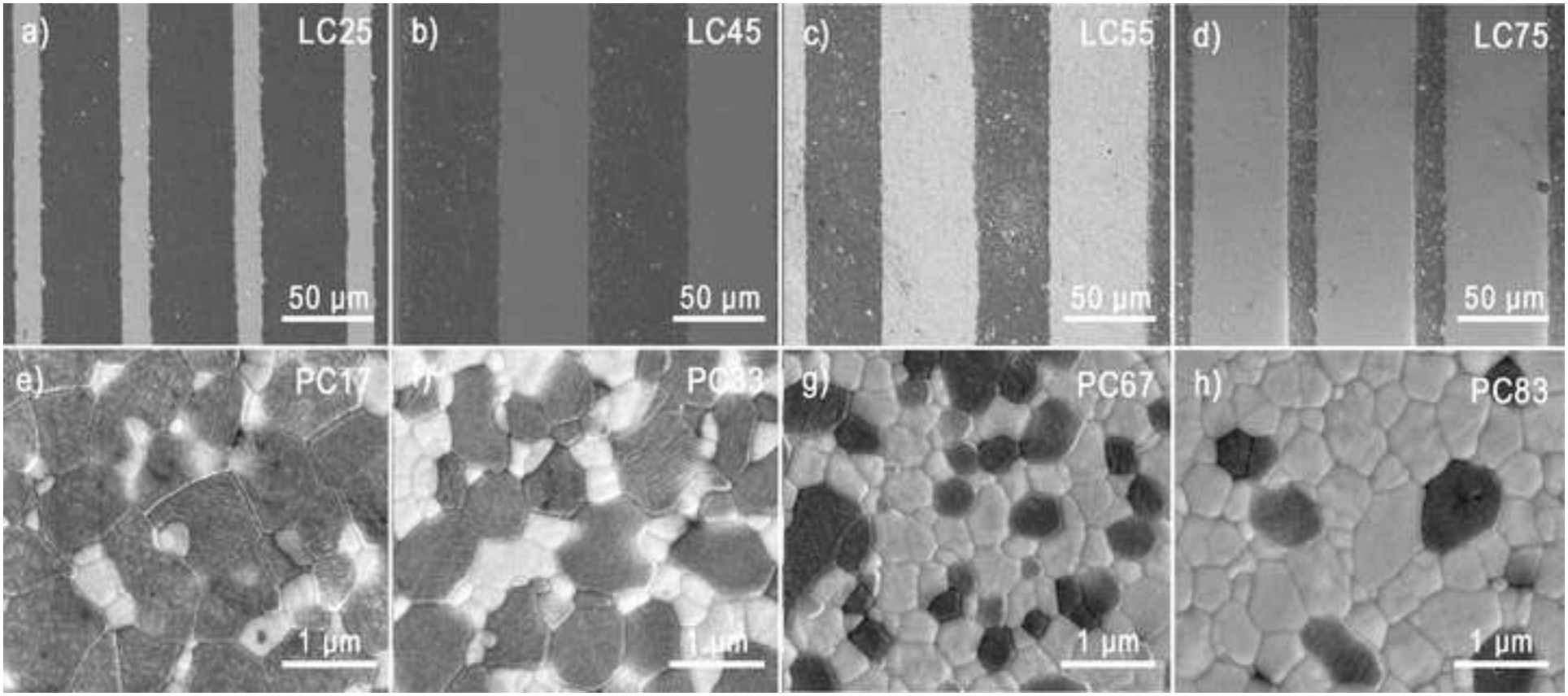

Figure 8

Click here to access/download;Figure;Fig. 8.tif

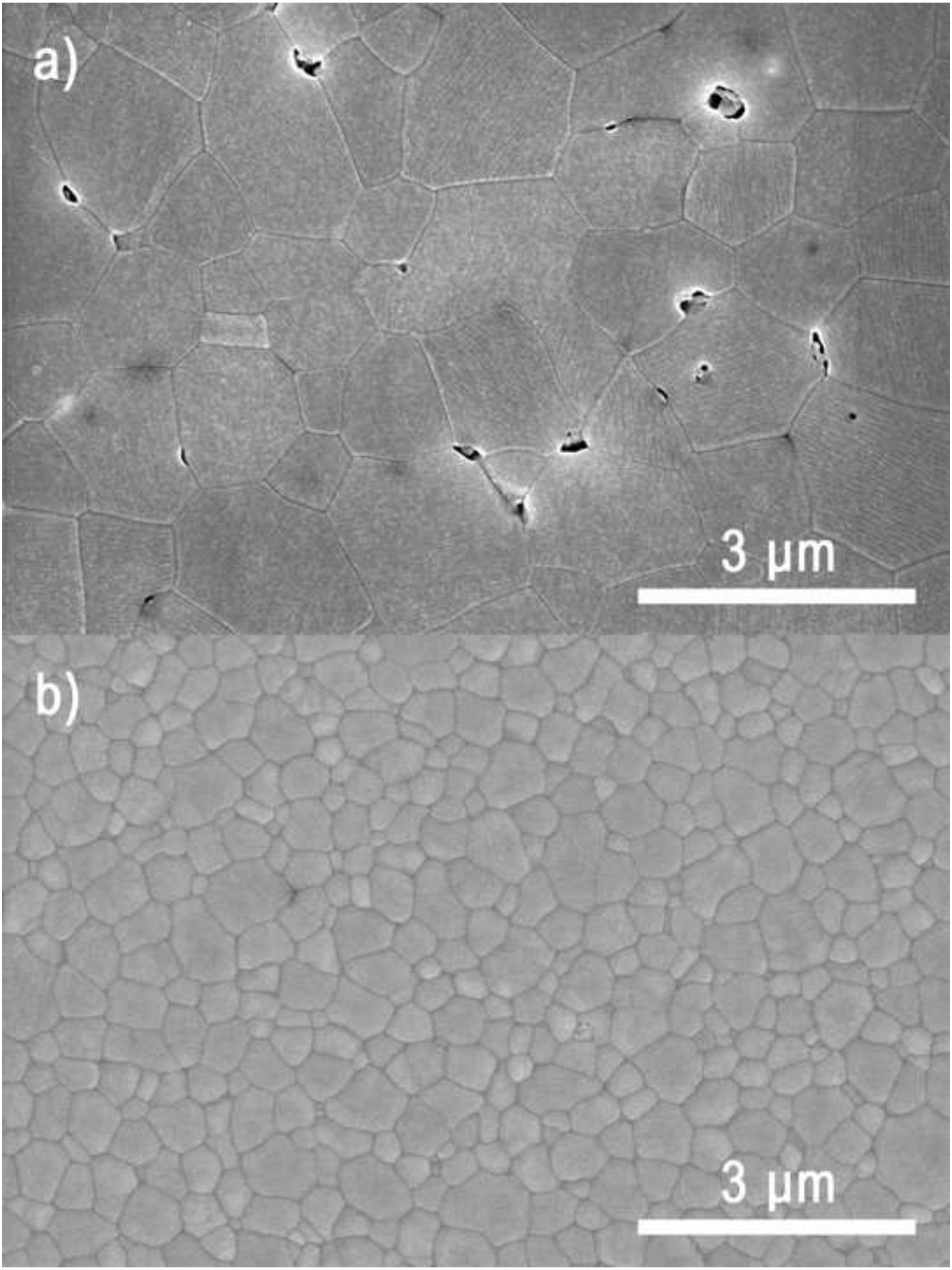

Figure 9

Click here to access/download;Figure;Fig. 9.tif

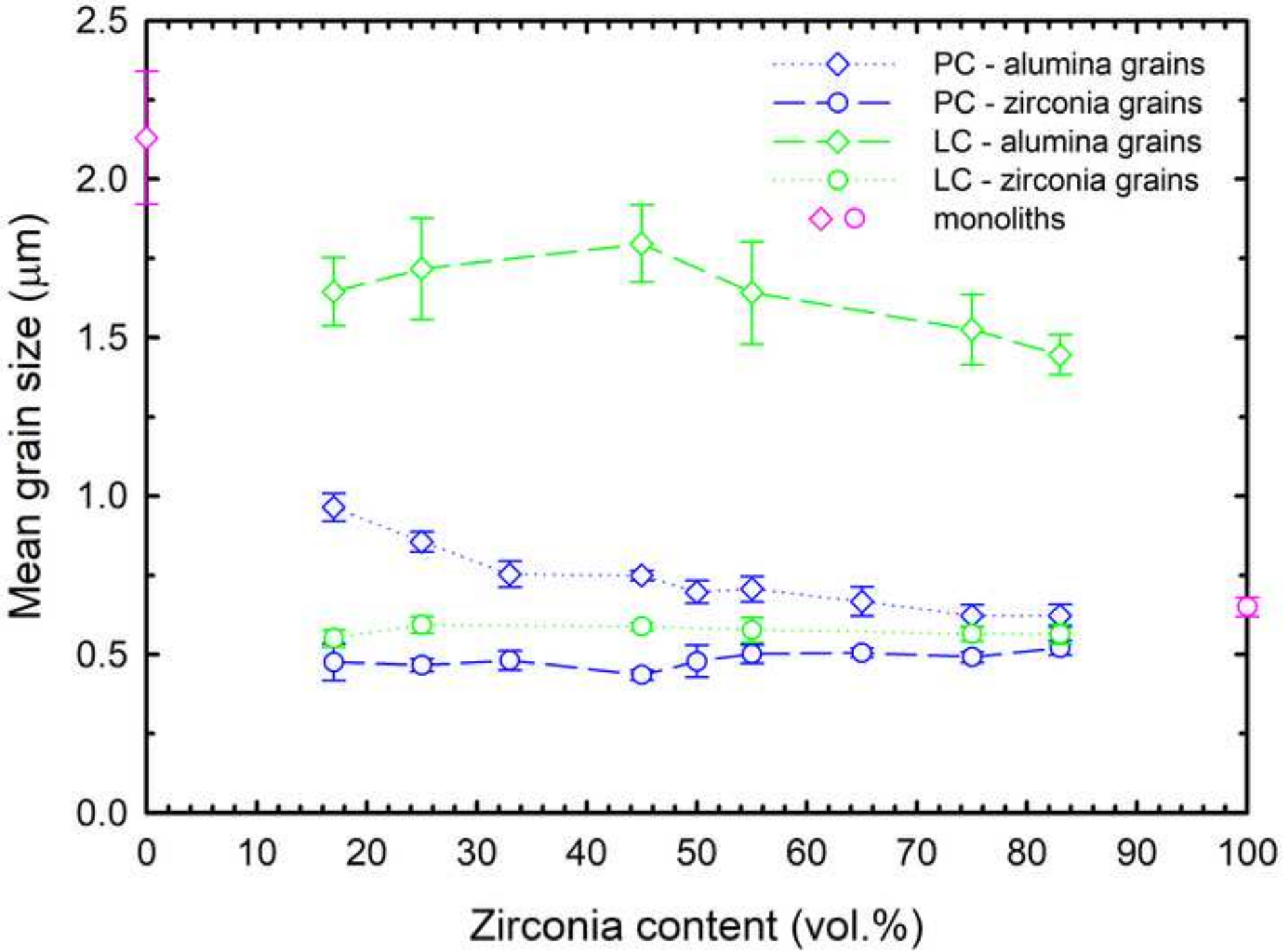

Figure 10

Click here to access/download;Figure;Fig. 10.tif

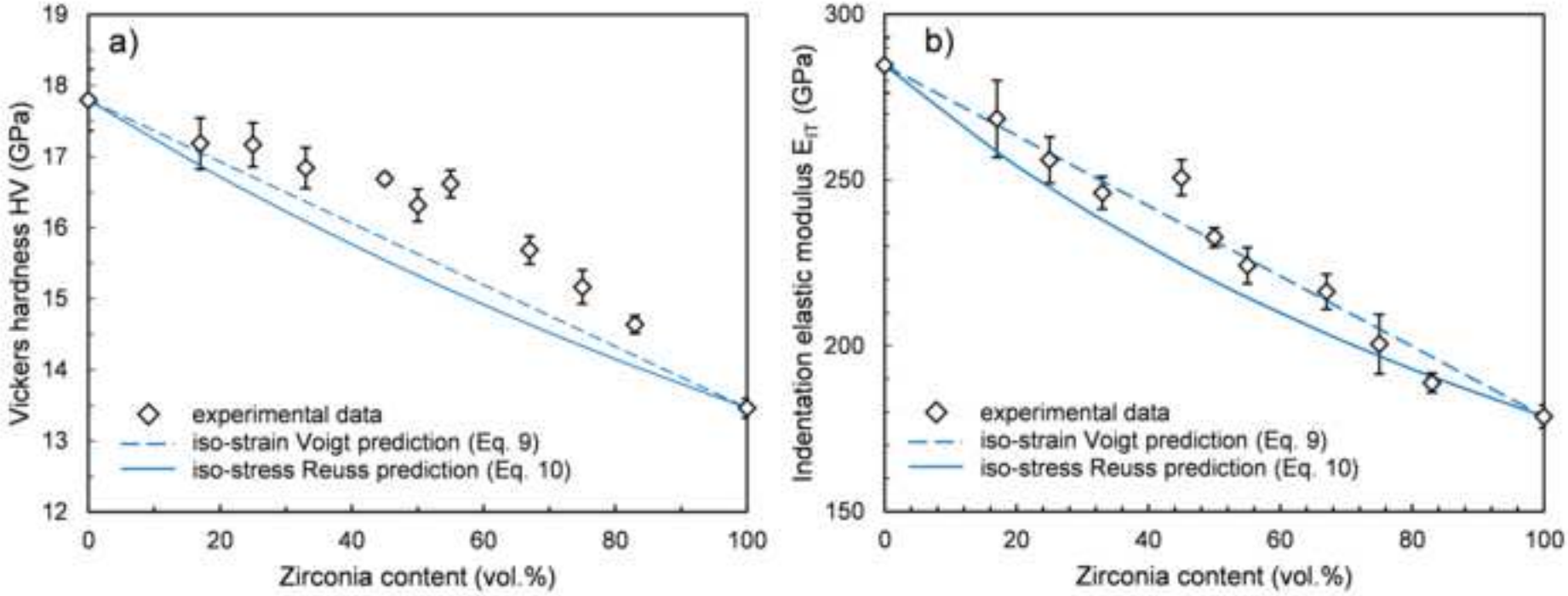

PUBLIKACE VIII

Journal of the European Ceramic Society 37 (2017) 2695–2703

Contents lists available at www.sciencedirect.com

Journal of the European Ceramic Society

journal homepage: www.elsevier.com/locate/jeurceramsoc

Luminescent Er^{3+} doped transparent alumina ceramics

Katarína Drdlíková[a,*], Róbert Klement[b], Daniel Drdlík[a], Tomáš Spusta[a], Dušan Galusek[b], Karel Maca[a]

[a] CEITEC—Central European Institute of Technology, Brno University of Technology, Brno, Czech Republic
[b] Joint Glass Centre of the IIC SAS, TnU AD, and FChFT STU, Trenčín, Slovakia

ARTICLE INFO

Article history:
Received 8 September 2016
Received in revised form 1 February 2017
Accepted 8 February 2017
Available online 16 February 2017

Keywords:
Alumina
Dopants/doping
Erbium/erbium compounds
Luminescence
Transparent ceramics

ABSTRACT

We report on successful preparation of Er^{3+} doped transparent alumina (0.1–0.17 at.%) exhibiting visible light photoluminescence using wet shaping method and hot isostatic pressing. The effects of dopant amount, type of doping powder and powder pre-treatment on final microstructure, real in-line transmittance and photoluminescence characteristics were studied.

The real in-line transmittance ranged between 28 and 56%, depending on processing parameters. The transparency decreased with increased amount of dopant. The decrease is dependent on the type of doping powder and its pre-treatment.

The photoluminescence spectra measured in both visible and NIR region showed typical emission bands due to the presence of Er^{3+} ions. The decay profiles of the $^4S_{3/2} \rightarrow {}^4I_{15/2}$ transition were fitted with a 2-exponential function, with faster component in the range of 360–700 ns and slower component around 1.6-2.4 μs. The intensity of emissions and lifetime of the $^4S_{3/2}$ level decrease significantly with increasing concentration of Er^{3+} ions.

© 2017 Elsevier Ltd. All rights reserved.

1. Introduction

Transparent polycrystalline alumina ceramics have been studied for decades as a material for optical applications and a cheaper alternative to sapphire single crystals [1]. Besides the economic and ecological benefits of such replacement, their applications could be extended due to better mechanical properties of polycrystalline materials and possibility of production complex shaped parts.

Moreover, doping with certain elements could lead to new interesting functional properties, thus expanding the application potential of transparent aluminas even further (e.g. dosimeters, phosphors for high-brightness LEDs or laser host materials). However, adding the required amount of dopant (mostly with very low solubility in alumina lattice) inevitably leads to formation of second phase inclusions, which impair transparency, and make the preparation of transparent alumina with luminescence properties a challenging topic.

There are only few works dealing with transparent or translucent alumina doped with optically (photoluminescence – PL) active rare earth (RE) or transition metal (TM) ions. Cr-doped transparent alumina exhibiting thermoluminescence (TL) and optically stimulated luminescence was designed as a potential TL dosimetry material [2]. Doping of alumina with Ti and Mg was proposed for the same purpose [3]. However, the mean grain size of prepared material is well within the micrometer size range as the result of pressure-less sintering at relatively high temperature, with adverse impact on transparency.

Penilla et al. [4] prepared by spark plasma sintering (SPS) Tb^{3+} doped transparent alumina with fine-grained microstructure with 75% of total transmission at a wavelength of 800 nm and with characteristic Tb^{3+} emission. According to the authors, this was the first instance when a birefringent (non-cubic) polycrystalline oxide bulk ceramic possessed both high transparency and induced light emission properties. The authors also suggested that only high heating and cooling rates accessible by SPS technique and operating out of thermodynamic balance could result in achieving high concentration of dopant while maintaining the transparency.

Alvarez-Clemares et al. [5] showed that doping of alumina with up to 0.7 wt.% of ceria hinders the growth of alumina grains during SPS and enables the preparation of transparent alumina with total transmission of up to 70% in the IR-VIS range. Although ceria-doped alumina exhibits photoluminescent properties [5], no measurement of the photoluminescence was performed in this work.

Sanamyan et al. [6] reported on preparation of Er – doped alumina powders (0.1–0.3 at.% of Er) subsequently sintered by SPS to transparent ceramics with submicron microstructure. All

* Corresponding author.
E-mail address: katarina.drdlikova@ceitec.vutbr.cz (K. Drdlíková).

http://dx.doi.org/10.1016/j.jeurceramsoc.2017.02.017
0955-2219/© 2017 Elsevier Ltd. All rights reserved.

samples prepared under optimized conditions exhibited sharp, well-resolved emission lines characteristic for RE^{3+} ions, indicating predominantly crystalline single-site Er^{3+} occupation. Obtained IR spectra were similar to those previously observed in Er^{3+}-doped Al_2O_3 powders prepared by sol–gel technique [7]. However, the effect of Er concentration on the PL intensity was not discussed, and no data of optical transmission were provided.

Wang et al. [8] studied the influence of the phase structure and the amount of dopant on PL intensity of alumina powders. The strongest emission intensity was detected at the lowest examined concentrations (0.5 and 1 mol% Er). Dramatic concentration quenching effect took place above 1.5 mol% Er^{3+} doping concentration. At 1 mol.% Er^{3+} doping, the PL intensity of the Er^{3+}-doped Al_2O_3 powders increased with the phase structure changed in the sequence $\gamma \rightarrow \theta \rightarrow \alpha$-$(Al, Er)_2O_3$. These findings indicate that relatively low amount of Er with controllable impact on the transparency are sufficient for obtaining adequate PL intensity of doped transparent Er^{3+}-doped alumina (α-$(Al, Er)_2O_3$).

The present study follows and extends our recent work dealing with rare-earth doped transparent alumina [9], with the aim to enhance important material properties significantly (real in-line transmission, PL intensity) by modifying of the processing parameters. More precisely, it is aimed at alternative way of producing Er^{3+}-doped transparent and photoluminescent alumina, combining colloidal processing (slip casting) for green body preparation, advanced pre-sintering in a conventional electric furnace and subsequent hot isostatic pressing. Our approach differs from all cited works concerned on preparation of transparent alumina with PL properties where spark plasma sintering was applied to achieve full densification. Transparent alumina ceramics prepared in this study are characterized in terms of their microstructure (mean grain size, presence and size of secondary phase(s) inclusions), real in-line transmittance and photoluminescence properties. Contrary to all mentioned studies dealing with transparent PL alumina, the present work examines also the effect of dopant concentration and pre-treatment of doping powder on all studied characteristics.

2. Experimental

High purity 99.99% commercial alumina powder (Taimicron TM-DAR, Taimei Chemicals Co., Ltd., Tokyo, Japan), with the primary particle size of 150 nm and specific surface area of 13.7 $m^2 g^{-1}$ was used as a starting material (the values were determined by the producer from SEM micrographs and by BET analysis, respectively).

Aqueous suspensions with the solid content of 45 vol.% of Al_2O_3 were stabilized electrosterically with the use of a commercial dispersant Darvan CN. De-ionized water with room temperature electric conductivity 25 ± 5.10^{-4} S m^{-1} was used as a dispersion medium. The optically active dopant (Er) in the amount equivalent to 0.1–0.17 at.% of Er with respect to Al_2O_3 was added in the form of oxide powders. Two different Er_2O_3 powders were used as starting materials.

First, a commercial coarse-grained Er_2O_3 powder (Treibacher Industrie AG, Austria) was used. In order to obtain a nano-powder, the commercial powder was dissolved in 65% HNO_3. Citric acid dissolved in deionized water and ethylene glycol was added to the nitrate solution and heated in oil bath for 2 h at 85–90 °C. The solvent was evaporated under continuous stirring. The product was dried and calcined at 800 °C for 1 h to remove organic residua. The powder was then milled in planetary mill (vessel and grinding balls from alumina) in order to reduce the number of aggregates. Residual aggregates were removed from diluted water suspension by centrifugal sedimentation at 800 rpm for 2 min. Only the particles, which remained in the suspension were dried and further used as dopants. This type of doping powder was further throughout the text denoted as P_S powder. Doped samples are denoted as P_S_x, The abbreviations are explained in Table 1.

Table 1
Abbreviation in designation of samples.

Abbreviation in designation of samples	Meaning in relation to the preparation of samples
P	Nano-powder prepared by modified Pechini method
C	Commercial nano-powder
S	Sedimentation used for removal of the aggregates
x	at.% of Er with respect to Al_2O_3

The nano-Er_2O_3 powder (purity 99.9%, particle size 20–30 nm, GNM – Getnanomaterials, USA) was used as received. Part of the nano-powder was also centrifugated, under the conditions described above, to remove aggregates. These types of doping powder were further throughout the text denoted as C and C_S powder, respectively. The samples doped with untreated commercial nano-powder were denoted as C_x and the samples doped with centrifuged commercial nano-powder were denoted as C_S_x.

The suspensions with added Er_2O_3 were homogenized on rollers for 24 h 40 g of alumina milling balls with diameter 4 mm were added to 10 ml of the suspension. After homogenization, the suspensions were poured into PVC dishes and allowed to dry at ambient conditions for three days. Green bodies were then dried at 80 °C for 5 h.

The samples were pre-sintered to 95–96 % of the theoretical density, which means only closed porosity was present [10,11]. The samples doped with the P_S powder were pre-sintered using two different regimes: single step pre-sintering (SSP) – and two-step pre-sintering (TSP) in order to establish more appropriate pre-sintering regime. Due to superior results achieved by the TSP regime only TSP was used in later experiments.

SSP was performed by heating the samples at the rate of 20 °C min^{-1} up to the maximal temperature 1480 °C without isothermal dwell, with subsequent cooling at the same rate. When the two-step pre-sintering (TSP) was applied, the specimens were first heated to a temperature T1 (1430–1440 °C) without isothermal dwell whereby achieving the relative density of 88–90%, and subsequently cooled down to a temperature T2 (1280 °C) at the rate of 20 °C min^{-1}. The isothermal dwell at the temperature T2 was 10 h.

The samples pre-sintered to closed porosity were hot isostatically pressed (HIP ABRA Shirp, Switzerland) at the temperature of 1280 °C for 3 h and the pressure of 200 MPa with argon used as a pressure medium. Molybdenum heating and shielding enables sintering without carbon contamination, which is usual in furnaces with graphite heating elements.

The density of sintered specimens was determined according to the Archimedes' principle. The theoretical density for all samples was calculated from the theoretical density of Al_2O_3 and Er_2O_3 by the rule of mixtures.

The microstructures were examined by scanning electron microscopy on polished and thermally etched cross sections (Lyra 3, Tescan, Czech Republic). The mean grain size was determined using the linear intercept method with a correction factor of 1.56. Minimum of 200 grains were measured in order to obtain statistically robust set of data. Distribution of Er in sintered alumina was determined using a high resolution (scanning) Transmission Electron Microscope FEI Titan Themis 60-300 (FEI, Czech Republic) equipped by Quantax EDS (Bruker Nano, Germany).

The real in-line transmission (RIT) of polished samples was measured with a non-polarized He–Ne laser (λ = 632.8 nm). The distance from the sample to the detector was 860 mm, with an opening angle of 0.5°. The real in-line transmission was measured in at least five different positions on each sample and was recalculated to constant thickness of 0.8 mm.

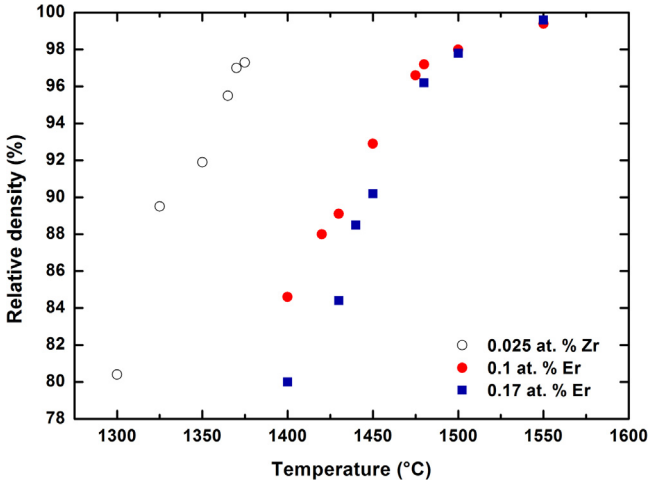

Fig. 1. Dependence of relative density of Er^{3+}-doped alumina on the sintering temperature (pressure-less sintering). For comparison, the densification data of alumina doped with 250 ppm Zr are also present.

The absorption spectra in the visible and NIR spectral range were recorded in the reflection mode using the Cary 5000 spectrometer equipped with the integrating sphere (module DRA-2500). The excitation and emission fluorescence spectra were measured using Fluorolog FL3-21 spectrometer (Horiba Jobin Yvon) with Xe-lamp (450 W) as an excitation source. For luminescence detection in visible and NIR spectral range, the PMT (R928) and InGaAs detector cooled with liquid nitrogen were used, respectively. The luminescence spectra of studied samples were recorded at room temperature. The luminescence decay curves were recorded at RT with the same instrument using time correlated single photon counting technique (TCSPC) with the pulsed laser diode at excitation wavelength 375 nm.

3. Results

3.1. Pre-sintering regime

Green bodies of Er^{3+}-doped alumina were prepared by mixing fine alumina powder with two types of Er_2O_3 nano-powders, in some cases further pre-treated by centrifugation in order to decrease the amount of aggregates present in starting Er_2O_3 powder. The designation of individual samples is related to the preparation process and is explained in Table 1. Green bodies were pre-sintered using two different regimes: single step pre-sintering (SSP) – and two-step pre-sintering (TSP) in order to establish more appropriate pre-sintering regime. For full densification hot isostatic pressing (HIP) was performed.

Polycrystalline alumina exhibits strong dependence of optical transmittance on grain size due to its birefrigent nature [12]. Therefore, the thorough optimization of all processing parameters is needed, with special emphasis on sintering conditions. Erbium oxide was observed to retard significantly the densification of alumina: the effect was more pronounced at higher dopant concentrations. Fig. 1 shows the comparison of sintered densities of Er^{3+}-doped samples with samples doped with negligible amount of Zr prepared in the same way in dependence on sintering temperature. The differences resulting from various amounts of the dopant were amplified at lower relative densities (RD); above 96% of the theoretical density (TD) the sintering behavior was almost identical. This allows the use of similar sintering regimes irrespective of the amount of the dopant.

Porosity in polycrystalline alumina ceramics is usually considered to be closed if the relative density exceeds 95% of the theoretical density [10,11]. In order to minimize the grain size the samples pre-sintered to relative densities ranging between 95.8 and 97.8% of TD were selected for HIP experiments. The used pre-sintering regimes and achieved relative densities are summarized in Table 2.

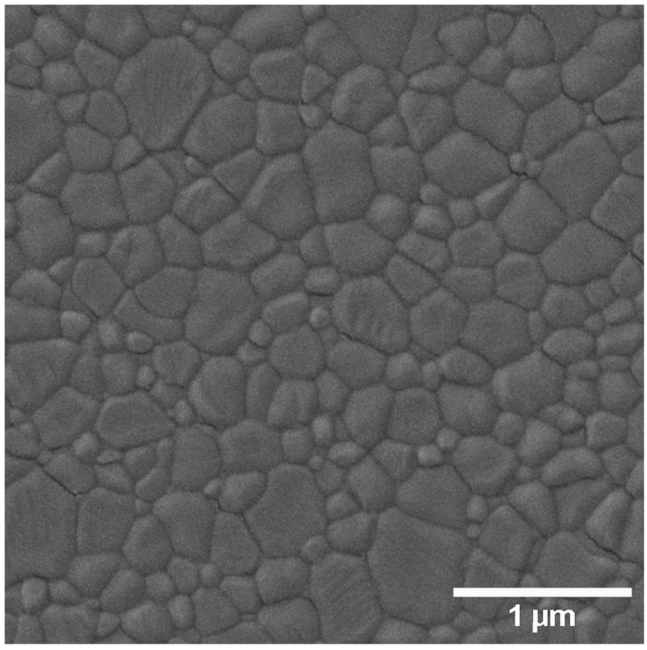

Fig. 2. The representative microstructure of HIPed alumina doped by Er.

Based on the results from previous work [10], the temperature 1280 °C and a holding time of 3 h was selected as the most suitable conditions for hot isostatic pressing (allowing full densification without observable grain growth). All samples sintered to full density (>99.9% of TD); no differences could be recorded using the applied measuring method.

The values of the mean grain size (MGS) of sintered Er^{3+}-doped ceramics after HIP are summarized in Table 3. The mean grain size of two-step pre-sintered samples seems to be slightly lower in comparison to single-step pre-sintered ones, but any difference lies within the range of the measurement error.

Microstructure of all HIP-ed samples is fine-grained and homogeneous without any second phase inclusions. Representative microstructure is shown in Fig. 2 and observable also in Fig. 3. However, some imperfections of used doping process resulted in rarely occurring aggregates of erbium oxide (Fig. 3a). This type of aggregates was found in samples doped with the P_S powder pre-sintered using single-step regime (the size of 10–20 μm taking into account the largest dimension). The aggregates in TSP samples were several fold smaller (3–10 μm) than in SSP samples (Fig. 3b). In samples doped with commercial nano-powder, SEM analysis in BSE mode (Fig. 3c) revealed only few grains with high Er content (0.3–0.6 μm). No larger aggregates were present. The high resolution TEM combined with EDX analysis showed enhanced concentration of Er on grain boundaries (Fig. 4), which confirmed presumed segregation of the dopant at grain boundaries. Based on SEM and TEM analyses of individual samples it can be assumed that the predominant part of the dopant is segregated at the grain boundaries. Rarely observed Er-enriched aggregates were probably the remains of aggregates present in starting powder.

3.1.1. Real in-line transmittance

Since the samples had thickness ranged between 0.8 and 1.6 mm, the measured values of RIT were recalculated to the constant thickness of 0.8 mm and are summarized in Table 4. The RIT

Table 2
Pre-sintering regimes for individual samples and achieved relative densities.

Sample	SSP – regime[a]	SSP – RD [%]	TSP – regime[a]	TSP – RD [%]
P_S_0.1	1480 °C	97.2	1430 °C → 1280 °C/10 h	96.9
P_S_0.17	1480 °C	96.4	1440 °C → 1280 °C/10 h	95.8
C_S_0.1	–	–	1440 °C → 1280 °C/10 h	97.4
C_S_0.125	–	–	1440 °C → 1280 °C/10 h	96.9
C_S_0.15	–	–	1440 °C → 1280 °C/10 h	96.2
C_ 0.11	–	–	1440 °C → 1280 °C/10 h	97.8

[a] SSP – without dwell; TSP – without dwell in the first step.

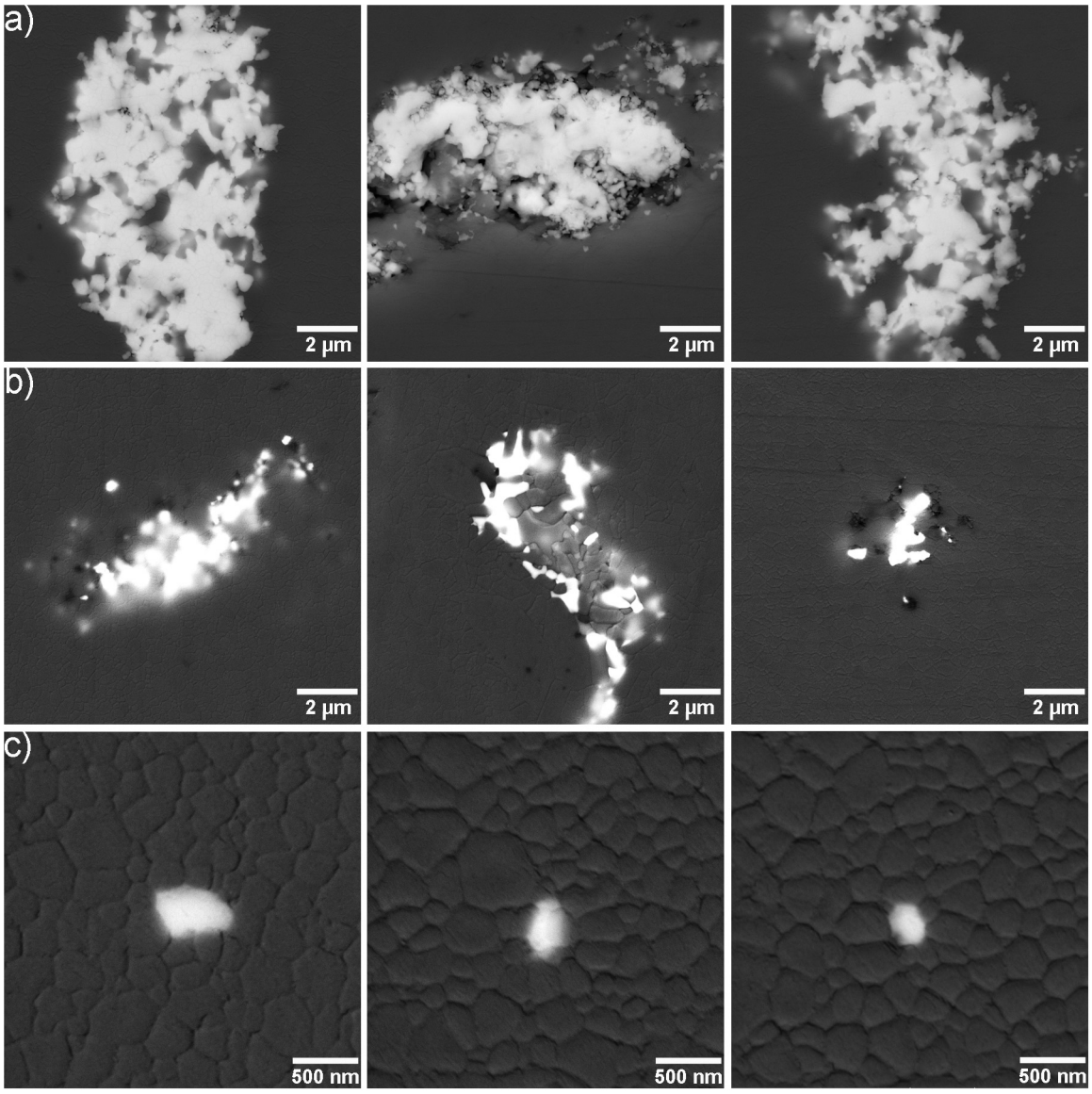

Fig. 3. The Er-enriched aggregates and grains found in the HIPed samples doped using: a) P_S powder pre-sintered by single step pre-sintering, b) P_S powder pre-sintered by two-step pre-sintering, c) C_S powder pre-sintered by two-step pre-sintering.

ranged between 28 and 56%, and was influenced markedly by the level of Er doping. The comparison between the samples doped with the P-S powder showed that higher concentration of doping ions resulted in substantial RIT decrease. RIT was also influenced by the pre-sintering regime in case of higher dopant amount.

On the other hand, the differences between samples doped with commercial nano-powder are relatively small (Table 4) as evidenced also from macrophotographs in Fig. 5. The decrease of RIT at higher Er contents was not as sharp as in case of the powder P. However, more significant decrease of the RIT seems to be related to the way how the commercial nano-powder was pre-treated. By marginal decrease of the Er content from 0.11 at.% in the material C_0.11 to 0.1 at.% in the sample C_S_0.1 the RIT increased by 6%, which was attributed to elimination of the aggregates by sedimentation in the material C_S_0.1.

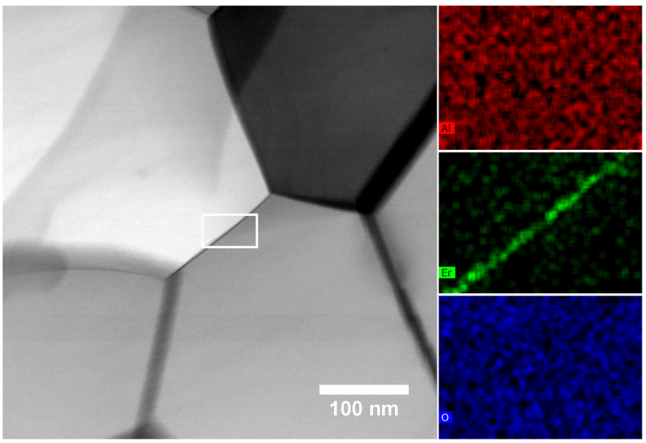

Fig. 4. TEM image of Er^{3+}-doped alumina (0.1 at.% of Er^{3+}) microstructure and EDS mapping for Al, O and Er elements on the grain boundary.

Table 3
Mean grain size of rare earth doped alumina after HIP (1280 °C/3 h, 200 MPa).

Sample	SSP + HIP		TSP + HIP	
	MGS [nm]	SD[a]/n[b] [nm/-]	MGS [nm]	SD[a]/n[b] [nm/-]
P_S_0.1	450	60/20	390	50/20
P_S_0.17	370	50/20	350	40/20
C_S_0.1	–	–	350	40/20
C_S_0.125	–	–	330	30/20
C_S_0.15	–	–	350	30/20
C_ 0.11	–	–	340	40/20

[a] SD is the standard deviation.
[b] n is the number of measurements.

Table 4
Real in-line transmittance of rare earth doped alumina after HIP (1280 °C/3 h, 200 MPa).

Sample	RIT afterSSP + HIP [%]	RIT afterTSP + HIP [%]
P_S_0.1	49	52
P_S_0.17	28	34
C_S_0.1	–	56
C_S_0.125	–	53
C_S_0.15	–	53
C_ 0.11	–	50

3.1.2. Absorption spectra

The UV–VIS-NIR spectra of the selected samples were recorded in the reflectance mode and are depicted in Fig. 6. Characteristic absorption bands identified in the spectra correspond to intra-configurational $4f^{11}$-$4f^{11}$ electronic transitions from the Er^{3+} ground state $^4I_{15/2}$. The spectra of Er^{3+}-doped Al_2O_3 in the spectral range 300–1700 nm Exhibit 12 absorptions. Particular transitions for Er^{3+} ion were labelled according to the report by Carnal et al. [13]. All the transitions are assumed to be electric dipole in nature, except for that to the $^4I_{13/2}$ first excited state that shows magnetic dipole contribution [14,15]. The hypersensitive transitions (sensitive to variation of local structure around RE ions) in Er^{3+} ($^4I_{15/2} \rightarrow {}^2H_{11/2}$; $^4I_{15/2} \rightarrow {}^4G_{11/2}$) are clearly identified by their strong intensity. The intensity of the absorption bands increases with increasing concentration of the Er^{3+} in the host matrix. The intense band at around 240 nm, strongly overlapped with the absorbance of the Al_2O_3 matrix, can be assigned to the $Er^{3+} - O^{2-}$ charge transfer state, although different $4f^{11} \rightarrow 4f^{10}5d$ inter-configurational transition bands of the Er^{3+} ion have also been reported in that region [16].

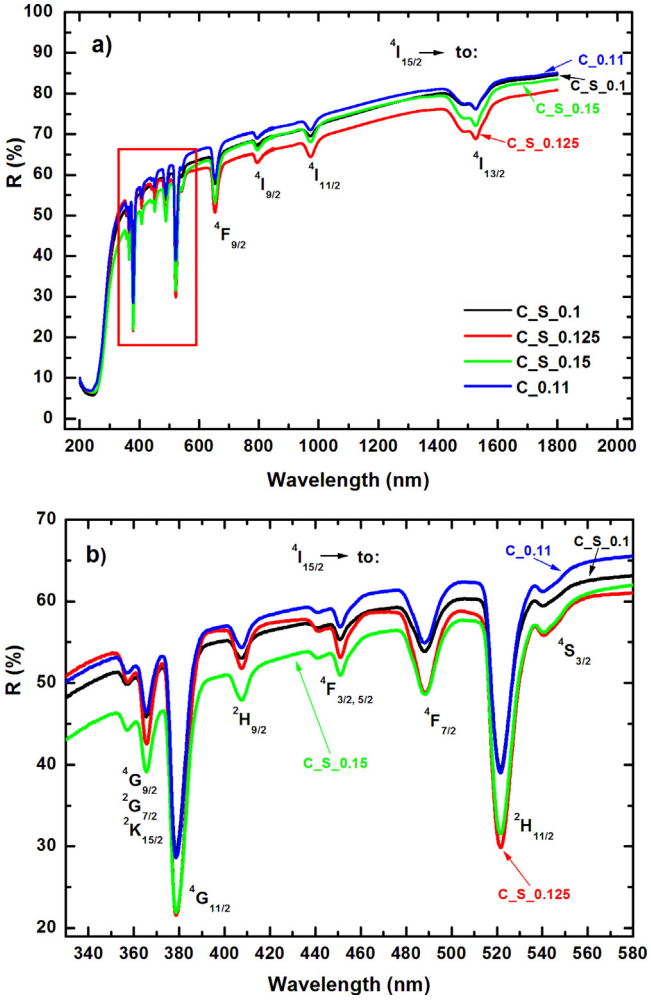

Fig. 6. Diffuse reflectance spectra of the Al_2O_3:Er^{3+} ceramics in the UV–VIS-NIR range recorded at RT (a). The expanded segment of the spectra with corresponding absorption bands assignment (b). All transitions start from $^4I_{15/2}$ ground state to the indicated levels.

3.1.3. Photoluminescence spectra

The photoluminescence spectra of the Er^{3+}-doped Al_2O_3 at the doping level ranging between 0.1 and 0.17 at.% are shown in Fig. 7.

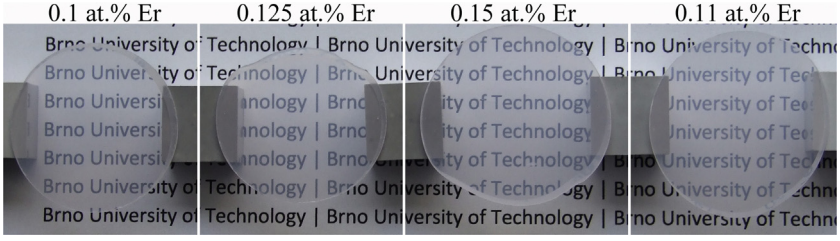

Fig. 5. Transparent Er^{3+}-doped alumina. The samples are ca 3 cm in diameter and they are positioned 1 cm above the text.

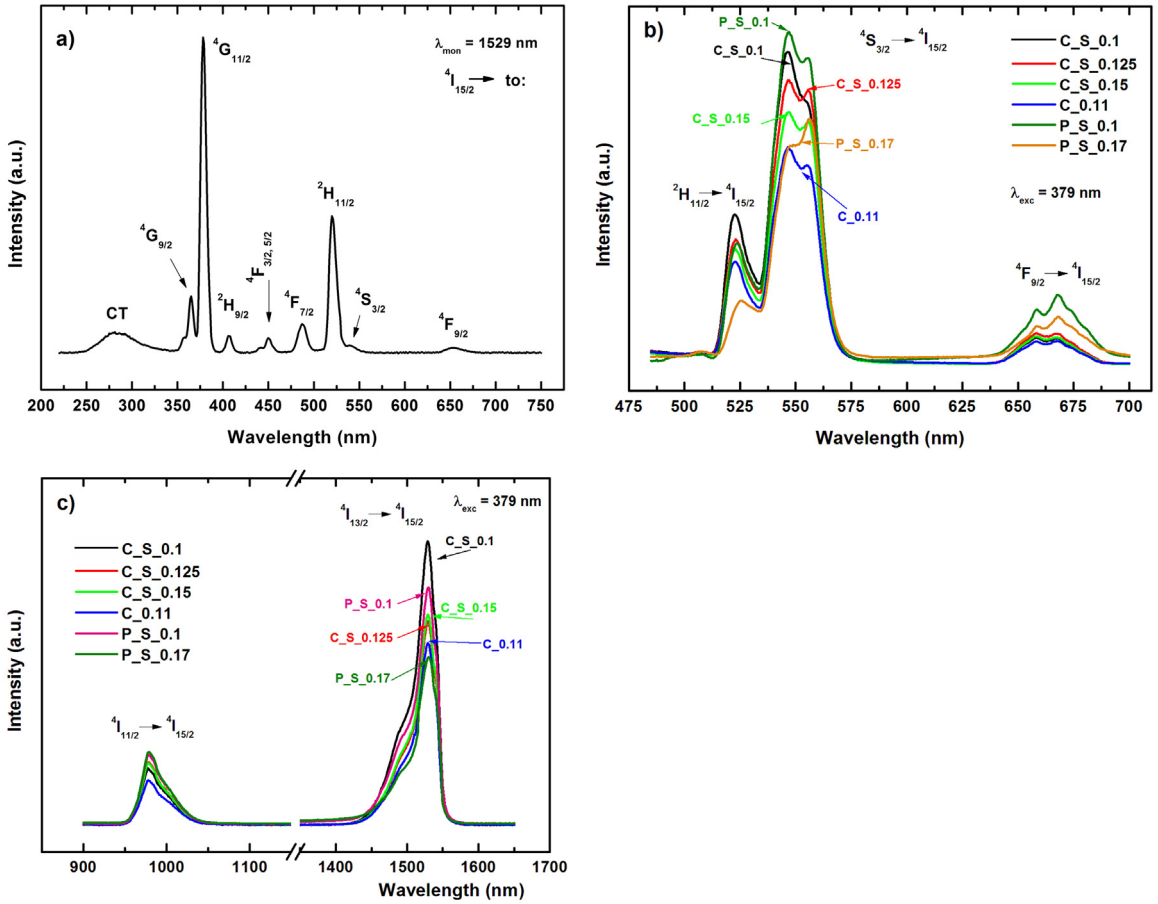

Fig. 7. Luminescence spectra of the Al_2O_3:Er^{3+} doped ceramics: (a) The representative excitation spectrum monitored at 1529 nm with corresponding band assignment; Emission spectra of the Er^{3+} doped Al_2O_3 ceramics monitored in VIS (b) and NIR (c) spectral region after sample excitation at 379 nm.

The measured excitation spectra monitored at 548 nm (spectrum not shown) and 1529 nm were almost identical. The excitation spectra (shown in Fig. 7a) monitored at 1529 nm exhibited ten bands with barycenters at 358, 365, 379, 407, 442, 450, 487, 520, 540, and 653 nm corresponding to the excited levels $^2G_{7/2}$, $^4G_{9/2}$, $^4G_{11/2}$, $^2H_{9/2}$, $^4F_{3/2}$, $^4F_{5/2}$, $^4F_{7/2}$, $^2H_{11/2}$, $^4S_{3/2}$, and $^4F_{9/2}$, respectively. The strongest band at 379 nm corresponded to the $^4I_{15/2} \rightarrow {}^4G_{11/2}$ hypersensitive transition. The broad band, centered at 284 nm, can be assigned to the $Er^{3+} - O^{2-}$ charge transfer state. The excitation spectra provide different possibilities of excitation to obtain green, red and near infrared (NIR) luminescence from the studied Er^{3+}-doped Al_2O_3.

The emission spectra (excited at 379 nm by Xe lamp) exhibited two green emission lines: one weaker green emission line centered at 524 nm ($^2H_{11/2} \rightarrow {}^4I_{15/2}$) and one strong emission centered at 549 nm ($^4S_{3/2} \rightarrow {}^4I_{15/2}$). Only weak red emission band corresponding to $^4F_{9/2} \rightarrow {}^4I_{15/2}$ transition was observed at about 668 nm. In the near infrared (NIR) spectral region (900–1600 nm), the emissions corresponding to $^4I_{11/2} \rightarrow {}^4I_{15/2}$ (centered at 980 nm) and $^4I_{13/2} \rightarrow {}^4I_{15/2}$ (centered at 1530 nm) transitions were observed, respectively. The broad emission band from the $^4I_{13/2}$ multiplet to the $^4I_{15/2}$ ground state is of special interest for optical amplification and laser application.

The intensity of the of green emissions in the group of samples denoted as C_S decreases with increasing concentration of Er^{3+} ions (Fig. 7b) while the intensity of the red emission only very slightly increases (i.e. no quenching of the red luminescence is observed); the relative intensity of the weak $^4F_{9/2} \rightarrow {}^4I_{15/2}$ red emission compared to green one increases. For the group of samples denoted as P_S both the green and red emission decrease with the doping concentration. The only exception is the sample C_0.11. When compared with the samples C_S_0.1 and P_S_0.1, i.e. these containing almost the same Er^{3+} doping concentration, the intensity of green emissions drops down significantly. This is most likely due to the presence of Er_2O_3 aggregates when the sedimentation step was not included during the sample preparation. The similar influence of Er^{3+} concentration on emission was observed also for emissions in NIR spectral region (Fig. 7c); the intensity of the $^4I_{13/2} \rightarrow {}^4I_{15/2}$ transition decreases, while the intensity of the $^4I_{11/2} \rightarrow {}^4I_{15/2}$ transition slightly increases with increasing Er^{3+} concentration.

3.1.4. Lifetime

For all samples studied the lifetime measurements have been performed in the visible spectral region for the strongest green emission centered at about 545 nm. The normalized decay profiles of the $^4S_{3/2} \rightarrow {}^4I_{15/2}$ (green) transition are shown in Fig. 8. The decay curves were fitted with double exponential equation and the average lifetime from decay curves was calculated using Eq. (1):

$$\tau_{ave} = \frac{\int_0^\infty tIdt}{\int_0^\infty Idt} = \frac{A_1\tau_1^2 + A_2\tau_2^2}{A_1\tau_1 + A_2\tau_2}. \quad (1)$$

where A_1 and A_2 are the weight factors of lifetimes τ_1 and τ_2, respectively. The corresponding lifetimes for all samples studied are summarized in Table 5.

The faster component of the decay was found to be in the range of 360–700 ns while the slower one in the range of 1.6–2.4 μs. However, in decays of the green emission the faster component dominates. The lifetime of the $^4S_{3/2}$ level decreases quite signif-

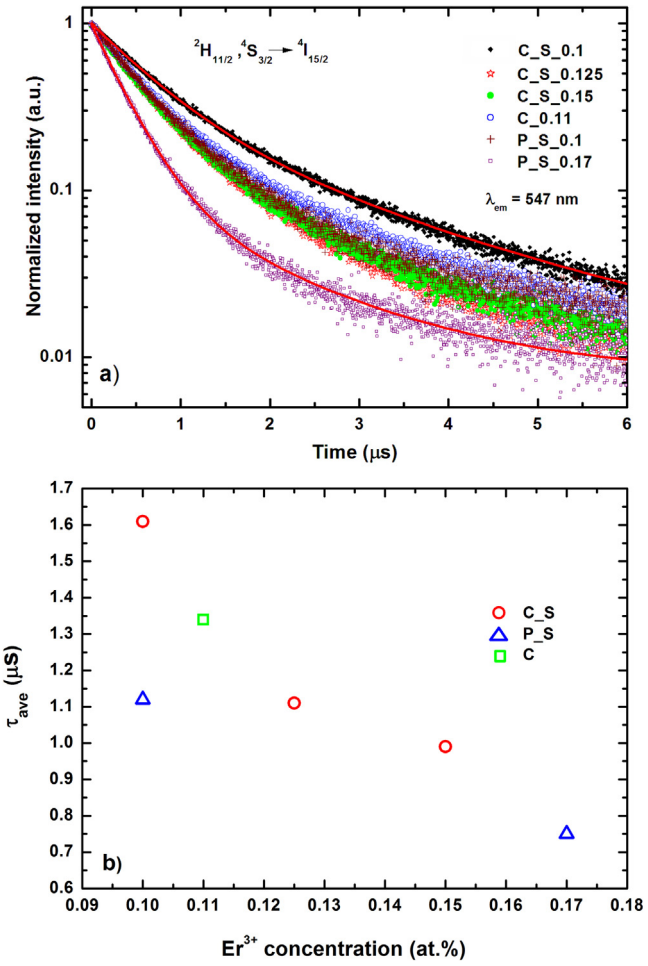

Fig. 8. Er^{3+} luminescence decay curves of the green emission ($^2H_{11/2}, ^4S_{3/2} \rightarrow ^4I_{15/2}$) recorded at RT under laser diode excitation at 375 nm: (a) The decay curves were fitted with 2-exponential decay function. (b) The dependence of τ_{ave} on Er^{3+} concentration. (For interpretation of the references to colour in this figure legend, the reader is referred to the web version of this article.)

Table 5
Lifetimes of the $^4S_{3/2}$ level at RT obtained under excitation at 375 nm.

Sample	Er^{3+}concentration [at.%]	τ_1[a] [ns]	τ_2[a] [μs]	τ_{ave} [μs]
C_S_0.1	0.1	694 (76%)	2.43 (24%)	1.61
C_0.11	0.11	566 (81%)	2.20 (19%)	1.34
C_S_0.125	0.125	545 (86%)	2.04 (14%)	1.11
C_S_0.15	0.15	517 (84%)	1.74 (16%)	0.99
P_S_0.1	0.1	564 (85%)	2.00 (15%)	1.12
P_S_0.17	0.17	360 (91%)	1.64 (9%)	0.75

[a] The numbers in parenthesis represent the weight of particular lifetime in the average lifetime value.

icantly with increasing concentration of Er^{3+} ions in the samples studied. The lifetime of the $^4F_{9/2}$ energy level could not be accurately measured under laser diode excitation due to the weak red emission from this level.

4. Discussion

4.1. The effect of parameters of doping on final microstructure and RIT

It was demonstrated that Er inhibits densification of alumina. However, the mean grain size of all fully dense HIP-ed samples

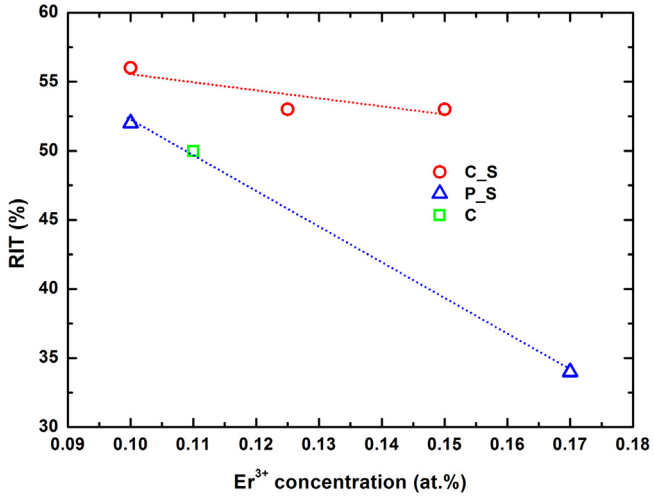

Fig. 9. The real in-line transmittance – Er content dependence.

was nearly identical (~350 nm) with differences falling within the standard deviation of the measurement. This indicates that the optimized conditions of sintering applied in the study were appropriate in terms of minimizing the grain growth while maximizing densification during sintering.

Due to almost identical values of the mean grain size of all prepared samples, the influence of other than sintering parameters, e.g. the content and the way of pre-treatment of the Er_2O_3 powders on the RIT could be traced. Generally, with increasing Er doping the RIT decreased. However, the extent of the decrease was strongly dependent on the type of used powder and its pre-treatment (performed by centrifugal sedimentation). The highest level of RIT and the smallest decrease with increasing amount of the dopant were achieved using commercial nano-powder further treated by sedimentation and denoted as C-S (Fig. 9). Careful elimination and removal of powder aggregates, which are always present even in commercial nano-powders, could reduce the decrease of RIT observed at higher concentrations of dopant in transparent ceramics.

The nano-powder prepared by modified Pechini method and then centrifugally treated (P-S) yielded lower values of RIT than commercial nano-powder (C-S) and stronger decrease of RIT values with increasing Er concentration (Fig. 9). On the other hand, the sedimented nano-powder P prepared by modified Pechini method (P-S) yields, in terms of the RIT, results similar to those of unsedimented commercial nano-powder (C) (Fig. 9). Although not clearly documented by SEM, this indicates certain level of aggregation of doping powder, especially in case of the powder C.

4.2. The effect of pre-sintering on final microstructure and RIT

The experiments made with P-S powder showed that pre-sintering regime has some effect on the RIT values of fully dense samples after HIP. As it can be seen from Table 4, prolonged TSP regime was beneficial for increase of transparency in comparison to conventional SSP pre-sintering. Since the final grain size of the samples were not statistically different (see Table 3) and the above mentioned results indicated the importance of dopant aggregation, we concerned our attention on microstructure of sintered samples.

The aggregates present in samples pre-sintered by prolonged TSP regime (Fig. 3) were considerably smaller (3–10 μm) than aggregates found in sample pre-sintered without dwell (10–20 μm). This confirmed the conclusions in our recently published paper [9] that long isothermal dwell (albeit at lower temperature) during two-step pre-sintering facilitates better redis-

tribution of dopants along grain boundaries, thus decreasing the size and/or number of second phase inclusions.

Since no practical doping process allows for removal of absolutely all aggregates, the prolonged pre-sintering can be recommended for minimizing of their size.

4.3. Photoluminescence spectra

The emission spectra of the Er^{3+} doped Al_2O_3 samples both in the visible and NIR spectral range exhibit relatively broad emissions and the emission bands are inhomogeneously broadened. For some transitions, e.g. from $^4S_{3/2}$ $^4F_{9/2}$, $^4I_{11/2}$ and $^4I_{13/2}$ this indicates that the band structure is due to the Stark splitting. This effect was found to be typical for highly disordered crystalline or amorphous materials, where optical centers experience quite different local environments that result in large inhomogeneous linewidths, in some cases approaching 100 cm^{-1} or even more for 4f-4f transitions [17]. Since the optical transition frequency of an ion depends on the strain, as well as local electric and magnetic fields affecting the ion, these environmental differences lead to a distribution of these frequencies for particular type of ion; the distribution of these frequencies produce an inhomogeneously broadened line. The broadened emissions were also found for the Er^{3+}-doped Al_2O_3 thin films with relatively higher concentration of the Er^{3+} ions (2.10^{19}– 4.10^{20} cm^{-3}) in the host matrix [18]. In contrast, very well resolved and sharp structured (Stark sublevels) emissions due to the Stark or crystal field splitting were observed for lower doping levels of Er^{3+} in Al_2O_3 matrix (0.026 at.%), as reported by Sanamyan et al. [6]. Similar results were found for other Er^{3+}-doped matrixes in which the Er^{3+} ions are incorporated into the structure of the host matrix [19], and Er^{3+} ion occupies defined positions in the structure. This, together with the fact that the emission intensity decreases with increasing concentration, point to the fact that local environment around the Er^{3+} ions is relatively disordered. The Er^{3+} ions aggregates are also possibly formed during the sample preparation that lead to the concentration quenching of luminescence due the direct interaction among Er^{3+} ions in the Al_2O_3 matrix.

4.4. Lifetime

The lifetime corresponding to $^4S_{3/2}$ level ($^4S_{3/2} \rightarrow {}^4I_{15/2}$ transition) exhibits strong dependence on the Er^{3+} concentration in Al_2O_3 host matrix (see Fig. 8, Table 5). All decay curves show non-mono-exponential profiles, even for the lowest concentrating sample containing 0.1 at.% of Er^{3+} ions ($2.38.10^{19}$ cm^{-3}), and were well fitted with double exponential decay function. It is well known that at very low concentrations of optically active ions, with negligible interactions between them, the decay of the luminescence can be described by a single exponential [20]. However, at higher concentrations the distances between active ions are shorter and the energy transfer processes become more efficient, resulting in a non-exponential decay [21]. All decay profiles thus exhibit a fast exponential decay in the initial part with a decay time of about 500 ns, followed by a slower decay with a decay time of ~ 2 μs. Similar double-exponential behavior of $^4S_{3/2}$ level decay was observed and reported by Agazzi [18] for Er^{3+}-doped Al_2O_3 films with dopant concentration in the range of 2.10^{19}–4.10^{20} cm^{-3}, with the lifetimes of 12.6 μs for faster and 30.8 μs for shorter decay process, respectively.

The observed non-exponential nature of the green luminescence decays, accompanied by shortening of the lifetimes with increasing Er^{3+} concentration is related to energy transfer processes (cross-relaxation processes) between Er^{3+} ions at higher concentrations and/or to different quenching traps (impurities and/or structural defective sites) [22]. During this process, an excited Er^{3+} ion (donor) is deactivated by transferring a part of its energy to another neighboring Er^{3+} ion (acceptor). The energy transfer is possible if there is a certain overlap in the fluorescence emission and absorption spectra of the donor and acceptor, which is the case of concentrated Er^{3+} systems; this means that there are matching differences in acceptor and donor energy levels. Some of the possible cross-relaxation channels that depopulate thermalized $^4S_{3/2}$ level can be described as (denoted as (initial sate Er^{3+}(I), Er^{3+}(II)→final state Er^{3+}(I), Er^{3+}(II)): ($^4S_{3/2}$, $^4I_{15/2} \rightarrow {}^4I_{13/2}$, $^4I_{9/2}$), ($^4S_{3/2}$, $^4I_{15/2} \rightarrow {}^4I_{9/2}$, $^4I_{13/2}$), ($^4I_{9/2}$, $^4I_{9/2} \rightarrow {}^4I_{11/2}$, $^4F_{9/2}$), ($^4I_{9/2}$, $^4I_{11/2} \rightarrow {}^4I_{13/2}$, $^4F_{9/2}$) and other [19]. For example, in the case of ($^4S_{3/2}$, $^4I_{15/2} \rightarrow {}^4I_{9/2}$, $^4I_{13/2}$) cross-relaxation channel, the donor is deactivated without emitting green fluorescence light and as a result the intensity and lifetime are diminished. However, as mentioned above, the structural defects may also play important role in the luminescence quenching.

5. Conclusion

Transparent photoluminescent aluminas doped with 0.1–0.17 at.% Er were successfully prepared by a combination of wet shaping technique (slip casting), pressure-less pre-sintering, and hot isostatic pressing (HIP). Fully dense samples with grain size less than 400 nm exhibited the RIT values ranging between 28 and 56%. The samples doped with Er_2O_3 nano-powder prepared by Pechini method exhibited slightly lower transparency (up to 52%) due to presence of Er agglomerates in the microstructure. The RIT value of 56% established for sample doped with commercial Er_2O_3 nano-powder is the highest real in-line transparency so far reported in the literature for luminescent RE doped aluminas. The positive influence of suspension centrifugation prior to slip casting on RIT and photoluminescence intensity was demonstrated. Upon excitation of the Er^{3+} ions in the UV range, intensive green, weak red and infrared emissions were observed, whose intensities and lifetime were described in dependence on the processing route. Based on the obtained results, future work to further improve the optical characteristics of this type of material will be focused on optimization of dopant concentration below 0.1 at% Er.

Acknowledgement

This work is part of the project 5SA14857, which has acquired the financial contribution from the EU Framework Programme for Research and Innovation Horizon 2020 within the scope of the Marie Sklodowska-Curie Actions co-financed by the South Moravian Region according to the Grant Agreement no. 665860.

The financial support of this work by the grant VEGA 1/0631/14 and GAČR 15-06390S is also gratefully acknowledged. This research has also been financially supported by the Ministry of Education, Youth and Sports of the Czech Republic under the project CEITEC 2020 (LQ1601). Part of the work was carried out with the support of core facilities of CEITEC open access project, ID number LM2011020, funded by the Ministry of Education, Youth and Sports of the Czech Republic under the activity “Projects of major infrastructures for research, development and innovations”.

References

[1] W.H. Rhodes, D.J. Sellers, T. Vasilos, Hot-working of aluminum-oxide. 2. Optical-properties, J. Am. Ceram. Soc. 58 (1–2) (1975) 31–34.
[2] Q. Liu, Q.H. Yang, G.G. Zhao, S.Z. Lu, H.J. Zhang, The thermoluminescence and optically stimulated luminescence properties of Cr-doped alpha alumina transparent ceramics, J. Alloy Compd. 579 (2013) 259–262.
[3] Q. Liu, Q.H. Yang, G.G. Zhao, S.Z. Lu, Titanium effect on the thermoluminescence and optically stimulated luminescence of Ti, Mg:alpha-Al2O3 transparent ceramics, J. Alloy Compd. 582 (2014) 754–758.
[4] E.H. Penilla, Y. Kodera, J.E. Garay, Blue-green emission in terbium-doped alumina (Tb:Al2O3) transparent ceramics, Adv. Funct. Mater. 23 (48) (2013) 6036–6043.

[5] I. Alvarez-Clemares, G. Mata-Osoro, A. Fernandez, S. Lopez-Esteban, C. Pecharroman, R. Torrecillas, J.S. Moya, Ceria doped alumina by Spark Plasma Sintering for optical applications, J. Eur. Ceram. Soc. 32 (11) (2012) 2917–2924.
[6] T. Sanamyan, R. Pavlacka, G. Gilde, M. Dubinskii, Spectroscopic properties of Er3+-doped alpha-Al2O3, Opt. Mater. 35 (5) (2013) 821–826.
[7] A.A. Kaplyanskii, A.B. Kulinkin, A.B. Kutsenko, S.P. Feofilov, R.I. Zakharchenya, T.N. Vasilevskaya, Optical spectra of triply-charged rare-earth ions in polycrystalline corundum, Phys. Solid State 40 (8) (1998) 1310–1316.
[8] X.J. Wang, M.K. Lei, T. Yang, H. Wang, Phase structure and photoluminescence Al2O3 powders prepared by the properties of Er3+-doped sol-gel method, Opt. Mater. 26 (3) (2004) 247–252.
[9] K. Bodišová, R. Klement, D. Galusek, V. Pouchlý, D. Drdlík, K. Maca, Luminescent rare-earth-doped transparent alumina ceramics, J. Eur. Ceram. Soc. 36 (12) (2016) 2975–2980.
[10] M. Trunec, K. Maca, R. Chmelik, Polycrystalline alumina ceramics doped with nanoparticles for increased transparency, J. Eur. Ceram. Soc. 35 (3) (2015) 1001–1009.
[11] T. Spusta, J. Svoboda, K. Maca, Study of pore closure during pressure-less sintering of advanced oxide ceramics, Acta Mater. 115 (2016) 347–353.
[12] R. Apetz, M.P.B. van Bruggen, Transparent alumina: a light-scattering model, J. Am. Ceram. Soc. 86 (3) (2003) 480–486.
[13] W.T. Carnall, H. Crosswhite, H.M. Crosswhite, Energy level structure and transitions probabilities of the trivalent lanthanides in LaF3 Argonne National Laboratory, Special Report, 1977.
[14] M.J. Weber, Probabilities for radiative and nonradiative decay of Er3+ in laf3, Phys. Rev. 157 (2) (1967) 262.
[15] C.M. Dodson, R. Zia, Magnetic dipole and electric quadrupole transitions in the trivalent lanthanide series: calculated emission rates and oscillator strengths, Phys. Rev. B 86 (12) (2012).
[16] P. Dorenbos, The 4f(n)⟨-⟩ 4f(n-1)5d transitions of the trivalent lanthanides in halogenides and chalcogenides, J. Lumin. 91 (1–2) (2000) 91–106.
[17] G. Liu, B. Jacquier, Spectroscopic Properties of Rare Earths in Optical Materials, Springer, Berlin, Heidelberg, 2006.
[18] L. Agazzi, Spectroscopic Excitation and Quenching Processes in Rare- Earth-Ion-Doped Al2O3 and Their Impact on Amplifier and Laser Performance, University of Twente, The Netherlands, 2012.
[19] V. Venkatramu, S.F. Leon-Luis, U.R. Rodriguez-Mendoza, V. Monteseguro, F.J. Manjon, A.D. Lozano-Gorrin, R. Valiente, D. Navarro-Urrios, C.K. Jayasankar, A. Munoz, V. Lavin, Synthesis, structure and luminescence of Er3+-doped Y3Ga5O12 nano-garnets, J. Mater. Chem. 22 (27) (2012) 13788–13799.
[20] P. Babu, H.J. Seo, C.R. Kesavulu, Y.H. Jang, C.K. Jayasankar, Thermal and optical properties of Er3+-doped oxyfluorotellurite glasses, J. Lumin. 129 (5) (2009) 444–448.
[21] B. Dibartolo, Energy Transfer Processes in Condensed Matter, Springer, US, 1984.
[22] V. Venkatramu, M. Giarola, G. Mariotto, S. Enzo, S. Polizzi, C.K. Jayasankar, F. Piccinelli, M. Bettinelli, A. Speghini, Nanocrystalline lanthanide-doped Lu3Ga5O12 garnets: interesting materials for light-emitting devices, Nanotechnology 21 (17) (2010).

PUBLIKACE IX

Journal of the European Ceramic Society 37 (2017) 4265–4270

Contents lists available at www.sciencedirect.com

Journal of the European Ceramic Society

journal homepage: www.elsevier.com/locate/jeurceramsoc

Feature article

Optical, mechanical and fractographic response of transparent alumina ceramics on erbium doping

Daniel Drdlik[a,*], Katarina Drdlikova[a], Hynek Hadraba[b], Karel Maca[a]

[a] CEITEC – Central European Institute of Technology, Brno University of Technology, Purkynova 123, 612 00 Brno, Czechia
[b] CEITEC IPM, Institute of Physics of Materials, Academy of Sciences of the Czech Republic, Zizkova 513/22, 616 62 Brno, Czechia

ARTICLE INFO

Article history:
Received 24 December 2016
Received in revised form 21 February 2017
Accepted 22 February 2017
Available online 1 March 2017

Keywords:
Alumina
Erbia
Transparency
Hardness
Fractography

ABSTRACT

Alumina ceramics found their utilisation in many applications which can be further extend by attaining functional properties; in our case the transparency obtained through precise processing and photoluminescence due to erbium (Er) doping. In order to examine the optical, mechanical and fractographic response of transparent alumina on Er doping, slip casted samples containing 0–0.15 at.% of erbium nano-oxide were pre-sintered by two-step sintering regime and then hot isostatically pressed. Prepared samples exhibited fully dense submicron microstructure and corresponding high transparency (RIT up to 60%). Positive influence of doping on the Vickers hardness resulted in values up to 27 GPa (at 10 N load). Moreover, the comparison of the Vickers hardness determined at different loadings with literature data showed that the Er doped alumina is one of the hardest material in this category. The samples were characterised also in terms of fracture toughness and fractographic behaviour.

© 2017 Elsevier Ltd. All rights reserved.

1. Introduction

Polycrystalline alumina is the most widely used structural ceramics in many common applications. When the alumina has extremely fine microstructure (low grain size) without residual porosity (final density ≥ 99.95%) then it becomes transparent [1]. Transparent polycrystalline alumina has a great technological potential for highly demanding applications which take advantage of its superior mechanical properties like high hardness, wear resistance, and high strength, in addition to its optical performance in the infrared and visible domain [2]. Moreover, in relation to the post-machining costs and inferior mechanical properties of sapphire (single crystal of alumina) the fine polycrystalline alumina exhibits economic and ecological benefits [3]. Krell et al. suggested application potential of this material in several directions: (i) lighting, (ii) optical components for different wavelengths, (iii) infrared emitters, (iv) orthodontic appliances and (v) ceramic armours [1,4].

To ensure transparency of the alumina few processing conditions must be fulfilled. The alumina powder should be extremely pure (99.99%) with nearly nanometre particle size and the grain growth during sintering has to be limited. The authors mainly utilise advantage of short sintering times using spark plasma sintering (SPS) [5–7]. However, to ensure other optical performances, i.e. photoluminescence, the doping with e.g. rare earth (RE) elements is needed [8–10]. By doping with the aim to obtain another functional property, it must be taken into account that the addition of sufficient amount of dopant can lead to the transparency deterioration. On the other hand, through the doping the alumina obtains interesting optical properties and pinning effect of dopant allows keeping low grain size. As doping elements for microstructure optimisation there are commonly used metals as chromium [11], titanium [12], magnesium [12–14], zirconium [15], or rare earth metals as yttrium [13], lanthanum [13]. Less common is doping with terbium [8], cerium [16], europium [9] or erbium [17,18].

Generally, mechanical properties and fractographic analysis of the transparent and/or photoluminiscent alumina is not well described in literature; only few publications on this topic can be found in the relevant literature. Krell et al. [19] doped commercial corundum powder with 0.03 wt.% MgO and 0.2 wt.% ZrO_2. In this transparent material no evidence of spinel phase and hardness 20–21 GPa (HV10) were obtained. The same combination of dopants used Braun et al. [20] to prepare transparent polycrystalline alumina with sub-micrometre microstructure. They studied the influence of different MgO and ZrO_2 dopant levels on the densification, microstructure development and in-line transmittance values. Nevertheless, authors provided information about hardness measurement valid only for undoped transparent alumina samples.

* Corresponding author.
E-mail addresses: daniel.drdlik@ceitec.vutbr.cz (D. Drdlik), katarina.drdlikova@ceitec.vutbr.cz (K. Drdlikova), hadraba@ipm.cz (H. Hadraba), karel.maca@ceitec.vutbr.cz (K. Maca).

http://dx.doi.org/10.1016/j.jeurceramsoc.2017.02.043
0955-2219/© 2017 Elsevier Ltd. All rights reserved.

The reported hardness ~11.6 GPa was relatively low probably due to higher value of grain size. In case of alumina doping with the rare earth elements Biswas et al. [3] reported hardness 21.4 GPa (HV5) of transparent sub-micrometre alumina doped with 0.1 wt.% lanthanum oxide.

Due to the lack of literature data this work is focused on investigation of optical, mechanical and fracture properties of transparent and/or photoluminescent alumina doped with various amount of erbia. Hardness measurement of alumina samples is extended to various load forces in order to enable better discussion with literature. Both hardness and fracture toughness are related to the observed microstructure. To the best of our knowledge, no similar study was carried out on this type of transparent and photoluminiscent material before.

2. Experimental

The commercial alumina powder (TM-DAR, Taimei Chemicals Co., Japan) with average particle size of 150 nm and commercial erbia powder (GNM, Getnanomaterials, USA) with average particle size of 20–30 nm were used for preparation of stable suspensions. Suspensions contain 45 vol.% of alumina, certain amount of erbia dopant (0, 0.10, 0.11, 0.125 and 0.15 at.%), electrostatic stabilizer (Darvan CN, Vanderbilt Minerals, USA) and deionized water. To remove aggregates the erbia powder was centrifugated at 800 rpm for 2 min before adding into suspension. Suspensions were homogenized for 24 h in a plastic bottles filled by alumina milling balls with diameter 4 mm. The balls to powder milling ratio of 2:1 was used.

The homogenous suspensions were casted into PVC dishes. Erbia doped alumina discs with diameter approximately 50 mm were first dried at room temperature for three days and then at 80 °C for 5 h. The discs were pressureless pre-sintered up to closed porosity stage (density range 95–96%) [18,21] using two-step sintering (TSS) in ambient atmosphere. The first step of TSS was realized at 1440 °C without dwell time followed by the cooling (20 °C/min) to the temperature 1280 °C with dwell time 10 h. The amount of open pores was checked by means of Archimedes method (EN 623-2). The two-step pre-sintered samples were consequently hot isostatically pressed under 200 MPa pressure of argon atmosphere at 1280 °C to completely eliminate residual closed porosity.

Sintered discs were grinded and polished up to 1 μm surface roughness, final thickness of the discs was approximately 0.8 mm. The real in-line transmittance (RIT) of the samples was measured with a non-polarized He-Ne laser (λ = 632.8 nm) at 860 mm sample to detector distance and 0.5° opening angle. The samples were thermally etched and investigated using a Lyra 3 microscope (Tescan, Czech Republic) and Titan Themis 60-300 (FEI, Czech Republic) equipped by Quantax EDX (Bruker Nano, Germany). During this investigation at least 5 micrographs of microstructure were obtained. The mean grain size (MGS) was determined on each micrograph using linear intercept method. The final average grain size value was multiplied by correction factor 1.56 [22].

Hardness was measured using an instrumented hardness tester (Z2.5, Zwick/Roel, Germany) at loading from 1 to 100 N. The number of measurements for each sample was set to 15. The fracture toughness was calculated from the length of the cracks originating from the corners of the indentation using equation [23]:

$$K_c = \propto \sqrt{\frac{E}{H}} \frac{P}{c^{3/2}}, \quad (1)$$

where α is an empirically determined constant (0.016), E is Young's modulus, H is the hardness, P is the applied load and c is the length of the crack grown from indent corner. Length of indent diagonals and cracks were measured using confocal microscope LEXT OLS 3100 (Olympus, Japan).

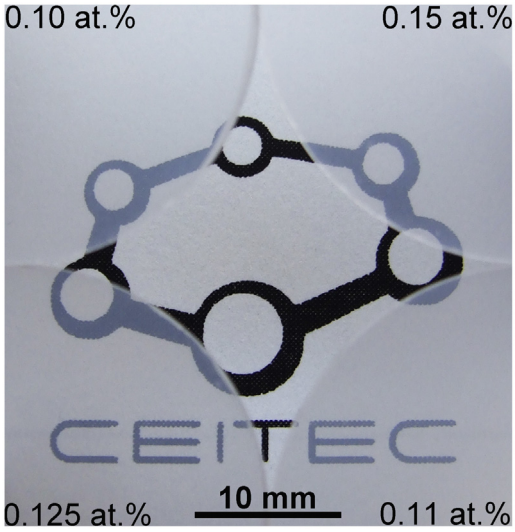

Fig. 1. Transparent alumina discs doped by different Er^{3+} concentration at 5 mm distance over the printed paper.

Table 1
Summary of microstructural and optical properties of undoped and Er^{3+}-doped alumina.

Concentration of Er^{3+} (at.%)	Density (%)	MGS (μm)	RIT (%)	RIT_r[a] (%)
undoped	≥99.95	0.50	60	64
0.10		0.35	56	59
0.11		0.34	–	–
0.125		0.33	53	55
0.15		0.35	53	55

[a] RIT_r = RIT recalculated to 1 mm thickness and related to the maximum theoretical transparency value for alumina (86% at 840 nm).

3. Results and discussion

Processing of the RE-doped transparent alumina was described in our previous work [18]. In the present work, one undoped and four Er^{3+}-doped transparent alumina discs were prepared. The photograph of transparent alumina discs doped by Er^{3+} in concentrations of 0.10, 0.11, 0.125 and 0.15 at.% is shown in Fig. 1. The samples were placed 5 mm above the printed paper. It is evident that transparency is similar for all samples. The real in-line transmittance of doped samples was in range 53–56% whereas the real in-line transmittance of undoped alumina was slightly higher (60%). Summary of RIT values is given in Table 1. The obtained RIT values were also recalculated to 1 mm thickness and related to the maximum theoretical transparency value for alumina (86% at 840 nm) for easier comparison with literature data [24]. The RIT of Er^{3+}-doped alumina in the range of 53–59% was already established in our previous work [18]. Here it was compared with RIT of undoped alumina prepared by the same way. The lower RIT value of doped alumina was expected because the relative high concentration of the dopant probably exceeded the amount being able to the segregate at the grain boundaries (e.g. lanthanum grain boundary solubility limit in alumina was observed at ~200 ppm [25]). Therefore, the higher content of the dopant then most likely results in decrease of optical transmittance.

Only few works reported optical transparency of photo- or thermoluminiscent alumina doped by Tb [8], Eu [9] and Ce [16]. In those cases the obtained transparencies were low, suffering from

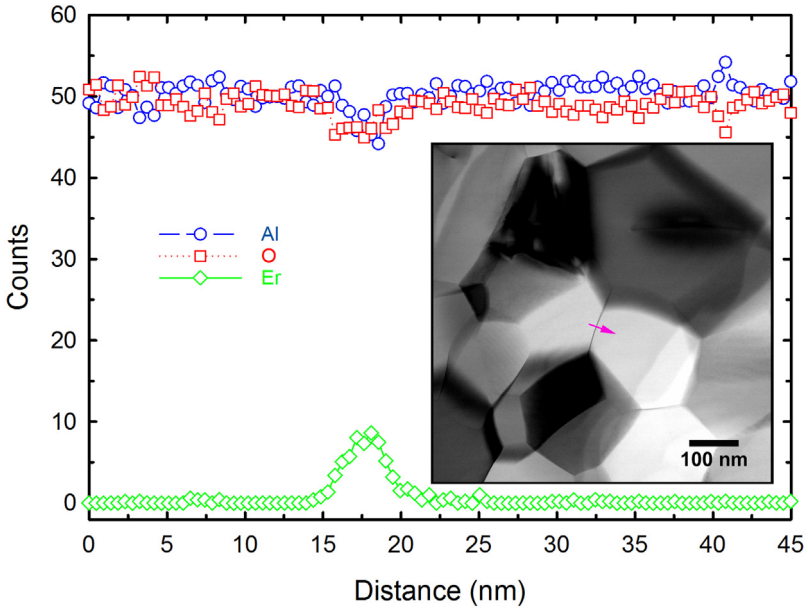

Fig. 2. EDX line scan of Al, O and Er elements on the grain boundary of Er^{3+}-doped alumina (0.10 at.% of Er^{3+}) with TEM detail of microstructure.

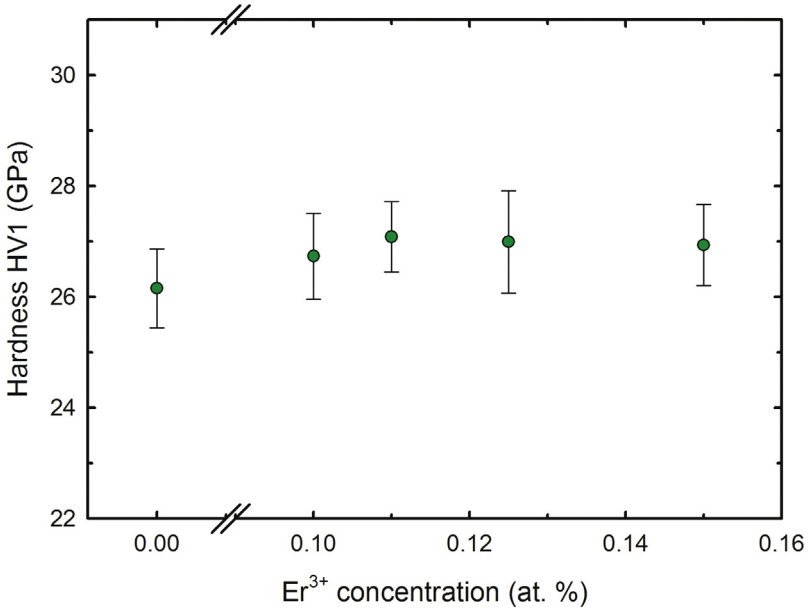

Fig. 3. Vickers hardness (at testing load of 10 N) of transparent alumina samples with different Er^{3+} concentration.

inclusions present as a result of high dopant concentration and the samples were rather translucent than transparent.

It is well known that transparency of the transparent ceramics is grain size dependent. However, the MGS of prepared Er^{3+}-doped transparent alumina exhibited no trend; the MGS was in narrow range of 0.33–0.35 μm (see Table 1) irrespective of dopant concentration. The slightly higher MGS of undoped alumina (0.50 μm) prepared at the same processing route confirmed grain growth inhibition (reduced mobility of grain boundaries) due to erbium presence at the grain boundaries. The segregation of Er^{3+} cations on the grain boundary was determined by EDX line scan. The EDX line scan of Al, O and Er elements through the grain boundary of Er^{3+}-doped alumina (0.10 at.% of Er^{3+}) with TEM detail of microstructure is showed in Fig. 2. The EDX line scan marked by pink arrow in detailed TEM micrographs of microstructure proved the presence of Er^{3+} cations on the grain boundary. The count of Er signal increased in this place (diamonds line) whereas signal of Al and O (circles and squares lines) atoms slightly decreased. This situation confirmed that the amount of dopant was higher than the bulk solubility limit (solubility in alumina is very low $\sim 10^{-3}$ at.% [26]) and the segregation of Er occurs on grain boundaries. Taking into account the observed values of grain boundary solubility for La and Zr for similar alumina microstructures, the amount of added Er very likely exceeded the grain solubility limit and the secondary phases should appear at grain boundaries and triple points [25]. Nevertheless, no secondary phases were observed during SEM and TEM investigation, which may suggest different (much higher) value of grain boundary solubility limit for Er or the situation where very homogeneous distribution of the dopant results in very small, barely perceptible inclusions.

The Vickers hardness (at testing load of 10N) of the transparent alumina samples with different Er^{3+} concentration is shown

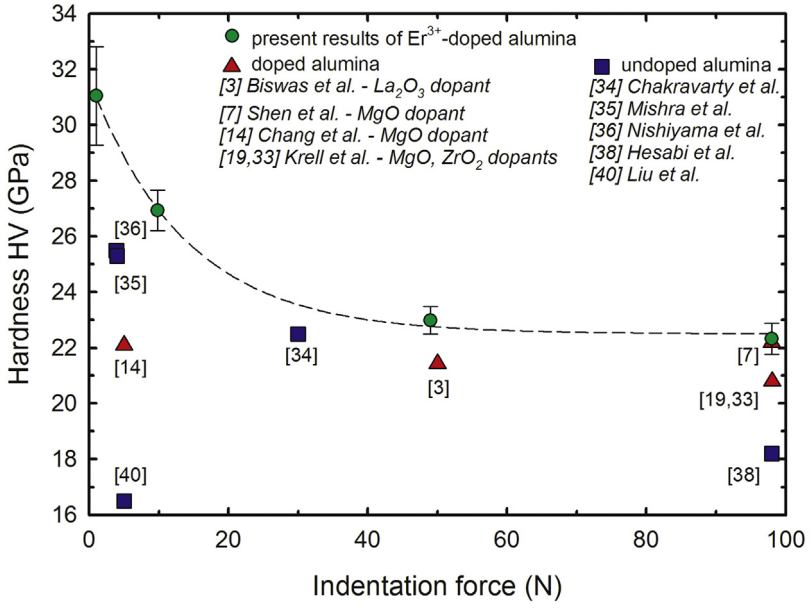

Fig. 4. Dependence of hardness of Er^{3+}-doped alumina (0.15 at.% of Er^{3+}) on the different indentation force [40].

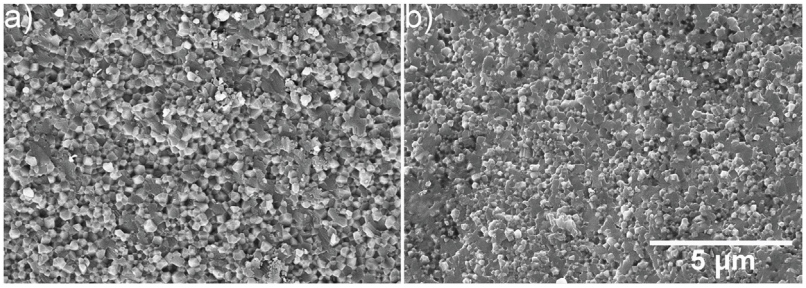

Fig. 5. Fracture surface micrographs of (a) undoped alumina sample and (b) alumina samples doped by 0.15 at.% of Er^{3+}.

in Fig. 3. From the hardness of undoped alumina (26.1 GPa), it is obvious that the high hardness of all samples is primarily related to the optimised processing (fine powders → optimised slip casting → TSS → HIP) leading to improved microstructure rather than possible hardening effect of erbia (which is anyway present in very small concentrations). The average hardness of Er^{3+}-doped transparent alumina samples (26.9 GPa) is slightly higher than undoped one. The hardness of the doped alumina samples varied only in the interval ±0.18 GPa. The improvement of the hardness due to erbia doping observed also Joshi et al. [27]. They reported 2% increase in the hardness of erbia doped polycrystalline silicon nitride in comparison with undoped silicon nitride. This result is in good agreement with our 3% increase of the hardness. Generally, the hardness of ceramics is dependent on its porosity and grain size [28,29]. However, the transparent ceramics contain porosity close to zero, so the main parameter influencing its hardness is the grain size. The slight increase of the hardness Er^{3+}-doped transparent aluminas in contrast to undoped alumina corresponds also with the Hall-Petch relationship where the hardness increases with the smaller grains [30]. The second reason of the hardness improvement in Er^{3+}-doped transparent alumina could be solute solution strengthening mechanism [31]. However, this mechanism is probably less of importance.

Krell [32,33] pointed out that hardness of polycrystalline alumina strongly depends on the indentation size (load), grain size and surface preparation. Neglecting of these conditions lead to the distortion of presented final hardness, especially in comparison with literature data. In our case both grain size (see Table 1) and surface preparation were constant. Therefore, only one sample of transparent alumina doped by 0.15 at.% of Er^{3+} was selected for Vickers hardness measurements at different loads. The dependence of hardness of Er^{3+}-doped alumina on the different indentation force is shown in Fig. 4. Our results (green circles) are compared with other authors who worked with polycrystalline (mostly transparent) doped (red triangles) or undoped (blue squares) aluminas. It is obvious from this comparison that the hardness of prepared transparent Er^{3+}-doped alumina is very high; higher than the published literature data. However, it is important to note that only hardness reported in works [34–36] was measured in alumina samples with the similar or lower MGS. The MGS of alumina samples reported by other authors was in range 0.5–0.8 μm.

The fracture toughness of transparent and/or photoluminiscent alumina materials is not quite well discussed in literature. The indentation fracture toughness of Er^{3+}-doped alumina was in range 2.1–2.2 MPa $m^{1/2}$. The indentation fracture toughness of undoped alumina was slightly higher 2.3 MPa $m^{1/2}$. These nearly the same fracture toughness values were expected because prepared ceramics contained uniform, equiaxed and fine grains [37]. On the other hand, it also indicates high strength [37]. The similar fracture toughness 2.9 and 3.2 MPa $m^{1/2}$ at undoped and MgO doped alumina were reported in works Nishiyama et al. [36] and Shen et al. [7], respectively. Hesabi et al. [38] provided fracture toughness 4.2 MPa $m^{1/2}$ and completely intergranular character of fracture surface of alumina sintered under optimised TSS regime. Nevertheless, their sample contained 2% porosity which could lead to reduction in the

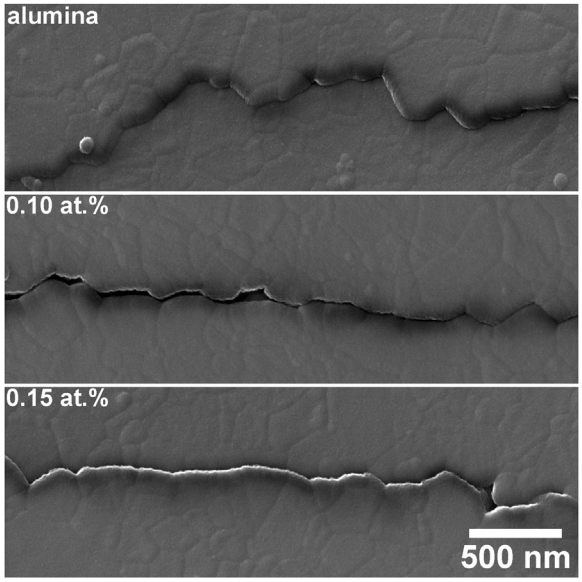

Fig. 6. Micrographs of cracks at the corners of Vickers indents of undoped alumina sample and alumina samples doped by 0.10 and 0.15 at.% of Er^{3+}.

crack length by stopping and re-initiation of the crack growth on the pores.

The micrographs of fracture surfaces of undoped and Er^{3+}-doped alumina are shown in Fig. 5. The fractographic analysis showed a higher transgranular character of fracture surface in Er^{3+}-doped alumina compare to undoped alumina. The observed proportional fracture is in apparent contradiction with observations in work of West et al. [39] where detailed study of fracture surfaces of RE-doped (Yb, Gd, La) and undoped alumina with various MGS was provided. On the other hand, it should be note that there are a number of studies with different conclusions, e.g. Rani et al. [37] reported dominant transgranular fracture of pressureless sintered Er- and La-doped alumina. Nevertheless, our results reveal that Er dopant promotes the grain boundary cohesion.

The micrographs of cracks at the corners of Vickers indents of the undoped alumina and Er^{3+}-doped alumina (0.10 and 0.15 at.%) are shown in Fig. 6. The crack path in undoped alumina sample was not as straight as in the case of Er^{3+}-doped samples which proved predominant intergranular character of fracture and it may explain slight increase in the fracture toughness of undoped alumina in comparison with doped one.

4. Conclusion

The optical, microstructural, mechanical and fracture properties of Er^{3+}-doped transparent and/or photoluminescent alumina was investigated within this article. The real in-line transmittance (RIT) of Er^{3+}-doped samples was in range of 55–59% (recalculated to 1 mm thickness and related to the maximum theoretical transparency value for alumina), which belongs to higher RIT values in comparison with RITs found in literature. The presence of segregated Er atoms on the grain boundaries was proved by EDX line scan. Segregation of Er atoms on the grain boundary probably caused reduction of grain boundaries mobility which led to decreasing of the mean grain size (0.33–0.35 μm) in comparison to undoped alumina (0.50 μm). The Vickers hardness of the Er^{3+}-doped alumina was measured at different loading conditions and compared with literature. The current results indicates, that prepared transparent and/or photoluminescent Er^{3+}-doped alumina is one of the hardest material in this category, e.g. the Vickers hardness at 10 N loading was 26.9 GPa (average value for all Er^{3+} concentrations). The fractographic analysis showed a higher transgranular character of fracture surface in Er^{3+}-doped alumina compare to undoped alumina which confirms the enhanced grain boundary cohesion due to Er doping. The indentation fracture toughness of Er^{3+}-doped alumina was in range 2.1–2.2 MPa $m^{1/2}$. In conclusion, we reported here processing and properties of unique material with combination of superior optical, functional and mechanical properties.

Acknowledgements

This work is part of the project 5SA14857, which has acquired the financial contribution from the EU Framework Programme for Research and Innovation Horizon 2020 within the scope of the Marie Sklodowska-Curie Actions co-financed by the South Moravian Region according to the Grant Agreement no. 665860. The financial support of this work by the grant GACR15-06390S is also gratefully acknowledged. This research has also been financially supported by the Ministry of Education, Youth and Sports of the Czech Republic under the project CEITEC 2020 (LQ1601). Part of the work was carried out with the support of core facilities of CEITEC open access project, ID number LM2011020, funded by the Ministry of Education, Youth and Sports of the Czech Republic under the activity “Projects of major infrastructures for research, development and innovations”.

References

[1] A. Krell, J. Klimke, T. Hutzler, Advanced spinel and sub-mu m Al(2)O(3) for transparent armour applications, J. Eur. Ceram. Soc. 29 (2) (2009) 275–281.
[2] A. Belenky, I. Bar-On, D. Rittel, Static and dynamic fracture of transparent nanograined alumina, J. Mech. Phys. Solids 58 (4) (2010) 484–501.
[3] P. Biswas, M.K. Kumar, K. Rajeswari, R. Johnson, U.S. Hareesh, Transparent sub-micrometre alumina from lanthanum oxide doped common grade alumina powder, Ceram. Int. 39 (8) (2013) 9415–9419.
[4] A. Krell, T. Hutzler, J. Klimke, Transmission physics and consequences for materials selection, manufacturing, and applications, J. Eur. Ceram. Soc. 29 (2) (2009) 207–221.
[5] L. Lallemant, G. Fantozzi, V. Garnier, G. Bonnefont, Transparent polycrystalline alumina obtained by SPS: green bodies processing effect, J. Eur. Ceram. Soc. 32 (11) (2012) 2909–2915.
[6] S. Grasso, H. Yoshida, H. Porwal, Y. Sakka, M. Reece, Highly transparent alpha-alumina obtained by low cost high pressure SPS, Ceram. Int. 39 (3) (2013) 3243–3248.
[7] Z.J. Shen, M. Johnsson, Z. Zhao, M. Nygren, Spark plasma sintering of alumina, J. Am. Ceram. Soc. 85 (8) (2002) 1921–1927.
[8] E.H. Penilla, Y. Kodera, J.E. Garay, Blue-green emission in terbium-doped alumina (Tb:Al2O3) transparent ceramics, Adv. Funct. Mater. 23 (48) (2013) 6036–6043.
[9] Y. Yang, H. Wei, L.H. Zhang, K. Kisslinger, C.L. Melcher, Y.Q. Wu, Blue emission of Eu2+-doped translucent alumina, J. Lumin. 168 (2015) 297–303.
[10] X.J. Wang, M.K. Lei, T. Yang, H. Wang, Phase structure and photoluminescence Al2O3 powders prepared by the properties of Er3+-doped sol-gel method, Opt. Mater. 26 (3) (2004) 247–252.
[11] Q. Liu, Q.H. Yang, G.G. Zhao, S.Z. Lu, H.J. Zhang, The thermoluminescence and optically stimulated luminescence properties of Cr-doped alpha alumina transparent ceramics, J. Alloy Compd. 579 (2013) 259–262.
[12] Q. Liu, Q.H. Yang, G.G. Zhao, S.Z. Lu, Titanium effect on the thermoluminescence and optically stimulated luminescence of Ti, Mg:alpha-Al2O3 transparent ceramics, J. Alloy Compd. 582 (2014) 754–758.
[13] M. Stuer, Z. Zhao, U. Aschauer, P. Bowen, Transparent polycrystalline alumina using spark plasma sintering: effect of Mg, Y and La doping, J. Eur. Ceram. Soc. 30 (6) (2010) 1335–1343.
[14] S. Chang, R.H. Doremus, L.S. Schadler, R.W. Siegel, Hot-pressing of nano-size alumina powder and the resulting mechanical properties, Int. J. Appl. Ceram. Technol. 1 (2) (2004) 172–179.
[15] M. Trunec, K. Maca, R. Chmelik, Polycrystalline alumina ceramics doped with nanoparticles for increased transparency, J. Eur. Ceram. Soc. 35 (3) (2015) 1001–1009.
[16] I. Alvarez-Clemares, G. Mata-Osoro, A. Fernandez, S. Lopez-Esteban, C. Pecharroman, R. Torrecillas, J.S. Moya, Ceria doped alumina by Spark Plasma Sintering for optical applications, J. Eur. Ceram. Soc. 32 (11) (2012) 2917–2924.
[17] T. Sanamyan, R. Pavlacka, G. Gilde, M. Dubinskii, Spectroscopic properties of Er3+-doped alpha-Al2O3, Opt. Mater. 35 (5) (2013) 821–826.

[18] K. Bodisova, R. Klement, D. Galusek, V. Pouchly, D. Drdlik, K. Maca, Luminescent rare-earth-doped transparent alumina ceramics, J. Eur. Ceram. Soc. 36 (12) (2016) 2975–2980.
[19] A. Krell, P. Blank, H.W. Ma, T. Hutzler, M.P.B. van Bruggen, R. Apetz, Transparent sintered corundum with high hardness and strength, J. Am. Ceram. Soc. 86 (1) (2003) 12–18.
[20] A. Braun, G. Falk, R. Clasen, Transparent polycrystalline alumina ceramic with sub-micrometre microstructure by means of electrophoretic deposition, Materialwiss Werkst 37 (4) (2006) 293–297.
[21] T. Spusta, J. Svoboda, K. Maca, Study of pore closure during pressure-less sintering of advanced oxide ceramics, Acta Mater. 115 (2016) 347–353.
[22] M.I. Mendelson, Average grain size in polycrystalline ceramics, J. Am. Ceram. Soc. 52 (8) (1969) 443–446.
[23] G.R. Anstis, P. Chantikul, B.R. Lawn, D.B. Marshall, A critical-evaluation of indentation techniques for measuring fracture-toughness: 1. Direct crack measurements, J. Am. Ceram. Soc. 64 (9) (1981) 533–538.
[24] J. Petit, P. Dethare, A. Sergent, R. Marino, M.H. Ritti, S. Landais, J.L. Lunel, S. Trombert, Sintering of alpha-alumina for highly transparent ceramic applications, J. Eur. Ceram. Soc. 31 (11) (2011) 1957–1963.
[25] L. Lallemant, N. Roussel, G. Fantozzi, V. Garnier, G. Bonnefont, T. Douillard, B. Durand, S. Guillemet-Fritsch, J.Y. Chane-Ching, D. Garcia-Gutierez, J. Aguilar-Garib, Effect of amount of doping agent on sintering, microstructure and optical properties of Zr- and La-doped alumina sintered by SPS, J. Eur. Ceram. Soc. 34 (5) (2014) 1279–1288.
[26] M.D. Chambers, D.R. Clarke, Doped oxides for high-temperature luminescence and lifetime thermometry, Annu. Rev. Mater. Res. 39 (1) (2009) 325–359.
[27] B. Joshi, Z. Fu, K. Niihara, S.W. Lee, Optical, mechanical and tribological properties of Y 2 o 3, Er 2 o 3 and Nd 2 O 3 doped polycrystalline silicon nitride ceramics, IOP Conf. Ser.: Mater. Sci. Eng. 18 (8) (2011) 082020.
[28] D. Drdlik, M. Slama, H. Hadraba, J. Cihlar, Hydroxyapatite/zirconia-microfibre composites with controlled microporosity and fracture properties prepared by electrophoretic deposition, Ceram. Int. 41 (9) (2015) 11202–11212.
[29] R.W. Rice, C.C. Wu, F. Borchelt, Hardness grain-size relations in ceramics, J. Am. Ceram. Soc. 77 (10) (1994) 2539–2553.
[30] C.S. Pande, K.P. Cooper, Nanomechanics of Hall-Petch relationship in nanocrystalline materials, Prog. Mater. Sci. 54 (6) (2009) 689–706.
[31] H.C. Ling, M.F. Yan, Microhardness measurements on dopant modified superconducting yba2cu3o7 ceramics, J. Appl. Phys. 64 (3) (1988) 1307–1311.
[32] A. Krell, A new look at the influences of load, grain size, and grain boundaries on the room temperature hardness of ceramics, Int. J. Refract. Met. Hard Mater. 16 (4–6) (1998) 331–335.
[33] A. Krell, Improved hardness and hierarchic influences on wear in submicron sintered alumina, Mater. Sci. Eng. A Struct. 209 (1–2) (1996) 156–163.
[34] D. Chakravarty, G. Sundararajan, Effect of applied stress on IR transmission of spark plasma-sintered alumina, J. Am. Ceram. Soc. 93 (4) (2010) 951–953.
[35] R.S. Mishra, C.E. Lesher, A.K. Mukherjee, High-pressure sintering of nanocrystalline gamma-Al2O3, J. Am. Ceram. Soc. 79 (11) (1996) 2989–2992.
[36] N. Nishiyama, T. Taniguchi, H. Ohfuji, K. Yoshida, F. Wakai, B.N. Kim, H. Yoshida, Y. Higo, A. Holzheid, O. Beermann, T. Irifune, Y. Sakka, K. Funakoshi, Transparent nanocrystalline bulk alumina obtained at 7.7 GPa and 800 degrees C, Scripta Mater. 69 (5) (2013) 362–365.
[37] D.A. Rani, Y. Yoshizawa, K. Hirao, Y. Yamauchi, Effect of rare-earth dopants on mechanical properties of alumina, J. Am. Ceram. Soc. 87 (2) (2004) 289–292.
[38] Z.R. Hesabi, A. Haghighatzadeh, M. Mazaheri, D. Galusek, S.K. Sadrnezhaad, Suppression of grain growth in sub-micrometer alumina via two-step sintering method, J. Eur. Ceram. Soc. 29 (8) (2009) 1371–1377.
[39] G.D. West, J.M. Perkins, M.H. Lewis, The effect of rare earth dopants on grain boundary cohesion in alumina, J. Eur. Ceram. Soc. 27 (4) (2007) 1913–1918.
[40] F.M. Liu, D.W. He, Q. Wang, W. Ding, J. Liu, Y.J. Liu, Bimodal transparent alumina ceramics prepared with micro/nano-particles under high pressure, Scripta Mater. 122 (2016) 54–58.

PUBLIKACE X

Science of Sintering, **55** (2023) 289-306

https://doi.org/10.2298/SOS221028017D

UDK: 53.086; 666.3.019; 622.785

Dilatometric and Microstructural Study of Particle and Functionally Graded Composites Based on Hydroxyapatite and Crystalline Bioglass

Daniel Drdlik[1,2*)], Katarina Drdlikova[1], Karel Maca[1]

[1]CEITEC BUT, Brno University of Technology, Purkynova 123, 612 00 Brno, Czech Republic

[2]Institute of Materials Science and Engineering, Brno University of Technology, Technicka 2, 616 00 Brno, Czech Republic

Abstract:

Hydroxyapatite (HA) and bioglass (BG) ceramics have become of prime importance in bone tissue engineering. Besides the appropriate composition, the microstructure of bone replacement plays a crucial role. In the present work, particle composites and functionally graded material (FGM) based on HA and BG prepared by electrophoretic deposition were thoroughly characterised in terms of the preparation method, sintering process, phase composition and microstructure. The sintering was monitored by high-temperature dilatometry in two directions, the sintering rates were calculated, and the overall sintering process was discussed. The SEM showed the continuous change in the microstructure of FGM with gradual interconnected porosity favourable for bio-applications. The fundamental fractographic analysis proved the crack development in FGM related to the sintering process, and the recommendations for the reduction of the crack development were given. The phase transformations during thermal treatment were analysed using X-ray diffraction analysis and deeply discussed.

Keywords*: Hydroxyapatite; Bioglass; Functionally graded material; Sintering; Microstructure.*

1. Introduction

Functionally graded materials (FGMs) are a special kind of composite in which the material properties vary smoothly and continuously from one surface to the other. The variation of the properties is attained by the gradual change of the material composition. FGMs attract great attention today in the materials science and engineering society because conventional composites do not achieve the necessary properties appropriate for many challenging applications [1]. FGMs are successfully applied in automobile, military, energy, machinery, aerospace or medical areas where a continuous chemical and structural change over the material is demanded [2]. In particular, regarding the medical area, the most important examples of FGMs are directly located in a human body. Bones or teeth have a gradual change in their structure and properties.

The most common strategy for hard tissue regeneration after some kind of trauma is to heal the bone by autograft or allograft. In the case of allograft, the utilisation of synthetic bioactive material with low risk of immune reaction is a highly discussed topic in the

*) **Corresponding author:** daniel.drdlik@ceitec.vutbr.cz

literature. Hydroxyapatite (HA) is being considered as a candidate for hard tissue substitution because of its 65% chemical similarity of the mineral constituent with the natural bone and excellent biocompatibility, bioactivity and cytocompatibility [3, 4].

Although the biocompatibility of HA is high, it can be improved further. It has been proposed that the addition of silicon to the apatite structure influences the material in biological environments [5]. The enhancement of HA bioactivity is due to the substitution of SiO_4^{4-} for PO_4^{3-} ions that affect HA surface chemistry or local bioavailable Si release [6]. The favourable results of the substitution were reported by several authors [7-9]. Therefore, the using of Bioglass® (BG) together with HA seems to be justified. Moreover, the addition of more bioactive BG [10] into HA composite can accelerate its dissolution rate because the dissolution rate of HA is relatively low [11], corresponding to ionic substitutions into the HA lattice and crystallinity [12].

Many studies have been made to describe HA/BG composite systems [5, 13-16]. The authors mainly focused their efforts to show manufacturability, microstructure and properties of the composites. However, it is hard to maintain the BG in an amorphous structure. The BG has a high crystallisation ability and it crystallises by a surface crystallisation mechanism, so that the material is highly crystalline even a low temperature (600-750 °C) [17]. Crystalline phase may affect its bioactivity and dissolution profile [18, 19]. Therefore, tailoring of manufacturing method with applied pressure [13, 14, 16] or thermal conditions [13, 14] has to be done.

Probably for these very reasons, only a few studies are available in the literature aiming on FGM from HA and BG [20-24]. Most of these studies deal preferably with coatings instead of bulk material. Moreover, all these works report specific types of multi-layered functionally graded HA/BG rather than FGM with continuous microstructural change. It is attributed to the fabrication techniques used, i.e. Spark Plasma Sintering (SPS) [20], plasma spraying [21, 22], pulsed laser deposition [23] or enamelling technique [24].

Another suitable method for preparation of non-composite [25, 26] or composite materials (particle [27] and fibre reinforced composites [28] or laminates [29]) including FGM [27, 30] is electrophoretic deposition (EPD). It is a versatile technique allowing fabrication of complicated objects from suspensions containing charged ceramic particles through their movement in an electric field applied between two electrodes. Contrary to previously mentioned methods, EPD offers the possibility of preparing FGM with continuous change of composition without any sharp phase interphase. Although, the EPD is widely used to prepare HA and BG composites [31, 32], but it has not yet been used to fabricate the FGM from these biomaterials. However, products of electrophoretic deposition are subsequently processed by conventional sintering, therefore crystallisation of BG in HA/BG composite is inevitable. Crystallisation of BG could consequently be suppressed by combining EPD with following SPS or Hot Isostatic Press methods (HIP).

Another challenging issues associated with the HA/BG FGM materials is coefficients of thermal expansion (CTE) of HA and BG and sintering shrinkage if the prepared green bodies do not have the same density and undergo phase changes during sintering. In the first case, the CTE of HA and BG are 15.9 and 9.7 $\times 10^{-6}$ K^{-1}, respectively, indicating the possible development of cracks during cooling from the sintering temperature. In the second case, the structural change during sintering, i.e. variation of grain or pore morphology and size, phase transformations are accompanied by volume change (a shrinkage). Generally speaking, the shrinkage of BG is considerably high (60 % at 1050 °C [17]) compared to HA (13 % at 1050 °C [33]), which may lead to crack development in the FGM as well. This situation is very well documented in the work of Luginina et al. [20]. Therefore, a deep description and understanding of the sintering process of FGM based on HA and BG are needed.

Present work as the first describes the preparation of bulk FGM based on HA and BG with continuous phase change using EPD. To accomplish this goal, the various bulk (several millimetres thick) HA/BG particle composites had to be prepared and evaluated as well. Since

conventional sintering of the prepared composites was chosen, the article brings original information about densification, crystallisation of bioglass and phase changes in HA/BG and FGM composites during sintering determined by high-temperature dilatometry and X-ray diffraction analysis.

2. Materials and Experimental Procedures

Two commercial powders, i.e. hydroxyapatite (HA, 99,95%, Nanografi Nanotechnology, Turkey) and bioglass 45S5 (BG, Schott AG, Germany) with mean particle size of 50 nm and 10 μm, respectively, were used to prepare functionally grade and particle composite materials as well as standards (pure HA or BG). The fine HA particles were chosen in order to use the lowest possible sintering temperature. The suspensions designed to prepare FGM consisted of 15 wt % HA or BG, 0.85 wt % of monochloroacetic acid (Merck, Germany) and 84.15 wt % of 2-propanol (Lachner, Czech Republic). The suspensions related to fabrication of the two standards and three particle composites had the same compositions of ingredients, but the ceramics loads had different weight ratios of powders (HA:BG): 100:0, 75:25, 50:50, 25:75, 0:100. After mixing all components, the suspensions were homogenised mechanically and ultrasonically for 30 minutes. The electrical conductivity of the suspensions was measured using a SevenCompact Conductivity S230 conductometer (Mettler Toledo AG, Switzerland).

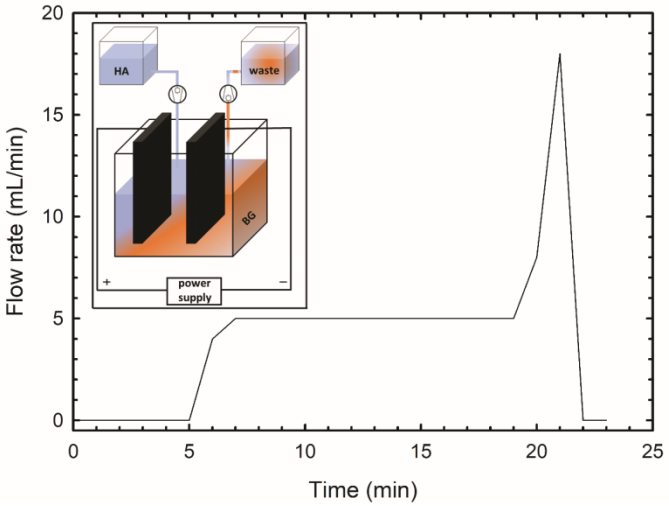

Fig. 1. Scheme of the flow rate of suspension change during fabrication of FGM.

The EPD apparatus was assembled from a glass cell, two stainless steel electrodes placed in vertical positions with 26 mm distance between them and a stable power source with applied constant current of 5 mA (current density of 0.27 mA/cm^2). The depositions of the pure ceramics and particle composites were interrupted each 5 minutes and the suspensions were stirred to avoid a sedimentation of the particles at an electrophoretic cell bottom (described elsewhere [25, 26, 28]). At the same time, a weight yield on the deposition electrode was monitored to obtain data about deposition kinetics required for preparation of FGM. The deposition time was up to 40 minutes to obtain robust set of kinetic data and thick enough deposits. Based on that, the FGM could be prepared using the continuous mode of EPD. The suspension containing only BG was drained continuously from the glass cell, and the fresh suspension with HA was fed into at the same rate. The flow rate was increased during the deposition process to respect the evolution of the deposition kinetics given by

materials change in the suspension, thickness and resistivity of the growing deposit. The schemes of the EPD apparatus and flow rate during the deposition (23 minutes) are given in Fig. 1.

The electrodes covered by deposits were allowed to dry in a desiccator for 24 hours at 25 °C. After then the several millimetres thick deposits were removed from electrodes, and the organic residues were burnt out at 600 °C for 1 hour. The samples were sintered at 1050 °C for 2 hours with heating rate of 10 °C/min, whereas the linear dimensional changes were recorded using a high-temperature dilatometer L70/1700 (Linseis, Germany) in longitudinal (parallel with electrode) and transversal (in the direction of deposition) direction. The samples for longitudinal direction had the shape of the prismatic bar with dimensions (length × width × thickness): 10×4×1-5 mm. The samples for transversal direction had the shape of a cylinder with dimensions (diameter × thickness): 5×1-5 mm. The thickness of the measured sample depended on the thickness of the deposit. The theoretical shrinkage based on the knowledge of green (ρ_{gb}) and final (ρ) densities of the ceramic body was calculated using equation [34]:

$$\varepsilon_{calc} = 1 - \sqrt[3]{\frac{\rho_{gb}}{\rho}}. \quad (1)$$

The density and pore size distribution of the samples were determined using the Archimedes method (EN 623-2) and an automatic pore size analyser (PoreMaster 60, Quantachrome Instruments, USA) equipped with low (1-340 kPa) and high (0.1-330 MPa) pressure stations with a measurable range of pores of 0.004-1000 μm, respectively. The phase composition of the samples was determined using X-ray diffraction analysis (XRD, SmartLab, Rigaku, Japan). Based on the phase compositions, the theoretical density of individual composites was calculated. The microstructures were observed using a Lyra3 scanning electron microscope (SEM, FEG/FIB, Tescan, Czech Republic).

3. Results and Discussion

3.1 Electrophoretic deposition

To determine a correct manufacturing process for preparation of FGM, the deposition kinetics of the pure HA and BG ceramics and their mixtures were studied first. Fig. 2a represents dependence of electrical conductivity on BG amount in the suspension. It is clearly evident that the electrical conductivity of the suspension increased with the BG amount. The suspension containing HA powder only had the electrical conductivity of 0.2 μS/cm. The addition of 25 and 50 wt % of BG in suspensions led to the electrical conductivity increase to 4.8 and 11.5 μS/cm, respectively, which was the highest measured value. The subsequent increase in BG concentration resulted in the electrical conductivity of the suspensions on the similar level. This behaviour can be explained in two ways. An adsorption capacity of individual material compositions in suspensions had a different ability to bind the MCCA molecules on the surface of ceramic particles and thus cause their dissociation [25]. The second phenomenon that may have occurred in BG-containing suspensions is slight dissolution of the BG due to the presence of MCAA because the conductive ion release from BG occurs significantly faster at lower pH [35].

The electrical conductivity of the suspensions markedly affected the EPD kinetics. The kinetic curves are given in Fig. 2b. It can be seen from the figure that the fastest deposition was achieved at the lowest electrical conductivity of the suspension. A high voltage is generated between the electrodes in suspension with low electrical conductivity, which causes the particles to move faster. Moreover, this also results in a very rapid depletion of the ceramic particles from the suspension and the deposition is completed in a relatively short time. In the extreme case, the deposited particle applied pressure on the surface of the

already created deposit, which can be separated from the electrode due to the development of cracks [36, 37]. In our case, HA:BG 100:0 and HA:BG 75:25 depositions had to be terminated soon, i.e. 10 and 15 minutes. The results described in Fig. 2b also corresponds to the measured thickness of the deposits, which decreased with increasing electrical conductivity of the suspension from 5.3 mm (HA:BG 100:0) to 0.9 mm (HA:BG 0:100). It is clear from the figure that the kinetic curves obtained from suspensions containing HA:BG 50:50 to HA:BG 0:100 are very similar, which corresponds to the measurement of the electrical conductivity shown in Fig. 2a.

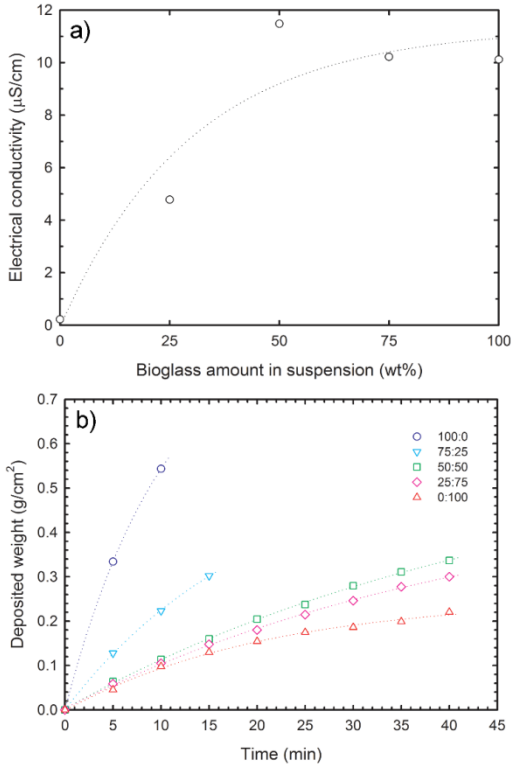

Fig. 2. Dependence of electrical conductivity on bioglass amount in suspension (a) and dependence of deposited weight on time of deposition during preparation of pure ceramics and HA:BG composites (b).

Based on the knowledge of the deposition kinetics for various HA and BG compositions it was possible to estimate an increment of ceramic deposit on the electrode (described in detail for different materials in [29]) and subsequently adjust the correct flow rate of the suspension during the preparation of FGM.

3.2 Physical properties of green bodies

The dependence of relative density on BG amount in the pure and composite green bodies is shown in Fig. 3a and Table I. The relative density increased with concentration of the BG in the HA structure from 25.8 % t.d. up to 47.5 % t.d. It is evident that the value of the relative density was affected mainly by the value of the electrical conductivity of the suspensions from which the pure HA and BG ceramics and HA:BG composites were prepared (see Fig. 2a). The higher values of the electrical conductivity in the suspensions led to the slower deposition rates resulting to better arrangement of ceramic particles to the most advantageous positions in the deposit, thereby increasing the density of the samples [38].

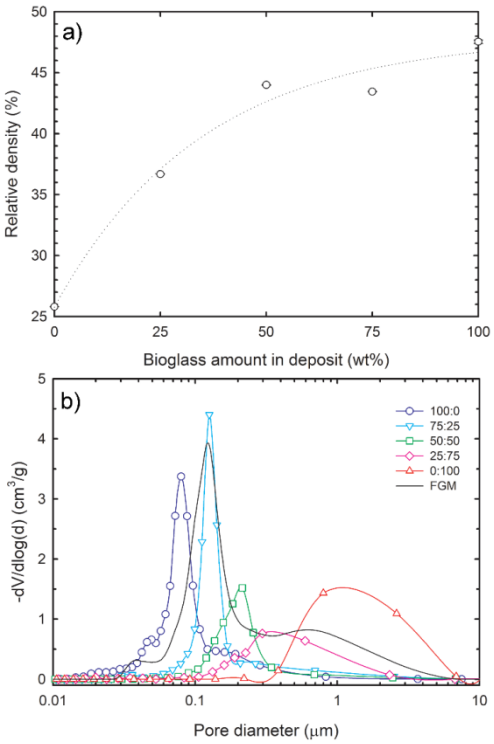

Fig. 3. Dependence of relative density on bioglass amount in annealed deposits (a) and pore size distribution of pure ceramics and HA:BG composites (b).

Tab. I Summary of relative densities and shrinkages of HA:BG composite and FGM samples measured in longitudinal (L) and transversal (T) directions.

Sample	Relative density (%)			Shrinkage (%)			
	ρ_{gb} (at 600 °C)	ρ_L (at 1050 °C)	ρ_T (at 1050 °C)	$\varepsilon_{L\ calc}$	ε_L	$\varepsilon_{T\ calc}$	ε_T
100:0	25.8 ±0.1	38.1 ±0.1	37.9 ±0.2	12.2	14.2	12.0	16.1
75:25	36.7 ±0.1	50.7 ±0.0	48.9 ±0.2	10.2	16.4	9.1	22.1
50:50	44.0 ±0.1	54.0 ±0.1	54.0 ±0.1	6.6	19.1	6.6	24.2
25:75	43.5 ±0.1	95.0 ±0.3	92.1 ±0.7	22.9	32.6	22.1	38.6
0:100	47.5 ±0.1	92.7 ±0.4	91.4 ±0.6	20.0	59.0	19.6	67.7
FGM	-	-	-	-	21.2	-	38.9

Green density of the samples did not change linearly with concentration. An explanation could be the different size of the HA and BG particles causing different porosity of deposits, whereby the small HA particles could fill the large pores between the big BG particles and thus reduce the overall porosity of the composite. The pore size distribution of these samples is displayed in Fig. 3b. The pure HA ceramic sample (HA:BG 100:0) showed a trimodal pore distribution with most frequent pore sizes of 0.04, 0.08 and 0.16 μm. As the content of the BG in the HA increased, the most frequent pore sizes increased as well. The HA:BG 75:25 composite also showed a trimodal pore size distribution with most frequent pore sizes of 0.03, 0.13 and 0.25 μm. Bimodal pore size distributions with most frequent pore sizes of 0.15, 0.21 μm and 0.19, 0.36 μm were measured for HA:BG 50:50 and HA:BG 25:75 samples, respectively. The measurement of HA:BG 0:100 pure ceramics showed an unimodal

pore size distribution with most frequent pore size of 1.21 μm. In contrast to the pure and composite materials, a broad distribution of pores in FGM was determined. This result can be expected as a superposition of performed measurements on the aforementioned samples. The broad size distribution in FGM may imply significant influence on physical, microstructural and mechanical (not studied here) properties.

3.3 Dilatometric evaluation

The sintering shrinkage (ε) of standards, HA:BG composites and FGM, measured in the longitudinal direction, is shown in Fig. 4a. An enormous difference can be seen between sintering shrinkage of pure HA (HA:BG 100:0 sample) and BG (HA:BG 0:100 sample) in both longitudinal and transversal directions. The temperature 1050 °C was selected not to exceed the melting point of the BG. At this temperature, the shrinkage of the BG in longitudinal direction was 59.0 %. A very similar result was reported before in the work of Bretcanu et al. [17]. Table I shows the calculated shrinkage values using Eq. 1. It should be noted that this equation is valid for isotropic shrinkage. Despite the obvious anisotropy of the studied materials, the calculation was performed in individual directions in order to demonstrate the contribution of more than one process to shrinkage. The calculated sintering shrinkage for pure BG is 20.0 % (see Table I) indicating the existence of more internal processes during thermal treatment including first and second glass transition, glass in glass phase separation and crystallisation processes [39, 40]. It is clear from the Table 1 that these processes were applied in all studied materials. Contrary to BG, the shrinkage of the HA was only 14.2 % as a consequence of the low sintering temperature and the low value of green body density. The shrinkage curve of the FGM was close to the measured HA:BG 50:50 composite with similar final shrinkages of 19.1 % and 21.2 %, as could be expected for correctly designed FMG.

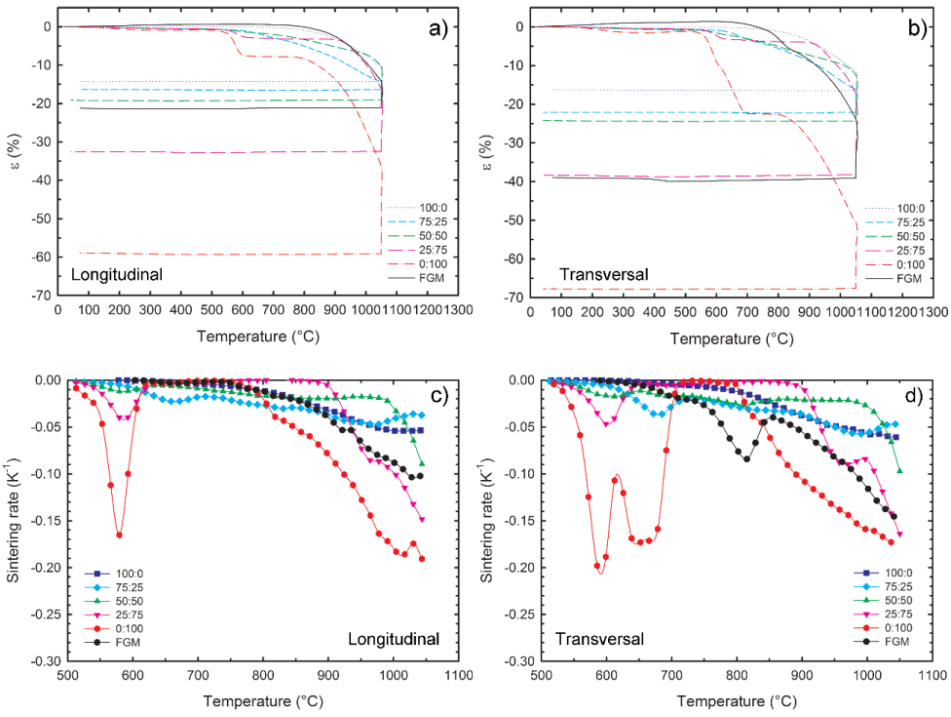

Fig. 4. Linear shrinkage of standards, HA:BG composites and FGM in (a) longitudinal and (b) transversal direction; sintering rate of standards, HA:BG composites and FGM in (c) longitudinal and (d) transversal direction.

The sintering shrinkage of standards, HA:BG composites and FGM, measured in transversal direction, is shown in Fig. 4b. It can be seen from Fig. 4b and Table 1 that shrinkage is slightly higher in the transversal direction than in the longitudinal direction for all measured samples. The visibly different sintering shrinkages in the longitudinal and transversal directions compared with density values in Table I, more evident in samples containing the BG, indicate sintering shrinkage anisotropy. The preferential packing of particles during EPD causes probably this phenomenon [41]. Concerning EPD, a similar behaviour was observed recently for the sintering characterisation of deposited alumina [42]. The explanation is strengthened by the fact that higher anisotropy was observed for big non-spherical BG particles.

The two significant sintering steps are often identified during sintering of the pure BG up to 1050 °C. The first densification step is seen to start at 530 °C (T1) and to end at 620 °C (T2), while the second densification step starts at 850 °C (T3), followed by a slight inflexion at 1000 °C attributed to a softening point when viscous flow starts [17]. Contrary to the literature data, our investigations for the same heating rate (10 °C/min) in longitudinal direction showed slight temperature deviations at the beginnings of the densifications steps and their shifting with composition change. The first densification step for HA:BG 100:0 sample started at 490 °C (T1) and ended at 610 °C (T2), while the second densification step started at 770 °C (T3). The shrinkage during the first step was 7.0 %. It should be noted that no inflexion was observed. The typical sharp sintering steps were also observed in HA:BG 25:75 sample, but the beginnings of the steps were recorded at higher temperatures, i.e. T1 was 505 °C, T2 was 620 °C, and the second densification step started at 900 °C with reduced shrinkage of 2.2 % in the first step. Higher content of the HA in the HA:BG 50:50 sample eliminated sharpness of typical plateau (between T2 and T3). In this sample, the densification started at 550 °C, followed by smooth curve descent with substantial bend at 990 °C. The record of HA:BG 75:25 sample shows no plateau with identified densification temperature at 590 °C. The curve of pure HA is smoothly descending as can be expected for this material with beginning of the densification at 640 °C. However, it is clear from this result that the second sintering phase did not develop for pure HA, which was mainly due to the low green body density and low sintering temperature.

The situation for the samples measured in transversal direction was similar to the longitudinal direction. In sample HA:BG 0:100, the first step started at 520 °C and ended at 700 °C. The shrinkage of 21.2 % during this step was much higher when compared to the longitudinal direction. The second densification step started at 790 °C. The beginning of densification of HA:BG 25:75 sample was determined at 530 °C, and the end of the first step was recorded at 640 °C accompanied by shrinkage of 2.8 %. The T3 was 900 °C. From this point of view, the densification in HA:BG 50:50 and HA:BG 75:25 samples began at temperatures about 10°C higher than those measured in longitudinal direction and HA:BG 100:0 sample revealed no change. To conclude, the higher HA content shifts the starts and ends of the individual sintering steps of BG to higher temperatures and reduces the typical plateau.

The derivate plot vs the temperature for longitudinal and transversal directions is given in Fig. 4c and Fig. 4d, respectively. It was found that the sintering rates of individual materials are similar in both directions. The sintering shrinkage rate of HA:BG 100:0 sample began to increase at 640 °C. The curve had no visible maximum. Such a situation is expected because the maximum densification rate occurs at 1080 °C, as Palard et al. [43] reported for pure HA having an analogous surface area. Moreover, this fact is reflected in all plots of measured samples containing HA, where no primary maxima of sintering rates were observed. Therefore, for samples HA:BG 75:25, HA:BG 50:50 and HA:BG 25:75, the only secondary maxima around 670 °C, 600 °C and 590 °C attributed to the first densification step of BG accompanied by its phase transformation were obtained, respectively. The pure BG sample (HA:BG 0:100) reached the secondary maxima of the densification rate at around

585 °C. Moreover, one more maximum at 650 °C is present in the transversal direction (see Fig. 4d), probably corresponding to the small inflexion visible on the shrinkage curve in Fig. 5b. The FGM started to shrink at 600 °C without distinct primary maximum and one measurable secondary maximum at 815 °C in the transversal direction. Based on the results, it is evident that BG accelerated the sintering rate in the composite materials.

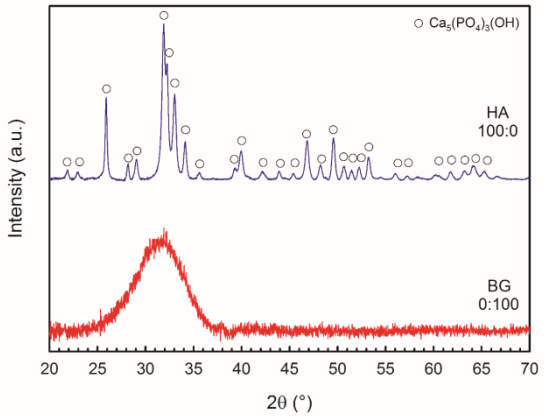

Fig. 5. X-ray diffraction patterns of HA and BG powders.

3.4 XRD analysis

Fig. 5 shows diffraction patterns of commercial HA and BG powders. The red line is a typical pattern for amorphous bioglass with a single flat peak 2θ = 32 ° and other types of glass [44, 45]. The measurement is in good agreement with previously published data [17, 40]. On the contrary, the hydroxyapatite powder exhibited sharp, well-defined peaks, patently indicating the high crystallinity [46]. No secondary phases or impurities were detected during both analyses.

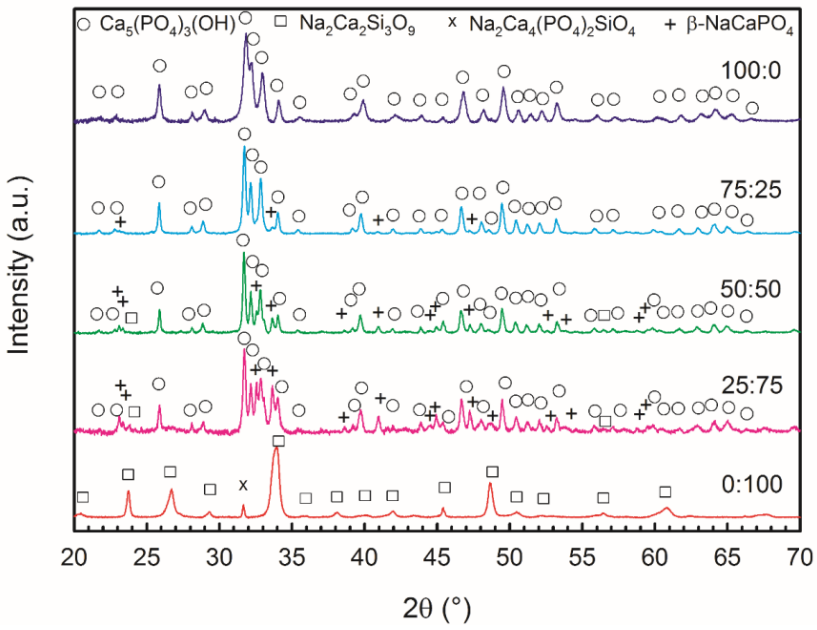

Fig. 6. X-ray diffraction patterns of standards and HA:BG composites annealed at 600 °C.

Further XRD analyses were performed only within standard and composite materials; analysis of FGM was not done for apparent reason. The XRD analyses of standard and composite samples annealed at 600 °C are plotted in Fig. 6. In the pure BG sample, the amorphous structure was completely transformed to a crystalline one, whereas combeite ($Na_2Ca_2Si_3O_9$) was identified as a dominant phase at the annealing temperature. Additionally, one single peak of the secondary phase identified as silicorhenanite ($Na_2Ca_4(PO_4)_2SiO_4$) was found. Surprisingly, this secondary phase is usually observed at higher temperatures (800 – 950 °C) [17, 47], and it is considered as a sintering aid because it significantly enhances the sinterability of hydroxyapatite at 1000 °C [48]. It should be noted that many authors identified $Na_2CaSi_2O_6$ phase as the main phase rather than $Na_2Ca_2Si_3O_9$ phase because of better agreement between measured diffraction patterns and calculated ones by the Rietveld refinement method [39, 47, 49, 50]. When BG is mixed with HA (HA:BG 25:75), the pattern shows mainly $Ca_5(PO_4)_3(OH)$ (hydroxyapatite) crystalline phase with secondary phase identified as β-rhenanite (β-$NaCaPO_4$) and minority phase of $Na_2Ca_2Si_3O_9$. Hydroxyapatite is a non-stoichiometric compound that accepts many substituting ions in its unit cell [51]. Therefore, it can be assumed that the hydroxyapatite was partially substituted by present ions, such as Na^+ or Si^{2+}, even at this low temperature. In the case of the secondary phase, it is well known that the crystalline phase β-rhenanite exhibits high biocompatibility and bioactivity [48, 52, 53]. The further increasing of the HA content in the composite structure (samples HA:BG 50:50 and HA:BG 75:25) resulted in lower or even negligible content of secondary phases. In the case of HA sample (HA:BG 100:0), the only detected phase was $Ca_5(PO_4)_3(OH)$.

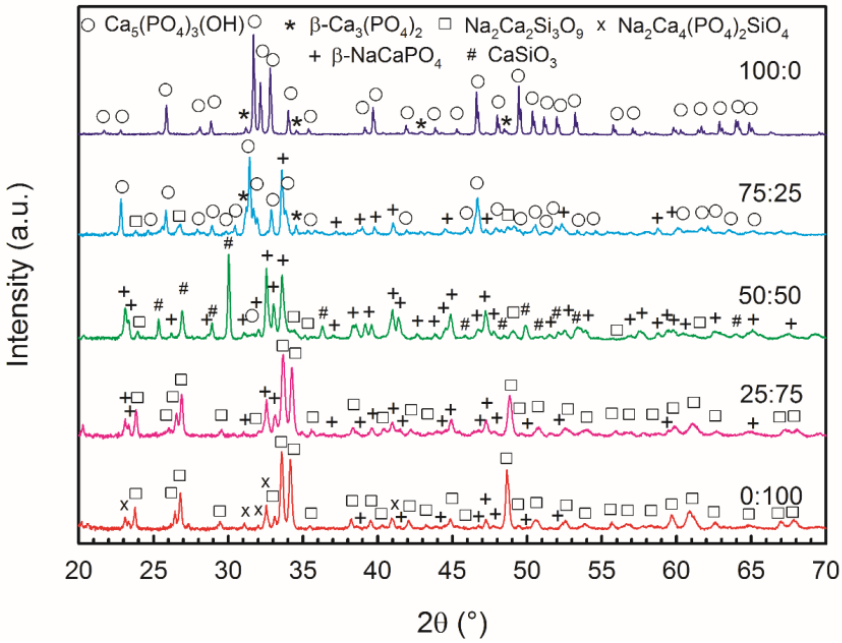

Fig. 7. X-ray diffraction patterns of standards and HA:BG composites sintered at 1050 °C.

The XRD analysis of standards and composite samples sintered at 1050 °C is shown in Fig. 7. The difference between annealed and sintered HA:BG 0:100 sample was in the more complex crystalline phase structure. The major phase was still identified as combeite, but more peaks of silicorhenanite appeared. This result was published many times, and thus it is not surprising [17, 54, 55]. On the other hand, the many published papers ignore the presence of β-rhenanite that was identified in the structure as well. When the HA:BG 25:75

composite is sintered at 1050 °C, no peaks corresponding to hydroxyapatite were detected. The structure was composed of combeite and more significant quantity of β-rhenanite as a product of the chemical reaction between HA and BG [52]. The phase composition of HA:BG 50:50 included β-rhenanite, combeite, β-wollastonite and hydroxyapatite phases. The hydroxyapatite was a dominant phase in HA:BG 75:25 composite, and several peaks of β-rhenanite and combeite were also identified. The structure of HA (HA:BG 100:0) contained beside $Ca_5(PO_4)_3(OH)$ phase also β-$Ca_3(PO_4)_2$ (TCP) phase, which is not usual at such low temperature [56-58]. Cihlar et al. [59] determined that hydroxyapatite decomposes to tricalcium phosphate at a temperature above 1200 °C. The explanation of this behaviour is in nanoparticle size of HA, which probably accelerated decomposition to TCP [60, 61].

3.5 Microstructure

The microstructure of composite samples was examined on the fracture surfaces, see Fig. 8. Fig. 8a shows microstructures of HA:BG 100:0 where small grain size and open porosity were observed. The considerable porosity can be expected because the closing of pores in HA occurs at a relative density higher than 90 % [62] that was not reached by the used sintering temperature, see Table 1. When the BG was incorporated into the composite (sample HA:BG 75:25 in Fig. 8b), the pores were still interconnected, but the detailed inset shows an increase in the grain size. Such growth is more evident in Fig. 8c, where the microstructure of HA:BG 50:50 is given. Moreover, a gradual decrease in the volume of pores at the expense of their size is clearly visible because of bigger BG particles and promoted the densification process [48]. This fact is quite well documented in other microstructures of HA:BG 25:75 and HA:BG 0:100 samples in Fig. 8d and Fig. 8e, respectively.

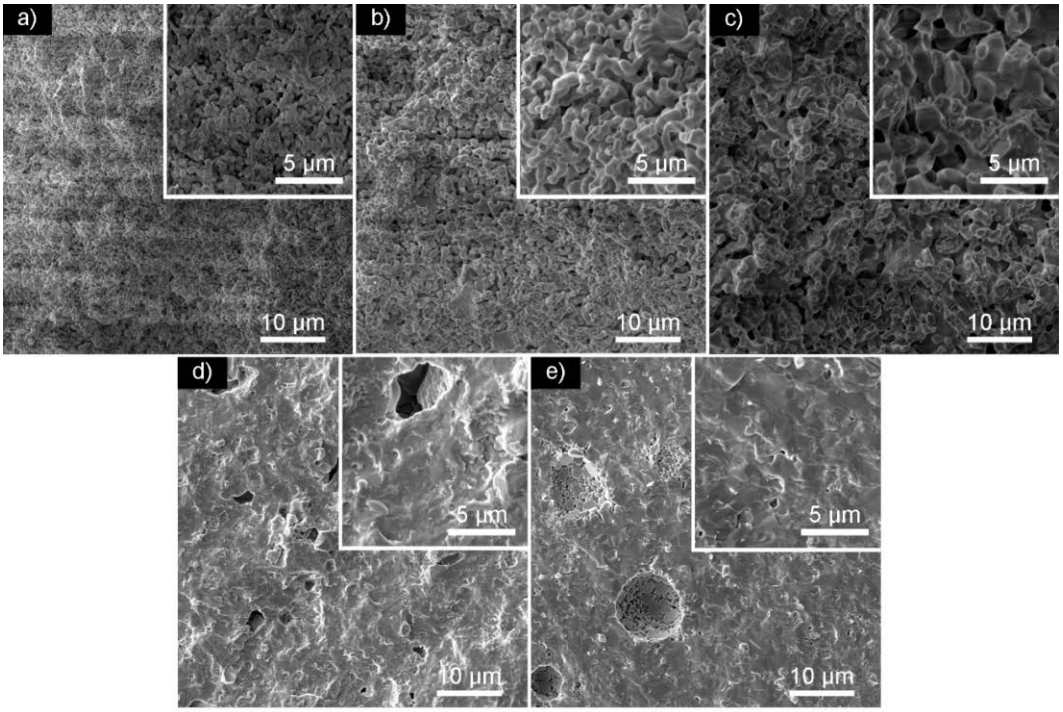

Fig. 8. Fracture surface micrographs of standards and particle composites sintered at 1050 °C: a) HA:BG 100:0, b) HA:BG 75:25, c) HA:BG 50:50, d) HA:BG 25:75 and e) HA:BG 0:100.

The microstructure of the prepared FGM is shown in Fig. 9a. The sample had a visually continuous change in the microstructure. In order to examine a microstructure

evolution during the preparation of FGM, several places were investigated; the marks in the FGM correspond with detailed images in Fig. 9b-f. The closer inspection of detailed microstructures indicated a perfect agreement with microstructures presented in Fig. 8, which proves that the FGM with continuous microstructural and chemical change was prepared.

The microstructure without presence of cracks is provided. However, more than one sample was sintered during experiments, and some cracks in transversal or even longitudinal directions were observed occasionally. The longitudinal cracks are most likely caused by too large difference in the shrinkage of the basic materials observed by dilatometric measurements. Related to this, the samples' bending was observed, which probably caused transversal cracks located mainly in the HA rich microstructures. The transversal cracks are often reported as inauspicious results of the material composition at other fabrication methods [20]. To reduce or suppress the crack development, the pure BG layer in the FGM should be thinner, or the final material composition of the FGM should be HA:BG 25:75. On the other hand, the visible crack bridging in Fig. 9a (see white arrows) suggests higher fracture toughness, which is beneficial for this composite material.

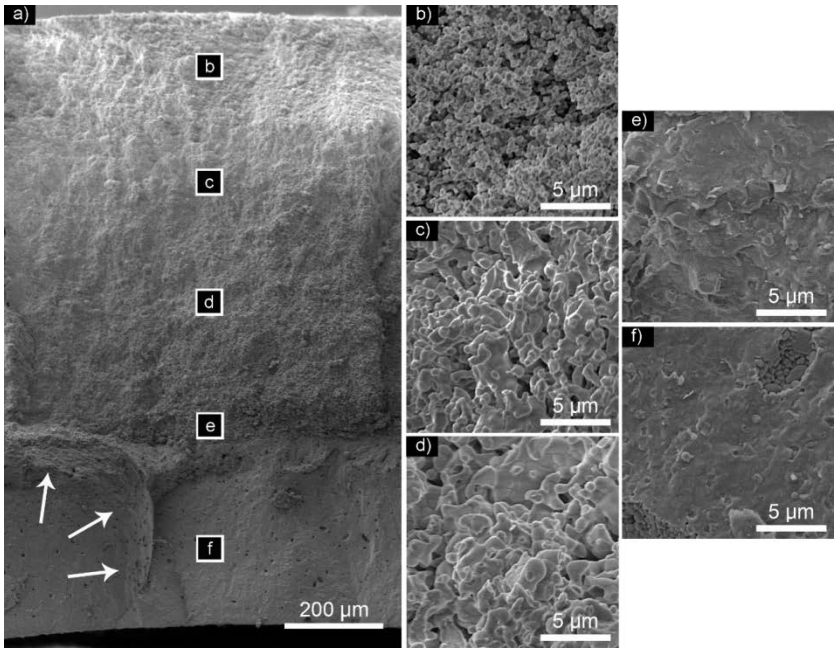

Fig. 9. Fracture surface micrographs of FGM sintered at 1050 °C; a) overall view with marked places corresponding to b) HA:BG 100:0, c) HA:BG 75:25, d) HA:BG 50:50, e) HA:BG 25:75, f) HA:BG 0:100 microstructures.

Therefore, the obtained microstructures of standards, composites and FGM are interesting from a fractographic point of view. The images of the HA rich microstructures show numerous fine ceramic grains connected to their neighbours by thin necks. The crack propagating through these necks caused their decohesion, and completely intergranular fracture-mode occurred. Contrary, the fracture-mode with increasing content of the BG in the microstructure was changed entirely, i.e. transgranular fracture was observed only. A fracture-mode transition from intergranular to transgranular fracture could be attributed to significantly different porosity found in the microstructures. Our conclusion is supported by works of Deng et al. [63] or later Pecqueux et al. [64], who reported that this phenomenon occurs during the transition from higher-porous to lower-porous microstructure.

4. Conclusion

In this paper, the particle composites and functionally graded bulk materials (FGM) based on hydroxyapatite (HA) and bioglass (BG) were studied. First, the kinetics of electrophoretic deposition from variously concentrated suspensions was studied that allowed the preparation of FGM. The key parameter of electrophoretic deposition affecting particle arrangement in deposits and, thus, their green density was identified. The sintering process was evaluated by high-temperature dilatometry in the longitudinal and transversal orientation of the samples. It was found that there exists an enormous difference between the sintering shrinkage of pure HA (14.2 %) and BG (59.0 %). The gradual change in shrinkage was observed related to composition change in composites. The higher content of HA in composite shifts the starts and ends of the individual sintering steps to higher temperatures and reduces the typical plateau. The shrinkage curve of the FGM in the longitudinal direction was close to the measured HA:BG 50:50 composite what indicated correctly designed FMG. The different sintering shrinkages obtained in longitudinal and transversal directions have been attributed to the sintering shrinkage anisotropy originating from ceramic particles' preferential packing during EPD. The sintering shrinkage rate of all samples was calculated. The microstructural inspection of the samples showed interconnected porosity that is favourable for bio-applications and confirmed the continuous material change in FGM. The porosity was also gradually changed in dependence on the corresponding composition. The fractographic analysis of FGM showed that the porosity completely changed the fracture mode from intergranular to transgranular when the material transition from HA to BG occurred. To reduce or suppress the crack development, the pure BG layer in the FGM should be thinner, or the final material composition of the FGM should be HA:BG 25:75, or the preparation route for HA particles must be optimised to provide green bodies with higher density. The X-ray diffraction analyses revealed a fully crystalline structure of all prepared materials changing significantly depending on the starting composition. The phase evolution during changing material composition and dependence on temperature was deeply evaluated. For further experiments, the crystallisation of BG, BG rich particle composites and FGM could consequently be suppressed by combining EPD with following pressure assisted sintering method, e.g. SPS or HIP.

Acknowledgments

The research has been financially supported by the Ministry of Education, Youth and Sports of the Czech Republic under projects LTT18013 and CEITEC 2020 (LQ1601). We acknowledge CzechNanoLab Research Infrastructure supported by MEYS CR (LM2018110).

5. References

1. B. Saleh, J. Jiang, R. Fathi, T. Al-hababi, Q. Xu, L. Wang, D. Song, A. Ma, 30 Years of functionally graded materials: An overview of manufacturing methods, Applications and Future Challenges, Composites Part B: Engineering 201 (2020) 108376.
2. W. Li, B. Han, Research and Application of Functionally Gradient Materials, IOP Conference Series: Materials Science and Engineering 394 (2018) 022065.
3. S.V. Dorozhkin, Calcium Orthophosphate-Based Bioceramics and Its Clinical Applications, in: K. G. (Ed.), Clinical Applications of Biomaterials, Springer, Cham2017, p. 104.

4. A. Haider, S. Haider, S.S. Han, I.-K. Kang, Recent advances in the synthesis, functionalization and biomedical applications of hydroxyapatite: a review, RSC Advances 7(13) (2017) 7442-7458.
5. R. Ravarian, F. Moztarzadeh, M.S. Hashjin, S.M. Rabiee, P. Khoshakhlagh, M. Tahriri, Synthesis, characterization and bioactivity investigation of bioglass/hydroxyapatite composite, Ceramics International 36(1) (2010) 291-297.
6. K.A. Hing, P.A. Revell, N. Smith, T. Buckland, Effect of silicon level on rate, quality and progression of bone healing within silicate-substituted porous hydroxyapatite scaffolds, Biomaterials 27(29) (2006) 5014-5026.
7. J.L. Xu, K.A. Khor, Chemical analysis of silica doped hydroxyapatite biomaterials consolidated by a spark plasma sintering method, Journal of Inorganic Biochemistry 101(2) (2007) 187-195.
8. E.S. Thian, J. Huang, S.M. Best, Z.H. Barber, R.A. Brooks, N. Rushton, W. Bonfield, The response of osteoblasts to nanocrystalline silicon-substituted hydroxyapatite thin films, Biomaterials 27(13) (2006) 2692-2698.
9. M. Palard, E. Champion, S. Foucaud, Synthesis of silicated hydroxyapatite Ca10(PO4)6−x(SiO4)x(OH)2−x, Journal of Solid State Chemistry 181(8) (2008) 1950-1960.
10. J. Ma, B.X. Huang, X.C. Zhao, C.Z. Wang, H.M. Zhang, Effect of zinc substitution for calcium on the structure, dissolution behavior and apatite formation of CaO–ZnO–SiO2–P2O5 bioceramics, Materials Letters 206 (2017) 154-157.
11. Y. Yang, K.-H. Kim, J.L. Ong, A review on calcium phosphate coatings produced using a sputtering process—an alternative to plasma spraying, Biomaterials 26(3) (2005) 327-337.
12. [12] M.T. Fulmer, I.C. Ison, C.R. Hankermayer, B.R. Constantz, J. Ross, Measurements of the solubilities and dissolution rates of several hydroxyapatites, Biomaterials 23(3) (2002) 751-755.
13. D. Bellucci, L. Desogus, S. Montinaro, R. Orrù, G. Cao, V. Cannillo, Innovative hydroxyapatite/bioactive glass composites processed by spark plasma sintering for bone tissue repair, Journal of the European Ceramic Society 37(4) (2017) 1723-1733.
14. M. Rizwan, M. Hamdi, W.J. Basirun, K. Kondoh, J. Umeda, Low pressure spark plasma sintered hydroxyapatite and Bioglass® composite scaffolds for bone tissue repair, Ceramics International 44(18) (2018) 23052-23062.
15. G. Goller, H. Demirkıran, F.N. Oktar, E. Demirkesen, Processing and characterization of bioglass reinforced hydroxyapatite composites, Ceramics International 29(6) (2003) 721-724.
16. D.G. Wang, C.Z. Chen, X.X. Yang, X.C. Ming, W.L. Zhang, Effect of bioglass addition on the properties of HA/BG composite films fabricated by pulsed laser deposition, Ceramics International 44(12) (2018) 14528-14533.
17. O. Bretcanu, X. Chatzistavrou, K. Paraskevopoulos, R. Conradt, I. Thompson, A.R. Boccaccini, Sintering and crystallisation of 45S5 Bioglass® powder, Journal of the European Ceramic Society 29(16) (2009) 3299-3306.
18. M. Parvizifard, S. Karbasi, H. Salehi, S. Soleymani Eil Bakhtiari, Evaluation of physical, mechanical and biological properties of bioglass/titania scaffold coated with poly (3-hydroxybutyrate)-chitosan for bone tissue engineering applications, Materials Technology 35(2) (2020) 75-91.
19. D. Bellucci, A. Sola, V. Cannillo, Hydroxyapatite and tricalcium phosphate composites with bioactive glass as second phase: State of the art and current applications, Journal of Biomedical Materials Research Part A 104(4) (2016) 1030-1056.
20. M. Luginina, D. Angioni, S. Montinaro, R. Orrù, G. Cao, R. Sergi, D. Bellucci, V. Cannillo, Hydroxyapatite/bioactive glass functionally graded materials (FGM) for

bone tissue engineering, Journal of the European Ceramic Society 40(13) (2020) 4623-4634.
21. A. Cattini, D. Bellucci, A. Sola, L. Pawłowski, V. Cannillo, Suspension plasma spraying of optimised functionally graded coatings of bioactive glass/hydroxyapatite, Surface and Coatings Technology 236 (2013) 118-126.
22. A. Cattini, D. Bellucci, A. Sola, L. Pawłowski, V. Cannillo, Microstructural design of functionally graded coatings composed of suspension plasma sprayed hydroxyapatite and bioactive glass, Journal of Biomedical Materials Research Part B: Applied Biomaterials 102(3) (2014) 551-560.
23. D. Tanaskovic, B. Jokic, G. Socol, A. Popescu, I.N. Mihailescu, R. Petrovic, D. Janackovic, Synthesis of functionally graded bioactive glass-apatite multistructures on Ti substrates by pulsed laser deposition, Applied Surface Science 254(4) (2007) 1279-1282.
24. J.M. Gomez-Vega, E. Saiz, A.P. Tomsia, T. Oku, K. Suganuma, G.W. Marshall, S.J. Marshall, Novel Bioactive Functionally Graded Coatings on Ti6Al4V, Advanced Materials 12(12) (2000) 894-898.
25. J. Cihlar, D. Drdlik, Z. Cihlarova, H. Hadraba, Effect of acids and bases on electrophoretic deposition of alumina and zirconia particles in 2-propanol, Journal of the European Ceramic Society 33(10) (2013) 1885-1892.
26. D. Drdlik, Z. Chlup, H. Hadraba, K. Drdlikova, Surface roughness improvement of near net shaped alumina by EPD, Journal of the Australian Ceramic Society 56(2) (2020) 721-727.
27. H. Hadraba, K. Maca, J. Cihlar, Electrophoretic deposition of alumina and zirconia: II. Two-component systems, Ceramics International 30(6) (2004) 853-863.
28. D. Drdlik, M. Slama, H. Hadraba, J. Cihlar, Hydroxyapatite/zirconia-microfibre composites with controlled microporosity and fracture properties prepared by electrophoretic deposition, Ceramics International 41(9, Part A) (2015) 11202-11212.
29. H. Hadraba, D. Drdlik, Z. Chlup, K. Maca, I. Dlouhy, J. Cihlar, Layered ceramic composites via control of electrophoretic deposition kinetics, Journal of the European Ceramic Society 33(12) (2013) 2305-2312.
30. S. Put, J. Vleugels, O. Van der Biest, Functionally graded WC–Co materials produced by electrophoretic deposition, Scripta Materialia 45(10) (2001) 1139-1145.
31. S. Khanmohammadi, M. Ojaghi-Ilkhchi, M. Farrokhi-Rad, Development of bioglass coating reinforced with hydroxyapatite whiskers on TiO_2 nanotubes via electrophoretic deposition, Ceramics International 47(1) (2021) 1333-1343.
32. S. Khanmohammadi, M. Ojaghi-Ilkhchi, M. Farrokhi-Rad, Evaluation of bioglass and hydroxyapatite based nanocomposite coatings obtained by electrophoretic deposition, Ceramics International 4616, Part A) (2020) 26069-26077.
33. A. Indra, Gunawarman, J. Affi, I.H. Mulyadi, Y. Wiyanto, Physical and Mechanical Properties of Hydroxyapatite Ceramics with a Mixture of Micron and Nano-Sized Powders: Optimising the Sintering Temperatures, Ceram-Silikaty 65(3) (2021) 224-234.
34. K. Maca, V. Pouchly, A.R. Boccaccini, Sintering densification curve - a practical approach for its construction from dilatometric shrinkage data, Sci Sinter 40(2) (2008) 117-122.
35. L. Bingel, D. Groh, N. Karpukhina, D.S. Brauer, Influence of dissolution medium pH on ion release and apatite formation of Bioglass® 45S5, Materials Letters 143 (2015) 279-282.
36. R. Drevet, N. Ben Jaber, J. Fauré, A. Tara, A. Ben Cheikh Larbi, H. Benhayoune, Electrophoretic deposition (EPD) of nano-hydroxyapatite coatings with improved mechanical properties on prosthetic Ti6Al4V substrates, Surface and Coatings Technology 301 (2016) 94-99.

37. D. Drdlik, M. Slama, H. Hadraba, K. Drdlikova, J. Cihlar, On the role of the indifferent electrolyte LiCl in electrophoretic deposition of hydroxyapatite from 2-propanol dispersions, Ceramics International 42(15) (2016) 16529-16534.
38. R.N. Basu, C.A. Randall, M.J. Mayo, Fabrication of dense zirconia electrolyte films for tubular solid oxide fuel cells by electrophoretic deposition, Journal of the American Ceramic Society 84(1) (2001) 33-40.
39. L. Lefebvre, J. Chevalier, L. Gremillard, R. Zenati, G. Thollet, D. Bernache-Assolant, A. Govin, Structural transformations of bioactive glass 45S5 with thermal treatments, Acta Materialia 55(10) (2007) 3305-3313.
40. L. Lefebvre, L. Gremillard, J. Chevalier, R. Zenati, D. Bernache-Assolant, Sintering behaviour of 45S5 bioactive glass, Acta Biomaterialia 4(6) (2008) 1894-1903.
41. S. Yang, W. Cai, G. Liu, H. Zeng, From Nanoparticles to Nanoplates: Preferential Oriented Connection of Ag Colloids during Electrophoretic Deposition, The Journal of Physical Chemistry C 113(18) (2009) 7692-7696.
42. K. Maca, V. Pouchly, D. Drdlik, H. Hadraba, Z. Chlup, Dilatometric study of anisotropic sintering of alumina/zirconia laminates with controlled fracture behaviour, Journal of the European Ceramic Society 37(14) (2017) 4287-4295.
43. M. Palard, J. Combes, E. Champion, S. Foucaud, A. Rattner, D. Bernache-Assollant, Effect of silicon content on the sintering and biological behaviour of Ca10(PO4)6-x(SiO4)x(OH)2-x ceramics, Acta Biomaterialia 5(4) (2009) 1223-1232.
44. R.A.A. Wahab, M.H.M. Zaid, K.A. Matori, M.K. Halimah, H.A.A. Sidek, Y.W. Fen, A. Abdu, M.F.M. Shofri, S.H. Jaafar, Synthesis and sintering impact on the properties of willemite based glass-ceramics using rice husk waste as silica source, Sci Sinter 54(2) (2022) 223-233.
45. V.G. Molina, A.P. Parra, P.A.M. Aguilar, R.G. Tapia, M.C.R. González, I. Rosales-Cadena, M. Vlasova, Peculiarities of glass ceramics formation from red clay-cullet-waste activated sludge-hematite mixtures, Sci Sinter 54(3) (2022) 249-264.
46. M. Rajkumar, N. Sundaram, V. Rajendran, Preparation of size controlled, stochiometric and bioresorbable hydroxyapatite nanorod by varying initial pH, Ca/P ratio and sintering temperature, Digest Journal of Nanomaterials and Biostructures 6(1) (2011) 169-179.
47. A.R. Boccaccini, Q. Chen, L. Lefebvre, L. Gremillard, J. Chevalier, Sintering, crystallisation and biodegradation behaviour of Bioglass®-derived glass–ceramics, Faraday Discussions 136(0) (2007) 27-44.
48. W. Suchanek, M. Yashima, M. Kakihana, M. Yoshimura, β-Rhenanite (β-NaCaPO4) as Weak Interphase for Hydroxyapatite Ceramics, Journal of the European Ceramic Society 18(13) (1998) 1923-1929.
49. L. Bertolla, I. Dlouhý, P. Tatarko, A. Viani, A. Mahajan, Z. Chlup, M.J. Reece, A.R. Boccaccini, Pressureless spark plasma–sintered Bioglass® 45S5 with enhanced mechanical properties and stress–induced new phase formation, Journal of the European Ceramic Society 37(7) (2017) 2727-2736.
50. S. Grasso, R.K. Chinnam, H. Porwal, A.R. Boccaccini, M.J. Reece, Low temperature spark plasma sintering of 45S5 Bioglass®, Journal of Non-Crystalline Solids 362 (2013) 25-29.
51. M. Vallet-Regí, J.M. González-Calbet, Calcium phosphates as substitution of bone tissues, Progress in Solid State Chemistry 32(1) (2004) 1-31.
52. I. Kangasniemi, K. De Groot, J. Wolke, Ö. Andersson, Z. Luklinska, J.G.M. Becht, M. Lakkisto, A. Yli-Urpo, The stability of hydroxyapatite in an optimized bioactive glass matrix at sintering temperatures, Journal of Materials Science: Materials in Medicine 2(3) (1991) 133-137.

53. I.M. Kangasniemi, E. Vedel, J. de Blick-Hogerworst, A.U. Yli-Urpo, K. de Groot, Dissolution and scanning electron microscopic studies of Ca,P particle-containing bioactive glasses, Journal of biomedical materials research 27(10) (1993) 1225-33.
54. X. Chatzistavrou, T. Zorba, E. Kontonasaki, K. Chrissafis, P. Koidis, K.M. Paraskevopoulos, Following bioactive glass behavior beyond melting temperature by thermal and optical methods, physica status solidi (a) 201(5) (2004) 944-951.
55. R. Xin, Q. Zhang, J. Gao, Identification of the wollastonite phase in sintered 45S5 bioglass and its effect on in vitro bioactivity, Journal of Non-Crystalline Solids 356(23) (2010) 1180-1184.
56. B. Le Thi, B.D. Long, T. Van Trung, N.T. Van Thanh, S. Ramesh, Nanocrystalline Hydroxyapatite Prepared at Different Precursor Concentrations: Thermal Stability, Morphology and in Vitro Cellular Response, Ceram-Silikaty 66(1) (2022) 19-27.
57. N.V. Bulina, S.V. Makarova, S.G. Baev, A.A. Matvienko, K.B. Gerasimov, O.A. Logutenko, V.S. Bystrov, A Study of Thermal Stability of Hydroxyapatite, Minerals-Basel 11(12) (2021).
58. A. Faeghinia, T. Ebadzadeh, Effect of Microwave Conditions on Sintering of Hydroxyapatite Ceramics, Sci Sinter 52(4) (2020) 469-479.
59. J. Cihlář, A. Buchal, M. Trunec, Kinetics of thermal decomposition of hydroxyapatite bioceramics, Journal of Materials Science 34(24) (1999) 6121-6131.
60. M.H. Fathi, A. Hanifi, V. Mortazavi, Preparation and bioactivity evaluation of bone-like hydroxyapatite nanopowder, Journal of Materials Processing Technology 202(1) (2008) 536-542.
61. Y.-M. Sung, J.-C. Lee, J.-W. Yang, Crystallization and sintering characteristics of chemically precipitated hydroxyapatite nanopowder, Journal of Crystal Growth 262(1) (2004) 467-472.
62. E. Champion, Sintering of calcium phosphate bioceramics, Acta Biomaterialia 9(4) (2013) 5855-5875.
63. Z.-Y. Deng, T. Fukasawa, M. Ando, G.-J. Zhang, T. Ohji, Microstructure and Mechanical Properties of Porous Alumina Ceramics Fabricated by the Decomposition of Aluminum Hydroxide, Journal of the American Ceramic Society 84(11) (2001) 2638-2644.
64. F. Pecqueux, F. Tancret, N. Payraudeau, J.M. Bouler, Influence of microporosity and macroporosity on the mechanical properties of biphasic calcium phosphate bioceramics: Modelling and experiment, Journal of the European Ceramic Society 30(4) (2010) 819-829.

Сажетак: *Керамике на бази хидроксиапатита (ХА) и биостакла (БС) су од највеће важности у инжењерству коштаног ткива. Поред одговарајућег састава, микроструктура коштане замене игра кључну улогу. У овом раду, композити честица и функционално градирани материјал на бази ХА и БС припремљени електрофоретским таложењем су детаљно окарактерисани у смислу методе припреме, процеса синтеровања, фазног састава и микроструктуре. Синтеровање је праћено високотемпературном дилатометријом у два правца, израчунате су брзине синтеровања и дискутовано је о целокупном процесу синтеровања. СЕМ је показао континуирану промену у микроструктури са постепеном међусобно повезаном порозношћу погодном за био-апликације. Фундаменталном фрактографском анализом доказан је развој прслине у материјалу у вези са процесом синтеровања и дате су препоруке за смањење развоја прслине. Фазне трансформације током термичке обраде анализиране су анализом дифракције рендгенских зрака и детаљно размотрене.*
Кључне речи*: хидроксиапатит; биостакло; функционални материјали; синтеровање; микроструктура.*

© 2023 Authors. Published by association for ETRAN Society. This article is an open access article distributed under the terms and conditions of the Creative Commons — Attribution 4.0 International license (https://creativecommons.org/licenses/by/4.0/).

PUBLIKACE XI

Journal of the European Ceramic Society 36 (2016) 365–371

Contents lists available at www.sciencedirect.com

Journal of the European Ceramic Society

journal homepage: www.elsevier.com/locate/jeurceramsoc

Micro-fibres containing composites prepared by EPD

Hynek Hadraba[a,*], Zdenek Chlup[a], Daniel Drdlik[b], Jaroslav Cihlar[b]

[a] CEITEC IPM, Institute of Physics of Materials, Academy of Sciences of the Czech Republic, Zizkova 513/22, 61662 Brno, Czech Republic
[b] CEITEC BUT, Brno University of Technology, Technicka 10, 61600 Brno, Czech Republic

ARTICLE INFO

Article history:
Received 15 March 2015
Received in revised form 13 July 2015
Accepted 27 July 2015
Available online 10 August 2015

Keywords:
Electrophoretic deposition
Zirconia
Fibres
Fibre reinforcement
Laminates

ABSTRACT

Presented article summarises preparation of fibre reinforced alumina and alumina laminates containing zirconia micro-fibres. Electrophoretic deposition was performed from concentrated isopropanolic suspensions stabilised by monochloracetic acid containing mixture of alumina powder and certain amount of zirconia micro-fibres. A method for in-situ monitoring the deposition of alumina and zirconia micro-fibres mass was applied to control deposition kinetics. Two different approaches for composite deposition were applied: (i) electrophoretic deposition of powders mixture and (ii) electrophoretic co-deposition from sonicated suspension containing stabilization aid. Applying the optimised procedure the alumina laminates reinforced with zirconia fibres were prepared. The co-deposition of ceramic micro-fibres and powder led to the preparation of microstructures having unique orthogonal fracture properties. Developed laminate with layers created by zirconia micro-fibres in the alumina matrix seems to be the most promising. This type of material exhibited potential of the crack trapping and deflection even when very small amount of micro-fibres was used.

© 2015 Elsevier Ltd. All rights reserved.

1. Introduction

Ceramic based composite materials can be prepared by variety of approaches; however, the common challenge is to minimize the defects size produced during processing. The reason is that the main mechanical properties are somehow connected to both the fracture toughness and the flaw size distribution. Therefore, the minimization of the defect size created during processing is one way how to enhance the mechanical properties of the material. The second approach uses enhancement of the fracture toughness of given material by application of suitable reinforcement [1]. The most effective is the incorporation of long fibres to the brittle matrix when the number of toughening mechanisms is acting simultaneously [2,3].

Colloidal routes are widely used due to their relative simplicity and the ability to reduce critical flaw size and possibility to combine different initial materials. The electrophoretic deposition is one of colloidal processing methods with proven ability to fabricate sophisticated structures based on combination of various ceramic materials [4–9]. The preparation of long fibres or fabric reinforced composites by the impregnation technique using electrophoretic route was already proven [10–13]. Preparation of particulate composite materials using mixture of various powders was also demonstrated by many authors [14–17]. Laminates as the special case of composites can be also prepared even thou selected layers can have composite structure to enhance their mechanical properties [18–24]. The electrophoretic deposition kinetic in such cases become more complicated and its knowledge is essential. Recently, thanks to advances in understanding of processes influencing the kinetics of electrophoretic deposition the tailored laminates with perfect and strong interfaces between layers with precise thickness management were prepared [25,26]. The mechanical properties of such layered structures can be designed based on numerical predictions [27,28]. To achieve such extraordinary mechanical properties the development of high internal stresses during material processing especially due to CTE's mismatch and/or phase transformation is utilised [29–35]. The systems combining alumina and zirconia are mainly used in such cases. The relatively high content of zirconia used in such composites affects negatively selected properties, mainly the wear resistance, chemical resistance and last but not least the overall composite weight.

This contribution is coming with the idea to prepare composites using zirconia micro-fibres incorporated in relatively small amounts into the alumina matrix. Two arrangements were investigated the volume composites and laminates with thin layers containing micro-fibres. The positive effect of micro-fibres can be seen in (i) suppressing of drying defects in the green body stage before sintering and (ii) enhancement of the fracture resistance of sintered body. The co-deposition of zirconia micro-fibres and alumina powder with the targeted final creation of homogenous

* Corresponding author.
E-mail address: hadraba@ipm.cz (H. Hadraba).

http://dx.doi.org/10.1016/j.jeurceramsoc.2015.07.031
0955-2219/© 2015 Elsevier Ltd. All rights reserved.

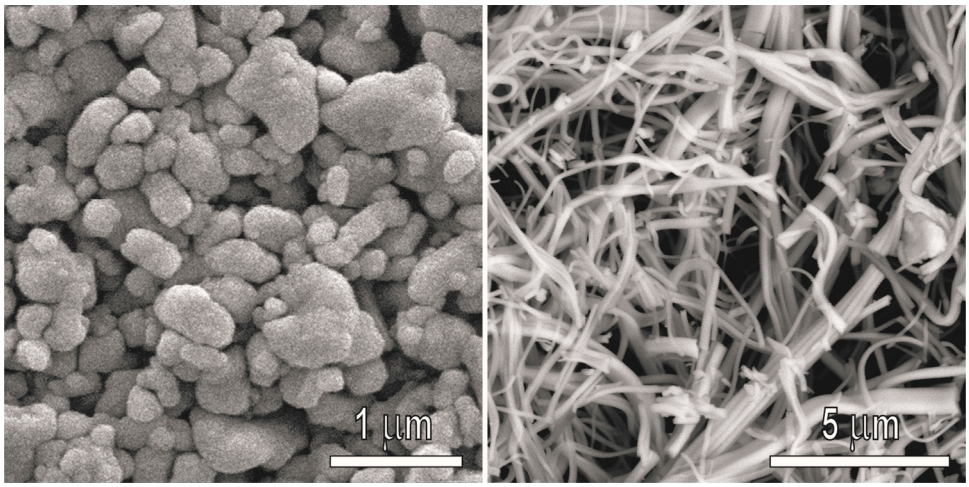

Fig. 1. Micrographs of alumina powder (left) and zirconia micro-fibres (right) used for EPD.

crack free ceramic material using EPD is unexplored field from the processing, microstructure and as well as mechanical properties point of view. The deposition kinetics of EPD powder and micro-fibre co-deposition will be described in the relation to the route of suspension preparation. The effects to the final microstructure will be also demonstrated.

2. Experimental methods

Micrographs of alumina powders and zirconia micro-fibres used in this work are provided in Fig. 1. Alumina powder (HP-DBM, Baikowski) with the particle size 80–900 nm was used (mean particle size of alumina powder was 470 nm). The tetragonal zirconia micro-fibres (Pardam Nanotechnology) prepared by electro-spinning method having diameter from 100 nm to 500 nm and length of hundreds of micrometres were used as reinforcing phase. Dispersion medium used for suspensions preparation was isopropanol (p.a., Onex). Monochloroacetic acid (99%, SigmaAldrich) was added to suspensions as a stabilization and dispersion aid. Suspensions used for electrophoretic deposition were prepared by mixing of 15 wt.% of solid content (mixture of 99 wt.% of alumina and 1 wt.% of zirconia micro-fibres) with 12.75 wt.% of monochloracetic acid and 72.25 wt.% of isopropanol. Two ways of suspension preparation were elaborated. In the first one mixture of alumina powder and zirconia micro-fibres was prepared by ball milling in isopropanol and subsequent drying of powder in air atmosphere (denoted as "pre-milled powder"). A stainless steel milling vial and zirconia balls were used. The ball-milling was performed for 15 min, 2 h, 4 h and 6 h in a planetary ball mill (Pulverisette, Fritsch). Suspensions for electrophoretic deposition using pre-milled powder were homogenized by mechanical mixing. The other way of suspension preparation consisted of intensive sonication of entire suspension (denoted as "sonicated suspension"). The sonication was performed for 15 min, 2 h, 4 h and 6 h in ultrasonic bath (S60, Elma). Zirconia reinforced alumina composites were prepared by several consecutive depositions with suspension containing 99 wt.% of alumina and 1 wt.% of zirconia micro-fibres, between which the suspension was stirred. Each partial deposition consumed 5 min and the total deposition time was 40 min. Alumina laminate consisted of 30 alumina layers of thickness 50 μm separated by thin zirconia micro-fibre layers. Such material was prepared by interrupted electrophoretic deposition, i.e., several consecutive depositions, alternately with the suspension containing 100 wt.% of alumina and with suspension containing 75 wt.% of alumina and 25 wt.% of zirconia micro-fibres, respectively. The total deposition time of layered composite materials was 35 min. Electrophoretic deposition was performed in electrophoretic cell with two vertical stainless steel electrodes. The details of used deposition technique were described elsewhere earlier [5,17,25]. Subsequently, the deposits were calcined (800 °C/1 h; heating rate + 2 °C/min) and sintered (1500 °C/2 h; heating rate + 5 °C/min) in air atmosphere. Density of the green (calcined) and sintered deposits was determined by Archimedes' method using high purity deionised water according to EN 623-2 standard. The green samples were soaked with high purity deionised water using a vacuum chamber before measurement for determination of the green density. Characterisation of the microstructure was conducted on the polished cross-sections prepared via standard ceramographic approaches using diamond suspension down to 1 μm grain size. Microstructure of composites was observed using a scanning electron microscopy (LYRA 3 XMU FEG/SEM, Tescan). Amount and area of micro-fibres embedded inside the deposits were analysed using an images analysis (ImageJ software) on the polished cross-sections. Each cumulative micro-fibre area curve was constructed for given composite material as a result of conducted analysis on 6 micrographs taken at different places over whole thickness of the composite. The cracks were introduced by application of Vickers indenter at load of 5 kg using a ZWICK Z2.5 testing machine equipped with instrumented micro hardness head ZHU0.2 (Zwick/Roell). The indents and indentations cracks length were measured using a laser confocal microscope Olympus LEXT OLS3100 (Olympus. Japan). The indentation fracture toughness K_{IC} [MPa m$^{1/2}$] was calculated separately for each direction (i.e., *X*-direction characterise the deposition plane and *Y*-direction characterise the deposition direction on the prepared cross-sections) using following equation [36]:

$$K_{\mathrm{Ic}} = \alpha \sqrt{\frac{E}{H}} \frac{P}{c^{\frac{3}{2}}} \tag{1}$$

where α [–] is calibration factor equal to 0.018, *P* [N] is the indentation load, *c* [m] is the crack length, *E* [MPa] elastic moduli and *H* [MPa] Vickers hardness. The indentation fracture toughness *Y*/*X* ratio between deposition direction and deposition plane was calculated to determine the level of anisotropy introduced in to the material by processing and by the micro-fibres arrangement.

3. Results and discussion

The tetragonal zirconia micro-fibres used for composites fabrication were forming bundles of fibres with length of hundreds

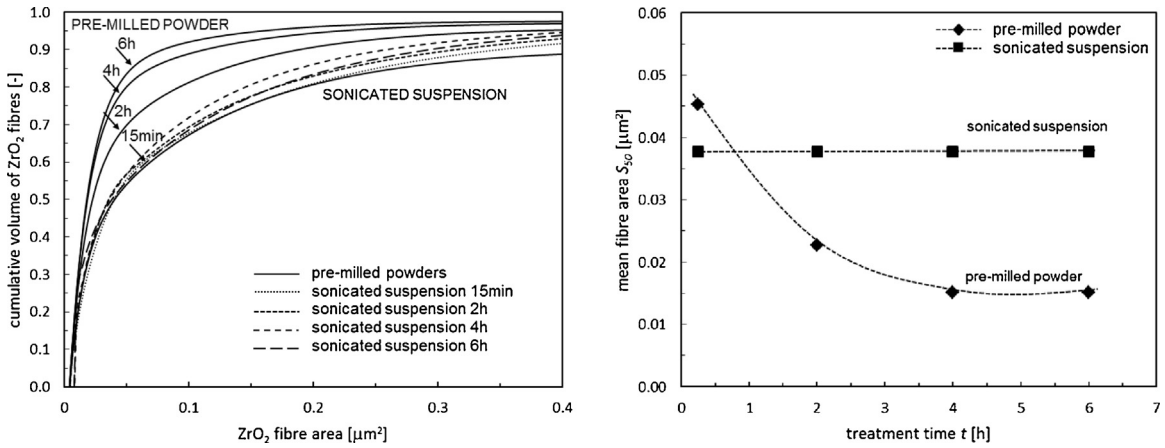

Fig. 2. Cumulative fibre area (left) and mean fibre area (right) of zirconia fibres in deposits prepared from pre-milled powders and sonicated suspensions.

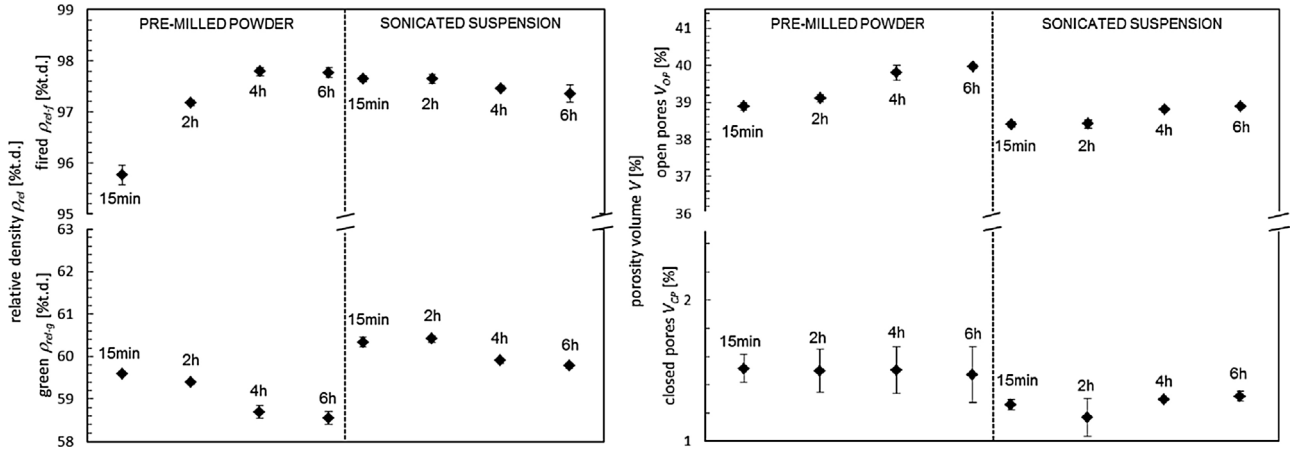

Fig. 3. Dependence of density (left) and porosity volume fraction (right) of alumina deposits on the time of treatment.

of micrometres. To obtain a good dispersion of the micro-fibres in the alumina suspension and in the final deposits, application of proper dispersing process was necessary. A ball milling and sonication of fibres suspended into liquid were used for fibres separation and broken up. The effect of used process of zirconia micro-fibres size reduction was observed by image analysis on micrographs of final microstructure. Cumulative zirconia fibre size (broken micro-fibres) in term of fibre area is given in Fig. 2 left. During ball-milling the fibres were broken and with increasing time of ball-milling zirconia micro-fibre size decreases and reached stable optimum after 4 h (see Fig. 2 right). During sonication of suspension the fibres were just separated from bundles and no reduction of fibre size was observed even with increasing sonication time (see Fig. 2).

Green and fired densities of zirconia micro-fibres reinforced alumina composites prepared are given in Fig. 3 left. The green densities of deposits decreased slightly with time of powder milling or suspension sonication. Decrease of green densities was caused particularly by increase in amount of open porosity (see Fig. 3 right). The amount of porosity captured between particles (closed porosity) remained constant for all deposits prepared and was not affected by time of powder and suspension treatment, respectively.

Evolution of deposited layer on the electrode during electrophoretic deposition was monitored by weighing of whole electrode in 5 min intervals between consecutive depositions with one suspension. Obtained mass represents the mass of deposit m_{dep} [g] consisting of the mass of deposited ceramics m_{cer} [g] and the mass of liquid phase m_{liq} [g] captured in the pores between ceramics particles. Equation describing mass of deposited ceramics m_{cer} [g] as a function of mass of whole wet deposit m_{dep} [g] containing suspension media having density ρ_{liq} [g cm^{-3}], density of deposited ceramics ρ_{cer} [g cm^{-3}] and relative density of deposited ceramics body ρ_{rel-g} [% t.d.] was derived in previous work [25]:

$$m_{cer} = \frac{m_{dep}}{1 + \frac{\rho_{liq}}{\rho_{cer}} \times \left(\frac{100}{\rho_{rel-g}} - 1\right)} \quad (2)$$

Time evolution of deposit mass m_{cer} [g], obtained by direct mass weighing method are represented by symbols in Fig. 4 left. From Fig. 4 it is evident, that deposition rate was almost constant and almost no influence of treatment time was observed. Efficiency of deposition can be represented as relative deposited mass defined as a ratio between final mass of dried deposit m_{cer} [g], and mass of ceramics powder placed between electrodes inside the suspension m_0 [g]. The dependence of relative deposited mass of all suspensions prepared is given in Fig. 4 right. The efficiency of deposition from suspensions prepared from pre-milled powder was comparable with the efficiency of deposition for pure alumina [5,25] and varied just slightly with time of powder treatment. The efficiency of electrophoretic co-deposition (and thus deposition rate) from sonicated suspensions increased with time of suspension sonication from 76% for 15 min to 84% for 4 h of sonication and then decreased to 76% for 6 h of sonication. The observed difference in deposition efficiency from sonicated suspensions can be explained by presence of stabiliser (monochloracetic acid) during sonication of suspension.

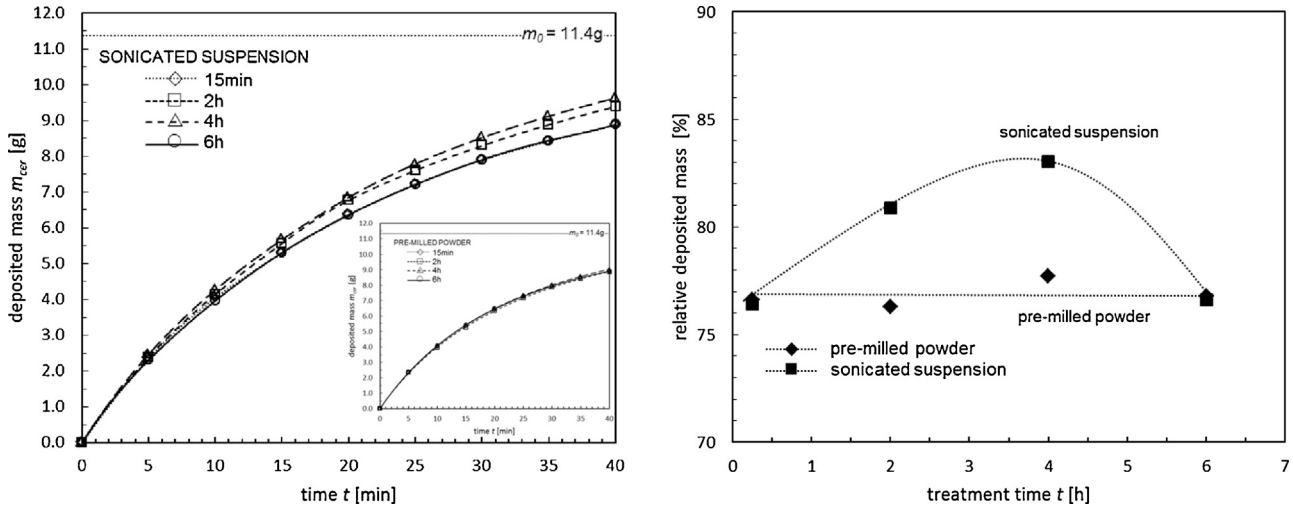

Fig. 4. Time dependence of the composite deposit weight (left) and dependence of relative deposited mass on tretament time (right).

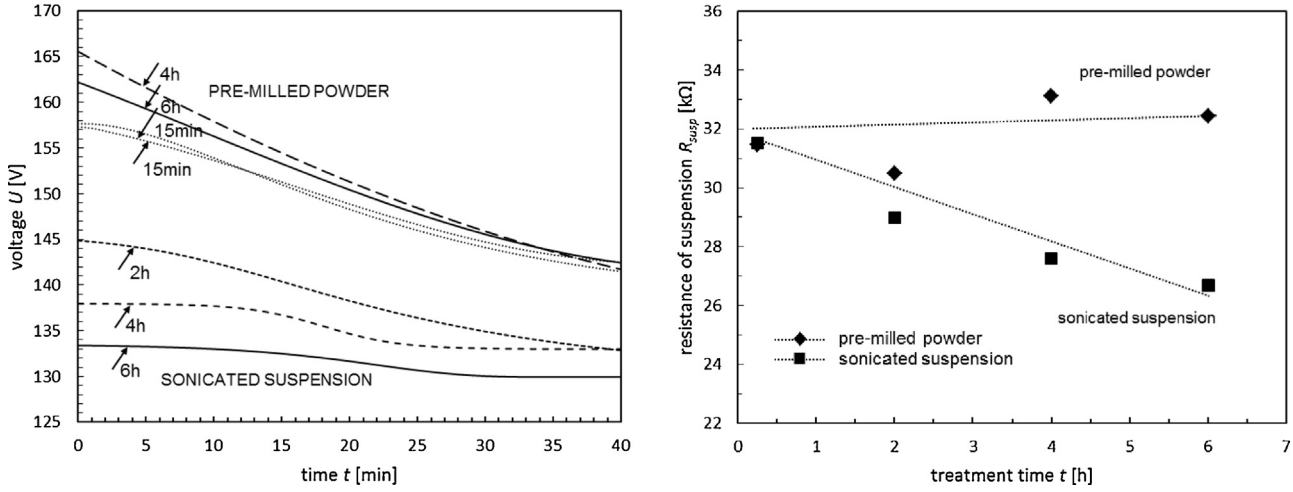

Fig. 5. Voltage course during electrophoretic depostion from ball-milled suspensions (left) and dependence of initial resistance of suspension on tretament time (right).

The kinetics of electrophoretic deposition, i.e., time dependence of deposited mass $m(t)$ [g] in constant-current regime, is theoretically described by Zhang's equation [25]:

$$m(t) = m_0 \times \left(1 - e^{-\frac{\mu E}{d}t}\right) \quad (3)$$

where m_0 [g] is starting amount of solid phase (ceramic powder) in the suspension, μ [$m^2\,V^{-1}\,s^{-1}$] is electrophoretic mobility of particles in the suspension, E [$V\,m^{-1}$] is intensity of applied electric field and d [m] is distance between electrodes immersed to the suspension. Predictions of kinetic curves for $m_0 = 11.4$ g, $\mu = 0{,}205\ m^2\,V^{-1}\,s^{-1}$, $d = 26$ mm and real voltage between electrodes monitored during deposition are given by lines in Fig. 4 left. The perfect coincidence of deposited mass measured and calculated by using Eq. (2) with prediction according to the Eq. (3) is evident.

Precise monitoring of voltage course during deposition is crucial point for the electrophoretic deposition kinetics prediction. Except electric field intensity E [$V\,m^{-1}$] all quantities entering Eq. (3) remains constant. It means that the rate of electrophoretic deposition is controlled by voltage applied between electrodes. Voltage U[V] applied between electrodes immersed into suspension is proportional to electric current I [A] and resistance R [Ω]. During electrophoretic deposition, the voltage is redistributed between deposit and suspension having magnitude proportional to resistance of suspension R_{susp} [Ω] and resistance of deposit R_{dep} [Ω], respectively:

$$U = R \times I = \left(R_{susp} + R_{dep}\right) \times I = R_{susp} \times I, \text{ for} t = 0 \quad (4)$$

Insulating ceramic layer grows on the electrode and thus, the resistance of deposit increases during deposition. In the case of suspensions stabilised by monochloracetic acid the increase of deposit resistance is balanced by increase of suspension resistance [25]. Just slight change of voltage applied between electrodes during deposition was monitored (see Fig. 5 left). The velocity of particles moving to the depositing electrode is proportional to the voltage applied between electrodes. Small change of voltage during electrophoretic deposition led to uniform particles settling onto electrode. Deposit obtained by this process exhibits uniform density and homogeneity over whole thickness [25].

Voltage course during electrophoretic deposition using pre-milled powders and sonicated suspension is given in Fig. 5 left. It is evident, that initial voltage (for $t = 0$) decreases with increasing time of suspension sonication. The decrease of initial voltage was caused by increase of conductivity of suspension due to sonication. In the case of suspensions prepared from pre-milled powders no substantial change of initial conductivity of suspension was observed and thus voltage course during deposition was almost identical. In the beginning of deposition no film is grown onto the electrode and

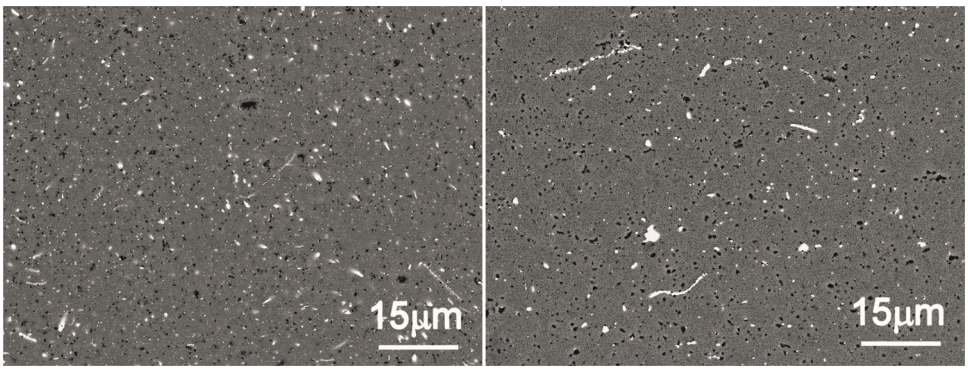

Fig. 6. Microstructure of zirconia micro-fibre reinforced alumina prepared from powder pre-milled for 4 h (left) and from suspension sonicated for 4 h (right).

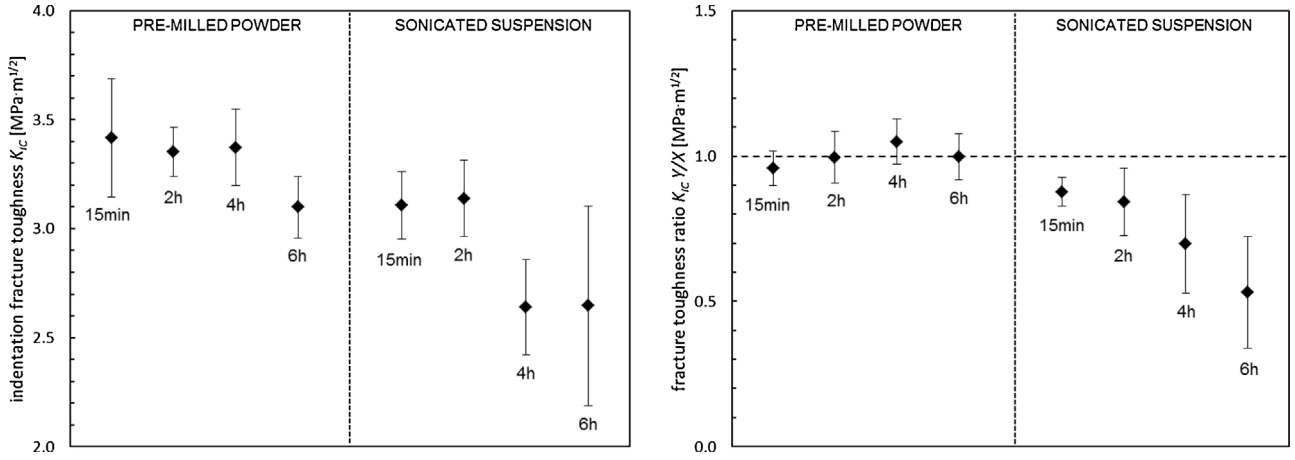

Fig. 7. Dependence of the average indentation fracture toughness values (left) and *Y*/*X* ratio of the indentation fracture toughness (right) on the material composition.

resistivity of all system is proportional just to the suspension resistance R_{susp} [Ω]. Dependence of resistance of suspension R_{susp} on time of powder or suspension treatment is given in Fig. 5 right. The pre-milled powders consisted of alumina particles and zirconia fibres separated from bundles during ball-milling. The resistance of suspension prepared from pre-milled powders was constant. The sonicated suspensions consisted of separated alumina and zirconia micro-fibres. The resistance of sonicated suspensions decreased with time of suspension treatment as a consequence of increased amount of zirconia micro-fibres separated from bundles serving as a charge carrier.

Micrographs of the microstructure of micro-fibre reinforced alumina prepared are given in Fig. 6. Composites with randomly oriented micro-fibres inside the alumina matrix were prepared by deposition using pre-milled and then dried powder (see Fig. 6 left). Microstructure of composites prepared by co-deposition of alumina particles and zirconia micro-fibres from sonicated suspension consisted of zirconia fibres arranged parallel to the depositing electrode. Sonication of suspension minimised damage of micro-fibres during dispersion process comparing to composites prepared from pre-milled suspensions (compare microstructures in Fig. 6). During ball-milling, the zirconia micro-fibres were separated from bundles and broken up during milling to smaller parts (compare Fig. 6 right and Fig. 2 right).

Fracture resistance of composite materials prepared was characterised by analysis of indentation cracks created from corners of Vickers indents. The ball milling time affects the microstructure texture what is hardly detectable from the average indentation fracture toughness values (see Fig. 7 left). From the ratio between indentation fracture toughness of both directions it is evident that the composite materials prepared from pre-milled powders shows symmetric (isotropic) behaviour as a consequence of randomly oriented zirconia micro-fibres (see Fig. 7 right). The significant anisotropy in fracture behaviour was observed when sonication was applied. The reinforcing effect of micro-fibres in these materials can't be responsible for such high level of anisotropy. The main reason was weakening of the material in the deposition plane direction, i.e., the indentation fracture toughness values in this direction were only 50% of the indentation fracture toughness observed in the deposition direction (see drop in average indentation fracture toughness in Fig. 7 left). It is evident that sonication affects the properties of deposits although the deposition kinetics didn't showed any abnormalities. From this point of view the sonicated suspensions are not suitable for preparation of more complex bulk materials. The most preferable results showed materials from pre-milled powders which exhibit isotropic microstructure and fracture behaviour. On the other hand observed anisotropy for sonicated suspensions can be beneficial when higher amount of micro-fibres is used.

An example of typical crack patterns obtained for both the composite material prepared from suspensions using pre-milled powder and the laminate using similar conditions consisting of cracks initiating from the indent corners is shown in Fig. 8a. The crack patterns are redrawn in to schematic drawings showing clearly the crack paths in Fig. 8b. Cracks had in both cases typically straight inter-granular character controlled mainly by the alumina grains up to the point of interaction with zirconia micro-fibres. The crack interaction with micro-fibres is in case of composites nearly negligible from the fracture resistance point of view due to one grain micro-fibre thickness (see Fig. 8c left). The crack deflection is

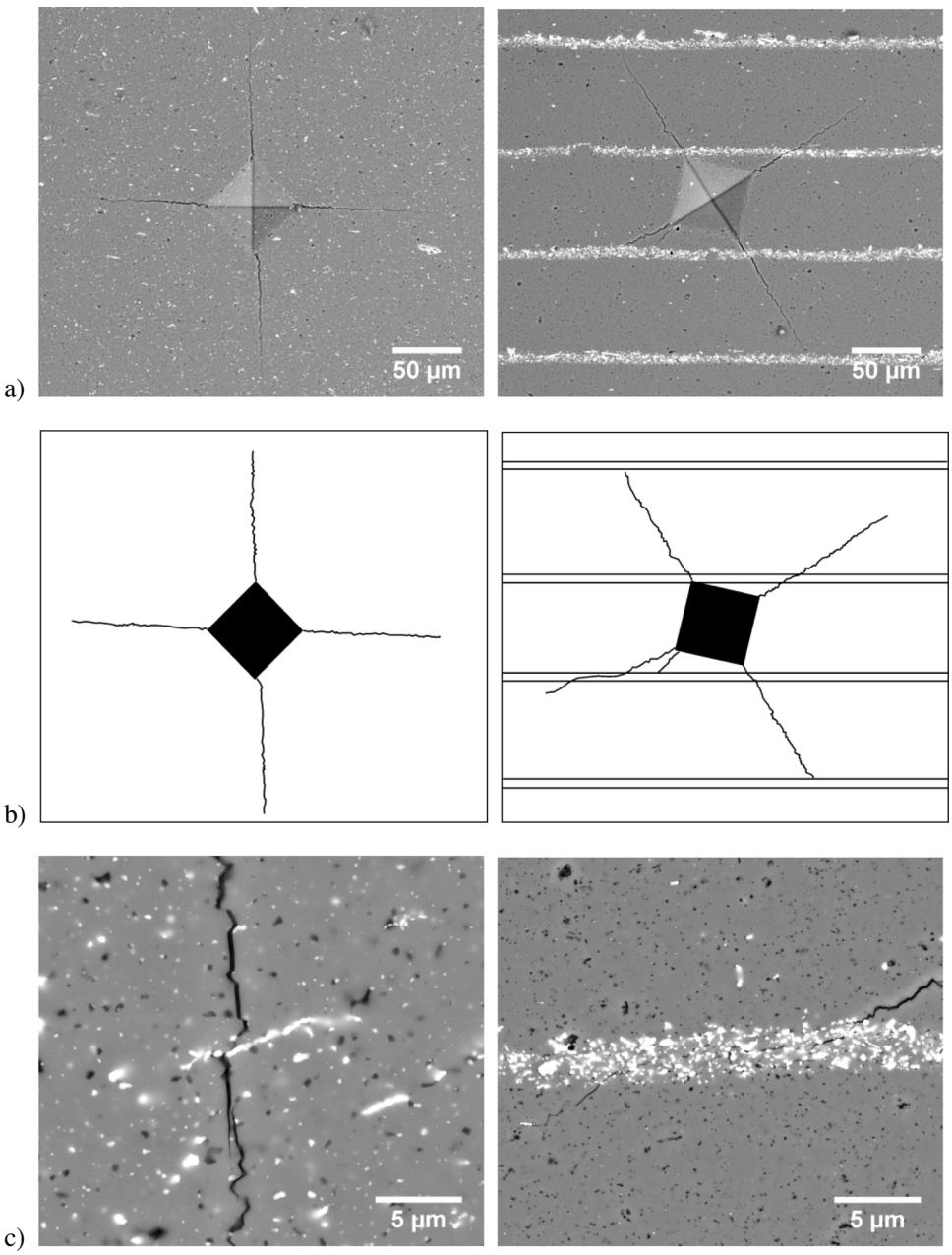

Fig. 8. Comparison of the fracture behaviour between composite (left) and laminate (right) prepared at the same conditions from powders pre-milled for 2 h. The overview of indentation cracks (a), schematic drowing of the crack pattern (b) and detail view of the crack interaction with the zirconia micro-fibres (c).

only few micrometres and affects the indentation fracture toughness minimally. On the other hand when micro-fibres are oriented the effect is measurable as was disused earlier. It was observed that the fracture behaviour can be more controlled when layered structure is used. Two main features can be found in the crack behaviour in the laminate material. One can be identified as a multiple crack initiation (re-initiation) from the indent corner when thin layer containing micro-fibre is nearby. The primary crack stops when reaches this thin layer and the secondary crack initiate. The detailed view of the secondary crack interaction with the thin layer containing zirconia micro-fibres is in Fig. 8c right. This behaviour indicates that electrophoretic deposition of pre-milled powders primarily creates orthotropic material via orienting of deposited particles (micro-fibres in this case) in the electric field [24]. The increased content of zirconia micro-fibres in the alumina matrix can strengthen the anisotropy effect as can be seen in the case of laminates. Here the crack deflection observed on the thin layer was more than ten micrometres. This effect, the crack deflection to the layer direction, is known at materials with weak interfaces and for strong interfaces only when high internal stresses are present [29–32]. The absolute values of the indentation fracture toughness values presented here have to be taken with caution and treated as only indicative information used for material comparison.

4. Conclusions

The article summarises preparation of alumina matrix composites reinforced by zirconia micro-fibres prepared by EPD. The electrophoretic deposition was performed from isopropanolic suspensions stabilised by monochloracetic acid containing mixture of alumina powder and certain amount of zirconia micro-fibres. Different ways of zirconia microfibers dispersion inside the alu-

mina matrix were applied. Mixed powder containing alumina and zirconia fibres were prepared by ball-milling in isopropanol and subsequent drying of powder in air atmosphere. Composites with randomly oriented micro-fibres inside the alumina matrix obtained by deposition using these pre-milled powder exhibited isotropic crack propagation. Other way of zirconia micro-fibres dispersion was based on co-deposition of alumina particles and zirconia micro-fibres. Sonication of suspension was used for zirconia micro-fibres dispersion in the alumina suspension. The co-deposition from mixed suspension led to obtaining composites with fibres arranged parallel to depositing electrode. Sonication of suspension minimised damage of micro-fibres during dispersion process. The co-deposition of ceramic micro-fibres and powder led to the preparation of composites exhibited increase fracture resistance in one direction. The laminated alumina materials consisted of thick alumina layers with thickness of 50 μm separated by thin layer of zirconia micro-fibres were successfully prepared. The help of knowledge of the powder and micro-fibres co-deposition kinetics allowed reaching perfect reproducibility in layers dimensions. The overall content of zirconia micro-fibres added to the alumina layers interfaces in the layered systems was comparable with other composites and it was on the level of 2 vol.%. The layered configuration brings significant change in the fracture behaviour. The symmetric alumina/zirconia laminate demonstrates the ability to significantly increase fracture resistance in one direction. The material containing thin layers of co-deposited micro-fibres exhibits also capability to change direction of the propagating crack even if only small amount of micro-fibres is added.

Acknowledgements

This work was realised in CEITEC-Central European Institute of Technology with research infrastructure supported by the project CZ.1.05/1.1.00/02.0068 financed from European Regional Development Fund and financially supported by Czech Science Foundation project No. 15-06390S.

References

[1] K.K. Chawla, Composite Materials: Science and Engineering, Springer, 2012.
[2] A.G. Evans, F.W. Zok, J. Davis, The role of interfaces in fibre-reinforced brittle matrix composites, Compos. Sci. Technol. 42 (1991) 3–24.
[3] D.B. Marshall, A.G. Evans, Failure mechanisms in ceramic-fibre/ceramic-matrix composites, J. Am. Ceram. Soc. 68 (1985) 225–231.
[4] P.S. Nicholson, P. Sarkar, S. Datta, Producing ceramic laminate composites by EPD, Am. Ceram. Soc. Bull. 75 (1996) 48–51.
[5] K. Maca, H. Hadraba, J. Cihlar, Electrophoretic deposition of alumina and zirconia—I. Single-component systems, Ceram. Int. 30 (2004) 843–852.
[6] B. Ferrari, I. Santacruz, M.a.I. Nieto, R. Moreno, Thermogelation of Al_2O_3/Y-TZP films produced by electrophoretic co-deposition, J. Eur. Ceram. Soc. 24 (2004) 3073–3080.
[7] I. Corni, M.P. Ryan, A.R. Boccaccini, Electrophoretic deposition: from traditional ceramics to nanotechnology, J. Eur. Ceram. Soc. 28 (2008) 1353–1367.
[8] L. Besra, M. Liu, A review on fundamentals and applications of electrophoretic deposition (EPD), Prog. Mater. Sci. 52 (2007) 1–61.
[9] A.R. Boccaccini, I. Zhitomirsky, Application of electrophoretic and electrolytic deposition techniques in ceramics processing, Curr. Opin. Solid State Mater. Sci. 6 (2002) 251–260.
[10] S. Novak, K. Konig, A. Ivekovic, A.R. Boccaccini, Infiltration of a 3-D fabric for the production of SiC/SiC composites by means of electrophoretic deposition electrophoretic deposition: fundamentals and applications III, Key Eng. Mater. 412 (2009) 237–242.
[11] K. König, S. Novak, A. Ivekovič, K. Rade, D. Meng, A.R. Boccaccini, S. Kobe, Fabrication of CNT-SiC/SiC composites by electrophoretic deposition, J. Eur. Ceram. Soc. 30 (2010) 1131–1137.
[12] A.R. Boccaccini, I. MacLaren, M.H. Lewis, C.B. Ponton, Electrophoretic deposition infiltration of 2-D woven SiC fibre mats with mixed sols of mullite composition, J. Eur. Ceram. Soc. 17 (1997) 1545–1550.
[13] A.R. Boccaccini, C.B. Ponton, Processing ceramic-matrix composites using electrophoretic deposition, JOM 47 (1995) 34–37.
[14] K. Moritz, R. Herbig, T. Damjanović, C. Argirusis, G. Borchardt, Development of mullite and mullite/Al_2O_3 precursor sols for electrophoretic deposition of oxidation protection coatings, Colloids Surf. A: Physicochem. Eng. Aspects 350 (2009) 13–21.
[15] S. Put, J. Vleugels, G. Anné, O. Van der Biest, Functionally graded ceramic and ceramic-metal composites shaped by electrophoretic deposition, Colloids Surf. A: Physicochem. Eng. Aspects 222 (2003) 223–232.
[16] P. Sarkar, S. Datta, P.S. Nicholson, Functionally graded ceramic/ceramic and metal/ceramic composites by electrophoretic deposition, Compos. Part B-Eng. 28 (1997) 49–56.
[17] H. Hadraba, K. Maca, J. Cihlar, Electrophoretic deposition of alumina and zirconia-II. Two-component systems, Ceram. Int. 30 (2004) 853–863.
[18] R. Bermejo, Y. Torres, A. Sanchez-Herencia, C. Baudin, M. Anglada, L. Llanes, Fracture behaviour of an Al_2O_3–ZrO_2 multi-layered ceramic with residual stresses due to phase transformations, Fatigue Fract. Eng. Mater. Struct. 29 (2006) 71–78.
[19] B. Ferrari, S. Gonzalez, R. Moreno, C. Baudin, Multilayer coatings with improved reliability produced by aqueous electrophoretic deposition, J. Eur. Ceram. Soc. 26 (2006) 27–36.
[20] R. Bermejo, Y. Torres, C. Baudin, A. Sanchez-Herencia, J. Pascual, M. Anglada, L. Llanes, Threshold strength evaluation on an Al_2O_3–ZrO_2 multilayered system, J. Eur. Ceram. Soc. 27 (2007) 1443–1448.
[21] P. Šajgalík, Z. Lenčéš, J. Dusza, Layered composites with self-diagnostic ability, Compos. Part B-Eng. 37 (2006) 515–523.
[22] Z. Chlup, H. Hadraba, L. Slabakova, D. Drdlik, I. Dlouhy, Fracture behaviour of alumina and zirconia thin layered laminate, J. Eur. Ceram. Soc. 32 (2012) 2057–2061.
[23] H. Hadraba, J. Klimes, K. Maca, Crack propagation in layered Al_2O_3/ZrO_2 composites prepared by electrophoretic deposition, J. Mater. Sci. 42 (2007) 6404–6411.
[24] Z. Chlup, H. Hadraba, D. Drdlik, K. Maca, I. Dlouhy, R. Bermejo, On the determination of the stress-free temperature for alumina–zirconia multilayer structures, Ceram. Int. 40 (2014) 5787–5793.
[25] H. Hadraba, D. Drdlik, Z. Chlup, K. Maca, I. Dlouhy, J. Cihlar, Layered ceramic composites via control of electrophoretic deposition kinetics, J. Eur. Ceram. Soc. 33 (2013) 2305–2312.
[26] H. Hadraba, D. Drdlik, Z. Chlup, K. Maca, I. Dlouhy, Control of electrophoretic deposition kinetics for preparation of laminated alumina/zirconia ceramic composites electrophoretic deposition: fundamentals and applications IV, Key Eng. Mater. 507 (2012) 209–213.
[27] L. Sestakova, R. Bermejo, Z. Chlup, R. Danzer, Strategies for fracture toughness, strength and reliability optimisation of ceramic–ceramic laminates, Int. J. Mater. Res. 102 (2011) 613–626.
[28] R. Bermejo, Z. Chlup, L. Sestakova, O. Sevecek, R. Danzer, D. Singh, J. Salem, M. Halbig, S. Mathur, Strategies to optimize the strength and fracture resistance of ceramic laminates, Mech. Prop. Perform. Eng. Ceram. Compos. VII (2013) 163–174.
[29] M. Lugovy, V. Slyunyayev, N. Orlovskaya, G. Blugan, J. Kuebler, M. Lewis, Apparent fracture toughness of Si_3N_4-based laminates with residual compressive or tensile stresses in surface layers, Acta Mater. 53 (2005) 289–296.
[30] M. Lugovy, V. Slyunyayev, V. Subbotin, N. Orlovskaya, G. Gogotsi, Crack arrest in Si_3N_4-based layered composites with residual stress, Compos. Sci. Technol. 64 (2004) 1947–1957.
[31] A.J. Sánchez-Herencia, C. Pascual, J. He, F.F. Lange, ZrO_2/ZrO_2 Layered Composites for Crack Bifurcation, J. Am. Ceram. Soc. 82 (1999) 1512–1518.
[32] R. Bermejo, Y. Torres, A. Sanchez-Herencia, C. Baudin, M. Anglada, L. Llanes, Residual stresses, strength and toughness of laminates with different layer thickness ratios, Acta Mater. 54 (2006) 4745–4757.
[33] V. Sergo, X.-L. Wang, D.R. Clarke, P.F. Becher, Residual stresses in alumina/ceria-stabilized zirconia composites, J. Am. Ceram. Soc. 78 (1995) 2213–2214.
[34] J. Pascual, T. Lube, R. Danzer, Fracture statistics of ceramic laminates strengthened by compressive residual stresses, J. Eur. Ceram. Soc. 28 (2008) 1551–1556.
[35] H. Hadraba, D. Drdlik, Z. Chlup, K. Maca, I. Dlouhy, J. Cihlar, Laminated alumina/zirconia ceramic composites prepared by electrophoretic deposition, J. Eur. Ceram. Soc. 32 (2012) 2053–2056.
[36] G.R. Anstis, P. Chantikul, B.R. Lawn, D.B. Marshall, A critical evaluation of indentation techniques for measuring fracture toughness: I, direct crack measurements, J. Am. Ceram. Soc. 64 (1981) 533–538.

PUBLIKACE XII

Available online at www.sciencedirect.com

ScienceDirect

Ceramics International 40 (2014) 5787–5793

CERAMICS INTERNATIONAL

www.elsevier.com/locate/ceramint

On the determination of the stress-free temperature for alumina–zirconia multilayer structures

Zdenek Chlup[a,*], Hynek Hadraba[a], Daniel Drdlik[b], Karel Maca[b], Ivo Dlouhy[a], Raul Bermejo[c]

[a]CEITEC IPM, Institute of Physics of Materials, Academy of Sciences of the Czech Republic, 616 62 Brno, Czech Republic
[b]CEITEC BUT, Brno University of Technology, 616 69 Brno, Czech Republic
[c]Institut fur Struktur- und Funktionskeramik, Montanuniversitaet Leoben, 8700 Leoben, Austria

Received 19 July 2013; received in revised form 16 October 2013; accepted 2 November 2013
Available online 13 November 2013

Abstract

Internal residual stresses can enhance the fracture resistance and mechanical reliability of layered ceramics. The magnitude of the stresses depends on the elastic and thermal properties of the layers and the typically assumed reference (stress-free) temperature, below which internal stresses develop. A novel combined experimental and numerical simulation approach has been developed to determine the reference temperature and experimentally proved in alumina–zirconia ceramic laminates. Dilatometric data of monolithic phases are input for the numerical simulation and experimental data on the laminate properties are used for the stress-free temperature determination. In contrast to typical assumptions, reference temperature very near the sintering temperature (i.e. approx. $T_{ref} \approx 1470$ °C) was found, which should be considered for the estimation of internal (residual) stresses in alumina/zirconia-based layered ceramics.
© 2013 Elsevier Ltd and Techna Group S.r.l. All rights reserved.

Keywords: A. Sintering; C. Thermal expansion; Zirconia; Alumina; Layered Ceramics

1. Introduction

The brittle fracture of ceramics is a consequence of the material defects located either within the bulk or at the surface, resulting from the processing and/or machining procedures [1–3]. Under external applied stress, the stress concentration associated with those defects is the common source of failure for ceramic components. If each defect is considered as a crack or a potential source for crack initiation, then it becomes clear that the size and type of these defects determine the mechanical strength of the material [4]. The distribution of defects within a ceramic component yields a statistically variable strength which can be described by the Weibull theory [5–7]. Since flaws are intrinsic to processing and in most cases unavoidable, the reliability of ceramic components in terms of strength is associated with such a flaw distribution. In an attempt to reduce the level of uncertainty in mechanical strength and to overcome the lack of toughness of monolithic ceramics, several processing routes have arisen in the last two decades which do not utilise the conventional "flaw elimination" approach, but rather use the implication of energy release mechanisms to obtain "flaw tolerant" (more reliable) materials, with improved fracture toughness. One strategy is to design multilayer structures combining layers of different materials. An effective way has proven to be layered ceramics with strong bond interfaces [8–16]. The strain mismatch between layers after cooling from sintering temperature (associated with differences in CTE and/or phase transformations [17–21]) can induce significant internal (residual) stresses within individual layers which can effectively change the crack path or even stop the crack during its propagation. In some cases layered ceramics can effectively act as a barrier to crack propagation, yielding a so-called "threshold strength", i.e. a stress level under which the material does not fail [10,12,22,23]. It has been recently shown that the layer thickness and exact ordering of layers (i.e. periodic or non-periodic) can be modelled by means of analytical and numerical calculations in order to obtain an optimal mechanical behaviour of the laminate in terms of strength and fracture resistance [24,25]. For tailoring

*Corresponding author. Tel.: +420 532 290 335.
E-mail address: chlup@ipm.cz (Z. Chlup).
http://www.ipm.cz

0272-8842/$ - see front matter © 2013 Elsevier Ltd and Techna Group S.r.l. All rights reserved.
http://dx.doi.org/10.1016/j.ceramint.2013.11.018

the design various methods including tape casting, slip casting and electrophoretic deposition (EPD) have been employed where a precise control of the kinetics during the deposition process is necessary to obtain accurate layer thicknesses [18,26–34].

The key feature in the design of laminates is the distribution of internal stresses in the layers, which depends on the elastic properties, thermal expansion coefficients, green densities, and volume ratio of the materials. The residual stresses in each layer may be assessed by means of experimental techniques such as X-Ray [35,36], neutron diffraction [37–40], Raman or fluorescent spectroscopy [41–43], among others. However, some limitations associated with the spatial resolution, edge effects, surface cracks, etc. may hinder the accurate stress measurement.

From the point of view of mechanical behaviour, the in-plane stresses in the bulk material (far from the free surfaces) can be calculated within each layer using the following equation:

$$\sigma_{\mathrm{res},i} = \frac{E_\mathrm{i}}{1-\nu_\mathrm{i}}(\overline{\alpha}-\alpha_\mathrm{i})\Delta T = \frac{E_\mathrm{i}}{1-\nu_\mathrm{i}}\Delta\varepsilon_\mathrm{i} \quad (1)$$

where E_i, ν_i and α_i are the Young's modulus, Poisson's ratio and coefficient of thermal expansion of the ith layer, respectively. $\Delta\varepsilon_\mathrm{i} = (\overline{\alpha}-\alpha_\mathrm{i})\Delta T$ is the mismatch strain of the ith layer. The coefficient $\overline{\alpha}$ is given as an averaged expansion coefficient of the thermal expansion of the laminate and depends on the materials volume fraction of the different layer types (for details see [24,25]). The temperature difference is $\Delta T = T_0 - T_\mathrm{ref}$, where T_0 is the room temperature and T_ref refers to the temperature above which the laminate is considered to be stress free.

The theoretical calculation of internal stresses in a layered structure using Eq. (1) can provide a good estimation only when exact input data are provided. The elastic properties and coefficients of thermal expansion and geometrical parameters can be obtained with high accuracy. However, the determination of the stress-free temperature above which stresses are relaxed seems to be the main course of uncertainty. Previous authors have assumed that for typical glass-phase free materials stress-free temperatures are in the range 1180–1300 °C [17,37,44]. They state that this temperature is influenced by the processing route, grain size, phase composition and/or cooling rate used after sintering [45–47]. Therefore it may be easily under or over estimated, thus resulting in inaccurate prediction of internal stresses. The present work introduces a novel approach to determine the stress-free temperature in layered ceramics based on combined numerical simulations and dilatometric measurements performed on alumina–zirconia laminates.

2. Experiments and simulations

2.1. Material of study

Materials for this study were prepared by the electrophoretic deposition technique. Two monolithic compounds (Al_2O_3 and ZrO_2) and a multilayer system combining both compounds in a layered structure were fabricated. The thickness of each layer was adjusted to approx. 50 μm, giving a volume ratio of approximately 1 between both materials see Fig. 1(a). Following powders were used: alumina (type HP-DBM, Malakoff Ind., USA) and tetragonal-zirconia stabilized with 3 mol% of Y_2O_3 (type TZ-3YSE, Tosoh, Japan) for manufacturing the monolithic Al_2O_3 (A), ZrO_2 (Z) and the alumina–zirconia laminate (L). The mean particle sizes of the alumina and zirconia powder were 470 nm and 140 nm, respectively. Isopropanol (p.a., Onex, Czech Republic) with addition of monochloroacetic acid (99%, Aldrich, Germany) were used for suspension preparation. The electrophoretic deposition was carried out in a constant current mode at 5 mA. Details about manufacturing process can be found elsewhere [28,32,33]. For all deposits three orientations were selected, where X was the deposition horizontal axis, Y was the vertical axis and Z was the axis in the direction of the deposition (see Fig. 1b). We caution the reader that the orientation may be important during the EPD process. The packaging may be affected by a number of factors such as (i) gravity (on the Y-direction), where heavier particles tend to deposit at the bottom part of the cell, (ii) shape of the powder particles, where particles have rather smaller dimension perpendicular to the electrode, (iii) electric field, which can orient particles based on their physical properties (i.e. domains oriented), and (iv) capillary forces which can affect the density of deposit in the vertical axis during withdrawing of the electrode with deposit from the suspension, etc. After the drying process, each deposit was annealed (800 °C/1 h; heating rate +2 °C/min in air) and finally cut and polished to the shape suitable for dilatometric measurements.

2.2. Dilatometer measurements

The relative length change of all specimens during sintering was monitored using a high-temperature dilatometer (L75/50, Linseis, Germany). The nominal sample geometry of $5 \times 5 \times 20\ \mathrm{mm}^3$ was used. Two different conditions covering standardly used conditions for sintering i.e. sintering temperature 1500 °C with dwell time 2 h; heating and cooling rate (5 °C/min or 10 °C in air) were applied for all materials. Two different heating and cooling rates were used to obtain an influence on the dilatometric results, if exists. Higher cooling rates were not tested because of physical limits of the furnace. Fig. 2 shows a scheme of the dilatometric set-up for both monolithic and laminate samples. The coefficients of thermal expansion were determined from the cooling part of the shrinkage curve fitted by a third order polynomial function of the form

$$\varepsilon = \frac{\Delta l}{l_0} = a_0 + a_1 T + a_2 T^2 + a_3 T^3, \quad (2)$$

where ε is the thermal strain given by the length increment Δl with respect to the initial length of sample l0. The polynomial fit provides better accuracy of measured data around the room temperature. Additionally it is possible to use instantaneous α

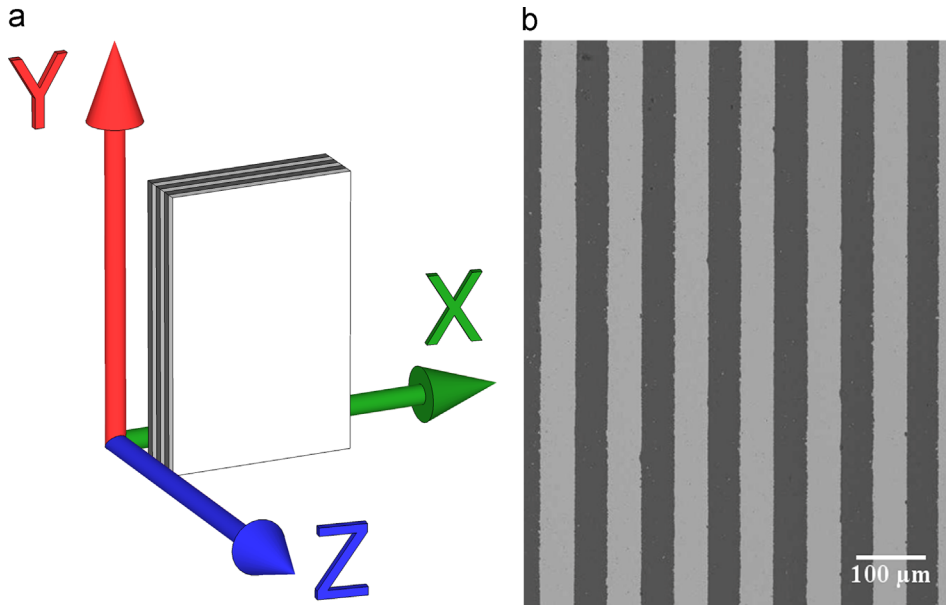

Fig. 1. Scheme of axes definition in the sample (a) and example of the microstructure of prepared laminate – *YZ* plane showing quality of the layers (b).

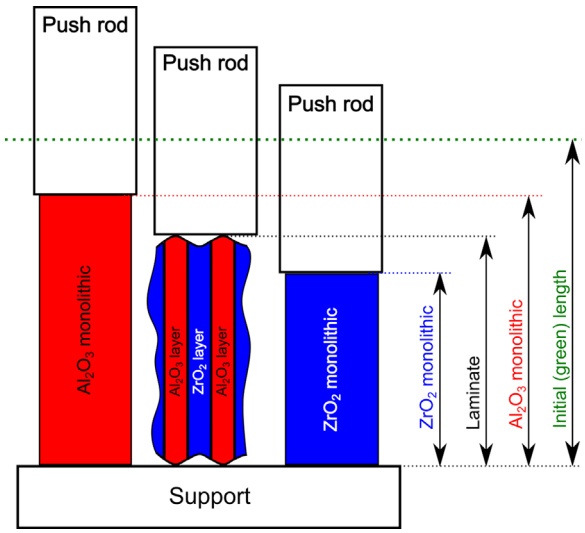

Fig. 2. Scheme of the dilatometric measurements showing the effect of sample composition and green density and the effect of surface features in the laminate.

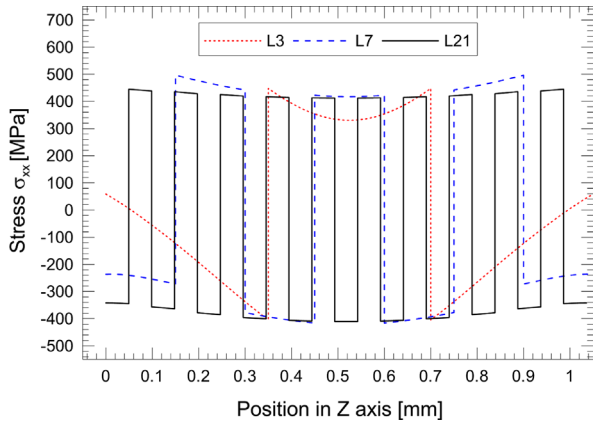

Fig. 3. Distribution of maximal principal stress in the centre of three laminate systems (L3, L7 and L21) containing 3, 7 and 21 layers, respectively.

temperature dependence as input for numerical simulation as will be described further. The technical CTEs were calculated for a given temperature interval ΔT using the following equation:

$$\mathrm{CTE} = \frac{\varepsilon}{\Delta T} = \frac{\Delta l}{l_0 \Delta T} \tag{3}$$

In this case the temperature interval was taken from 10 °C to 1500 °C (i.e. from sintering to the room temperature).

2.3. Numerical simulations

Coupled temperature–displacement numerical simulations were performed to estimate the thermal strains (and stresses) in the layers of the laminate upon cooling from the sintering temperature. The input parameters involved elastic properties of the layers (i.e. Young's modulus and Poisson's ratio) as well as the CTE of the individual layer materials. Young's modulus and Poisson's ratio were taken as $E_A = 380$ GPa, $\nu_A = 0.26$, $E_B = 210$ GPa, $\nu_B = 0.31$, as determined elsewhere [16,28].

The FEM model consists of 21 layers (11 made of Al_2O_3 and 10 made of ZrO_2), containing 6400 elements (C3D20T), which gives a total of 134,400 elements. In this case a periodic and symmetric layered structure with external compressive layers was analysed. The number of layers was chosen in order to obtain representative results and reasonable computation time. With low number of layers, surface effects would become significant on the stress distribution within the outer layers, whereas a high number of layers would result in very high computational times. This can be demonstrated in Fig. 3 where the maximal principal stresses σ_{xx} calculated along the *Z*-axis (perpendicular to the layer plane) going through the

centre of the laminate is displayed for three multilayer systems (L3, L7 and L21) containing 3, 7 and 21 layers respectively. The strong effect of the free surface is visible in case of systems having a low number of layers (e.g. 3 layers), where the compressive stresses in the outer layers are not at the same level as predicted from the analytical solution given for materials with the same volume ratio. On the other hand the model with 21 layers provides estimation of the stress distribution with sufficient accuracy for the purpose of this study.

2.4. Methodology

The estimation of the stress field in the layered structure when internal stresses are developed during the manufacturing process is essential for the design of the laminate. There is a possibility to calculate internal stresses using an analytical solution (see Eq. (1)). This approach is simply based on the knowledge of elastic and thermal properties of laminate component and is convenient from the application point of view. The only uncertain variable is the temperature interval where the stress development takes place, $\Delta T = T_0 - T_{ref}$, where T_0 is the room temperature and T_{ref} refers to the temperature at which the laminate is considered to be stress free. In order to determine T_{ref}, the following approach combining numerical simulations and dilatometric measurements performed on alumina (A) and zirconia (B) monoliths as well as on alumina–zirconia laminates (L) has been implemented. The combined method is schematically shown in Fig. 4 and can be described as follows:

The first step is to measure dilatometric parameters (thermal strains and/or CTE) of the A and B monolithic materials (i.e. CTE^A, CTE^B or α^A, α^B or ε^A, ε^B).

The second step is the FE calculation of the shrinkage of the laminate during cooling down from the sintering temperature. The information about thermal expansion coefficients of monolithic materials as a function of temperature are used as input data for each layer. The numerical calculation is conducted for the maximal range of temperature where T_{ref} is set initially as the sintering temperature, i.e. for this particular case 1500 °C.

The strains obtained in the laminate with the simulation (i.e. ε^L_{FEM}) are now compared with the thermal strains measured on the laminate with dilatometry in the range of $\Delta T = T_0 - T_{sint}$, i.e. ε^L. If there are some differences, the reference temperature T_{ref} has to be adjusted in order to match the experimental measured strains in the laminate. When both strains are in good agreement, T_{ref} can be set and residual stresses in the layers can be calculated accurately by selected method using this reference temperature.

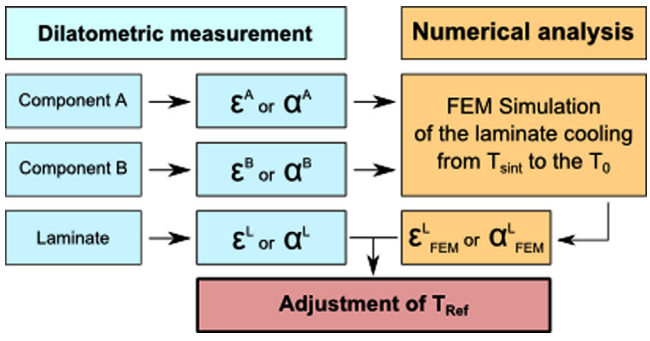

Fig. 4. Schematic of the combined experimental and numerical procedure for determination of the stress filed distribution in a layered ceramic.

Additionally, if necessary and significant deviation from isotropic material of each layer exists (for example caused by processing used) then is possible to extend this method for all three directions as will be presented in this work. It implies to obtain thermal expansion coefficients for all the three materials (A, B and L) in *X*, *Y* and *Z* directions, respectively, which can be accompanied by experimental limits.

3. Results and discussion

The dilatometric curves were obtained for all prepared specimens and strains were calculated. The technical coefficients of thermal expansion of the monolithic and laminate materials were calculated as a function of temperature from the cooling part of the curves. The relative error of CTE evaluation was determined from at least 5 measurements (performed with

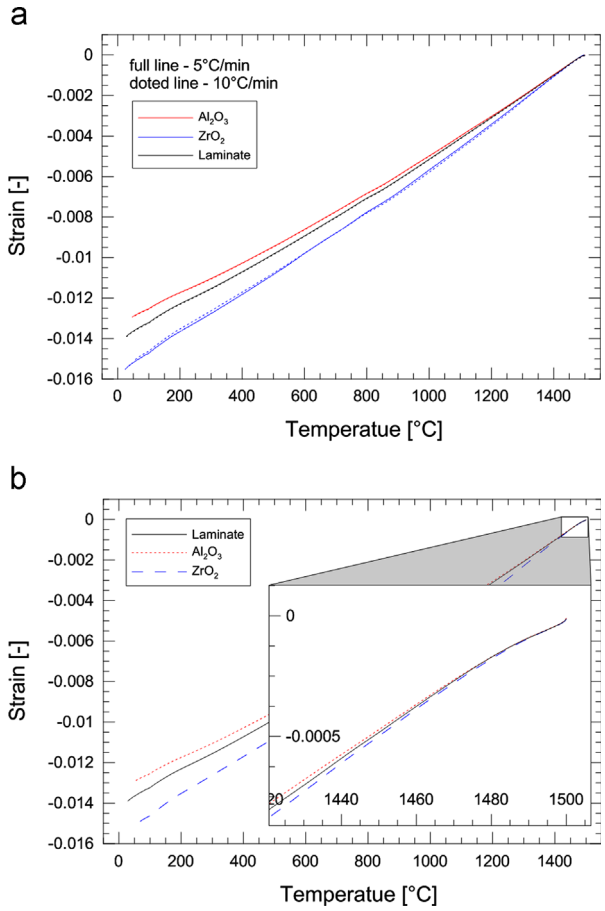

Fig. 5. Cooling part of the dilatometric curves obtained in *X*-direction for alumina and zirconia monoliths and laminate (a) comparison both cooling rates of 5 and 10 °C and (b) detailed view of the high temperature region cooling rate 10 °C/min.

both monolithic materials) and resulted in a maximum scatter of 2.5%. An example of the dilatometric measurements obtained on samples with different cooling rates (5 and 10 °C/min) is displayed in Fig. 5(a). The shrinkage of the ZrO_2 monolithic sample is significantly higher than that of the Al_2O_3 monolithic sample, therefore the ZrO_2 monolithic sample has higher CTE comparing with Al_2O_3 sample. However, the shrinkage of the laminate reads very similar to that of the Al_2O_3 monolith. This can be related to the different stiffness of both alumina and zirconia layers, the former being higher and thus dominating the shrinkage process. Detailed view of measured dilatometric curves for the cooling rate 10 °C/min close to the sintering temperature is displayed in Fig. 5(b). In order to find an experimental evidence of the different shrinkages of the layers in the laminate sample, a confocal microscopy analysis was performed on the laminate sample used for the dilatometry. The resulting surface 3D reconstruction of some layers of the laminate sample is shown in Fig. 6. Surface rippling can be observed corresponding to convex Al_2O_3 and concave ZrO_2 layers. Note that the magnitude of the reconstructed ripples contains both the effect of CTE mismatch and also the effects connected to the differences in green densities, which cannot be separated. This can explain the fact that the dilatometry curve corresponding to the laminate is close to the one measured for Al_2O_3 monolith (see Fig. 5), the dilatometer push rod (as shown in Fig. 2) being in contact with the (convex) Al_2O_3 layers during the measurement. Likewise, the small difference can be associated with the constraining effect of the ZrO_2 layers.

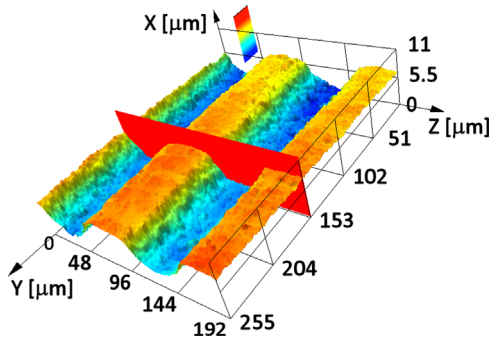

Fig. 6. 3D surface reconstruction of the free surface of the laminate sample using confocal microscopy, showing convex Al_2O_3 and concave ZrO_2 layers.

All measured thermal strains and coefficients of thermal expansion for the monoliths and for the laminate are summarised in Table 1. The FE calculated strains corresponding to a T_{ref} of 1500 °C (i.e. $T_{ref}=T_{sint}$) are also listed in the referred table. In order to find the best fit for T_{ref}, the strain results obtained from the FE calculation of the laminate structure for different T_{ref} are plotted in Fig. 7 as a function of temperature. A linear behaviour can be observed, as predicted by the elasticity theory. The thermal strain measured on the laminate in *X*-direction is plotted as a broken line. The shadowed area shows the expected maximal scatter of the measurements. From the comparison, the reference temperature can be easily obtained where both strains are equal, resulting in $T_{ref}=1470\pm40$ °C.

A similar analysis can be done for *Y* and *Z* directions. According to the strain values reported in Table 1 strains measured in the *Y*-direction lead to a reference temperature close to the sintering temperature (similar to the *X*-direction). However, for the *Z*-direction (perpendicular to the layer plane) the difference between dilatometric measurements and FEM is detectable (thermal strains in this direction are higher than the calculated ones), the reference temperature resulting even higher than the sintering temperature which is not physically feasible. This fact can be associated with the presence of interfaces (including effects of pores, interface roughness etc.), which are not considered in the numerical model. Additionally, the measured CTE in this direction is affected by the size of the initial specimen length given by limited laminate thickness (i.e. 5 mm in this particular case) which significantly influences precision of the dilatometric measurement.

Considering these facts the reference temperature is taken based on the *X* and *Y* results, which were estimated to be very close to the sintering temperature (i.e. $T_{ref}=1470\pm40$ °C vs $T_{sint}=1500$ °C). This result is in contrast with published data for others alumina/zirconia based composite materials, where a stress-free temperature is given in the range of 1180–1300 °C, as was mentioned earlier (see [17,37,44]). This discrepancy can be associated with possible processes taken place during the sintering: (i) grain growth, (ii) diffusion along the grain boundaries and (iii) plastic deformation etc. as was reported by mentioned authors. It is necessary to point out that presence of glassy phase on the grain boundaries having lower melting temperature can influence the kinetics of grain growth during cooling stage; however no glassy phase was present in the

Table 1
Measured thermal strains and coefficients of thermal expansion for the alumina and zirconia monoliths and for the laminate in the temperature range of 20–1500 °C. The FE calculated strains corresponding to a T_{ref} of 1500 °C (i.e. $T_{ref}=T_{sint}$) are also listed for comparison.

	Al_2O_3 (A)			ZrO_2 (B)			Laminate (L)		
	X	*Y*	*Z*	*X*	*Y*	*Z*	*X*	*Y*	*Z*
Dilatometry									
Strains [$\times 10^{-2}$]	1.319	1.320	1.265	1.538	1.504	1.388	1.387	1.384	1.427
CTE [$\times 10^{-6}$ K^{-1}]	8.91	8.92	8.55	10.39	10.16	9.38	9.37	9.35	9.64
FE calculations for $T_{ref}=1500$ °C									
Strains [$\times 10^{-2}$]	–	–	–	-	–	–	0.01413	0.01402	0.01407
CTE [$\times 10^{-6}$ K^{-1}]	–	–	–	–	–	–	9.55	9.47	9.51

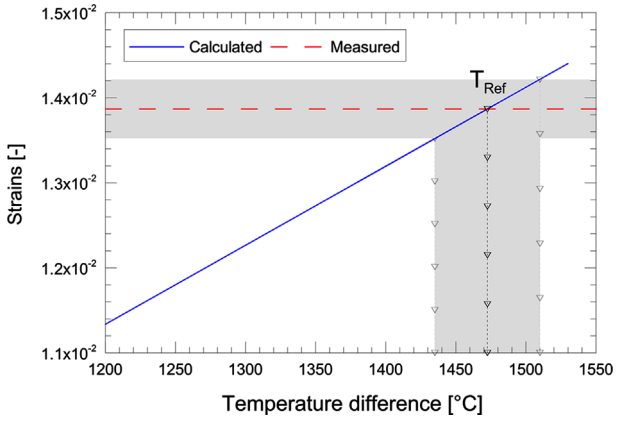

Fig. 7. Strain results in *X*-direction obtained from the FE calculation of the laminate structure for different T_{ref} as a function of temperature. The thermal strain measured on the laminate in *X*-direction is plotted as a broken line. The shadowed area shows the scatter of the measurements.

system under investigation. The determination of the stress-free temperature can be also affected by the method of evaluation (for example widely used curvature method exhibits with increasing temperatures higher inaccuracy thanks to radiation of the sample), the sintering process itself (e.g. presence of higher porosity at final stage of sintering can leads to the not equilibrium energetic state) and additionally by the effects connected to the processing route (i.e. assistance of pressure, etc.). It needs to be mentioned that this work reports measurements on layered ceramics and not on particulate composites, where such relatively low T_{ref} was mainly reported.

Based on the numerical calculations and conducted experiments in this work the stress-free temperature for layered materials prepared by EPD is found to be close to the sintering temperature. This consideration is supported by the fact that all processes mentioned earlier are saturated at the end of the dwell time at the sintering temperature. Therefore, there is no available driving force for activation of stress releasing processes and additionally, the cooling rate is high enough to eliminate time connected effects as a creep deformation. This result shows that there is no evidence of any significant stress relaxation process (such as creep, grain growth, diffusion, etc.) during the cooling stage of the sintering of these laminates for given range of cooling rates. It implies that for internal stress calculation it is necessary to use this estimated temperature difference on the level of $\Delta T = 1470 \pm 40$ °C. As a consequence, the residual stress levels obtained in the laminate may be higher than anticipated by following previous assumptions using a reference temperature of 1200 °C (i.e. approx. 20% higher). Although high compressive stresses have proven to be beneficial for strength and toughness in layered ceramics, cracking of layers may occur associated with high internal residual stresses. For instance, in-plane stresses in tensile layers which are high enough to overcome the material strength can cause the development of tunnelling cracks [13,48]. In addition, too high compressive stresses may yield (out-of-plane) stresses perpendicular to the layer plane which can lead to edge cracks in the compressive layers [13,49–51]. Cracking can be avoided with proper design as demonstrated elsewhere [25], the reference temperature being an important parameter to be taken into account.

The methodology proposed in this work for the determination of the reference temperature was presented for laminate systems with relatively linear shrinkage behaviour. Nevertheless, it could be used for laminates exhibiting additional processes influencing development of the internal stresses (for example phase transformations or chemical reactions within particular layers). In this case the temperature dependence of instantaneous thermal expansion coefficients will be essential.

4. Conclusions

A new approach combining dilatometric experiments and numerical analyses of thermal strains in layered ceramics has been presented, which allows simple way to determine the reference (i.e. stress-free) temperature, T_{ref}, under which internal (residual) stresses may develop after cooling down from the sintering temperature. Dilatometric measurements on monolithic layers served as input for the numerical simulation of strains in the laminate. Results were matched to the measured strains in the layered sample and T_{ref} was estimated.

The reference temperature estimated in this work for alumina–zirconia laminates (i.e. $T_{ref} = 1470 \pm 40$ °C) was rather higher than previously assumed in other published works on glass-phase free materials, and very close to the sintering temperature. A higher T_{ref} can imply higher internal stresses (approx. 20%) which may lead to cracking of the layers and should be considered in the design of crack-free alumina/zirconia-based layered ceramics. The methodology can be extended from isotropic to orthotropic monolithic materials as was demonstrated.

Acknowledgements

The authors are grateful for financial support to project GAP108-11-1644 under Czech Science Foundation and Institutional Research Plan no. 68081723. This work was realised in CEITEC – Central European Institute of Technology with research infrastructure supported by the project CZ.1.05/1.1.00/02.0068 financed from European Regional Development Fund. Special thanks are dedicated to V. Pouchly for the dilatometric measurements.

References

[1] A.A. Griffith, The phenomenon of rupture and flow in solids, Phil. Trans. R. Soc. Lond. A 221 (1921) 163–198.
[2] W.D. Kingery, H.K. Bowen, D.R. Uhlmann, in: Introduction to Ceramics, John Wiley & Sons, New York; London, 1960.
[3] R. Danzer, A general strength distribution function for brittle materials, J. Eur. Ceram. Soc. 10 (1992) 461–472.
[4] B.R. Lawn, Fracture of Brittle Solids, second ed., Cambridge University Press, Cambridge, 1993, p. 378.
[5] W. Weibull, A statistical distribution function of wide applicability, J. Appl. Mech. 18 (1951) 253.

[6] D. Munz, T. Fett, Ceramics: Mechanical Properties, Failure Behaviour, Materials Selection, Springer, Berlin, 1999.
[7] R. Danzer, P. Supancic, J. Pascual, T. Lube, Fracture statistics of ceramics – Weibull statistics and deviations from Weibull statistics, Eng. Fract. Mech. 74 (18) (2007) 2919–2932.
[8] D.J. Green, R. Tandon, V.M. Sglavo, Crack arrest and multiple cracking in glass through the use of designed residual stress profiles, Science 283 (5406) (1999) 1295–1297.
[9] M. Rao, J. Sanchez-Herencia, G. Beltz, R.M. McMeeking, F. Lange, Laminar ceramics that exhibit a threshold strength, Science 286 (1999) 102–105.
[10] M. Lugovy, V. Slyunyayev, V. Subbotin, N. Orlovskaya, J. Kübler, Crack arrest in Si_3N_4-based layered composites with residual stress, Comp. Sci. Tech. 64 (2004) 1947–1957.
[11] R. Bermejo, L. Llanes, M. Anglada, P. Supancic, T. Lube, Thermal shock behavior of an Al_2O_3/ZrO_2 multilayered ceramic with residual stresses due to phase transformations, Key Eng. Mater. 290 (2005) 191–198.
[12] V.M. Sglavo, M. Paternoster, M. Bertoldi, Tailored residual stresses in high reliability alumina-mullite ceramic laminates, J. Am. Ceram. Soc. (10) (2005) 2826–283288 (10) (2005) 2826–2832.
[13] R. Bermejo, A.J. Sanchez-Herencia, C. Baudin, L. Llanes, Residual stresses in Al_2O_3–ZrO_2 multilayered ceramics: nature, evaluation and influence on the structural integrity, Bol. Soc. Esp. Ceram. V. 45 (5) (2006) 352–357.
[14] J. Pascual, T. Lube, R. Danzer, Fracture statistics of ceramic laminates strengthened by compressive residual stresses, J. Eur. Ceram. Soc. 28 (8) (2008) 1551–1556.
[15] Z. Chlup, H. Hadraba, Alumina and zirconia based layered composites, Fract. Response. Key Eng. Mater. (2009) 412.
[16] Z. Chlup, H. Hadraba, L. Slabakova, D. Drdlik, I. Dlouhy, Fracture behaviour of alumina and zirconia thin layered laminate, J. Eur. Ceram. Soc. 32 (9) (2012) 2057–2061.
[17] K.B. Alexander, P.F. Becher, X.-L. Wang, C.-H. Hsueh, Internal stresses and the martensite start temperature in alumina-zirconia composites: effects of composition and microstructure, J. Am. Ceram. Soc. 78 (2) (1995) 291–296.
[18] J. Sanchez-Herencia, J. Moya, A. Tomsia, Microstructural design in alumina-alumina/zirconia layered composites, Scr. Mater. 38 (1) (1998) 1–5.
[19] D.J. Green, P.Z. Cai, G.L. Messing, Residual Stresses in alumina–zirconia laminates, J. Eur. Ceram. Soc. 19 (13–14) (1999) 2511–2517.
[20] M.G. Pontin, M.P. Rao, A.J. Sánchez-Herencia, F.F. Lange, Laminar ceramics utilizing the zirconia tetragonal-to monoclinic phase transformation to obtain a threshold strength, J. Am. Ceram. Soc. 85 (12) (2002) 3041–3048.
[21] R. Bermejo, Y. Torres, A.J. Sanchez-Herencia, C. Baudin, M Anglada, L. Llanes, Fracture behaviour of an Al_2O_3–ZrO_2 multi-layered ceramic with residual stresses due to phase transformations, Fatigue Fract. Eng. Mater. Struct. 29 (1) (2006) 71–78.
[22] R. Bermejo, Y. Torres, C. Baudin, A.J. Sánchez-Herencia, J. Pascual, M. Anglada, L. Llanes, Threshold strength evaluation on an Al_2O_3–ZrO_2 multilayered system, J. Eur. Ceram. Soc. 27 (2–3) (2007) 1443–1448.
[23] R. Bermejo, Y. Torres, M. Anglada, L. Llanes, Fatigue behavior of alumina–zirconia multilayered ceramics, J. Am. Ceram. Soc. 91 (5) (2008) 1618–1625.
[24] R. Bermejo, J. Pascual, T. Lube, R. Danzer, Optimal strength and toughness of Al_2O_3–ZrO_2 laminates designed with external or internal compressive layers, J. Eur. Ceram. Soc. 28 (8) (2008) 1575–1583.
[25] L. Sestakova, R. Bermejo, Z. Chlup, R. Danzer, Strategies for fracture toughness, strength and reliability optimisation of ceramic–ceramic laminates, Int. J. Mater. Res. 102 (6) (2011) 613–626.
[26] J. Requena, R. Moreno, J Moya, Alumina and alumina/zirconia multilayer composites obtained by slip casting, J. Am. Ceram. Soc. 72 (1989) 1511.
[27] K. Maca, H. Hadraba, J. Cihlar, Electrophoretic deposition of alumina and zirconia I. Single-component systems, Ceram. Int. 30 (2004) 843–852.
[28] H. Hadraba, K. Maca, J. Cihlar, Electrophoretic deposition of alumina and zirconia II. Two-component systems, Ceram. Int. 30 (2004) 853–863.
[29] P. Šajgalík, Z. Lenčéš, J. Dusza, Layered composites with self-diagnostic ability, Compos. Part B: Eng. 37 (6) (2006) 515–523.
[30] G. de Portu, L. Micele, G. Pezzotti, Laminated ceramic structures from oxide systems, Compos. Part B 37 (6) (2006) 556–567.
[31] R. Bermejo, C. Baudin, R. Moreno, L. Llanes, A.J. Sanchez-Herencia, Processing optimisation and fracture behaviour of layered ceramic composites with highly compressive layers, Comp. Sci. Tech. 67 (9) (2007) 1930–1938.
[32] H. Hadraba, K. Maca, Z. Chlup, Alumina and zirconia based composites: Part 1.Preparation, Key Eng. Mater. 412 (2009) 221–226.
[33] H. Hadraba, D. Drdlik, Z. Chlup, K. Maca, I. Dlouhy, J. Cihlar, Layered ceramic composites via control of electrophoretic deposition kinetics, J. Eur. Ceram. Soc. 33 (12) (2013) 2005–2012.
[34] H. Hadraba, D. Drdlik, Z. Chlup, K. Maca, I. Dlouhy, J. Cihlar, Laminated alumina/zirconia ceramic composites prepared by electrophoretic deposition, J. Eur. Ceram. Soc. 32 (9) (2012) 2053–2056.
[35] T. Adachi, T. Sekino, T. Nakayama, T. Kusunose, K. Niihara, Measurement of microscopic stress distribution of multilayered composite by X-ray stress analysis, Mater. Lett. 57 (2003) 3057–3062.
[36] M. Leoni, M. Ortolani, M. Bertoldi, V.M. Sglavo, P. Scardi, Nondestructive Measurement of the residual stress profile in ceramic laminates, J. Am. Ceram. Soc. 91 (4) (2008) 1218–1225.
[37] Q. Ma, W. Pompe, J.D. French, D.R. Clarke, Residual stresses in Al_2O_3–ZrO_2 composites: a test of stochastic stress models, Acta Metall. Mater. 42 (5) (1994) 1673–1681.
[38] X.-L. Wang, C.R. Hubbard, K.B. Alexander, P.F. Becher, J. A. Fernandez-Baca, S. Spooner, Neutron diffraction measurements of the residual stresses in Al_2O_3–ZrO_2 (CeO_2) ceramic composites, J. Am. Ceram. Soc. 77 (6) (1994) 1569–1575.
[39] P. Lukas, M. Vrana, P. Mikula, J Vleugels, G. Anne, O. Van der Biest, Neutron diffraction study of the phase-specific stresses in graded alumina/zirconia ceramics, Physica B 350 (2004) e517–e520.
[40] G.A. Maier, J. Keckes, J. Brechbuehl, H. Guerault, R. Bermejo, Position resolved residual stress determination in alumina–zirconia multilayered ceramics, Mater. Sci. Forum (2008) 571–572.
[41] V. Sergo, D.R. Clarke, W. Pompe, Deformation Bands in Ceria-Stabilized tetragonal Zirconia/Alumina: I. Measurement of Internal Stresses, J. Am. Ceram. Soc. 78 (3) (1995) 633–640.
[42] M. Popa, J.M.C. Moreno, P. Hvizdos, R. Bermejo, G. Anne, Residual stress profile determined by piezo-spectroscopy in alumina/alumina-zirconia layers separated by a compositionally graded intermediate layer, Key Eng. Mater. 290 (2005) 328–331.
[43] G. de Portu, L. Micele, Y. Sekiguchi, G. Pezzotti, Measurement of residual stress distributions in Al_2O_3/3Y-TZP multilayered composites by fluorescence and Raman microprobe piezo-spectroscopy, Acta Mater. 53 (2005) 1511–1520.
[44] V. Sergo, X.-L. Wang, D.R. Clarke, P.E. Becher, Residual stresses in alumina/ceria-stabilized zirconia composites, J. Am. Ceram. Soc. 78 (8) (1995) 2213–2214.
[45] V. Sergo, G. Pezzotti, O. Sbaizero, T. Nishida, Grain size influence on residual stresses in alumina/zirconia composites, Acta Mater. 46 (5) (1998) 1701–1710.
[46] P.Z. Cai, D.J. Green, G.L. Messing, Constrained densification of alumina/zirconia hybrid laminates, I: experimental observation of processing defects, J. Am. Ceram. Soc. 80 (8) (1997) 1929–1939.
[47] P.Z. Cai, D.J. Green, G.L. Messing, Constrained densification of alumina/zirconia hybrid laminates, II: viscoelastic stress computation, J. Am. Ceram. Soc. 80 (8) (1997) 1940–1948.
[48] S. Ho, Z. Suo, Tunneling cracks in constrained layers, J. Appl. Mech. 60 (1993) 890–894.
[49] S. Ho, C. Hillman, F.F. Lange, Z. Suo, Surface cracking in layers under biaxial, residual compressive stress, J. Am. Ceram. Soc. 78 (9) (1995) 2353–2359.
[50] A.J. Sánchez-Herencia, C. Pascual, J. He, F.F. Lange, ZrO_2/ZrO_2 layered composites for crack bifurcation, J. Am. Ceram. Soc. 82 (6) (1999) 1512–1518.
[51] K. Hbaieb, R. McMeeking, F. Lange, Crack bifurcation in laminar ceramics having large compressive stress, Int. J. Solids Struct. 44 (10) (2007) 3328–3343.

PUBLIKACE XIII

Journal of the European Ceramic Society 37 (2017) 4287–4295

Contents lists available at www.sciencedirect.com

Journal of the European Ceramic Society

journal homepage: www.elsevier.com/locate/jeurceramsoc

Dilatometric study of anisotropic sintering of alumina/zirconia laminates with controlled fracture behaviour

Karel Maca[a,b,*], Vaclav Pouchly[a,b], Daniel Drdlik[a,b], Hynek Hadraba[c], Zdenek Chlup[c]

[a] CEITEC BUT, Brno University of Technology, Purkynova 123, 61669 Brno, Czech Republic
[b] Institute of Materials Science and Engineering, Brno University of Technology, Technicka 2896/2, 61669 Brno, Czech Republic
[c] CEITEC IPM, Institute of Physics of Materials, Academy of Sciences of the Czech Republic, Zizkova 513/22, 61662 Brno, Czech Republic

ARTICLE INFO

Article history:
Received 22 January 2017
Received in revised form 10 April 2017
Accepted 11 April 2017
Available online 23 April 2017

Keywords:
Alumina/zirconia laminate
Sintering shrinkage
Master sintering curve
Crack deflection

ABSTRACT

Al_2O_3 and ZrO_2 monoliths as well as layered Al_2O_3/ZrO_2 composites with a varying layer thickness ratio were prepared by electrophoretic deposition. The sintering shrinkage of these materials in the transversal (perpendicular to the layers, i.e. in the direction of deposition) as well as in the longitudinal (parallel with layers interfaces) direction were monitored using high-temperature dilatometry. The sintering of layered composites exhibited anisotropic behaviour. The detailed study revealed that sintering shrinkage in the longitudinal direction was governed by alumina (material with a higher sintering temperature), whilst in the transversal direction it was accelerated by the directional sintering of zirconia layers. For interpretation of such anisotropic sintering kinetics, the Master Shrinkage Curve model was developed and applied. Crack propagation through laminates with a different alumina/zirconia thickness ratio was described with the help of scanning electron microscopy and confocal laser microscopy.

© 2017 Elsevier Ltd. All rights reserved.

1. Introduction

Layered ceramic composites (laminates) can be prepared by various techniques like tape casting, slip casting, or electrophoretic deposition (EPD). EPD is an experimentally simple and cheap method enabling the formation of deposits from stable suspensions. EPD is a powerful method for the preparation of ceramic laminates [1,2], but also of monoliths [3] or structural composites such as particle mixed composites and functionally gradient materials [4–6]. In the last decades, ceramic laminates have been one of the main areas of focus for material scientists particularly for their crack deflection behaviour [7,8].

Internal stresses are responsible for unique crack propagation in ceramic laminates [9]. The tension arising during sintering is usually described by the constrained sintering model. Unfortunately, this model is designed for the sintering of one layer on a rigid substrate [10]. However, laminate composites consist of hundreds of individual layers supporting each other. Constrained sintering causes hindering of sintering and very often the generation of cracks, or crack like defects [11,12]. Additionally, internal stresses that are due to a mismatch in the coefficient of thermal expansion (CTE) are generated during cooling as well [11].

The magnitude of residual tensile stress (σ_r) in the ZrO_2 layer can be calculated using the following relation [9,13].

$$\sigma_{rZrO_2} = \frac{(\alpha_{ZrO_2} - \alpha_{Al_2O_3}) \cdot \Delta T \cdot E_{ZrO_2}}{1 - \upsilon_{ZrO_2}} \cdot \left(1 + \frac{d_{ZrO_2}}{d_{Al_2O_3}} \cdot \frac{E_{ZrO_2} \cdot (1 - \upsilon_{Al_2O_3})}{E_{Al_2O_3} \cdot (1 - \upsilon_{ZrO_2})}\right)^{-1}, \quad (1)$$

where d is the layer thickness, α is the coefficient of linear thermal expansion, ΔT is the difference between the sintering and the current temperature, ν is Poisson's ratio, and E is the modulus of elasticity. Stress in the Al_2O_3 phase can be obtained analogously. In contrast with ZrO_2, stress in the alumina layer is compressive. The stresses are directed parallel with the interfaces.

For a better understanding of the fracture properties of ceramic laminates, the detailed study of crack propagation in laminates with various values of internal stresses appears appropriate. It follows from Eq. (1) that internal stresses can be designed by the proper choice of thicknesses ratio of individual layers. To tailor the thicknesses of the layers in the final laminate, the exact control of the deposition kinetics as well as sintering shrinkage is needed. Since the detailed study of deposition kinetics was presented in our previous papers [1,14], the goal of this work is the study of sintering behaviour carried out with the help of high-temperature dilatometry [15].

The concept of Master Sintering Curve (MSC in the following) is a good engineering tool for optimizing and predicting the sintering

* Corresponding author at: CEITEC BUT, Brno University of Technology, Purkynova 123, 61669 Brno, Czech Republic.
E-mail address: karel.maca@ceitec.vutbr.cz (K. Maca).

http://dx.doi.org/10.1016/j.jeurceramsoc.2017.04.030
0955-2219/© 2017 Elsevier Ltd. All rights reserved.

process which can also be used for the determination of sintering activation energy [16]. The MSC model was derived under conditions of validity of some geometrical and physical conditions [16] and it is used in the form of relation between density and function Θ (describing the thermal history of the sintering with the help of parameter Q):

$$\frac{k}{\gamma\Omega D_0}\int_{\rho_0}^{\rho}\frac{(G(\rho))^n}{3\rho\Gamma(\rho)}d\rho \equiv f(\rho) = \int_0^t \frac{1}{T}\exp\left(-\frac{Q}{RT}\right)dt \equiv \Theta, \quad (2)$$

where γ is the surface energy, Ω is the atomic volume, k is the Boltzmann constant, R is the gas constant, T is the thermodynamic temperature, G is the mean grain size, D_0 is the coefficient of a diffusion process (only one dominant diffusion process is considered), Γ represents scaling parameters that relate different geometric features as the driving force of sintering and the mean diffusion distance to the grain size, t is the time, ρ is sample density, Q is the activation energy of sintering, and n has a value of 3 (for volume diffusion) or 4 (for grain boundary diffusion).

Not only does the construction of MSC require several sintering experiments performed at different heating schedules, but also time consuming mathematical iteration. Recently, some mathematical approaches enabling the easy construction of MSC from few dilatometric sintering experiments have been published [17,18], shown by the dramatic rise of references being made to MSC in the literature. The basic MSC model has already been modified for many special purposes. An and Han [19,20] extended the MSC model to pressure-assisted sintering and Enneti et al. to field-assisted sintering [20,21]. An et al. [22] and Raether et al. [23] used the MSC model for construction of sintering kinetics diagrams. Di Antonio et al. [24] and Wang et al. [25] showed that MSC can be extended to all Arrhenius type equations. Recently, Song et al. [26] and Pouchly et al. [27] showed that MSC can also be used for the description of sintering behaviour when the change of the controlling sintering mechanism has to be taken into account.

The limitations of the MSC model arise when a more complicated sintering material is examined. For example, in the case of a lamellar composite, the shrinkage is not isotropic [28], and therefore the geometrical assumption of the MSC model is not fulfilled [29]. The densification curve of the sample cannot be calculated from one-dimensional dilatometric shrinkage. Hence, the second goal of this work is modification of the MSC model from density related to shrinkage related. Such a modified MSC can then be applied to lamellar composites with the aim to use the results of such analysis for the description of processes which occur during sintering.

For this study, the Al_2O_3/ZrO_2 laminates prepared by EPD were chosen since the authors have much experience with the preparation of these laminates with strongly bonded layers. Using sintered composites with various layer designs, the crack propagation was demonstrated and discussed.

Table 1
Ceramic powder materials used for electrophoretic deposition.

Material	Manufacturer	Grade	Mean particle size[a] [μm]
Al_2O_3	Malakoff Ind., USA	HP-DBM	0.47
ZrO_2	Tosoh, Japan	TZ-3YS-E	0.14

[a] Values were calculated from specific surface area given by the producer.

2. Experimental

2.1. Electrophoretic deposition

For preparation of ceramic monoliths and laminates, alumina and tetragonal zirconia (stabilized by 3 mol% of Y_2O_3) powders were used. Detailed information about ceramic powders is shown in Table 1. Suspensions contained 15 wt.% of alumina or zirconia, 12.75 wt.% of monochloroacetic acid (99%, Aldrich, Germany) used as a stabilizer and 72.25 wt% of the dispersion medium – 2-propanol (p.a., Onex, Czech Republic).

Electrophoretic deposition was performed in an electrophoretic glass cell with the constant current mode of 5 mA. The distance between stainless steel electrodes with an effective area of 18.2 cm^2 was set to 26 mm. In order to prevent particles from settling on the bottom of the EPD cell, the suspension was repeatedly stirred every 5 min during electrophoretic deposition. The repeated transfer of the deposition electrode from the alumina to the zirconia suspension (and vice versa) enabled the preparation of ceramic laminates with about 100 alternating alumina and zirconia layers with a thickness ratio of 2:1, 1:1, and 1:2 (denoted as Z33, Z50, and Z67, respectively). The precise control of deposition kinetics enabled the preparation of ceramic laminates with well defined thicknesses of individual layers [30]. For comparison, alumina (denoted as A), and zirconia (denoted as Z) monoliths were prepared during 90 min and 140 min long depositions, respectively. A detailed description of all prepared deposits is given in Table 2. All deposits were dried after the deposition for at least 24 h at room temperature. After the drying, the deposits were annealed at 800 °C/1 h in air.

2.2. Sintering of ceramic samples and constructing of the modified MSC

The sintering of the test samples was done in a contact high-temperature dilatometer (L70/1700, Linseis, Germany), where the sample shrinkage was in-situ monitored both in the transversal direction (perpendicular to alumina/zirconia interfaces, i.e. parallel to the direction of deposition) as well as in the longitudinal one (parallel to alumina/zirconia interfaces, i.e. perpendicular to the direction of deposition). Samples were cut from the deposits in the shape of prismatic bars, with a cross-section ca 4 × 4 mm, height ca 10 mm (longitudinal sample) resp. ca 5 mm (transversal sample).

The coefficient of thermal expansion (α) of all the samples was calculated according to Eq. (3):

$$\alpha = \frac{\varepsilon_{room} - \varepsilon_{T\max}}{(T_{room} - T_{\max})\cdot 100}, \quad (3)$$

Table 2
Characteristics of deposited and sintered samples.

Laminate	Al_2O_3/ZrO_2 thickness [μm/μm]	ZrO_2 content [vol%]	Green density [%TD]	Final density [%TD]	Grain size Al_2O_3/ZrO_2 [μm/μm]	Final shrinkage	
						T [%]	L [%]
A	50/0	0	62.0	99.40	1.3/-	17.5	14.2
Z33	50/25	33.3	57.3	99.20	1.6/0.6	22.7	14.9
Z50	50/50	50.0	55.0	99.57	1.2/0.4	24.2	15.4
Z67	25/50	66.7	52.7	98.02	1.6/0.6	27.2	16.1
Z	0/50	100	48.0	99.92	-/0.3	22.4	21.4

Note: T = transversal, L = longitudinal.

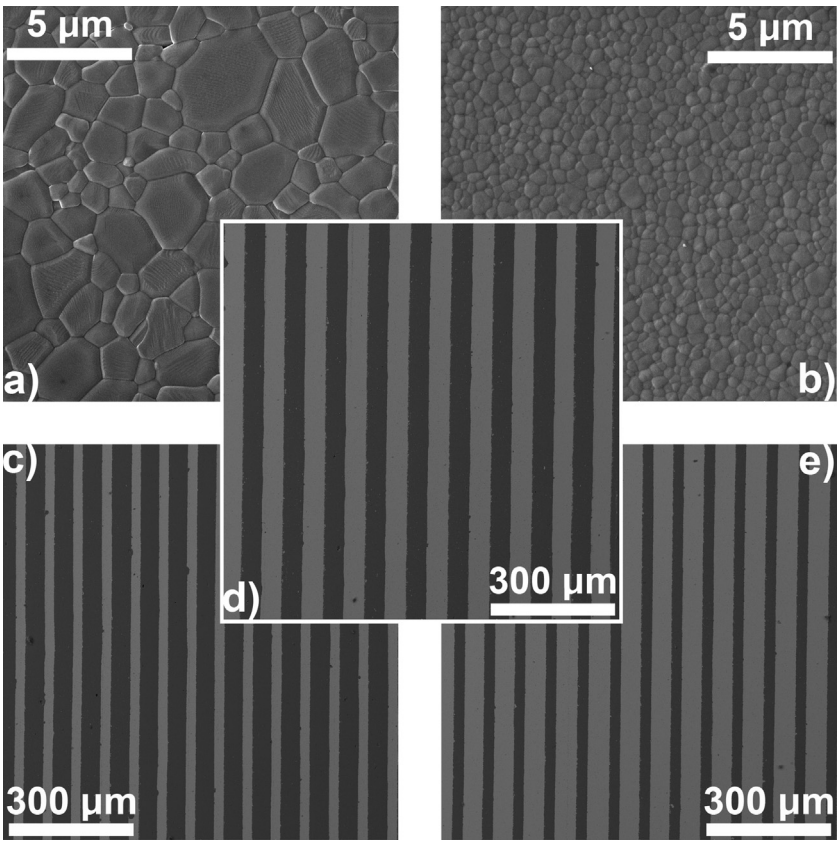

Fig. 1. Microstructure of sintered materials a) A, b) Z, c) Z33 d) Z50 e) Z67. In the case of composites, the bright layers consist of zirconia and the dark ones of alumina.

where ε_{room} is the shrinkage after cooling, ε_{Tmax} is the shrinkage at the end of the dwell, T_{room} is the temperature after cooling, and T_{max} is the temperature at the end of the dwell.

Knowing the values of α, the sample length changes caused by thermal dilatation can be eliminated which leads to so called sintering shrinkage:

$$\varepsilon(t, T) = \varepsilon_{instant}(t, T) - \alpha \cdot 100 \cdot (T - T_{room}), \quad (4)$$

where $\varepsilon_{instant}$ (t,T) is instantaneous measured shrinkage, t is time, and T is actual temperature.

The sintering was performed at 1500 °C and 2 h dwell with a heating rate of 10 °C/min and a cooling rate of 5 °C/min. In order to obtain different heating profiles for MSC construction, samples A, Z50, and Z were also sintered with heating rates of 2, 5, and 20 °C/min. All calculations associated with the modified MSC model were performed with the help of an automatic procedure which uses Mean Perpendicular Curves Distance (MPCD) for estimating the best overlap of individual curves [17]. This procedure was in this work adjusted for analysis of sintering shrinkage. The 95% confidence interval for sintering activation energy Q was established by fitting of MPCD = f(Q) dependence using the weighted nonlinear regression.

2.3. Microstructure of sintered samples

Green as well as final densities of layered monoliths and composites were determined using Archimedes' method (EN 623-2) with distilled water as a liquid media. The theoretical densities (TD) used for the relative densities calculation were 3.99 g cm^{-3} for alumina and 6.08 g cm^{-3} for zirconia. Theoretical densities of laminates were calculated by a rule of mixtures according to the volume fractions of alumina and zirconia. The samples were ground and polished by the standard ceramographic methods and then thermally etched at 1400 °C for 5 min (heating rate of 20 °C/min) to expose the grain boundaries. The microstructure of the samples was examined using scanning electron microscopy (Lyra 3, Tescan, Czech Republic). The grain size was estimated by the linear intercept method (EN 623-3) with a correction factor of 1.56. Minimum of 250 grains were measured at magnifications 15kx and 30kx for alumina and zirconia, respectively.

2.4. Fracture behaviour of laminates

Crack propagation in laminates was observed on the fracture surfaces of fracture toughness experiments using the Single Edge V-Notch Beam (SEVNB in the following) technique. The test samples had a shape of bars with a rectangular cross-section and a starting notch was prepared using a razor blade and subsequent application of diamond paste. The typical notch radius reached by described technique was about 10 µm. Note that notch radius had no influence on subsequent crack propagation. The loading of the samples of nominal dimensions 2×1.6 mm was conducted in a three point bending configuration with the span of 10 mm aiming to have a controlled stress field in the vicinity of the notch. A confocal laser microscope (LEXT OLS 3100, Olympus, Japan) was employed for the fractographic observations, 3D surface reconstruction, and measurements.

3. Results and discussion

3.1. Microstructure properties of sintered materials

Fig. 1 shows the microstructure of sintered ceramic samples A, Z33, Z50, Z66, and Z. The final relative densities of all samples exceeded 98%TD. The interface between individual layers after sintering is smooth and does not contain any extra porosity. In this

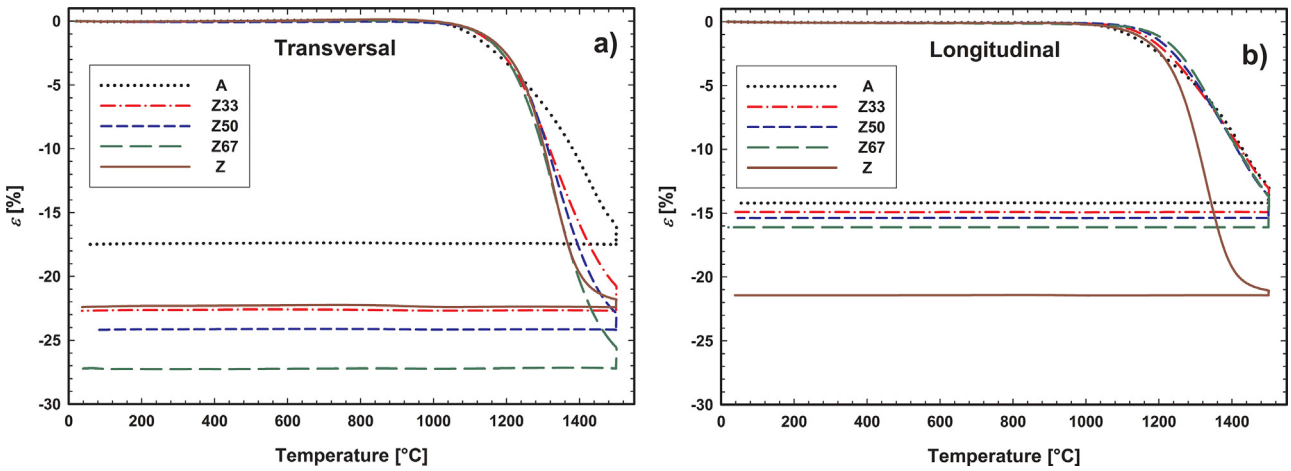

Fig. 2. Sintering shrinkage of all samples in the a) transversal and b) longitudinal direction.

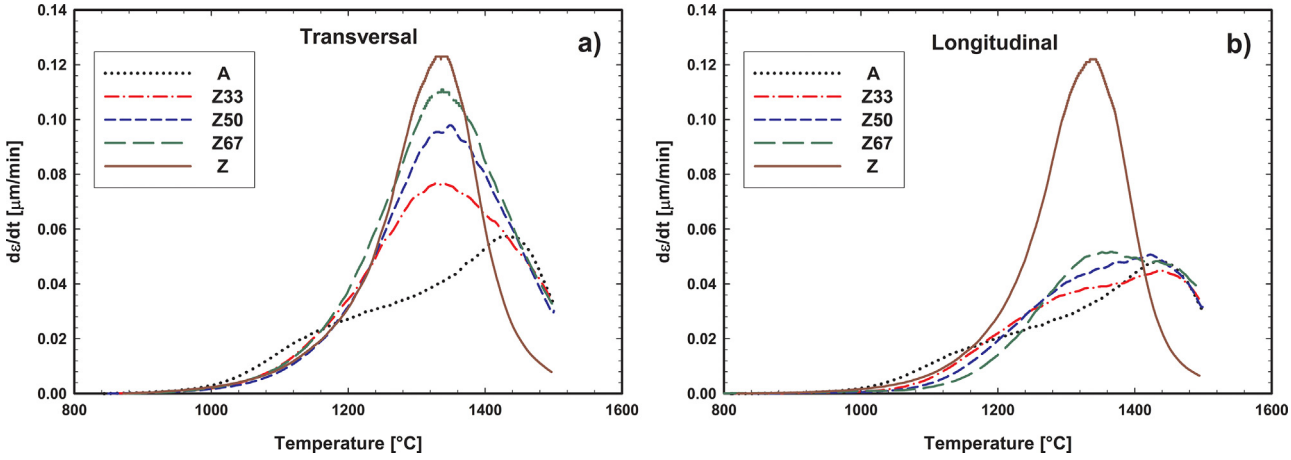

Fig. 3. Sintering shrinkage rate of all samples in the a) transversal and b) longitudinal direction.

regard, EPD was found as the more promising method in preparation of laminate composites than the commonly used methods of tape-casting [31,32], sequential slip casting [33], centrifugal casting [34], or screen printing [35].

Generally, ceramic laminate materials can be separated into two types. The first ones are laminates with weakly bonded layers. Typically, these laminates have fracture behaviour under loading known as delamination. The second types of laminates have interfaces between individual layers strongly bonded resulting in internal stresses. The crack path during loading is, therefore, influenced by tensile or compressive stresses developed during cooling from the sintering temperature. The interfaces between individual layers in presented laminates are flat and strongly bonded.

3.2. Dilatometric analysis of sintering shrinkage

The sintering shrinkage of all deposits, measured in transversal as well as longitudinal directions, is given in Fig. 2. It can be seen that sintering shrinkage of the alumina monolith is smaller than that of the zirconia (refer to Fig. 2a for transversal direction, resp. Fig. 2b for longitudinal). The reason is the lower green density of the zirconia green body (48%TD for zirconia, resp. 62%TD for alumina). The difference of green densities may be caused by particle size and shape, orientation of particles in the electrical field, capillary forces, etc. [36]. Fig. 2a, resp. b, and Table 2 also show different sintering shrinkage in the longitudinal and transversal directions of alumina (difference in the final shrinkage of 3.3%) as well as zirconia (difference in the final shrinkage of 1.0%) monoliths. The possible explanation of sintering shrinkage anisotropy of both monoliths can be preferential packing during the EPD [37]. This hypothesis is strengthened by the fact that shrinkage anisotropy is larger for alumina with oval (anisotropic) initial powder particles.

In the case of shrinkage in the transversal direction (see Fig. 2a), one could expect that laminates shrinkage in this direction will be the superposition of alumina and zirconia shrinkages and after sintering it will reach a value between 17.5% (final transversal shrinkage of alumina monolith) and 22.4% (final transversal shrinkage of zirconia monolith). In reality, the final sintering shrinkage of all three composites was higher: 22.7% for Z33, 24.2% for Z50, and even 27.2% for Z67 (refer to Table 2). To explain this apparent disproportion, we need to heed the sintering shrinkage in the longitudinal direction. As can be seen in Fig. 2b, in this direction the sintering shrinkage of all laminates is very similar to the shrinkage of the alumina monolith, therefore zirconia layers are forced to densify preferentially in the transversal direction [1,32]. This is supported by the observation of an increasing degree of shrinkage anisotropy with an increasing content of zirconia (see Table 2).

The shrinkage rate of both monoliths and their laminate composites is shown in Fig. 3. It is well known [38] that with decreasing particle size the sintering temperature decreases as well. In our case, the maximal shrinkage of zirconia (particle size 140 nm) occurred at ca 1340 °C, whilst that of alumina (particle size 470 nm) was at ca 1410 °C. This fact, together with the strong bond between alumina and zirconia layers, is probably responsible for the high

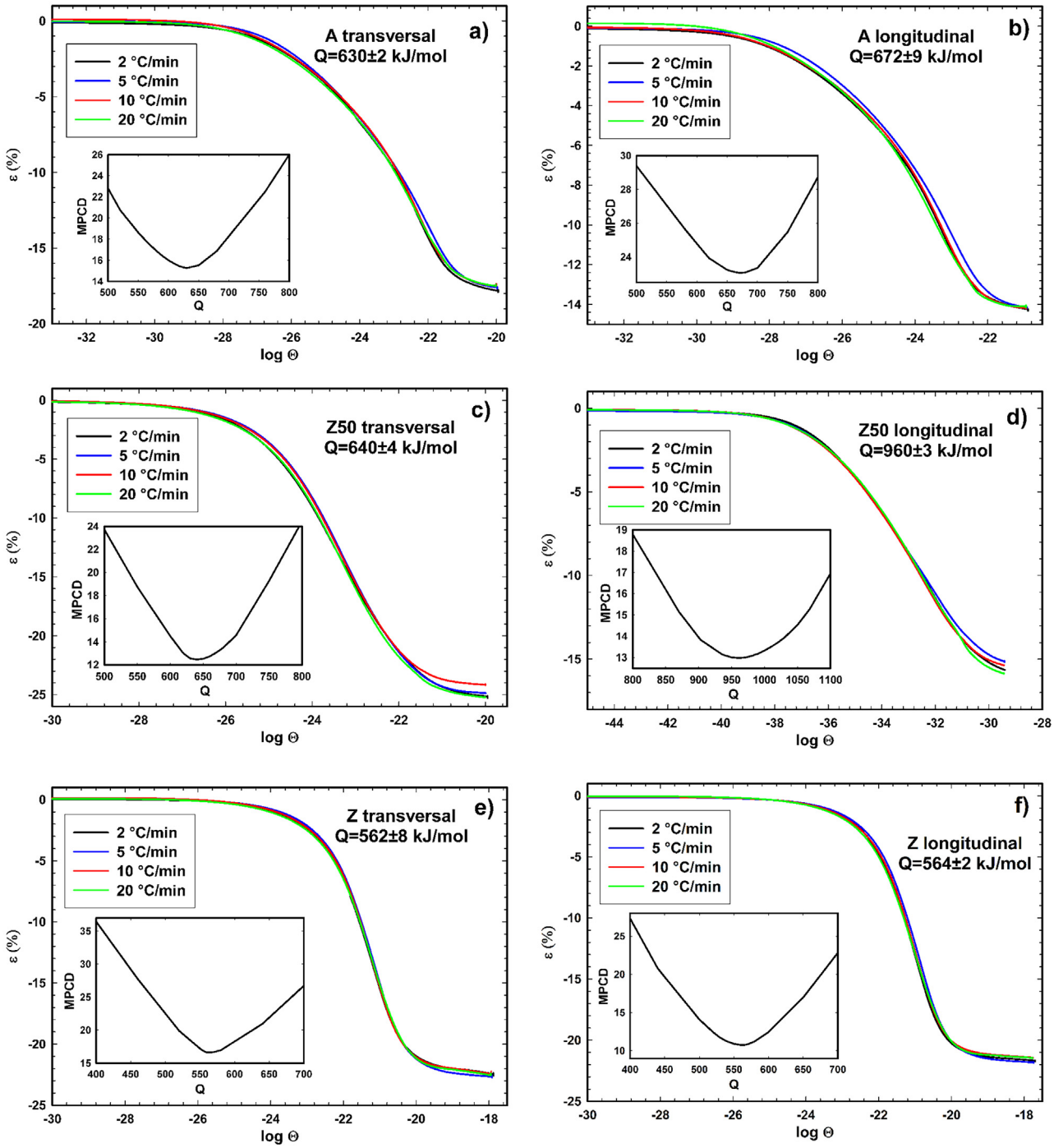

Fig. 4. Master Shrinkage Curves of samples: (a, b) A, (c, d) Z50, and (e, f) Z in the longitudinal and transversal directions.

degree of anisotropy of the laminates. Zirconia layers tend to shrink at temperatures of around 1300 °C, but in the longitudinal direction they are bound at inter-layers by alumina which is still rigid at this temperature. Therefore, zirconia shrinks particularly in the transversal direction. It can be seen in Fig. 3b that the maximal shrinkage rate of laminates in the longitudinal direction is shifted to temperatures of about 1400 °C, which is the temperature appropriate for the sintering of alumina. Therefore, the sintering of the composite in the longitudinal direction is controlled by the material with a higher sintering temperature. As a consequence, the sintering shrinkage of the zirconia layers is smaller in the longitudinal direction than without this constraint. The degree of the sintering anisotropy of the zirconia increased with its increasing volume concentration and it is necessary to take into account this effect when we design a laminate with precise thickness of individual layers.

3.3. Modified Master Sintering Curve – Master Shrinkage Curve

The model of MSC can be used for the calculation of activation energy of sintering, which allows a deeper view into the physical background of the sintering process. However, the results in the previous chapter showed that the sintering of ceramic laminates exhibits a significant degree of anisotropy, so the utilization of MSC in its original form is not possible. The following part shows the

way to modify the MSC model to make it suitable for describing anisotropic sintering.

Hansen and co-workers [39] formulated the model of sintering in the open and closed porosity stage which relates the linear shrinkage rate of a compact to grain boundary and volume diffusion coefficient, surface tension, and microstructure variables

$$-\frac{d\varepsilon}{dt} = \frac{\gamma\Omega}{kT}\left(\frac{\Gamma_v D_v}{G^3} + \frac{\Gamma_b \delta D_b}{G^4}\right), \quad (5)$$

where D_v resp. D_b are the coefficients of volume, resp. grain boundary diffusion, Γ_v, and Γ_b represent scaling parameters that relate different geometric features as the driving force of sintering and the mean diffusion distance to the grain size, and δ is the grain boundary thickness.

Assuming that

- the grain size evolution in the course of sintering is independent of thermal history and it is only a function of density; and
- one sintering mechanism dominates the whole sintering process,

we can rearrange Eqs. (5) to (6)

$$\frac{-k}{\gamma\Omega D_0}\int_0^{\varepsilon_f}\frac{(G(\varepsilon))^n}{\Gamma(\varepsilon)}d\varepsilon = \Theta = \int_0^t \frac{1}{T}\exp\left(-\frac{Q}{RT}\right)dt, \quad (6)$$

which relates microstructural parameters with thermal history of the sample.

The modified Master Sintering Curve (Master Shrinkage Curve) is now defined as a relationship between ε and the right side of Eq. (6). If the concept of Master Shrinkage Curve is correct, there must exist one activation energy Q for which all functions of $\varepsilon = f(\Theta)$ (calculated for all used heating profiles) converge onto a single (master) curve. The criterion of Mean Perpendicular Curve Distance (MPCD) [20] can be used to find the best overlap of individual curves. Both monoliths and one laminate (Z50) were sintered with heating rates of 2, 5, 10, and 20 °C in transversal as well as in longitudinal directions and the constructed Master Shrinkage Curves are shown in Fig. 4.

Fig. 4a–f show a good overlap of individual curves and the MPCD criterion exhibits a single sharp minimum. The values of activation energies established from the Master Shrinkage Curve model can be seen in Fig. 5.

The sintering activation energy established from the MSC concept is commonly interpreted as apparent activation energy for the mechanism that controls sintering [40]. The published values of sintering activation energies vary through the literature very strongly (Al_2O_3: 342–1064 kJ/mol [41–43]; t-ZrO_2 310–1220 kJ/mol [27,44]), which is probably caused by the different processing methods, level of impurities, temperature range, and also by the used models. For this given experimental procedure, the

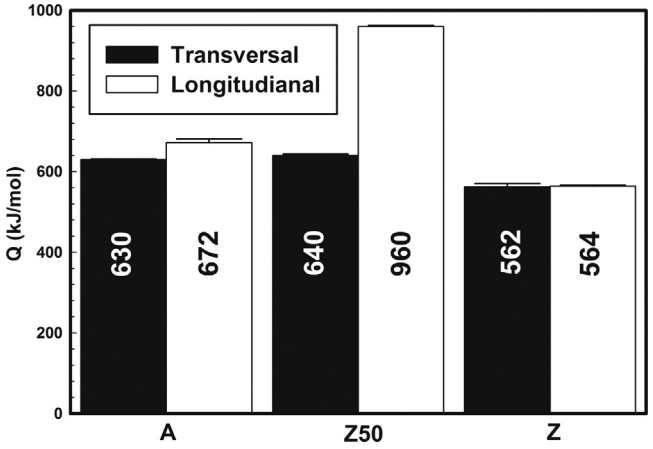

Fig. 5. Activation sintering energies of alumina monolith, Z50 laminate, and zirconia monolith.

activation energies of sintering of alumina and zirconia monoliths are in the range presented by other authors and they do not exhibit either no (for zirconia) or minimal (for alumina) difference between the transversal and the longitudinal direction.

Despite the final longitudinal shrinkage of the Z50 composite being similar to alumina, the sintering of Z50 laminate is characterized by a significant increase of the sintering activation energy in the longitudinal direction. The increase of activation energy of sintering shrinkage was expected due to a constrained sintering [45] which influences the shape of the shrinkage curves (see Fig. 2b). In view of the dilatometric analysis of sintering shrinkage performed within this work, we believe that the increase of sintering activation energy of the composite can be caused by preferential sintering of zirconia in the transversal direction (see Fig. 6) which resulted in the deformation of the originally isotropic pores (see Fig. 7).

3.4. Crack propagation through the laminates with different layer thickness ratio

The crack propagation through laminates with a different alumina/zirconia thickness ratio (namely 2:1, 1:1, and 1:2) was studied by SEM and confocal laser microscopy. SEM microphotographs in the upper part of Fig. 8 show the side surface view of the fracture surface in the central part of the crack propagating from the notch after fracture toughness experiments using the SEVNB technique. The 3D reconstructions of fracture surfaces together with their height profiles showing variations in the crack deflection according to the layer are given in the middle, resp. bottom part of Fig. 8. Note that the darker phase is alumina and the brighter one is a zirconia layer, and that crack propagation direction is along the X-axis. It clearly follows from Fig. 8 that the declination of the crack propagation from its original direction is strongly influenced by the

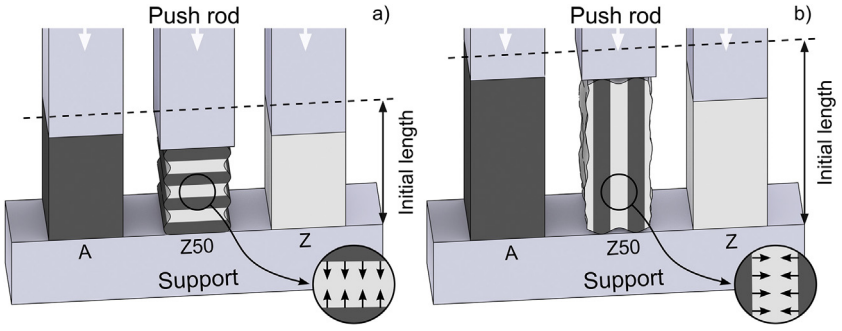

Fig. 6. Scheme of sintering shrinkage in alumina/zirconia laminates in the a) transversal and b) longitudinal direction. Arrows indicate preferential shrinkage.

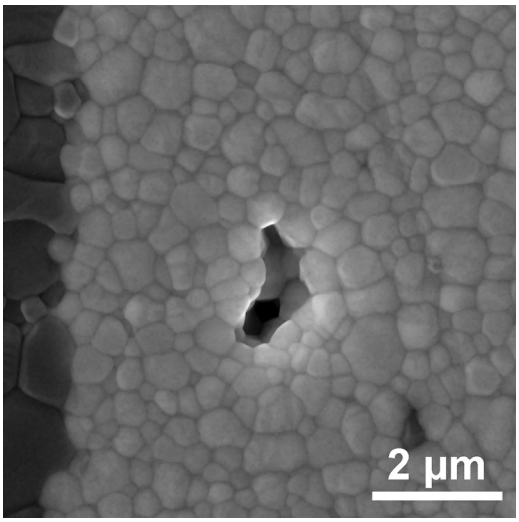

Fig. 7. SEM evidence of elongated pores in zirconia layer.

laminate design (see declination angles in Fig. 8). The highest crack declination was reached in sample Z67 (Fig. 8c), where the crack was deflected by about 550 μm at a distance of 250 μm, whilst in Z33 laminate (Fig. 8a) it was only 30 μm at the same distance. The fracture behaviour of the laminates prepared by the optimised sintering of the EPD green bodies that have strong bonds is influenced by the developed internal stresses within the layers during cooling from the sintering temperature. The stresses retained in the material as a consequence of constrained sintering are negligible compared to previous ones (due to a difference of two orders of magnitude) [11]. The values of internal stresses calculated according to Eq. (1) and given material constants [13,46] are listed in Table 3.

Due to the higher thermal expansion of zirconia [46], tensile stress is present in zirconia layers. It led to the crack propagation inclining to the loading direction (i.e. along the X-axis as is shown in Fig. 8). This behaviour is typical and it can be attributed to the tensile stresses being similar and relatively low for all laminates under investigation. The main difference in the fracture behaviour of laminates under investigation was observed in the alumina layers with substantially different compressive stresses. The deviation of the crack from the loading axis propagating through the alumina layer (see Fig. 8) is the result of a combination of three effects: the difference in the elastic modulus, the tilt of the laminae plane to the loading axis, and the influence of internal compressive stresses. The effect of the elastic modulus can be expected to be the same for all laminates, not being affected by the layer thickness. The effect of

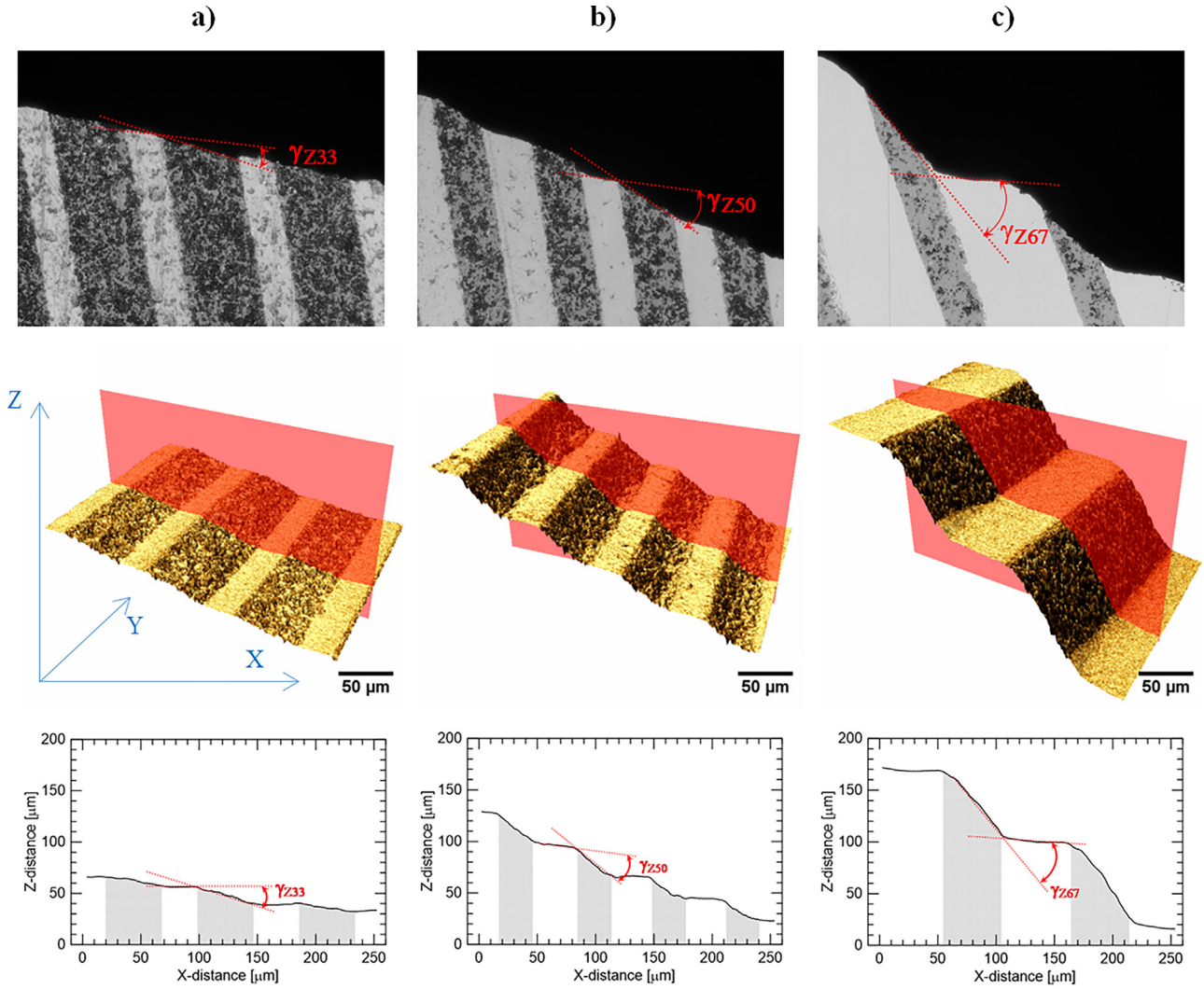

Fig. 8. Fracture surfaces side view (upper line of figures), their confocal microscope image (middle line of figures) and quantitative analysis (bottom line of figures) describing declination angles at alumina/zirconia interfaces for a) Z33, b) Z50), and c) Z67 laminates.

Table 3
Internal stresses developed during cooling down from sintering temperature (A – alumina, Z – zirconia, sign in stress means: minus = compressive; plus = tensile).

Monolith	α [10^{-6} K^{-1}]	E [GPa]	Poisson ratio [–]	Laminate	Nominal internal stress [MPa]	
					layer A	layer Z
A	8.915	380	0.26	Z33	−279	447
Z	10.275	210	0.31	Z50	−440	352
				Z67	−617	247

the laminate tilt predetermining the entering angle of the starting crack from the notch plays an important role, but it is independent of the volume ratio, too. Contrary to that, the effect of the internal compressive stresses affects the declination angle significantly as demonstrated in Fig. 8 and it is dependent only on the materials volume ratio. According to expectation and observation, the higher the compressive stresses are the higher the deviation of the crack from the loading direction.

4. Conclusions

Alumina and zirconia monoliths, as well as their lamellar composites with three different thickness ratios, were prepared by electrophoretic deposition. The detailed dilatometric study of their sintering shrinkage revealed that sintering shrinkage of laminates was constrained in the longitudinal direction (parallel with layers interfaces) by alumina which was densified at higher temperatures than zirconia. As a consequence, sintering shrinkage in the transversal direction (perpendicular to layers) was accelerated by the preferential shrinkage of zirconia in this direction. The model of Master Sintering Curve was modified in order to describe the sintering of anisotropic systems. The enhanced sintering activation energy in the longitudinal direction confirmed the constrained sintering of laminates. The detailed fractographic analysis of crack propagation in laminates with well-defined layer thickness ratios revealed the importance of individual parameters on its declination.

Acknowledgements

The authors acknowledge the support of the Grant agency of the Czech Republic under grant no. 15-06390S. The research has also been financially supported by the Ministry of Education, Youth and Sports of the Czech Republic under the project CEITEC 2020 (LQ1601).

References

[1] H. Hadraba, D. Drdlik, Z. Chlup, K. Maca, I. Dlouhy, et al., Layered ceramic composites via control of electrophoretic deposition kinetics, J. Eur. Ceram. Soc. 33 (2013) 2305–2312.
[2] L. Vandeperre, O. VanDerBiest, W.J. Clegg, Silicon carbide laminates with carbon interlayers by electrophoretic deposition, Key Eng. Mater. 127–131 (1997) 567–573.
[3] D. Drdlik, E. Bartonickova, H. Hadraba, J. Cihlar, Influence of anionic stabilization of alumina particles in 2-propanol medium on the electrophoretic deposition and mechanical properties of deposits, J. Eur. Ceram. Soc. 34 (2014) 3365–3371.
[4] E. Askari, M. Mehrali, I.H.S.C. Metselaar, N.A. Kadri, M.M. Rahman, Fabrication and mechanical properties of Al_2O_3/SiC/ZrO_2 functionally graded material by electrophoretic deposition, J. Mech. Behav. Biomed. 12 (2012) 144–150.
[5] P. Hvizdos, D. Jonsson, M. Anglada, G. Anne, O. Van Der Biest, Mechanical properties and thermal shock behaviour of an alumina/zirconia functionally graded material prepared by electrophoretic deposition, J. Eur. Ceram. Soc. 27 (2007) 1365–1371.
[6] M. Mehrali, H. Wakily, I.H.S.C. Metselaar, Residual stress and mechanical properties of Al_2O_3/ZrO_2 functionally graded material prepared by EPD from 2-butanone based suspension, Adv. Appl. Ceram. 110 (2011) 35–40.
[7] H. Moon, M.G. Pontin, F.F. Lange, Crack interactions in laminar ceramics that exhibit a threshold strength, J. Am. Ceram. Soc. 87 (2004) 1694–1700.
[8] W.A. Cutler, F.W. Zok, F.F. Lange, P.G. Charalambides, Delamination resistance of two hybrid ceramic-composite laminates, J. Am. Ceram. Soc. 80 (1997) 3029–3037.
[9] C. Hillman, Z.G. Suo, F.F. Lange, Cracking of laminates subjected to biaxial tensile stresses, J. Am. Ceram. Soc. 79 (1996) 2127–2133.
[10] Y. Zhao, L.R. Dharani, Theoretical-model for the analysis of a ceramic thin-film sintering on a non-sintering substrate, Thin Solid Films 245 (1994) 109–114.
[11] P.Z. Cai, D.J. Green, G.L. Messing, Constrained densification of alumina/zirconia hybrid laminates. 1. Experimental observations of processing defects, J. Am. Ceram. Soc. 80 (1997) 1929–1939.
[12] R.K. Bordia, R. Raj, Sintering behavior of ceramic films constrained by a rigid substrate, J. Am. Ceram. Soc. 68 (1985) 287–292.
[13] H. Hadraba, J. Klimes, K. Maca, Crack propagation in layered Al_2O_3/ZrO_2 composites prepared by electrophoretic deposition, J. Mater. Sci. 42 (2007) 6404–6411.
[14] K. Maca, H. Hadraba, J. Cihlar, Electrophoretic deposition of alumina and zirconia – I. Single-component systems, Ceram. Int. 30 (2004) 843–852.
[15] K. Maca, V. Pouchly, A.R. Boccaccini, Sintering densification curve – a practical approach for its construction from dilatometric shrinkage data, Sci Sinter. 40 (2008) 117–122.
[16] H.H. Su, D.L. Johnson, Master sintering curve: a practical approach to sintering, J. Am. Ceram. Soc. 79 (1996) 3211–3217.
[17] V. Pouchly, K. Maca, Master sintering curve – a practical approach to its construction, Sci. Sinter. 42 (2010) 25–32.
[18] D.C. Blaine, S.J. Park, R.M. German, Linearization of master sintering curve, J. Am. Ceram. Soc. 92 (2009) 1403–1409.
[19] K. An, M.K. Han, Microstructural evolution based on the pressure-assisted master sintering surface, Mater. Sci. Eng. A—Struct. 391 (2005) 66–70.
[20] V. Pouchly, K. Maca, Y. Xiong, J.Z. Shen, Master sintering surface –A practical approach to its construction and utilization for spark plasma sintering prediction, Sci. Sinter. 44 (2012) 169–175.
[21] R.K. Enneti, M.G. Bothara, S.J. Park, S.V. Atre, Development of master sintering curve for field-assisted sintering of HfB2-20SiC, Ceram. Int. 38 (2012) 4369–4372.
[22] K.J. An, M.K. Han, H.J. Kim, The pressure-Assisted master sintering surface of metallic powder mixture, Mater. Trans. 51 (2010) 822–825.
[23] F. Raether, P.S. Horn, Investigation of sintering mechanisms of alumina using kinetic field and master sintering diagrams, J. Eur. Ceram. Soc. 29 (2009) 2225–2234.
[24] C.B. DiAntonio, K.G. Ewsuk, D. Bencoe, Extension of master sintering curve theory to organic decomposition, J. Am. Ceram. Soc. 88 (2005) 2722–2728.
[25] S.Y. Wang, M.H. Teng, Why a master sintering curve model can be applied to the sintering of nano-sized particles? J. Alloy Compd. 504 (2010) S336–S339.
[26] X.C. Song, J. Lu, T.S. Zhang, J. Ma, Two-stage master sintering curve approach to sintering kinetics of undoped and Al(2)O(3)-doped 8 mol% yttria-stabilized cubic zirconia, J. Am. Ceram. Soc. 94 (2011) 1053–1059.
[27] V. Pouchly, K. Maca, Z. Shen, Two-stage master sintering curve applied to two-step sintering of oxide ceramics, J. Eur. Ceram. Soc. 33 (2013) 2275–2283.
[28] R. Bjork, H.L. Frandsen, N. Pryds, Modeling the microstructural evolution during constrained sintering, J. Am. Ceram. Soc. 98 (2015) 3490–3495.
[29] L.S. Arias-Maya, Free and constrained sintering of 3-mol% yttria stabilised zirconia, Dyna-Colombia 81 (2014) 158–167.
[30] H. Hadraba, D. Drdlik, Z. Chlup, K. Maca, I. Dlouhy, et al., Laminated alumina/zirconia ceramic composites prepared by electrophoretic deposition, J. Eur. Ceram. Soc. 32 (2012) 2053–2056.
[31] J.B. Davis, A. Kristoffersson, E. Carlstrom, W.J. Clegg, Fabrication and crack deflection in ceramic laminates with porous interlayers, J. Am. Ceram. Soc. 83 (2000) 2369–2374.
[32] A.J. Sanchez-Herencia, J. Gurauskis, C. Baudin, Processing of Al_2O_3/Y-TZP laminates from water-based cast tapes, Compos. B—Eng. 37 (2006) 499–508.
[33] J. Requena, R. Moreno, J.S. Moya, Alumina and alumina zirconia multilayer composites obtained by slip casting, J. Am. Ceram. Soc. 72 (1989) 1511–1513.
[34] E. Lucchini, O. Sbaizero, Alumina/zirconia multilayer composites obtained by centrifugal consolidation, J. Eur. Ceram. Soc. 15 (1995) 975–981.
[35] X. Wang, A. Atkinson, Microstructure evolution in thin zirconia films: experimental observation and modelling, Acta Mater. 59 (2011) 2514–2525.
[36] R. Chaim, M. Levin, A. Shlayer, C. Estournes, Sintering and densification of nanocrystalline ceramic oxide powders: a review 2, Adv. Appl. Ceram. 107 (2008) 159–169.
[37] S.K. Yang, W.P. Cai, G.Q. Liu, H.B. Zeng, From nanoparticles to nanoplates: preferential oriented connection of Ag colloids during electrophoretic deposition, J. Phys. Chem. C 113 (2009) 7692–7696.
[38] M.J. Mayo, Processing of nanocrystalline ceramics from ultrafine particles, Int. Mater. Rev. 41 (1996) 85–115.
[39] J.D. Hansen, R.P. Rusin, M.H. Teng, D.L. Johnson, Combined-stage sintering model, J. Am. Ceram. Soc. 75 (1992) 1129–1135.

[40] G. Bernard-Granger, A. Addad, G. Fantozzi, G. Bonnefont, C. Guizard, et al., Spark plasma sintering of a commercially available granulated zirconia powder: comparison with hot-pressing, Acta Mater. 58 (2010) 3390–3399.
[41] Z.M. He, J. Ma, Constitutive modeling of alumina sintering: grain-size effect on dominant densification mechanism, Comput. Mater. Sci. 32 (2005) 196–202.
[42] W.Q. Shao, S.O. Chen, D. Li, H.S. Cao, Y.C. Zhang, et al., Prediction of densification and microstructure evolution for alpha-Al(2)O(3) during pressureless sintering at low heating rates based on the master sintering curve theory, Sci. Sinter. 40 (2008) 251–261.
[43] K. Maca, V. Pouchly, K. Bodisova, P. Svancarek, D. Galusek, Densification of fine-grained alumina ceramics doped by magnesia, yttria and zirconia evaluated by two different sintering models, J. Eur. Ceram. Soc. 34 (2014) 4363–4372.
[44] G. Bernard-Granger, C. Guizard, Apparent activation energy for the densification of a commercially available granulated zirconia powder, J. Am. Ceram. Soc. 90 (2007) 1246–1250.
[45] F.F. Lange, M.M. Hirlinger, Hindrance of grain-growth in Al_2O_3 by ZrO_2 inclusions, J. Am. Ceram. Soc. 67 (1984) 164–168.
[46] M.G. Pontin, M.P. Rao, A.J. Sanchez-Herencia, F.F. Lange, Laminar ceramics utilizing the zirconia tetragonal-to-monoclinic phase transformation to obtain a threshold strength, J. Am. Ceram. Soc. 85 (2002) 3041–3048.

PUBLIKACE XIV

Journal of the European Ceramic Society 40 (2020) 5810–5818

Contents lists available at ScienceDirect

Journal of the European Ceramic Society

journal homepage: www.elsevier.com/locate/jeurceramsoc

Effect of residual stresses to the crack path in alumina/zirconia laminates

Zdeněk Chlup[a,*], Lenka Novotná[b], Filip Šiška[c], Daniel Drdlík[b,d], Hynek Hadraba[a]

[a] CEITEC IPM, Institute of Physics of Materials, Czech Academy of Sciences, Zizkova 22, 616 00 Brno, Czech Republic
[b] CEITEC BUT, Brno University of Technology, Purkynova 123, 612 00 Brno, Czech Republic
[c] Institute of Physics of Materials, Czech Academy of Sciences, Zizkova 22, 616 00 Brno, Czech Republic
[d] Institute of Materials Science and Engineering, Brno University of Technology, Technicka 2, 616 00 Brno, Czech Republic

ARTICLE INFO

Keywords:
Laminates
Alumina
Zirconia
Residual/internal stresses
Crack path

ABSTRACT

Laminates with alternating layers are well known from nature. The strongly bonded alumina/zirconia (Al_2O_3/ZrO_2) layers can combine high fracture resistance with high strength and stiffness when properly tailored. The presence of compressive residual stresses formed in Al_2O_3 layers can suppress and deflect cracks propagating through the layers. The crack path is governed by both the elastic properties and the internal stress field of individual layers. The laminates with various layer-thickness ratios ranging from 0.1 to 3 were used to investigate the effect of residual stresses and influence of crack formation pattern on the crack path development. The indentation surface cracks observed in various alumina-zirconia laminates exhibit the same crack deflection independently on the level of internal stresses. The crack deflection observed on the fracture surfaces of bending specimens was related to the indentations cracks. The complicated crack path was explained experimentally by 3D reconstruction with the support of numerical simulations.

1. Introduction

Ceramic materials in the layered form can exhibit enhanced fracture resistance in comparison with individual monolithic components [1–3]. Generally, two main strategies of reaching such a goal exist. The first one is based on the existence of weak interfaces between layers as it is known from nature where fracture energy is consumed predominately by layer delamination [4–8]. The second strategy is based on the development of tailored residual stresses within the layers by strain changes during cooling from the sintering temperature accompanied by strong interlayer bound [9–14].

Upon the second approach, the development of residual/internal stresses can be done through the strains developed due to *CTE* mismatch of used materials, phase transformation or some combination of both [15–18]. The level of residual/internal stresses within the individual layers when CTE mismatch is only applicable can be standardly estimated from the thicknesses of layers or alternatively by the material volume ratio calculating average CTE. The application of material volume instead of layer thicknesses simplifies the situation and allows comparing of periodic and non-periodic systems easily [19]. The determination of T_{ref} is critical from the estimated stress level point of view and should be determined carefully [20–22]. Another approach is based on the exact determination of elastic strain differences experimentally by dilatometry supported by numerical simulations [23]. Alternatively, an application of experimentally determined strains for a given laminate for residual/internal stresses estimation can be done using the following equation:

$$\sigma_{res,i} = \frac{E_i}{1-\mu_i}\Delta\varepsilon_i \quad (1)$$

The usual design of laminate is using two materials which alternate. Symmetric design is essential to reach a flat laminate structure with no curvature by a non-equilibrium stress field.

Many authors have described the crack deflection or crack bifurcation for a crack propagating through the bi-material interface. The crack deflection is governed by two factors, the elastic properties mismatch and the residual/internal stresses. Generally, the indentation cracks or fracture surfaces of bending bars (with or without pre-cracks) are used to experimentally characterise intensity/effectiveness of the crack deflection [7,12,14,19,24–27].

Two main criteria are applied for the prediction of crack propagation. The first one is based on the maximum tangential tensile stress (MTTS) [28,29] This criterion is based on the assumption that cracks preferably propagate in mode I. Therefore, it follows the path of the maximal opening stress perpendicular to its flanks. This, this criterion is local. The second criterion takes into account minimum strain energy density (MSED) [30,31] According to this criterion, the crack grows along a path that leads to the minimization of the strain energy density

* Corresponding author.
E-mail address: chlup@ipm.cz (Z. Chlup).

https://doi.org/10.1016/j.jeurceramsoc.2020.06.044
Received 31 March 2020; Received in revised form 9 June 2020; Accepted 13 June 2020
Available online 16 June 2020
0955-2219/ © 2020 Elsevier Ltd. All rights reserved.

Nomenclature

t_{Al2O3}	The thickness of the Al_2O_3 layer, μm
t_{ZrO2}	The thickness of the ZrO_2 layer, μm
α	Entering angle, °
β	Exit angle, °
γ	The tilt angle of the sample for SEVNB, °
c	Fitting coefficient
E	Young modulus, GPa
μ	Poisson's ratio
S	The span at three-point bending, mm
σ_{max}	The maximum stress level, MPa
σ_{yy}	Stress component, MPa
σ_{zz}	Stress component, MPa
σ_{rAl2O3}	Calculated residual/internal stresses in the Al_2O_3 layer, MPa
σ_{rZrO2}	Calculated residual/internal stresses in the ZrO_2 layer, MPa
CTE, α	Thermal expansion coefficient, K^{-1}
N	Number of layers
ν	Volume fraction

in the loaded volume, which makes it non-local. Both criteria have been used for predictions of crack propagation [32,33]. In the present work, the MTTS criterion is used, because the tested material is brittle. The brittle fracture mechanism is based on atomic layers debonding when the applied stress exceeds the bonding strength. Therefore, the MTTS criterion is more suitable in our case.

Both, the simulations and experiments show the obvious effect of residual/internal stresses on the crack path in the laminate. In general, two limit situations can occur i) crack perpendicular to the interface plane and ii) crack parallel to the interface. Besides these two limit situations is a range of crack entering angels (0°,90°) where the residual/internal stresses should play a significant role. Generally, if the external load is applied in-plane with layers (acting in opening mode I) the tensile residual/internal stresses will lead to the crack inclination to the normal direction whilst the compressive stresses will cause declination from the normal direction. In other words the tensile stresses will shorten the crack path and the compressive stresses will extend it.

This paper aims to demonstrate and explain the role of the residual/internal stresses on the crack trajectory and clarify observed discrepancies between surface indentation cracks and fracture surfaces of notched bending bars. The effectiveness of the indentation technique will be discussed in the context of residual/internal stresses surface effect in 3D.

2. Experimental

2.1. Material preparation

The experimental bulk laminated ceramics were prepared via alternating electrophoretic deposition (EPD) from stabilised suspensions. The suspensions consisted from 15 wt.% of alumina (denoted as A, HP-DBM, Malakoff Ind., USA) or tetragonal-zirconia stabilized with 3 mol% of Y_2O_3 (denoted as Z, TZ-3YSE, Tosoh, Japan) powders having mean particle sizes of 470 nm and 140 nm, respectively, 12.75 wt% of monochloroacetic acid (p.a., Merck, Germany) and 2-propanol (p.a., Lachner, Czech Republic). The suspensions prepared were 30 min mechanically stirred in an ultrasonic field before the EPD.

The EPD was performed in an electrophoretic glass cell with the constant current mode of 5 mA. The distance between stainless steel electrodes with an effective area of 18.2 cm^2 was set to 26 mm. To prevent particles from settling on the bottom of the EPD cell, the suspension was repeatedly stirred every 5 min during electrophoretic deposition. To create laminates with given thicknesses of individual layers the deposition kinetics curves studied earlier was applied [24,34–36]. Prepared deposits were slowly dried, annealed at 800 °C for 1 h and sintered at 1500 °C for 2 h as was reported elsewhere [37]. The list of examined laminates, layers thicknesses, volume ratio, number of total deposited layers, calculated expected residual stresses and crack formation method is summarised in Table 1. All laminates were prepared as symmetric (odd number of layers) and periodic (alternating layers of given thickness) structures with ratios of layers (A:Z) 3:1, 2:1, 1:1, 1:2, 1:3, 1:5, 1:10 to eliminate all effects connected with possible curvature and not evenly distributed residual/internal stresses.

The residual stresses were calculated according to the material volume ratios and corresponding E, μ and *CTEs* (see Table 2) following Eq. 2 with $T_{ref} - T_0 = 1480\,°C$.

$$\sigma_{res,i} = \frac{E_i}{1-\mu_i}(\bar{\alpha} - \alpha_i)(T_{ref} - T_0) \tag{2}$$

where E_i, μ_i and α_i are material characteristics (Young modulus, Poisson ratio and *CTE*, respectively), T_{ref} is the reference temperature when thermally induced elastic strains started to develop and T_0 is the target temperature of use, here room temperature. The average *CTE* was calculated as follows:

$$\bar{\alpha} = \frac{\sum_{i=1}^{n} \frac{E_i \nu_i \alpha_i}{1-\mu_i}}{\sum_{i=1}^{n} \frac{E_i \alpha_i}{1-\mu_i}} \tag{3}$$

where ν_i is the volume fraction of i^{th} material in the laminate.

2.2. Crack path characterisation

Two approaches for crack path analysis were adopted in this study i) the indentation technique for surface cracks and ii) the three-point bending method for volume cracks. Laminates used for three-point bending had a thickness of several millimetres to allow the preparation

Table 1
Layers thicknesses and nominal stresses of laminates analysed by a given method.

Laminate	t_{Al2O3} [μm]	t_{ZrO2} [μm]	N [−]	AZ ratio [−]	σ_{rAl2O3} [MPa]	σ_{rZrO2} [MPa]	Indentation HV10	Bending SEVNB
A3Z1	40.0	13.0	59	3.18	–164	+520	X	
A2Z1	36.3	18.0	59	2.09	–231	+480	X	
A2Z1	52.5	25.5	151	2.09	–231	+481		X
A1Z1	43.0	43.0	59	1.03	–380	+392	X	
A1Z1	52.5	53.0	151	1.00	–387	+387		X
A1Z2	21.6	43.4	59	0.51	–558	+286	X	
A1Z2	26.0	60.0	151	0.44	–598	+262		X
A1Z3	12.7	46.4	59	0.28	–705	+199	X	
A1Z5	14.7	77.9	151	0.19	–788	+150		X
A1Z10	5.0	50.0	59	0.10	–888	+91	X	

Table 2
Material parameters used in the FE simulations [23].

Material	E [GPa]	μ	*CTE* [10^{-6} K^{-1}]
Al_2O_3	380	0.26	8.91
ZrO_2	210	0.31	10.28

of specimens with various angles of layers plane to the loading direction.

Laminate structures predetermined for indentation cracks were embedded into a resin and polished using standard diamond tools and diamond suspensions. The indentation cracks were initiated from indents corners by the application of a Vickers indenter. The indents were created by a universal fully instrumented Vickers hardness head ZHU02 mounted on a Z5 machine (Zwick/Roell, Germany). The maximum load of 98.07 N (HV10) was applied. The scheme of crack entering and exit angle measurement is shown in Fig. 1a**)**.

The second method, a single edge V-notch beam (SEVNB) technique applied on the specimens cut tilted to the direction of layers by angle γ. The extraction of samples from ceramic laminates is illustrated in Fig. 2a**)**. The specimens were notched by a razor blade technique (see Fig. 2b). The three-point bending using an Instron 8862 (Instron, USA) universal testing system was conducted at a cross-head speed of 0.1 mm/min. The fracture surfaces were analysed by a laser confocal microscope LEXT OLS3100 (Olympus, Japan). The central part of the 3D reconstruction of fracture surface (top view) and the surface crack pattern (side view) was used for entering and exit angle determination in SEVNB specimens (see Fig. 1b). The surface crack paths were determined from 2D side images of broken specimens taken after bending tests.

The 3D reconstruction of indentation cracks was created from 2D trajectories of indentation cracks observed by a DSX1000 microscope (Olympus, Japan). Inner indentation crack trajectories were revealed by the step slice removal method by polishing at an automatic polishing system Sapphire 550 (ATM, Germany) with the step between recordings of approximately 5 μm. The 3D reconstruction of crack patterns was done with the help of 3DSlicer software (www.slicer.org).

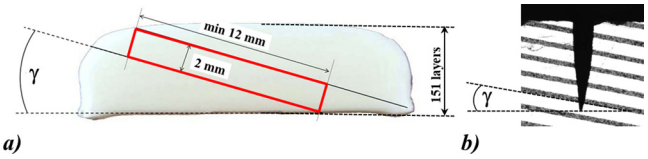

Fig. 2. a) scheme of SEVNB specimen placement into the laminate, and b) detailed view of the notch and tilted layers.

3. Numerical modelling

The FE simulations were used to investigate the stress field in front of the crack tip with the presence of residual stresses inside the laminate. The location of the maximum of the tangential (opening) stress in front of the crack was searched which predicts the future crack propagation. The numerical model used for the analysis of results was created in FE code Abaqus. It represented the symmetrical periodic laminate with the materials volume ratio of 1 (i.e. A1Z1). There were two types of FE models (2D and 3D) used to support the analysis of the measurements. The 2D models with conditions of the plane strain and plane stress were used to analyse limit situations at the surface (plane stress) and inside the material (plane strain). The geometry and boundary conditions of the FE model are shown in Fig. 3a**)**. The crack had the length equal to one laminate layer (L = 53 μm) and its tip was located at the layers interface. The crack opening was executed by the prescribed displacement (U) of the three nodes in the middle of the crack flanks. These nodes were moved perpendicularly to the flanks by 0.5 μm. Seven variants of the crack orientation were assumed. The angle between the crack and interface (α) was set from 0° to 90° with 15° steps. Two variants of layers ordering (Material 1 - Material 2) were made to simulate crack in Al_2O_3 and also in ZrO_2. The sides of the model cell were kept plane-parallel during the simulations. Such a setup represented conditions inside the small volume of material embedded by a larger body. The mesh is shown in Fig. 3b**)**. The 2D quadratic elements were used (CPE8, CPS8) in the model. The elements were arranged concentrically around the crack tip with the element size of 0.1 μm. The materials' behaviour was purely elastic and their parameters E, μ, and *CTE* are summarised in Table 2. The simulations were divided into two models. The first one calculated the stress field caused by the crack without thermal stresses and the second model represented material without crack subjected to cooling by 1480 °C which induced

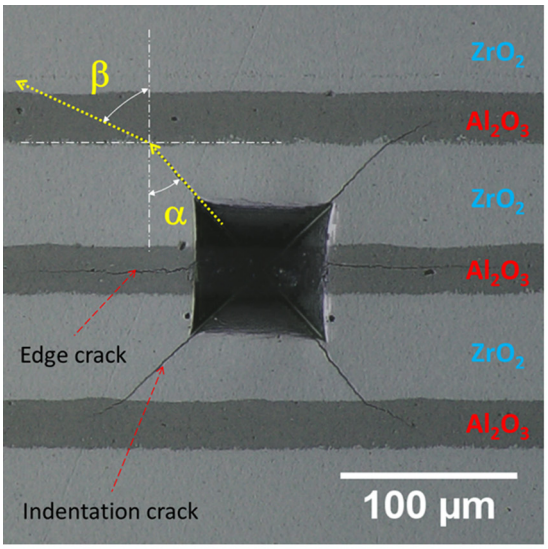

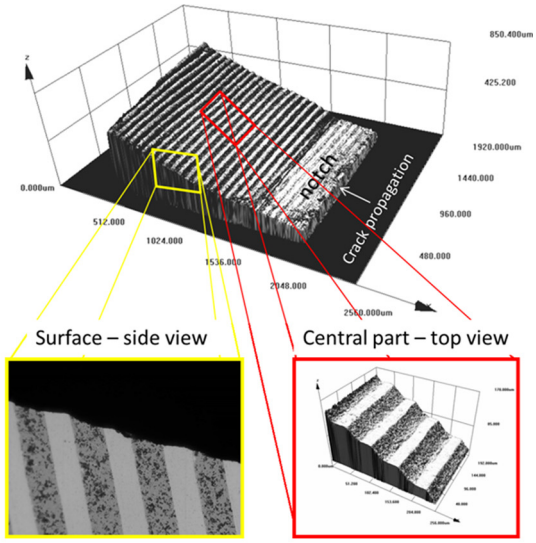

Fig. 1. Scheme of a) Vickers indentation cracks formation in the laminate with indicated angles used for crack deflection (example for laminate 1A2Z), and b) 3D reconstruction of the SEVNB specimen fracture surface with indicated places of crack trajectory analysis (example for laminate 1A1Z).

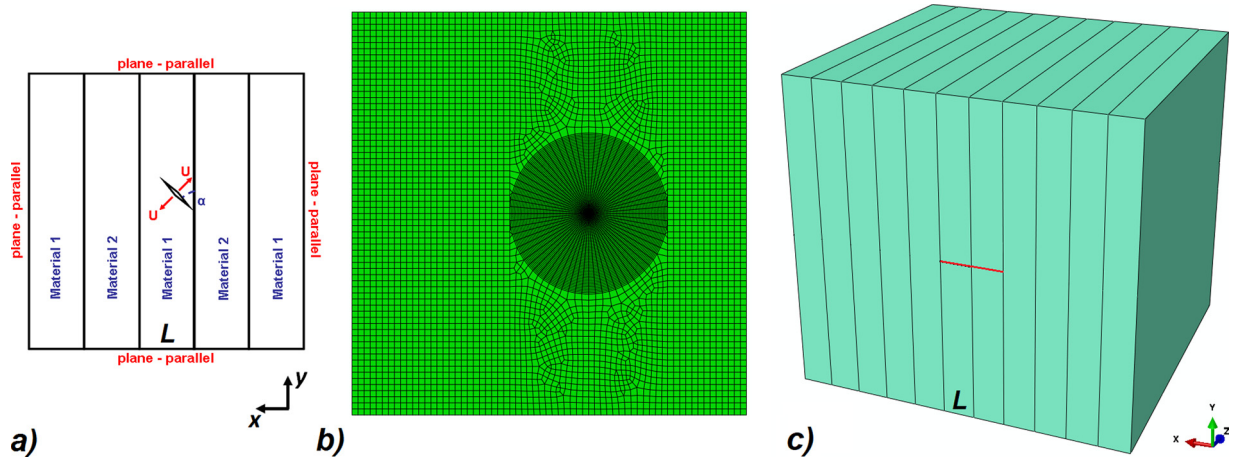

Fig. 3. Illustration of a) geometry and boundary conditions of the 2D FE model, b) FE mesh used in the model and c) geometry of the 3D model for the analysis of the thermal stresses through the thickness of the laminate (along Z-axis).

the thermal stresses. These two stress fields were then combined and analysed. Such combination is possible as the material behaviour is purely elastic and allows using a combination of simple models without loss of validity. The model contained only static crack but the location of the maximal tangential stress could reveal the direction of the crack propagation.

The 3D model was used to analyse the evolution of the thermal stresses through the thickness of the laminate structure (Z-axis) and to establish the length of the transition region from plane stress condition at the surface to plane strain conditions inside the material. The geometry of the model is shown in Fig. 3c). It represents a cube with 11 equal size laminate layers (L = 53 μm). The boundary conditions were similar to the 2D model. The surfaces perpendicular to the X and Y axis were kept plane-parallel while surfaces perpendicular to Z-axis were free. The model contained 613000 3D temperature-displacement coupled elements (C3D8T). The size of the element in the analysed region in the centre of the front face (red line in Fig. 3c) was 2 μm. The thermal stresses were induced by the application of the homogeneous thermal field representing cooling by 1480 °C. The material parameters were the same as in the 2D model.

4. Results

The laminates prepared to have various Al_2O_3 to ZrO_2 ratios of layer thicknesses (volume fractions) were subjects of the Vickers indentation on the polished cross-sections. Indentation cracks formed from the indent corners before they enter the interface and after they passed the interface were analysed from the trajectory point of view. Entering and exit angles counted from the interface normal were measured and are displayed in Fig. 4a). The individual points in the plot create two distinguished branches depending on the type of material into which the crack propagates. The data points are fitted by sinus function with the correlation coefficient higher than 0.9 for both branches even the scatter of data is significant. The exit angle β can be calculated directly from the entering angle α using the following equation:

$$\beta = \alpha \pm c.\ \sin(\alpha) \tag{4}$$

where c is the maximum angle deviation and it seems to be dependent only on the material used because the influence of residual stresses was not proven in this case.

$$\Delta = ABS(\beta - \alpha) \tag{5}$$

All data are shown in Fig. 4a) and can be expressed also as the absolute deviation between entering and exit angles as is shown in

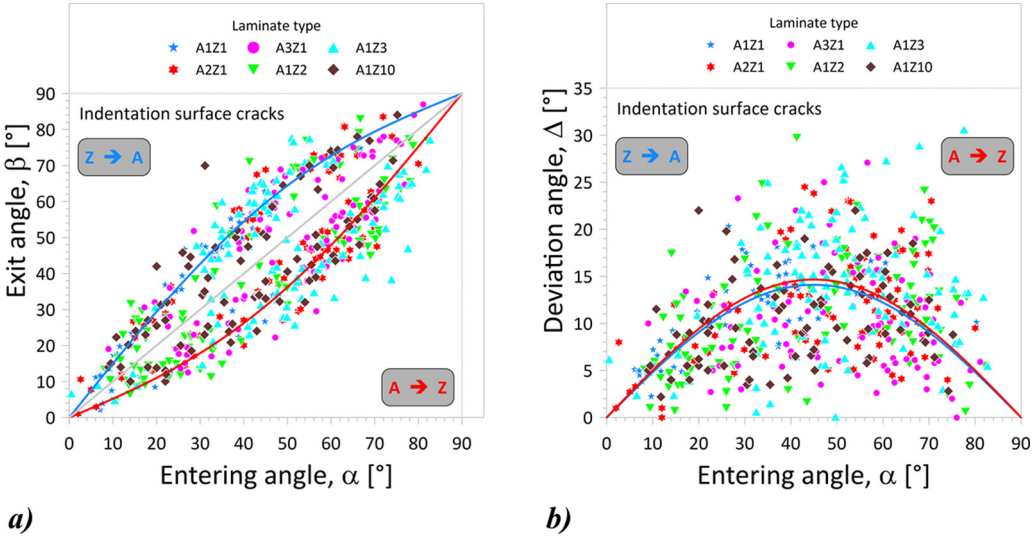

Fig. 4. a) The summary plot of crack path deflection at the interface for indentation cracks measured for different laminates with indicated fit according to Eq. 4 and b) representation of the same data as the dependence of the deviation angle on the entering angle of cracks with indicated fit according to Eq. 5.

Fig. 4b). The deviation angle can be calculated according to the Eq. 5, where the absolute value of the entering and exit angle is calculated for each analysed crack. This representation of data by regression fits (see full lines in Fig. 4b) indicates the symmetry of the indentation crack behaviour (i.e. the deviation is nearly the same if the crack enters either from ZrO_2 or Al_2O_3 layer) even if a relatively high scatter of data is noticeable.

A crack propagation for the indentation cracks was usually only through two neighbouring layers. On the contrary, in the case of bending SEVNB specimens, there was a crack propagating through all layers included in the ligament. No delamination on the interfaces was observed in case of bending. Variation of the entering angle α from 0° up to ~30° was reached by application of different specimen tilting angle γ as shown in Fig. 2. The initial entering angles slightly deviate from the individual entering angles taken along the specimen thickness; however, the coverage of entering angles range is relatively narrow for the given materials volume ratio anyway. All data obtained from the side of the surface of bending specimens are summarised in Fig. 5a) and all data obtained from the measurements at the central part of the fracture surface (i.e. plane strain area) are displayed in Fig. 5b) plotted in the same form as the crack propagation trajectory changes measured for indentation cracks.

The results of the numerical simulations of crack behaviour in the vicinity of the interface are shown in Fig. 6 for both the plane stress and plane strain configuration. The calculation of angles deflection was done for the laminate type 1A1Z. The estimates of the exit angles made by the FE model depend on the distance taken from the crack tip. The location of the maximal tangential stress changes with the distance from the crack tip. This is caused by the superposition of the stress field induced by the crack and the thermal stress field. The former one decreases further from the crack tip while the latter one is constant but non-uniform if recalculated into the tangential direction. Therefore, it is necessary to specify the proper distance. It can be related to the microstructural features, like grain size which is within the micron range. The estimates of the angles for both materials and distances 0.1–5 μm are shown in Fig. 6 with highlighted curves for a distance of 0.5 μm corresponding to the expected process zone. The plots are shown in the same style as data represented in Fig. 4 for a better comparison.

The evolution of the thermally induced (residual) stresses along the out of plane direction inside the laminate is shown in Fig. 7. The numerical analysis shows that the stress in the Y-direction (i.e. parallel with the interface) that influences the crack propagation decreases towards the surface of the laminate (see Fig. 7a). The stress decrease is more significant in the centre of each material layer due to the smaller displacement restrictions compared to the layers interface. However, the stresses do not vanish at the surface completely and they reach the constant value (corresponding with the analytical solution – see Eq. 1) in the depth of about 0.5 of the thickness of the individual material layer. The stress component in the Z-direction (i.e. out of plane direction) shows a larger difference between the interface and the centre of the layer (see Fig. 7 b). At the interface, it is still present at the surface while in the central part of the layers it decreases to zero due to the free surface effect. There is also a difference in the stress level saturation. The interface stresses level at the distance $0.25 - 0.75L$ from the surface while in the central part of the layers experience the stress levelling in the depth of $2L$. These results show that the effect of free surface on thermal stress distribution is quite significant and its range is comparable to the thickness of the laminate layers.

5. Discussion

The results obtained by the indentation technique (see Fig. 4) show uneven deviation in the dependence on the entering and exit angle of the observed crack trajectory. The closer 45° an entering angle is the higher deviation from this direction after passing interface is identified (see Fig. 4b). The effect of the presence of residual stresses within the individual layers is not visible even though a large variety of laminate designs were analysed (material volume ratio from 0.1–3). The situation of the indentation crack was modelled using FE simplified model. The model based on the microstructural morphology of prepared materials was found to describe well the indentation cracks development. Especially, the experimentally obtained trend was the same as calculated by this simplified model, see Fig. 8 for comparison. The trajectory of cracks propagating in the limit situations, i.e. crack perpendicular or parallel to the interface, is not affected by both the elastic characteristic mismatch and the presence of residual/internal stresses and deviation is equal to zero. This finding is in good agreement with other calculations and experiments [38–40]. Note, to theoretically or experimentally prove the limit situations in laminates is always hardly reachable especially for the crack parallel to the interface [41–44].

The observed situation in the indentation crack trajectories (see Fig. 4) seems to be independent on the level of residual stresses present in the layers because of all laminates with Al_2O_3 to ZrO_2 ratio from 0.1 to 3 exhibit the same crack deviation. This fact can be ascribed to the effect of the free surface where in-plane residual/internal stresses (σ_{yy} and σ_{zz}) lower or vanishes completely as can be demonstrated on the

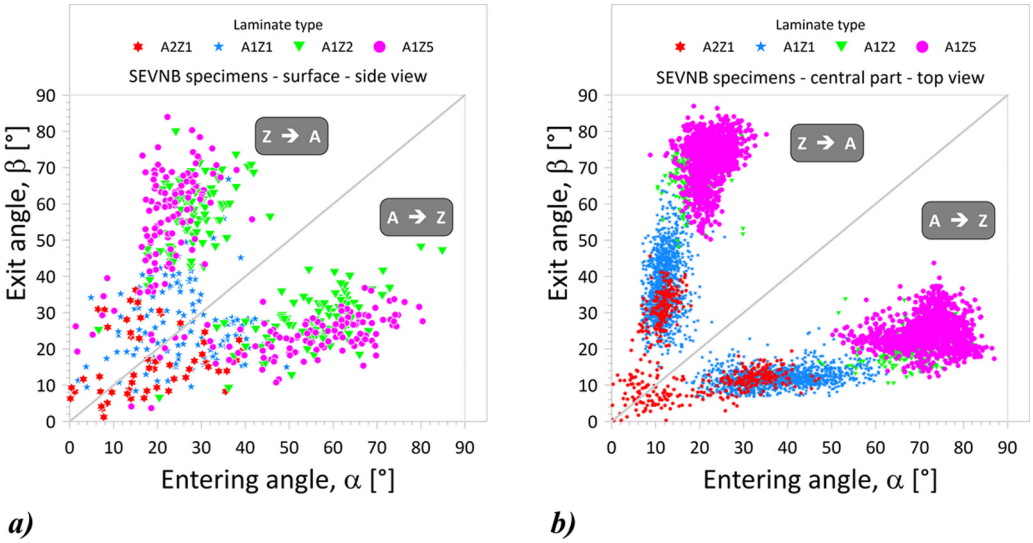

Fig. 5. The summary plot of crack path deflection at the interface for cracks measured for different laminates a) from the side of the bending bars and b) on the central part of the fracture surface.

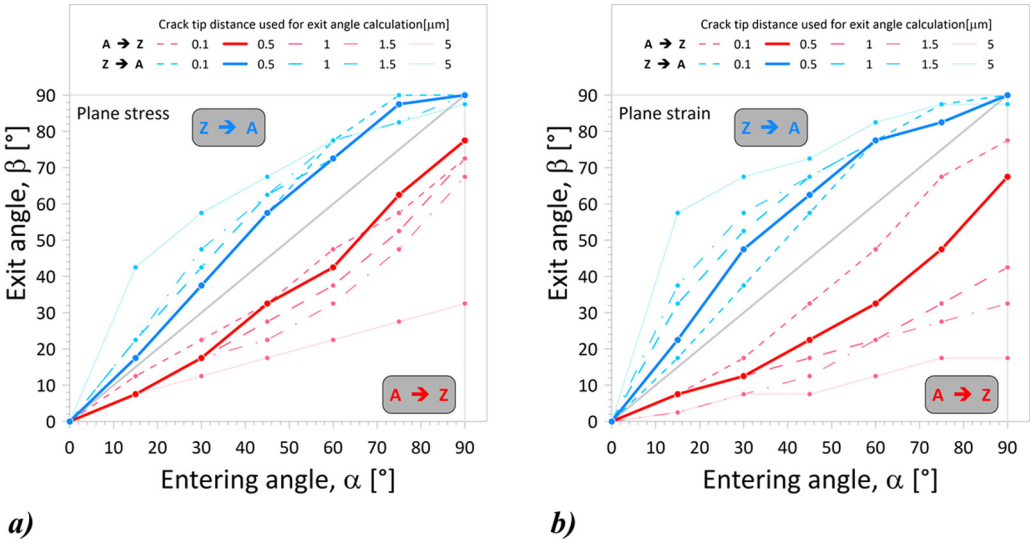

Fig. 6. The evolution of crack path change predicted using numerical calculations for various crack tip distances from the interface (0.1-5 μm) for a) plane stress, and b) plane strain conditions.

calculated stress profiles shown in Fig. 7. Therefore, the elastic mismatch of layer materials is mainly responsible for the crack deflection which corresponds well with the literature [45]. The stress-free zone is expected to be in the range of 10 − 100 μm dependent on the material volume ratios and layer thickness. The effect of the surface on the crack path trajectory was experimentally proved by the 3D analysis of indentations cracks as well as fracture surfaces of bending bars in the vicinity of the free surface.

The 3D reconstructions of indentation cracks patterns are demonstrated in Fig. 9 for two typical situations. Indent is placed into the compressive Al_2O_3 layer and cracks are propagating form ZrO_2 to Al_2O_3 layers (Fig. 9a–d) or indent is placed into the tensile ZrO_2 layer and cracks are propagating from Al_2O_3 to ZrO_2 layers (Fig. 9e–h).

From the 3D reconstructed crack patterns can be concluded several facts. The cracks depth is significantly larger than the indent depth itself, for example, compare the depth of indent shown in Fig. 9e–h) of A = 21 μm with the largest crack depth approximately B = 270 μm, i.e. more than 10 fold, depending on the type of crack. The cracks depth is influenced by the present stress field. In the case of indent placed into the compressive layer (Al_2O_3), the crack pattern is simple and individual cracks coming from the indent corners have a half elliptical shape (i.e. Palmqvist cracks). The deflection of the individual indentation cracks at the interface changes with the depth as is visible in Fig. 9b). The presence of edge cracks induced by the indents stress field superposed with compressive stresses within the Al_2O_3 layer was proved. The edge cracks depth significantly decreases with the distance from the indent and the crack shape is triangular. The different situation can be observed in the case of indent placed into a zirconia tensile layer. The development of cracks is more extensive and the crack paths are longer. The bending of the cracks with increasing depth is more pronounced (see Fig. 9f). Interestingly, the crack trajectories within one layer are not straight as can be expected and they are usually modelled [19,32]. Additionally, the formation of so-called tunnelling cracks in the tensile zirconia layers was observed [46,47]. This effect is marked by arrows in Fig. 9e). It can be stated that cracks are not propagating directly from the indent's corner but can be formed in the volume when a suitable stress field is formed resulting in a stress intensity factor overcoming fracture toughness of the material. Also, delamination cracks were found at the layer interfaces in the vicinity of the indent together with other secondary cracks. The individual Palmqvist type cracks are formed in this case when indent is placed into the ZrO_2 layer. They have closed-form of cracks, i.e. in the depth, they are joined together in the form of lateral cracks. The crack deflection for the crack marked by the yellow circle in Fig. 9e) was monitored thought the

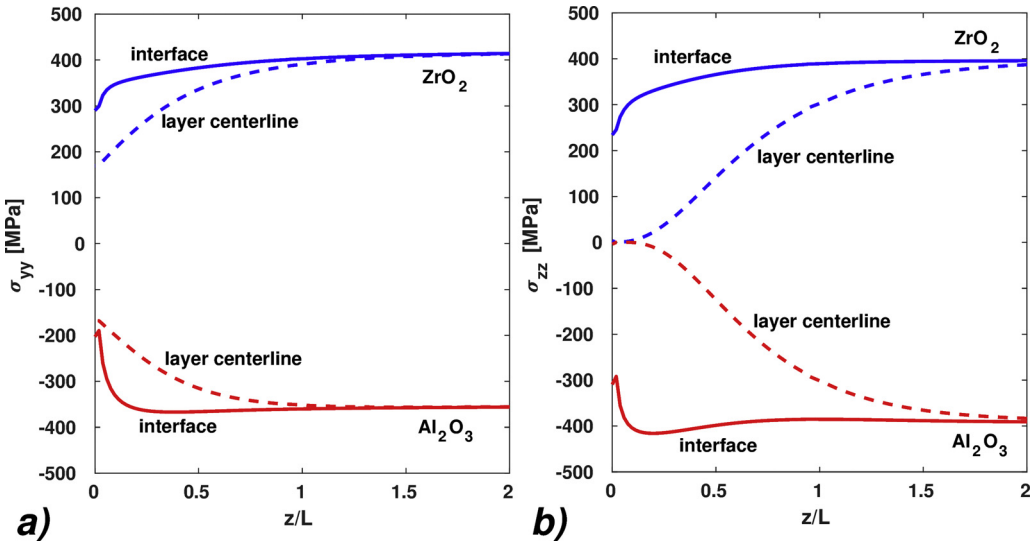

Fig. 7. The evolution of the thermally induced (residual) stresses through the out of the plane thickness of the laminate structure (*Z*-axis): a) normal stress component in the *Y*-axis direction (parallel with the interface), b) normal stress component in the *Z*-axis direction. The distance from the surface *z* is normalized by the thickness of the individual laminate layer *L*. Solid lines show the results for the interface between the material layers. Dashed lines show the stress evolution along the centreline of each material layer.

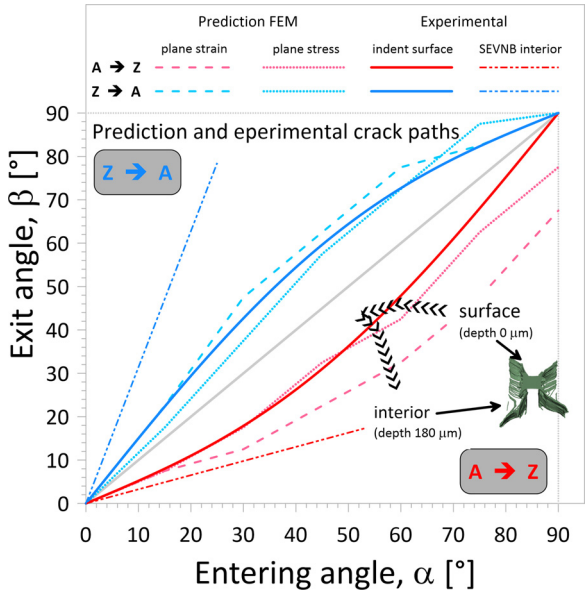

Fig. 8. Comparison of experimentally determined crack deflection development with results from FEM calculations for crack tip distance of 0.5 μm. The development of crack deflection for an indentation crack on its depth from the surface (see Fig. 10 for details) is also inserted.

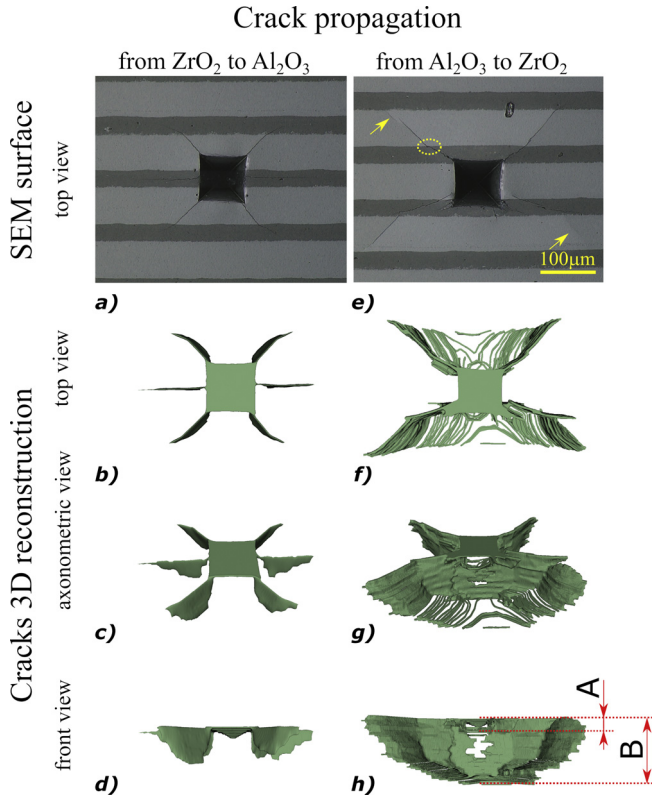

Fig. 9. An example of 3D indentation crack reconstruction for indent placed into a-d) alumina layer with cracks propagation from ZrO_2 to Al_2O_3, and e-h) zirconia layer with crack propagation from Al_2O_3 to ZrO_2 where a, e) is a top view by SEM, b, f) represents a corresponding top view of the 3D reconstructed cracks pattern, c, g) represents an axonometric view of the 3D reconstructed cracks pattern and d, h) represents a side view of the 3D reconstructed cracks pattern.

depth in detail. The dependence of crack deflection development on the distance from the surface is shown in Fig. 10 accompanied by micrographs of the indentation crack at various depths. The visibly marked knee of the curve corresponds well with the stress field of the indent and from that point the deflection increases. In the comparison shown in Fig. 8 are inserted results from detailed crack deflection analysis (shown in Fig. 10) as a depth-dependent trajectory. In this comparison is visible an effect of increasing level of internal/residual stresses with increasing depth which well corresponds with the results of FE simulations presented in Fig. 7. Also vanishing effect of the indent stress field with the depth corresponds well to the formation of stress "crossroad" as marked in Fig. 10 at the depth of approximately 55 – 60 μm and visible better in the sharp change of the crack trajectory in Fig. 8 where the entering angle α is changing from approximately 70° to 55° resulting in the exit angle β equal to 45°.

The crack trajectory obtained on the surface of the notched bending bars is slightly different in comparison with the indentation cracks as can be noticed from Figs. 4 and 5. The difference is dependent on the entering angle as well as residual/internal stress level. These discrepancies can be a result of the overall three-dimensional character of the crack path and an effect of crack propagation direction, i.e. if the crack propagates from the surface to the interior (from corners of indents) or vice versa (from the notch in bending bars). In the case of indentation cracks, the direction of propagation is from the nearly stress-free surface to the interior of laminate where residual stresses are high, i.e. only elastic mismatch is controlling the trajectory at the beginning. In the case of notched bending bars, the crack front is usually curved as well-known from the literature [48–50]. In the central part, plane strain conditions increase stress triaxiality which enhances brittle fracture and thus crack propagates faster in the interior than at the surface with plane stress region [51]. Taking into account results measured in the central part of the fracture surface where larger deviation was observed (see Fig. 6) and the fact that crack propagates from interior to the surface it can be stated that the trace observed on the bar side surface (free surface) is influenced by the dominant crack path in the plane strain region. The crack direction can't change stepwise even when passing the interface or changing stress conditions as one can deduct from the rough numerical simulations [32]. The complexity of the crack trajectory can be seen also in the 3D reconstruction of the fracture surface for bending bars Fig. 11. The even steps are observable for the laminate interior (central part of the fracture surface) Fig. 11a). The noticeable change of crack trajectory in the vicinity of the surface is shown in Fig. 11b) and the crack profiles are summarised and compared in Fig. 11c). The smooth crack path change in the three-dimensional space is obvious. This finding is in good correlation with the calculated stress field shown in Fig. 7 where the gradient of thermally induced stresses is changing trough the layer thickness.

The comparison between crack paths formed by indentation and bending approach for laminates with internal stresses can result in the recommendation to use crack propagation in bulk samples which reflects better the effect of present stresses. The indentation provides not relevant information on the surface. It was also reported based on the 3D crack pattern reconstructions that the resulting crack pattern is influenced by the stress field created by the indentation itself although the structural ceramic material is used [52,53].

6. Conclusions

The crack deflection magnitude observed in laminates with strongly bonded layers depends heavily on both the experimental technique used for crack formation and the location of observation. Based on the experimental results supported by numerical analysis the main findings of this investigation can be summarised as follows:

- Deflection of the indentation cracks observed at the surface reflects mostly dissimilar elastic properties of individual materials and does not reflect the level of residual/internal stresses.
- Crack path of the indentation cracks is changed in the depth

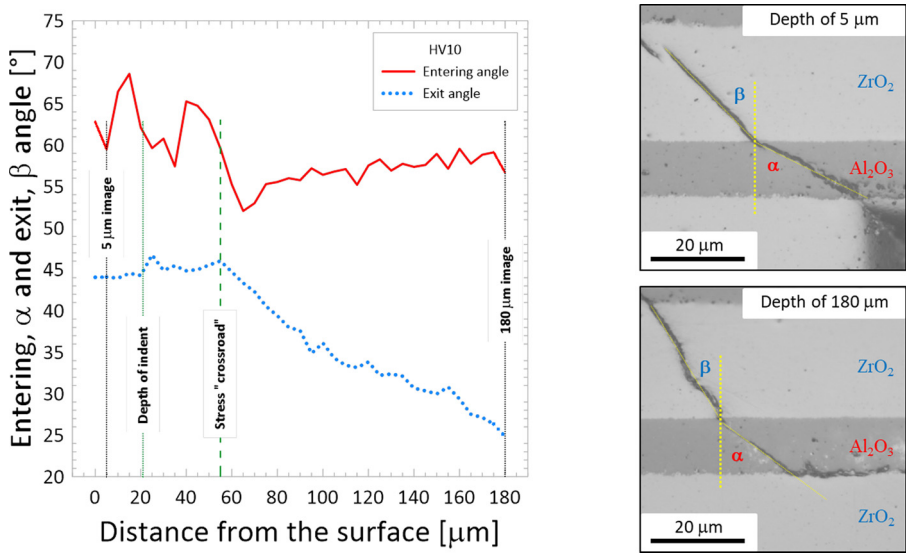

Fig. 10. The development of the indentation crack angles and corresponding micrographs for 5 μm and 180 μm depth.

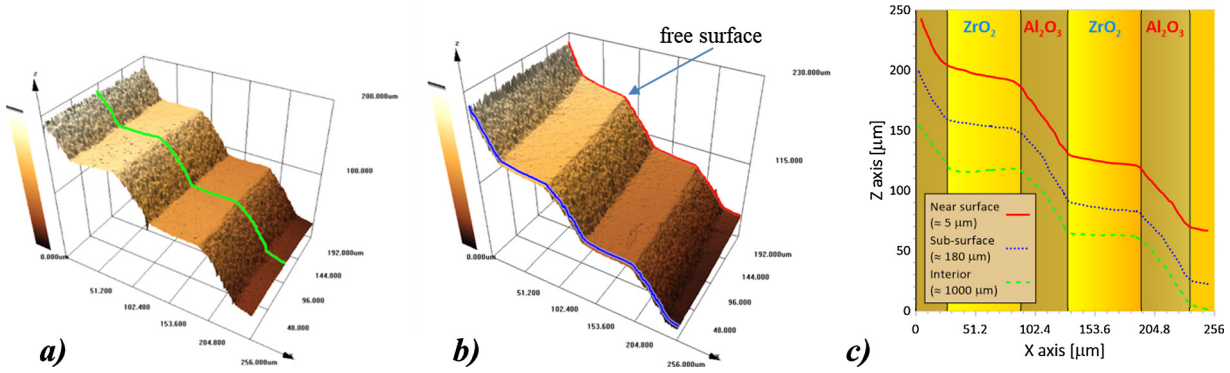

Fig. 11. Detail of fracture surface 3D reconstruction a) central part, b) near the side surface of the SEVNB specimen, and c) comparison of selected fracture path profiles.

significantly when residual/internal stresses are present.

- The formation of tunnelling cracks can be observed when the stress fields created during indentation and induced by the crack tip interacts with the present residual/internal stresses.
- The crack path of SEVNB specimens observed from the side surface (similarly to indentation cracks) differs when compared with the trajectory of indentation cracks.
- The crack path of SEVNB specimen in the interior is strongly affected by the presence of residual/internal stresses.
- The direction of crack propagation, i.e. surface to the interior (for indent) or vice versa (for SEVNB), is an important factor for the resulting crack path (crack deflection at the interface).
- Change of the crack propagation angle depends on the distance in front of the crack tip at which the new crack initiates. This was verified by the numerical simulations. The initiation distance is determined by the microstructure.
- It was numerically and experimentally proven that the depth at which residual stresses are influenced by the free surface is comparable to the thickness of the layers in the ceramic laminate.

Declaration of Competing Interest

The authors declare that they have no known competing financial interests or personal relationships that could have appeared to influence the work reported in this paper.

Acknowledgements

This work has been supported through a grant number 17-08153S of the Czech Science Foundation. The research has also been financially supported by the Ministry of Education, Youth and Sports of the Czech Republic under the project CEITEC 2020 (LQ1601).

References

[1] W.J. Clegg, K. Kendall, N.M. Alford, T.W. Button, J.D. Birchall, A simple way to make tough ceramics, Nature 347 (6292) (1990) 455–457.
[2] F.D. Minatto, P. Milak, A. De Noni, D. Hotza, O.R.K. Montedo, Multilayered ceramic composites – a review, Adv. Appl. Ceram. 114 (3) (2015) 127–138.
[3] L. Cheng, M. Sun, F. Ye, Y. Bai, M. Li, S. Fan, L. Zhang, Structure design, fabrication, properties of laminated ceramics: a review, Int. J. Lightweight Mater. Manuf. 1 (3) (2018) 126–141.
[4] M. Lugovy, V. Slyunyayev, V. Subbotin, F. Liang, J. Gou, N. Orlovskaya, T. Graule, J. Kuebler, Mechanical behavior and failure mechanisms of boron carbide based three-layered laminates with weak interfaces, Ceram. Int. 37 (7) (2011) 2255–2261.
[5] E. Munch, M.E. Launey, D.H. Alsem, E. Saiz, A.P. Tomsia, R.O. Ritchie, Tough, bio-inspired hybrid materials, Science 322 (5907) (2008) 1516.
[6] P. Šajgalík, Z. Lenčéš, J. Dusza, Layered composites with self-diagnostic ability, Compos. Part B: Eng. 37 (6) (2006) 515–523.
[7] D. Kovar, M.D. Thouless, J.W. Halloran, Crack deflection and propagation in layered silicon nitride/boron nitride ceramics, J. Am. Ceram. Soc. 81 (4) (1998) 1004–1112.
[8] M. Sun, Y. Bai, M. Li, S. Fan, L. Cheng, Structural design and energy absorption mechanism of laminated SiC/BN ceramics, J. Eur. Ceram. Soc. 38 (11) (2018) 3742–3751.
[9] T. Chartier, T. Rouxel, Tape-cast alumina-zirconia laminates: processing and mechanical properties, J. Eur. Ceram. Soc. 17 (2) (1997) 299–308.
[10] M. Lugovy, V. Slyunyayev, N. Orlovskaya, G. Blugan, J. Kuebler, M. Lewis,

Apparent fracture toughness of Si3N4-based laminates with residual compressive or tensile stresses in surface layers, Acta Mater. 53 (2) (2005) 289–296.
[11] V.M. Sglavo, M. Paternoster, M. Bertoldi, Tailored residual stresses in high reliability alumina-mullite ceramic laminates, J. Am. Ceram. Soc. 88 (10) (2005) 2826–2832.
[12] R. Bermejo, Y. Torres, A. Sanchez-Herencia, C. Baudin, M. Anglada, L. Llanes, Residual stresses, strength and toughness of laminates with different layer thickness ratios, Acta Mater. 54 (18) (2006) 4745–4757.
[13] R. Bermejo, "Toward seashells under stress": bioinspired concepts to design tough layered ceramic composites, J. Eur. Ceram. Soc. (2017).
[14] C. Liu, J. Sun, G. Li, B. Li, F. Gong, Fabrication, mechanical properties and fracture behaviors of the laminated Al2O3–ZrB2–MgO / Al2O3–TiN–MgO ceramic composite, Ceram. Int. 46 (1) (2020) 857–865.
[15] R. Bermejo, Y. Torres, A. Sanchez-Herencia, C. Baudin, M. Anglada, L. Llanes, Fracture behaviour of an Al2O3-ZrO2 multi-layered ceramic with residual stresses due to phase transformations, Fatigue Fract. Eng. Mater. Struct. 29 (1) (2006) 71–78.
[16] M. Lugovy, V. Slyunyayev, V. Subbotin, N. Orlovskaya, G. Gogotsi, Crack arrest in Si3N4-based layered composites with residual stress, Compos. Sci. Technol. 64 (13–14) (2004) 1947–1957.
[17] A.J. Sánchez-Herencia, J.S. Moya, A.P. Tomsia, Microstructural design in alumina-alumina/zirconia layered composites, Scr. Mater. 38 (1) (1997).
[18] D.J. Green, P.Z. Cai, G.L. Messing, Residual stresses in alumina–zirconia laminates, J. Eur. Ceram. Soc. 19 (13) (1999) 2511–2517.
[19] L. Sestakova, R. Bermejo, Z. Chlup, R. Danzer, Strategies for fracture toughness, strength and reliability optimisation of ceramic-ceramic laminates, Int. J. Mater. Res. 102 (6) (2011) 613–626.
[20] Q. Ma, W. Pompe, J.D. French, D.R. Clarke, Residual stresses in Al2O3 ZrO2 composites: A test of stochastic stress models, Acta Metall. Mater. 42 (5) (1994) 1673–1681.
[21] V. Sergo, X.-L. Wang, D.R. Clarke, P.F. Becher, Residual stresses in alumina/ceria-stabilized zirconia composites, J. Am. Ceram. Soc. 78 (8) (1995) 2213–2214.
[22] A. Atkinson, A. Selçuk, Residual stress and fracture of laminated ceramic membranes, Acta Mater. 47 (3) (1999) 867–874.
[23] Z. Chlup, H. Hadraba, D. Drdlik, K. Maca, I. Dlouhy, R. Bermejo, On the determination of the stress-free temperature for alumina-zirconia multilayer structures, Ceram. Int. 40 (4) (2014) 5787–5793.
[24] H. Hadraba, K. Maca, J. Cihlar, Electrophoretic deposition of alumina and zirconia - II. Two-component systems, Ceram. Int. 30 (6) (2004) 853–863.
[25] R. Bermejo, C. Baudin, R. Moreno, L. Llanes, A. Sanchez-Herencia, Processing optimisation and fracture behaviour of layered ceramic composites with highly compressive layers, Compos. Sci. Technol. 67 (9) (2007) 1930–1938.
[26] K. Hbaieb, R.M. McMeeking, F.F. Lange, Crack bifurcation in laminar ceramics having large compressive stress, Int. J. Solids Struct. 44 (10) (2007) 3328–3343.
[27] Z. Chlup, H. Hadraba, L. Slabakova, D. Drdlik, I. Dlouhy, Fracture behaviour of alumina and zirconia thin layered laminate, J. Eur. Ceram. Soc. 32 (9) (2012) 2057–2061.
[28] Y.G. Matvienko, Maximum average tangential stress criterion for prediction of the crack path, Int. J. Fract. 176 (1) (2012) 113–118.
[29] D. Zhang, W. Zhu, S. Li, B. Zhang, W. Wang, A modified maximum tangential tensile stress criterion for three-dimensional crack propagation, J. Rock Mech. Geotech. Eng. 4 (1) (2012) 62–72.
[30] G.C. Sih, Strain-energy-density factor applied to mixed mode crack problems, Int. J. Fract. 10 (3) (1974) 305–321.
[31] S. Lin, F. Narita, Y. Shindo, Comparison of energy release rate and energy density criteria for a piezoelectric layered composite with a crack normal to interface, Theor. Appl. Fract. Mech. 39 (3) (2003) 229–243.
[32] L. Náhlík, L. Šestáková, P. Hutař, R. Bermejo, Prediction of crack propagation in layered ceramics with strong interfaces, Eng. Fract. Mech. 77 (11) (2010) 2192–2199.
[33] D. Leguillon, E. Martin, O. Ševeček, R. Bermejo, Application of the coupled stress-energy criterion to predict the fracture behaviour of layered ceramics designed with internal compressive stresses, Eur. J. Mech.-A/Solids 54 (2015) 94–104.
[34] K. Maca, H. Hadraba, J. Cihlar, Electrophoretic deposition of alumina and zirconia - I. Single-component systems, Ceram. Int. 30 (6) (2004) 843–852.
[35] H. Hadraba, K. Maca, Z. Chlup, A. Boccaccini, O. VanDerBiest, R. Clasen, T. Uchikoshi, Alumina and zirconia based composites: Part 1 preparation, Electrophoretic Deposition: Fundam. Appl. III 412 (2009) 221–226.
[36] H. Hadraba, D. Drdlik, Z. Chlup, K. Maca, I. Dlouhy, J. Cihlar, Layered ceramic composites via control of electrophoretic deposition kinetics, J. Eur. Ceram. Soc. 33 (12) (2013) 2305–2312.
[37] H. Hadraba, D. Drdlik, Z. Chlup, K. Maca, I. Dlouhy, A. Boccaccini, O. VanDerBiest, R. Clasen, J. Dickerson, Control of electrophoretic deposition kinetics for preparation of laminated Alumina/Zirconia ceramic composites, Electrophoretic Deposition: Fundam. Appl. Iv 507 (2012) 209–213.
[38] A. Tambat, G. Subbarayan, Simulations of arbitrary crack path deflection at a material interface in layered structures, Eng. Fract. Mech. 141 (2015) 124–139.
[39] B.M. Sundaram, H.V. Tippur, Dynamics of crack penetration vs. branching at a weak interface: an experimental study, J. Mech. Phys. Solids 96 (2016) 312–332.
[40] M. Alam, J.P. Parmigiani, J.J. Kruzic, An experimental assessment of methods to predict crack deflection at an interface, Eng. Fract. Mech. 181 (2017) 116–129.
[41] M. Ryvkin, A mode I crack parallel to the interfaces in a periodically layered medium, Int. J. Fract. 99 (3) (1999) 173–188.
[42] A. Nishide, T. Yamamoto, Y. Momoi, M.V. Swain, Cracks formed by Vickers indentation adjacent to the interface in bonded dental ceramics with various marginal angles, Dent. Mater. J. 30 (3) (2011) 308–314.
[43] Y. Bao, F. Kuang, Y. Sun, Y. Li, D. Wan, Z. Shen, D. Ma, L. He, A simple way to make pre-stressed ceramics with high strength, J. Mater. 5 (4) (2019) 657–662.
[44] Y. Chang, R. Bermejo, G.L. Messing, Improved fracture behavior of alumina microstructural composites with highly textured compressive layers, J. Am. Ceram. Soc. 97 (11) (2014) 3643–3651.
[45] H. Ming-Yuan, J.W. Hutchinson, Crack deflection at an interface between dissimilar elastic materials, Int. J. Solids Struct. 25 (9) (1989) 1053–1067.
[46] O. Ševeček, M. Kotoul, D. Leguillon, E. Martin, R. Bermejo, Assessment of crack-related problems in layered ceramics using the finite fracture mechanics and coupled stress-energy criterion, Procedia Struct. Integr. 2 (2016) 2014–2021.
[47] C. Hillman, Z. Suo, F.F. Lange, Cracking of laminates subjected to biaxial tensile stresses, J. Am. Ceram. Soc. 79 (8) (1996) 2127–2133.
[48] L. Náhlík, K. Štegnerová, B. Máša, P. Hutař, A failure scenario of ceramic laminates with strong interfaces, Eng. Fract. Mech. 167 (2016) 56–67.
[49] L. Zhao, D. Bardel, A. Maynadier, D. Nelias, Velocity correlated crack front and surface marks in single crystalline silicon, Nat. Commun. 9 (1) (2018) 1298.
[50] C.L. Quackenbush, V.D. Frechette, Crack-front curvature and glass slow fracture, J. Am. Ceram. Soc. 61 (9–10) (1978) 402–406.
[51] G.C. Sih, Y.D. Lee, Review of triaxial crack border stress and energy behavior, Theor. Appl. Fract. Mech. 12 (1) (1989) 1–17.
[52] A. Baggott, M. Mazaheri, B.J. Inkson, 3D characterisation of indentation induced sub-surface cracking in silicon nitride using FIB tomography, J. Eur. Ceram. Soc. 39 (13) (2019) 3620–3626.
[53] F.A. Elfallagh, B.J. Inkson, 3D tomographic analysis of crack morphologies in alumina and glass using FIB microscopy, J. Phys. Conf. Ser. 126 (2008) 012080.

PUBLIKACE XV

Materials Letters 355 (2024) 135424

Contents lists available at ScienceDirect

Materials Letters

journal homepage: www.elsevier.com/locate/matlet

A way for densification of lead-free $BaTiO_3$-based/ZrO_2 laminates for energy harvesting applications prepared by electrophoretic deposition

Daniel Drdlik [a,b,*], Vojtech Marak [a], Hynek Hadraba [c], Zdenek Chlup [c]

[a] CEITEC BUT, Brno University of Technology, Purkynova 123, 612 00 Brno, Czech Republic
[b] Institute of Materials Science and Engineering, Brno University of Technology, Technicka 2, 616 00 Brno, Czech Republic
[c] Institute of Physics of Materials, Czech Academy of Sciences, Zizkova 22, 616 00 Brno, Czech Republic

ARTICLE INFO

Keywords:
EPD
SPS
Piezoceramics
Harvester
Layer interface
Indentation/hardness

ABSTRACT

In this paper, the concept of multi-layer ceramics based on a combination of piezoelectric layers $BaTiO_3$ (BT) or $(Ba_{0.85}Ca_{0.15})(Zr_{0.1}Ti_{0.9})O_3$ (BCZT) alternated with mechanically durable ZrO_2 (Z) layers is investigated. Both BT/Z and BCZT/Z laminates were successfully electrophoretically deposited (EPD) due to knowledge of the deposition kinetics of individual materials and their green densities allowing precise layer thickness control. The EPD was followed by conventional sintering (CS) or spark plasma sintering (SPS). The CS resulted in the development of cracks, pores, and significant chemical reactions at the layers interfaces in both types of laminates. Laminates sintered by SPS were crack free with suppressed or none chemical reactions at the interfaces. The mechanical properties development across layers was monitored using nanoindentation. This approach identified interlayer porosity evolution and estimated the significance of the reaction zone at the interface.

1. Introduction

Piezoelectric harvesting devices are designed to generate a small amount of energy for low-power electrical devices [1,2]. One of the feasible harvester designs is a multi-layer (or laminate) form [3]. However, these multi-layer materials are usually packaged piezoelectric ceramics using epoxy resin as protective layers. From the mechanical point of view, such structural organization has some limitations in low resistance against mechanical impact and scratches. Therefore, the challenging solution could be addressed with fully ceramic multi-layer laminates.

The mechanically durable ceramic protective layers can enhance the reliability and fracture resistance of the inherently brittle piezoceramics. However, several issues must be taken into consideration: i) the different green densities of the ceramic layers in multi-layer ceramics before sintering may lead to crack propagation along layer interface (delamination) due to high internal stresses at the sintering temperature, ii) if the ceramics have dissimilar coefficients of thermal expansion then cracks perpendicular to the layers are developed during cooling from sintering temperature, iii) the piezoceramics, typically $BaTiO_3$, are known for their strong tendency to undergo chemical reactions with surrounding ceramic materials giving formation of new phases [4–6]. Related to the harvesting application, there is also a question of electrodes being as close to the piezoelectric layers as possible. Hence, new approaches must be applied to overcome these issues.

In the paper, the concept of multi-layer ceramics with alternating piezoceramics of $BaTiO_3$ (BT) or $(Ba_{0.85}Ca_{0.15})(Zr_{0.1}Ti_{0.9})O_3$ (BCZT) and mechanically durable ZrO_2 (Z) layers for possible harvesting application is investigated. The brief study covers combined preparation using electrophoretic deposition (EPD) and spark plasma sintering (SPS), microstructural analysis, evaluation of changes in the reaction zone at the interface between layers and local mechanical characterization.

2. Experimental

Selected materials were commercial ZrO_2 (Tosoh, Japan), $BaTiO_3$ (Nanografi, Turkey) and synthesized $(Ba_{0.85}Ca_{0.15})(Zr_{0.1}Ti_{0.9})O_3$ powders. More information about the synthesis of BCZT is in the work [7]. Multi-layer materials were prepared using EPD from suspensions containing 15 wt% ceramic powder, 12.75 wt% of monochloroacetic acid (Merck, Germany) and isopropyl alcohol (Lachner, Czech Republic). Description of suspension handling and details about EPD of single- and multi-layered materials used in this work are available in the literature [7,8].

* Corresponding author at: CEITEC BUT, Brno University of Technology, Purkynova 123, 612 00 Brno, Czech Republic.
E-mail address: daniel.drdlik@ceitec.vutbr.cz (D. Drdlik).

https://doi.org/10.1016/j.matlet.2023.135424
Received 14 June 2023; Received in revised form 22 August 2023; Accepted 15 October 2023
Available online 16 October 2023
0167-577X/© 2023 Elsevier B.V. All rights reserved.

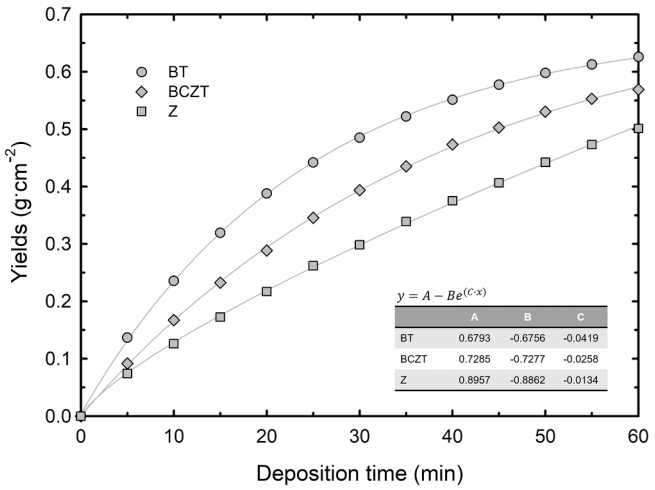

Fig. 1. Dependence of yields on deposition time.

The BT/Z and BCZT/Z laminates of several millimetres in thickness containing 31 alternating BT and Z or BCZT and Z layers were calcinated at 800 °C for 1 h and shaped into cylinders with a diameter of 12 mm. Such pellets were conventionally sintered (CS) at 1300 °C for BT/Z or 1500 °C for BCZT/Z for 2 h in the air or inserted into a graphite die with the same diameter followed by SPS at 1250 °C for BT/Z or 1350 °C for BCZT/Z for 5 min with a heating rate of 100 °C/min and applied pressure of 50 MPa.

The density of the laminates was measured according to Archimedes' principle. The microstructure was observed using scanning electron microscopy (Mira, Tescan, Czech Republic) equipped with EDS. The samples' Vickers hardness was determined using a machine ZHN (Zwick/Roel, Germany) at a maximum load of 50 mN. The QCSM method was used to estimate the elastic modulus. Indentation hardness was calculated from the loading curves data and the geometric function of the indenter. At least 150 indents were measured and analysed.

3. Results and discussion

The multi-layer ceramics were prepared using knowledge of the kinetics of each material. The kinetic curves can be seen in Fig. 1, where the dependence of yields on deposition time is plotted. To reduce the inclination of multi-layer ceramics to delaminate during sintering, the EPD process was optimized to reach similar green densities for all materials. As a result, the green densities were 44.7 ± 0.1 % t.d. for BT, 46.7 ± 0.1 % t.d. for BCZT, 47.4 ± 0.1 % t.d. for Z. The slowest deposition was recorded for Z material. The slow deposition rate generally results in favourable particle packing during deposition, i.e., particles have enough time to take advantageous positions in a deposit [9]. Therefore, increasing deposition rates of BT and BCZT resulted in slightly lower green densities. Adopting the kinetic data and green densities of the deposited ceramics allowed the estimation of a schedule covering precise time per layer in laminate according to the work [8], so it was possible to prepare the multi-layer systems with precise control of layer thickness.

Fig. 2 shows SEM images of prepared multi-layer ceramics prepared using EPD and densified by CS or SPS. The CS BT/Z laminate shown in Fig. 2a consisted of 31 periodically repeating layers with a thickness of 60 μm. The layer interfaces were strong and narrow after EPD; however, a significant reaction during sintering occurred. The reaction was more

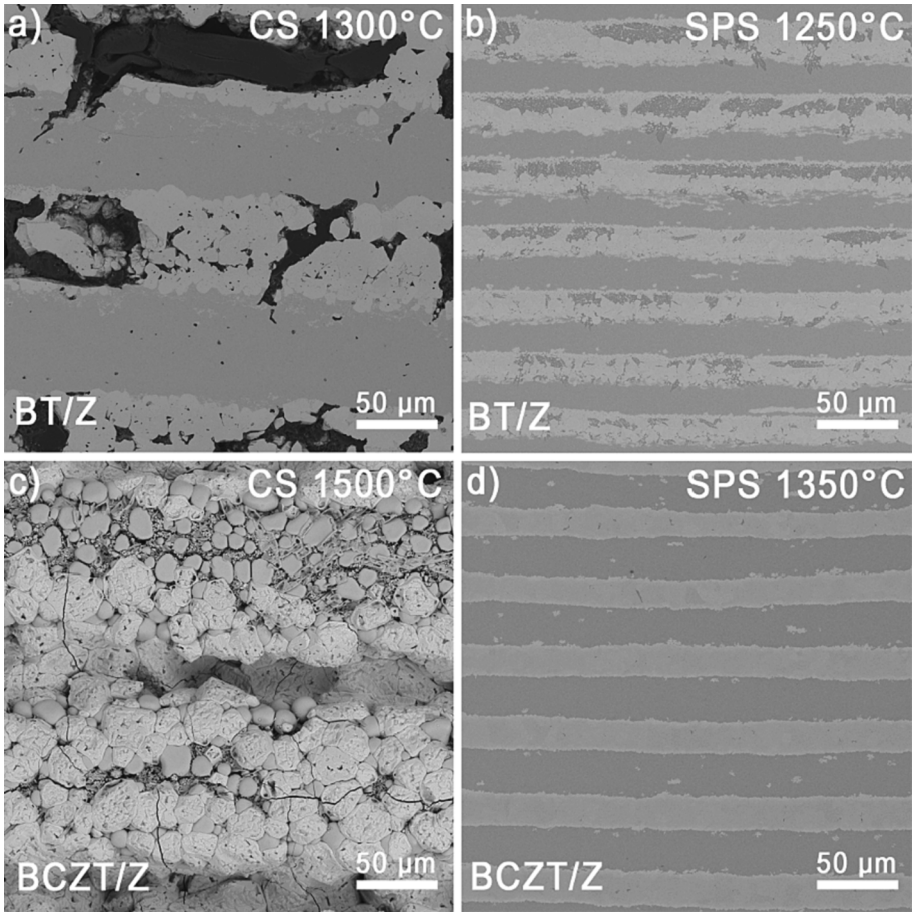

Fig. 2. SEM micrographs of a,b) BT/Z and c,d) BCZT/Z laminates after conventional sintering (CS) and spark plasma sintering (SPS).

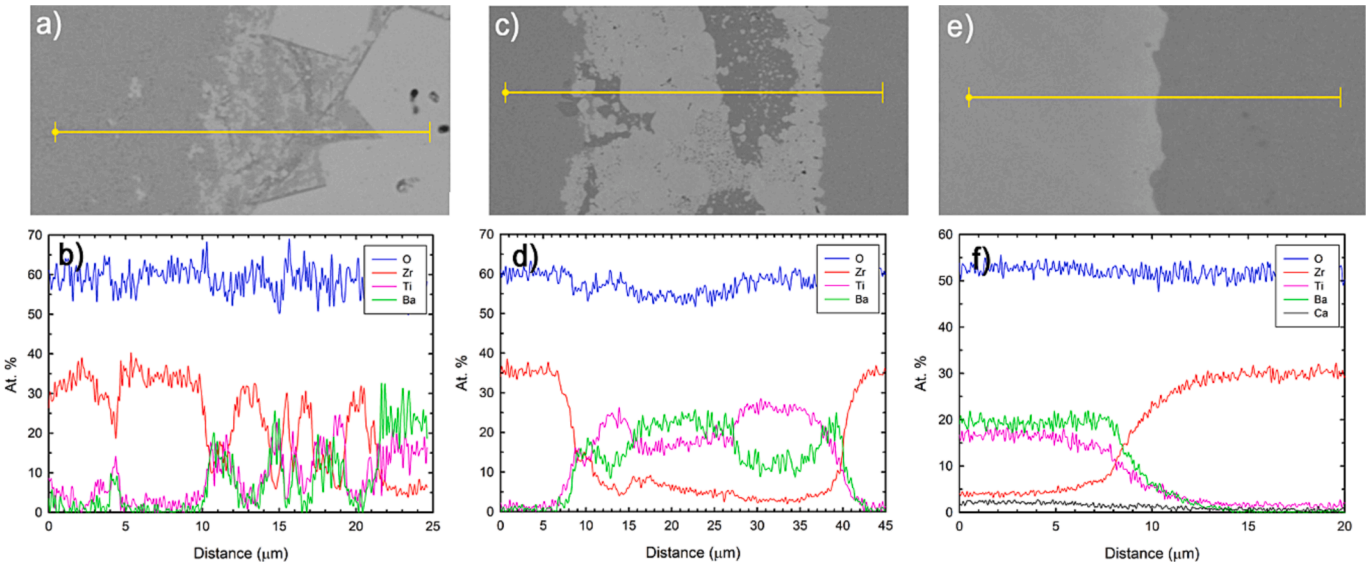

Fig. 3. EDS measurement at layer boundaries of a,b) BT/Z sintered in a furnace; c, d) BT/Z and e,f) BCZT/Z sintered using SPS.

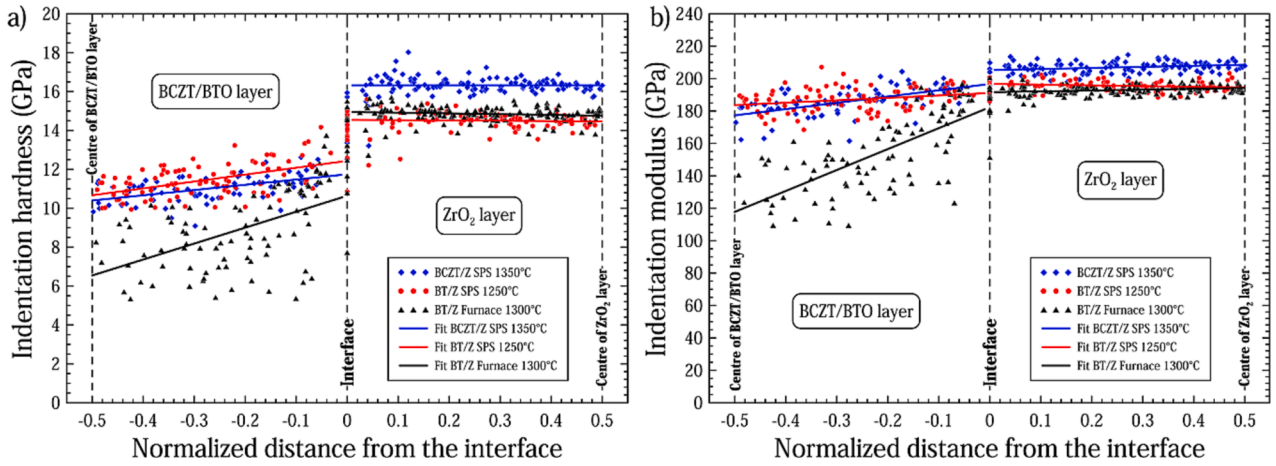

Fig. 4. Indentation a) hardness and b) modulus development on normalised distance from the interface for BT/Z sintered in a conventional furnace, BT/Z and BCZT/Z sintered using SPS.

evident in BT layers (bright ones) resulting in the formation of large pores. Moreover, BT layers contain perpendicular cracks and coarse BT grains due to high sintering temperature and dwell time [10]. The same laminate sintered using SPS had a crack-free microstructure with a narrow and strong layer interface after densification (see Fig. 2b). The applied pressure promoted densification resulting in 17 μm thick layers. However, isolated reaction zones were present. The significant propagation of cracks (parallel and perpendicular to layers) was observed in CS BCZT/Z laminate (see Fig. 2c). The tendency to crack was probably due to a significant chemical reaction, which also made it impossible to determine the thickness of the layers. On the other hand, BCZT/Z laminate sintered by SPS (see Fig. 2d) was crack-free with no observable reaction between BCTZ and Z layers with a thickness of ~22 μm. White areas in grey Z layers, visible in Fig. 2b,d, are processing artefacts originating from contaminated suspension by BT or BCZT materials.

Fig. 3 shows results from EDS measurement at layer boundaries of BT/Z laminate prepared by CS and BT/Z and BCZT/Z laminates sintered by SPS. The measurement proved a strong chemical reaction at the layer interface in CS BT/Z laminate resulting in the substitution of the B cation site in the ABO_3 perovskite structure of BT (see Fig. 3a,b) into probable phase structure of $BaTi_{0.75}Zr_{0.25}O_3$ [11]. It is known, that such stoichiometry imbalance in BT decreases its tetragonality and negatively affects electric properties [12]. The situation was more favourable in BT/Z laminate sintered by SPS. The chemical reaction between BT and Z was suppressed; however, some isolated areas enriched by Ti (most probably $Ba_6Ti_{17}O_{40}$ or $BaTi_2O_5$ [11]) were observed (see Fig. 3c,d). In contrast, no reaction was detected using EDS analysis in BCZT/Z laminate sintered by SPS, as seen in Fig. 3e,f. Suppressed reactivity in the laminates sintered by SPS can be attributed to faster thermal treatment, reduced atmosphere, applied pressure and the fact that BCZT already contains Z leading to slower diffusion processes due to concentration gradient.

The indentation data obtained across layers shown in Fig. 4 corresponds well with the changes in the chemical composition shown in Fig. 3. The indentation hardness, as well as modulus, exhibits sharp changes in BCZT/Z sintered by SPS at 1350 °C contrary to BT/Z CS where except reaction zone a significant porosity was formed (note the indents affected by pores are not shown). The SPS of BT/Z at 1250 °C led to the elimination of microporosity in the BT layer, which was mirrored in the reduced scatter of hardness data coming from the BT layer. The indentation modulus of the Z layer sintered by SPS changed from ~208 GPa to ~194 GPa for the drop of sintering temperature by 100 °C. The lower sintering temperature (1250 °C) led to modulus reduction corresponding to increased porosity of ~3 % by the Ishai Cohen model

[13]. In the case of the BT or BCZT layer, the porosity increased from the interface to the layer centre (see the fitted lines), which was most pronounced for CS BT. The SPS technique was beneficial from the mechanical properties point of view by reducing porosity and the extent of the reaction zone.

4. Conclusions

The multi-layer ceramics with precise layer thickness control were successfully prepared by EPD using knowledge about deposition kinetics and green densities of BT, BCZT and Z ceramics. However, the substantial development of cracks and chemical reactions was observed and measured in the microstructure of conventionally sintered BT/Z and BCZT/Z laminates. SPS significantly improved the durability of the laminates and suppressed undesirable chemical reactions between materials. From the mechanical point of view, a gradient still existed caused by increased porosity in the direction from the interface to the layer centre when SPS was applied but was significantly suppressed. The results indicate that combining EPD and SPS is a promising concept for preparing multi-layer ceramics for energy harvesting applications.

CRediT authorship contribution statement

Daniel Drdlik: Conceptualization, Methodology, Investigation, Writing – original draft. **Vojtech Marak:** Formal analysis, Writing – review & editing. **Hynek Hadraba:** Formal analysis, Validation, Writing – review & editing. **Zdenek Chlup:** Formal analysis, Investigation, Writing – original draft.

Declaration of Competing Interest

The authors declare that they have no known competing financial interests or personal relationships that could have appeared to influence the work reported in this paper.

Data availability

Data will be made available on request.

Acknowledgements

Financial support of the Czech Science Foundation under project no. 21–24805S is gratefully acknowledged. We acknowledge CzechNanoLab Research Infrastructure supported by MEYS CR (LM2023051).

References

[1] T. Paul, S. Maiti, U. Mukherjee, S. Mondal, A. Sahoo, K.K. Chattopadhyay, Mater. Lett. 301 (2021), 130264, https://doi.org/10.1016/j.matlet.2021.130264.
[2] K. Li, S. Cong, H. Zheng, T. Wang, Z. Zhao, X. Qi, W. Gong, Mater. Lett. 317 (2022), 132127, https://doi.org/10.1016/j.matlet.2022.132127.
[3] H.-C. Song, H.-C. Kim, C.-Y. Kang, H.-J. Kim, S.-J. Yoon, D.-Y. Jeong, J. Electroceramics 23 (2) (2009) 301–304, https://doi.org/10.1007/s10832-008-9439-9.
[4] G.M. Gladysz, K.K. Chawla, Compos. A Appl. Sci. Manuf. 32 (2) (2001) 173–178, https://doi.org/10.1016/S1359-835X(00)00144-5.
[5] C. Zhao, Y. Huang, J. Wu, InfoMat 2 (6) (2020) 1163–1190, https://doi.org/10.1002/inf2.12147.
[6] P.Z. Cai, D.J. Green, G.L. Messing, J. Am. Ceram. Soc. 80 (8) (1997) 1929–1939, https://doi.org/10.1111/j.1151-2916.1997.tb03075.x.
[7] D. Drdlik, D. Zeman, P. Tofel, Z. Chlup, H. Hadraba, K. Drdlikova, Ceram. Int. 47 (2) (2021) 2034–2042, https://doi.org/10.1016/j.ceramint.2020.09.035.
[8] H. Hadraba, D. Drdlik, Z. Chlup, K. Maca, I. Dlouhy, J. Cihlar, J. Eur. Ceram. Soc. 33 (12) (2013) 2305–2312, https://doi.org/10.1016/j.jeurceramsoc.2013.01.026.
[9] R.N. Basu, C.A. Randall, M.J. Mayo, J. Am. Ceram. Soc. 84 (1) (2001) 33–40, https://doi.org/10.1111/j.1151-2916.2001.tb00604.x.
[10] M. Bäurer, M. Syha, D. Weygand, Acta Mater. 61 (15) (2013) 5664–5673, https://doi.org/10.1016/j.actamat.2013.06.007.
[11] H.Y. Lu, J.S. Bow, W.H. Deng, J. Am. Ceram. Soc. 73 (12) (1990) 3562–3568, https://doi.org/10.1111/j.1151-2916.1990.tb04258.x.
[12] T.R. Armstrong, L.E. Morgens, A.K. Maurice, R.C. Buchanan, J. Am. Ceram. Soc. 72 (4) (1989) 605–611, https://doi.org/10.1111/j.1151-2916.1989.tb06182.x.
[13] O. Ishai, L.J. Cohen, Int. J. Mech. Sci. 9 (8) (1967) 539–546, https://doi.org/10.1016/0020-7403(67)90053-7.

PUBLIKACE XVI

Key Engineering Materials
ISSN: 1662-9795, Vol. 784, pp 67-72
doi:10.4028/www.scientific.net/KEM.784.67
© 2018 Trans Tech Publications, Switzerland
Submitted: 2017-12-08
Revised: 2018-05-13
Accepted: 2018-05-30
Online: 2018-10-29

Study of Alumina and Alumina-Silicon Carbide Layered Composite Sintered by SPS

Daniel Drdlík[1,2,a*], Vojtěch Mařák[1,b], Jakub Roleček[1,c], Katarína Drdlíková[1,3,d], Jiří Kratochvíl[4,e] and David Salamon[1,2,f]

[1]CEITEC BUT, Brno University of Technology, Purkynova 123, 612 00 Brno, Czech Republic

[2]Institute of Materials Science and Engineering, Brno University of Technology, Technicka 2, 616 69 Brno, Czech Republic

[3]Military Research Institute, Department of Technology, Veslarska 230, 637 00 Brno, Czech Republic

[4]BOGGES, Rudice 1, 679 06 Rudice, Czech Republic

[a]daniel.drdlik@ceitec.vutbr.cz, [b]vojta.marak@gmail.com, [c]jakub.rolecek@ceitec.vutbr.cz, [d]drdlikova@vvubrno.cz, [e]jiri.kratochvil@bogges.cz, [f]david.salamon@ceitec.vutbr.cz

Keywords: slip casting, spark plasma sintering, composite, mechanical properties.

Abstract. A laminate composed from alumina and mixture of alumina and 5 vol.% of SiC as well as standards with composition of each layer were prepared using a slip-casting method for green body preparation with following spark plasma sintering. The laminate had a sharp interface between layers and no delamination was observed. Prepared materials were characterized in terms of their microstructure, hardness and fractographic analysis. Because of supposed ballistic potential all prepared ceramics were also subjected to depth of penetration testing.

Introduction

In the last decade, the layered ceramics have received much attention in the material research. The engineering laminates consisting of ceramic layers are used rather in very special applications. Proper tailoring of the layer composition allows enhancing of the final electrical, optical or mechanical properties of laminate [1-3]. Moreover, the other beneficial effect of layered structure is existence of internal stresses between layers affecting mainly the fracture behavior.

Further improvement of material properties can be obtained when the layers of the laminate are formed as a nanocomposite structure. One of the most studied nanocomposite system based on alumina matrix contains added particles or whiskers of different oxide (ZrO_2, YAG etc.) or non-oxide (SiC, Si_3N_4, B_4C etc.) [4]. In the case of alumina matrix with added fine SiC particles to the matrix usually occurs significant increase in strength, hardness, fracture toughness and creep resistance [5]. However, the alumina densification is suppressed by the extensive addition of carbide or nitride and may results in the formation of porous microstructure [6].

In present work, the ceramic three-layer laminate composed of pure alumina layer and layers of alumina with 5 vol.% SiC and standards with the same composition as layers were prepared. Motivation of alumina doping by nano SiC was to increase the hardness of such layer in the laminate. An unusual combination of slip-casting method with following spark plasma sintering (SPS) was applied. Prepared materials were subjected to microstructure analysis, measurement of Vickers hardness and fractographic analysis. The suitability of the prepared materials for ballistic applications was verified by depth of penetration (DOP) test.

Experimental

The suspensions used for slip casting contained alumina powder (A, d = 450 nm, Sumitomo Chemical, Japan) or alumina powder with 5 vol.% of silicon carbide powder (A5SiC, d = 50 nm, Goodfellow Cambridge, UK), 2.5 % solution of water and polyvinyl alcohol (PVA, Mowiol 10-98,

All rights reserved. No part of contents of this paper may be reproduced or transmitted in any form or by any means without the written permission of Trans Tech Publications, www.scientific.net. (#111029713-21/11/18,09:19:15)

Sigma-Aldrich, USA), sucrose (Cukrovar Vrbatky, Czech Republic), Darvan C-N (Vanderbilt Chemicals, Netherlands) and Octanol (1 drop per 25 mL of suspension). The exact composition of both type suspensions is shown in Table 1.

Table 1 Composition of suspensions

Compounds	Suspensions	
	A [vol. %]	A5SiC [vol. %]
solution of water and PVA	49	49
Darvan C-N	4	4
sucrose	4	4
alumina powder	43	41
silicon carbide powder	-	2*

* volume fraction of SiC is calculated relative to the suspension volume

All components of the suspensions were stirred together with zirconia balls in ratio of 1:3 for 24 hours. A gypsum-cement plate served as a porous mold during slip casting. The shape of green bodies was created using cylindrical silicon form with diameter of 49.5 mm and height of 20 mm. Laminate was prepared using a gradual casting with 40 minutes period between casting of individual layers. The ceramic bodies were left on the mold for 4 days. Dried green bodies were annealed at 600 °C (1 °C/min) for 1 hour in air and then sintered by spark plasma sintering (Fuji Electronic Industrial, Japan) at 1450 °C (50 °C/min) for 2 minutes with applied pressure of 40 MPa and using graphitic die with diameter of 50.5 mm.

The sample densities were measured using Archimedes' principle (EN 623-2). The phase composition was determined using an X-ray diffractometer (XRD, SmartLab Rigaku, Japan). The hardness of samples was measured using an instrumented hardness tester Z2.5 (Zwick/Roel, Germany) at 50 N load. The number of measurements for standards and each layer in laminate was set to 10. The microstructure was observed using a scanning electron microscope Lyra 3 (Tescan, Czech Republic). The depth of penetration experiments were conducted with projectile 7.62 mm x 54R B32 API at velocity of 854 ± 20 m/s. The used backings were aluminum cylinders. The impact craters were analyzed using XRD on at least five samples of each type of ceramic material.

Results and Discussion

In general, the slip-casting method allows preparation of relatively huge crack free green bodies. We fabricated three types of green bodies; A and A5SiC served as a standards and laminate with three layers (A5SiC/A/A5SiC) were prepared. Typical green bodies prepared by slip casting method are shown in Fig. 1.

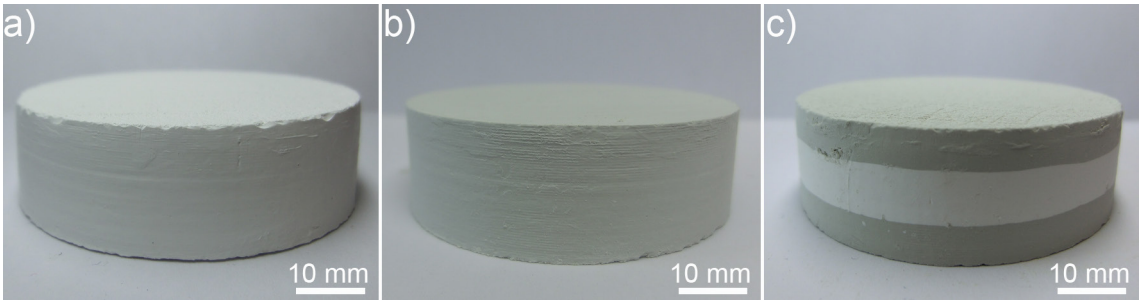

Fig. 1 Green bodies of a) alumina, b) A5SiC composite and c) three-layer A5SiC/A/A5SiC laminate after slip-casting.

The laminate had a sharp interface between layers and no delamination was observed. Casted green bodies have already been used in few papers [7, 8] instead of ceramic powders for sintering via SPS. Such approach has two positive effects: i) reduction of the graphite die wear and ii) controlled preparation of layered materials.

The X-ray diffraction patterns of A and A5SiC layers in the sintered laminate are plotted in Fig. 2. From the diffraction pattern of A layer is evident that the microstructure is formed by pure alumina phase. In the case of A5SiC layer only the several peaks belonging to SiC phase were found beside the alumina peaks. This is an important observation confirming that the SiC phase reacted noticeably neither with the liquid during slip casting nor with oxygen in alumina. Based from the literature [9] the presence of more than one secondary phase could be expected but no more phases were detected.

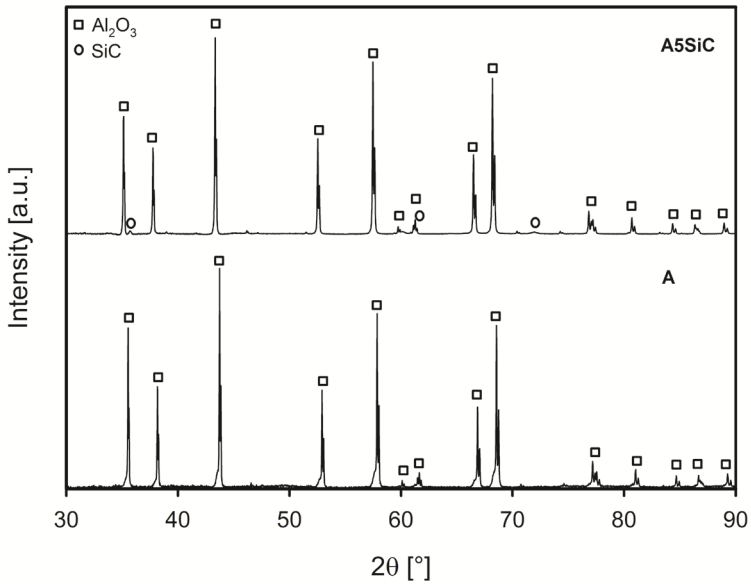

Fig. 2 X-ray diffraction patterns of A and A5SiC layers in sintered laminate.

The relative density of prepared A standard was 99.4 % contrary to A5SiC standard with relative density of 98.2 %. The higher degree of porosity in A5SiC may have two reasons. The first one is the worse dispergation of the SiC particles in alumina matrix during suspension preparation. Such agglomerates then preserved in the microstructure after SPS. The second reason is the suppressed densification of alumina by SiC particles [6]. The relative density of three-layer laminate was 98.9 %.

The hardness of A (red triangles), A5SiC (black rings) and A5SiC/A/A5SiC laminate (green squares) is shown in Fig. 3. The Vickers hardness of A and A5SiC standards was 19.6 ± 0.3 and 19.3 ± 0.4 GPa, respectively. The similar result was reported before [10, 11] and it indicates that the addition of SiC did not improve the mechanical properties. Nevertheless, in the works of Jaafar et al. [4] and Shi et al. [5] the measured hardness was substantially higher (more than 20 GPa). The hardness of the layers in the three-layer laminate was almost similar. The hardness of the first A5SiC layer was 19.9 ± 0.3 GPa, hardness of the second and third layers were 19.8 ± 0.7 GPa and 20.7 ± 0.5 GPa, respectively. The higher hardness of the last layer can be attributed to inhomogeneous densification by pressing during SPS. The similar hardness of A and A5SiC (see Fig. 3) can be attributed to the higher porosity in the ceramics containing SiC. This porosity is clearly visible in the image of an indent near the layer interface in Fig. 3 and is very likely caused by insufficient SiC dispersion. The observed pores are flattened what suggests that a sinter-forging takes place. Furthermore, the interesting result is that the high hardness of SiC grains can compensate porosity in A5SiC layers.

From the image in Fig. 3 can also be seen that the propagating indentation crack pointing to the layer interface did not or only slightly changed its direction on the interface. This behavior suggests minimal internal tension or pressure stresses between layers. Presumably, the internal stresses would take on greater importance when the amount of SiC would be higher.

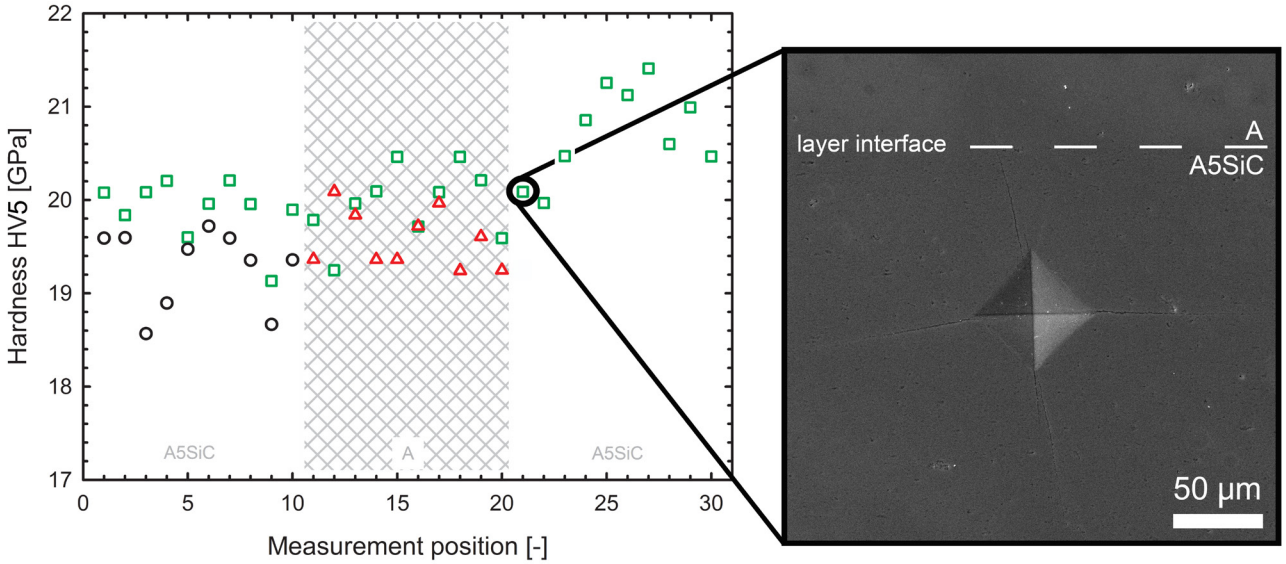

Fig. 3 Vickers hardness of A (red triangles), A5SiC (black rings) and A5SiC/A/A5SiC laminate (green squares) with detailed micrographs of indent near the layer interface.

The side view of propagating indentation cracks in A and A5SiC layers are shown in Fig. 4a, b. The path of the crack in A5SiC layer is straighter than in A layer. This corresponds with the micrographs of the open crack surfaces (see Fig. 4c, d) where predominantly intergranular and transgranular fractures are documented. The transgranular fracture was probably caused by a higher compressive stress on the grain boundary of SiC generated due to the mismatch of thermal coefficients (CTE) between alumina (CTE = $8.8 \cdot 10^{-6}$ °C^{-1}) matrix and SiC (CTE = $4.4 \cdot 10^{-6}$ °C^{-1}) [5].

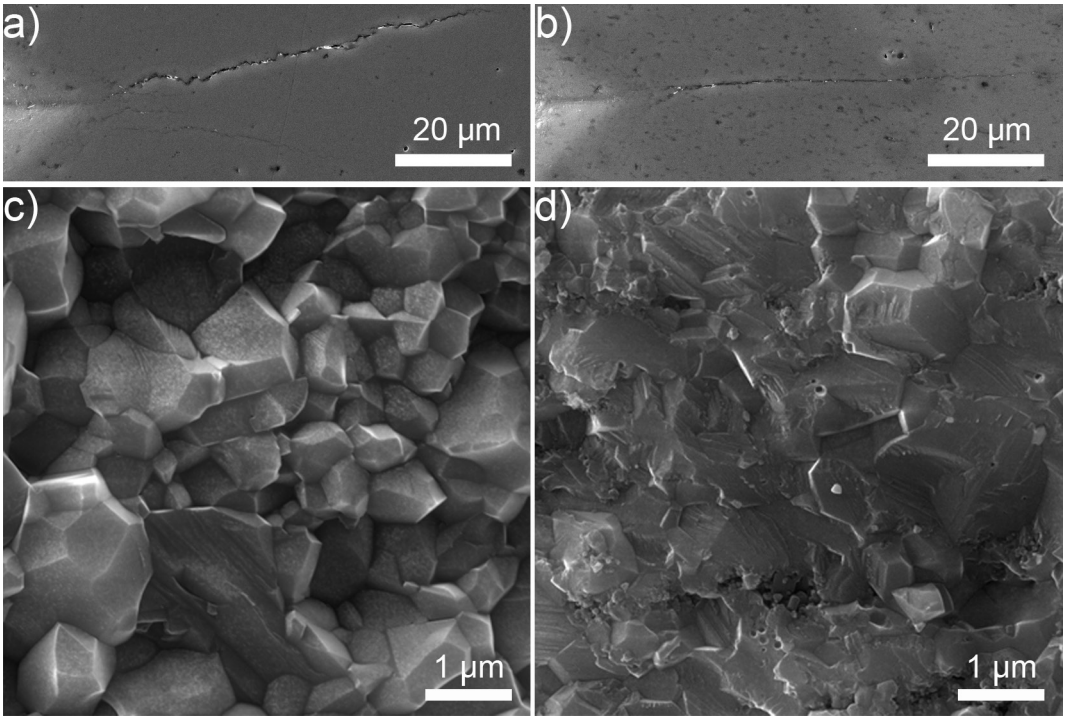

Fig. 4 Micrographs of propagating indentation cracks and open surfaces in (a, c) A and (b, d) A5SiC layers.

The DOP tests of prepared ceramics are summarized in Fig. 5. The DOP value increased with content of SiC in the microstructure due to its higher porosity. On the other hand, the differences are only seemingly high. Obtained results were compared to data from work Savio et al. [12] where alumina and zirconia-toughened alumina (ZTA) ceramics at lower thickness were investigated. Normalized data from the mentioned paper supplemented by current results clearly show linear

dependence of DOP on thickness of alumina ceramics. Our DOP values for pure alumina perfectly fit into this dependence. Moreover, such comparison showed that 7.62API projectile (at velocity of 854 m/s) can be completely stopped in the alumina armor when the ceramics is ≥7.4 mm thick. Slightly higher DOP values for prepared composite and laminates confirmed that the added amount of SiC with higher hardness was not completely able to compensate the negative influence of increased porosity. However, the optimization of added SiC amount and the sintering regime, which will be the subject of future work, could very likely lead to increased ballistic efficiency of the laminate.

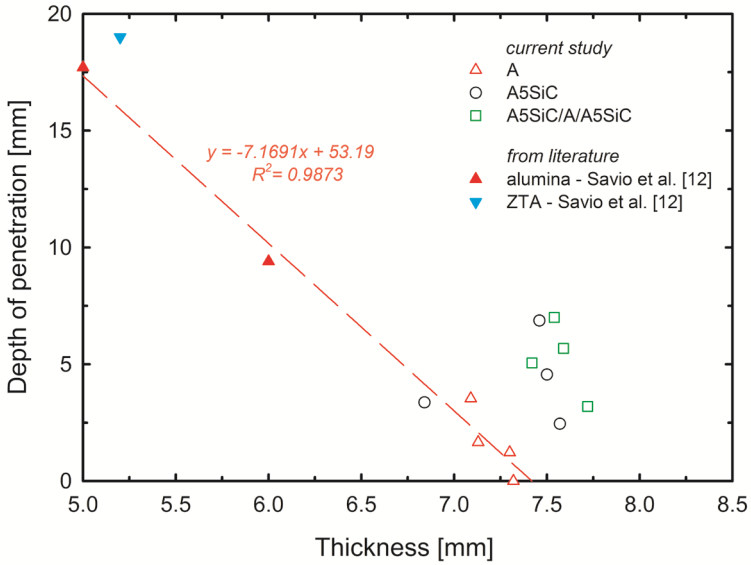

Fig. 5 Dependence of depth of penetration on thickness of ballistic tested samples.

Conclusions

The green bodies of three-layer laminate containing alumina and mixture of alumina with 5 vol.% of SiC as well as standards were prepared using slip-casting with following spark plasma sintering. All the prepared ceramics were crack free and the laminates did not exhibit any delamination. The XRD analysis proved presence of only alumina and SiC phases in the microstructure. The Vickers hardness of the samples varied from 18.1 to 20.7 GPa. The lower hardness of layers containing SiC was caused by higher porosity. However, this negative porosity effect can be compensated to certain extent due to the higher hardness of SiC grains. The minimal influence of internal stresses on the crack propagating on layer interface was found. The layers with added SiC in laminates had predominantly transgranular fracture behavior contrary to intergranular fracture in alumina layers. The DOP test of prepared ceramics showed that the porosity is (beside the hardness) another key parameter for successful ballistic protection. Present work clearly showed that the positive effect of SiC will require full densification, which was in our case limited especially by insufficient SiC dispersion. Therefore, the future work will be concerned on adjusting the processing parameters (mainly dispersing procedure) in order to obtain completely pore free structure.

Acknowledgement

The authors wish to express their gratitude and sincere appreciation to the authority of The Technology Agency of the Czech Republic, project TE02000162 for financial support. This research was also carried out under the project CEITEC 2020 (LQ1601) with financial support from the Ministry of Education, Youth and Sports of the Czech Republic under the National Sustainability Programme II. Part of the work was carried out with the support of CEITEC Nano Research Infrastructure (ID LM2015041, MEYS CR, 2016–2019), CEITEC Brno University of Technology. The MSE study of V. Marak was supported by the project FSI-S-17-4308.

References

[1] B. Dubus, G. Haw, C. Granger, O. Ledez, Characterization of multilayered piezoelectric ceramics for high power transducers, Ultrasonics 40 (1-8) (2002) 903-906.

[2] L. Gan, Y.J. Park, H. Kim, J.M. Kim, J.W. Ko, J.W. Lee, Fabrication and microstructure of hot pressed laminated Y_2O_3/Nd:Y_2O_3/Y_2O_3 transparent ceramics, J. Eur. Ceram. Soc. 36 (3) (2016) 911-916.

[3] J.X. Deng, D.L. Yun, H.M. Zhou, Y.Q. Tan, Layered structures in ceramic nozzles for improved erosion wear resistance in industrial coal-water-slurry boilers, Ceram. Int. 36 (1) (2010) 299-306.

[4] M. Jaafar, H. Reveron, C. Esnouf, G. Fantozzi, Highly creep-resistant alumina-SiC nanocomposites processed by spark plasma sintering, Scripta Mater. 68 (2) (2013) 134-137.

[5] X.L. Shi, F.M. Xu, Z.J. Zhang, Y.L. Dong, Y. Tan, L. Wang, J.M. Yang, Mechanical properties of hot-pressed Al_2O_3/SiC composites, Mat. Sci. Eng. a-Struct. 527 (18-19) (2010) 4646-4649.

[6] B.-K. Jang, M. Enoki, T. Kishi, H.-K. Oh, Effect of second phase on mechanical properties and toughening of Al_2O_3 based ceramic composites, Compos. Eng. 5 (10) (1995) 1275-1286.

[7] R. Boulesteix, R. Epherre, S. Noyau, M. Vandenhende, A. Maître, C. Sallé, G. Alombert-Goget, Y. Guyot, A. Brenier, Highly transparent Nd:Lu_2O_3 ceramics obtained by coupling slip-casting and spark plasma sintering, Scripta Mater. 75 (Supplement C) (2014) 54-57.

[8] A. Borrell, M.D. Salvador, V.G. Rocha, A. Fernández, T. Molina, R. Moreno, Enhanced properties of alumina–aluminium titanate composites obtained by spark plasma reaction-sintering of slip cast green bodies, Compos. Part B-Eng. 47 (Supplement C) (2013) 255-259.

[9] C.E. Borsa, H.S. Ferreira, R.H.G.A. Kiminami, Liquid phase sintering of Al_2O_3/SiC nanocomposites, J. Eur. Ceram. Soc. 19 (5) (1999) 615-621.

[10] S. Gustafsson, L.K.L. Falk, E. Liden, E. Carlstrom, Pressureless sintered Al_2O_3-SiC nanocomposites, Ceram. Int. 34 (7) (2008) 1609-1615.

[11] L. Carroll, M. Sternitzke, B. Derby, Silicon carbide particle size effects in alumina-based nanocomposites, Acta Mater. 44 (11) (1996) 4543-4552.

[12] S.G. Savio, V. Madhu, A.K. Gogia, Ballistic performance of alumina and zirconia-toughened alumina against 7.62 armour piercing projectile, Defence Sci. J. 64 (5) (2014) 477-483.